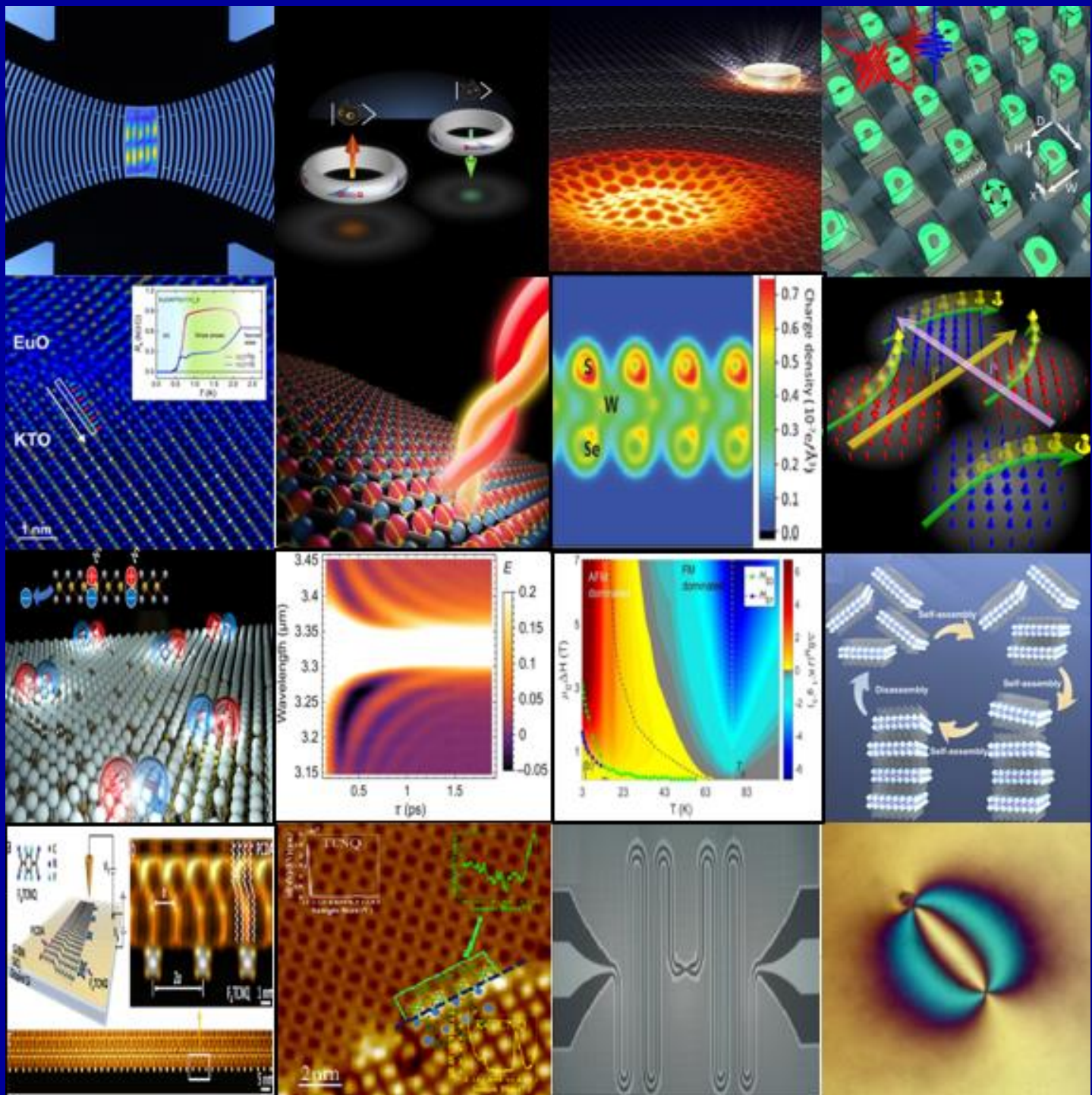


DOE-BES Principal Investigators' Meeting
Physical Behavior of Materials
March 10-12, 2021, Virtual Meeting
Program and Abstracts



U.S. Department of Energy
Office of Science – Basic Energy Sciences
Division of Materials Sciences and Engineering



1	2	3	4
5	6	7	8
9	10	11	12
13	14	15	16

COVER IMAGES

- 1- Spin–phonon interactions in silicon carbide addressed by Gaussian acoustics. D.D. Awschalom
- 2- Observation of half-quantum flux in an unconventional superconductor. C-L. Chien
- 3- Mid-Infrared Radiative Emission from Bright Hot Plasmons in Graphene. H.A. Atwater
- 4- Frequency Conversion in a Time-variant Dielectric Metasurface. I. Brener
- 5- Two-dimensional superconductivity and anisotropic transport at KTaO₃ (111) interfaces. A. Bhattacharya
- 6- Colossal mid-infrared bulk photovoltaic effect in a type-I Weyl semimetal. K.S. Burch
- 7- Anomalous Behavior of 2D Janus Excitonic Layers under Extreme Pressures. S. Tongay
- 8- Critical spin fluctuation mechanism for the spin Hall Effect. T. Egami
- 9- Electrical suppression of all nonradiative recombination pathways in monolayer semiconductors. A. Javey
- 10- Time-variant metasurfaces enable tunable spectral bands of negative extinction. H. Harutyunyan
- 11- Evolution of Competitive Magnetic Phases in Multiferroic and Skyrmion lattice Systems. H. Srikanth
- 12- Self-Assembly of 2D Perovskite Nanosheet Building Blocks into Ordered Ruddlesden–Popper Perovskite Phase. P. Yang
- 13- Frustrated Supercritical Collapse in Tunable Charge Arrays on Graphene. M.F. Crommie
- 14- Mixed Valence Effects on Insulator-to-Metal Transition in Organic Salt. P. Zhang
- 15- Fabrication of Quantum Meta-Atoms and Quantum Transmission Line. S. Anlage
- 16- Elastic colloidal monopoles and reconfigurable self-assembly in liquid crystals. I.I. Smalyukh

This document was produced under contract number DE-SC0014664 between the U.S. Department of Energy and Oak Ridge Associated Universities.

The research grants and contracts described in this document are supported by the U.S. DOE Office of Science, Office of Basic Energy Sciences, Materials Sciences and Engineering Division.

FOREWORD

This booklet is a summary of projects presented at the seventh Physical Behavior of Materials Principal Investigators' meeting. This meeting is sponsored by the Division of Materials Sciences and Engineering (MSE) of the Department of Energy, Office of Basic Energy Sciences (BES), and is held on March 10–12, 2021.

The purpose of the Principal Investigators' meeting is to bring together all the principal investigators and their co-PIs who are supported by the Physical Behavior of Materials program to facilitate the exchange of ideas, promote collaborations and share the latest exciting scientific knowledge and discoveries. For BES and the participating investigators, the meeting serves the purpose of providing an overview and assessment of the whole program, which helps BES to identify new research areas and future directions for the program. This meeting brings together leading experts in topical areas of research supported by our program and is designed to stimulate and inspire new ideas.

The Physical Behavior of Materials program supports transformative and innovative research activities at the crossroads of materials science and condensed-matter physics. The primary mission of the program is to support both fundamental and use-inspired basic scientific research that promises to advance our knowledge of materials' behavior. The primary scientific interests of the program include electronic, electromagnetic, magnetic, and thermal properties of materials, including novel light-matter interactions and quantum-information sciences that are relevant to the BES mission. The program has a rich portfolio in many groundbreaking, exciting, and high-risk high-reward projects in both experimental and theoretical areas.

The 2021 Principal Investigators' meeting is being held virtually. The meeting format has been modified to include shortened oral presentations, short "poster talks", and special sessions to introduce "new projects" recently added to the Physical Behavior of Materials program. This meeting brings together over 85 scientists and is organized to include 25 regular presentations, 40 virtual poster talks, and 17 new project introductions. The presentations are grouped in topics of similar research interests.

We appreciate the contributions of all the attendees and thank all Physical Behavior of Materials investigators for sharing their exciting ideas and latest findings. We are also grateful to the outstanding support of Linda Severs of Oak Ridge Institute for Science and Education and Teresa Crockett of MSE.

Refik Kortan, Ph.D.
Athena S. Sefat, Ph.D.
Program Managers,
Physical Behavior of Materials Program
Division of Materials Sciences and Engineering
Office of Basic Energy Sciences
Department of Energy
March 2021

Table of Contents

Agenda	xi
 Session I	
Quantum Metamaterials	
<i>David Awschalom, Joseph Heremans, Stephan Hruszkeywycz, and Gary Wolfowicz</i>	3
Light-Matter Quantum Control: Coherence and Dynamics	
<i>Jigang Wang, Zhe Fei, Kai-Ming Ho, Liang Luo, Joseph Shinar, Cai-Zhuang Wang, and Yongxin Yao</i>	8
A Nonlinear Approach to Topological Semimetals	
<i>Kenneth S. Burch</i>	15
 Session II	
Coherent Control of Strongly Interacting Spins in the Solid-State	
<i>Jeff Thompson</i>	21
Emergent Properties of Magnons Coupled to Microwave Photons	
<i>M. Benjamin Jungfleisch</i>	24
Observation of the Modification of Quantum Statistics in Plasmonic Systems	
<i>Omar S. Magana-Loaiza</i>	28
DNA-Controlled Dye Aggregation – A Path to Create Quantum Entanglement	
<i>William B. Knowlton</i>	32
Electron Transfer in Heterostructures Based on Two-Dimensional Materials	
<i>Hui Zhao</i>	36
Optically Controlled Quantum Phase Transitions at Van der Waals Interfaces	
<i>Cheng Cen, Lian Li, and Xin Li</i>	41
 Session III	
Phase-Sensitive Measurements of Triplet Superconductors	
<i>Chia-Ling Chien</i>	47
Spin-Dependent Quantum Phenomena in 2D Heterostructures	
<i>Jing Shi</i>	50

Spin Functionality at Interfaces through Complex Oxide Heteroepitaxy	
<i>Yuri Suzuki</i>	53
Tunable Excitons and Pseudospins in Transition Metal Dichalcogenide Homobilayers	
<i>Xiaoqin Elaine Li</i>	57
Session IV	
Physical Behavior of Quantum Metamaterials	
<i>Steven M. Anlage</i>	65
Non-Equilibrium Quantum Dynamics of Multi-Qubit Superconducting Circuits	
<i>Hakan E. Türeci</i>	70
Quantum Nanoplasmonics Theory	
<i>Vadym Apalkov</i>	73
Optical, Electrical and Magnetic Studies of Hybrid Organic-Inorganic Perovskite Semiconductors	
<i>Z. Valy Vardeny</i>	77
Coherent Control of Spin States in Organic Electronics – Discovery and Investigation of Complex Room-Temperature Magnetic Quantum Excitations	
<i>Christoph Boehme and John M. Lupton</i>	82
Spin Transport in Group IV Materials and 2D Membranes	
<i>Hanan Dery, Dinh Van Tuan, and Min Yang</i>	87
Tunnel Magnetoresistance Detection of Skyrmions	
<i>Sara A. Majetich</i>	92
Complex Magnetism and Emergent Phenomena in Correlated Electron Oxide Materials	
<i>Hari Srikanth and Manh-Huong Phan</i>	96
Topological Phases in Aperiodic Systems and Flat-Band Material	
<i>Feng Liu</i>	103
Quantifying Exciton Heterogeneities in Metal Halide Perovskites	
<i>Luisa Whittaker-Brooks</i>	109
Unique Optical Excitations in Topological Insulators	
<i>Stephanie Law</i>	114
Electron Spin Polarization in Large Electric Fields	
<i>Vanessa Sih</i>	119

Control of Energy Transfer and Molecular Transport via Strong Coupling <i>Stephen R. Forrest and Vinod Menon.....</i>	122
---	-----

Session V

Digital Synthesis: A Pathway to Create and Control Novel States of Condensed Matter <i>Anand Bhattacharya, Dillon D. Fong, and Sam Jiang.....</i>	131
Electronic Materials Program <i>Joel W. Ager, Daryl C. Chrzan, Oscar D. Dubon, Wladek Walukiewicz, Junqiao Wu, and Ali Javey</i>	137
Uncovering and Surmounting Loss Mechanisms in Light Emitters <i>Chris G. Van de Walle</i>	143
Lateral Heterostructures of Organic Charge Transfer Complexes and Inorganic Two-Dimensional Materials <i>Pengpeng Zhang</i>	149
Plasmon and Photon Excitations in Layered Heterostructures <i>Harry A. Atwater</i>	154

Session VI

Physical Mechanisms and Electric-Bias Control of Phase Transitions in Quasi-2D Charge-Density-Wave Quantum Materials <i>Alexander A. Balandin</i>	161
Singlet and Triplet Exciton Interaction and Dynamics in Molecular Crystals <i>Ivan Biaggio.....</i>	166
Discovery of Goniopolar Metals with Zero-Field Hall and Nernst Effects <i>Joseph P. Heremans</i>	170
Elucidating Chirality-Induced Magnetism and Magnetoelectric Functionalities in Layered Chiral Hybrid Metal Halide Perovskites <i>Dali Sun</i>	175
The Synthesis 2D Janus vdW Crystals and Novel Quantum Phenomena Arising from Mirror-Symmetry Breaking <i>Sefaattin Tongay</i>	179

Session VII

Physical Chemistry of Inorganic Nanostructures	
<i>A. Paul Alivisatos, Peidong Yang, Stephen R. Leone, Eran Rabani, and David T. Limmer</i>	187
Characterization of Functional Nanomachines	
<i>Michael F. Crommie, A. P. Alivisatos, C. Bustamante, M. L. Cohen, F. R. Fischer, S. G. Louie, and A. Zettl.....</i>	196
Superatomic Clusters and Cluster-Based Materials – Structure, Stability, and Applications	
<i>Purusottam Jena</i>	202
Stimuli-Responsive Mesostructured Hybrid Materials	
<i>Ivan I. Smalyukh</i>	208

Session VIII

Light-Matter Interactions in Nanoscale Systems for Energy Applications	
<i>Shanhui Fan and Mark Brongersma</i>	217
Metamaterials	
<i>Costas M. Soukoulis, Thomas Koschny, and Jigang Wang</i>	222
Light-Matter Interaction Phenomena using Subwavelength Engineering of Material Properties	
<i>Igal Brener, Michael B. Sinclair, Willie Luk, John Klem, Jayson Briscoe, and Raktim Sarma.....</i>	228
Opening New Frontiers of Near-Zero-Index (NZI) Optics: from Photonic Time Crystals to Non-Reciprocity and Novel Localization Regimes	
<i>Alexandra Boltasseva</i>	234
Metamaterials as a Platform for the Development of Novel Materials for Energy Applications	
<i>Willie J. Padilla</i>	240
Semiconductor Excitonic Nanoshells for Energy Conversion Applications	
<i>Mikhail Zamkov</i>	245
Wavelength Conversion through Plasmon-Coupled Surface States	
<i>Mona Jarrahi</i>	250
Defects in Gallium Oxide	
<i>Matthew D. McCluskey and Leah Bergman</i>	255

Establishing Microscopic Photophysics of Local Cation and Anion Phase Segregation in Hybrid Perovskite Solar Cells <i>Masaru Kuno and Prashant Kamat</i>	260
Nanocrystal-Based Dyads for Solar to Electric Energy Conversion <i>David H. Waldeck, David N. Beratan, and Ron Naaman</i>	263
Exploring the Impact of the Local Environment on Charge Transfer States at Molecular Donor-Acceptor Heterojunctions <i>Barry P. Rand, Antoine Kahn, and Noel C. Giebink</i>	268
Tuning Organic Semiconductor Packing and Morphology through Nonequilibrium Solution Processing <i>Zhenan Bao</i>	274
Exploring the Design Principles of Low-Dimensional Organometal Halide Perovskites Assisted by Machine Learning <i>Yiying Wu</i>	278
Interfaces in Electronic and Structural Materials <i>Yuri Mishin</i>	284

Session IX

Excitons in Low-Dimensional Perovskites <i>William A. Tisdale</i>	291
Control of Light-Matter Interactions in Hybrid Structured Environments with Novel Nanomaterials of Different Dimensionalities <i>Anton V. Malko, Yuri N. Gartstein, and J. A. Robinson</i>	296
Describing Light-Matter Interaction at the Nanoscale through Coupled Simulation of Quantum Electronic Transport and Electrodynamics <i>Irena Knezevic</i>	301
Hot Carrier Dynamics in Low Dimensional Systems <i>Ian R. Sellers</i>	306

Session X

Disorder in Topological Semimetals <i>Kirstin Alberi, Brian Fluegel, Anthony Rice, Stephan Lany, Mark van Schilfgaarde, Matt Beard, and Daniel Dessau</i>	313
Overcoming Optical Selection Rules in Materials by Extreme Localization of Light <i>Hayk Harutyunyan</i>	317

Weyl Semimetals for High-Thermopower Transverse Thermoelectric Transport	
<i>Sarah J. Watzman</i>	322

Orienting Strained Interfaces Designed to Direct Energy Flow	
<i>Dongkyu Lee</i>	326

Tailoring Photophysical Energy Transfer for Selective Separations of Critical Lanthanides	
<i>Andrew Ferguson, Christopher Chang, Mark Steger, Mark Jensen, Alan Sellinger, Thomas Mallos, Anastasia Kuvayskaya, Eric Schelter, and Kevin Ruoff</i>	331

Design, Synthesis, and Atomic Scale Characterization of Rare-Earth Based Supramolecular Nano-graphene and Nanoribbons	
<i>Saw Wai Hla, Larry A. Curtiss, Xuedan Ma, Eric Masson, Anh T. Ngo, Volker Rose, Tijana Rajh, and Sergio E. Ulloa</i>	336

Session XI

Understanding and Probing Phonon Transport in Emerging Quantum Materials	
<i>Bolin Liao</i>	343

Spin-Mediated Heat Conduction and Thermoelectric Effects in Novel Materials	
<i>Joshua L. Cohn</i>	348

Tuning Anisotropic Bonding via Chemistry and Pressure in Layered Pnictides and Chalcogenides	
<i>Alexandra Zevalkink and Olivier Delaire.....</i>	353

Generating Metastable Magnetostructural Phases in Solid-State Caloric Systems	
<i>Shane Stadler, Naushad Ali, and Saikat Talapatra</i>	358

Session XII

Phase Transitions in Mesoscopic Systems	
<i>Raymond L. Orbach, E. Dan Dahlberg, and Gregory G. Kenning</i>	367

Atomic Dynamics in Metallic and Other Liquids and Glasses	
<i>T. Egami, Y. Shinohara, E. Zarkadoula, C. Hua, J. R. Morris, and W. Dmowski.....</i>	372

Machine-Learned Structure-Property Relationship in Metallic Glass	
<i>Michael L. Falk.....</i>	379

Phase-Field Modeling of Materials Interfaces and Nanostructures	
<i>Alain Karma.....</i>	382

Extraordinary Responsive Magnetic Rare Earth Materials	
<i>Vitalij K. Pecharsky, Yaroslav Mudryk, and Anis Biswas</i>	387

Harnessing Order Parameter in Ternary II-IV-V₂ Semiconductors	
<i>Adele C. Tamboli</i>	394
Effect of Spatial Variation of Photon Chemical Potential on Near-Field Thermophotovoltaics	
<i>Zhuomin Zhang</i>	400
Synthesis of Ta₂S₅ Wires with Steel-Like Strength and Superconductivity in Ta₂O_{5-x}S_x Wires	
<i>Shermane M. Benjamin, Nathaniel F. Rieders, M. G. Smith, and John J. Neumeier</i>	405
Properties, Electrochemical Activity, and Stability of Solid Oxide Cell Materials under Extreme Conditions	
<i>Scott A. Barnett</i>	410
Collective Energy Transport of Excitons in Two-Dimensional Materials	
<i>Steve Cronin and Li Shi</i>	415
Organic Multiferroics	
<i>Shenqiang Ren</i>	420
Collective Energy Transport of Excitons in Two-dimensional Materials	
<i>Li Shi and Steve Cronin</i>	426
Thermodynamic, Kinetic and Electrochemical Studies on Mixed Proton, Oxygen Ion and Electron (Hole) Conductors	
<i>Anil V. Virkar</i>	430
Author Index	437
Participant List	441

DOE-BES, Division of Materials Sciences and Engineering, Virtual Program PI Meeting

Physical Behavior of Materials Program

March 10–12, 2021

All times are in Eastern Time

March 10, 2021 Wednesday

10:50-11:00 Zoom login

Welcome and Updates

11:00-11:30 **Welcome and Materials Sciences and Engineering Division Update**
Andrew Schwartz, Acting Division Director, *MSED, DOE-BES*

Physical Behavior of Materials (PBM) Program Update
Refik Kortan, Athena Sefat, *Program managers, MSED, DOE-BES*

***Session I: Quantum Behavior of Materials*, Moderator: Christoph Boehme**

11:30-11:50 “**Quantum Metamaterials**”
David Awschalom, *Argonne National Laboratory*

11:50-12:10 “**Light-Matter Quantum Control: Coherence and Dynamics**”
Jigang Wang, *Ames Laboratory*

12:10-12:30 “**A Nonlinear Approach to Weyl Transport**”
Kenneth Burch, *Boston College*

12:30-13:00 Break

***Session II: New Projects I* (3 Slides), Moderator: Hakan Tureci**

13:00-13:05 “**Coherent Control of Strongly Interacting Spins in the Solid-State**”
Jeffrey Thompson, *Princeton University*

13:05-13:10 “**Emergent Properties of Magnons Coupled to Microwave Photons**”
Benjamin Jungfleisch, *University of Delaware*

- 13:10-13:15 “Multiphoton Quantum Simulation through the Control of Electromagnetic Near-Fields in Photonic Networks”
 Omar Magana-Loaiza, *Louisiana State University*
- 13:15-13:20 “DNA-Controlled Dye Aggregation – A Path to Create Quantum Entanglement”
 William Knowlton, *Boise State University*
- 13:20-13:25 “Electron Transfer in Heterostructures Based on Two-Dimensional Materials”
 Hui Zhao, *University of Kansas*
- 13:25-13:30 “Optically Controlled Quantum Phase Transitions at Van der Waals Interfaces”
 Cheng Cen, *West Virginia University*

Session III: Spin Behavior of Materials, Moderator: Z. Valy Vardeny

- 13:30-13:50 “Materials, Physics, and Nanostructures for Next Generation Spintronics”
 Chia-Ling Chien, *Johns Hopkins University*
- 13:50-14:10 “Study of Materials and Interface Properties for High-Efficiency Spin Injection”
 Jing Shi, *University of California, Riverside*
- 14:10-14:30 “Spin Functionality through Complex Oxide Heteroepitaxy”
 Yuri Suzuki, *Stanford University*
- 14:30-14:50 “Tunable Excitons and Pseudospins in Transition Metal Dichalcogenide Homobilayers”
 Elaine Li, *University of Texas, Austin*

14:50-15:15 Break

Session IV: Three Slides Poster Talks I, Moderator: Kenneth Burch

- 15:15-15:23 “Physical Behavior of Quantum Metamaterials”
 Steven Anlage, *University of Maryland*
- 15:23-15:31 “Photon-Mediated Interactions in Superconducting Circuits as a New Tool to Study Emergent Phenomena Far from Equilibrium”
 Hakan Türeci, *Princeton University*

- 15:31-15:39 “Quantum Nanoplasmonics Theory”
Vadym Apalkov *Georgia State University*
- 15:39-15:47 “Optical, Electrical and Magnetic Studies of Hybrid Organic-Inorganic Perovskite Semiconductors”
Zeev Vardeny, *University of Utah*
- 15:47-15:55 “Coherent Control of Spin-States in Organic Electronics”
Christoph Boehme, *University of Utah*
- 15:55-16:03 “Spin Transport in Group IV Materials and 2D Membranes”
Hanan Dery, *University of Rochester*
- 16:03-16:11 “Magnon Current Transmission through Insulators”
Sara Majetich, *Carnegie Mellon University*
- 16:11-16:19 “Magnetization Dynamics and Cooperative Phenomena in Charge and Spin Frustrated Correlated Electron Materials”
Hariharan Srikanth, *University of South Florida*
- 16:19-16:27 “Topological Phases in Aperiodic Systems and Flat-Band Material”
Feng Liu, *University of Utah*
- 16:27-16:35 “Understanding and Enhancing Rashba Splitting in Doped 2D Organic-Inorganic Halide Perovskites: Towards Efficient Spintronics and IR Photodetectors”
Luisa Whittaker-Brooks, *University of Utah*
- 16:35-16:43 “Unique Optical Excitations in Topological Insulators”
Stephanie Law, *University of Delaware*
- 16:43-16:51 “Electron Spin Polarization in Large Electric Fields”
Vanessa Sih, *Michigan University*
- 16:51-16:59 “Control of Energy Transfer and Molecular Excitations via Strongly Coupled Light-Matter Quasiparticles”
Stephen Forrest, *University of Michigan*; Vinod Menon, *City College of New York*

March 11, 2021 Thursday

Session V: Electronic Behavior of Materials, Moderator: Mona Jarrahi

- 11:00-11:20 “Digital Synthesis: A Pathway to Create and Control Novel States of Condensed Matter”
Anand Bhattacharya, *Argonne National Laboratory*
- 11:20-11:40 “Electronic Materials Programs”
Daryl Chrzan, *Lawrence Berkeley National Laboratory*
- 11:40-12:00 “Uncovering and Surmounting Loss Mechanisms in Nitride Light Emitters”
Chris Van de Walle, *University of California, Santa Barbara*
- 12:00-12:20 “Microscopic Understanding of Thin Film Growth and Substrate Engineering of Organic Charge Transfer Complexes”
Pengpeng Zhang, *Michigan State University*
- 12:20-12:40 “Plasmonic Photovoltaics”
Harry Atwater, *California Institute of Technology*

12:40-13:10 Break

Session VI: New Projects II (3 Slides), Moderator: Prashant Kamat

- 13:10-13:15 “Physical Mechanisms and Electric-Bias Control of Phase Transitions in Quasi-2D Charge-Density- Wave Quantum Materials”
Alexander Balandin, *University of California, Riverside*
- 13:15-13:20 “Singlet and Triplet Exciton Interaction and Dynamics in Molecular Crystals”
Ivan Biaggio, *Lehigh University*
- 13:20-13:25 “Discovery of Goniopolar Metals with Zero-Field Hall and Nernst Effect”
Joseph Heremans, *Ohio State University*
- 13:25-13:30 “Elucidating Chirality-Induced Magnetism and Magnetoelectric Functionalities in Layered Chiral Hybrid Metal Halide Perovskite”
Dali Sun, *North Carolina State University*

- 13:30-13:35 “The Synthesis 2D Janus vdW Crystals and Novel Quantum Phenomena Arising from Mirror-Symmetry Breaking”
Sefaattin Tongay, *Arizona State University*

Session VII: Nano-Enabled Behavior of Materials, Moderator: Matthew McCluskey

- 13:35-13:55 “Physical Chemistry of Inorganic Nanostructures”
Peidong Yang, *Lawrence Berkeley National Laboratory*
- 13:55-14:15 “Characterization of Functional Nanomachines”
Michael Crommie, *Lawrence Berkeley National Laboratory*
- 14:15-14:35 “In Search of Metastable Forms of Matter: Discovery of 3D Magnetic Carbon”
Puru Jena, *Virginia Commonwealth University*
- 14:35-14:55 “Nanostructured Colloidal Self-assembly and Controlled Alignment of Anisotropic Nanoparticles”
Ivan Smalyukh, *University of Colorado*

14:55-15:20 Break

Session VIII: Three Slide Poster Talks II, Moderator: Stephanie Law

- 15:20-15:28 “Nanophotonics-Enhanced Solar Cells”
Shanhui Fan, *Stanford University*
- 15:28-15:36 “Metamaterials”
Thomas Koschny, *Ames Laboratory*
- 15:36-15:44 “Light-Matter Interaction Phenomena using Subwavelength Engineering of Material Properties”
Igal Brener, *Sandia National Laboratories*
- 15:44-15:52 “Control of Light-Matter Interaction with Epsilon-Near-Zero Homogeneous Alternative Plasmonic Materials”
Alexandra Boltasseva, *Purdue University*
- 15:52-16:00 “Metamaterials as a Platform for the Development of Novel Materials for Energy Applications”
Willie Padilla, *Duke University*

- 16:00-16:08 “Solution-Processed Photovoltaic Devices Utilizing Semiconductor Excitonic Nanoshells”
Mikhail Zamkov, *Bowling Green State University*
- 16:08-16:16 “Plasmonic Photoconductive Nanostructures for High-Power Terahertz Wave Generation”
Mona Jarrahi, *University of California, Los Angeles*
- 16:16-16:24 “Defects in Gallium Oxide”
Matthew McCluskey, *Washington State University*
- 16:24-16:32 “Probing Local, Hybrid Perovskite Photophysics through Spatially- and Temporally-Resolved Absorption/Emission Microscopy”
Masaru Kuno, *University of Notre Dame*
- 16:32-16:40 “Nanocrystal-Based Dyads for Solar to Electric Energy Conversion”
David Waldeck, *University of Pittsburgh*
- 16:40-16:48 “Exploring the Impact of the Local Environment on Charge Transfer States at Molecular Donor-Acceptor Heterojunctions”
Barry Rand, *Princeton University*
- 16:48-16:56 “Tuning Organic Semiconductor Packing and Morphology through Non-equilibrium Solution Processing”
Zhenan Bao, *Stanford University*
- 16:56-17:04 “Design Principles of Low-Dimensional Halide Perovskites Assisted by Machine Learning”
Yiying Wu, *Ohio State University*
- 17:04-17:12 “Interfaces in Electronic and Structural Materials”
Yuri Mishin, *George Mason University*

March 12, 2021 Friday

Session IX: Excitonic Behavior of Materials, Moderator: Antoine Kahn

11:00-11:20 “Excitons in Low-Dimensional Perovskites”
William Tisdale, *Massachusetts Institute of Technology*

11:20-11:40 “Control of Light-Matter Interactions in Hybrid Structured Environments with Novel Nanomaterials of Different Dimensionalities”
Anton Malko, *University of Texas, Dallas*

11:40-12:00 “Coupling Electrons, Phonons, and Photons: Efficient Multiphysics Simulation of Nonequilibrium Quantum Transport in Electrically and Optically Excited Semiconductor Nanostructures”
Irena Knezevic, *University of Wisconsin*

12:00-12:20 “Hot Carrier Dynamics in Low-Dimensional Systems”
Ian Sellers, *University of Oklahoma*

12:20-12:45 Break

Session X: New Projects III (Three Slides), Moderator: Igal Brener

12:45-12:50 “Disorder in Topological Semimetals”
Kirstin Alberi, *National Renewable Energy Laboratory*

12:50-12:55 “Overcoming Optical Selection Rules in Materials by Extreme Localization of Light”
Hayk Harutyunyan, *Emory University*

12:55-13:00 “Weyl Semimetals for High-Thermopower Transverse Thermoelectric Transport”
Sarah Watzman, *University of Cincinnati*

13:00-13:05 “Orienting Strained Interfaces Designed to Direct Energy Flow”
Dongkyu Lee, *University of South Carolina, Columbia*

13:05-13:10 “Tailoring Photophysical Energy Transfer for Selective Separations of Critical Lanthanides”
Andrew Ferguson, *National Renewable Energy Laboratory*

- 13:10-13:15 “Design, Synthesis, and Atomic Scale Characterization of Rare-Earth Based Supramolecular Nanographene and Nanoribbons”
Saw Hla, *Argonne National Laboratory*

Session XI: Phonon related Behavior of Materials, Moderator: Stephen Cronin

- 13:15-13:35 “Probing Coherence in Nanoscale Energy Transport with High Spatial-Temporal Resolution”
Bolin Liao, *University of California, Santa Barbara*
- 13:35-13:55 “Extreme Thermoelectric Behavior in Low-Dimensional Oxide Conductors”
Joshua Cohn, *University of Miami*
- 13:55-14:15 “Tuning Anisotropic Bonding via Chemistry and Pressure in Layered Pnictides and Chalcogenides”
Olivier Delaire, *Duke University*
- 14:15-14:35 “Phase Transitions in Metastable Multicaloric Materials”
Shane Stadler, *Louisiana State University*

14:35-15:00 Break

Session XII: Three Slide Poster Talks III, Moderator: Alexandra Boltasseva

- 15:00-15:08 “Phase Transitions in Mesoscopic Systems”
Raymond Orbach, *University of Texas, Austin*
- 15:08-15:16 “Atomistic and Mesoscopic Study of Metallic Glasses”
Takeshi Egami, *Oak Ridge National Laboratory*
- 15:16-15:24 “Amorphous Structures and Polymorphic Transitions in Metallic Glasses”
Michael Falk, *Johns Hopkins University*
- 15:24-15:32 “Bridging Atomistic and Continuum Scales in Phase-Field Modeling of Solid-Liquid Interface Dynamics and Coalescence”
Alain Karma, *Northeastern University*
- 15:32-15:40 “Extraordinary Responsive Magnetic Rare Earth Materials”
Vitalij Pecharsky, *Ames Laboratory*
- 15:40-15:48 “Harnessing Order Parameter in Ternary II-IV-V₂ Semiconductors”
Adele Tamboli, *National Renewable Energy Laboratory*

- 15:48-15:56 “Measurement of Near-Field Thermal Radiation Between Flat Surfaces with a Nanogap”
Zhuomin Zhang, *Georgia Institute of Technology*
- 15:56-16:04 “Investigations of Dimensionally-Constrained Fermions”
John Neumeier, *Montana State University*
- 16:04-16:12 “Properties, Electrochemical Activity, and Stability of Solid Oxide Cell Materials Under Extreme Conditions”
Scott Barnett, *Northwestern University*
- 16:12-16:20 “Structure-Optical-Thermal Relationships of Carbon Nanotubes”
Stephen Cronin, *University of Southern California*
- 16:20-16:28 “Collaborative Research: Polymeric Multiferroics”
Shenqiang Ren, *University of Buffalo*
- 16:28-16:36 “Structure-Optical-Thermal Relationships of Carbon Nanotubes”
Li Shi, *University of Texas*
- 16:36-16:44 “Thermodynamic and Kinetic Studies of High Temperature Proton Conductors (HTPC) Using Thin Films and Porous Bodies”
Anil Virkar, *University of Utah*

16:45 - 17:00 Closeout, PBM program managers

Session I

Quantum metamaterials

Principal Investigator:

David Awschalom – Argonne National Lab

Co-Principal Investigators:

Joseph Heremans – Argonne National Lab

Stephan Hruszkeywycz – Argonne National Lab

Support Staff:

Gary Wolfowicz – Argonne National Lab

Program Scope

The quantum metamaterials effort at Argonne National Lab has continued to extend the fundamental understanding to defect-based solid-state quantum systems, while building up a toolbox of materials growth, characterization, and fabrication techniques. Herein, we highlight some of our recent experimental progress focusing on several new defects in silicon carbide (SiC) including Chromium (Cr^{4+}) [1] and Vanadium (V^{4+}) [2], and on confirming predictions for how a local change in the SiC crystal stacking order (e.g. stacking fault) could enable intrinsic coherent defects with spin-contrast persisting to room temperature [3]. Additionally, we highlight a recent effort in creating a set of guidelines for designing new quantum defect-host systems for specific applications, discussing the important interplay of spin, optical, and charge defect properties and how they relate to the intrinsic and engineerable aspects of their host materials [4]. We also highlight opportunities for magnon- mediated long-range quantum entanglement using NV centers [5], as well as more broadly explore how spin qubit / magnon hybrid quantum systems can be used for controlling and mediating the transfer of quantum information [6]. Finally, we highlight some new work integrating these defects with nanoscale structures and combine diamond membranes with nanophotonics [7] and engineered nanoparticles for XRD characterization techniques [8].

These diverse experiments provide key insights toward improving the defect coherence properties through fundamental materials studies, defect creation and integration, as well as the development of a materials characterization toolkit to advance our fundamental understanding of quantum defects by design.

Recent Progress

Beyond our recent manuscripts, we continue to develop novel diamond chemical vapor deposition recipes for nitrogen (^{15}N) delta-doped diamond, diamond (^{12}C) membrane overgrowth, and poly-isotopic growth. We are extending our capabilities by adding ^{13}C isotopic growth and are expanding our dopant repertoire. This past autumn, we added annealing capabilities and a tri-acid (perchloric, nitric, and sulfuric acid) cleaning procedure along with the necessary safety infrastructure to allow for the surface treatment and sample preparation needed for coherent near surface defects. Additionally, we are developing new methods to extend our delta-doped diamond techniques to integrate these defects into membrane structures only a few hundred nanometers thick. To date, we have grown more than 60 new samples using our tool as we continue to build expertise and expand our capabilities.

Using insight developed and discussed in our recent review article on defect guidelines [4], we are exploring new defect host materials tailored to specific quantum applications. Of particular interest, through collaborations with the Galli group and others, are oxide materials with known low nuclear spin concentrations that should theoretically serve as a host material with long spin coherence [9]. We have begun exploring these systems by gathering high quality materials from commercial vendors as well as collaborators, with initial spin resonance measurements to determine crystal quality and dopant impurities ongoing.

Building on our experience with integrating spin qubits with other quantum systems using a hybrid quantum architecture approach, we continue to develop nanomechanical devices with integrated defects to improve the spin-phonon interaction, as well hybrid spin-magnon devices. Our recently published theory of magnon-mediated NV-NV entanglement [5] and quantum magnonics review [6] highlight our recent efforts in this area. In addition, we have been making progress towards integrating magnetic thin films with bulk and diamond nanoparticles, as well as developing a scanning microscopy system to study both spin-magnon interactions and to use these defects as quantum sensors for probing magnon transport physics.

We have also continued our efforts in integrating high quality defects in engineered nanostructures. Related to this, we have had recent success in combining smart-cut membrane fabrication techniques with in-situ doped diamond overgrowth. We are currently characterizing not only these defects' remarkably long spin coherence but also exploring methods to control the local strain within these suspended membranes as a means for coherent control of the defect's quantum state. We have also been adapting these thin membrane fabrication techniques, both using smart-cut method for diamond and a selective photo-electrochemical etch for suspended silicon carbide, to create engineered nanoparticles. The aim is to create defect ensembles within these nanoparticles both for quantum sensing applications as well as fundamental study of defect creation processes using synchrotron x-ray imaging techniques. These imaging techniques will explore embedded engineered nanoparticles using adapted Bragg Coherent Diffraction Imaging (BCDI) techniques at the Argonne Advanced Photon Source in collaboration with the Synchrotron Radiation Studies

(SRS) FWP in MSD, to image the full 3D strain profile of these nanoparticles as fabricated, after ion implantation and irradiation for defect creation, and during the subsequent annealing process.

Personnel-wise we have integrated the new staff and post-doc hires over the last two years and have hired a joint post-doc with the SRS FWP who started in November 2019. Additionally, we have the pleasure to be joined by a new Maria Goeppert Meyer Fellow (Katherine Harmon) who will work jointly in our group along with the SRS FWP starting in mid-February 2021 to study defects in heterostructures with engineered phonon dispersions.

Future Plans

We present some of our future plans related to materials synthesis and defect creation, defect qubit search, and hybrid quantum systems.

We will continue to develop advanced techniques based on growth and local vacancy creation/mobilization in an effort to improve the material quality, lengthen the defect's spin coherence times, increase the defect creation efficiency and density, and improve localization of defects and nuclear spin baths. We will extend our knowledge of NV center defect creation in diamond to other defects including SiV and GeV centers in diamond, and divacancy complexes in SiC. Continuing our collaborative work with the XRD scientists in the SRS FWP, we will study this defect creation process using in-situ novel techniques at the APS.

We will also continue to characterize newly discovered transition metal defects (e.g. chromium, vanadium, etc.) in SiC and relevant oxide host materials as viable qubit candidates using optical spectroscopy and EPR techniques. This includes taking experimental data to corroborate our recent simulations and theoretical calculations on the importance of nuclear spin density. To aid in the defect qubit search, we are also expanding our broadband optical capabilities for fast sample characterization as well as implement a thermoelectrically cooled cryostat for studying near-room-temperature defects.

Finally, in collaboration with the Superconductivity and Magnetism (SM) FWP in MSD, we will fabricate magnonic waveguides to study NV centers coupled to spin waves in the context of quantum hybrid systems research. We are working to develop a multimodal magnetometry sensing platform that incorporates both NV quantum sensing and micro-Brillouin light scattering spectroscopy (BLS), in collaboration with the SM FWP, to paint a complete picture of magnon-single spin interactions over both submicron and millimeter length scales. Additionally, we continue to explore spin-phonon hybrid approaches with progress toward suspended fabricating nanomechanical devices coupled to chromium defects in SiC, where we expect a significantly larger spin-strain coupling strength, as compared to the divacancy defects.

References

- [1] B. Diler, S. J. Whiteley, C. P. Anderson, G. Wolfowicz, M. E. Wesson, E. S. Bielejec, F. J. Heremans, and D. D. Awschalom, “Coherent control and high-fidelity readout of chromium ions in commercial silicon carbide”, *npj Quantum Information* **6**, 1 (2020).
- [2] G. Wolfowicz, C. P. Anderson, B. Diler, O. G. Poluektov, F. J. Heremans, D. D. Awschalom, “Vanadium spin qubits as telecom quantum emitters in silicon carbide”, *Sci. Adv.* **6**, eaaz1192 (2020).
- [3] V. Ivády, J. Davidsson, N. Delegan, A. L. Falk, P. V. Klimov, S. J. Whiteley, S. O. Hruszkewycz, M. V. Holt, F. J. Heremans, N. T. Son, D. D. Awschalom, I. A. Abrikosov, A. Gali, “Stabilization of point-defect spin qubits by quantum wells” *Nat. Commun.* **10**, 5607 (2019).
- [4] G. Wolfowicz, F. J. Heremans, C. P. Anderson, S. Kanai, H. Seo, A. Gali, G. Galli, D. D. Awschalom, “Qubit guidelines for solid-state spin defects.”, arXiv:2010.16395, *Nature Review Materials* (accepted).
- [5] M. Fukami, D. R. Candido, D. D. Awschalom, M. E. Flatté, “Opportunities for long-range magnon-mediated entanglement of spin qubits via on- and off-resonant coupling”, arXiv:2101.09220.
- [6] D. D. Awschalom, C. H. R. Du, R. He, F. J. Heremans, A. Hoffmann, J. T. Hou, H. Kurebayashi, Y. Li, L. Liu, V. Novosad, J. Sklenar, S. E. Sullivan, D. Sun, H. Tang, V. Tiberkevich, C. Trevillian, A. W. Tsien, L. R. Weiss, W. Zhang, X. Zhang, L. Zhao, C. W. Zollitsch, “Quantum engineering with hybrid magnonics systems and materials”, arXiv:2102.03222, *IEEE Transactions on Quantum Engineering* (accepted).
- [7] A. Butcher, X. Guo, R. Shreiner, N. Delegan, K. Hao, P. J. Duda, D. D. Awschalom, F. J. Heremans, Alexander A High, “High- Q Nanophotonic Resonators on Diamond Membranes using Tempered Atomic Layer Deposition of TiO 2”, *Nano Lett.* **20**, 4603 (2020).
- [8] S. Maddali, P. Li, A. Pateras, D. Timbie, N. Delegan, A.L. Crook, H. Lee, I. Calvo-Almazan, D. Sheyfer, W. Cha, F. J. Heremans, D. D. Awschalom, V. Chamard, M. Allain, S. O. Hruszkewycz, “General approaches for shear-correcting coordinate transformations in Bragg coherent diffraction imaging. Part I.” *J. Appl. Crystallogr.* **53**, 393 (2020).
- [9] S. Kanai, F. J. Heremans, H. Seo, G. Wolfowicz, C. P. Anderson, S. E. Sullivan, G. Galli, D. D. Awschalom, H. Ohno, “Generalized scaling of spin qubit coherence in over 12,000 host materials”, arXiv:2102.02986.

Publications - 2-year list of publications SUPPORTED BY BES

1. D. D. Awschalom, C. H. R. Du, R. He, F. J. Heremans, A. Hoffmann, J. T. Hou, H. Kurebayashi, Y. Li, L. Liu, V. Novosad, J. Sklenar, S. E. Sullivan, D. Sun, H. Tang, V. Tiberkevich, C. Trevillian, A. W. Tsai, L. R. Weiss, W. Zhang, X. Zhang, L. Zhao, C. W. Zollitsch, "Quantum engineering with hybrid magnonics systems and materials", arXiv:2102.03222, *IEEE Transactions on Quantum Engineering* (accepted).
2. G. Wolfowicz, F. J. Heremans, C. P. Anderson, S. Kanai, H. Seo, A. Gali, G. Galli, D. D. Awschalom, "Qubit guidelines for solid-state spin defects.", *Nature Review Materials* (accepted).
3. G. Wolfowicz, C. P. Anderson, B. Diler, O. G. Poluektov, F. J. Heremans, D. D. Awschalom, "Vanadium spin qubits as telecom quantum emitters in silicon carbide", *Sci. Adv.* **6** (18), eaaz1192 (2020).
4. S. Maddali, P. Li, A. Pateras, D. Timbie, N. Delegan, A.L. Crook, H. Lee, I. Calvo-Almazan, D. Sheyfer, W. Cha, F. J. Heremans, D. D. Awschalom, V. Chamard, M. Allain, S. O. Hruszkewycz, "General approaches for shear-correcting coordinate transformations in Bragg coherent diffraction imaging. Part I. ,", *J. Appl. Crystallogr.* **53**, 393 (2020).
5. A. Butcher, X. Guo, R. Shreiner, N. Delegan, K. Hao, P. J. Duda, D. D. Awschalom, F. J. Heremans, Alexander A High, "High- Q Nanophotonic Resonators on Diamond Membranes using Templated Atomic Layer Deposition of TiO 2", *Nano Lett.* **20**, 4603 (2020).
6. B. Diler, S. J. Whiteley, C. P. Anderson, G. Wolfowicz, M. E. Wesson, E. S. Bielejec, F. J. Heremans, and D. D. Awschalom, "Coherent control and high-fidelity readout of chromium ions in commercial silicon carbide ", *npj Quantum Information* **6**, 1 (2020).
7. V. Ivády, J. Davidsson, N. Delegan, A. L. Falk, P. V. Klimov, S. J. Whiteley, S. O. Hruszkewycz, M. V. Holt, F. J. Heremans, N. T. Son, D. D. Awschalom, I. A. Abrikosov, A. Gali, "Stabilization of point-defect spin qubits by quantum wells" *Nat. Commun.* **10**, 5607 (2019).
8. S. J. Whiteley, F. J. Heremans, G. Wolfowicz, D. D. Awschalom, M. V. Holt, "Correlating dynamic strain and photoluminescence of solid-state defects with stroboscopic x-ray diffraction microscopy.", *Nature Commun.* **10**, 1 (2019).
9. M. Fukami, C. G. Yale, P. Andrich, X. Liu, F. J. Heremans, P. F. Nealey, D. D. Awschalom, "All-optical cryogenic thermometry based on nitrogen-vacancy centers in nanodiamonds", *Phys. Rev. Appl.*, **12**, 014042 (2019).

Light-Matter Quantum Control: Coherence and Dynamics

Principal investigator: Jigang Wang

Co-investigators: Zhe Fei, Kai-Ming Ho, Liang, Luo, Joseph Shinar, Cai-Zhuang Wang, Yongxin Yao

Materials Science and Engineering Division, Ames Laboratory, Ames, IA 50011
e-mail: jwang@ameslab.gov

Program Scope There is growing evidence that harnessing coherence and non-equilibrium dynamics may push initial charge transfer into simultaneously the multi-terahertz and multi-nanometer regime. If so, this could overcome the grain boundaries required as the first step for efficient photoconversion systems. This also offers promise of realizing coherence-protected, robust current transport against impurity scattering for topological electronics and quantum computation. Furthermore, understanding how to measure, manipulate, and harvest these coherent and non-equilibrium carriers before they dissipate and cool might help exceed the fundamental Shockley-Queisser limit in thermodynamic equilibrium for photoconversion efficiency. The proposed research aims to advance our understanding of the pathways of photoenergy conversion and robust photocurrent transport through the study of coherence- and dynamics-mediated charge transfer, especially against impurities, across grain boundaries and microstructures. The work will characterize space, time, and energy evolution of electronic, vibrational, chiral states, with extreme but important resolutions (nanometer, femtosecond, and terahertz), in a variety of model systems such as photovoltaic materials and topologically protected states. Special emphases are on dynamic stability and coherent switching enabled by light-matter quantum coherence and periodic driving of lattice motions. The work brings together a team of experimentalists, including experts in ultrabroadband, multi-modal spectroscopy and nano-imaging, from visible to terahertz, and advanced materials synthesis, with theorists skilled in out-of-equilibrium simulations.

Recent Progress We will discuss some highlights of our program during past two years.

1. Quantum beats unveils hidden Rashba effects in perovskite photovoltaics

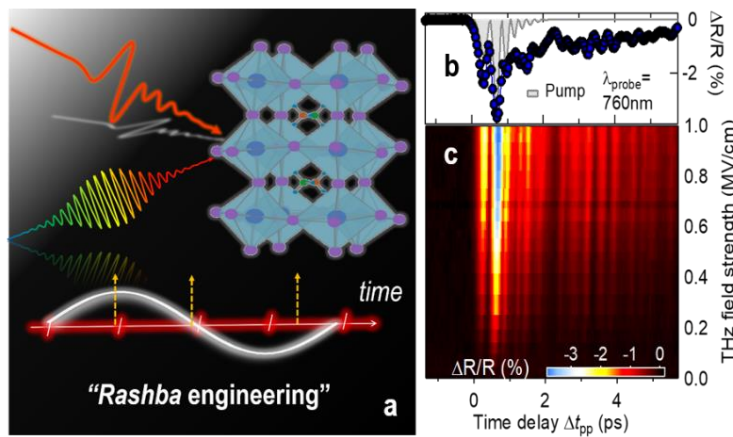


Figure 1: Quantum beats unveils hidden Rashba fine structure in perovskite photovoltaics. (a) Schematics for THz quantum beat spectroscopy for discovering vibronic (or coupled electron-phonon) coherence and demonstrating “Rashba engineering” in metal halide perovskites. (b) Representative exciton dynamics measured by differential reflectivity $\Delta R/R$ at 760 nm after $E_{THz}=938$ kV/cm pumping and (c) a 2D false-color plot for quantum beat temporal oscillations. Squared THz pump field is plotted together in (b) (gray shade) [1].

The presence of the momentum- and spin-dependent splitting of electronic bands, known as the Rashba effect in metal halide perovskites, has been an intensely debated mechanism. It underlies the entire field of spintronics, photovoltaics, light emitting diodes and lasers based on this category of revolutionary materials. Demonstrating the Rashba effect in bulk perovskites settles this debate. This is achieved by detecting “quantum beating” that relate to Rashba electronic bands, i.e., an interference pattern between multiple periodic back-and forth quantum motion of atoms and electrons of slightly different frequencies. This was achieved by employing a single-cycle terahertz pump field which reveals vibronic quantum beats that modulate the dark and bright excitonic fine structure splitting. The long-lived quantum beats, exclusively from the dark Rashba states, are more than ten times longer than the bright Rashba states. The different coherence times arise from the selective modulation of the Rashba bands by lattice vibrations of two symmetries, i.e., infrared vs Raman. Some beating signals are shown to survive even at room temperature in the form of polarons. By steering quantum motions of atoms and electrons to manipulate the excitonic fine structure splitting, we also achieve “Rashba engineering” of Rashba-type bands. This is a significant leap for perovskite quantum control, and for spintronic and photovoltaic applications.

Paper reference: *Physical Review Letters*. 124(15), art. no. 157401 2020).

2. Light induced exceptional ballistic transport in a Dirac material ZrTe₅

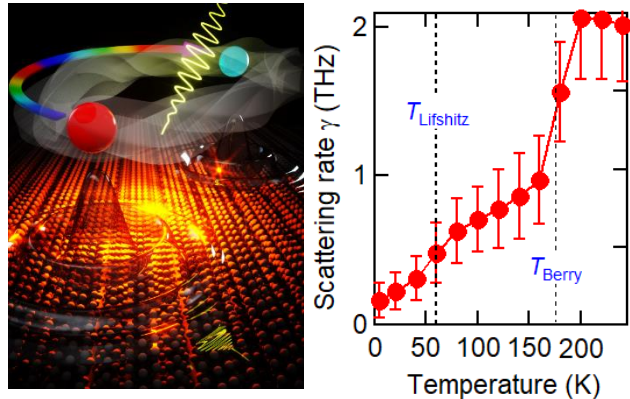


Figure 2: Light induced Weyl semimetals with exceptional ballistic transport. (Left) Schematics of light-induced coherent phonons that break inversion symmetry and lead to the formation of Weyl points. (Right) Temperature-dependent scattering rate of photocurrent, which appears dissipationless towards low temperature. Berry curvature dominance below T_{Berry} (black dashed line) marks the sharp suppression of impurity scattering due to chiral protection [2].

Wide-scale adoption of quantum computing and large scale data center requires building devices in which fragile quantum states are protected from their noisy environments and energy consumption is minimized. One approach is based on “symmetry-protected” topological quasiparticles that are theoretically immune to noise and enable spin and/or chirality switching by quantum coherent motion with minimum energy loss. A new light-induced symmetry switch, that works by twisting the crystal lattice of a Dirac material, coherently splits Dirac points to two pairs of Weyl points and photogenerates giant low dissipation current with an exceptional ballistic transport protected by induced Weyl band topology. Such topological control principles are demonstrated using a few-cycle terahertz pulse to driven coherent infrared phonons and, in turn, induce a topological phase transition from Dirac to Weyl semimetal states ZrTe₅. Experimental

results combined with first-principles modeling shows that indicate two pairs of Weyl points dynamically created by mode-selective phonon pumping of broken inversion symmetry. Such phononic terahertz control breaks ground for coherent manipulation of Weyl nodes and robust quantum transport without application of static electric or magnetic fields. The discovery holds great promise for spintronics, topological effect transistors, and quantum computing.

Paper reference: *Nature Materials*, 10.1038/s41563-020-00882-4 (2021)

3. Nano-imaging of plasmon spatial coherence in pentacene-graphene heterostructures

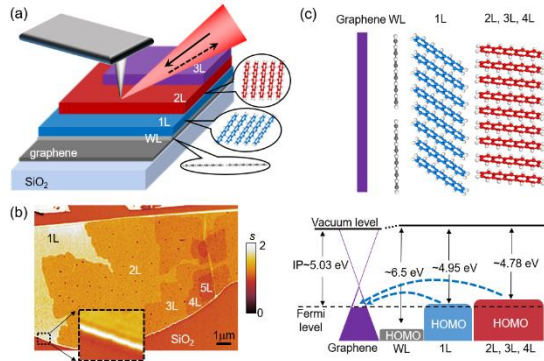


Figure 3. (a) Illustration of the nano-imaging study of a pentacene/graphene heterostructure (HS). (b) The IR amplitude (s) image of the pentacene/graphene HS taken at $E = 116$ meV. Inset plots a zoom-in view that shows plasmon fringes at the sample edges. (c) Illustration of the graphene/pentacene HS (top) and the energy level alignment diagram (bottom). The energies values are ionization potentials (IP) and the blue arrows mark the direction of electron transfer. In all panels ‘WL’, ‘1L’ to ‘4L’ represent wetting-layer, 1-layer to 4-layer pentacene on graphene.

Advanced nanotechnology can allow us to play ‘Legos’ at the nanometer length scale using emerging two-dimensional (2D) semiconductors. For example, it is possible to stack atomic layers of 2D material together into a Wan der Waals (vdW) heterostructure. Interlayer interactions between these 2D materials lead to new properties and functionalities that are different from individual components. Recently, the Ames team performed a nano-plasmonic study of vdW heterostructures that consist of ordered molecular layers of pentacene on graphene [3]. We find through nano-infrared imaging that coherent charge transfer between graphene and pentacene affects dramatically the plasmonic responses of graphene. Further analysis and density functional theory calculations indicate that charge transfer is controlled by pentacene thickness and orientation. Our work unveils a new method for tailoring graphene plasmons by interlayer charge transfer. We are currently extending this to characterize coherence in an organic superlattice of donor/acceptor monolayer photovoltaic architectures.

Paper reference: *Nano Lett.*, 2019, 19, 9, 6058-6064

4. Topological Quantum Switching via Light-Driven Raman Coherence

A topological switching control principle is demonstrated using a few-cycle THz pulse to driven coherent Raman phonons and, in turn, induce a topological phase transition in a Dirac semimetal ZrTe₅[4]. This is achieved by periodically driving using vibrational coherence of the lattice due to excitation of its lowest Raman-active mode. Above a critical THz pump field threshold, there emerges a long-lived (~100 ps) metastable phase ~100 ps with unique Raman phonon-assisted topological switching dynamics, which is absent for optical pumping. This quantum control principle is achieved by a mode-selective Raman phonon coherent oscillations, i.e. light-induced atomic motions of Raman symmetry about the equilibrium position. Experimental results combined with first-principles modeling shows that the system transitions from strong to weak topological insulators with a Dirac semimetal phase in-between. The critical atomic

displacements are controlled by the phonon coherent pumping. This work opens a new arena of light-wave speed topological electronics and phase transitions controlled by quantum coherence.

Paper reference: *Physical Review X* 10, 021013 (2020).

Future Plans Supporting the overarching science goals discussed in the program scope are the following *six projective-level objectives and plans* during the next period.

#1: Achieve coherent control of the Rashba splitting, polarons and optical conductivity in perovskite photovoltaics by tailoring multiple pulse excitation protocols to excite phonons of selective Raman and IR symmetries.

#2: Generate charge, spin and magnetoo-gyrotropic photocurrents and control their long range transport in perovskite absorbers and interfaces using control knobs such as THz “push” electric field pulses to improve power conversion efficiency.

#3: Realize coherent control of quantum geometric and topological properties, such as Weyl, Dirac points and surface Fermi arcs, by tailoring multiple pulse excitation protocols to selectively excite phonons of different symmetry.

#4: Photogenerate a giant, dissipationless chiral current with exceptionally robust quantum transport.

#5: Non-equilibrium tuning of charge transport in 2D materials using phonon pumping of few-layer graphene or using gate tuning of exciton polaritons in atomic layers of WSe₂.

#6: Understand the measured quantum and non-adiabatic dynamics by computing coherent time-frequency spectra and underpinning key observables in them such as Raman/IR coherent peaks, phonon anharmonicity, pump-probe and wave-mixing and high harmonic generation peaks.

References

- [1] Liu, Z., Vaswani, C., Yang, Zhao, X., Yao, Y., Song, Z., Cheng, d., Shi, Y., Luo, L., Mudiyanselage, D.-H., Huang, C., Park, J.-H., Kim, R.H.J., Zhao, J., Yan, Y., Ho, K.-M., Wang, J. 2020. Ultrafast control of excitonic rashba fine structure by phonon coherence in the metal halide perovskite CH₃NH₃PbI₃. *Physical Review Letters.* 124(15), art. no. 157401. <https://doi.org/10.1103/PhysRevLett.124.157401>.
- [2] L. Luo, D. Cheng, B. Song, L-L. Wang, C. Vaswani, P. M. Lozano, G. Gu, C. Huang, R. H. J. Kim, Z. Liu, J-M. Park, Y. Yao, K-M. Ho, I. E. Perakis, Q. Li and J. Wang, “A Light-induced Phononic Symmetry Switch and Giant Dissipationless Topological Photocurrent in ZrTe₅,” *Nature Materials*, 10.1038/s41563-020-00882-4 (2020)
- [3] Hu, F., Kim, M., Zhang, Y., Luan, Y., Ho, K.H., Shi, Y., Wang, C.Z., Wang, X., Fei, Z. 2019. Tailored plasmons in pentacene/graphene heterostructures with interlayer electron transfer. *Nano Letters.* 19(9), pp. 6058-6064. <https://doi.org/10.1021/acs.nanolett.9b01945>
- [4] C. Vaswani, L.-L. Wang, D. H. Mudiyanselage, Q. Li, P. M. Lozano, G. Gu, D. Cheng, B. Song, L. Luo, R. H. J. Kim, C. Huang, Z. Liu, M. Mootz, I. E. Perakis, Y. Yao, K. M. Ho, J. Wang, "Light-Driven Raman Coherence as a Non-Thermal Route to Ultrafast Topology Switching in a Dirac Semimetal." *Physical Review X* 10, 021013 (2020).

A 2-year publication list of papers supported by this BES funding

Publications intellectually led by this FWP

1. L. Luo, D. Cheng, B. Song, L-L. Wang, C. Vaswani, P. M. Lozano, G. Gu, C. Huang, R. H. J. Kim, Z. Liu, J-M. Park, Y. Yao, K-M. Ho, I. E. Perakis, Q. Li and J. Wang, “A Light-induced Phononic Symmetry Switch and Giant Dissipationless Topological Photocurrent in ZrTe₅,” *Nature Materials*, 10.1038/s41563-020-00882-4 (2020)
2. Jialu Chen*, Zijun Zhang*, Liang Luo*, Yunhao Lu, Cheng Song, Di Cheng, Xing Chen, Wei Li, Zhaohui Ren, Jigang Wang, He Tian, Ze Zhang, Gaorong Han, “Reversible magnetism transition at ferroelectric oxide heterointerface”, *Science Bulletin*, 65, 2094 (2020) *equal contributions
3. Liu, Z ., Vaswani, C., Luo, L., Cheng, D., Yang, X., Zhao, X., Yao, Y., Song, Z., Brenes, R., Kim, R., Jean, J., Bulovic, V., Yan, Y., Ho, K.-M., Wang, J. 2020. Coherent band-edge oscillations and dynamic longitudinal-optical phonon mode splitting as evidence for polarons in perovskites. *Physical Review B*. 101(11), art. no. 115125. <https://doi.org/10.1103/PhysRevB.101.115125>.
4. Liu, Z., Vaswani, C., Yang, Zhao, X., Yao, Y., Song, Z., Cheng, d., Shi, Y., Luo, L., Mudiyanselage, D.-H., Huang, C., Park, J.-H., Kim, R.H.J., Zhao, J., Yan, Y., Ho, K.-M., Wang, J. 2020. Ultrafast control of excitonic rashba fine structure by phonon coherence in the metal halide perovskite CH₃NH₃PbI₃. *Physical Review Letters*. 124(15), art. no. 157401. <https://doi.org/10.1103/PhysRevLett.124.157401>.
5. Vaswani, C., Wang, L.L., Mudiyanselage, D.H., Li, Q., Lozano, P.M., Gu, G.D., CCheng, D., Song, B., Luo, L., Kim, R.H., Huang, C., Liu, Z., Mootz, M., Perakis, I.E., Yao, Y., Ho, K.M., Wang, J. 2020. Light-driven Raman coherence as a nonthermal route to ultrafast topology switching in a Dirac semimetal. *Physical Review X*. 10, art. no. 021013. <https://doi.org/10.1103/PhysRevX.10.021013>.
6. Yang, X.*, Luo, L.* , Vaswani, C., Zhao, X., Yao, Y., Cheng, D., Liu, Z., Kim, R. H.J., Liu, X., Dobrowolska, M., Furdyna, J.K., Perakis, I.E., Wang, C.Z., Ho, K.M., Wang, J. 2020. Light control of surface-bulk coupling by terahertz vibrational coherence in a topological insulator. *npj Quantum Materials*. 5(1), art. no. 13. <https://doi.org/10.1038/s41535-020-0215-7>. (* co-first author)
7. Luan, Y., McDermott, L., Fei, Z. 2020. Tip- and plasmon-enhanced infrared nanoscopy for ultrasensitive molecular characterizations. *Physical Review Applied*. 13, art. no. 034020. <https://doi.org/10.1103/PhysRevApplied.13.034020>.
8. Cheng, D., Liu, Z., Luo, L., Vaswani, C., Park, J.-M., Yao, Y., Song, Z., Huang, C., Mudiyanselage, D.-H., Kim, R.H.J., Yan, Y., Ho, K.-M., Wang, J. 2019. Helicity-dependent terahertz photocurrent and phonon dynamics in hybrid metal halide perovskites. *The Journal of Chemical Physics*. 151(24), art. no. 244706. <https://doi.org/10.1063/1.5127767>.

9. Hu, F.R., Fei, Z. 2019. Recent progress on exciton polaritons in layered transition-metal dichalcogenides. *Advanced Optical Materials.* art. no. 1901003. <https://doi.org/10.1002/adom.201901003>.
10. Hippola, C., Danilovic, D., Bhattacharjee, U., Perez-Bolivar, C., Niradha Sachinthani, K.A., Nelson, T.L., Anzenbacher, P., Petrich, J.W., Shinar, R., Shinar J.. 2019. Bright deep blue TADF OLEDs: The role of triphenylphosphine oxide in NPB/TPBi:PPh₃O exciplex emission. *Advanced Optical Materials.* 8(1), art. no. 0191282. <https://doi.org/10.1002/adom.201901282>
11. Zhaoyu Liu, et al., "Cryogenic spatial-temporal imaging of surface photocarrier dynamics in MAPbI₃ at the single grain level", *AIP Advances*, 10, 125108 (2020)
12. Hu, F., Luan, Y., Speltz, J., Zhong, D., Liu, C.H., Yan, J., Mandrus, D.G., Xu, X., Fei, Z. 2019. Imaging propagative exciton polaritons in atomically thin WSe₂ waveguides. *Physical Review B.* 100(12), art. no. 121301(R). <https://doi.org/10.1103/PhysRevB.100.121301>
13. Hu, F., Fei, Z. 2019. Recent progress on exciton polaritons in layered transition-metal dichalcogenides. *Advanced Optical Materials.* art. no. 1901003. <https://doi.org/10.1002/adom.201901003>
14. Hu, F., Kim, M., Zhang, Y., Luan, Y., Ho, K.H., Shi, Y., Wang, C.Z., Wang, X., Fei, Z. 2019. Tailored plasmons in pentacene/graphene heterostructures with interlayer electron transfer. *Nano Letters.* 19(9), pp. 6058-6064. <https://doi.org/10.1021/acs.nanolett.9b01945>
15. Luo, L., Yang, X., Liu, X., Liu, Z., Vaswani, C., Cheng, D., Mootz, M., Zhao, X., Yao, Y., Wang, C.Z., Ho, K.M., Perakis, I.E., Dobrowolska, M., Furdyna, J.K., Wang, J. 2019. Ultrafast manipulation of topologically enhanced surface transport driven by mid-infrared and terahertz pulses in Bi₂Se₃. *Nature Communications.* 10(1), art. no. 607. <https://doi.org/10.1038/s41467-019-08559-6>
16. Park, J.M., Cheng, D., Patz, A., Luo, L., Liu, Z.Y. Fungura, F., Shinar, R., Ho, K.M., Shinar, J., Wang, J. 2019. Ultrafast nonlinear transparency driven at a telecom wavelength in an organic semiconductor system. *AIP Advances.* 9(2), art. no. 025303. <https://doi.org/10.1063/1.5042542>
17. Cheng, D., Park, J., Luo, L., Kim, R.; Meier, W.R., Bud'ko, S.L., Canfield, P.C., Mootz, M., Perakis, I.E., Wang, J. 2019. Ultrafast spin dynamics and phase competition in a spin vortex crystal superconductor. *OSA Technical Digest (Optical Society of America, 2019).* paper FW4M.5. https://doi.org/10.1364/CLEO_QELS.2019.FW4M.5

Collaborative Publications

1. C. Vaswani, J. H. Kang, M. Mootz, L. Luo, X. Yang, C. Sundahl, D. Cheng, C. Huang, R. H. J. Kim, Z. Liu, Y. G. Collantes, E. E. Hellstrom, I. E. Perakis, C. B. Eom and J. Wang, "Light Quantum Control of Persisting Higgs Modes in Iron-Based Superconductors", *Nature Communications*, 12, 258 (2021). 10.1038/s41467-020-20350-6 (2021) Arxiv/2011.13036

2. Harris, D.T., Campbell, N.G., Di, C., Park, J.M., Luo, L., Zhou, H., Kim, G.Y., Song, K., Choi, S.Y., Wang, J., Rzchowski, M.S., Eom, C.B.. 2020. Charge density wave modulation in superconducting BaPbO₃/BaBiO₃ superlattices. *Physical Review B.* 101(6), art. no. 064509. <https://doi.org/10.1103/PhysRevB.101.064509>
3. Dey, K., Chowdhury, S.R., Dykstra, E., Koronatov, A., Lu, H.P., Shinar, R., Shinar, J., Anzenbacher, P.. 2020. Diazirine-based photo-crosslinkers for defect free fabrication of solution processed organic light-emitting diodes. *Journal of Materials Chemistry C.* 8(34), pp. 11988-11996. <https://doi.org/10.1039/d0tc02317e>
4. Mootz, M., Wang, J., Perakis, I.E.. 2020. Lightwave terahertz quantum manipulation of non-equilibrium superconductor phases and their collective modes. *Physical Review B.* 102(5), art. no 054517. <https://doi.org/10.1103/PhysRevB.102.054517>
5. Gamage, E.H., Greenfield, J.T., Unger, C., Kamali, S., Clark, J.K., Harmer, C.P., Luo, L., Wang, J., Shatruk, M., Kovnir, K.. 2020. Tuning Fe-Se tetrahedral frameworks by a combination of [Fe(en)₃]²⁺cations and Cl-anions. *Inorganic Chemistry.* 59(18), pp. 13353-13363. <https://doi.org/10.1021/acs.inorgchem.0c01727>
6. Xu, H., Zhao, Y., Zhang, J., Zhang, D., Miao, Y., Shinar, J., Shinar, R., Wang, H., Xu, B.. 2019. Low efficiency roll-off phosphorescent organic light-emitting devices using thermally activated delayed fluorescence hosts materials based 1, 2, 4-triazole acceptor. *Organic Electronics.* 74, pp. 13-22. <https://doi.org/10.1016/j.orgel.2019.06.041>
7. Ryan, B.J., Hanrahan, M.P., Wang, Y., Ramesh, U., Nyamekye, C.K.A., Nelson, R.D., Liu, Z., Huang, C., Whitehead, B., Wang, J., Roling, L.T., Smith, E.A., Rossini, A.J., Panthani, M.G.. 2019. Silicene, siloxene, or silicane? Revealing the structure and optical properties of silicon nanosheets derived from calcium disilicide. *Chemistry of Materials.* 32(2), pp. 795-804. <https://doi.org/10.1021/acs.chemmater.9b04180>
8. Zhang, J., Zhao, Y., Xu, H., Zhang, D., Miao, Y., Shinar, R., Shinar, J., Wang, H., Xu, B., Wu, Y. 2019. Novel blue fluorescent emitters structured by linking triphenylamine and anthracene derivatives for organic light-emitting devices with EQE exceeding 5%. *Journal of Materials Chemistry C.* 7, pp. 10810-10817. <https://doi.org/10.1039/C9TC02773D>
9. Wang, F., Zhao, Y., Xu, H., Zhang, J., Miao, Y., Guo, K., Shinar, R., Shinar, J., Wang, H., Xu, B. 2019. Two novel bipolar hosts based on 1,2,4-triazole derivatives for highly efficient red phosphorescent OLEDs showing a small efficiency roll-off. *Organic Electronics: physics, materials, applications.* 70, pp. 272-278. <https://doi.org/10.1016/j.orgel.2019.04.030>
10. Herklotz, A., Rus, S.F., Balke, N., Rouleau, C., Guo, E.J., Huon, A., KC, S., Roth, R., Yang, X., Vaswani, C., Wang, J., Orth, P.P., Scheurer, M.S., Ward, T.Z. 2019. Designing morphotropic phase composition in BiFeO₃. *Nano Letters.* 19(2), pp. 1033-1038. <https://doi.org/10.1021/acs.nanolett.8b04322>

A Nonlinear Approach to Topological Semimetals

Kenneth Stephen Burch (Boston College)

Program Scope

The program is focused on exploration of the nonlinear and inelastic optical responses of topological semimetals (TSM), towards understanding their dynamics and unleashing their potential for plasmonics, nonreciprocal photothermoelectrics, high speed interconnects, efficient nonlinear optoelectronic elements, and magneto-resistive sensors. Topological semimetals possess an array of novel transport and nonlinear responses, including ultrahigh mobilities, chiral anomalies, extreme magneto-resistance, and nonlinear responses. These properties' origins remain controversial, such as whether the nontrivial topology is responsible for the ultrahigh mobility and enormous nonlinearities. Typically TSM are described by the Hamiltonian $H = \chi \vec{k} \cdot \vec{\sigma}$, where the nodes of opposite χ are degenerate for a Dirac semimetal (DSM). By applying a magnetic field (or breaking inversion), the Zeeman term will shift the \vec{k} position of the nodes, removing their degeneracy and producing a Weyl semimetal (WSM). These Weyl nodes are monopoles of spin in momentum space, and as such, have diverging Berry curvature ($\Omega(k)$). Thus, by changing the separation between the nodes, one tunes the quantum geometry and dispersion of the bands. Additionally, these bands create a large phase space for phonons to scattering into electrons. Simultaneously the heavy atoms limit the bandwidth of the acoustic modes and thus minimize phonon-phonon scattering. These, in combination, could lead to a novel regime where phonon-electron scattering exceeds phonon-phonon, thus creating a high mobility phonon-electron fluid.

The PI is using his unique combination of expertise in optical spectroscopy and device fabrication to uncover the mechanisms governing the dynamic and topological properties of Semimetals. This requires deciphering the intertwined roles of the band dispersion, symmetry, phonons, and quantum geometry. In particular, one must controllably tune one of these components and observe the effects on various physical responses.

Recent Progress

The PI investigated phonon-electron scattering in a series of ultrahigh mobility semimetals. His group was the first to demonstrate that phonon-electron scattering was far dominant over phonon-phonon scattering in TaAs and NbAs. Through high temperature and energy resolution Raman spectra, the phonon linewidth was found to rapidly grow and eventually saturate. This behavior is quite anomalous as optical modes typically decay into a pair of acoustic phonons,

leading to the linewidth being governed by Bose statistics and thus rising without saturation (Fig. 1). The dominance of phonon-electron scattering over phonon-phonon could produce a non-equilibrium phonon-electron fluid. Such a fluid would lead to large mobility since momentum of the electrons that was lost to phonons, would generally be returned. This strongly suggested it was the phonon-electron scattering that produced the large mobility of this particular WSM family. To test this hypothesis, the PI carefully investigated β -WP₂, where previous experiments revealed an enormous low temperature mobility and evidence for electronic hydrodynamic behavior. While this material is a type-II Weyl semimetal, the Weyl node is ≈ 250 meV below the Fermi surface, suggesting topology is not relevant to the transport. In β -WP₂ the rather low thermal conductivity and specific heat at low temperatures required careful optimization of the Raman measurements to avoid laser heating (as seen by others). Here the PI found Raman modes with similar energy but different symmetry, as well as modes with the same symmetry but different energies that all revealed different relative strength of the phonon-phonon versus phonon-electron scattering. Thus, he established the importance of symmetry and phase space in the dominance of phonon-electron scattering. Working closely with the Narang group (Harvard), they found excellent agreement between the first-principles calculations and experimental results. This work suggested the importance of phonon-electron scattering, and thus high mobility, results from nearly degenerate electronic bands and bunching of acoustic modes that reduces phonon-phonon scattering.

The PI also established optics for probing topological materials, especially the quantum geometry of the electrons and spins. In TaAs, the PI provided the first observation of the colossal bulk photovoltaic effect (BPVE), and the first demonstration of BPVE in the mid-IR. As described in his article featured on the cover of *Nature Materials*, these observations are closely tied to TaAs being a Weyl semimetal. The BPVE results from changes in Berry connection between the initial and final states. Thus the WSM states of TaAs enabled BPVE at low energies, with large enhancements expected close to the node. Crucial to this observation was his development of

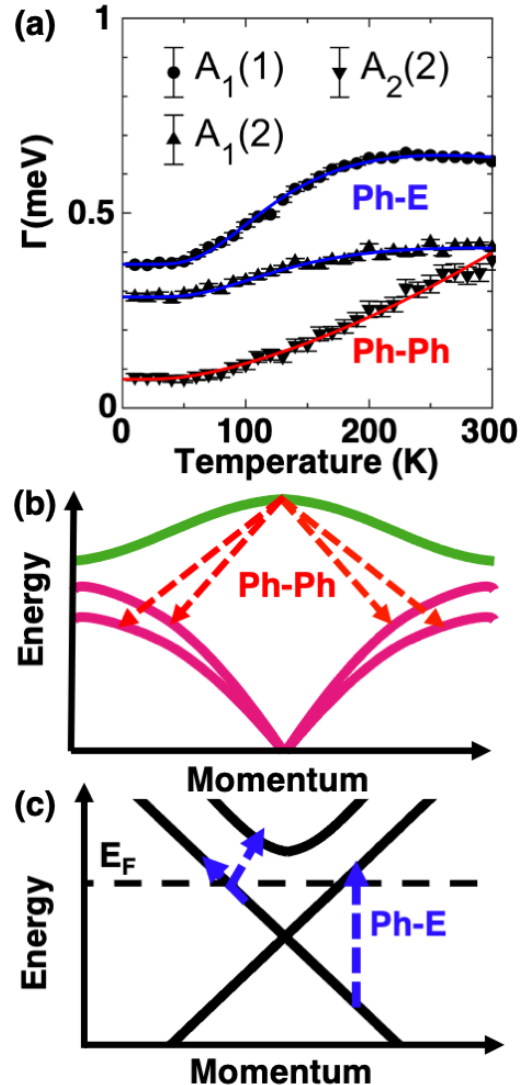


Figure 1 (a) β -WP₂ Phonon linewidths. The $A_2(2)$ mode widens with temperature from phonon-phonon scattering (red line), and A_1 plateau from phonon-electron scattering (blue lines). (b) Phonon-phonon scattering, governed by Bose statistics and the acoustic modes' phase space. (c) Phonon-electron scattering controlled by Fermi statistics and band structure.

WSM devices, photocurrent protocols for the spatial and symmetry analysis to remove extrinsic photothermal responses. These advances also allowed the PI to be first to reveal nonlinear photocurrent responses in a WSM at room temperature, confirmed by THz generation experiments. Still unclear are the roles of scattering, separation of Weyl nodes, specific band structure regions, trivial bands, and resonant enhancements close to the nodes.

Studying nonlinear photocurrent and phonon-electron coupling poses numerous challenges. Often the Fermi level is far from the Weyl node, the materials are air sensitive, unwanted thermal signals or poor temperature control from laser heating, and only bulk samples are available. This is especially challenging in Raman and nonlinear photocurrent studies where signals are small and lowered by poor surface quality. Additionally, for nonlinear studies inhomogeneity and poor contacts can produce spurious signals due to the photothermal and photovoltaic effects (built in electric fields). The PI solved these issues by developing a series of new approaches. This included techniques to freshly cleave/exfoliate and/or produce high quality contacts in inert atmosphere, then transfer materials from his "cleanroom in a glovebox" via a vacuum suitcase to the low-T Raman and photocurrent setups (Fig 2 a-b). In addition, it was crucial to optimize the Raman setup for high throughput, full symmetry analysis and minimal heating by the laser (checked with Stokes/Anti-Stokes ratios). These capabilities were crucial to a number of works in quantum materials.

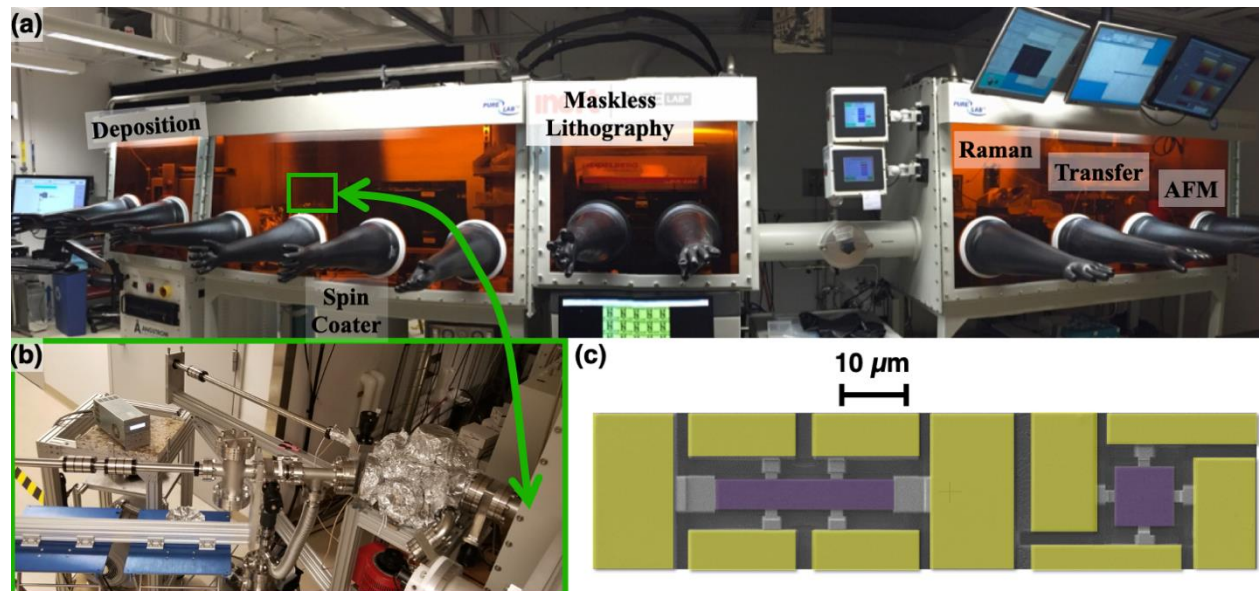


Figure 2 (a) Cleanroom in a glovebox with fabrication and characterization. Techniques and transfer via vacuum suitcase (b), in UHV, to/from low T optics/electronics and MBE(not shown) were developed with DOE support. (c) False-color TEM image of an FIB fabricated device made from a single slab of β -WP₂. The hall bar enables photoinduced and standard Hall or longitudinal resistance measurements. The highly symmetric square reduces unwanted thermal signals along with accurate centering of the beam in the center of the device.

Working with P. Moll, the PI designed and optimized the FIB fabrication of devices from bulk crystals, the first use of this technology for nonlinear experiments (Fig. 2C). Here it was

crucial to engineer the device to minimize accidental polarization and inhomogeneous photo-thermal signals. Thus the PI devised means to produce a Hall bar alongside a square device, cut from the same lamela. This enables transport characterization and nonlinear measurements on the Hall bar, along with spatially symmetric photocurrent experiments along particular crystallographic axis. When combined with new symmetry analysis outlined in his *Nature Material*'s article, the PI unambiguously separated thermal from nonlinear responses. Lastly, in an attempt to tune the Fermi level, the PI investigated a number of organic materials that are highly charged interacting with Dirac systems. While this work to tune the Fermi level in WSM, it enabled a new ability to detect various pathogens rapidly and cheaply.

Future Plans

It is highly desirable to expand nonlinear techniques to provide more detailed information about the quantum geometry from particular momentum regions of the band structure. To this end, the PI is developing and performing nonlinear photocurrent measurements in magnetic fields, along with new angular resolved, current-induced photocurrents. The scattering and role of phonons will be disentangled through Raman experiments, performed on a series of well-chosen materials, that tune either the Fermi level or phonon spectra. Lastly, these experiments are performed in a magnetic field to uncover what role, if any, the quantum geometry plays in the novel phonon-electron scattering.

Publications

- 1) G. B. Osterhoudt, et al., PRX 11, 011017 (2021)
- 2) M. J. Gray, et al., Review of Scientific Instruments 91, 073909 (2020)
- 3) Y. Wang, et al., Nano Letters (2020)
- 4) Y. Wang, et al., npj Quantum Materials 5, 14 (2020)
- 5) T. A. Tartaglia, et al., Science Advances 6 (2020)
- 6) N. Kumar, et al., MEDICAL DEVICES & SENSORS, e10121 (2020)
- 7) N. Kumar, et al., Biosensors and Bioelectronics p. 112123 (2020)
- 8) G. B. Osterhoudt, et al., Nature Materials 18, 471 (2019)
- 9) J. Coulter, et al., Phys. Rev. B 100, 220301 (2019)

Session II

Coherent control of strongly interacting spins in the solid-state

PI: Jeff Thompson, Princeton University

Program Scope

This proposal aims to study the coherent quantum behavior and dynamics of strongly interacting spin systems in the solid state. The central experimental tool is a technique that we have recently developed, which allows the spins of single Erbium (Er^{3+}) ion impurities in a crystal host to be optically initialized and measured through a nanophotonic cavity [1,2]. Importantly, the addressing of individual ions is achieved in the frequency domain [3], instead of spatially, allowing for control of individual spins with sub-10 nm separation, and therefore strong interactions.

Using this platform, we plan to carry out fundamental investigations of strongly interacting spin systems in solids, studying the interplay of different interaction mechanisms and developing spectroscopy techniques to identify the governing Hamiltonian in a particular instance of the system with randomly positioned spins. Furthermore, we will develop quantum control techniques to generate arbitrary effective Hamiltonians. This will allow many-body quantum states to be protected from noise and unwanted interactions, and is important to explore the potential of strongly interacting spin systems for quantum information processing and quantum-enhanced metrology.

Recent Progress

After submission of this proposal, but before the funding started, we made a very significant advance in controlling and manipulating closely-spaced Er^{3+} ions. In particular, using frequency domain addressing inside a nanophotonic cavity, instead of spatial addressing, we were able to coherently manipulate and perform single-shot readout on six individual Er^{3+} ions within a sub-diffraction-limited volume [3]. Although these ions were still too far apart to interact strongly (~80 nm on average), this technique has no fundamental lower bound on the ion separation that can be resolved, and will form the foundation of our future studies of strongly interacting Er^{3+} ion clusters.

In recent months, with BES support, we have also begun to explore interacting systems comprised of one Er^{3+} spin and up to three nearby nuclear spins. We are

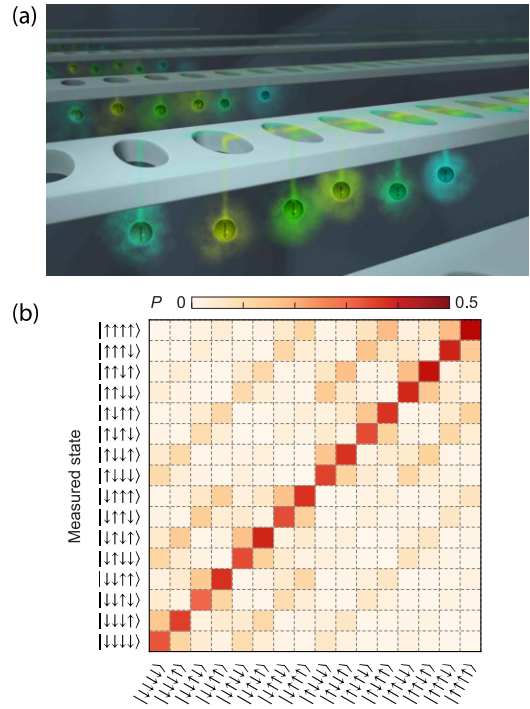


Figure 1 - (a) Schematic depiction of frequency-domain optical control of Er spins with small spacing (b) Simultaneous initialization and single-shot readout of four-ion spin states [3].

able to perform single-shot readout of all three nuclear spins using electron-nuclear CNOT gates, and also use the nuclear spins as a highly coherent probe of environmental noise. Through careful measurement of the interaction strengths, we have also been able to localize the relative position of the electron and one particular nuclear spin with sub- \AA^3 accuracy (on top of a separation of more than 20 \AA). We are currently preparing this work for publication, along with a companion theoretical paper describing novel approaches to electron-nuclear spin gates with $S=1/2$ electrons, which are quite distinct from recent work with $S=1$ spin systems like the NV center in diamond.

Furthermore, we have made significant progress on a key milestone for years 1 and 2, which is developing new host material platforms that will enable creating ensembles of highly coherent Er^{3+} ions with controllable density. Our current host crystal, Y_2SiO_5 (YSO), is not ideal in this regard as it is very noisy (from 100% abundant ^{89}Y nuclear spins) and has a >100ppb background of Er^{3+} impurities. However, Er can be implanted into a wide range of materials.

We have observed fluorescence and characterized the energy level structure of Er in nearly a dozen materials, including TiO_2 [4], MgO , CaWO_4 and related compounds, SrTiO_3 and related compounds, ZnS and ZnO . In most of these materials, we have developed satisfactory theoretical models for the spectrum based on a crystal field Hamiltonian, which gives us insight into the nature of the eigenstates, selection rules and dipole moment orientations. We have also fabricated nanophotonic devices on many of these materials. Recently, we have observed strongly Purcell-enhanced emission ($P > 1000$) from single implanted Er^{3+} ions in MgO , and have begun characterizing single ion spin properties and performing spin readout. Because of the low abundance of nuclear magnetic moments in this host compared to YSO, we anticipate longer spin coherence times. Equally importantly, we have found that we can implant Er ions at densities anywhere from 10^{15} cm^{-3} to 10^{19} cm^{-3} with similar properties (in particular, implantation yield and inhomogeneous optical linewidth). This is a promising starting point for creating strongly interacting spin clusters using patterned ion implantation.

Future Plans

In the coming year, we believe we will be able to leverage our results on single ion addressing in the frequency domain, and ion implantation of controlled densities of Er into highly coherent materials, to realize strongly interacting Er spin clusters with single particle addressability and control. This will allow us to begin work on our Year 3-4 milestones of developing

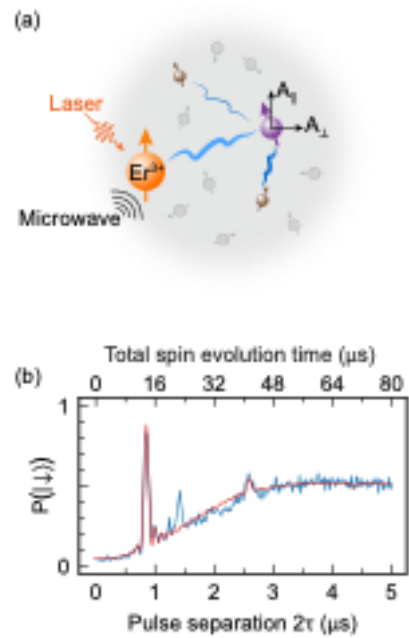


Figure 2 – (a) Schematic depiction of Er^{3+} interacting with three nuclear spins. (b) Sharp spectral signature of one of the nuclear spins, a ^1H (proton) observed as electron spin echo envelope modulation (ESEEM) on the Er^{3+} .

spectroscopy techniques to map out interactions in such an ensemble, which will also leverage our recent work on mapping out electron-nuclear spin interactions.

References

- [1] A. M. Dibos, M. Raha, C. M. Phenicie, and J. D. Thompson, *Atomic Source of Single Photons in the Telecom Band*, Phys. Rev. Lett. **120**, 243601 (2018).
- [2] M. Raha, S. Chen, C. M. Phenicie, S. Ourari, A. M. Dibos, and J. D. Thompson, *Optical Quantum Nondemolition Measurement of a Single Rare Earth Ion Qubit*, Nat. Commun. **11**, 1605 (2020).
- [3] S. Chen, M. Raha, C. M. Phenicie, S. Ourari, and J. D. Thompson, *Parallel Single-Shot Measurement and Coherent Control of Solid-State Spins below the Diffraction Limit*, Science **370**, 592 (2020).
- [4] C. M. Phenicie, P. Stevenson, S. Welinski, B. C. Rose, A. T. Asfaw, R. J. Cava, S. A. Lyon, N. P. de Leon, and J. D. Thompson, *Narrow Optical Linewidths in Erbium Implanted in TiO₂*, Nano Lett. **19**, 8928 (2019).

Publications

We have 3 publications in various stages of preparation with BES support, but none submitted yet.

Emergent Properties of Magnons Coupled to Microwave Photons

M. Benjamin Jungfleisch, Department of Physics and Astronomy, University of Delaware

Program Scope

The goal of the proposed research is to achieve precise control of light-matter interaction in magnetic hybrid systems and nanostructures, where the light part is carried by microwave photons, and the matter component is carried by magnons in engineered magnetic metamaterials. This includes implementing new measurement techniques for systematic studies of new material systems for efficient control of magnon-photon coupling. The underlying mechanisms of the interaction of magnons with photons, magnons with phonons, and magnons with magnons are determined, as these interactions are essential for utilizing magnons as coherent information transduction platforms between carriers. This project explores the mechanism by which non-uniform magnons interact with photons in the strong coupling regime, determines the spatial distribution of the hybrid excitations, and identifies how to dynamically and spatially control the interaction. Therefore, it is essential to broaden the range of material platforms and the measurement techniques that can be applied to understand magnon-photon coupling mechanisms. Controlling the collective properties of magnons is a transformative advance; as such, its impact extends beyond spintronics to the wider research arenas of quantum science. The gains are not limited to basic science - they might also help accelerate the development of applied engineering for quantum information applications.

Recent Progress

The development, optimization, and fabrication of high-quality microwave antenna structures are essential to achieve this objective, in particular planar antennas. Equally important is the optimization of the growth of low-damping magnetic materials, including insulators such as yttrium iron garnet (YIG) and metals such as NiFe, CoFe, and Heusler alloys.

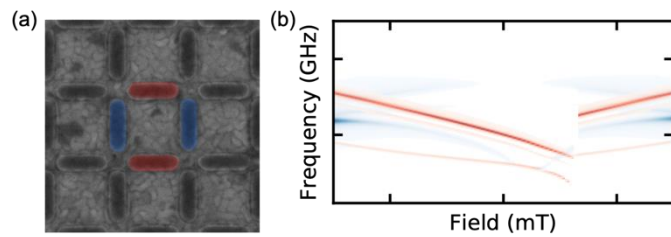


Fig. 1: Characterization of bicomponent artificial spin ices. (a) Scanning electron microscopy images of studied square lattices for bi-component artificial spin ice, NiFe – blue, CoFe – red. (b) Corresponding ferromagnetic resonance spectrum.

Recently, we studied angular-dependent spin dynamics in arrays of ferromagnetic nanodisks arranged on a honeycomb lattice using ferromagnetic resonance. We observed a rich spectrum of modes that is strongly affected by the microstate of the network. Comparing the experimental data with micromagnetic simulations revealed that different subsections of the lattice predominantly contribute to the high-frequency response of the array. This was confirmed by optical characterizations using micro-focused Brillouin light scattering (BLS). These findings

bring up new perspectives for designing magnonic devices that combine geometric frustration in gyrotrropic vortex crystals at low frequencies with magnonic crystals at high frequencies.

Recent work showed evidence for strong magnon-magnon coupling in various hybrid systems [1-4], including nanocross arrays [4] and arrays of nanomagnets [5]. These works have solely relied on inductive and electric detection methods. However, to understand the spatial distribution of the coupling, an optical detection scheme is advantageous. We recently studied the dynamic properties of a square array of interacting NiFe nano-ellipses (artificial spin ice) by three complementary techniques: (1) angular-dependent ferromagnetic resonance spectroscopy, (2) micro-focused BLS, and (3) micromagnetic modeling. We observe a spin-wave mode splitting facilitated by the inter-element interactions that depends on both the in-plane field angle and magnitude. The two-dimensional micromagnetic modeling results reveal that the split modes observed in the experiment reside in different regions of a single ASI vertex, suggesting that it is possible to control which portion of the network oscillates. In addition to the observed mode splitting, we show that the thermal spin-wave spectrum is sufficiently strong to be detected by micro-focused BLS and that using this approach, we can detect modes inaccessible by other commonly used methods such as microwave spectroscopy.

Moreover, we introduced a new kind of artificial spin ice based on two dissimilar ferromagnetic metals (NiFe and CoFe) arranged on complimentary lattice sites in a square lattice, Fig. 1. We show that the interaction between the lattice sites can be finely tuned and that ferromagnetic resonance spectroscopy is an effective tool to probe this interaction: We discover unique spectra attributed to each sublattice, and – even more importantly – the observation of intra- and inter-lattice dynamics facilitated by the distinct static magnetization properties of the two materials, Fig. 1. This is also a critical tuning mechanism for magnon-magnon coupling and could control hybridized magnonic states. The dynamics are systematically studied by angular-dependent broadband ferromagnetic resonance and confirmed by micromagnetic simulations. Our results demonstrate the ability to realize a novel type of two-dimensional magnonic crystals enabling new concepts in nano-magnonics. The results will serve as the basis for the planned studies on the band structure engineering in hybrid solid-state-based systems based on magnonic crystals.

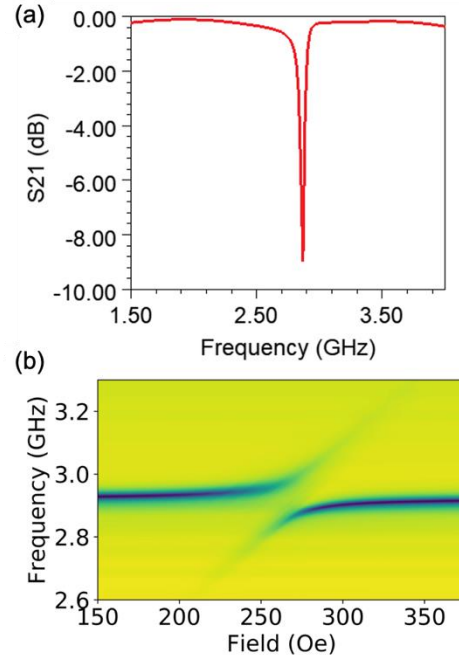


Fig. 2: Hybridization of magnon mode with microwave photon mode. (a) Results of our HFSS modeling results for a split-ring resonator. (b) Experimentally observed frequency vs magnetic field map for a splitting resonator loaded with a $2.4 \mu\text{m}$ YIG film shows an avoided crossing.

Furthermore, we employed HFSS to design and model various types of antenna structures such as split-ring resonators and double split-resonators. We tested and benchmarked our modeling results by comparing them to the literature. Exemplarily, Fig. 2(a) shows the simulated resonance behavior of a split-ring resonator. We fabricated various planar antenna structures with different dimensions, quality factors, and resonance frequencies based on these simulations. Preliminary experimental results obtained for a split-ring resonator loaded with a 2.4 μm -thick YIG film is shown in Fig. 2(b). This data suggest that we can observe magnon-photon coupling using these antennas.

Future Plans

We will continue the optimization and experimental realization of the planar antenna structures we have so far studied by HFSS modeling. The first inductive measurements of YIG thin films appear to be promising, see Fig. 2. The next step will be the characterization of the same samples by BLS spectroscopy:

1. We aim to reproduce the inductive measurements by BLS and optically detect magnon-photon coupling.
2. We will determine the spatial distribution of the magnonic hybrid excitation. Using this approach, we expect to determine the critical length scales and relevant time scales for magnon-polariton interaction.
3. We will identify the temporal characteristics of the hybridization by the recently implemented time-resolved measurement capabilities.

Upon successfully observing magnon-photon coupling by BLS in thick YIG films, we will focus on thin YIG films. We have already started the fabrication of nanometer-thick YIG films by pulsed-laser deposition. However, the growth requires further optimization to achieve a smaller Gilbert damping.

Furthermore, we plan to investigate magnon-magnon interaction in micropatterned YIG/NiFe bilayers by micro-focused BLS. Upon successfully demonstrating an avoided crossing between acoustic and optical modes in the bilayer system, we will explore the magnon-magnon coupled system's emergent properties when strongly coupled to a planar microwave antenna. In particular, we will seek to understand the temporal dynamics of the triple resonant excitation using time-resolved BLS.

References

- [1] Y. Xiong, Y. Li, M. Hammami, R. Bidthanapally, J. Sklenar, X. Zhang, H. Qu, G. Srinivasan, J. Pearson, A. Hoffmann, V. Novosad, and W. Zhang, *Sci. Rep.* **10**, 070101 (2020).
- [2] D. MacNeill, J. T. Hou, D. R. Klein, P. Zhang, P. Jarillo-Herrero, and L. Liu, *Phys. Rev. Lett.* **123**, 047204 (2019).

- [3] Y. Li, W. Cao, V. P. Amin, Z. Zhang, J. Gibbons, J. Sklenar, J. Pearson, P. M. Haney, M. D. Stiles, W. E. Bailey, V. Novosad, A. Hoffmann, and W. Zhang, Phys. Rev. Lett. **124**, 117202 (2020).
- [4] K. Adhikari, S. Sahoo, A. K. Mondal, Y. Otani, and A. Barman, Phys. Rev. B **101**, 054406 (2020).
- [5] J. C. Gartside, A. Vanstone, T. Dion, K. D. Stenning, D. M. Arroo, H. Kurebayashi, and W. R. Branford, arXiv:2101.07767 (2021).
- [6] G. B. G. Stenning, G. J. Bowden, L. C. Maple, S. A. Gregory, A. Sposito, R. W. Eason, N. I. Zheludev, and P. A. J. de Groot, Optics Express **21**, 1456 (2013).

Publications

- [1] S. Lendinez, M. T. Kaffash, and M. B. Jungfleisch. Emergent spin dynamics enabled by lattice interactions in a bicomponent artificial spin ice, Nano Lett., in press, <https://dx.doi.org/10.1021/acs.nanolett.0c03729> (2021).
- [2] M. B. Jungfleisch. ‘Inelastic scattering of light by spin waves’ in “Optomagnonic structures: Novel architectures for simultaneous control of light and spin waves”, pages 175 - 211, edited by E. Almpanis, Word Scientific Publishing, 2021.
- [3] S. Lendinez, J. E. Pearson, A. Hoffmann, V. Novosad, and M. B. Jungfleisch. Temperature-dependent collective magnetization reversal in a network of ferromagnetic nanowires, AIP Adv. **11**, 025222 (2021). *Selected as Featured Article in AIP Advances*.
- [4] W. Bang, R. Silvani, A. Hoffmann, J. B. Ketterson, F. Montoncello, and M. B. Jungfleisch. Ferromagnetic resonance in clusters and of lattices macro-dipoles in two dimensions: measurements and simulations, J. Phys.: Condens. Matter **33**, 065803 (2021).
- [5] W. Bang, J. Sturm, R. Silvani, M. T. Kaffash, A. Hoffmann, J. B. Ketterson, F. Montoncello, and M. B. Jungfleisch. Influence of vertex region on spin dynamics in artificial Kagome spin ice, Phys. Rev. Applied **14**, 014079 (2020). *Selected as Editor’s Suggestion*.
- [6] S. Lendinez, T. Polakovic, J. Ding, M. B. Jungfleisch, J. E. Pearson, A. Hoffmann, and V. Novosad, Spin-orbit-torque-driven vortex dynamics in a single microdisk, J. Appl. Phys. **127**, 243904 (2020).
- [7] M. T. Kaffash, W. Bang, S. Lendinez, A. Hoffmann, J. B. Ketterson, and M. B. Jungfleisch. Control of spin dynamics in artificial honeycomb spin-ice-based nanodisks, Phys. Rev. B **101**, 174424 (2020).

Observation of the Modification of Quantum Statistics in Plasmonic Systems

Omar S. Magana-Loaiza, Quantum Photonics Laboratory, Department of Physics & Astronomy, Louisiana State University, Baton Rouge, LA 70803, USA

Program Scope

This research program aims to develop hybrid photonic-plasmonic networks for quantum transport simulation. This novel platform for quantum simulation relies on the exquisite control of multiphoton scattering through dissipative near fields induced by single surface plasmons [1]. The presence of dissipative near fields provides additional paths that increase the complexity of multiparticle interactions in the network [1]. These exotic dynamics will be exploited to speed-up the quantum simulation of light transport. This quantum technology has important implications for the development of new schemes for light harvesting [2, 3].

Recent Progress

The first milestone of this four-year research program is devoted to identifying novel multiparticle quantum dynamics induced by dissipative near fields in hybrid photonic-plasmonic networks. In the past six months, the PI together with his postdoc and two students have made important progress towards the completion of the first milestone. *For the first time, the team has demonstrated that multiparticle scattering mediated by dissipative near fields enables the modification of the quantum statistics of plasmonic systems.* This possibility represents a paradigm shift in the understanding of the quantum properties of plasmonic systems [2, 3]. As described below, the team has solid experimental results and plans to complete the first milestone in the next few months. There is an additional set of measurements that will be collected. This material will be used to prepare a research article.

For almost two decades, it has been believed that the quantum statistical properties of bosons are preserved in plasmonic systems [2, 3]. This idea has been stimulated by experimental work reporting the possibility of preserving nonclassical correlations in light-matter interactions mediated by scattering among photons and plasmons [2]. Furthermore, it has been assumed that similar dynamics underlies the conservation of the quantum fluctuations that define the nature of light sources [3]. *We demonstrate that quantum statistics are not always preserved in plasmonic systems and report the first observation of their modification.* We found that plasmonic near-field effects enable the manipulation of multiparticle scattering. This possibility leads to a modification of the statistical properties of hybrid photonic-plasmonic circuits. We quantify the change in the quantum statistical fluctuations through the degree of second-order coherence. The reported observations are validated through the quantum theory of optical coherence [4].

The team initiated this study motivated by the idea that electromagnetic near fields can be used to control scattering among multiple interfering particles. This concept is illustrated in **Fig. 1a**, this fundamental process enables the manipulation of the quantum statistical properties of

hybrid photonic-plasmonic systems. The team built the plasmonic structure in **Fig. 1b** to experimentally demonstrate this effect. The experimental setup is shown in **Fig. 1c**.

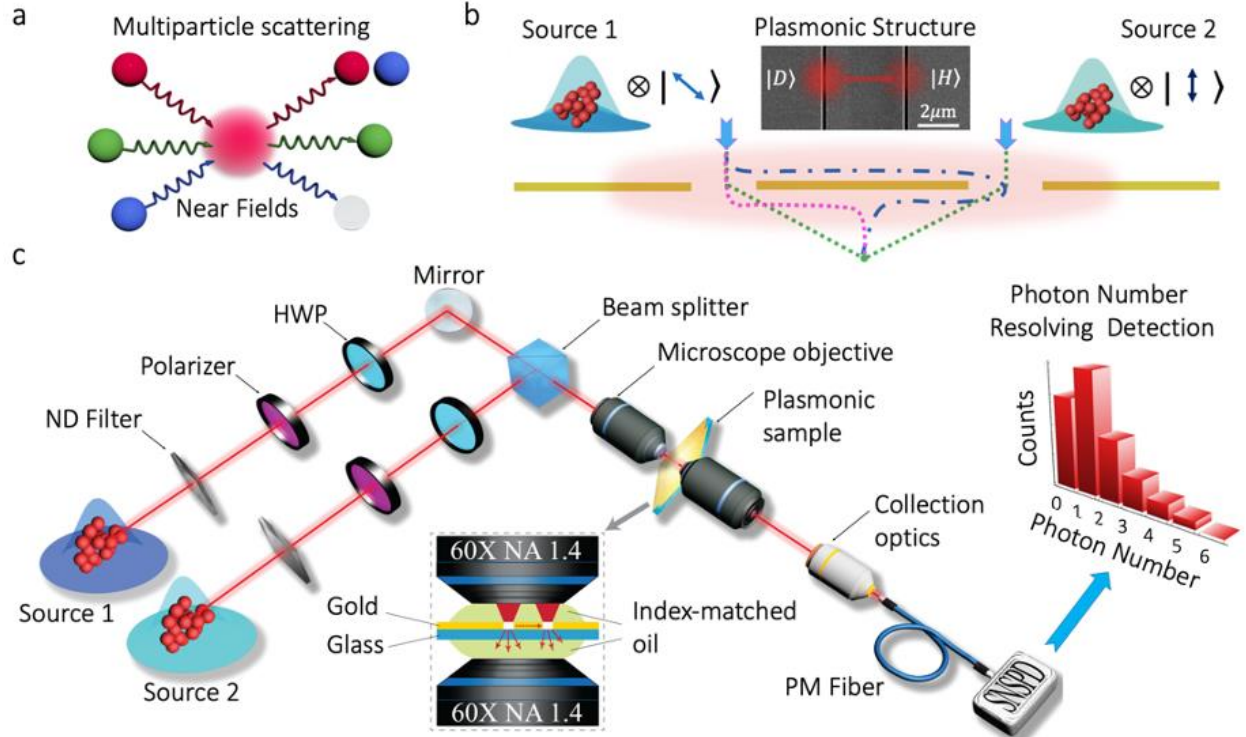


Figure 1. The possibility of controlling multiparticle scattering through electromagnetic near fields is shown in **a**. This idea is implemented through the plasmonic nanostructure shown in **b**. The fabricated sample is illuminated by two thermal sources of light with specific polarizations. The strength of the plasmonic near-fields is controlled through the polarization of the multiphoton sources. The plasmonic near-field is always polarized in the horizontal plane. The experimental setup for the observation of the modification of quantum statistics in plasmonic systems is shown in **c**. We generate two independent thermal beams using a rotating ground glass (not shown). The polarization of these two thermal beams is individually controlled by a polarizer (Pol) and half-wave plate (HWP). Then, the two sources are injected into a beam splitter (BS) and then focused onto the gold sample through an oil-immersion objective. The refractive index of the immersion oil matches that of the glass substrate creating a symmetric index environment around the gold film. The transmitted photons are collected with another oil-immersion objective. We measure the photon statistics in the far field by performing photon-number-resolving detection using superconducting nanowire single-photon detectors (SNSPDs).

The modification of the photon-number distribution induced by the system described in **Fig. 1b** can be described using the quantum theory of coherence as described by Glauber [4]. For this purpose, we first define the P-function associated to the field produced by the indistinguishable combination of the vertical components of the photonic modes of the two sources

$$P_s(\alpha) = \int P_{V_1}(\alpha - \alpha')P_{V_2}(\alpha')d\alpha'. \quad (1)$$

This expression enables one to obtain the following photon-number distribution for the combined sources $p_s(n) = [(1 + \eta)\bar{n}]^n/[1 + (1 + \eta)\bar{n}]^{n+1}$. In this case η represents the number of vertically-polarized photons given the initial polarization angle θ of one of the sources, see **Fig. 1b**. The mean photon number of the sources and the photon number are represented by \bar{n} and n ,

respectively. To account for the contributions from the horizontally polarized plasmonic fields $p_{pl}(m)$, we write the final photon-number distribution at the detector as $p_f(n) = \sum_{m=0}^n p_s(n-m)p_{pl}(m)$. This expression permits one to obtain a final photon-number distribution $p_f(n)$ which is defined by the strength of the plasmonic near fields \bar{n}_{pl}

$$p_f(n) = \sum_{m=0}^n \frac{\bar{n}_s^{n-m} \bar{n}_{pl}^m}{(\bar{n}_s + 1)^{n-m+1} (\bar{n}_{pl} + 1)^{m+1}}. \quad (2)$$

This probability function indicates the possibility of modifying the degree of coherence of a hybrid photonic-plasmonic system. Remarkably, it is possible to use plasmonic near fields to induce coherence in the multiparticle system. As shown in **Fig. 2**, the PI and his team have performed experimental measurements that confirm the validity of the theory described above. The results in **Fig. 2** show for the first time the modification of quantum statistics in plasmonic systems.

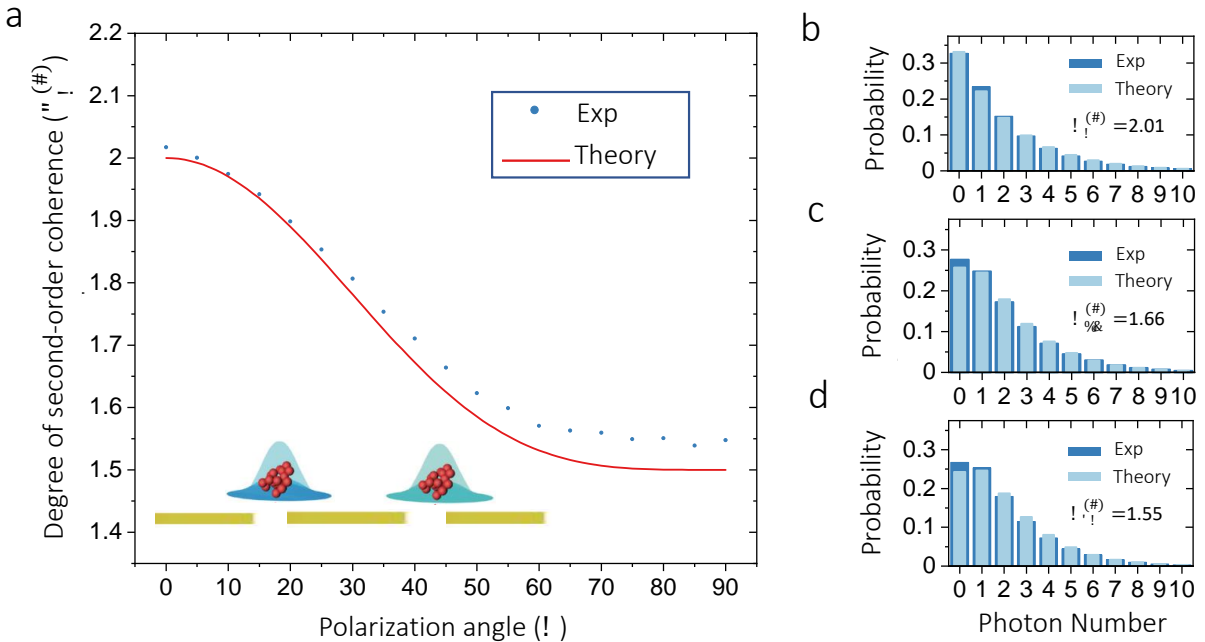


Figure 2. The possibility of modifying and controlling quantum statistics of plasmonic systems is shown in panel **a**. Here, the team plots experimental data together with a theoretical prediction for the degree of second-order coherence. The theoretical model is based on the photon-number distribution in Eq. 2. As demonstrated in **b**, the photon-number distribution is thermal for the system in the absence of near-fields ($\theta = 0^\circ$). However, an anti-thermalization effect takes place as the strength of the plasmonic near fields is increased ($\theta = 45^\circ$), see **c**. Remarkably, as shown in **d**, the degree of second-order coherence of the hybrid photonic-plasmonic system is 1.5 when the plasmonic near fields are strong ($\theta = 90^\circ$).

For more than two decades, the quantum plasmonics community has assumed that the quantum statistical properties of hybrid photonic-plasmonic systems are always preserved [2, 3]. The work reported by the PI in this document changes this paradigm and demonstrates the enormous potential of hybrid photonic-plasmonic platforms for applications in quantum information science.

Future Plans

The team will measure the spatial profile of photons after the plasmonic structure in **Fig. 1 b.** This will be measured as a function of the strength of the plasmonic near fields. These properties will be used to study the single-mode nature of the interactions described above. This information will enable the team to finalize the preparation of a scientific article reporting these achievements. As planned in the proposal, the team expects to submit this paper for publication before the summer.

The completion of this first goal will place the PI and his team in a suitable position to successfully demonstrate the second trust which aims to implement multiparticle control of Hong-Ou-Mandel interference in plasmonic networks. Both milestones are essential to demonstrate quantum transport simulation through the control electromagnetic near fields in hybrid photonic-plasmonic networks. This will be demonstrated in the third and fourth years of the research program.

References

- [1] O. S. Magana-Loaiza et al., Nature Communications, 7, 13987 (2017).
- [2] M. S. Tame et al., Nature Physics 9(6), 329 (2013).
- [3] C. You, C. Nellikka, I. De Leon, and O.S. Magana-Loaiza, Nanophotonics 9(6), 1243 (2020).
- [4] R. J. Glauber, Physical Review 131, 2766 (1963).

Publications

In addition to the work reported in this document, postdoctoral researcher (Chenglong You), graduate student (Mingyuan Hong), and undergraduate student (Joshua Fabre), have published the following papers in the last six months. Funding from DOE is acknowledged in the following papers:

1. N. Bhusal*, S. Lohani, C. You*, M. Hong, J. Fabre, P. Zhao, E. M. Knuston, R. T. Glasser, and O. S. Magana-Loaiza, Advanced Quantum Technologies 2000103 (2021).
2. M. A. Quiroz-Juarez, C. You, J. Carrillo-Martinez, D. Montiel-Alvarez, J. L. Aragon, O. S. Magana-Loaiza*, and R. de J. Leon-Montiel*, Physical Review Research 3(1), 013010 (2020).
3. O.S. Magana-Loaiza*, Physics Today 73, 10, 30 (2020).
4. C. You, M. Hong, P. Bierhorst, A. E. Lita, S. Glancy, E. Knill, S. W. Nam, R. P. Mirin, O. S. Magana-Loaiza*, and T. Gerrits, arXiv 2011.02454 (2020).

In reference 2, the team demonstrated an analog device for quantum simulation using electrical oscillators. This information will be useful to complete the third and fourth milestones. The work reported in reference 4 will be valuable for the team to demonstrate the second milestone.

DNA-Controlled Dye Aggregation – A Path to Create Quantum Entanglement

William B. Knowlton, Micron School of Materials Science and Engineering and Department of Electrical and Computer Engineering, Boise State University

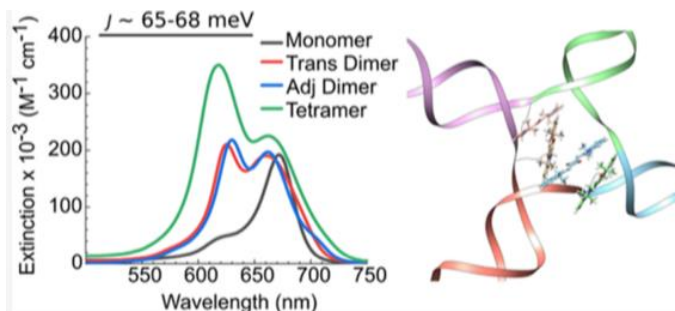
Program Scope

The overarching research goal is to assemble dye aggregates via deoxyribonucleic acid (DNA) templating and to study how fundamental properties of molecular exciton delocalization and coherence can be controlled to enable quantum entanglement. Our research is motivated by the hypothesis that exciton delocalization and exciton-exciton interactions can be tuned through the controlled arrangement of dyes into aggregates of dyes to create and control exciton quantum entanglement that is at the center of the DOE's quantum information science (QIS) initiative. The technical approach involves experiment, theory development, and computational modeling. These approaches are accomplished in an integrated and complementary manner across our now five research teams. Squaraine (SQ) and squarainerotaxane (SR) dyes assembled into dye aggregates by the deoxyribonucleic acid (DNA) self-assembly process by which a variety of DNA scaffolded architectures can be used to assemble dye aggregates; they are the primary materials system of interest. Dyes are functionalized to assess their structure-property relationships, the aggregates characterized via steady-state and transient ultrafast spectroscopy techniques, dye orientation precision assessed by single molecule microscopy approaches, and aggregate properties modeled through our in-house Kühn-Renger-May (KRM)¹ model tool that uses spectral data to determine the spatial orientation and proximity of dyes within an aggregate. Our results to date have indicated that SQ and SR-templated dyes hold significant promise for use in creating, measuring, and controlling quantum entanglement.

Recent Progress

Our grant started on August 15, 2019. We hired several new professional staff early on and brought on board a number of graduate students, many of whom have been heavily involved in our initial research outcomes. The three projects briefly described here have been accomplished despite significant impacts due to COVID-19 on access to laboratory facilities, visa processing, and subsequent hiring of personnel.

For the first project, we examined the ability of SQ dyes to undergo exciton delocalization when aggregated via a DNA Holliday junction (HJ) template.² We chose a commercially available indolenine SQ dye for the study given its strong structural resemblance to Cy5, a commercially

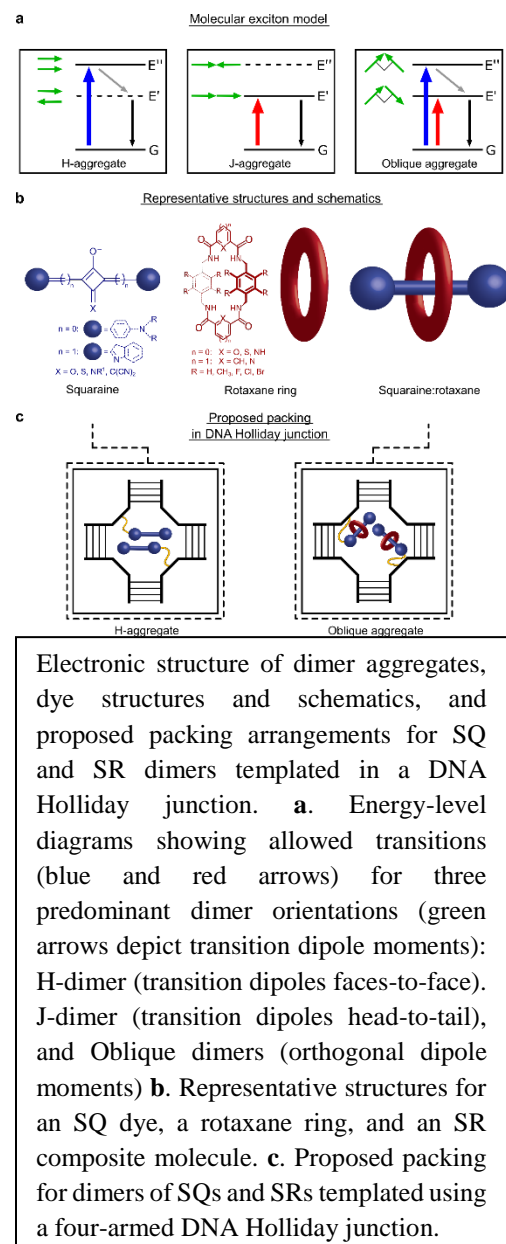


Right: Conceptual schematic of a DNA-templated SQ tetramer covalently tethered to and templated by a DNA HJ.
Left: Absorbance spectra of two SR dimer aggregates and a tetramer aggregate relative to a SR monomer all templated by a HJ. J , the exciton hopping parameter, refers to the transition dipole-dipole coupling strength between the SR dyes in the aggregate and is responsible for exciton delocalization. Note that J is over 2 times greater than kT at room temperature.²

available cyanine dye previously shown to undergo exciton delocalization in DNA HJs.^{3, 4} Three types of DNA-dye aggregate configurations—transverse dimer, adjacent dimer, and tetramer—were investigated. Signatures of exciton delocalization were observed in all dye-DNA aggregates. In particular, we observed a strong blue shift and Davydov splitting in our steady-state absorption spectroscopy measurements, and exciton-induced features also were evident in circular dichroism (CD) spectroscopy. Strongly suppressed fluorescence emission provided additional, indirect evidence for exciton delocalization in these DNA-templated dye aggregates. The excitonic hopping strength (J) within indolenine SQ dyes was comparable to that of the analogous Cy5 DNA-templated aggregate. The SQ aggregates adopted primarily an H-type (dyes oriented parallel to each other) spatial arrangement.

The second project involved demonstrating that adding rotaxane rings to SQ dyes templated with DNA promotes a difficult to achieve oblique packing arrangement with highly desirable excitonic optical properties.⁵ Specifically, dimers of these SR dyes exhibit an absorption spectrum with near-equal intensity, excitonically split absorption bands. Theoretical analysis using our KRM model tool indicates that the transitions are mostly electronic in nature and only have similar intensities over a narrow range of packing angles. Compared with SQ dimers, SR dimers also exhibit extended excited-state lifetimes and less structural heterogeneity. The approach proposed here of adding a macrocycle to a dye to mitigate interactions of the dye with the bath (environment) may be generally useful for optimizing excitonic materials for a variety of applications ranging from solar energy conversion to quantum information science.

To complement the two preceding experimental projects, a third project explored the role of substituent effects on the electronic and photophysical properties of SQ dyes from a theoretical perspective. To date, few studies of this nature have been accomplished. *Ab initio* theoretical methods were applied to determine the preceding effects for a series of nine different SQ dyes. In addition to electronic properties, solvation free energy was investigated as an insight into changes in hydrophobic behavior from substituents. The study considers the role of molecular symmetry on these properties via conformer and substituent placement. We expect submission of this work for publication soon.⁶



Future Plans

Given our promising initial results, we plan to expand on the previous studies in several ways. In particular, we are well underway in designing custom-made SQ and SR dyes whose specific structures are informed by our ongoing theoretical modeling using density functional theory (DFT), time-dependent DFT, and molecular dynamics, as well as our experimental results. Using custom dyes of our own design enables us to fine-tune the dye structure-property relationships that allow us to optimize specific parameters of interest—such as J —that are important for entanglement. We are assessing a series of differentially functionalized SQ dyes and with the SR dyes also assessing different structural configurations of the rotaxane ring for the effect on dye aggregate behavior.

At the same time, given our jurisdiction as a DOE EPSCoR state, we are leveraging DOE and other funding sources to build our capacity in dye synthesis, DNA construct design, ultrafast laser spectroscopy and single molecule microscopy instrumentation and techniques, and Frenkel exciton theory development as it relates to entanglement. Our recent move into the new Micron Center for Materials Research at Boise State University and its state-of-the-art laser labs will further enhance our measurement capabilities for determining the coherence of key parameters of interest that relate to entanglement.

References

1. O. Kühn, T. Renger and V. May, *Theory of exciton-vibrational dynamics in molecular dimers*, **Chemical Physics**, **204** (1), 99-114 (1996).
2. O. A. Mass, C. K. Wilson, S. K. Roy, M. S. Barclay, L. K. Patten, E. A. Terpetschnig, J. Lee, R. D. Pensack, B. Yurke and W. B. Knowlton, *Exciton delocalization in indolenine squaraine aggregates templated by DNA holliday junction scaffolds*, **The Journal of Physical Chemistry B**, **124** (43), 9636-9647 (2020).
3. B. L. Cannon, L. K. Patten, D. L. Kellis, P. H. Davis, J. Lee, E. Graugnard, B. Yurke and W. B. Knowlton, *Large davydov splitting and strong fluorescence suppression: An investigation of exciton delocalization in DNA-templated holliday junction dye aggregates*, **The Journal of Physical Chemistry A**, **122** (8), 2086–2095 (2018).
4. B. L. Cannon, D. L. Kellis, L. K. Patten, P. H. Davis, J. Lee, E. Graugnard, B. Yurke and W. B. Knowlton, *Coherent exciton delocalization in a two-state DNA-templated dye aggregate system*, **The Journal of Physical Chemistry A**, **121** (37), 6905-6916 (2017).
5. M. S. Barclay, S. K. Roy, J. S. Huff, O. A. Mass, D. B. Turner, C. K. Wilson, D. L. Kellis, E. A. Terpetschnig, J. Lee, P. H. Davis, B. Yurke, W. B. Knowlton and R. D. Pensack, *Rotaxane rings promote oblique packing and extended lifetimes in DNA-templated molecular dye aggregates*, **Communications Chemistry**, **4** (19), 1-11 (2021).
6. G. Barcenas, A. Biaggne, K. Wilson, O. Mass, W. Knowlton, B. Yurke, J. Lee, R. Pensack and L. Li, *First-principles studies of substituent effect on squaraine dyes*, (in preparation), will submit to **RSC Advances (Royal Society of Chemistry)** (2021).

Publications

*Denotes a graduate student

1. O. A. Mass, C. K. Wilson, S. K. Roy*, M. S. Barclay, L. K. Patten, E. A. Terpetschnig, J. Lee, R. D. Pensack, B. Yurke and W. B. Knowlton, *Exciton delocalization in indolenine squaraine aggregates templated by DNA holliday junction scaffolds*, **The Journal of Physical Chemistry B**, **124** (43), 9636–9647 (2020). doi.org/10.1021/acs.jpcb.0c06480
2. M. S. Barclay, S. K. Roy*, J. S. Huff*, O. A. Mass, D. B. Turner, C. K. Wilson, D. L. Kellis, E. A. Terpetschnig, J. Lee, P. H. Davis, B. Yurke, W. B. Knowlton and R. D. Pensack, *Rotaxane rings promote oblique packing and extended lifetimes in DNA-templated molecular dye aggregates*, **Communications Chemistry**, **4** (19), 1–11 (2021). doi.org/10.1038/s42004–021–00456–8
3. G. Barcenas*, A. Biaggne*, K. Wilson, O. Mass, W. Knowlton, B. Yurke, J. Lee, R. Pensack and L. Li, *First-principles studies of substituent effect on squaraine dye s*, (in preparation), will submit to **RSC Advances (Royal Society of Chemistry)** (2021).

Electron Transfer in Heterostructures based on Two-Dimensional Materials

Hui Zhao, University of Kansas, Lawrence, Kansas

Program Scope

The discovery of graphene has created an exponentially growing interest in 2D materials, which are attractive to both fundamental research and applications [1]. These materials provide a new route to fabricating van der Waals multilayers, which can potentially transform material discovery [2-4]. One key issue in van der Waals multilayers is the interlayer electron transfer, which is the fundamental process to integrate the individual layer for harnessing emergent properties for various electronic and optoelectronic applications [5]. Recently, efficient interlayer charge transfer has been generally demonstrated in hetero-bilayers formed by transition metal dichalcogenides [6,7], illustrating the feasibility of integrating multiple monolayers into a van der Waals stack. This program aims to provide experimental results for developing fundamental understanding on electron transfer, including charge and energy transfer, in van der Waals multilayer structures. The research goal is achieved through three thrusts. In Thrust 1, the material library to fabricate van der Waals heterostructures with novel electron transfer properties is expanded. Thrust 2 focuses on understanding electron transfer through thin barriers in van der Waals multilayers. In Thrust 3, effect of electric field on electron transfer is studied.

Recent Progress

In the first 6 months of this program, we have made progress in all three thrusts.

Thrust 1: Electron transfer in crystallographically incommensurate heterostructures

We performed steady-state spectroscopic and time-resolved pump-probe measurements on photocarrier dynamics of a number of 2D materials to evaluate their potential integration with other 2D materials with novel electron transfer properties. These materials include $\text{Bi}_2\text{O}_2\text{Se}$, MoO_3 , AsSbS_3 , GeS , TlGaS_3 , and PtSe_2 . For each material, we achieved transient absorption measurements of their photocarrier dynamics through either interband resonant absorption or Drude-like intraband absorption. Hot carrier dynamics and carrier lifetime were deduced. These materials bring new elements to several fronts of interlayer electron transfer. They can form type-I, type-II, and type-III band alignments with the most commonly studied transition metal dichalcogenide (TMD) monolayers, allowing a comprehensive study on charge and energy transfer in different potential landscapes. We observed ultrafast charge transfer between bulk TlGaS_3 and monolayer WS_2 [8]. We obtained unpublished results on ultrafast charge transfer between monolayer $\text{Bi}_2\text{O}_2\text{Se}$ and TMD monolayers, and between monolayer PtSe_2 and TMD monolayers. Furthermore, we exfoliated MoO_3 monolayers and are trying to make their heterostructures with TMD monolayers to form type-III band alignments.

Thrust 2: Carrier tunneling and energy transfer through thin barriers

We time-resolved tunneling of holes between two MoSe₂ monolayers through a monolayer barrier of WS₂. In this unpublished work, we designed and fabricated a 4-layer heterostructure with a layer sequence of MoSe₂/WS₂/MoSe₂/graphene, and with a band alignment as shown in Fig. 1(a). We used a 100-fs and 1.85-eV pump pulse to excite the two MoSe₂ layers. Since the electrons are expected to transfer to WS₂ within 100 fs [9] and the holes in the second MoSe₂ layer can transfer to graphene on a sub-picosecond time scale [10], after these transient processes, the population of the electrons and holes among the four layers will reach the state illustrated in Fig. 1(a). The rest of the population decay is dominated by the tunneling of the holes from the first to the second MoSe₂ layer, which is time-resolved by measuring differential reflectance of a 1.59-eV probe pulse that is tuned to the optical bandgap of MoSe₂.

Panel (b) of Fig. 1 summarizes the key results of our measurements. Since the differential reflectance signal ($\Delta R/R_0$) is approximately proportional to the carrier density in MoSe₂, its decay reflects the loss of hole population. To analyze the dynamics, each curve is fit by a multiple-exponential function (not shown). We found that in all heterostructures without the WS₂ barrier, the majority of the

signal decays on a 2-ps time scale, due to the fast electron and hole transfer in these heterostructures. However, the decay time constant of the four-layer sample is about 17 ps. Along with additional control experiments and analysis, we attributed the 17-ps process to the tunneling process of the holes from the first to the second MoSe₂ layers across the WS₂ barrier, followed by their rapid transfer to graphene. The tunneling rate deduced is also consistent with a simple tunneling model.

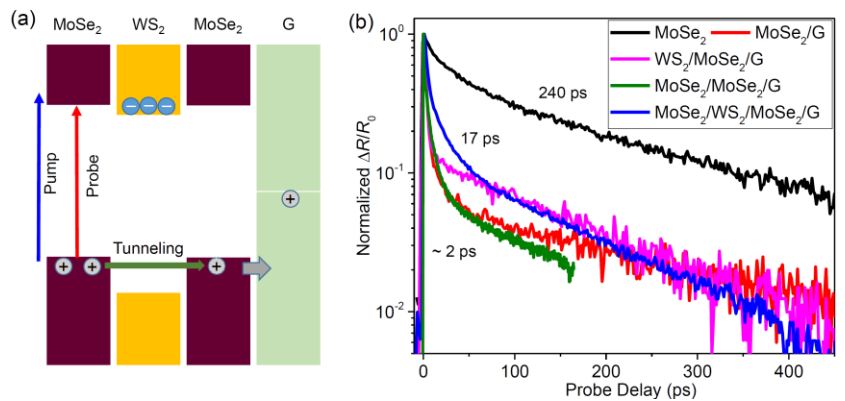


Figure 1: (a) Schematics of the four-layer heterostructure and hole tunneling. (b) Normalized differential reflectance signal measured from different samples as labeled.

In our next steps of this thrust, the barrier thickness will be used as an important parameter. As such, we studied how the interlayer electron transfer property evolves as the layer thickness is changed. By using electron transfer from MoSe₂ to MoS₂ as an example, we showed that the electron transfer time changes from sub-100-fs in 1L-MoSe₂/1L-MoS₂ and 1L-MoSe₂/2L-MoS₂ to several picoseconds in 1L-MoSe₂/3L-MoS₂ [11]. The significant thickness dependence was hypothesized as an effect of the phonon-assisted charge transfer. This result has important implications for our future studies on tunneling through multilayer barriers.

Thrust 3: Effect of electric field on electron transfer

We proposed two approaches to study the effect of electric fields on electron transfer in van der Waals multilayers, by using (i) optically generated fields and (ii) material built-in fields. In the first 6 months, we have made progress on both fronts.

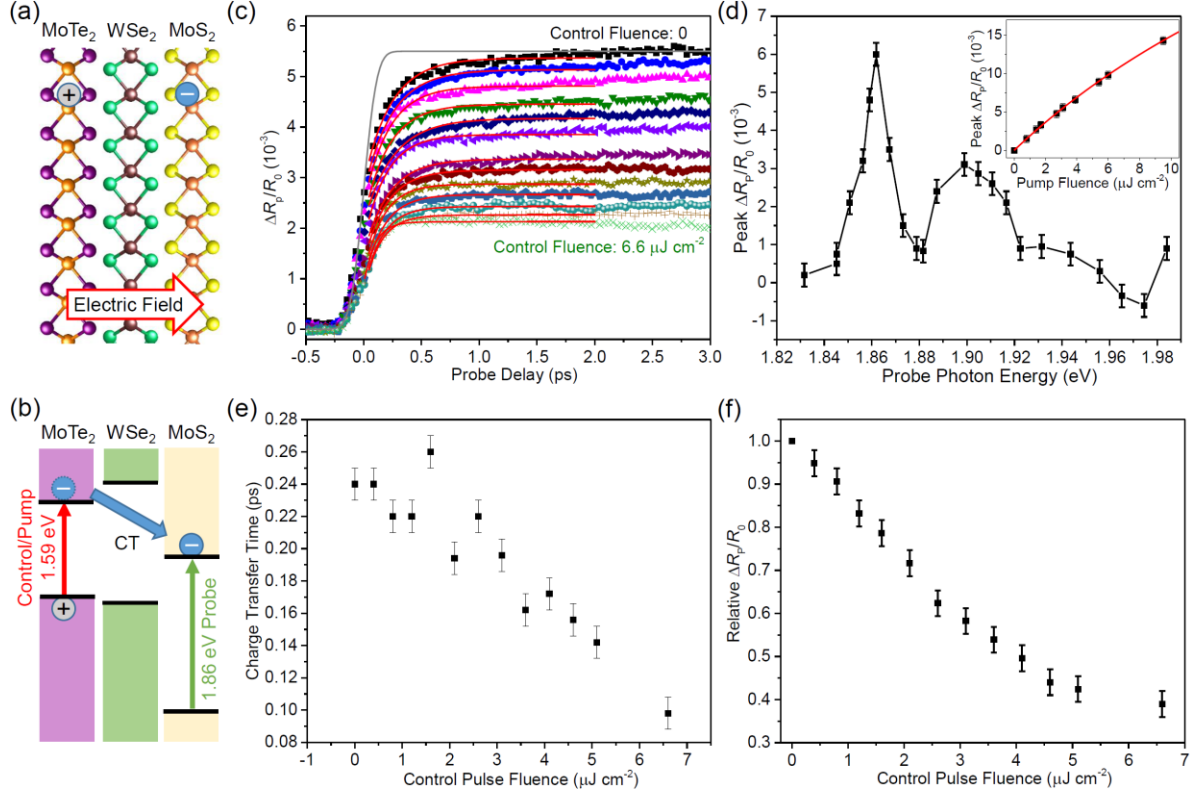


Figure 2: (a) and (b) Schematics of the three-pulse technique and charge transfer in the MoTe₂/WSe₂/MoS₂ trilayer heterostructure. (c) Differential reflectance signal with 1.59-eV control/pump and 1.86-eV probe pulses. The control fluence increases from top to bottom. The red curves are fits. The gray curve represents the instrumental response. (d) Peak differential reflectance signal as a function of the probe photon energy (the main panel) and the pump fluence (the inset). (e) Charge transfer time as a function of the control fluence. (f) Relative differential reflectance signal as a function of the control fluence.

With the first approach, we used a three-pulse control-pump-probe technique to study charge transfer under the influence of photo-generated carriers and fields in three heterostructures, MoSe₂/MoS₂, MoSe₂/WS₂, and MoTe₂/WSe₂/MoS₂. Here we use the last heterostructure as an example, as illustrated in Fig. 2(a). A 1.59-eV control pulse first excites the MoTe₂ layer. As shown in Fig. 2(b), electrons are expected to transfer to MoS₂, setting up layer-separated electron and hole populations in MoS₂ and MoTe₂ and an electric field pointing from MoTe₂ to MoS₂. Several picoseconds later, a 1.59-eV pump pulse excites electrons in MoTe₂ again, and the electron transfer to MoS₂ under the influence of the field is studied by monitoring the electron population in MoS₂ by a 1.86-eV probe. As shown in Fig. 2(c), as the fluence of the control pulse (and thus the photo-generated electric field) is increased, the signal magnitude decreased and the signal rise is faster.

By fitting the rise of each curve with a charge transfer model, we found that the charge transfer time decreases with the control fluence, as summarized in Fig. 2(e). Furthermore, the reduction of the peak signal by the control pulse, as shown in Fig. 2(f), illustrates that the electric field pushes the electron wavefunction in MoS₂ towards the van der Waals gap, and thus reduces the dipole moment of the interlayer excitons.

On the second approach of utilizing material built-in field, we obtained Janus MoSSe and WSSe monolayers through a collaboration with ORNL. Janus TMDs were first synthesized in 2017 [12,13]. These monolayer structures are composed of a transition metal layer sandwiched by two different chalcogen layers. The asymmetry in the vertical direction of the structure results in a built-in electric field. As our first step, we studied the optical properties and the excitonic dynamics in Janus MoSSe and WSSe monolayers and compare them with their pristine counterparts. We found that the exciton radiative recombination lifetimes in Janus structures are significantly longer than those in pristine TMDs due to the separation of the electron and hole wavefunctions. This result demonstrated the strong built-in field in such structures [14].

Future Plans

Building on the progress, we will continue pursuing the proposed research activities. In Thrust 1, we will study electron transfer in heterostructures involving the identified new 2D materials. In Thrust 2, we will design heterostructures and study carrier tunneling through barriers of TMDs, h-BN, and MoO₃. In Thrust 3, we will study electron transfer formed by Janus and pristine TMDs to probe the effect of the built-in fields on electron transfer. With optically generated fields, we will study four- and five-layer heterostructures to separate the field and population regions, so that their effects on electron transfer can be independently studied.

References

- [1] K. S. Novoselov *et al.* Science, 353, aac9439 (2016).
- [2] A. K. Geim and I. V. Grigorieva. Nature, 499, 419 (2013).
- [3] Y. Liu *et al.* Nat. Rev. Mater., 1, 16042 (2016).
- [4] K. F. Mak and J. Shan. Nat. Photo., 10, 216 (2016).
- [5] C. H. Jin *et al.* Nat. Nanotechnol., 13, 994 (2018).
- [6] X. Hong *et al.* Nat. Nanotechnol., 9, 682 (2014).
- [7] F. Ceballos, M. Z. Bellus, H. Y. Chiu, and H. Zhao. ACS Nano, 8, 12717 (2014).
- [8] Y. Fu *et al.* ACS Appl. Nano Mater., 3, 8702 (2020).
- [9] F. Ceballos, M. Z. Bellus, H. Y. Chiu, and H. Zhao. Nanoscale, 7, 17523 (2015).
- [10] M. Asadi *et al.* Nat. Commun., 5:4470, 2014.
- [11] T. Zheng *et al.* ACS Appl. Mater. Interfaces, 13, 6489 (2021).
- [12] A. Y. Lu *et al.* Nat. Nanotechnol., 12, 744 (2017).
- [13] J. Zhang *et al.* ACS Nano, 11, 8192 (2017).
- [14] T. Zheng *et al.* Nano Lett., 21:931–937, 2021.

Publications

1. Y. Fu, D. He, J. He, X. Han, J. Bai, Y. Wang, and H. Zhao, Photocarrier Dynamics in TlGaS₂ Nanoflakes and van der Waals Heterostructures with Hexagonal Boron Nitride and WS₂ Nanoflakes: Implications for Optoelectronic Applications, ACS Applied Nano Materials 3, 8702-8707 (2020).
2. T. Zheng, P. Valencia-Acuna, P. Zereshki, K. M. Beech, L. Deng, Z. Ni, and H. Zhao, thickness-Dependent Interlayer Charge Transfer in MoSe₂/MoS₂ Heterostructures Studied by Femtosecond Transient Absorption Measurements, ACS Applied Materials & Interfaces 13, 6489-6495 (2021).
3. T. Zheng, Y.-C. Lin, Y. Yu, P. Valencia-Acuna, A. A. Puretzky, R. Torsi, C. Liu, I. N. Ivanov, G. Duscher, D. B. Geohegan, Z. Ni, K. Xiao, and H. Zhao, Excitonic Dynamics in Janus MoSSe and WSSe Monolayers, Nano Letters 21, 931-937 (2021).

Optically Controlled Quantum Phase Transitions at Van der Waals Interfaces

Cheng Cen (PI), Lian Li (Co-PI), Xin Li (Co-PI), West Virginia University

Program Scope

It is often said that “the interface is the device”⁴. Nowhere is this more evident than in low dimensional Van der Waals (VdW) materials, whose properties can be most meaningfully discussed only when their interfaces are clearly defined. This effect is best demonstrated in monolayer (1uc) FeSe grown on SrTiO₃ (STO) (001) substrate (Fig. 1a), where the superconducting T_c is enhanced by more than one order of magnitude comparing to bulk FeSe⁵⁻⁸. The mechanism of superconductivity in 1uc-FeSe/STO, however, presents a conundrum. Due to charge doping from the substrate, its Fermi surface consists of only electron pockets centered at the Brillouin zone (BZ) corner (M), with the zone center (Γ) states pushed below the Fermi level⁵⁻⁸. This poses a challenge for pairing theories that involve both pockets^{9, 10}. More interestingly, we recently discovered that the superconducting transition in 1uc-FeSe/STO can be manipulated optically³. A brief exposure to a continuous wave (CW) ultraviolet (UV) light, with photon energy above the optical bandgap of STO, can raise the TC in 1uc-FeSe/STO by 25% (Fig. 1b). Using tailored sequence of UV light pulses and voltage pulses applied to the back of the STO substrate, the interface can be persistently driven between the superconducting state and its normal ground state (Fig. 1d). We attribute this effect to the strong photocarrier-phonon coupling in STO and the resultant metastable polar lattice distortion occurred at the FeSe/STO interface. In the quantum paraelectric phase of STO¹¹⁻¹⁴, photoexcited electrons can quadratically couple to the T_{1u} soft mode¹⁵⁻¹⁸ which, under the influence of the interface band bending^{19, 20}, gives rise to a

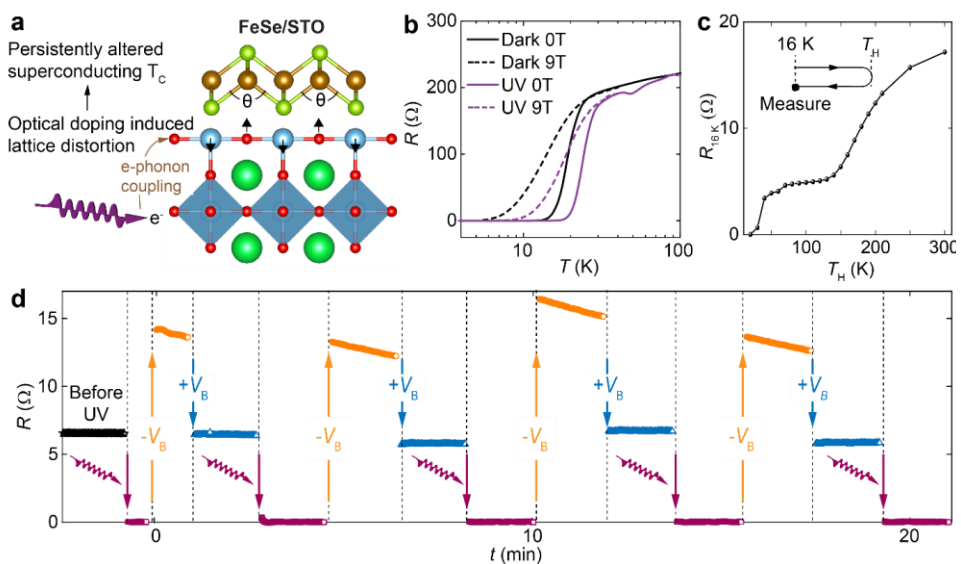


Figure 1 Light induced non-volatile switching of superconductivity in 1uc-FeSe/STO
(a) UV excitation can cause persistent phonon softening SrTiO₃ and polar structural distortion at the interface. These effects can be utilized to control the superconducting state in FeSe grown on top. (b) Temperature dependent resistances measured in 1uc-FeSe/STO (capped by 10 uc FeTe) with and without UV illumination or external magnetic field. (c) A series of thermal cycles of 16 K \rightarrow T_H \rightarrow 16 K were performed after turning off the UV light. At the end of each thermal cycle, sample resistance at 16 K was measured and plotted as a function of the maximum temperature (T_H) reached during sample heating. (d) Non-volatile switching between normal and superconducting states at 17 K by sequence of UV light pulses and back bias voltage pulses. (Ref 3)

In the quantum paraelectric phase of STO¹¹⁻¹⁴, photoexcited electrons can quadratically couple to the T_{1u} soft mode¹⁵⁻¹⁸ which, under the influence of the interface band bending^{19, 20}, gives rise to a

ferroelectric distortion with relative out-of-plane shifts between the Ti and O ions. As a result, it is viable that the Se-Fe-Se angle in the FeSe monolayer, a parameter sensitively modulates the electron correlation strength²¹, will be perturbed (Fig. 1a) and lead to an enhanced T_C.

While this proposed theory well explains our experimental observations, many open questions are still present. The most pressing task is to verify this theory by directly mapping the light-induced atomic displacements at the interface. Also, it is important to explore alternative heterostructures built from other 2D superconductors and substrate materials. These studies will allow us to extract more generalized interface design principles for realizing on-demand optical manipulation of quantum phases and enabling significant T_C enhancements. The objective of this project is to understand and control the emerging quantum phases in Van der Waals (VdW) materials through the innovative design of epitaxial heterostructures, implementation of novel optical excitations, and atomic-scale lattice tracing using cutting edge synchrotron tools. Specifically, the research activities in this project will be organized toward two specific aims: 1. To elucidate the light-induced quantum phase transitions at FeSe/SrTiO₃ interfaces; 2. To develop interface-aided optical quantum phase control capability in other analogous VdW heterostructures.

Recent Progress

Light-induced atomic displacements at the buried VdW interface are beyond the reach of common atomic-scale imaging tools (e.g., STM, TEM) that are either only sensitive to the surface or require invasive sample preparations that can alter the optical responses. In comparison, in-situ Crystal Truncation Rod (CTR) measurements and Coherent Bragg Rod Analysis (COBRA) experiments performed using the synchrotron X-rays are much better suited for this task. With the help of our collaborator at the Advanced Photon Source (APS) of Argonne National Lab (ANL),

Figure 2 Surface X-ray diffraction crystal truncation rod measurements of 1uc-FeSe/STO samples (a) Preliminary CTR/COBRA measurements of 1uc-FeSe/STO heterostructure taken at APS 33ID-D beamline at room temperature. The surface amorphous Se or S capping layer does not affect the interface structural quality, therefore having negligible effect on CTR data quality. (b) Preliminary CTR/COBRA measurements of annealed SrTiO₃ surface taken at 25 K before and after in-situ exposure to a UV light pulse. Signatures of a light induced surface lattice distortion can be clearly observed.

preliminary CTR/COBRA measurements were performed on 1uc-FeSe/SrTiO₃, 1uc-FeS/SrTiO₃, and TiO₂-terminated bare SrTiO₃ substrates (Fig.2). In order to study the lattice responses to the light excitation directly, we built an in-situ illumination assembly by integrating multiple LEDs with different emission wavelengths inside the cryostat chamber on the X-ray beamline. This assembly allows us to programmably switch on the excitation light during CTR measurements and control the excitation wavelength, strength, duration flexibly. Fig. 2b shows the CTR data obtained on a TiO₂-terminated bare SrTiO₃ substrate at 25 K in its quantum paraelectric phase. Pronounced differences can be seen comparing the CTR spectra taken before and after the sample is exposed to a short UV light pulse, supporting our theory of a light induced nonvolatile lattice distortion.

In the meanwhile, we are also pursuing the development of alternative heterostructures with structural instabilities that can potentially be manipulated by light. One example is shown in Fig.3. While WSe₂ normally crystallizes in the 1H structure at the single layer limit, by controlling the growth temperature, we are able to obtain single layer WSe₂ in 1T' phase. Due to small cohesive energy differences between the different polymorphic phases, metastable structural switching might be possible upon tailored external excitations.

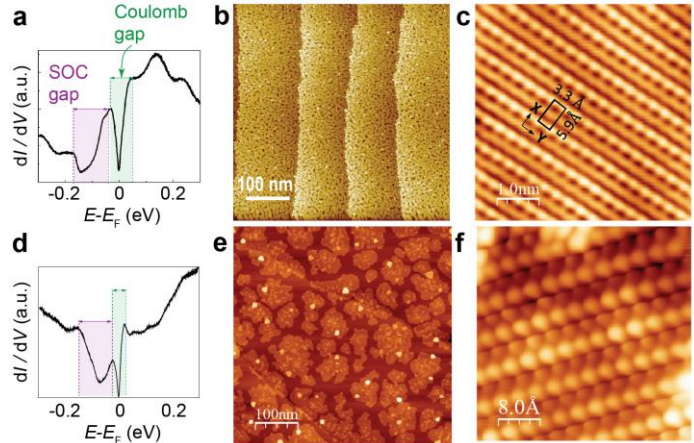


Figure 3 1T' WTe₂ films grown on different substrates (a-c) STS tunneling spectrum and STM images of WTe₂ film grown on SrTiO₃ substrate. (d-f) Similar data obtained on WTe₂ film grown on epitaxial graphene/SiC substrate.

Future Plans

While preliminary measurements as shown in Fig.2 has demonstrated the feasibility of producing significant and metastable surface lattice distortions using weak continuous-wave light, more systematic measurements on 1uc FeSe/SrTiO₃ heterostructures at different temperatures and with different excitation energies are needed. Our newly submitted APS beamtime proposal has recently been approved, which allocates us adequate beamtime in the first quarter of 2021 to perform the above-mentioned CTR measurements. The structural results obtained from COBRA analysis will reveal how the interface lattice configuration changes as FeSe and STO undergo their own structural phase transitions and how the interface changes under different photon energies in different bulk structural phases. Comparing the obtained structural data to the electronic band structure and transport properties, we will be able to paint a much clearer picture of the interfacial material coupling. The result will also be compared to theory to help elucidate the origin of the optically tunable superconducting phase.

Building upon the knowledges learned in FeSe/STO, different VdW interfaces built from epitaxial 2D quantum materials (e.g., FeSe, FeS, WSe₂) and complex oxides (e.g. SrTiO₃, SrNbO₃, LaAlO₃) will be designed to pursuit higher T_c, more effective optical tunability, and tailored active

polymorph control. The topographic, electronic, transport and optical properties of these samples will be first characterized at WVU using scanning tunneling microscope (STM), atomic force microscope (AFM), angle-resolved photoemission spectroscopy (ARPES), magnetotransport, and linear/nonlinear optical spectroscopy measurements. Selected samples will be sent to APS for the interface structural characterizations by surface x-ray diffraction measurement, including CTR/COBRA and time-resolved X-ray diffraction. Tailored optical tuning recipes that have been tested in STM and transport measurements at WVU will also be passed to APS. Depending on the optical wavelength and power required, optical excitations in the synchrotron measurement setup will be produced by either the compact LED source or lasers coupled through an x-ray transparent optical window.

Once the proposed research has been successfully carried out, well-understood methodology that uses light to manipulate the quantum phase transitions at the VdW interfaces will be established. We will also obtain a much clearer understanding of how high TC superconductivity and topological orders emerge from the VdW interfacial coupling. With this knowledge, it will become possible to deterministically tailor quantum interfaces with desired optical tunability, which can lead to unprecedented capability in designing and fabricating active quantum devices such as optically tunable superconducting qubits and ultrafast VdW electronics.

References

1. Fedorov, A., et al. *Scientific Reports* 2016, 6, 36834.
2. Schrecongost, D., et al. *Advanced Functional Materials* 2019, 29, (49), 1905585.
3. Yang, M., et al. *Nature Communications* 2019, 10, (1), 85.
4. Kroemer, H. *Reviews of Modern Physics* 2001, 73, (3), 783-793.
5. Liu, D., et al. *Nature Communications* 2012, 3, 931.
6. Tan, S., et al. *Nature Materials* 2013, 12, 634.
7. Lee, J. J., et al. *Nature* 2014, 515, 245.
8. Zhang, P., et al. *Physical Review B* 2016, 94, (10).
9. Hirschfeld, P. J., et al. *Reports on Progress in Physics* 2011, 74, (12), 124508.
10. Chubukov, A. *Annual Review of Condensed Matter Physics* 2012, 3, (1), 57-92.
11. Viana, R., et al. *Physical Review B* 1994, 50, (1), 601-604.
12. Fleury, P. A., et al. *Physical Review* 1968, 174, (2), 613-623.
13. Müller, K. A., et al. *Zeitschrift für Physik B Condensed Matter* 1991, 84, (2), 277-283.
14. Müller, K. A., et al. *Physical Review B* 1979, 19, (7), 3593-3602.
15. Nozawa, S., et al. *Physical Review B* 2005, 72, (12), 121101.
16. Qiu, Y., et al. *Physical Review B* 2005, 72, (22), 224105.
17. Nasu, K. *Physical Review B* 2003, 67, (17), 174111.
18. Koyama, Y., et al. *Physical Review B* 2010, 81, (2), 024104.
19. Zhao, W., et al. *Science Advances* 2018, 4, (3), eaao2682.
20. Zhang, H., et al. *Nature Communications* 2017, 8, (1), 214.
21. Mandal, S., et al. *Physical Review Letters* 2017, 119, (6), 067004.

Publications

This project starts in the Fall of 2020. New manuscripts are still in preparation.

Session III

Phase-Sensitive Measurements of Triplet Superconductors

C. L. Chien
The Johns Hopkins University

Program Scope

Exploration of pure spin current phenomena in ferromagnetic metals, antiferromagnetic insulators, materials with strong spin orbit coupling, quantum materials, and topological triplet superconductors,

Recent Progress

In a superconductor (SC), electrons are paired into Cooper pairs, which undergo Bose-Einstein condensation at the transition temperature T_c [1]. The Cooper pairs of two electrons can be either a spin singlet with spin 0 (*s*-wave and *d*-wave with *even parity*), or a spin triplet with spin 1 (*p*-wave with *odd parity*). To date, the known SCs are overwhelmingly singlet, mostly *s*-wave (e.g., Nb) and some *d*-wave (cuprates). Triplet SCs, essential for Majorana physics [2] and quantum computing, are rare but must be identified

For decades, thermodynamic properties (e.g., specific heat, upper critical field, etc.) have been used to identify possible triplet pairing in heavy fermions and Sr₂RuO₄, but without success [3,4]. Indeed, Sr₂RuO₄, has been a likely triplet *p*-wave SC for nearly three decades. In 2019, the key evidence of NMR Knight Shift was deemed unreliable, ending its triplet prospect [5]. The only established triplet *p*-wave is He³, a superfluid [6].

It is important to note that the gap values of singlet SCs (*s*-wave and *d*-wave) and triplet SCs (*p*-wave) have *opposite* parity [1]. The gap value of the even-parity singlet SCs does not, whereas that of the odd-parity triplet SCs does, change sign upon inversion. This fundamental difference allows unequivocal identification of singlet and triplet SCs by *phase-sensitive* measurements of the symmetry of the gap. We recently demonstrated β-Bi₂Pd as a triplet SC using flux quantization [7].

Flux quantization is a unique feature of all SCs, where the magnetic flux enclosed by a SC ring can only change in units of $\Phi_o = hc/2e = 20.7 \text{ G-}\mu\text{m}^2$, where h is the Planck constant, c the speed of light, and $2e$ the charge of the Cooper pair. Because $\Phi_o = 20.7 \text{ G-}\mu\text{m}^2$, μm-sized rings are the preferred sizes for measurements as shown in *Fig. 1*. For singlet SCs with even-parity gaps, the resistance minima of the ring device occur at $\Phi = n\Phi_o$, where n is an integer, as shown in *Fig. 1* for the case of singlet Nb. This is the *integer* flux quantization, first demonstrated in the Little-

Parks experiments [8] and has been universally observed in numerous singlet SCs of *s*-wave (e.g., Nb) and *d*-wave (e.g., cuprates), in both polycrystalline and epitaxial rings [9,10].

The situation is entirely different in the case of triplet SCs with an odd parity gap. A grain boundary may separate two grains with gaps of opposite signs, introducing a phase of π . In a polycrystalline triplet SC ring, when the total phase of all the grain boundaries adds up to an odd number of π , one observes half flux quantization of $\Phi = (n+1/2)\Phi_0$ as first shown theoretically [11]. Thus, the observation of the *half-integer* flux quantization is an unequivocal evidence of triplet pairing, which we have observed in polycrystalline β -Bi₂Pd as shown in *Fig. 1*.

More rigorously, since π phase shift occurs at the grain boundaries, one must observe *both* integer flux and half-integer flux of roughly equal proportion in polycrystalline triplet SC rings. Furthermore, one must observe *only* integer flux in epitaxial triplet SC rings without grain boundaries and sign change in gap value. These stringent criteria have indeed been observed in β -Bi₂Pd rings. In polycrystalline β -Bi₂Pd rings, we have observed both integer and half-integer flux. Equally important, we have patterned 30 epitaxial β -Bi₂Pd rings, epitaxially grown on MgO substrates. Not a single half-integer flux, and only integer flux, has been observed. These experiments conclusively demonstrate that β -Bi₂Pd is a triplet SC [7].

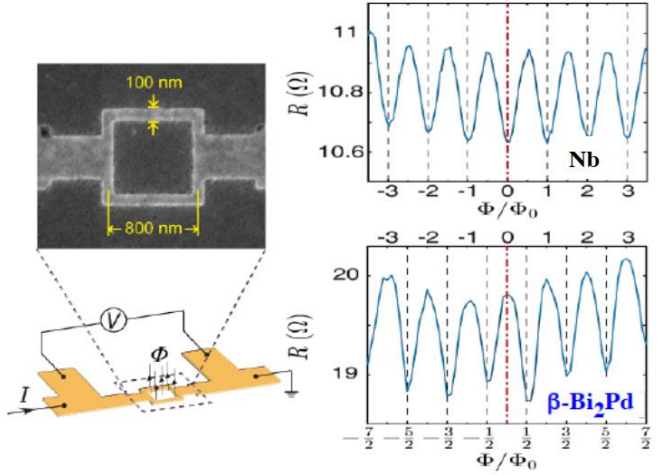


Fig. 1. Integer (Nb) and half-integer (β -Bi₂Pd) flux quantization observed in polycrystalline superconducting rings, with structures shown on the left. [Li, Xu, Lee, Chu, and Chien, *Science* **366**, 238 (2019)].

of the half-integer flux quantization is an unequivocal evidence of triplet pairing, which we have observed in polycrystalline β -Bi₂Pd as shown in *Fig. 1*.

More rigorously, since π phase shift occurs at the grain boundaries, one must observe *both* integer flux and half-integer flux of roughly equal proportion in polycrystalline triplet SC rings. Furthermore, one must observe *only* integer flux in epitaxial triplet SC rings without grain boundaries and sign change in gap value. These stringent criteria have indeed been observed in β -Bi₂Pd rings. In polycrystalline β -Bi₂Pd rings, we have observed both integer and half-integer flux. Equally important, we have patterned 30 epitaxial β -Bi₂Pd rings, epitaxially grown on MgO substrates. Not a single half-integer flux, and only integer flux, has been observed. These experiments conclusively demonstrate that β -Bi₂Pd is a triplet SC [7].

Future Plans

We plan to explore some promising topological SCs to identify other triplet SCs. Triplet SC ring exhibit half-flux in zero external field and can be exploited as flux qubits.

References

1. M. Tinkham, *Introduction to Superconductivity* (McGraw-Hill, New York, 1996), 2 edn.
2. C. W. J. Beenakker. Search for Majorana Fermions in Superconductors. *Annual Review of Condensed Matter Physics* **4**, 113 (2013).
3. e.g., G. R. Stewart, Z. Fisk, J. O. Willis, and J. L. Smith. Possibility of Coexistence of Bulk Superconductivity and Spin Fluctuations in UPt₃. *Physical Review Letters* **52**, 679 (1984).

4. A. P. Mackenzie and Y. Maeno. The superconductivity of Sr₂RuO₄ and the physics of spin-triplet pairing. *Reviews of Modern Physics* **75**, 657 (2003).
5. A. Pustogow1, Yongkang Luo, A. Chronister, Y.-S. Su, D. A. Sokolov, F. Jerzembeck, A. P. Mackenzie, C. W. Hicks, N. Kikugawa, S. Raghu, E. D. Bauer & S. E. Brown, “Constraints on the superconducting order parameter in Sr₂RuO₄ from oxygen-17 nuclear magnetic resonance,” *Nature* **574**, 72 (2019).
6. D. D. Osheroff, R. C. Richardson, and D. M. Lee. Evidence for a New Phase of Solid He³. *Physical Review Letters* **28**, 885 (1972).
7. Y. Li, X. Xu, M. H. Lee, M. W. Chu, and C. L. Chien, “Observation of half-quantum flux in the unconventional superconductor β-Bi₂Pd,” *Science*, **366**, 238 (2019).
8. W. A. Little and R. D. Parks. Observation of Quantum Periodicity in the Transition Temperature of a Superconducting Cylinder. *Physical Review Letters* **9**, 9 (1962).
9. P. L. Gammel, P. A. Polakos, C. E. Rice, L. R. Harriott, D. J. Bishop, *Phys. Rev. B* **41**, 2593–2596 (1990).
10. I. Sochnikov, A. Shaulov, Y. Yeshurun, G. Logvenov, I. Božović, *Nat. Nanotechnol.* **5**, 516(2010).
11. V. B. Geshkenbein, A. I. Larkin, and A. Barone. Vortices with half magnetic flux quanta in "heavy-fermion" superconductors. *Physical Review B* **36**, 235 (1987).

Publications supported by DOE

1. Yufan Li, Xiaoying Xu, M. H. Lee, M. W. Chu, and C. L. Chien, “Observation of Half-Quantum Flux in Unconventional Superconductor β-Bi₂Pd,” *Science*, **366**, 238 (2019).
2. C. C. Chiang, S. Y. Huang, D. Qu, P. H. Wu, and C. L. Chien, “Absence of evidence of electrical switching of antiferromagnetic Néel vector,” *Phys. Rev. Lett.* **123**, 227203 (2019) [Editor’s Suggestion, Featured in Physics].
- 3.. Xiaoying Xu, Yufan Li, and C. L. Chien, “Spin-Triplet Pairing State Evidenced by Half-Quantum Flux in a Noncentrosymmetric Superconductor,” *Phys. Rev. Lett.* **124**, 167001 (2020).
4. Qinli Ma, Yufan Li, Young-suk Choi, Wei-Chuan Chen, Shu Jen Han, and C. L. Chien, “Spin orbit torque switching of synthetic Co/Ir/Co trilayers with perpendicular anisotropy and tunable interlayer coupling,” *Appl. Phys. Lett.* **117**, 172403 (2020)
5. S. Y. Huang, D. Qu, T. C. Chuang, C. C. Chiang, Weiwei Lin, and C. L. Chien, “Pure spin current phenomena,” *Appl. Phys. Lett.* **117**, 190501 (2020). [Perspective, Editor’s Pick].
6. P. H. Wu, Y. T. Chan, T. C. Hung, Y. H. Zhang, D. Qu, T. M. Chuang and, C. L. Chien, and S. H. Huang, “Effect of demagnetization factors on spin current transport,” *Phys. Rev. B* **102**, 174426 (2020).
7. Jinsong Xu and C. L. Chien, “Voltage-controlled spin-orbit torque switching in W/CoFeB/MgO,” *Appl. Phys. Lett.* **118**, 052409 (2021).

Spin-Dependent Quantum Phenomena in 2D Heterostructures

Jing Shi, Department of Physics & Astronomy, University of California, Riverside

Program Scope

The proposed program focuses on exploring interfacial spin interactions in all-2D van der Waals (vdW) heterostructures fabricated with exfoliated or epitaxially-grown monolayer and few-layer quantum materials. The goal of this research is to demonstrate and develop in-depth understanding of novel quantum phenomena in all-2D vdW heterostructures with enhanced spin interactions.

Recent Progress

- (a) vdW heterostructure nanodevice fabrication by exfoliation, pickup and transfer. The 1T'-phase of monolayer WTe₂ is known to be a 2D quantum spin Hall insulator with a sizable gap [1-3]. We are interested in studying induced ferromagnetism and induced magneto-transport properties in this interesting material. We have demonstrated fabrication of vdW heterostructure devices (Figure 1) consisting of monolayer WTe₂ and multilayer Cr₂Ge₂Te₆ (CGT) using an automated transfer stage operated inside a glovebox. The exfoliation and subsequent pickup, transfer, and alignment have been carried out in this protected environment. The monolayer WTe₂ flake (labeled in blue) is picked up by the CGT flake (labeled in yellow) which is vdW bound to the hexagonal boron nitride marked as “Top hBN”. This vdW heterostructure stack is then placed onto a set of pre-fabricated electrodes on a large sheet of hBN (labeled in red), under which there is a piece of few-layer graphene (FLG, labeled in black) serving as the back gate to control the Fermi level of the monolayer WTe₂, the only conducting material in the stack. CGT is an insulating ferromagnet with T_c ~ 61 K, which is expected to induce proximity effects to break the time reversal symmetry in the monolayer WTe₂. Furthermore, the induced effects will be studied as the gate voltage, temperature, and magnetic field are varied. In addition to electrical transport properties, we are also interested in studying the mechanism behind the recently reported non-reciprocal transport phenomena in similar heterostructures.

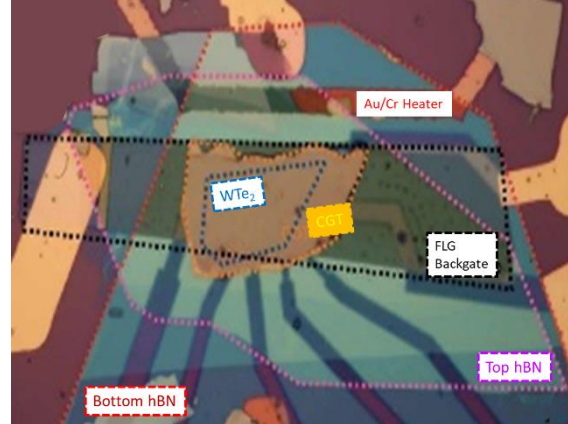


Figure 1 Multilayered, backgated nanodevice containing heterostructure of monolayer WTe₂ and CGT. The side heater generates a controlled temperature gradient across the WTe₂ flake. The color of dotted contours matches the color of the labels of the materials.

(b) Demonstration of induced ferromagnetism in monolayer WTe₂. Proximity coupling between monolayer WTe₂ and CGT (device shown in Figure 1) can lead to induced ferromagnetism in the former which has not been experimentally studied. Consequently, this induced exchange interaction combined with the strong spin-orbit coupling in monolayer WTe₂, a quantum spin Hall insulator, can induce new quantum states. An interesting non-reciprocal second harmonic phenomenon was recently reported [4], but its physical origin remain unexplored. One possible cause is the induced anomalous Nernst effect in magnetized monolayer WTe₂. In the device shown in Figure 1 with controlled temperature gradient, we obtained strong evidence in our preliminary data to support this scenario. The magnetization orientation dependence in our observed anomalous Nernst effect can give rise to non-reciprocity, and the effect itself is a temperature gradient-driven thermoelectric phenomenon; therefore can produce second harmonic responses to an ac current through the heater.

Future Plans

We will further investigate the induced ferromagnetism and related quantum phenomena in the monolayer WTe₂ quantum spin Hall insulator through systematic gate voltage, temperature, and magnetic field dependence measurements in combination with density functional theory calculations performed by our collaborators. From both electrical and thermoelectric transport, we will determine the proximity induced anomalous Hall effect and anomalous Nernst effect. Furthermore, we will identify contributions from the 2D bulk bands and edge states. Then, in similar vdW heterostructure devices fabricated with dual-gates, we plan to separately tune the Fermi level position and the strength of the electric field. The former enables us to access different regions of the band structure and the latter controls the topological phases.

References

1. Z. Fei, T. Palomaki, S. Wu, W. Zhao, X. Cai, B. Sun, P. Nguyen, J. Finney, X. Xu, D. H. Cobden, Edge conduction in monolayer WTe₂. Nat. Phys. **13**, 677–682 (2017).
2. S. Tang et al., Quantum spin Hall state in monolayer 1T'-WTe₂. Nat. Phys. **13**, 683-687 (2017).
3. S.F. Wu et al., Observation of the quantum spin Hall effect up to 100 kelvin in a monolayer crystal. Science **359**, 76-79 (2018).
4. W. Zhao et al., Magnetic proximity and nonreciprocal current switching in a monolayer WTe₂ helical edge. Nat. Mat. **19**, 503-507 (2020).

Publications

1. Mark Lohmann, Tang Su, Ben Niu, Yusheng Hou, Mohammed Alghamdi, Mohammed Aldosary, Wenyu Xing, Jiangnan Zhong, Shuang Jia, Wei Han, Ruqian Wu, Yongtao Cui, and Jing Shi, *Probing magnetism in insulating Cr₂Ge₂Te₆ by induced anomalous Hall effect in Pt*. Nano Lett. **19**, 2397 (2019). DOI: 10.1021/acs.nanolett.8b05121.

2. Mohammed Alghamdi, Mark Lohmann, Junxue Li, Palani R. Jothi, Qiming Shao, Mohammed Aldosary, Tang Su, Boniface P. T. Fokwa, and Jing Shi, *Highly efficient spin-orbit torque and switching of layered ferromagnet Fe₃GeTe₂*. Nano Lett. **19**, 4400 (2019). DOI: 10.1021/acs.nanolett.9b01043.
3. Fei Wang, Di Xiao, Wei Yuan, Jue Jiang, Yi-Fan Zhao, Ling Zhang, Yunyan Yao, Wei Liu, Zhidong Zhang, Chaoxing Liu, Jing Shi, Wei Han, Moses H. W. Chan, Nitin Samarth, and Cui-Zu Chang, *Observation of interfacial antiferromagnetic coupling between magnetic topological insulator and antiferromagnetic insulator*. Nano Lett. **19**, 2945 (2019). DOI: 10.1021/acs.nanolett.9b00027.
4. Ben Niu, Tang Su, Brian A. Francisco, Subhajit Ghosh, Fariborz Kargar, Xiong Huang, Mark Lohmann, Junxue Li, Yadong Xu, Takashi Taniguchi, Kenji Watanabe, Di Wu, Alexander Balandin, Jing Shi, and Yong-Tao Cui, *Coexistence of magnetic orders in two-dimensional magnet CrI₃*. Nano Lett. **20**, 553 (2020). DOI: 10.1021/acs.nanolett.9b04282.
5. Tang Su, Mark Lohmann, Junxue Li, Yadong Xu, Ben Niu, Mohammed Algamdi, Haidong Zhou, Yongtao Cui, Ran Cheng, Takashi Taniguchi, Kenji Watanabe, and Jing Shi, *Current-induced CrI₃ surface spin-flop transition probed by proximity magnetoresistance in Pt*. 2D Materials **7**, 045006 (2020). DOI:10.1088/2053-1583/ab9dd5.
6. Jothi, P. R., Scheifers, J. P., Zhang, Y., Alghamdi, M., Stekovic, D., Itkis, M. E., Shi, J. & Fokwa, B. P. T. *Fe_{5-x}Ge₂Te_{2-a} New Exfoliable Itinerant Ferromagnet with High Curie Temperature and Large Perpendicular Magnetic Anisotropy*. Physica Status Solidi (RRL) – Rapid Research Letters **14**, 1900666 (2020). DOI: 10.1002/pssr.201900666.

Spin Functionality at Interfaces through Complex Oxide Heteroepitaxy
PI: Yuri Suzuki
Department of Applied Physics, Stanford University

Program Scope

The *main research objectives* of the program are to develop new emergent ground states at complex oxide interfaces and to develop atomically precise complex oxide thin films and heterostructures for spin current generation, propagation and detection. In this program we have focused on generating ferromagnetism localized at the interface from materials that are not ferromagnetic in the bulk and demonstrating spin current generation, propagation and detection in newly developed low damping ferrite thin films. Atomically precise complex oxide thin films and heterostructures with spin functionality comprise a new class of oxide materials that will form the basis for the development of a more energy efficient spin-based electronics.

Our recent focus has been on the following categories of materials based on epitaxial films of *transition metal oxide compounds*:

- (i) low damping epitaxial oxide spinel ferrite thin films of $Mg(Al,Fe)_2O_4$ and $Li_{0.5}Fe_{2.5}O_4$ and associated heterostructures with strongly spin-orbit coupled complex oxides for spin current detection
- (ii) ultra-thin nickelate films of $LaNiO_3$ in which octahedral rotations at the interfaces generate unexpected spin functionality not observed in the bulk
- (iii) atomically precise $LaNiO_3/CaMnO_3$ superlattices with (111) orientation in which strong interfacial ferromagnetism is observed

Recent Progress

Highlights of recent work include (i) the discovery and synthesis of $Mg(Al,Fe)_2O_4$ and $Li_{0.5}Fe_{2.5}O_4$ epitaxial thin films with extremely low damping, (ii) demonstration of emergent ferromagnetism in ultra-thin $LaNiO_3$ films, and (iii) demonstration of strong interfacial ferromagnetism in (111) $LaNiO_3/CaMnO_3$ superlattices attributed to double exchange interactions and polar mismatch at the interface.

New Low Loss Spinel Ferrite Thin Films. (Publication #2,3,4,5) Materials with spin functionality in the bulk and at interfaces have enormous potential in transforming future energy relevant technologies. The manipulation of electrons via their spin has been recognized as a potentially more energy efficient alternative to charge-based microelectronics. Spin transport via the generation and control of angular momentum flow in spin currents offer low power information processing.[1] Low loss ferromagnetic insulators are a class of materials that can sustain spin current without accompanying charge current and have been recognized as important for spin-wave spin current phenomena and electronics.

We have identified spinel ferrite thin films as excellent candidates for low damping ferromagnetic insulators.[2] We believe the key factors in minimizing damping to be: (i) the presence of only one magnetic species of Fe^{3+} ($3d^5$) which has very low single ion anisotropy and $L=0$; (ii) minimal defects due to the close lattice match and isostructural film and substrate.

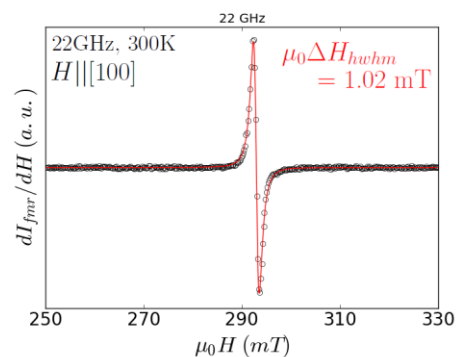


Figure 1. Ferromagnetic resonance of a $Li_{0.5}Fe_{2.5}O_4$ thin film at 22GHz gives rise to narrow linewidths on the order of 1mT at room temperature.

The most exciting result has been our stabilization of epitaxial $\text{Li}_{0.5}\text{Fe}_{2.5}\text{O}_4$ films that can be grown as thin as 3nm with low damping comparable to the gold standard of $\text{Y}_3\text{Fe}_5\text{O}_{12}$ films. [3] In terms of magnetic properties, these $\text{Li}_{0.5}\text{Fe}_{2.5}\text{O}_4$ films exhibit bulk saturation magnetization values and are robustly ferromagnetic at room temperature. Figure 1 shows the narrow ferromagnetic linewidth of a typical sample. Moreover this and other oxide spinel films can be integrated with silicon whereas $\text{Y}_3\text{Fe}_5\text{O}_{12}$ films can only exhibit low damping properties when grown on a single crystal garnet structure substrate.

We also performed a compositional study of magnesium aluminum ferrite thin films by varying the relative Fe to Al composition and found that the $x \sim 1.5$ composition minimizes the room-temperature magnetic damping with a typical Gilbert damping parameter of $\alpha \sim 1.8 \times 10^{-3}$. [4] Figure 1 shows a typical ferromagnetic resonance spectrum of a $\text{MgAl}_{0.5}\text{Fe}_{1.5}\text{O}_4$ film. This minimized damping is governed by a competition between the more robust magnetic ordering with increased iron content, x , and the more defective structure due to larger film-substrate lattice mismatch with increased iron content. The temperature-dependent magnetization curves indicate that T_c is suppressed below room temperature for iron content $x \sim 1.2$ and eventually suppressed entirely for $x \sim 0.8$. X-ray magnetic circular dichroism results indicate that for all x the magnetic moment is dominated by Fe^{3+} cations distributed in a 60:40 ratio on the octahedral and tetrahedral sites, with minimal contribution from Fe^{2+} cations. A typical FMR spectrum for a $x=1.5$ sample is shown in Figure 2(a). Films with $x \sim 1.4 - 1.6$ are shown in Figure 2(b) with low Gilbert damping parameters ($\alpha_{\text{eff}} \sim 1$ to 6×10^{-3}) as deduced from the slope of the frequency dependence of the linewidths, making them ideal candidates for microwave and spintronic applications.

For the optimally doped $\text{MgAl}_{0.5}\text{Fe}_{1.5}\text{O}_4$ films, we have found that there is an optimum thickness of 10–15nm for lowest damping. [5] While defects due to strain relaxation in the bulk of the film contribute to increased damping for large film thickness, the damping increase in thinner films is attributed to the presence of a chemically disordered magnetic dead layer at the film/substrate interface. This interfacial dead layer arises from an Fe-deficient MAFO layer. Notably, this layer is only about one-sixth the thickness of that found at the interface between yttrium iron garnet films and gadolinium gallium garnet substrates, making MAFO an ideal thin-film insulator for spin-torque applications.

Emergent Ferromagnetism in Ultra-thin LaNiO_3 Thin Films.(Publication #6) LaNiO_3 (LNO), a paramagnetic metal at all temperatures in the bulk, has elicited attention because theory predicts interesting topological phases in (111)-oriented LNO grown on LaAlO_3 (LAO).[6-8] While a suppression of metallicity has been achieved in

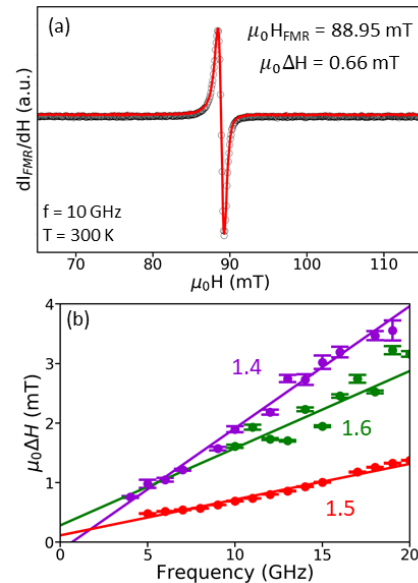


Figure 2. (a) Ferromagnetic resonance spectrum of a $\text{MgAl}_{0.5}\text{Fe}_{1.5}\text{O}_4$ film and (b) frequency dependence of the linewidth as a function of Fe composition in $\text{MgAl}_{2-x}\text{Fe}_x\text{O}_4$ films from which damping is deduced.

(001)-oriented LNO films with thicknesses of 2-4 unit cells, no long range magnetic order has been observed. [9-12] We have recently discovered the emergence of ferromagnetism in LNO films grown on LAO(111) in a wide range of thicknesses (8-26 unit cells thick) in both insulating and metallic films.[13] The emergent ferromagnetism in ultrathin LNO films grown on (111) LaAlO₃ (LAO) substrates can be correlated with transport and structure, indicating that NiO₆ octahedral distortions stabilize a ferromagnetic insulating phase at the film/substrate interface. Away from this interface, the distortions relax and bulk-like conduction is regained, ultimately dominating transport in thicker films.

Detailed structural characterization, including synchrotron x-ray diffraction and dynamical x-ray diffraction simulations confirm a consistent out-of-plane expansion at the interface of all our films. This distorted region results in a thickness-dependent metal-insulator transition, seen via transport data to occur at $t = 8$ unit cells. X-ray absorption spectroscopy reveals that this distortion stabilizes an increased concentration of Ni²⁺ ions at the LNO/LAO interface. The anomalous Hall effect (shown in Figure 3) and hysteretic magnetoresistance indicate long-range magnetic order although the magnetic signal is too small to be detected via bulk SQUID magnetometry or X-ray magnetic circular dichroism. Together the structural changes at the LNO/LAO(111) interface and the increased concentration of Ni²⁺ ions in ultra-thin LNO films facilitate ferromagnetic superexchange interactions among Ni²⁺ and Ni³⁺ ions. The emergent ferromagnetism in ultrathin LNO(111) films therefore relies both on the growth constraints imposed by lattice mismatch in the (111) interface geometry and on the presence of Ni²⁺ ions. These results also suggest that the unique distortions present in (111)-oriented films allow us to access emergent functionalities in materials than are unavailable in bulk or (001)-oriented thin films and may lead to fundamentally new phases in correlated materials.

Interfacial Ferromagnetism in (111) LaNiO₃/CaMnO₃ superlattices. (Publication #1) Emergent phenomena at the interface of two different materials have been attributed to electronic, magnetic or other types of reconstruction at the interface. We have focused on exploring emergent ferromagnetism at the interface of two materials which do not exhibit ferromagnetism in the bulk. [14-17] With our success in synthesizing atomically precise LaNiO₃/CaMnO₃ superlattices with (111) orientation by interval pulsed laser deposition, we have realized emergent ferromagnetism at the (111) LaNiO₃/CaMnO₃ interface gives rise to robust ferromagnetism with a T_c~200 K, which is much higher than the bulk antiferromagnetic CaMnO₃ ordering temperature of 140 K. The significant saturated interfacial moment is attributed to double exchange interactions at the fully uncompensated (111) CaMnO₃ surface.[18] This enhanced magnetization in (111) superlattices is much larger than the interfacial moment from compensated spin structures in (001) LaNiO₃/CaMnO₃. There is also an additional contribution to the interfacial magnetism from the Ni-Mn superexchange interactions associated with screening effects caused by polar mismatch.

Future Plans

In order to generate, propagate and detect spin currents in our low loss epitaxial Li_{0.5}Fe_{2.5}O₄ films, we will incorporate these lithium ferrite films in spin-current heterostructures with spin-

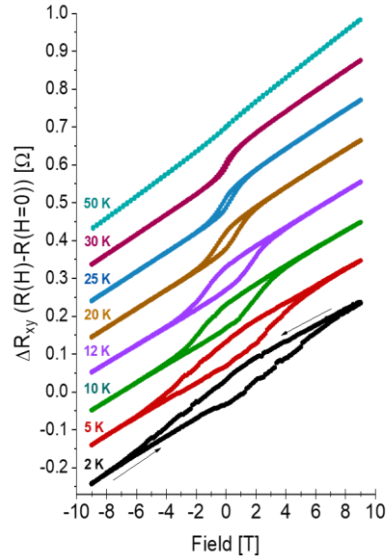


Figure 3. Hall resistance of a 10 unit cell (111) LaNiO₃ thin film indicates an anomalous Hall signal.

orbit coupled materials. We will perform experiments demonstrating magnetization switching of the ferrite via electrical current as well as spin torque ferromagnetic resonance. We also plan to explore Al doping of the $\text{Li}_{0.5}\text{Fe}_{2.5}\text{O}_4$ films to improve lattice match of the film and substrate, minimize defects and hence reduce damping further.

We will also explore possible topological phases and magnetic textures in our ultra-thin LNO thin films via transport measurements.

References

1. Ken-ichi Uchida et al., Solid State Physics **64** 1-26 (2013).
2. Satoru Emori et al., Nano Lett. **18** 4273 (2018).
3. X.Y. Zhang et al., Appl. Phys. Lett. **117** 092407 (2020).
4. Jacob J. Wisser et al., Appl. Phys. Lett. **116** 142406 (2020).
5. Jacob J. Wisser et al., Appl. Phys. Lett. **115** 132404 (2019).
6. D. Doennig, W.E. Pickett, R. Pentcheva, Phys. Rev. B **89** 121110 (2014).
7. A. Ruegg, C. Mitra, A.A. Demkov, G.A. Fiete, Phys. Rev. B **88** 115146 (2013).
8. K.-Y. Yang et al., Phys. Rev. B **84** 201104 (2011).
9. J. Son et al., Appl. Phys. Lett. **96** 062114 (2010).
10. R. Schwerwitzl et al., Phys. Rev. Lett. **106** 246403 (2011).
11. E.J. Moon et al., New J. Physics **13** 073037 (2011).
12. J. Fowlie et al., Adv. Mater. **29** 18 (2017).
13. Margaret Kane et al.,” under review at *npj Quantum Materials* (2021).
14. C. He et al., Phys. Rev. Lett. **109** 076603 (2012).
15. A.J. Grutter et al., Phys. Rev. Lett. **111** 087202 (2013).
16. C. L. Flint et al., Phys. Rev. Mater. **1** 024404 (2017).
17. C. L. Flint et al., Phys. Rev. B **96** 144438 (2017).
18. C. L. Flint et al., Phys. Rev. Mater. **3** 064401 (2019).

Publications

1. C. L. Flint, D. Yi, E. Karapetrova, A. T. N'Diaye, P. Shafer, E. Arenholz, and Y. Suzuki, “Enhanced Interfacial Magnetism and Exchange Bias in (111)-oriented $\text{LaNiO}_3/\text{CaMnO}_3$ Superlattices,” *Physical Review Materials* **3** 064401 (2019).
2. Lauren J. Riddiford, Jacob J. Wisser, Satoru Emori, Peng Li, Debangsu Roy, Egecan Cogulu, Olaf van t'Erve, Yong Deng, Shan X. Wang, Berend T. Jonker, Andrew D. Kent, Y. Suzuki, “Efficient Spin Current Generation in Low Damping $\text{Mg}(\text{Al},\text{Fe})_2\text{O}_4$ Thin Films,” *Applied Physics Letters* **115** 122401 (2019).
3. Jacob J. Wisser, Satoru Emori, Lauren Riddiford, Aaron Altman, Peng Li, Krishnamurthy Mahalingham, Brittany T. Urwin, Brandon M. Howe, Michael R. Page, Alexander J. Grutter, Brian J. Kirby and Yuri Suzuki, “Ultrathin interfacial layer with suppressed room temperature magnetization in magnesium aluminum ferrite thin films,” *Applied Physics Letters* **115** 132404 (2019).
4. Jacob J. Wisser, Lauren J. Riddiford, Aaron Altman, Peng Li, Satopru Emori, Padraig Shafer, Christoph Klewe Alpha N'Diaye, Elke Arenholz, Yuri Suzuki, “The Role of Iron in Magnetic Damping of $\text{Mg}(\text{Al},\text{Fe})_2\text{O}_4$ Thin Films,” *Applied Physics Letters* **116** 142406 (2020).
5. Xin Yu Zheng, Lauren J. Riddiford, Jacob J. Wisser, Satoru Emori, Yuri Suzuki, “Ultra-low magnetic damping in $\text{Li}_{0.5}\text{Fe}_{1.5}\text{O}_4$ Films,” *Applied Physics Letters* **117** 092407 (2020).
6. Margaret Kane, Lauren Riddiford, Charles Flint, A. Vaillionis, Apurva Mehta, Y. Suzuki, “Anomalous Ferromagnetism and Structural Distortions in Ultrathin (111)-oriented LaNiO_3 ,” under review at *npj Quantum Materials* (2021).

Tunable Excitons and Pseudospins in Transition Metal Dichalcogenide Homobilayers

Xiaoqin Elaine Li, Physics Department at the University of Texas-Austin

Report for DOE BES grant # DESC0019398, 02/15/2021

Program Scope

Transition metal dichalcogenides (TMDs) (MX_2 with $\text{M}=\text{Mo, W}$ and $\text{X}=\text{S, Se, and Te}$) are van der Waals (vdW) semiconductors which exhibit new and interesting optical properties. While a consistent understanding of exciton and valley pseudospin properties in monolayer TMDs has started to emerge in the last few years, many exciting opportunities to investigate topological exciton bands and quantum emitters in moiré superlattices formed by two vertically stacked monolayers have yet to be explored experimentally.

We aim to understand fundamental quantum dynamic properties and transport of tunable excitons and pseudospins in twisted TMD bilayers. In particular, we investigate

- New exciton resonances and their properties in the presence of a moiré potential
- Quantum dynamics of excitons and valley pseudospins in moiré superlattices

Questions of interest to us include the following. Will new exciton resonances emerge in the presence of moiré superlattice. How does twist angle influence exciton and valley lifetimes and decoherence time? Do valley pseudospins exhibit improved characteristics as information carriers?

Recent Progress

- Discovery of exciton diffusion is controllable by the twist angle of a moiré superlattice

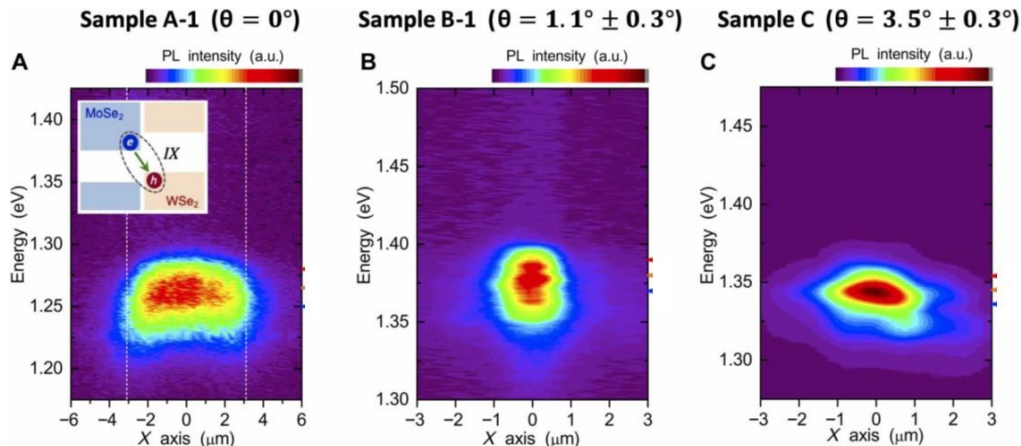


Fig. 1: Energy and spatially resolved photoluminescence from interlayer excitons in three $\text{MoSe}_2/\text{WSe}_2$ bilayers. (a) long diffusion is observed in a CVD grown bilayer without moiré potential. (b) excitons are localized by moiré potential in a stacked bilayer with 1° twist angle. (c) exciton diffusion observed in a 3° twisted bilayer.

Whether or not excitons are localized within each moiré supercell is an important fundamental question with great implications for applications. For example, a regular array of localized excitons may find exciting applications in quantum information science as quantum emitters with tunable chirality.¹ While most previous experiments have suggested long diffusion length for excitons in

TMD bilayers,^{2–4} excitons are likely localized within moiré supercell if the moiré potential is deep and the supercell size is 2–20 times of the exciton Bohr radius. If the supercells are too large, excitons essentially experience a 2D potential. If the supercell is too small, on the other hand, the picture of a bound electron-hole pair moving in a smooth potential breaks down.

Recently, we compared interlayer exciton diffusion in several WSe₂/MoSe₂ bilayers using steady-state PL mapping. A CVD-grown bilayer forms a commensurate structure, i.e., no moiré lattice is present. In this sample, a long exciton diffusion length of ~10 μm was observed (Fig. 1a). The interlayer exciton diffusion was truncated by the boundary of the heterostructure as evidenced by an abrupt drop in signal. In a stacked bilayer with 1° twist angle ((Fig. 1b), no evidence of exciton diffusion beyond the optical diffraction limit was found at either low or high excitation density under the continuous-wave laser excitation. It is important to compare the PL spatial profile with the laser spot size at the same wavelengths with the exciton energy to correctly determine the optical diffraction limit. In the bilayer with ~3° twist angle, interlayer exciton diffusion became observable, especially at high excitation density (Fig. 1c). These experimental observation of twist-angle dependent exciton diffusion is consistent with a recent theoretical study that calculates exciton dispersions in WSe₂/MoSe₂ bilayers. The flat exciton dispersion for a 1° twisted bilayer indicates spatial localization. In contrast, the calculated exciton dispersion have changed significantly for a 3° twisted bilayer, suggesting delocalized excitons. Our finding has been reported in a paper published in Science Advances in 2020.

- Discovery of atomic reconstruction of moiré superlattice in twisted MoS₂ homobilayers

We recently investigated a series of twist MoS₂ homobilayers prepared by mechanical stacking and discovered that atomic-scale reconstructions occur over a surprisingly broad range of twist angles ($0^\circ < \theta < 6^\circ$). The atomic reconstruction of the moiré pattern is determined by twist-angle-dependent competition between intrinsic strain and interlayer coupling. We identify three regimes of the lattice reconstruction (Fig. 2). In the relaxed regime $0^\circ < \theta < 2.5^\circ$, substantial lattice relaxation leads to large triangular regions with the energetically favorable AB(BA) stacking (Fig. 2c). These regions are separated by sharp domain boundaries and topological defects with AA stacking. As the twist angle increases and real space supercell size decreases (Fig. 2d), the area occupied by the domain walls

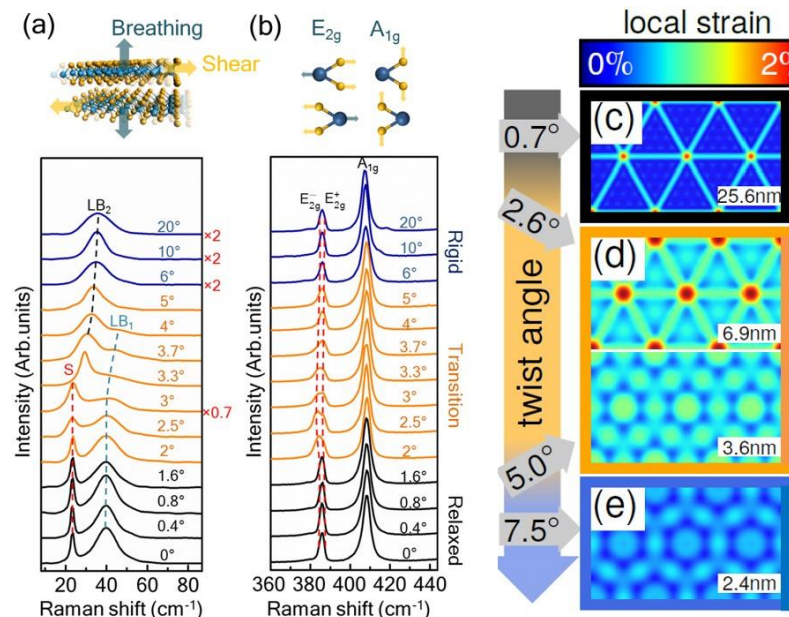


Fig 2: (a) First-principles calculation of moiré lattice reconstruction in three regimes. (b) low-frequency and (c) high-frequency Raman spectra evolves with the twist angles. Accepted by Nature Materials.

that interpolate between them increases steadily across a transition regime ($2.5^\circ < \theta < 6^\circ$). Finally, the TBL reaches the rigid regime at large twist angles $\theta > 6^\circ$ where the layers behave largely decoupled (Fig. 2e). Remarkably, far-field Raman experiments can be used to identify these regimes as shown in Fig. 2a-b. Two types of low-frequency modes are identified: the interlayer shear (S) mode and layer-breathing (LB) mode,⁵ that correspond to the in-plane (tangential) and out-of-plane (normal) relative motions of the two monolayers, respectively. Their rapid evolution can be related to the interlayer coupling and coupling between different phonon modes (Fig. 2a). In the high frequency range, the A_{1g} mode has remained almost the same for all twist angles. In contrast, the E_{2g} mode evolves into a doublet in the transition regime ($2^\circ < \theta < 6^\circ$) as shown in Fig. 2b. These results have been reported in a manuscript recently accepted by Nature Materials.

- Phonon dephasing in MoS₂ monolayers and bulk

Considering exciton-phonon interaction may act as a dephasing process, we adapted a spectroscopy method to investigate phonon dephasing in TMD monolayers. This method can be readily extended to study phonons in moiré superlattices. Since this topics is not the focus of our proposed program, we briefly describe the finding. we directly measure intrinsic optical phonon decoherence in a monolayer and a bulk MoS₂ by observing the temporal evolution of the spectral interference of Stokes photons generated by pairs of laser pulses. We find that a prominent optical phonon mode E_{2g} exhibit room-temperature dephasing time of ~ 7 ps in both the monolayer and bulk. This dephasing time extends to ~ 20 ps in the bulk crystal at ~ 15 K, which is longer than previously thought possible. First-principles calculations suggest that optical phonons decay via two types of three-phonon processes, in which a pair of acoustic phonons with opposite momentum are generated. The result is recently published in Nano Letters.

Future Plans

A key component of our proposed program is to investigate exciton quantum coherence using a powerful spectroscopy method known as the two dimensional electronic coherent spectroscopy (2DECS). While our group has successfully applied this spectroscopy method to investigate exciton coherence in TMD monolayers using experiments performed in the so-called box geometry. We realize that this geometry has serious limitations in studying twisted bilayers.

Starting in the second year of the program, we began building a new experimental set-up in the collinear geometry⁶ as illustrated in Fig. 3. Temporal modulation of the excitation pulses, paired with a co-propagating reference laser, allows not only the recovery of FWM signals from nanoscale objects with lock-in detection but also enables real-time

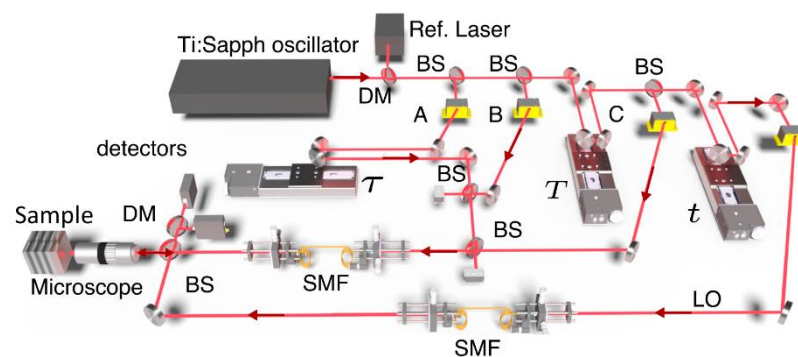


Fig. 3. Representative schematic of the proposed collinear 2DCES experiment. Adapted from Ref 6.

compensation for signal phase fluctuations arising from mechanical vibrations in the setup, surpassing the signal to noise levels achievable with the active stabilization method used in our current 2DCES experiment. Using this new collinear geometry, individual nanostructures such as single semiconductor quantum dots have been studied^{7,8}, demonstrating unprecedented sensitivity in detecting weak nonlinear signals. Removing the need for active stabilization also simplifies data acquisition and shorten the measurement time by a factor ~ 10 . We plan to study quantum coherence of excitons in natural bilayers and twisted bilayers using this set-up. We anticipate that phonon assisted inter-valley scattering would influence the quantum dynamics of TMD bilayers due to the emergence of other low energy valleys. These results will guide our future studies of moiré excitons in twisted bilayers.

References

- (1) Yu, H.; Liu, G.-B.; Tang, J.; Xu, X.; Yao, W. Moiré Excitons: From Programmable Quantum Emitter Arrays to Spin-Orbit-Coupled Artificial Lattices. *Sci. Adv.* **2017**, *3* (11), e1701696. <https://doi.org/10.1126/sciadv.1701696>.
- (2) Jauregui, L. A.; Joe, A. Y.; Pistunova, K.; Wild, D. S.; High, A. A.; Zhou, Y.; Scuri, G.; De Greve, K.; Sushko, A.; Yu, C.-H.; Taniguchi, T.; Watanabe, K.; Needleman, D. J.; Lukin, M. D.; Park, H.; Kim, P. Electrical Control of Interlayer Exciton Dynamics in Atomically Thin Heterostructures. *Science* **2019**, *366* (6467), 870–875. <https://doi.org/10.1126/science.aaw4194>.
- (3) Unuchek, D.; Ciarrocchi, A.; Avsar, A.; Watanabe, K.; Taniguchi, T.; Kis, A. Room-Temperature Electrical Control of Exciton Flux in a van Der Waals Heterostructure. *Nature* **2018**, *560* (7718), 340–344. <https://doi.org/10.1038/s41586-018-0357-y>.
- (4) Unuchek, D.; Ciarrocchi, A.; Avsar, A.; Sun, Z.; Watanabe, K.; Taniguchi, T.; Kis, A. Valley-Polarized Exciton Currents in a van Der Waals Heterostructure. *Nat. Nanotechnol.* **2019**, *14* (12), 1104–1109. <https://doi.org/10.1038/s41565-019-0559-y>.
- (5) Wu, J.-B.; Hu, Z.-X.; Zhang, X.; Han, W.-P.; Lu, Y.; Shi, W.; Qiao, X.-F.; Ijiäs, M.; Milana, S.; Ji, W.; Ferrari, A. C.; Tan, P.-H. Interface Coupling in Twisted Multilayer Graphene by Resonant Raman Spectroscopy of Layer Breathing Modes. *ACS Nano* **2015**, *9* (7), 7440–7449. <https://doi.org/10.1021/acsnano.5b02502>.
- (6) Autry, T. M.; Moody, G.; Fraser, J.; McDonald, C.; Mirin, R. P.; Silverman, K. Single-Scan Acquisition of Multiple Multidimensional Spectra. *Optica, OPTICA* **2019**, *6* (6), 735–744. <https://doi.org/10.1364/OPTICA.6.000735>.
- (7) Kasprzak, J.; Patton, B.; Savona, V.; Langbein, W. Coherent Coupling between Distant Excitons Revealed by Two-Dimensional Nonlinear Hyperspectral Imaging. *Nature Photon* **2011**, *5* (1), 57–63. <https://doi.org/10.1038/nphoton.2010.284>.
- (8) Fras, F.; Mermilliod, Q.; Nogues, G.; Hoarau, C.; Schneider, C.; Kamp, M.; Höfling, S.; Langbein, W.; Kasprzak, J. Multi-Wave Coherent Control of a Solid-State Single Emitter. *Nature Photon* **2016**, *10* (3), 155–158. <https://doi.org/10.1038/nphoton.2016.2>.

Publications

1. “Moiré potential impedes interlayer exciton diffusion in van der Waals heterostructures” Junho Choi, Wei-Ting Hsu, Li-Syuan Lu, Liuyang Sun, Hui-Yu Cheng, Ming-Hao Lee, Jiamin Quan, Kha Tran, Chun-Yuan Wang, Matthew Staab, Kayleigh Jones, Takashi Taniguchi, Kenji Watanabe, Ming-Wen Chu, Shangjr Gwo, Suenne Kim, Chih-Kang Shih, **Xiaoqin Li**, Wen-Hao Chang, *Science Advances*, 2020, 6, eaba8866.
2. “Phonon Dephasing Dynamics in MoS₂”, Liuyang Sun, Parveen Kumar, Zeyu Liu, Junho Choi, Bin Fang, Sebastian Roesch, Kha Tran, Joshua Casara, Eduardo Priego, Yu-Ming Chang, Galan Moody, Kevin L Silverman, Virginia O Lorenz, Michael Scheibner, Tengfei Luo, **Xiaoqin Li**, *Nano Letters*, 21, 1434, 2021.
3. “Phonon Renormalization in Reconstructed MoS₂ Moire Superlattices”, Jiamin Quan, Lukas Linhart, Miao-Ling Lin, Daehun Lee, Jihang Zhu, Chun-Yuan Wang, Wei-Ting Hsu, Junho Choi, Jacob Embley, Carter Young, Takashi Taniguchi, Kenji Watanabe, Chih-Kang Shih, Keji Lai, Allan H. MacDonald, Ping-Heng Tan, Florian Libisch, **Xiaoqin Li**, *Nature Materials*, Accepted

Session IV

Physical Behavior of Quantum Metamaterials

**Steven M. Anlage, Quantum Materials Center, Physics Department,
University of Maryland**

i) Program Scope

The goal is to investigate the physical properties of both natural and artificial quantum matter. The *natural* quantum materials under investigation have unique topological properties and are being examined through quantitative and unique electromagnetic measurements. We have performed the first electromagnetic experimental investigations of proximity-coupled superconducting topological insulators, and investigated the electrodynamic response of a new topological superconductor with protected surface states. The technical approach involves high-resolution and broad bandwidth microwave resonator measurements, along with nonlinear Meissner effect imaging techniques,[1, 2] all at mK temperatures. Our measurements give fundamental insights into the nature of superconductivity in topological materials. The *artificial* quantum materials are being investigated through engineered structures that mimic natural atoms and create new electronic and electromagnetic behavior not observed in nature. Our objective is to explore new quantum states of matter through creation of engineered quantum meta-atoms and their arrangement into structures that create qualitatively new types of quantum coherent behavior, especially in terms of their interaction with electromagnetic fields. The technical approach involves assembly of superconducting quantum devices that are nominally identical and strongly interacting with each other, and with a bath of microwave photons, and measuring their emergent behavior through electromagnetic response. The results will give fundamental insights into the nature of condensed matter and specific outcomes include investigation of proposed but unrealized states of matter, emergent quantum phenomena, and controlled super-radiant behavior. The work builds on metamaterials consisting of macroscopic quantum radio frequency Superconducting Quantum Interference Devices (rf SQUIDs), which have proven to be a rich nonlinear medium for creating new collective properties of artificial matter.

ii) Recent Progress

The grant commenced on 07/01/2018 and 2 graduate students were recruited to begin work. One of the students graduated in 2020, and a post-doc was hired in 2019 to accelerate the quantum metamaterials effort. Two efforts have been undertaken - one building on our strengths in surface impedance of new superconducting materials and the other to investigate both macroscopic-quantum and fully-quantum metamaterials. The first project utilized our newly-developed dielectric resonator surface impedance and nonlinear Meissner effect imaging technique.[2] We examined the electrodynamic properties of a unique superconductor / topological insulator proximity-coupled bilayer system (YB_6/SmB_6) down to mK temperatures.[3] We found that superconductivity could be induced into the surface states of the topological insulator SmB_6 , and measured the Meissner screening length in that material for the first time. We then went on to study the electrodynamic properties of the unique heavy Fermion material UTe_2 . We measured the complex conductivity of this material down to mK temperatures ($T_c = 1.6$ K) and a broad range of microwave frequencies.[4] We see clear evidence of chiral spin-triplet superconductivity with intrinsic surface states. This material is believed to be the first definitive experimental example of a Weyl superconductor with topologically protected surface states. Our findings suggest that UTe_2

can be a new platform to study exotic (Majorana) topological excitations in higher dimension. These landmark results are under review in Nature Communications.[4]

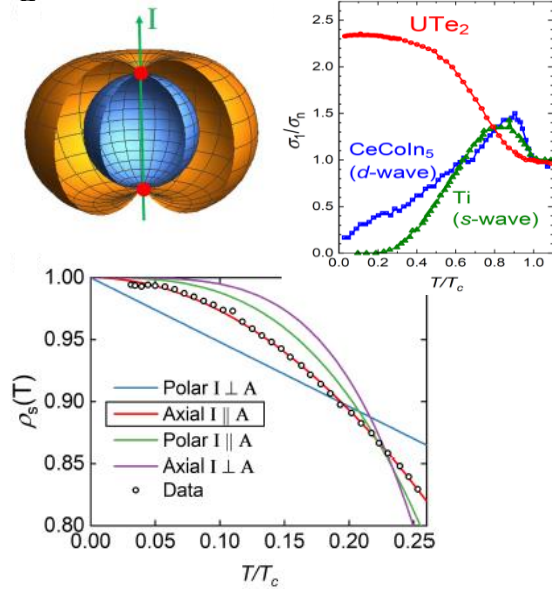


Fig. 1 Microwave complex conductivity data on superconducting UTe₂ single crystals made and measured at the University of Maryland Quantum Materials Center. The lower left plot shows the superfluid density vs reduced temperature T/T_c of UTe₂. The temperature dependence fits that of a spin-triplet axial p-wave superconductor with the vector potential aligned with the gap symmetry direction \vec{I} (shown above). These results indicate that the nodal points lie in or near the ab-plane of the material. The upper right plot shows the real part of the complex conductivity and its contrast with conventional s-wave and d-wave superconductors. We believe that the enhanced $\sigma_1(T)$ below T_c is a sign of Majorana arc states in this Weyl superconductor.[4]

The first metamaterials project is to explore collective properties of metamaterials made up of radio frequency (rf) Superconducting Quantum Interference Devices (SQUIDs). Experiments were conducted to image the *collective response* of the metamaterial as a function of external rf and dc driving magnetic flux.[5] These studies examine the fundamental properties of strongly-coupled nonlinear meta-atoms, and act as a surrogate for understanding the basic physics of condensed matter from the bottom up. A remarkable transition from incoherent and disordered behavior at low rf flux amplitude to a strongly coherent and nearly uniform response at higher rf power can be attributed to activation of the Josephson nonlinearity in the SQUIDs. A set of realistic fully-nonlinear simulations on an high-performance computing cluster reveals this transition arises from dramatic rearrangement of collective modes of the system.[5]

We also developed the world's first tunable Josephson electric metamaterial. This is the first example of an electrically-active macroscopic quantum metamaterial that is tuned by the Josephson effect. Superconducting wires decorated with Josephson junctions interact with electromagnetic waves, creating a tunable dielectric metamaterial.[6] By current-biasing the Josephson junctions we can tune the plasma edge of the artificial medium. This is also a highly nonlinear medium, both in terms of rf and dc responses.

An important part of our project aims to transition the macroscopic quantum metamaterials work discussed above into the fully quantum regime by replacing the rf SQUIDs with superconducting Qubits having two dominant quantum states, and coupling the Qubits together through collective electromagnetic modes. The initial setting for the experiment is the Quantum Transmission Line (QTL) metamaterial shown in Fig. 2. The objective is to create a discrete transmission line medium made up of quantum "meta-atoms" that are each endowed with a discrete energy level spectrum. The post-doc and student have designed and fabricated rf flux qubits by e-beam lithography inside superconducting co-planar waveguide resonant device structures (see Fig. 2). The co-planar waveguide (CPW) Aluminum (Al) transmission line resonators operate with high quality factors in the superconducting state at mK temperatures. We have optimized their performance through a series of experiments at mK temperatures and over a broad frequency and magnetic flux range. We have designed the flux Qubits to have strong

interactions with each other, and with the QTL, so that quantum collective effects will play a dominant role in their behavior. Our first quantum meta-atom has been integrated into the CPW as shown in Fig. 2. Our ability to fabricate and test these metamaterials has been severely compromised by the COVID-19 pandemic. We have been granted a 1-year no-cost extension by DOE to complete this research.

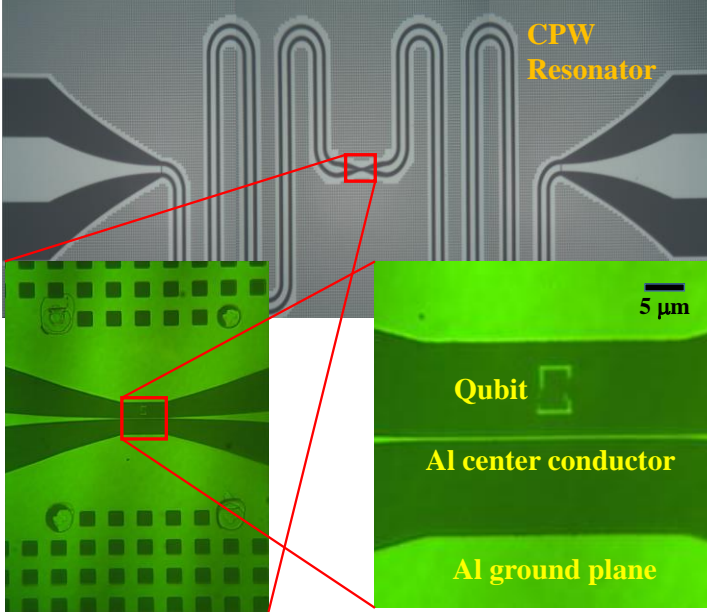


Fig. 2 Quantum Transmission Line (QTL) hosting a superconducting Qubit made from Aluminum (Al) and Al-oxide Josephson junctions. The flux qubit is created by electron-beam lithography and is designed to have a transition between the ground state and first excited state at 5 GHz, which lies between two resonant frequencies of the co-planar waveguide (CPW) resonator. Photons are injected on the left in the upper figure and enter the CPW resonator. These photons interact with the Qubit to prepare or evolve its quantum state, and to read-out the quantum state of the Qubit. The quantum metamaterial will be created by placing multiple Qubits together surrounding the Al center conductor.

iii) Future Plans

Our rf SQUID macroscopic-quantum metamaterial work has spawned a small theoretical community dedicated to making predictions for new collective phenomena to observe in this unique nonlinear medium [7]-[9]. Predicted phenomena include Chimera states, which are spatially separated regions of coherent and incoherent response, and they can form spontaneously in an otherwise homogeneous nonlinear media like our SQUID metamaterials. Other possibilities include chaos, breathers (long-lived nonlinear excitations), and novel collective modes that require a strongly nonlinear medium for their existence. A new round of samples to test these theories, and to discover new phenomena, have been designed and are now in fabrication. We are also performing detailed measurements and modelling of the *nonlinear* response of our rf SQUID metamaterials, with much of the work being done by a UMD undergraduate in collaboration with members of our theoretical community.

The Quantum Transmission Line structures are now being produced in number since we have recently perfected the intricate Qubit device fabrication processes. The immediate goal is to build QTLs with single qubits for basic characterization of vacuum Rabi splitting, Rabi oscillations, coherence time and de-phasing mechanisms. The student and post-doc will perform quantum tomography of the meta-atoms to demonstrate coherent quantum control and utilize collective know-how at UMD to optimize the coherence time of the individual meta-atoms. At the same time multiple-qubit QTLs will be fabricated on the same wafer and tested in the BlueFors dilution refrigerator, which can handle up to six samples on each cooldown.

iv) References

- [1] A. P. Zhuravel, B. G. Ghamsari, C. Kurter, P. Jung, S. Remillard, J. Abrahams, A. V. Lukashenko, A. V. Ustinov, Steven M. Anlage, "**Imaging the Anisotropic Nonlinear Meissner Effect in Nodal $\text{YBa}_2\text{Cu}_3\text{O}_{7-\delta}$ Thin-Film Superconductors**," Phys. Rev. Lett. 110, 087002 (2013).
- [2] Seokjin Bae, Yuewen Tan, Alexander P Zhuravel, Lingchao Zhang, Shengwei Zeng, Yong Liu, Thomas A. Lograsso, Ruslan Prozorov, Ariando, T. Venkatesan, Steven M. Anlage, "**Dielectric Resonator Method For Determining Gap Symmetry Of Superconductors Through Anisotropic Nonlinear Meissner Effect**," Rev. Sci. Instrum. 90, 043901 (2019).
- [3] Seokjin Bae, Seunghun Lee, Xiaohang Zhang, Ichiro Takeuchi, Steven M. Anlage, "**Microwave Meissner screening properties of proximity-coupled topological-insulator / superconductor bilayers**," Phys. Rev. Materials 3, 124803 (2019).
- [4] Seokjin Bae, Hyunsoo Kim, Sheng Ran, Yun Suk Eo, I-Lin Liu, Wesley Fuhrman, Johnpierre Paglione, Nicholas P Butch, Steven Anlage, "**Anomalous normal fluid response in a chiral superconductor**," [arXiv:1909.09032](https://arxiv.org/abs/1909.09032). Under review in Nature Communications.
- [5] Alexander P. Zhuravel, Seokjin Bae, Alexander V. Lukashenko, Alexander S. Averkin, Alexey V. Ustinov and Steven M. Anlage, "**Imaging collective behavior in an rf-SQUID metamaterial tuned by DC and RF magnetic fields**," Appl. Phys. Lett. 114, 082601 (2019).
- [6] Melissa Trepanier, Daimeng Zhang, Lyudmila Filippenko, Valery Koshelets, Steven M. Anlage, "**Tunable Superconducting Josephson Dielectric Metamaterial**," AIP Advances 9, 105320 (2019). (Editor's Pick).
- [7] N. Lazarides, G. Neofotistos, and G. P. Tsironis, "**Chimeras in SQUID metamaterials**," Phys Rev B 91 (5), 054303 (2015).
- [8] Amitava Banerjee and Debopriya Sikder, "**Transient chaos generates small chimeras**," Phys Rev E 98 (3), 032220 (2018).
- [9] J. Hizanidis, N. Lazarides, and G. P. Tsironis, "**Pattern formation and chimera states in 2D SQUID metamaterials**," Chaos: An Interdisciplinary Journal of Nonlinear Science 30 (1), 013115 (2020).

Publications supported by this grant

1. Alexander P. Zhuravel, Seokjin Bae, Alexander V. Lukashenko, Alexander S. Averkin, Alexey V. Ustinov and Steven M. Anlage, “**Imaging collective behavior in an rf-SQUID metamaterial tuned by DC and RF magnetic fields,**” *Appl. Phys. Lett.* **114**, 082601 (2019).
2. Seokjin Bae, Yuewen Tan, Alexander P Zhuravel, Lingchao Zhang, Shengwei Zeng, Yong Liu, Thomas A. Lograsso, Ruslan Prozorov, Ariando, T. Venkatesan, Steven M. Anlage, “**Dielectric Resonator Method For Determining Gap Symmetry Of Superconductors Through Anisotropic Nonlinear Meissner Effect,**” *Rev. Sci. Instrum.* **90**, 043901 (2019).
3. Shukai Ma, Bo Xiao, Yang Yu, Kueifu Lai, Gennady Shvets, Steven M. Anlage, “**Topologically Protected Photonic Modes in Composite Quantum Hall/Quantum Spin Hall Waveguides,**” *Phys. Rev. B* **100**, 085118 (2019).
4. Shaomao Xu, Geng Zhong, Chaoji Chen, Min Zhou, Dylan J. Kline, Rohit Jiji Jacob, Hua Xie, Shuaiming He, Zhennan Huang, Jiaqi Dai, Alexandra H. Brozena, Reza Shahbazian-Yassar, Michael R. Zachariah, Steven M. Anlage, Liangbing Hu, “**Uniform, Scalable, High-Temperature Microwave Shock for Nanoparticle Synthesis through Defect Engineering,**” *Matter* **1**, 759-769 (2019).
5. Melissa Trepanier, Daimeng Zhang, Lyudmila Filippenko, Valery Koshelets, Steven M. Anlage, “**Tunable Superconducting Josephson Dielectric Metamaterial,**” *AIP Advances* **9**, 105320 (2019). (Editor's Pick).
6. Tristin Metz, Seokjin Bae, Sheng Ran, I-Lin Liu, Yun Suk Eo, Wesley T. Fuhrman, Daniel F. Agterberg, Steven M. Anlage, Nicholas P. Butch, Johnpierre Paglione, “**Point Node Gap Structure of Spin-Triplet Superconductor UTe₂,**” *Phys. Rev. B* **100**, 220504(R) (2019). (Editors' Suggestion).
7. Seokjin Bae, Seunghun Lee, Xiaohang Zhang, Ichiro Takeuchi, Steven M. Anlage, “**Microwave Meissner screening properties of proximity-coupled topological-insulator / superconductor bilayers,**” *Phys. Rev. Materials* **3**, 124803 (2019).
8. Seokjin Bae, Hyunsoo Kim, Sheng Ran, Yun Suk Eo, I-Lin Liu, Wesley Fuhrman, Johnpierre Paglione, Nicholas P Butch, Steven Anlage, “**Anomalous normal fluid response in a chiral superconductor,**” *arXiv:1909.09032*. Under review in Nature Communications.

Non-Equilibrium Quantum Dynamics of Multi-Qubit Superconducting Circuits

Hakan Türeci, Department of Electrical Engineering, Princeton University

Program Scope

The overarching goal of this project is to develop computational techniques that are able to accurately capture the evolution of the quantum state of multiple Josephson junction (JJ) artificial atoms embedded in large-scale complex planar circuitry or 3D cavities, and driven by microwave and RF signals. This effort will build on quantum electrodynamic modeling tools we developed for superconducting circuits in the previous performance period [1,2], and extend them further to address phenomena that are of current interest in the field of superconducting circuits. The major goals are:

1. **3D Quantum Electrodynamic Modeling of Cavity QED systems:** The Heisenberg-Langevin (HL) approach developed in the previous period for planar circuit electrodynamic systems will be extended to three-dimensional solid state structures.
2. **Radiative corrections in solid state Cavity QED systems:** Based on the formulation developed in 1. we will look into the calculation of radiative corrections of natural and artificial atoms in open resonators.
3. **Non-equilibrium dynamics in multi-qubit quantum circuits:** A general method will be developed to derive and parametrize effective Quantum Master Equations for microwave-driven superconducting quantum circuits.
4. **Dynamics of qubits coupled to high-impedance resonators:** The phase-diagram of driven-dissipative high-impedance resonators with embedded superconducting qubits will be studied.

Recent Progress

Towards the major goals 2 and 4, we are completing an in-depth study of quantum electrodynamics of superconducting high-impedance cavity QED systems. Recent experiments show that the system of a Josephson atom coupled to a high impedance transmission line provides a tunable platform for realizing light-matter interactions across a wide range of coupling strength regimes [3,4]. These systems have also been considered as effective experimental platforms for quantum simulation of quantum impurity systems in novel regimes [5].

In recent work, we show that the notion of radiative corrections to the properties of an atom (e.g. the Lamb shift, spontaneous emission rate) can become ill-defined in a high-impedance environment. The origin of this failure can be traced to the fact that the effective coupling of the atom to its electromagnetic environment can become so large in certain experimental realizations that the combined atom+cavity system finds itself in a non-perturbative regime of the associated 1+1D effective field theory. What then becomes of concepts such as the spontaneous emission

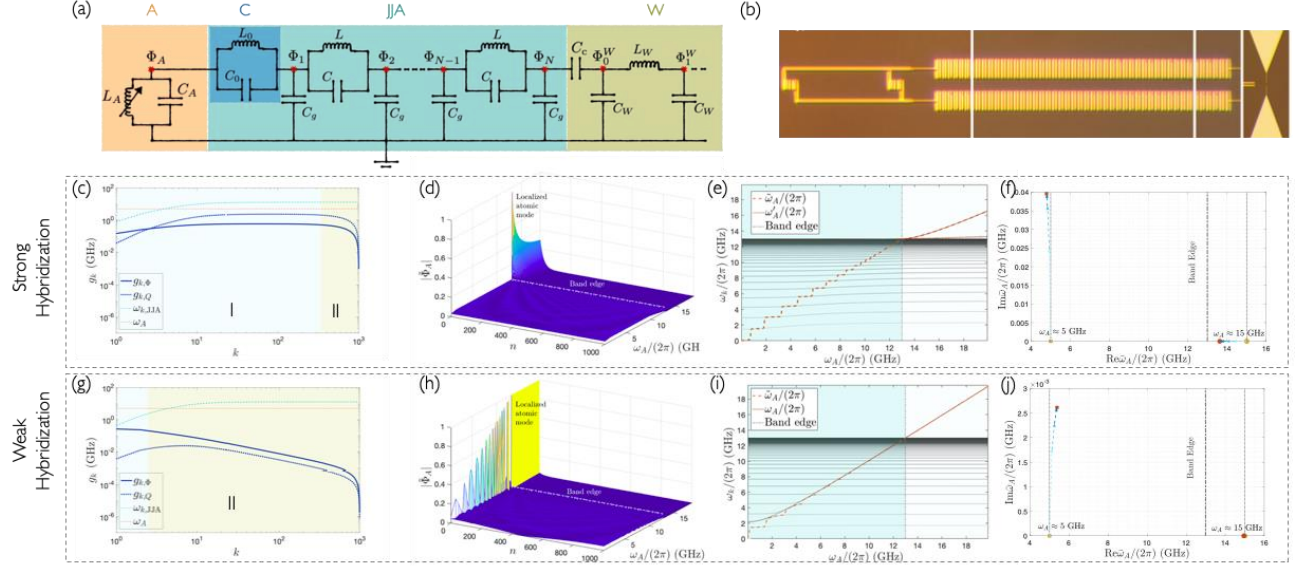


Fig.1 (a) Lumped-element circuit model for an artificial atom [A] galvanically coupled [C] to a high-impedance transmission line realized by a long array of JJs [JJA] capacitively coupled to an infinite 50Ω transmission line [W]. (b) Experimental implementation of a similar model (from Ref. [4]). We study the two cases of strong hybridization (SH) ((c)-(f)) and weak hybridization (WH) ((g)-(j)) between the atomic and the JJA modes realized by a tunable coupling element [C]. Coupling coefficients between the atomic and multiple array modes can be comparable to the bare excitation frequencies, in region I as indicated by the blue shaded area. (d,h) The variation of the atomic mode as a function of its bare plasma frequency. In the SH regime, for atomic frequency within the photonic band, the atomic mode is spatially delocalized over the entire array. We find a similar delocalization for the WH case when the atomic mode is only near-resonant with one of the array modes. (e, i) Tuning the atomic frequency via a SQUID loop, we note that in the SH regime it is not possible to spectrally distinguish the atomic mode. In the WH regime the atomic mode goes through a series of avoided crossings as it hybridizes with the array modes. (f, j) Movement of complex eigenfrequencies of the open atom+JJA system coupled to external waveguide as the coupling is switched on.

rate that are based on perturbative notions? We answer this question using the HL formulation of circuit quantum electrodynamics [1,2] describing the open system (atom+high-imdedance cavity coupled to free space) in terms of the complex-valued poles of its hybridized resonances (see Fig.1). We find in particular that the atomic mode spectrally and spatially ‘melts’ into the modes of its environment and cannot be distinguished from other hybridized resonances (see Fig.1e). This picture is quantitatively provided through the access to the spatial structure of the quasi-modes of the hybridized system (Fig.1 d, h), and is consistent with findings of recent experimental studies.

The above findings underline the limitations of the perturbative approach to quantum electrodynamics. Perhaps more importantly, the theoretical approach employed to arrive at these findings indicate a new conceptual structure (QED in terms of complex-valued resonance poles of the open system) that retains its validity across all parametric regimes. The work concludes by explicitly showing how this new approach reproduces perturbative results in its proper regime of validity.

Future Plans

Our work in the next funding period will focus on (1) the non-equilibrium quantum dynamics of high-impedance cavity QED systems under continuous driving. Various non-linear optical dynamical instabilities are expected (as e.g. observed in our recent theory-experiment collaboration [6] on a different system) which in contrast to [6] can be induced already in the few-photon regime. This requires the development of a field theoretic description that is valid across the quantum-to-classical transition, (2) The development of a coarse-graining approach to the dynamics of driven dissipative superconducting oscillator systems.

References

- [1] **Non-Markovian dynamics of a superconducting qubit in an open multimode resonator**, M. Malekakhlagh, A. Petrescu, Hakan E. Tureci, Phys. Rev. A **94**, 063848 (2016).
- [2] **Cutoff-free Circuit Quantum Electrodynamics**, Moein Malekakhlagh, Alexandru Petrescu, Hakan E. Tureci, Phys. Rev. Lett. **119**, 073601 (2017).
- [3] **A tunable Josephson platform to explore many-body quantum optics in circuit-QED**, S. Leger et al., npj Quantum Information 5, 19 (2019).
- [4] **Superstrong coupling in circuit quantum electrodynamics**, R. Kuzmin et al., npj Quantum Information 5, 20 (2019).
- [5] **Photon decay in circuit quantum electrodynamics**, R. Kuzmin et al., arxiv:2010.02099
- [6] **Nearly quantum-limited Josephson-junction Frequency Comb synthesizer**, P. Lu et al., arXiv:2005.10193

Publications

1. **Lifetime renormalization of weakly anharmonic superconducting qubits. I. Role of number nonconserving terms**, Moein Malekakhlagh, Alexandru Petrescu, and Hakan E. Türeci, Phys. Rev. B **101**, 134509 (2020).
2. **Lifetime renormalization of weakly anharmonic superconducting qubits. II. The readout problem**, Moein Malekakhlagh, Alexandru Petrescu, and Hakan E. Türeci, Phys. Rev. B **101**, 134510 (2020).
3. **Nearly quantum-limited Josephson-junction Frequency Comb synthesizer**, P. Lu et al., arXiv:2005.10193

Quantum Nanoplasmonics Theory

Vadym Apalkov

Department of Physics and Astronomy,

Georgia State University, Atlanta, GA 30303

E-mail: vapalkov@gsu.edu

Program Scope

Major goals of this Program is in theoretical research devoted to new phenomena in two dimensional (2D) materials and metal nanostructures subjected to strong ultrafast optical fields. We consider such novel and promising 2D systems as graphene (a 2D semimetal), transition metal dichalcogenides (2D semiconductors), and surfaces (2D boundaries) of three-dimensional topological insulators. We focus on effects in the reciprocal space that are related to topological properties of the Bloch wave functions: Topological curvature, Berry phase, valley polarization, etc. These properties are protected by fundamental symmetries of nature: time reversal (T-symmetry) and spatial reflection (P-symmetry), which are in the focus of this Proposal.

Recent Progress

Topological resonance in Weyl semimetals: ultrafast electron dynamics:

Three dimensional Weyl semimetals bring extra dimensionality into the problem of ultrafast electron dynamics in topological materials. Weyl semimetals can be considered as a combination of two dimensional gapped-graphene-like systems with variable bandgap and dispersion relation. We have theoretically studied the effect of topological resonance, which is an intrinsic property of ultrafast dynamics, in such three dimensional materials [1].

The ultrafast electron dynamics in Weyl semimetals is controlled by competition between the dynamic and the topological phases, which occurs in the field of a circularly polarized femtosecond long optical pulse. When these two phases cancels each other the system exhibit the topological resonance, which manifests itself in large residual conduction band population. For Weyl semimetals, for the pulse propagating along, for example, \mathbf{z} direction, the topological resonance results in predominant conduction band population of the region in the reciprocal space near one of the Weyl points, say W , for $k_z < 0$ and the region near another Weyl point, W' , for $k_z > 0$. Exactly at $k_z = 0$, the conduction bands at both Weyl points are equally populated. The reason for such behavior is that for each cross-section $k_z = \text{const}$, the Weyl semimetal behaves as a two dimensional gapped graphene system with the bandgap that is proportional to k_z .

Since the strength of the topological resonance in gapped graphene systems increases with the magnitude of the bandgap and manifests itself in the predominant population of one of the valleys, then the similar features of topological resonance is visible in three dimensional Weyl semimetals. Thus, the dynamics of Weyl semimetals in circularly polarized pulse provides an extra tool to study the properties of topological resonance, i.e., its dependence on the bandgap and energy dispersion of the material, and profile and intensity of the optical pulse.

Gapped graphene-like materials in ultrashort optical pulse: nonlinear absorption.

Topological properties of graphene-like materials can be controlled by tuning their bandgap. One of the characteristics of the system is its response to ultrashort optical pulse, which can coherently probe the ultrafast electron dynamics. Such dynamics is highly irreversible and leave the system in highly excited residual state, which also determines the nonlinear ultrafast optical absorption. We have studied theoretically the nonlinear absorption of an ultrafast optical pulse by gapped graphene monolayer [2]. At low field amplitudes, the absorbance in pristine graphene is equal to the universal value of 2.3 %. Although, the ultrafast optical absorption for low field amplitudes is independent on polarization, linear or circular, of an applied optical pulse, for high field amplitudes, the absorption strongly depends on the pulse polarization. For a linearly polarized pulse, the optical absorbance is saturated at the value of ~ 1.4 % for the pulse's amplitude of > 0.4 V/A, but no such saturation is observed for a circularly polarized pulse. For the gapped graphene systems, the absorption of a linearly polarized pulse has weak dependence on the bandgap, while for a circularly polarized pulse, the absorption is very sensitive to the bandgap.

The ultrafast absorption of optical pulses in gapped graphene is determined by specific properties of ultrafast electron dynamics, both intraband and interband, in the field of the pulse. Such dynamics strongly depends on polarization of the optical pulse, whether it is linear or circular. The fundamental difference between these two types of polarization is that for a single oscillation pulse the electron trajectory in the reciprocal space passes twice through the region with large interband coupling for linear polarization and only once for circular polarization of the pulse. As a result the interference pattern with the dark and bright fringes is clearly visible in the conduction band population distribution for a linearly polarized pulse, but no such interference is observed at small field amplitudes for a circularly polarized pulse. Due to this effect the absorption of linearly and circularly polarized pulses is quite different. Such difference is well pronounced for relatively large field amplitudes, > 0.1 V/A. For small field amplitudes, the absorbance for both types of polarization behaves similarly. This is because for small field amplitudes the size of the electron displacement in the reciprocal space is less than or comparable to the size of the region with large interband coupling. In this case, during the whole trajectory, both for linearly and circularly polarized pulses, there is a strong interband coupling. Thus no interference pattern can be formed and no difference between the linear and circular polarizations can be observed.

Topological nanospaser: topologically protecting spasing dynamics and spontaneous symmetry breaking

Bringing topology into plasmonic systems opens unique topological control of the system, such topologically protected states of the systems and topologically nontrivial dynamics. In this relation, we combined topology and coherent generation of surface plasmons, and proposed two types of topological nanospaser: topological nanospaser of type I [3] and topological nanospaser of type II [4]. In the topological nanospaser of type I the topology is introduced in the plasmonic modes of spaser, while in the topological spaser of type II the gain medium has nontrivial topology.

A topological spaser of type I consists of a honeycomb lattice of spherical metal nanoshells containing a gain medium [3]. The two sublattices, A and B, are built from two different types of nanoshells. A meta-atoms of such lattice is plasmonic metal nanoshell containing an achiral gain medium. The A and B sublattices differ in size and shape of the constituent nanoshells, so their individual spasers have different eigenfrequencies. Such a spaser generates one of two chiral plasmonic collective modes characterized by topological charge +1 or -1 whose local field rotate clockwise or counterclockwise, respectively. Which of these two modes is generated is determined by a spontaneous violation of symmetry as defined by the initial conditions. The chirality of the

spasing mode is stable and topologically protected. The macroscopic fields of the spasing mode are localized along the edge of the lattice despite the absence of the edge states. The edge fields propagates clockwise (for topological charge +1) or counterclockwise (for topological charge -1). Due to a very high lattice momentum they are dark in contrast to the original lasing spaser. Nevertheless, they can be outcoupled by using a corresponding coupler, e.g., grating.

A topological nanospaser of type II, proposed by us in Ref. [4] that consists of a plasmonic metal spheroid as the surface plasmon resonator and a nanoflake of a semiconductor TMDC as the gain medium. This spaser has two mutually-T-reserved dipole modes with identical frequencies but opposite chiralities (topological charges $m = 1$ and $m = -1$). Only one mode whose chirality matches that of the active (pumped) valley, i.e., $m = 1$ for the K valley and $m = -1$ for the K' valley can be generated while the conjugated mode does not go into generation at any pumping level. The topological spaser is stable with respect to even large perturbations: the surface plasmon with mismatched topological charge injected into the system even in large numbers decay exponentially within a 100 fs time. This implies a strong topological protection. This protection is not trivial because the exact valley selection rule matching its chirality to that of the surface plasmons is strictly valid on the symmetry axis of the metal spheroid (in the center of the TMDC gain-medium flake). Off-axis, there is a coupling of the gain to the chirally-mismatched surface plasmons. However, the strong topological protection appears due to the fact that the spaser is a highly nonlinear, threshold phenomenon. In fact, it is the nonlinear saturation of the gain and the concurrent clamping of the inversion that cause the strong mode competition. The topologically matched mode ($m = 1$ for the K valley and $m = -1$ for the K' valley) reaches the threshold first and saturates the gain, thus, preventing the mismatched mode from generation under any pumping or any perturbations.

The proposed topological nanospasers are promising for use in nanooptics and nanospectroscopy where strong rotating nano-localized fields are required. It may be especially useful in applications to biomolecules and biological objects, which are typically chiral.

Future Plans

The properties of topological nanospaser of type II, which consists of metal nanospheroid and TMDC nanoflake, strongly depend on the size of the gain medium, i.e., TMDC system. Our preliminary results show that in this case we should expect a special two-threshold regime, when the transition from generation of only one plasmonic mode to simultaneous generation of two modes occurs. It happens at large radius of TMDC nanopatch. We will study in details how the dynamics of topological nanospaser depends on the parameters of the system: size of TMDC nanoflake and also on initial condition, i.e., initial number of plasmons. Another problem, which will be addressed in this relation, is control of the stationary regime of nanospaser by ultrashort optical pulse. Such pulse can switch the system from one regime, when only one type of plasmons is generated, to another regime, which is characterized by multi plasmon generation.

References

- [1] F. Nematollahi, Azar Oliaei Motlagh, J.S. Wu, R Ghimire, V. Apalkov, M.I. Stockman, “*Topological resonance in Weyl semimetals in a circularly polarized optical pulse*”, **Physical Review B** 102 (12), 125413 (2020)
- [2] Azar Oliaei Motlagh, A.J. Zafar, A. Mitra, V. Apalkov, M.I. Stockman, “*Ultrafast strong-field absorption in gapped graphene*”, **Physical Review B** 101 (16), 165433 (2020).

[3] Jhih-Sheng Wu, Vadym Apalkov, and Mark I. Stockman, “*Topological Spaser*”, **Physical Review Letter**: 124, 017701 (2020).

[4] R .Ghimire, J.S. Wu, V. Apalkov, M.I. Stockman, “*Topological nanospaser*”, **Nanophotonics** 9 (4), 865-874 (2020).

Publications

[1] F. Nematollahi, Azar Oliaei Motlagh, J.S. Wu, R Ghimire, V. Apalkov, M.I. Stockman, “*Topological resonance in Weyl semimetals in a circularly polarized optical pulse*”, **Physical Review B** 102 (12), 125413 (2020)

[2] Azar Oliaei Motlagh, A.J. Zafar, A. Mitra, V. Apalkov, M.I. Stockman, “*Ultrafast strong-field absorption in gapped graphene*”, **Physical Review B** 101 (16), 165433 (2020).

[3] R .Ghimire, J.S. Wu, V. Apalkov, M.I. Stockman, “*Topological nanospaser*”, **Nanophotonics** 9 (4), 865-874 (2020).

[4] Jhih-Sheng Wu, Vadym Apalkov, and Mark I. Stockman, “*Topological Spaser*”, **Physical Review Letter**: 124, 017701 (2020).

[5] S. Azar Oliaei Motlagh, F. Nematollahi, A. Mitra, A.J. Zafar, V. Apalkov, M.I. Stockman, “*Ultrafast optical currents in gapped graphene*”, **Journal of Physics: Condensed Matter** 32 (6), 065305 (2019).

[6] S. Azar Oliaei Motlagh, F. Nematollahi, V. Apalkov, M.I. Stockman, “*Topological resonance and single-optical-cycle valley polarization in gapped graphene*”, **Physical Review B** 100 (11), 115431 (2019).

[7] S. Azar Oliaei Motlagh, V. Apalkov, M.I. Stockman, “*Laser pulse waveform control of Dirac fermions in graphene*”, **Quantum Nanophotonic Materials, Devices, and Systems**, 11091 (2019).

[8] F. Nematollahi, S. A. Oliaei Motlagh, V Apalkov, M.I. Stockman, "Weyl semimetals in ultrafast laser fields", **Physical Review B** 99 (24), 245409 (2019).

[9] S. A. Oliaei Motlagh, J. S. Wu, V. Apalkov, and M. Stockman, "Ultrafast laser pulse induced topological resonance in MoS₂ monolayer" in **Lasers and Electro-Optics**, OSA Technical Digest (Optical Society of America), paper JT4M.3 (2019).

[10] Fatemeh Nematollahi, Vadym Apalkov, and Mark I. Stockman, “*Weyl semimetals in circularly-polarized ultrafast laser field*”, **Frontiers in Ultrafast Optics: Biomedical, Scientific, and Industrial Applications XIX**; 1090803 (2019).

Optical, Electrical and Magnetic Studies of Hybrid Organic-Inorganic Perovskite Semiconductors

PI: Z. Valy Vardeny; Physics & Astronomy Department, University of Utah

Program Scope

Magneto-Optical and spin responses of carriers and excitons in organic inorganic perovskite semiconductors. During the last two years we have investigated: (i) The photocarriers spin response in various 2D and 3D hybrid organic-inorganic perovskite (HOIP) semiconductors using the circular-photogalvanic effect; (ii) The nonlinear optical response of these compounds; (iii) The magneto-optic response of these materials using the high magnetic field national laboratory (NFMFL) in Tallahassee Florida.

Recent Progress

(i) Probing Rashba splitting in 2D-HOIP using the circular photogalvanic effect (CPGE)

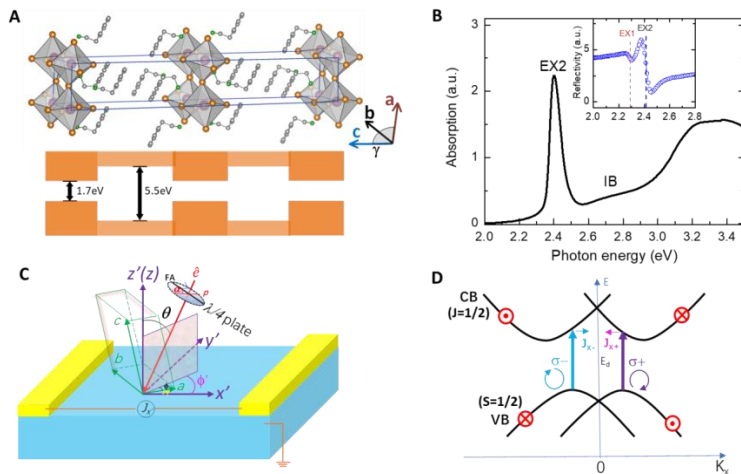


Figure 1: Rashba splitting in 2D hybrid organic-inorganic perovskite (2D-PEPI) crystal: **A**, Schematic of the 2D-PEPI structure with alternating ($C_6H_5C_2H_4NH_3^+$) and $[PbI_6]^{4-}$ layers, which form natural multiple quantum wells (MQW), where the inorganic layer is the potential ‘well’ and organic layer is the potential ‘wall’. The crystal structure is monoclinic. **B**, Room temperature absorption (black line) spectrum of a thin film 2D-PEPI where the exciton (EX) and interband (IB) transitions are denoted. The inset shows the reflectivity spectrum of a single crystal (blue symbol), having two different spectra features. **C**, Experimental set-up for measuring the CPGE using $\lambda/4$ plate; the angles, α , θ , and ϕ are denoted. x' indicates the current flow direction. **D**, Schematic diagram of the continuum bands (VB and CB) having **Rashba spin splitting**, and related optical transitions with circular polarized light. The electron group velocity (and current) change polarity when the light changes helicity. E_d is the direct energy difference between the CB and VB at the Dirac points. From Liu *et al.* [1]

The two-dimensional (2D) Ruddlesden–Popper organic-inorganic halide perovskites such as (2D)-phenylethyl ammonium lead iodide (2D-PEPI) have layered structure that resembles multiple quantum wells (MQW) [1]. The heavy atoms in 2D-PEPI contribute a large spin-orbit coupling (SOC) that influences the electronic band structure. Upon breaking the inversion symmetry, a spin splitting (‘Rashba splitting’) occurs in the electronic bands [2]. We have studied the spin splitting in 2D-HOIP single crystals using the circular photogalvanic effect (CPGE) [1]. We have confirmed

the existence of Rashba splitting at the electronic band extrema of 35 ± 10 meV, and identify the main inversion symmetry breaking direction perpendicular to the MQW planes. The CPGE action spectrum above the gap reveals spin-polarized photocurrent generated by ultrafast relaxation of hot photocarriers separated in momentum space. However the helicity dependent photocurrent with below-gap excitation is due to spin-galvanic effect of the ionized spin-polarized excitons, where spin polarization occurs in the spin-split bands due to asymmetric spin-flip.

In the published work [1] we studied the CPGE using both cw and picosecond transient spectroscopies. For the cw studies we measured the CPGE action spectrum, from which we concluded that there are two different PGE effects in this compounds; the CPGE when excited carriers over the gap, and the spin PGE when excited directly into the exciton level. For the transient CPGE we have used the ps transient THz spectroscopy where the hot photocarriers relaxation was measured by THz emission. We obtained CPGE THz emission when excited over the gap, but no THz emission when excited into the exciton level, which show that the latter PGE process occurs at longer times, which is determined by the exciton dissociation rate.

(ii) Broken inversion symmetry and Rashba splitting in HOIP revealed through two-photon absorption spectroscopy

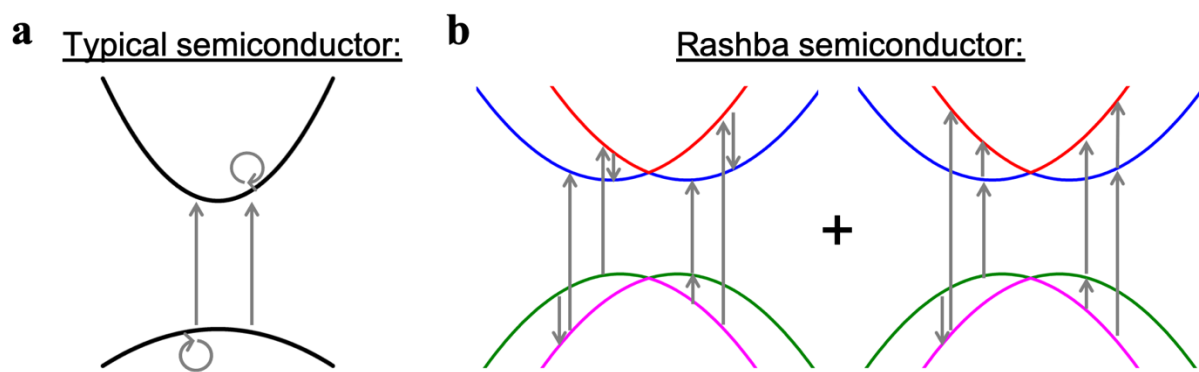


Figure 2: Schematic illustration of the two-photon absorption pathways for semiconductors with and without Rashba splitting. **a.** Two-photon pathways for transitions between initial, intermediate and final states limited to highest valence and lowest conduction bands in a typical semiconductor. **b.** Examples of additional two-photon pathways for transitions between initial, intermediate and final states available in a semiconductor that exhibits Rashba splitting. Under review in *Nature Commun* [3].

The Rashba effect describes the splitting of spin degeneracy in the band structure of solids due to the presence of spin-orbit coupling and lack of inversion symmetry [2]. The development of materials that support large Rashba splitting is rapidly growing, but the means of its experimental detection is substantially limited. The Rashba-splitting in HOIP is particularly promising and yet controversial, due to questions surrounding the presence or absence of inversion symmetry. We have utilized two-photon absorption (TPA) spectroscopy to study inversion symmetry breaking in different phases of these materials. We have demonstrated this nonlinear optical technique as a new method to observe and quantify the Rashba effect [3]. In particular, we have measured two-photon excitation spectra of the photoluminescence in HOIP crystals, and show that an additional band above, but close to the optical gap is the signature of new two-photon transition channels that originate from the Rashba splitting. This provides an all-optical technique that is distinct as it probes the bulk of the materials.

Figure 3: Broken inversion symmetry and Rashba splitting in $(\text{PEA})_2\text{PbI}_4$. Two-Photon Photoluminescence Excitation (TP-PLE) spectrum of $(\text{PEA})_2\text{PbI}_4$ (blue circles); compared to the linear absorption spectrum of the corresponding thin film (dashed line). The TP-PLE spectrum is plotted vs. twice the excitation energy, $2\hbar\omega$, whereas the absorption is plotted vs. $\hbar\omega$. The exciton region is indicated; also, the inter-band onset is designated. Under review in *Nature Communications* [3].

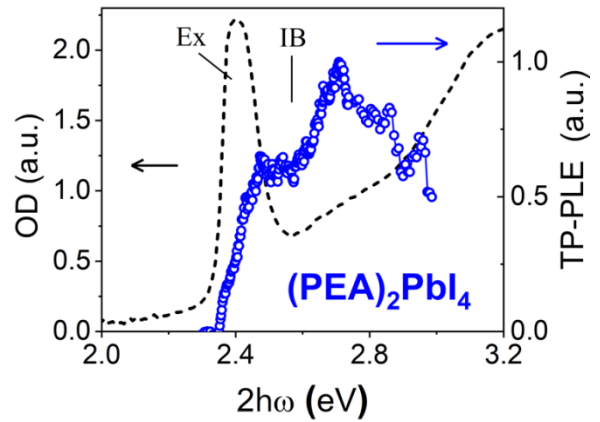


Figure 3 demonstrates the TPA spectrum of $(\text{PEA})_2\text{PbI}_4$ (PEPI) measured at room temperature using the technique of two-photon photoluminescence (TP-PLE). It is seen that the exciton band contributes to the TP-PLE spectrum; this shows that the compound does not possess inversion symmetry. Since PEPI has strong SOC it thus indicates that there is Rashba splitting in the continuum bands, as shown in (i) above by the CPGE spectroscopy. Importantly there is a second peak in the TP-PLE at ~ 2.7 eV which is ~ 140 meV above the band gap in this material. From the analysis shown in Fig. 2, we thus conclude that the Rashba energy, E_R is $\sim 150/4 = 35$ meV, in agreement with other experiments [2].

(iii) Magneto optic studies of 2D-HOIP at high field

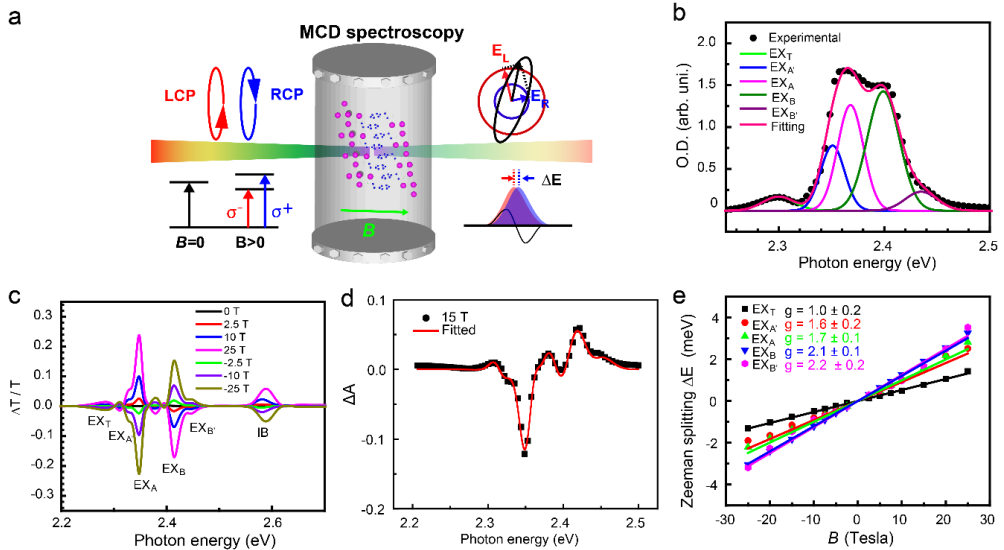


Figure 4: MCD spectroscopy of 2D-PEPI using Faraday configuration. **a**, Schematics of the MCD working principle. **b**, The absorption spectrum of the complex exciton structure in 2D-PEPI, which is fitted using five exciton bands as labeled. **c**, MCD spectra of 2D-PEPI measured at various magnetic field strengths and polarities, as labeled. **d**, Fit of a typical MCD spectrum in the range of the complex exciton structure. **e**, Magnetic field dependence of the obtained Zeeman splitting for the five excitons. The Landé g -factors determined from the linear fits are given for each exciton band. Under review.

We have used magnetic circular dichroism (MCD) spectroscopy for studying the excitons and charge carriers in 2D-HOIP (namely $\text{C}_6\text{H}_5\text{C}_2\text{H}_4\text{NH}_3)_2\text{PbI}_4$ or PEPI) at magnetic fields up to 25 T,

where Landau levels (LL) form. The measurements were carried on at the national high field magnet laboratory (NHMFL) in Tallahassee Florida [4]. From the MCD spectra we have obtained the Landé gyromagnetic factors of the three main excitons and the band-edge electron-hole (e-h) pairs. These measurements have revealed that the exciton spectrum contain three different excitons of which origin is under discussion [5]. We also observed sharp oscillations in the MCD and EA spectra above the band edge that we believe are caused by optical transitions from LL of holes in the valence band (VB) to electrons LL in the conduction band (CB). In PEPI these transitions may not be equally spaced due to the large Rashba SOC. From the LL dispersion with the magnetic field, we may thus determine the Rashba coefficients of electrons and holes.

Future Plans

During the 5th support year of our program we work on several projects that involve circular dichroism (CD) and magneto-circular dichroism (MCD) of 2D and 3D organic/inorganic perovskites. We have already preliminary data that show MCD of Landau Levels (LL) in 2D HOIP. We plan to study the interband LL transitions upon the application of an external electric field, F . Because the Rashba SOC is sensitive to the application of an electric field, it would be interesting to determine the change of the SOC coefficient with F .

References

- [1] Liu, X. *et al.*, *Nature Communications* **11**, 323 (2020). CPGE spectroscopy in 2D HOIP).
- [2] Zhai, Y *et al.*, *Science Advances* **3**, e1700704 (2017). Rashba splitting in 2D HOIP.
- [3] Lafalce E. *et al.*, *Nature Communications* (under review). NLO spectroscopy of HOIP.
- [4] Zhang,C. *et al.*, *Phys. Rev. B* **97**, 134412(2018). Field-induced circular dichroism in MAPbI₃.
- [5] Liu. H. *et al.*, *Nature Physics* (under review). LL spectroscopy in 2D-HOIP.

Publications that resulted from the present DOE grant (01.2019- 02.2021)

- [1] “Novel Spin Physics in Organic-Inorganic Perovskites”, Chuang Zhang, Dali Sun, and Z. Valy Vardeny, chapter 4.1 in “Halide Perovskites; Photovoltaics, Light Emitting Devices and Beyond”, Willey-VCH, Ed. T.C. Sum and N. Mathews, pp 251-272 (2019); ISBN 978-3-527-34111-5
- [2] “Field-induced spin splitting and anomalous photoluminescence circular polarization in CH₃NH₃PbI₃ films at high magnetic field”, Chuang Zhang, Dali Sun, Zhi-Gang Yu, Chuan-Xiang Sheng, Stephen McGill, Dmitry Semenov, and Zeev Valy Vardeny, *Physical Rev. B* **97**, 134412 (2018). DOI: 10.1103/PhysRevB.97.134412
- [3] “Spin-Optoelectronic Devices Based on Hybrid Organic-Inorganic Trihalide Perovskites”, Jingying Wang, Chuang Zhang, Haoliang Liu, Ryan McLaughlin, Yixin Zhai, Shai R. Vardeny, Xiaojie Liu, Stephen McGill, Dmitry Semenov, Hangwen Guo, Ryuichi Tsuchikawa, Vikram V. Deshpande, Dali Sun, Z. Valy Vardeny, *Nature Communications* **10**, 129 (2019) <https://doi.org/10.1038/s41467-018-07952-x>
- [4] “Surface-enhanced spin current to charge current conversion efficiency in CH₃NH₃PbBr₃-based devices”, Dali Sun, Chuang Zhang, Marzieh Kavand, Jingying Wang, Hans Malissa, Haoliang Liu, Henna Popli, Jaspal Singh, Shai R. Vardeny, Wei Zhang, Christoph Boehme, and Z. Valy Vardeny, *Journal of Chemical Physics* **151**, Issue 17, November 2019. <https://doi.org/10.1063/1.5125230>

[5] “Tunable spin characteristic properties in spin valve devices based on hybrid organic-inorganic perovskites”, Jingying Wang, Chuang Zhang, Haoliang Liu, Xiaojie Liu, Hangwen Guo, Dali Sun, Z. Valy Vardeny, *Advanced Materials*, August 2019, 1904059. DOI: [10.1002/adma.201904059](https://doi.org/10.1002/adma.201904059)

[6] “Circular photogalvanic spectroscopy of Rashba splitting in 2D hybrid organic-inorganic perovskite multiple quantum wells”, X. Liu, A. Chanana, U. Huynh, F. Xue, P. Haney, S. Blair, X. Jiang and Z. V. Vardeny, *Nature Communication* **11**, 323 (2020). DOI: [10.1038/s41467-019-14073-6](https://doi.org/10.1038/s41467-019-14073-6)

[7] “Magneto-electroluminescence response in 2D and 3D hybrid organic inorganic perovskite light emitting diodes”, Xin Pan, Haoliang Liu, Uyen Huynh and Z. Valy Vardeny, *J. Chem. Phys.* **152**, 044714 (2020). <https://doi.org/10.1063/1.5132982>

[8] 652. “Quantifying Exciton Heterogeneities in Mixed-Phase Organometal Halide Multiple Quantum Wells via Stark Spectroscopy Studies”, Eric Amerling, Sangita Baniya, Evan Lafalce, Steve Blair, Zeev Valy Vardeny, and Luisa Whittaker-Brooks, *ACS Appl. Mater. & Interfaces* **12**, 47, 52538 – 52548 (2020). <https://doi.org/10.1021/acsami.0c13564>

[9] Spin-photovoltaic and photogalvanic responses of optoelectronic devices based on chiral two-dimensional hybrid organic-inorganic perovskites”, Jingying Wang, Haipeng Lu, Xin Pan, Junwei Xu, Haoliang Liu, Xiaojie Liu, Michael F. Toney, Matthew C. Beard, and Z. Valy Vardeny, *ACS Nano* (November 2020) : <https://dx.doi.org/10.1021/acsnano.0c05980>

Coherent control of spin states in organic electronics – discovery and investigation of complex room-temperature magnetic quantum excitations

PI: Christoph Boehme, co-PI: John M. Lupton
University of Utah, Department of Physics and Astronomy,
115S 1400E, Salt Lake City, Utah, 84112, boehme@physics.utah.edu
Award # DE-SC0000909

Program Scope

The focus of this program has been to address, in the context of organic semiconductors, the long-term challenges set forward by the Department of Energy's Basic Energy Sciences Advisory Committee, such as "How do we control materials processes at the level of electrons?", "How do we characterize and control matter away - especially very far away - from equilibrium?" and "How do remarkable properties of matter emerge from complex correlations of the atomic or electronic constituents and how can we control these properties?".

Specifically, this program pursues the study of ***complex room-temperature magnetic quantum excitations (CoRMQE)***, which include ***higher-spin systems with $s > 1/2$*** (excitons, exciton-polaron pairs or exciton pairs) [1] as well as ***resonantly induced collective charge-carrier spin pair ensembles*** that emerge under ultrastrong resonant driving fields B_1 [2-4] for weakly spin-orbit coupled electronic states, as found in materials based on carbon, silicon, and other elements with low atomic order numbers. Central to how these phenomena affect spin-dependent electronic transitions and, thus, physical materials behaviors such as electronic, optoelectronic and magneto-optoelectronic properties, are, therefore, the strengths of ***spin-hyperfine interactions (HFIs)*** as well as ***spin-orbit coupling (SOC)*** [2]. While ***HFIs*** are typically strong in organic materials due to the all-abundant hydrogen, ***SOC*** is generally weak, yet still not negligible for the behavior of paramagnetic charge carrier states. Thus, this project will

focus in particular on the following questions: **(i) What is the influence of spin-spin interactions, SOC, and the HFI on charge carriers and thus on the formation of CoRMQEs?** Using recent demonstrations of differentiation between charge-carrier SOC and HFI with electrically detected magnetic resonance (EDMR) spectroscopy [5, 6], the influence of HFI and SOC on CoRMQEs is

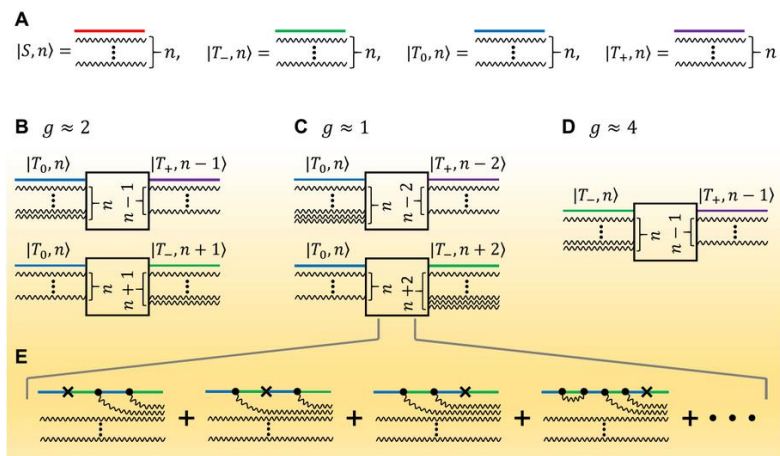


Figure. 1: Illustrations of multiquantum transitions of spin pairs in the singlet-triplet basis. (A) Floquet states controlling a spin-dependent recombination current in a polymer layer under magnetic resonance are defined by the photon number n (wavy lines before and after the interaction) and the spin wavefunction (red, green, blue, purple). (B) The spin- $1/2$ resonance of the pair at an effective g -factor of $g \approx 2$ corresponds to a raising or lowering of n . (C), (D) Resonances also arise at $g \approx 1$ and $g \approx 4$ due to two-photon and half-field transitions. (E) Examples of diagrams of the two-photon transitions. The vortices indicate the creation or annihilation of a photon (\bullet) or spin scattering not involving a photon (\times), e.g. due to hyperfine or dipolar coupling. An infinite number of higher-order loops exists. Magnetoresistance on resonance is calculated by summation over all transitions [10].

studied. (ii) **What is the nature of the dynamics of CoRMQEs?** Previous pulsed EDMR measurements showed that spin-coherence times (T_2) of paramagnetic charge carrier states in organic semiconductors are typically below $1\mu\text{s}$ [7], due to the random HFI, limiting their utilization for quantum applications. As CoRMQEs can form when $B_1 > \text{HFI}$, it is conceivable that long T_2 emerge under strong drive when coherence is protected by the strong driving fields. (iii) **What is the quantum mechanics of resonantly induced collective charge-carrier spin ensembles?** The study of charge-carrier spin collectivity has revealed an unexpected wealth of conductivity effects related to the formation of CoRMQEs, raising questions of whether multiphoton transitions, avoided level crossings, examples of which are illustrated in Fig. 1 for the spin-states of weakly spin-spin coupled electron-hole pairs, and spin-spin interactions can influence the way collectivity affects the macroscopic materials behavior.

Recent Progress

During the past 24 months, much progress [9,10] has been made on the exploration of multiphoton and fractional g -factor transitions of magnetic dipoles that are illustrated in Fig. 1. The illustration scheme follows a description of Cohen-Tannoudji [8], where an ensemble of n photons form Floquet states together with the spin-pair eigenstates of the charge-carrier pair exposed to this radiation (see Fig. 1A). When transitions with one or more photons occur (see Fig. 1B through D), the Floquet states change following transition probabilities depending on various contributions (see Fig. 1E for the example of one $g \approx 1$ transition). By applying the known [11] hyperfine field B_{hyp} and spin-orbit coupling conditions under which pairs of charge-carrier spins with $s = \frac{1}{2}$ occur in a fully deuterated form of the polymer semiconductor poly[2-methoxy-5-(2-ethylhexyloxy)-1,4-phenylenevinylene] (d-MEH-PPV), we have obtained predictions for how multiphoton magnetic dipole transitions affect changes to spin-dependent transition rates and, thus, to electric device currents, for any given applied combination of the static magnetic field B_0 as well as the amplitude of B_1 . Figure 2A shows the results of these calculations for spin-dependent changes in charge-carrier recombination current δI in d-MEH-PPV. This plot shows a wealth of previously entirely

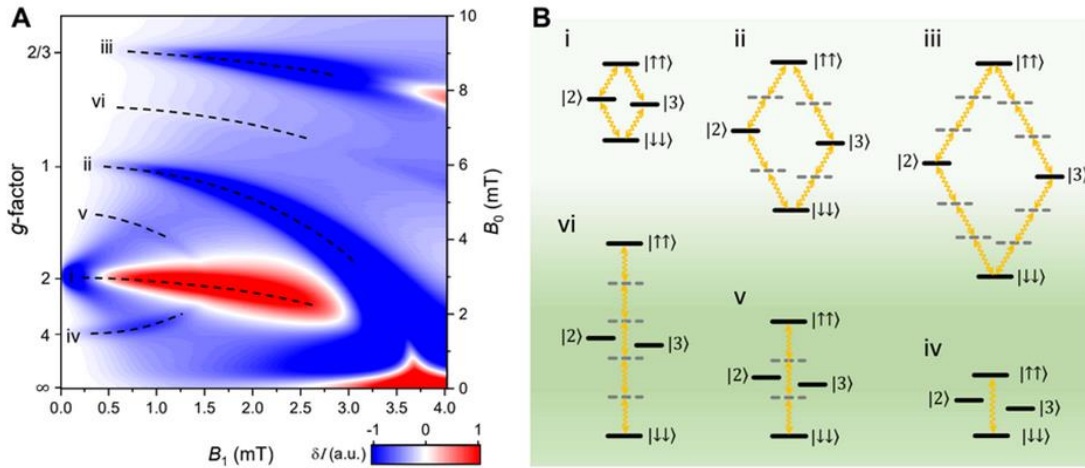


Figure 2: Floquet spin states in OLED magnetoresistance. (A) Calculated change of spin-dependent recombination current as a function of static field B_0 and oscillating field B_1 for a frequency of 85 MHz. (B) Term diagrams of integer and fractional g -factor multiphoton transitions. Adapted from [10].

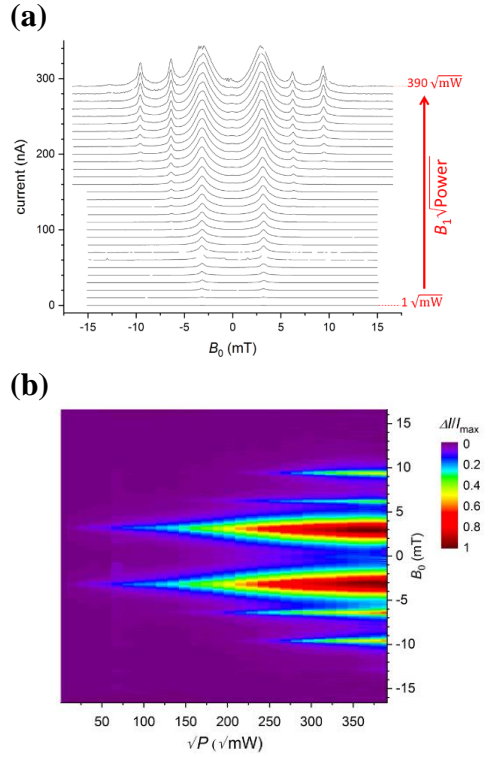


Figure 3: Plots of quadrature lock-in detected EDMR spectra obtained from SY-PPV polymer devices with MoO_3 hole injectors and Ca electron injectors for a variety of applied drive amplitudes with an excitation frequency off = 100 MHz. The data in (a) represents waterfall plots of magnetic field slices taken out of the complete data set displayed in (b), plotted with an arbitrary offset.

which changes very sensitively when spin-dependent electron–hole recombination rates change. As shown by the plots in panels (a) and (b), the high signal-to-noise ratios obtained in these experiments, even under application of high drive powers, allows for the study of the properties of these transitions, i.e. their dependencies on the driving field amplitude, B_1 .

The experimental access to two-photon magnetic dipole transitions has allowed us to study their helicity dependence in order to compare their behavior with the single-photon magnetic dipole transitions at $g \approx 2$. We carried out EDMR measurements under close to fully circularly polarized excitation shown in Fig. 4. From this data, we see that under strong drive, the ratio between the $g \approx 2$ resonances changes significantly, even though, due to the spin-Dicke effect [9], the out-of-cycle peak does not disappear entirely. However, within the given SNR, the $g \approx 1$ resonances are reduced significantly, i.e. below the detection limit, compared to the case of linear excitation. This helicity dependence of the $g \approx 1$ EDMR charge-carrier resonance suggests that it is caused by more complex CoRMQEs involving two-photon transitions within charge carrier spin states.

unexplored resonance signatures, which we were able to attribute to integer as well as fractional Landé-factors, i.e. one, two-, and three-photon transitions between $s=1/2$ as well as $s=1$ manifolds [10]. Figure 2B displays term diagrams illustrating which of the underlying spin transitions apply for the various predicted current changes shown in Fig. 2A.

For the experimental verification and exploration of the nature of the two-photon transition with Landé factor $g \approx 1$, under strong magnetic resonant drive, an electrically detected magnetic resonance (EDMR) setup was built allowing the observation of spin-dependent currents when $B_1 > B_0 > B_{\text{hyp}}$. We implemented a newly developed lock-in detection protocol, which not only greatly improved the separation of the signal from the noise (usually the goal of lock-in detection), but also allowed to separate the contributions of non-magnetic resonance related radiation-induced effects on the measured sample conductivity from the studied spin-dependent current. By using amplitude modulation of the magnetic resonance drive power at frequencies which match the dynamics, i.e. the transition times of the spin-dependent recombination processes, but not the much faster dynamics of the radiation-induced conductivity artifacts, signals resembling the subtle multiphoton transitions are captured by the out-of-phase component of the measured electric currents, while the radiation artifacts are separated into the in-phase component. Fig. 3 displays data of electric current changes in a “superyellow” (SY)-PPV polymer layer under electron and hole injection, using suitable injector materials that sandwich the active polymer layer [5].

Under forward bias, a constant current is established

which changes very sensitively when spin-dependent electron–hole recombination rates change.

As shown by the plots in panels (a) and (b), the high signal-to-noise ratios obtained in these experiments, even under application of high drive powers, allows for the study of the properties of these transitions, i.e. their dependencies on the driving field amplitude, B_1 .

The experimental access to two-photon magnetic dipole transitions has allowed us to study their helicity dependence in order to compare their behavior with the single-photon magnetic dipole transitions at $g \approx 2$. We carried out EDMR measurements under close to fully circularly polarized excitation shown in Fig. 4. From this data, we see that under strong drive, the ratio between the $g \approx 2$ resonances changes significantly, even though, due to the spin-Dicke effect [9], the out-of-cycle peak does not disappear entirely. However, within the given SNR, the $g \approx 1$ resonances are reduced significantly, i.e. below the detection limit, compared to the case of linear excitation. This helicity dependence of the $g \approx 1$ EDMR charge-carrier resonance suggests that it is caused by more complex CoRMQEs involving two-photon transitions within charge carrier spin states.

Future Plans

We are currently in the process of corroborating and further exploring the $g \approx 1$ resonance shown in Figs. 3 and 4, as well as the other multi-photon transitions illustrated in Fig. 2. Goal of this work is to confirm the different Bloch-Siegert-type resonance shifts under strong drive conditions that are expected from the calculations shown in Fig. 2 and that reflect an increasing light-matter hybridization. At the same time, we will continue to collaborate with theory groups in order to develop a better qualitative and quantitative understanding of these phenomena, especially the selection rules that determine the observed helicity dependencies. Remarkably, theoretical descriptions of two-photon magnetic dipole transitions are scarce in the literature, likely because their development was considered to be a futile effort for a long time due to the lack of experimental access to such phenomena with traditional magnetic resonance detection schemes. Through low magnetic field/frequency EDMR which we have pursued in the course of this project, we are now able to study these previously inaccessible drive-field domains and this makes the development of new theoretical descriptions

meaningful. Experimentally, we will pursue in the coming year also, the time domain of the studied CoRMQEs. We are currently in the verification phase of a pulsed low magnetic field/frequency setup based on the use of digital signal processors for arbitrary waveform generation. Using this setup, room temperature coherent control of electron spin states in near complete absence of local magnetic fields will be possible. This setup will then be used for the measurements of CoRMQE spin quantum coherence times in order to scrutinize their currently hypothesized long T_2 values.

References

- [1] W. J. Baker et al., *Phys. Rev. B* **84**, 165205 (2011); [2] R. C. Roundy & M. E. Raikh, *Phys. Rev. B* **88**, 125206 (2013); [3] D. P. Waters et al., *Nature Physics* **11** (11), 910 (2015); [4] S. Jamali et al., *Nano Lett.* **17** (8), 4648 (2017); [5] G. Joshi et al., *J. Am. Chem. Soc.* **140**, 6758 (2018); [6] H. Malissa et al., *Phys. Rev. B* **97**, 161201 (R) (2018) (Rapid Communication); [7] H. Malissa et al., *Science* **345** (6203), 1487 (2014); [8] C. Cohen-Tannoudji, J. Dupont-Roc, G. Grynberg, *Atom-Photon Interactions: Basic Processes and Applications*. (Wiley, New York, 2004).

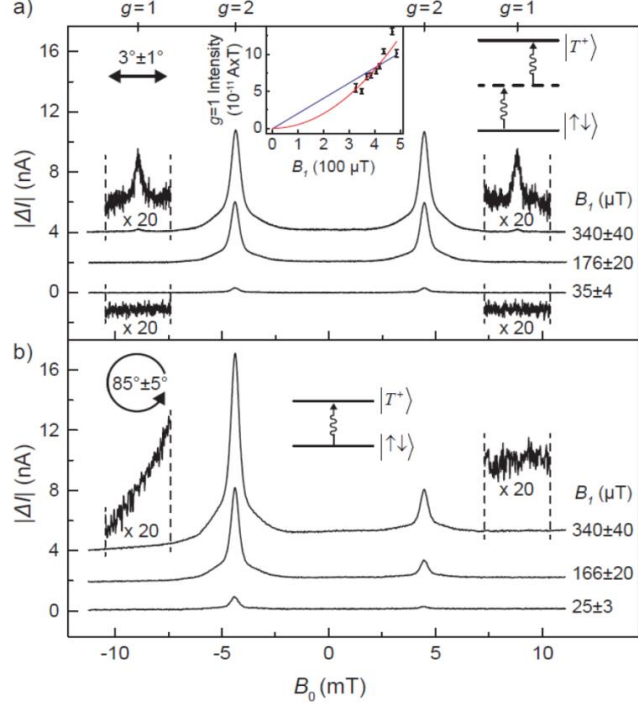


Figure 4: (a) EDMR spectra for the $g=2$ and $g=1$ resonances in SY-PPV. The spectra are measured using near-linearly polarized B_1 fields at 125 MHz with three different powers. At high values of B_1 (high power), the $g=1$ resonance appears, indicating the two-photon transition depicted by the term diagram in the upper right corner. The middle inset is a plot of the intensity of the $g=1$ resonance peak as a function of B_1 with linear and quadratic fits. (b) EDMR spectra using near-circularly polarized B_1 with three different powers. Only the $g=2$ resonance appears regardless of B_1 strength.

Two-year publication list with articles acknowledging award # DE-SC0000909

[1] V. V. Mkhitaryan, C. Boehme, J.M. Lupton, M.E. Raikh, Two-photon absorption in a two-level system enabled by noise, *Phys. Rev. B* **100** (21), 214205 (2019).

<https://doi.org/10.1103/PhysRevB.100.214205>

[2] S. Jamali, V. V. Mkhitaryan, H. Malissa, A. Nahlawi, H. Popli, T. Grünbaum, S. Bange, S. Milster, D. Stoltzfus, A. E. Leung, T. A. Darwish, P. L. Burn, J. M. Lupton, and C. Boehme Floquet spin-state control of OLED magnetoresistance. *Nature Commun.* **12** (1), 465 (2021).
<https://www.nature.com/articles/s41467-020-20148-6>

[3] D.M. Stoltzfus, G. Joshi, H. Popli, S. Jamali, M. Kavand, S. Milster, T. Grünbaum, S. Bange, A. Nahlawi, M. Y Teferi, S. I. Atwood, A. E. Leung, T. A Darwish, H. Malissa, P. L. Burn, J. M. Lupton, C. Boehme, Perdeuteration of poly[2-methoxy-5-(2'-ethylhexyloxy)-1,4-phenylenevinylene] (d-MEHPPV): control of microscopic charge-carrier spin-spin coupling and of magnetic-field effects in optoelectronic devices, *J. Mater. Chem. C* **8**, 2764 (2020).
<https://doi.org/10.1039/C9TC05322K>

[4] T. Grünbaum, S. Milster, H. Kraus, W. Ratzke, S. Kurrmann, V. Zeller, S. Bange, C. Boehme and J. M. Lupton, OLEDs as models for bird magnetoreception: detecting electron spin resonance in geomagnetic fields, *Faraday Discuss.* **221**, 92 (2020).
<https://doi.org/10.1039/C9FD00047J>

[5] D. L. Baird, A. Nahlawi, K. Crossley, K. J. van Schooten, M. Y. Teferi, H. Popli, G. Joshi, S. Jamali, H. Malissa, J. M. Lupton, C. Boehme, Electric Field Effects on Photoluminescence-Detected Magnetic Resonance of a π -Conjugated Polymer, *Phys. Stat. Sol. (B)* **257**, 1900493 (2020). <https://doi.org/10.1002/pssb.201900493>

[6] X. Liu, H. Popli, O. Kwon, H. Malissa, X. Pan, B. Park, B. Choi, S. Kim, E. Ehrenfreund, C. Boehme, Z V. Vardeny, Isotope Effect in the Magneto-Optoelectronic Response of Organic Light-Emitting Diodes Based on Donor–Acceptor Exciplexes, *Adv. Mater.* **32** (48), 2004421 (2020). <https://doi.org/10.1002/adma.202004421>

[7] H. Popli, J. Wang, X. Liu, E. Lafalce, T. H. Tennahewa, H. Malissa, Z. V. Vardeny, C. Boehme, Spin-transport in an organic semiconductor without free charge carrier involvement, arXiv preprint arXiv:2101.02140. <https://arxiv.org/abs/2101.02140>

[8] N. Bunzmann, D. L. Baird, H. Malissa, S. Weissenseel, C. Boehme, V. Dyakonov, A. Sperlich, Thermal Activation Bottleneck in TADF OLEDs based on m-MTDATA:BPhen arXiv preprint arXiv:2008.05781. <https://arxiv.org/abs/2008.05781>

Spin Transport in group IV materials and 2D membranes

Hanan Dery, Dinh Van Tuan, and Min Yang

Depts. of Electrical and Computer Engineering and of Physics, University of Rochester

Program Scope

During the last two years, this program was focused on two studies. The first one is our continuous effort to understand many-body interactions in monolayer transition-metal dichalcogenides (ML-TMDs), manifested through the exciton spectrum. The second study focuses on the nature of optical transitions in ML-TMDs. While we have made progress in both fronts [see 2-year list of publications], I will focus on the latter in this short document.

Recent Progress: optical properties of ML-WSe₂

To understand the optical properties of ML-WSe₂, we should first note the unique structure of the conduction-band valleys, shown in Figs. 1(a)-(d), where the optically active electron in the exciton complex comes from the top spin-split valleys. The other electron of the negative trion comes from the bottommost valleys, which are also the valleys populated with electrons when a positive gate voltage is applied. As a result, there are two negative trion species depending on the quantum numbers of the two electrons in the complex: opposite spins but similar valley (singlet or intravalley trion) versus opposite valleys but similar spin (triplet or intervalley trion) [1].

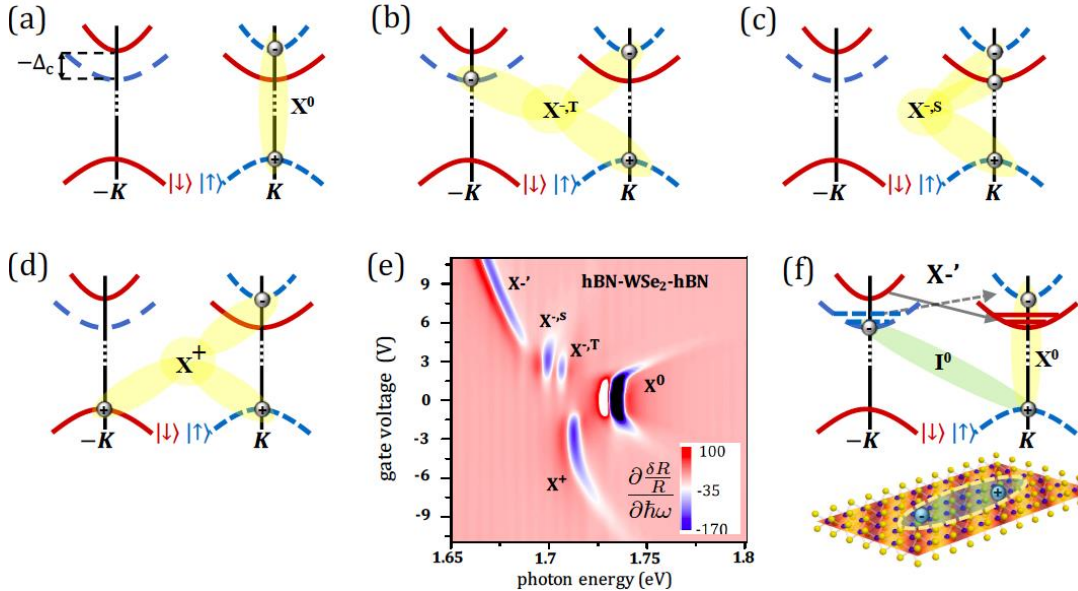


FIG. 1: The state composition of bright excitonic complexes in ML-WSe₂, including (a) the neutral exciton X⁰, (b) the intervalley (triplet) negative trion X^{-T}, (c) the intravalley (singlet) negative trion X^{-S}, and (d) the positive trion X⁺. (e) Low-temperature differential reflectivity of ML-WSe₂ embedded in hexagonal boron nitride (hBN). The data is taken from Ref. [3]. In addition to the expected bright exciton complexes, the spectrum reveals a unique many-body feature that emerges when the monolayer is highly electron-doped. This feature, dubbed as X'-, has not been documented in conventional quantum-well semiconductors. Our previous attempt to decipher its origin was based on the coupling between indirect and direct excitons through collective shortwave charge excitations (intervalley plasmons), as shown in (f) [2, 3, 4].

Figure 1(e) shows the differential reflectivity spectrum, where each 1V corresponds approximately to a charge density of 10^{12} cm^{-2} . In addition to the detection of the four complexes in Figs. 1(a)-(d), we notice a new feature that emerges when the monolayer is heavily electron doped, dubbed as X' in Fig. 1(e). The seemingly incidental change in the order of the conduction band valleys in ML-WSe₂ compared with other cases, such as ML-MoSe₂, gives rise to this exotic many-body feature. Unlike the other spectral features, this feature is a genuine new phenomenon not seen before in bulk or quantum-well semiconductor systems [2,3,4].

Switching to the emission spectrum, Fig. 2(a) shows the unprecedentedly rich low-temperature photoluminescence (PL) spectrum of high-quality ML-WSe₂. The monolayer is excited with righthanded circularly polarized light where the photon energy is 1.775 eV. The PL is detected for left-handed circularly polarized emission (to prevent interference with Raman lines). Here, we focus on the regime where the monolayer is neutral or moderately doped with electrons or holes (gate voltage amplitude is smaller than 1V). The reason for the rich PL spectrum of ML-WSe₂ compared with ML- MoSe₂ is that its bright excitonic species, shown in Figs. 1(a)-(d), are no longer the ground state complexes. The dark and indirect excitonic complexes in ML-WSe₂, shown in Fig. 2(b)-(d), have lower energies. As a result, photoexcited bright excitons and trions complexes can relax to these dark states prior to emitting light. The PL

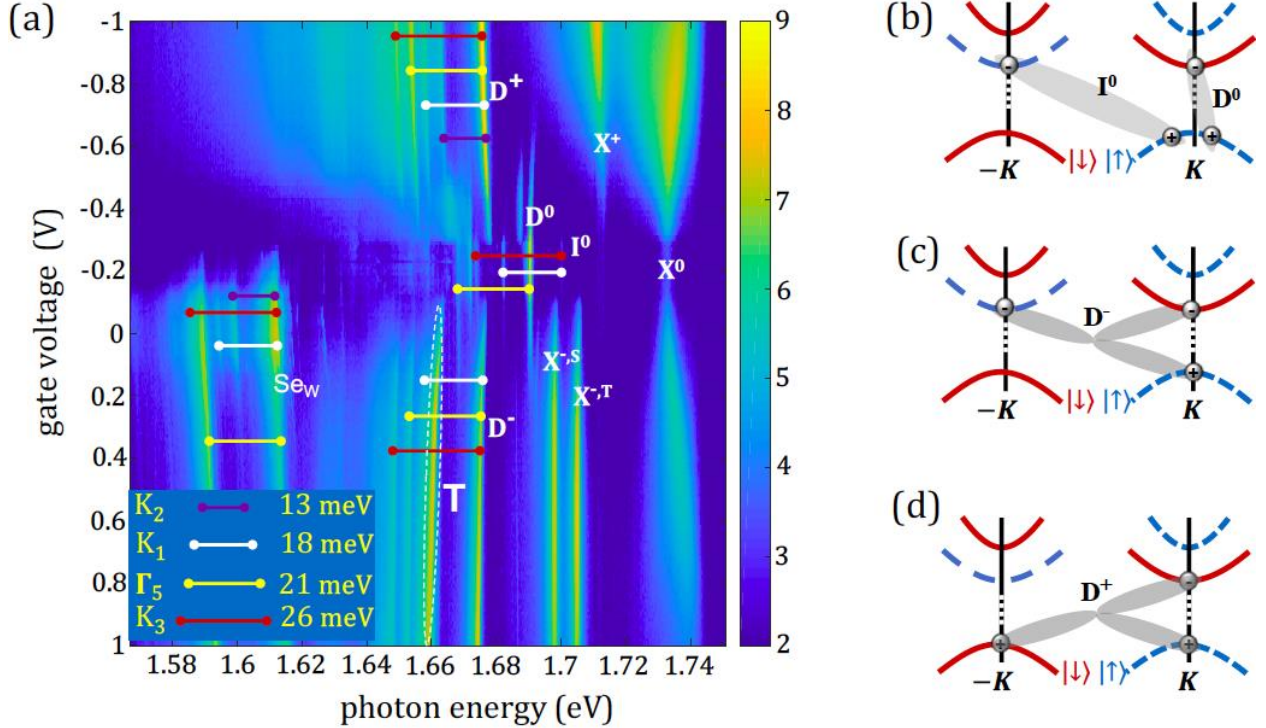


FIG. 2: (a) Low-temperature PL of high-quality ML-WSe₂ [5,6]. The phonon replica of dark/indirect complexes are indicated by the horizontal lines, and the corresponding phonon energies are shown in the bottom-left legend. The spectral lines indicated by T around 1.66 eV and Sew around 1.62 eV are discussed in the text. (b)-(d) The state composition of non-bright exciton complexes in ML-WSe₂, including (b) the indirect and dark excitons, I^0 & D^0 , (c) negative trion D^- , and (d) positive trion D^+ . The energy of these complexes is lower than that of bright ones in Figs. 1(a)-(d) because now the electrons are only from the bottommost conduction-band valleys.

spectrum in Fig. 2(a) reveals many features whose identification and interpretation was made possible as a result of prior work made by the PI group on selection rules and classification of dark exciton complexes in ML-TMDs [7, 8]. For example, we were able to identify the phonon replicas of dark trion optical transitions with dominant role played by the zone-center Γ_5 and zone-edge K_3 phonon modes [5,7].

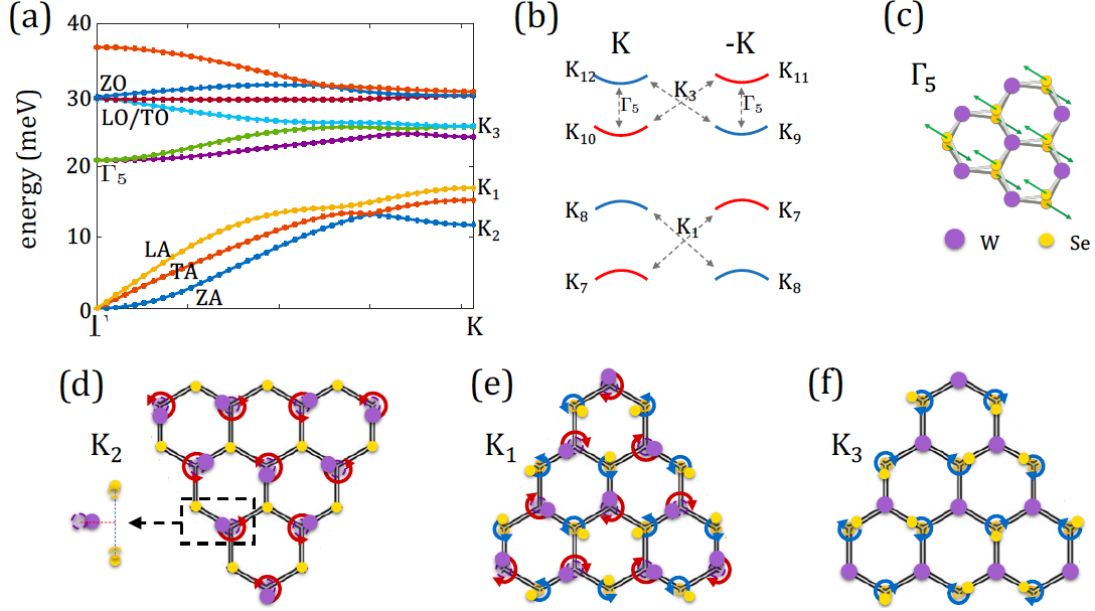


FIG. 3: (a) The phonon dispersion of ML-WSe₂ along the axis between the high-symmetry Γ and K points. Pertinent zone-center and zone-edge phonon modes are indicated. (b) Scheme of low-energy valleys in the conduction and valence bands. Spin-flip intravalley transitions in the conduction band are mediated by the phonon-mode Γ_5 , while spin-conserving intervalley transitions in the conduction (valence) bands are mediated by the phonon mode K_3 (K_1). Phonon-induced intervalley spin-flip scattering is relatively weak (the transition matrix element between time-reversed states vanishes). (c) Atomic displacement of the zone-center phonon mode Γ_5 . (d)-(f) Atomic motions of zone-edge phonon modes that are marked in (a). The curved arrows denote the in-plane circular motion of atoms around their equilibrium positions.

Figure 3(a) shows the phonon energy dispersion in ML-WSe₂, along with specification of the relevant phonons. As shown in Fig. 3(b), the coupling between opposite spin states in the conduction-band is governed by the long wavelength (intravalley) phonon mode Γ_5 . Its energy is ~21 meV in ML-WSe₂ and its atomic vibration is shown in Fig. 3(c), corresponding to out-of-phase and in-plane motion of the two chalcogen atoms in the unit cell. In addition, Fig. 3(b) shows that spin-conserving intervalley selection rules are governed by the zone-edge phonon mode K_3 for electrons and K_1 for holes. The energies of these phonons in ML-WSe₂ are ~26 and ~18 meV, respectively, and their atomic vibrations involve circular motion of the atoms in the unit-cell as shown in Figs. 3(e) and (f). The PL spectrum in Fig. 2(a) also reveals a signature of the zone-edge phonon mode with lowest energy, K_2 (~13 meV). The observation of a relatively strong replica from this mode is attributed to emission of dark exciton complexes next to shallow defects wherein crystal momentum selection rules are mitigated. Finally, we were able to identify the elusive indirect exciton in the charge neutral regime [5], indicated by the faint line I_0 in Fig. 2(a), along with its two possible phonon replicas K_1 and K_3 .

Finally, the PL spectrum in Fig. 2(a) reveals two more interesting features. The first feature is the salient spectral line, referred to as the T-peak, which emerges around 1.66 eV when the monolayer is electron doped. This peak does not emerge in the absorption spectrum and should not be confused with the many-body peak X-' that was discussed in the context of Fig. 1(e). The peak X-' first emerges around 1.685 eV when the electron charge density is of the order of a few times 10^{12} cm^{-2} , whereas the T peak emerges only in the PL around 1.66 eV as soon as the monolayer becomes electron doped (charge density of $\sim 10^{11} \text{ cm}^{-2}$). Similar to the X-' peak, the origin of the T peak is still a mystery. The second interesting feature in Fig. 2(a) is the group of spectral lines between 1.58 and 1.62 eV. Using defect-controlled crystal synthesis and scanning tunneling microscopy measurements, these spectral lines are associated to excitonic emissions next to donor anti-sites, wherein Se atoms substitutes W ones [6].

In conclusions, many of the predictions we made in 2013 and 2015 [7, 8] have been confirmed experimentally [5,6,9]. The original predictions, which largely relied on symmetry arguments, are now being supported in experiment through (i) matching of the phonon energy with the energy difference between the optical transition of a dark/indirect species and its phonon replica, (ii) measuring the g-factor of these complexes finding distinct values for bright, dark and indirect species, and (iii) analyzing the emitted-light polarization (the theory correctly predicts when reversed polarization is expected compared to the laser polarization). Being able to check all of these checkboxes, our physical picture is becoming the accepted way to explain the optical transitions in charge neutral or moderately doped ML-WSe₂.

Future Plans

1. We plan to perform a detailed study, showing how exciton complexes are formed, relax in energy, and recombine (either radiatively or non-radiatively). This study will include the aforementioned various species of trions and excitons (bright, dark and indirect). To test our results, we will use empirical data provided by our collaborators (the groups of Xavier Marie and Xiaodong Xu) for the emission spectrum dependence on charge density in gated devices, magnetic field, pump laser intensity and pump photon energy.
2. We will continue investigating many-body interaction in ML-TMDs. First, we plan to study long-wavelength collective spin excitations that couple the spin-split conduction bands of the same valley (intravalley). The quantum of these excitations is the magnon, which can couple between the bright and dark exciton states through flipping of the electron spin. Second, we plan to study the behavior of correlated trion states, wherein the three-body bound states (trions) are coupled to anti-particles in the Fermi sea (also referred to as coulomb holes). In real space, the Coulomb hole comes from the lack of charge in the vicinity of an electron due to Pauli exclusion. The purpose of both studies is to examine how and if correlated trions can support the emergence of the many-body peak [X-' in Fig. 1(e)].

References

- [1] A. M. Jones *et al.*, Nature Phys. **12**, 323 (2016).
- [2] D. Van Tuan, B. Scharf, I. Zutic, and H. Dery, Phys. Rev. X **7**, 041040 (2017).
- [3] D. V. Tuan *et al.*, Phys. Rev. B **99**, 085301 (2019).
- [4] B. Scharf, D. Van Tuan, I. Zutic, and H. Dery, J. Phys.: Condens. Matter. **31**, 203001 (2019).
- [5] M. He *et al.*, Nature Commun. **11**, 618 (2020).
- [6] P. Rivera *et al.*, Nature Commun. **12**, 871 (2021).
- [7] H. Dery and Y. Song, Phys. Rev. B **92**, 125431 (2015).
- [8] Y. Song and H. Dery, Phys. Rev. Lett. **111**, 026601 (2013).
- [9] C. Robert *et al.*, Phys. Rev. Lett. **126**, 067403 (2021).

Publications (2-year list of publications supported by BES)

- [i]. C. Robert, H. Dery, L. Ren, D. Van Tuan, E. Courtade, M. Yang, B. Urbaszek, D. Lagarde, K. Watanabe, T. Taniguchi, T. Amand, and X. Marie, *Measurement of con- duction and valence bands g-factors in a transition metal dichalcogenide monolayer*, Phys. Rev. Lett. **126**, 067403 (2021).
- [ii]. P. Rivera, M. He, B. Kim, S. Liu, C. Rubio-Verd, H. Moon, L. Mennel, D. A. Rhodes, H. Yu, T. Taniguchi, K. Watanabe, J. Yan, D. G. Mandrus, H. Dery, A. Pasupathy, D. Englund, J. Hone, W. Yao, and X. Xu, *Intrinsic donor-bound excitons in ultraclean monolayer semiconductors*, Nature Commun. **12**, 871 (2021).
- [iii]. M. Yang, C. Robert, Z. Lu, D. V. Tuan, D. Smirnov, X. Marie, and H. Dery, *Exciton valley depolarization in monolayer transition-metal dichalcogenides*, Phys. Rev. B **101**, 115307 (2020).
- [iv]. M. He, P. Rivera, D. V. Tuan, N. P. Wilson, M. Yang, T. Taniguchi, K. Watanabe, J. Yan, D. G. Mandrus, H. Yu, H. Dery, W. Yao, and X. Xu, *Valley phonons and exciton complexes in a monolayer semiconductor*, Nature Commun. **11**, 618 (2020).
- [v]. Z. Lu, D. Rhodes, Z. Li, D. Van Tuan, Y. Jiang, J. Ludwig, Z. Jiang, Z. Lian, S.-F. Shi, J. Hone, H. Dery, and D. Smirnov, *Magnetic field mixing and splitting of bright and dark excitons in monolayer MoSe₂*, 2D Mater. **7**, 015017 (2020).
- [vi]. D. Van Tuan, M. Yang, A. M. Jones, X. Xu, and H. Dery, *Virtual triions in the photoluminescence of monolayer transition-metal dichalcogenides*, Phys. Rev. Lett. **122**, 217401 (2019).
- [vii]. I. Zutic, A. Matos-Abiague, B. Scharf, H. Dery, and K. Belashchenko, *Proximity-induced Materials*, Materials Today **22**, 85 (2019).
- [viii]. D. Van Tuan, B. Scharf, Z. Wang, J. Shan, K. F. Mak, I. Zutic, and H. Dery, *Probing Many-Body Interactions in Monolayer Transition-Metal Dichalcogenides*, Phys. Rev. B **99**, 085301 (2019).

Tunnel Magnetoresistance Detection of Skyrmions

Sara A. Majetich, Physics Department, Carnegie Mellon University, Pittsburgh, PA 15213

Program Scope

This research program has focused on development of conductive atomic force microscopy methods to detect nanoscale magnetization patterns. While the objective remains to do this experimentally, for the past year the work has had to proceed through simulations. The specific emphasis during the past year has been on modeling the detectability of skyrmions (Figure 1) through the time dependence of tunnel magnetoresistance. Skyrmions are stable non-collinear spin patterns that in 2013 were proposed for use as 1's and 0's in racetrack memory (Figure 2) [1]. For this to work, it must be possible to uniquely detect the passage of a skyrmion as well as features that could be used to represent 1's and 0's, such as the magnetization direction of the core or the chirality for a Bloch skyrmion. Bloch skyrmions are particularly interesting due to their topological protection. There are still many questions about the best way to detect them electronically. The most promising approaches so far have used the transverse voltage due to the skyrmion Hall effect, but the signal is still very weak [2, 3]. Here we use simulations to examine alternative vertical detection methods using magnetoresistance, which could be more compact and have a greater signal-to-noise ratio. Our results show that there are unique signatures for detection of the skyrmion core direction for Néel and Bloch skyrmions, as well as the chirality for Bloch skyrmions.

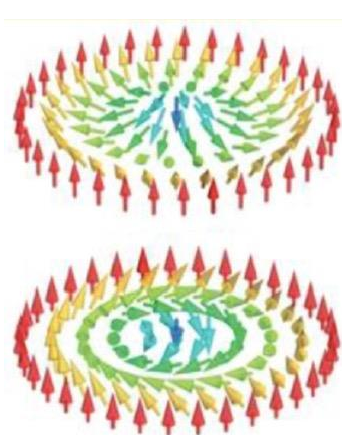


Fig. 1. Néel (top) and Bloch (bottom) skyrmions. Both have cores ~ 10 nm in diameter. Bloch skyrmions also have chirality and are topologically protected.

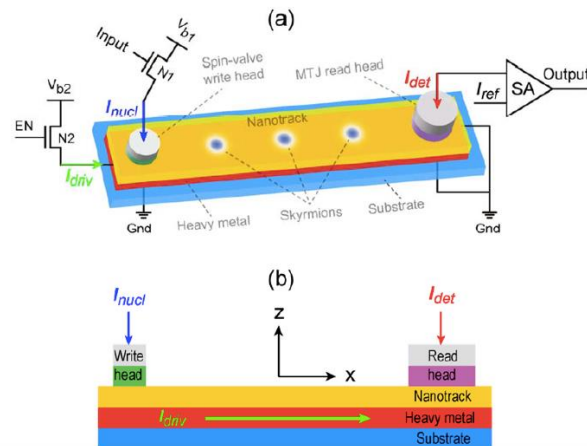


Fig. 2. Schematic of proposed skyrmion racetrack memory with magnetoresistive reading and writing, which has not yet realized experimentally [4].

Recent Progress

A spin polarized current was used to simulate movement of a Néel skyrmion down a racetrack that contains a circular magnetic dot above it. When the dot is flush with the racetrack, exchange interactions dominate, while when it is separated by a 1 nm thick tunnel barrier, the interactions are mainly magnetostatic. The trajectory of the skyrmion over a period of ~ 4 ns is calculated using mumax³ micromagnetics simulation software. Results for different dot and skyrmion core magnetization directions are used as a guide to predict the magnetoresistance as a function of time, which would be used to detect individual skyrmions.

For these model studies, a saturation magnetization of 5.8×10^5 A/m, exchange stiffness 1.5×10^{-12} J/m, anisotropy 8×10^5 J/m³, and damping parameter 0.1 were used for both the racetrack and 20 nm diameter detection dot. In addition, to stabilize 20 nm diameter skyrmions, the racetrack also had a Dzyaloshinskii-Moriya Interaction strength of 3×10^{-3} J/m². A current density of 1×10^{12} A/m² with spin polarization 0.4 was used to move the skyrmions.

In all cases there was a transverse deflection due to the skyrmion Hall effect. When the dot is flush with the racetrack, exchange coupling to the skyrmion spin texture background can be treated as an effective magnetic field with an antiskyrmion texture [5]. When there is a 1 nm MgO tunnel barrier separating the dot and racetrack, magnetostatic effects dominate and the magnitude of the interaction field is much smaller. However, simulations show that the vertical tunnel current is dominated by the volume directly below the dot. There will be a transient change in the magnetoresistance as a skyrmion passes by the dot detector.

With magnetostatic coupling both the trajectory and skyrmion size as a function of time differ, depending on whether the dot and skyrmion core magnetizations are parallel or antiparallel. When they are parallel (Figure 3), the skyrmion diameter grows slightly as it approaches the dot, since the dipolar field tends to orient misaligned spins. The spatial field gradient due to the dot causes a repulsive deflection around the dot. When the skyrmion core and dot magnetization are antiparallel (Figure 4), the skyrmion slightly shrinks in diameter as it approaches the dot, and there is an attractive interaction. The magnitudes of the deflection depend on the dot and skyrmion stack diameters and thicknesses, but as long as part of the skyrmion passes under the dot, it should also be possible to differentiate core up and core down skyrmions. For Figure 3 there would be a transient drop in resistance, and for Figure 4 a transient rise. If in-plane magnetization dot detectors were used, there would also be characteristic magnetoresistance transients that are sensitive to the in-plane component of the skyrmion spins. This could enable Néel and Bloch skyrmions to be differentiated, if magnetized along the racetrack axis, and chirality detection of Bloch skyrmions, if magnetized perpendicular to the racetrack axis.

In order to quantitatively compare the effect of different detector dot thicknesses and diameters, as well as the influence of the skyrmionics material, the vertical tunnel magnetoresistance across the detector dot and the skyrmionic stack is calculated. Based on

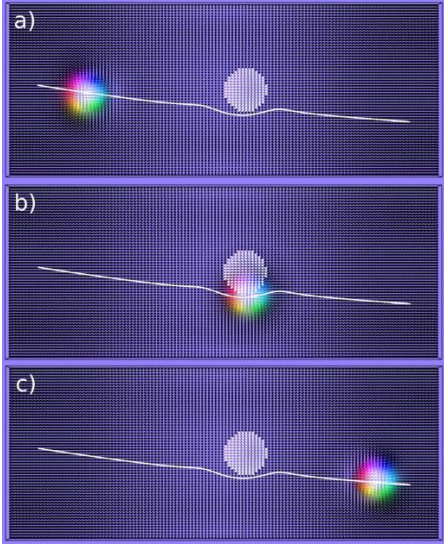


Fig. 3. 20 nm Néel skyrmion trajectory along a 200 nm x 80 nm racetrack, passing by a 20 nm diameter dot separated by a 1 nm tunnel junction barrier. The skyrmion core and dot have parallel magnetizations. a) at beginning, b) repulsion near the dot, and c) at the end of the racetrack.

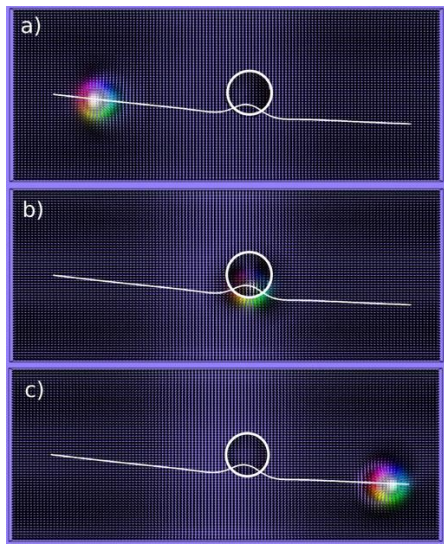


Fig. 4. Trajectory for similar conditions to those of Figure 3, except that the dot magnetization direction has been reversed, so that it is antiparallel to that of the skyrmion core. Here the interaction near the dot is attractive.

previous simulations, the amount of current spreading is small, and the vast majority of the current is collected from the volume of the skyrmionic stack directly beneath the detection dot [6]. A grid size of $(1 \text{ nm})^2$ was used to pixelate the detector dot, so that the magnetoresistance contributions could be treated like resistors in parallel. The electron polarization was assumed to be determined by the local magnetization orientation at the top of the skyrmionic stack, and the magnetoresistance for a given pixel was assumed to follow the empirical $\cos(\theta)$ relation found experimentally by Moodera and Kinder [7].

Future Plans

For the immediate future, a manuscript based on the simulations alone will be submitted for publication. There will also be a presentation of this work at the virtual Intermag Conference April 26-30, 2021. Experimental verification of the simulations is important, and this will proceed as soon as the student's visa is approved and he can safely return to the US. Demonstration of Néel skyrmion core detection will be the first goal, since that can be done with multilayer film stacks that have skyrmion excitations at room temperature. Extension to Bloch skyrmion detection will require low temperature and focused ion beam sectioning of a B20 material.

References

1. A. Fert, V. Cros, J. Sampaio, Nat. Nanotech. **8**, 152 (2013).
2. D. Macciarello, et al., Nat. Nanotech. **13**, 233 (2018).
3. K. Zeissler, et al., Nat. Commun, **11**, 428 (2020).
4. X. Chen, W. Kang, D. Zhu, X. Zhang, N. Lei, Y. Zhang, Y. Zhou, and W. Zhao, Appl. Phys. Lett. **111** 202406 (2017).
5. K. Hamamoto, M. Ezawa, and N. Nagaosa, Phys. Rev. B **92**, 115417 (2015).
6. H. Chen, I-H. Kao, and S. A. Majetich, “TMR Detection of Skyrmions: Simulations of Current Spreading and Magnetostatic Interactions”, CF-11, Magnetism and Magnetic Materials Conference, Las Vegas, Nov. 5, 2019.
7. J. S. Moodera and L. R. Kinder, J. Appl. Phys. **79**, 4724 (1996).

Publications

I.-H. Kao, B. Parks, and S. A. Majetich, “Magnetoresistive Imaging of Magnetic Bubbles, Skyrmions, and Skyrmion Fabric”, CF-11, Magnetism and Magnetic Materials Conference, Las Vegas, November 4, 2019.

H. Chen, I-H. Kao, and S. A. Majetich, “TMR Detection of Skyrmions: Simulations of Current Spreading and Spin Polarization”, AW-01, Magnetism and Magnetic Materials Conference, Las Vegas, November 5, 2019.

W. Bouckaert, H. Chen, and S. A. Majetich (manuscript in preparation); digest “Simulations of Magnetoresistance Detection of Skyrmions” is accepted for presentation HP-09 at the upcoming Virtual Intermag 2021 Conference April 26-30, 2021.

Project Title: Complex magnetism and emergent phenomena in correlated electron oxide materials

Principal Investigator: Prof. Hari Srikanth
University of South Florida, Department of Physics, ISA2019
4202 East Fowler Ave, Tampa, FL 33620
E-mail: sharihar@usf.edu

Co-Principal Investigator: Prof. Manh-Huong Phan
University of South Florida, Department of Physics, ISA2019
4202 East Fowler Ave, Tampa, FL 33620
E-mail: phanm@usf.edu

Program Scope:

The overall goal of our DOE funded project is to employ a unique approach that combines DC and AC magnetic susceptibility measurements, neutron diffraction, synchrotron X-ray diffraction with relatively unconventional RF transverse susceptibility (TS), magnetocaloric effect (MCE), and spin Seebeck effect (SSE) to yield new insights into the ground state magnetism in a wide variety of complex oxides and emerging magnetic systems. In particular, we have demonstrated the important impacts of phase coexistence, reduced dimensionality, magnetic proximity, strain, and anisotropy on the exotic magnetic properties in multicaloric double perovskites $A_2BB'O_6$ ($A = Y, La$; $B = Co, Ni$ and $B' = Mn$), exchange-coupled core/shell nanoparticles ($Fe_3O_4/Co_xZn_{1-x}Fe_2O_4$), and the discovery of the giant spin Seebeck effect in $Y_3Fe_5O_{12}$ (YIG)/ C_{60}/Pt multilayers. Other research efforts include the exploration of exotic magnetism in strongly correlated systems that host topologically nontrivial states as well as the new discovery of robust, tunable room-temperature ferromagnetism in semiconducting monolayers of V-doped WSe_2 and WS_2 .

Recent Progress:

1. Complex magnetic phases in multifunctional double perovskite oxides $A_2BB'O_6$ ($A = Y; B = Co, Ni$ and $B' = Mn$)

Double perovskite (DP) oxides are a versatile class of materials showing exotic physical properties, arising from the interplay between spin, charge and orbital degrees of freedom. By exploiting DC and AC magnetometry, and neutron diffraction experiments, we have observed for the first time the presence of two distinct cluster-glass-like states at low temperatures in the long-range ferromagnetically ordered La_2CoMnO_6 . (*Phys. Rev. B* **99**, 104436 (2019)). Magnetism in both YCMO and YNMO is guided by the superexchange interaction between the transition metal ions, $Mn^{4+}-O^{2-}-Co^{2+}$ and $Mn^{4+}-O^{2-}-Ni^{2+}$, giving rise to the FM coupling. We synthesized the polycrystalline samples of $Y_2Ni_xCo_{1-x}MnO_6$ (YNCMO) for $x= 0, 0.5$ and 1.0 with space group $P2_1/n$ using the sol-gel method. The collinear long-range FM ordering in YCMO down to 5 K was established by the neutron diffraction experiments (Fig. 1(a)). The presence of both FM and AFM orders results in an exchange bias effect at low temperatures. The co-existence of these two competing magnetic phases is further established by the temperature- and field-dependent magnetic entropy change. As a result, the comprehensive magnetic phase diagrams of $Y_2Ni_xCo_{1-x}MnO_6$ are plotted as a function of temperature and magnetic field.

x MnO₆ (for $x = 0.0, 0.5$ and 1) are constructed for the first time (Fig. 1(b)-(d)). A part of this work has recently been published (*J. Magn. Magn. Mater.* **507**, 166821 (2020)).

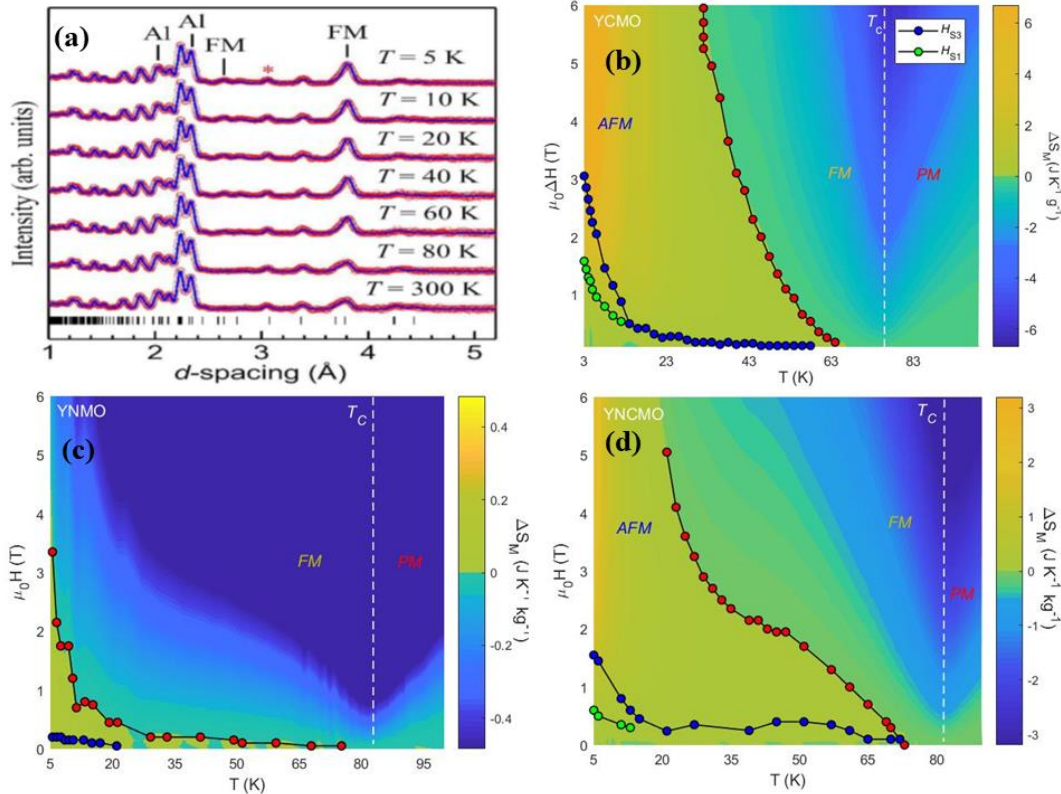


Figure 1: (a) Neutron diffraction (ND) patterns for Y₂CoMnO₆ at low temperatures processed by the Rietveld method. The experimental points and calculated profiles are shown in the figure. The magnetic FM contributions are denoted by symbol “FM”. The most intense peaks of Al used as a sample cover and impurity of Y₂O₃ are marked by symbol Al and *, respectively. (b) The H - T phase diagram of Y₂CoMnO₆. The surface plot shows the magnetic entropy change (ΔS_M) over a full range of temperatures for different magnetic field changes. $T = T_C$ (the dashed yellow line) marks the PM-FM phase transition corresponding to Co²⁺-O-Mn⁴⁺ 180° superexchange interactions. The critical fields for the dominant FM region are marked with the dashed black lines. The blue (HS1) and green (HS3) circles mark the peaks in the $d\Delta S_M/dH$ vs. H curves. (c) and (d) The H - T phase diagrams of Y₂NiMnO₆ and Y₂Ni_{0.5}Co_{0.5}MnO₆, respectively. It is evident that the AFM contribution arising from antiphase boundaries increases with Co²⁺ content.

2. Shell-mediated control of surface chemistry of magnetite nanoparticles

Iron oxide nanomaterials are being proposed for multiple applications ranging from biomedicine to spintronics. However, most nanomaterials contain variable amounts of Fe₃O₄ and γ -Fe₂O₃ due to the relatively easy oxidation of Fe²⁺ to Fe³⁺ under environmental conditions. Such a process, decreases both the overall magnetic moment and the magnetocrystalline anisotropy and leads to a decreased electrical conductivity. In addition, the chemical stability of Fe₃O₄ NPs is relevant in the biomedical field as Fe₃O₄ NPs can play an important role in cellular oxidative stress and toxicity. In addition to our discovery of the giant heating power in core/shell Fe₃O₄/Co_xZn_{1-x}Fe₂O₄ nanoparticles synthesized in our labaoratory (*ACS Applied Nano Materials* **3**, 1755 (2020)), we have proposed a novel strategy to control the surface chemistry of monodisperse 12 nm magnetite nanoparticles by means of a 3 nm-thick Zn-ferrite epitaxial coating in core/shell nanostructures (*Nanoscale* **12**, 13626 (2020)). We have carried out a combined Mössbauer spectroscopy, dc magnetometry, X-ray photoelectron spectroscopy and spatially

resolved electron energy loss spectroscopy study on iron oxide and $\text{Fe}_3\text{O}_4/\text{Zn}_{0.6}\text{Fe}_{2.4}\text{O}_4$ core/shell nanoparticles under aging conditions. Our results reveal that while the aged iron oxide nanoparticles consist of a mixture of γ - Fe_2O_3 and Fe_3O_4 , the Zn-ferrite-coating preserves a highly stoichiometric Fe_3O_4 core (Fig. 2).

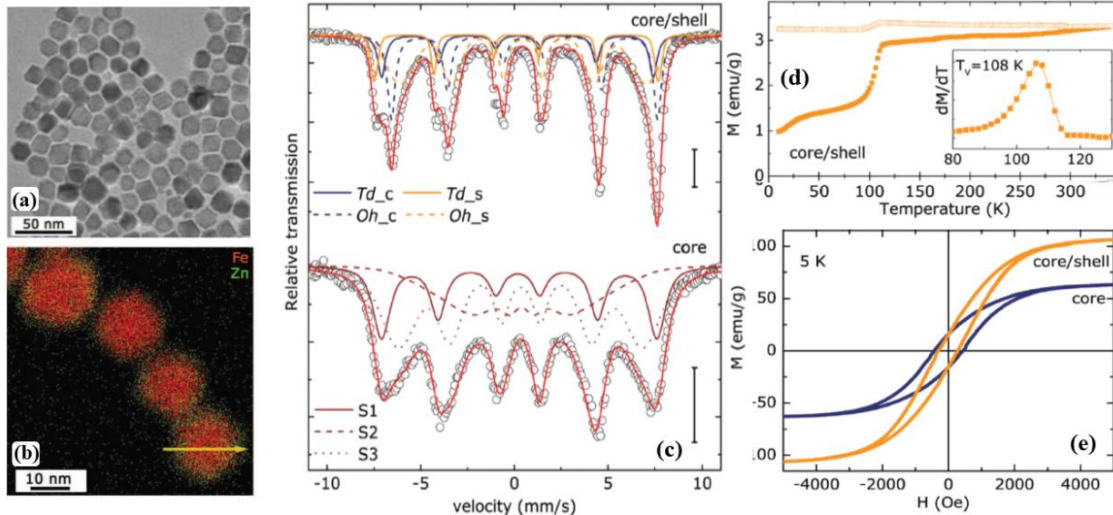


Figure 2: (a) Representative TEM image of $\text{Fe}_3\text{O}_4/\text{Zn}_{0.6}\text{Fe}_{2.4}\text{O}_4$ core/shell NPs. (b) Fe and Zn EDS elemental mapping for the core/shell NPs. (c) Room temperature Mössbauer spectra for 6 month-aged iron oxide cores (lower spectrum) and core/shell $\text{Fe}_3\text{O}_4/\text{Zn}_{0.6}\text{Fe}_{2.4}\text{O}_4$ NPs (upper spectrum). Lines indicate the fits associated with different sextets. Td_c , Oh_c , Td_s and Oh_s subspectra are associated with iron in tetrahedral (Td) and octahedral (Oh) sites in the core and shell, respectively. The bars indicate a relative transmission of 1%. (d) Zero-field cooled (ZFC, full symbols) and field-cooled (FC, open symbols) temperature dependence of the magnetization for 6 month aged core/shell NPs. The inset shows the derivative of the ZFC curve and the Verwey transition temperature. (e) $M(H)$ hysteresis loops measured at 5 K for the bare aged cores and core/shell NPs.

3. Organic semiconductor mediated giant spin Seebeck effect in ferromagnetic insulator/ C_{60} /heavy metal heterostructures

Over the past few years, generation of pure spin polarized current by the longitudinal spin Seebeck effect (LSSE) has gained substantial attention of the spintronic community. LSSE refers to the injection of spin current from a ferromagnetic (FM) insulator to the adjacent normal metal (NM) with strong spin orbit coupling under the application of a temperature gradient across the NM/FM bilayer. The efficiency of spin current injection is sensitive to multiple factors, e.g., the spin coherence length of the NM layer, magnetic properties of the FM layer as well as the quality of the interface between the FM-NM bilayers which is primarily controlled by the spin mixing conductance (G) at the interface. Large conductivity mismatch between YIG and Pt hinders the efficient spin transport in YIG/Pt. Several efforts have been devoted towards enhancing the value of G and hence the LSSE voltage by inserting various thin intermediate layers, such as Cu, NiO, CoO, $\text{Fe}_{70}\text{Cu}_{30}$, NiFe between $\text{Y}_3\text{Fe}_5\text{O}_{12}$ (YIG) and Pt. Despite the enhancement of LSSE reported in these systems, the underlying mechanism(s) associated with the role of the intermediate layer on the LSSE have remained an open question. An organic semiconductor such as C_{60} (buckminster fullerene) has a low spin-orbit coupling that essentially results in weak spin scattering and consequently a large spin diffusion length. These attractive properties of C_{60} led us to propose a new approach to enhance the injection of spin-polarized current across FM/NM bilayer structure such as YIG/Pt by inserting a thin intermediate layer of C_{60} .

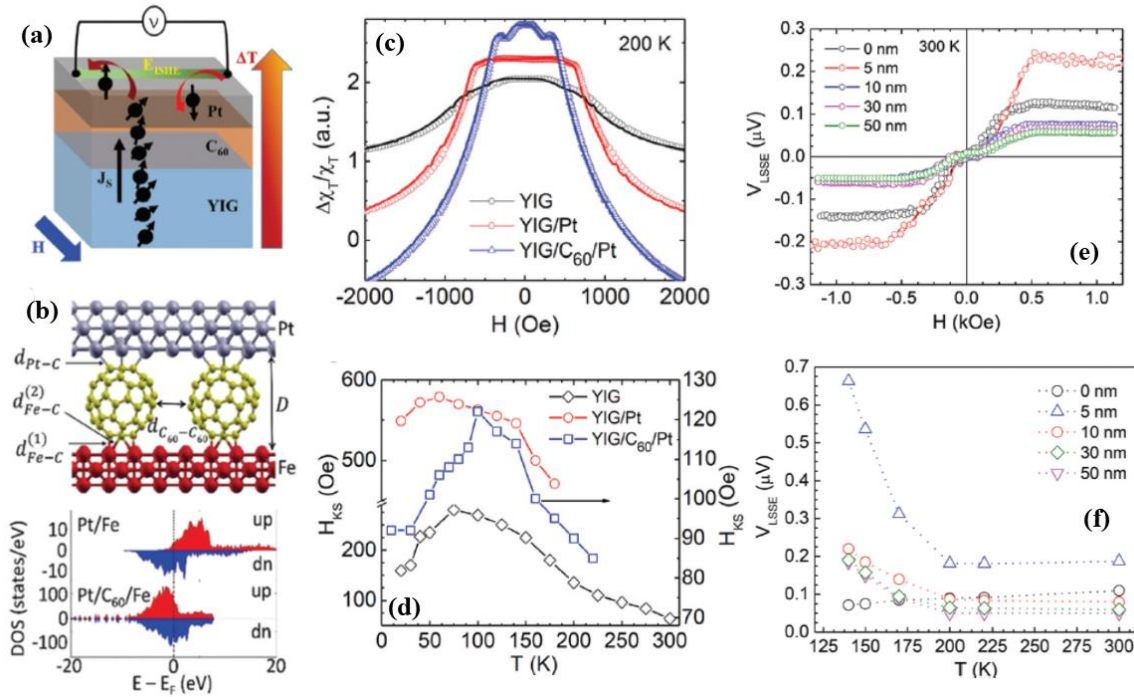


Figure 3: (a) Measurement geometry and spin transport through the $\text{Y}_3\text{Fe}_5\text{O}_{12}$ (YIG)/ C_{60} /Pt layer; (b) Top panel: the Pt/ C_{60} /Fe heterostructure, where Pt and Fe atoms. Bottom panel: spin resolved density of states (DOS) for the Pt and Fe layers, with and without the C_{60} molecule; (c) Transverse susceptibility spectra taken at 200 K for YIG, YIG/Pt, and YIG/ C_{60} /Pt heterostructures. For YIG/ C_{60} /Pt, as the field was swept from positive to negative saturation, the first peak corresponds to the bulk magnetocrystalline anisotropy field (H_K) and the second peak corresponds to the surface/interface magnetic anisotropy field (H_{SK}) of the system; (d) temperature dependence of surface/interface perpendicular magnetic anisotropy field (H_{SK}) for YIG, YIG/Pt, and YIG/ C_{60} /Pt structures; (e) The longitudinal spin Seebeck effect (LSSE) signal vs. magnetic field curves taken at 300 K; and (f) Temperature dependence of LSSE voltage for YIG/ C_{60} /Pt with different thicknesses of C_{60} .

We have demonstrated, for the first time, through the LSSE experiments and density functional theory calculations that the presence of C_{60} significantly reduces the conductivity mismatch between YIG and Pt and the surface perpendicular magnetic anisotropy of YIG, giving rise to an enhanced spin mixing conductance across YIG/ C_{60} /Pt interfaces (Fig. 3). We have observed a 600% increase in the SSE voltage in YIG/ C_{60} /Pt relative to YIG/Pt. Our study provides a new pathway for developing novel spincaloric devices (*Materials Horizons* **7**, 1413 (2020)).

Future plans:

Multicaloric double perovskites ($A_2BB'\text{O}_6$: $A=\text{La}, \text{Y}, \text{Pb}$; $B=\text{Co}, \text{Fe}$; $B'=\text{Mn}, \text{W}$), noncollinear spin textures (MnSi, MnP), spin-caloritronic heterostructures $\text{CoFe}_2\text{O}_4/\text{TMD}/\text{Pt}$, $\text{NiFe}_2\text{O}_4/\text{TMD}/\text{Pt}$ and YIG/TMD/Pt, YIG/graphene, YIG/h-BN, TmIG/graphene, gate controlled LSSE etc. will be explored (where monolayers of transition metal dichalcogenide (TMD) are V-doped WSe_2 , MoS_2 , and MoSe_2). Our research efforts over the next few years will be targeted towards elucidating these emergent aspects of correlated magnetic systems that could have important impacts on quantum spintronics and science information.

Publications:

List of papers acknowledging DoE grant support during the 2-year period (2019-2020):
(Students and postdocs' names are italicized, PI and co-PI names are in bold)

1. *E.M. Clements, R. Das, G. Pokharel, **M.H. Phan**, A.D. Christianson, D. Mandrus, J.C. Prestigiacomo, M.S. Osofsky, and **H. Srikanth**, Robust cycloid crossover driven by anisotropy in the skyrmion host GaV₄S₈, Physical Review B* 101, 094425, 2020 (**Editor's choice**)
2. *R.P. Madhogaria, R. Das, N.T. Dang, E. Clements, V. Vijaysankar, D.P. Kozlenko, **M.H. Phan**, and **H. Srikanth**, Evidence of long-range ferromagnetic order and spin frustration effects in the double perovskite La₂CoMnO₆, Physical Review B* 99, 104436 (2019)
3. *V. Kalappattil, R. Geng, R. Das, H. Luong, M. Pham, T. Nguyen, A. Popescu, L. M. Woods **H. Srikanth**, and **M.H. Phan**, Giant Spin Seebeck effect through an Interface Organic Semiconductor, Materials Horizons* 7, 1413 (2020)
4. *G. Lavorato, R. Das, Y. Xing, J. Robles, F. Jochen Litterst, E. Baggio-Saitovitch, **M.H. Phan**, and **H. Srikanth**, Origin and Shell-Driven Optimization of the Heating Power in Core/Shell Bimagnetic Nanoparticles, ACS Applied Nano Materials* 3, 1755 (2020)
5. *G.C. Lavorato, A.A. Ruberta, Y. Xing, R. Das, J. Robles, F. Jochen Litterst, E.B. Saitovitch, **M.H. Phan**, **H. Srikanth**, C. Vericat, and M.H. Fonticellia, Shell-Mediated Control of the Surface Chemistry in Highly Stoichiometric Magnetite Nanoparticles, Nanoscale* 12, 13626 (2020)
6. *R. Das, R. Prabhu, N. Venkataramani, S. Prasad, L. Li, **M.H. Phan**, V. Keppens, D. Mandrus, and **H. Srikanth**, Giant Low-field Magnetocaloric Effect and Refrigerant Capacity in Reduced Dimensionality EuTiO₃ Multiferroics, Journal of Alloys and Compounds* 850, 156819 (2021)
7. *R.P. Madhogaria, N.T. Dang, R. Das, E.M. Clements, V. Kalappattil, N.S. Bingham, D. P. Kozlenko, **M.H. Phan**, and **H. Srikanth**, Metamagnetism and kinetic arrest in a long-range ferromagnetically ordered multicaloric double perovskite Y₂CoMnO₆, Journal of Magnetism and Magnetic Materials* 507, 166821 (2020)
8. *R. Das, N.T. Dang, V. Kalappattil, R.P. Madhogaria, D.P. Kozlenko, S.E. Kichanov, E.V. Lukin, A.V. Rutkaukas, T.P.T. Nguyen, L.T.P. Thao, N.S. Bingham, **H. Srikanth**, and **M.H. Phan**, Unravelling the nature of Fe-doping mediated inter- and intra-chain interactions in Ca₃Co₂O₆, Journal of Alloys and Compounds* 851, 156897 (2021)
9. *P. Lampen, E. Clements, B. Casas, **M.H. Phan**, J. Marcin, I. Skorvanek, H.T. Yi, S.W. Cheong, and **H. Srikanth**, Impact of reduced dimensionality on the correlation length and magnetization dynamics of the spin chain cobaltite Ca₃Co₂O₆, Journal of Magnetism and Magnetic Materials* 493, 165690 (2020)
10. *R. Das, V. Kalappattil, **M.H. Phan**, and **H. Srikanth**, Magnetic anomalies associated with domain wall freezing and coupled electron hopping in magnetite nanorods, Journal of Magnetism and Magnetic Materials* 522, 167564 (2021)
11. *Y.T. Hai Pham, M. Liu, V.O. Jimenez, F. Zhang, V. Kalappattil, Mauricio Terrones, and **M.H. Phan**, Tunable Ferromagnetism and Thermally Induced Spin Flip in Vanadium-*

- doped Tungsten Diselenide Monolayers at Room Temperature, *Advanced Materials* 32, 2003607 (2020)
12. F. Zhang, B.Y. Zheng, A. Sebastian, H. Olson, M.Z. Liu, K. Fujisawa, *Y.T.H. Pham*, V. Ortiz Jimenez, V. Kalappattil, T. Zhang, R. Pendurthi, Y. Lei, A. Laura Elias, Y. Wang, Patrick E. Hopkins, S. Das, V.H. Crespi, **M.H. Phan**, and M. Terrones, Monolayer Vanadium-doped Tungsten Disulfide: An Emerging Room-Temperature Diluted Magnetic Semiconductor, *Advanced Science* 7, 2001174 (2020)
 13. V.O. Jimenez, V. Kalappattil, T. Eggers, M. Bonilla, S. Kolekar, P. T. Huy, M. Batzill, **M.H. Phan**, A magnetic sensor using a 2D van der Waals ferromagnetic material, *Scientific Reports* 10, 4789 (2020)
 14. Z. Nemati , M. Reza Zamani Kouhpanji, F. Zhou, R. Das, K. Makielski, J. Um, **M.H. Phan**, A. Muela, M.L. Fdez-Gubieda, R. R Franklin, Bethanie J. H. Stadler, J.F. Modiano, and J. Alonso, Isolation of Cancer-Derived Exosomes Using a Variety of Magnetic Nanostructures: From Fe₃O₄ Nanoparticles to Ni Nanowires, *Nanomaterials* 10, 1662 (2020)
 15. C. Kons, **M.H. Phan**, **H. Srikanth**, and D.A. Arena, Z.N. Porshokouh, J.A. Borchers, and K. L. Krycka, Investigating spin coupling across a three-dimensional interface in core/shell magnetic nanoparticles, *Physical Review Materials* 4, 034408 (2020)
 16. N. Thi My Duc, C.M. Hung, N.T. Huong, and **M.H. Phan**, Magnetic Interactions and Magnetocaloric Effect in (La_{0.5}Pr_{0.5})_{0.6}Ba_{0.4}MnO₃: Effect of A-Site Co-doping, *Journal of Electronic Materials* 49, 2596 (2020)
 17. R. Das, C. Witanachchi, Z. Nemati, V. Kalappattil, I. Rodrigo, J. Ángel García, E. Garaio, J. Alonso, V.D. Lam, A.T. Le, **M.H. Phan**, and **H. Srikanth**, Magnetic Vortex and Hyperthermia Suppression in Multigrain Iron Oxide Nanorings, *Applied Sciences* 10, 787 (2020)
 18. N.T.M. Duc, H.X. Shen, O. Thiabgoh, N.T. Huong, J.F. Sun, and **M.H. Phan**, Melt-extracted Gd_{73.5}Si₁₃B_{13.5}/GdB₆ ferromagnetic/antiferromagnetic microwires with excellent magnetocaloric properties, *Journal of Alloys and Compounds* 818, 153333 (2020)
 19. D. Gandia, L. Gandarias, I. Rodrigo, J. Robles-García, **R. Das**, E. Garaio, J. Á. García, A. García Prieto, **M.H. Phan**, **H. Srikanth**, I. Orue, J. Alonso, A. Muela, and M.L. Fdez-Gubieda, Unlocking the potential of Magnetotactic Bacteria as Magnetic Hyperthermia agents, *Small* 15, 1902626 (2019)
 20. R. Geng, H.M. Luong, **R. Das**, K. Stojak, M.T. Pham, T.A. Duong, P.T. Huy, N.D. Lai, **M.H. Phan**, T.D. Nguyen, Magnetically Tunable Organic Semiconductors with Superparamagnetic Nanoparticles, *Materials Horizons* 6, 1913 (2019)
 21. P.M. Coelho, H.-P. Komsa, K. Lasek, V. Kalappattil, J. Karthikeyan, **M.H. Phan**, A. V Krasheninnikov, and M. Batzill, Room temperature ferromagnetic MoTe₂ by post-growth incorporation of vanadium impurities, *Advanced Electronic Materials* 5, 1900044 (2019)
 22. R. Das, J.A. Cardarelli, **M.H. Phan**, and **H. Srikanth**, Magnetically tunable iron oxide nanotubes for multifunctional biomedical applications, *Journal of Alloys and Compounds* 789, 323 (2019)
 23. N.T.M. Duc, H.X. Shen, E. Clements, O. Thiabgoh, J.L. Sanchez Llamazares, C.F. Sanchez-Valdes, N.T. Huong, J.F. Sun, **H. Srikanth**, and **M.H. Phan**, Enhanced

- refrigerant capacity in melt-extracted amorphous $\text{Gd}_{60}\text{Fe}_{20}\text{Al}_{20}$ microwires with high Curie temperature, *Journal of Alloys and Compounds* 807, 151694 (2019)
24. N. T. Dang, D. P. Kozlenko, N. Tran, B. W. Lee, T. L. Phan, V. Kalappattil, D. S. Yang, S. E. Kichanov, E.V. Lukin, B. N. Savenko, P. Czarnecki, T. A. Tran, V. L. Vo, T. P. T Le, T. K. Dinh, S. H. Jabarov and **M.H. Phan**, Structural, magnetic and electronic properties of Ti-doped $\text{BaFeO}_{3-\delta}$ exhibiting colossal dielectric permittivity, *Journal of Alloys and Compounds* 808, 151760 (2019)
25. N.T.M. Duc, H.X. Shen, E. Clements, O. Thiabgoh, J.L. Sanchez Llamazares, C.F. Sanchez-Valdes, N.T. Huong, J. F. Sun, **H. Srikanth**, and **M.H. Phan**, Critical magnetic and magnetocaloric behaviors of amorphous melt-extracted $\text{Gd}_{50}(\text{Co}_{69.25}\text{Fe}_{4.25}\text{Si}_{13}\text{B}_{13.5})_{50}$ microwires, *Intermetallics* 110, 106479 (2019)
26. R.P. Madhogaria, R. Das, E. M. Clements, V. Kalappattil, N. S. Bingham, **M.H. Phan**, and **H. Srikanth**, Effect of antiphase boundaries on the magnetic properties of $\text{La}_2\text{CoMnO}_6$, *AIP Advances* 9, 035142 (2019)
27. R. Das, J. Robles, M. Glassell, V. Kalappattil, **M.H. Phan**, and **H. Srikanth**, Magnetic anisotropy and switching behavior of exchange coupled $\text{Fe}_3\text{O}_4/\text{CoFe}_2\text{O}_4$ core/shell nanoparticles, *Journal of Electronic Materials* 48, 1461 (2019)

Topological Phases in Aperiodic Systems and Flat-Band Material

Feng Liu
University of Utah

Program Scope

This project, titled “Topological Phases in Aperiodic Systems and Flat-Band Materials”, encompasses a comprehensive study of physical mechanisms underlying the formation of exotic quantum phases of electronic states associated with topological order in quasicrystals and disordered systems and in materials hosting topological flat bands. It covers three correlated research topics: (1) topological phase in quasicrystal lattices and materials; (2) topological phase in disordered systems; (3) flat-band materials. The common theme of the proposed research is to understand topological phases in aperiodic systems without translational symmetry, the robustness of topological order in crystals against disorder, and a new class of topological materials hosting two-dimensional (2D) or 3D flat bands.

Our theoretical/computational project will employ a multiscale approach, combining several state-of-the-art theoretical and computational techniques, ranging from first-principles density-functional-theory (DFT) electronic structure calculations to semi-empirical tight-binding (TB) model Hamiltonian analyses and calculations and to non-equilibrium Green's function transport calculations. Specifically, electronic band structure will be studied using both DFT and TB methods with the TB parameters fit to the DFT band structures, e.g., in supercells of ribbon geometry to represent an edge. Topological invariants of electronic states will be revealed by analyzing Bloch wavefunctions for crystalline lattices using conventional methods of calculating (spin) Chern numbers or single electron states for aperiodic lattices using our newly developed methods of calculating (spin) Bott indices. In addition, the topological surface (edge) states will be calculated using DFT/TB/Wannier function based methods, while the transport properties including surface/edge conductance will be investigated using the TB/Wannier function based non-equilibrium Green's function methods.

Our studies will significantly improve our fundamental understanding of physical origins of topological states in non-crystalline and disordered material systems, in terms of lattice geometry (or lack of), spin-orbit coupling, orbital composition and degree of disorder. Both the continuations and new initiatives of the proposed research will significantly improve our fundamental understanding of topological order and phase transition in 2D quasicrystal materials and crystals with disorder, and a new class of topological flat-band materials. They will provide useful guidelines for future experimental efforts in synthesis and characterization of new 2D and 3D topological materials. They will also have direct technological impact on advancing quantum materials and devices for energy applications, to fulfill the mission of the Department of Energy.

Recent Progress

During the last two years, we have published 33 journal papers fully or partially supported by this DOE grant, including 2 Physical Review Letters, 3 Nano Letters, 1 Nature Communications, 1 ACS Nano, 1 Adv Materials, 1 Research; plus one invited review (published on Jan. 5, 2021). Two postdoctoral research associates and three graduate students have been fully or partially supported by this DOE project. The PI gave 9 invited talks at national/international conferences, and 12 departmental colloquium/seminar presentations. Below is a brief summary of four topics of research achievements pertaining to this project.

(1) A Unified View of Topological Phase Transition in Band Theory:¹ We develop a unified view of topological phase transitions (TPTs) in solids by revising the classical band theory with the inclusion of topology. Reevaluating the band evolution from an “atomic crystal” [a normal insulator (NI)] to a solid crystal, such as a semiconductor, we demonstrate that there exists ubiquitously an intermediate phase of topological insulator (TI), whose critical transition point displays a linear scaling between electron hopping potential and average bond length, underlined by deformation-potential theory. The validity of the scaling relation is verified in various two-dimensional (2D) lattices regardless of lattice symmetry, periodicity, and form of electron hoppings, based on a generic tight-binding model. Significantly, this linear scaling is shown to set an upper bound for the degree of structural disorder to destroy the topological order in a crystalline solid, as exemplified by formation of vacancies and thermal disorder. Our work formulates a simple framework for understanding the physical nature of TPTs with significant implications in practical applications of topological materials.

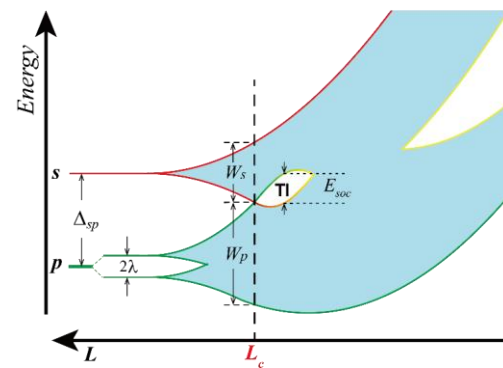


Fig. 1. Fig. 1. Schematic illustration of topological phase transition (TPT) in band evolution diagram. By decreasing average bond length L . The bandwidth increases gradually and a TPT occurs at L_c , which is inversely proportional to the electron hopping potential $\gamma = dE_g/dL$, where E_g is band gap.

(2) Realization of an Antiferromagnetic Superatomic Graphene: Dirac Mott Insulator and Circular Dichroism Hall Effect:

² Using first-principles calculations, we investigate the electronic and topological properties of an antiferromagnetic (AFM) superatomic graphene lattice superimposed on a bipartite honeycomb lattice governed by Lieb’s theorem of itinerant magnetism. It affords a concrete material realization of the AFM honeycomb model with a Dirac Mott insulating

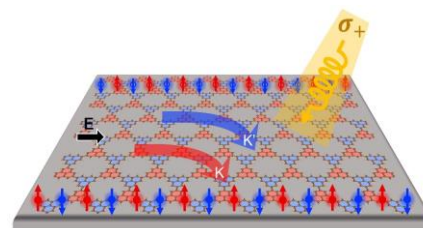


Fig. 2. Schematic illustration of CD Hall effect of AFM superatomic graphene excited by left-handed circularly polarized light ($\sigma+$).

state, characterized by a gap opening at the Dirac point due to inversion symmetry breaking by long-range AFM order. The opposite Berry curvatures of the K and K' valleys induce a circular dichroism (CD) Hall effect. Different from the valley Hall effect that activates only one valley, the CD Hall effect activates carriers from both K and K' valleys, generating the opposite directions of transversal Hall currents for the left- and right-handed circularly polarized light, respectively.

(3) A Lieb-Like Lattice in a Covalent-Organic-Framework and its Stoner Ferromagnetism:¹⁷

Lieb lattice has been extensively studied as a model system to realize ferromagnetism due to its exotic flat band. However, its material realization has remained elusive; so far only artificial Lieb lattices have been made experimentally. Recently, based on first-principles and tight-binding calculations, we discover that a recently synthesized two dimensional sp₂ carbon-conjugated covalent-organic framework (sp₂c-COF) represents a material realization of a Lieb-like lattice. The experimentally observed ferromagnetism upon doping is shown to arise from a Dirac (valence) band in a non-ideal Lieb lattice with strong electronic inhomogeneity (EI) rather than the topological flat band in an ideal Lieb lattice. The EI, as characterized with a large on-site energy difference and a strong dimerization interaction between the corner and edge-center ligands, quenches the kinetic energy of the usual dispersive Dirac band, subjecting to an instability against spin polarization. Furthermore, we predict an even higher spin density for monolayer sp₂c-COF to accommodate a higher doping concentration with reduced interlayer interaction.

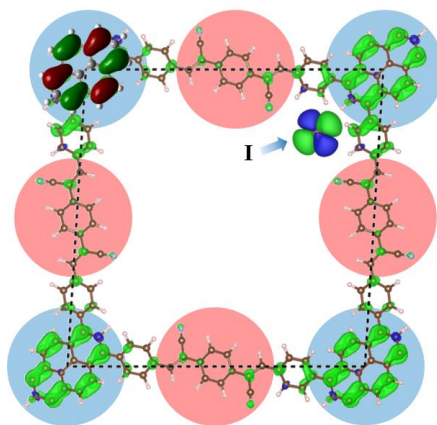


Fig. 3. Lattice structure of the sp₂c-COF, illustrating first real material realization of a long-sought Lieb lattice. Spin distribution upon iodine doping is shown in green lobes. Top left corner shows the molecular orbital of the corner ligand.

(4) Unidirectional Spin–Orbit Interaction Induced by the Line Defect in Monolayer Transition Metal Dichalcogenides for High-Performance Devices:¹⁸

Spin–orbit (SO) interaction is an indispensable element in the field of spintronics for effectively manipulating the spin of carriers. However, in crystalline solids, the momentum-dependent SO effective magnetic field generally results in spin randomization by a process known as the Dyakonov–Perel spin relaxation, leading to the loss of spin information. To overcome this obstacle, the persistent spin helix (PSH) state with a unidirectional

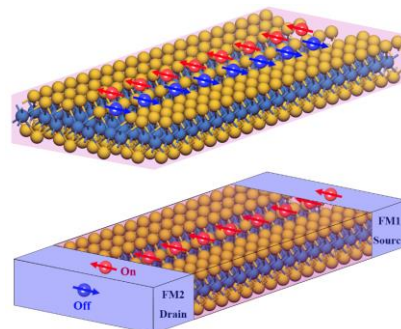


Fig. 4. Schematic diagrams of (upper panel) line defect in TMD with unidirectional spin texture (red and blue arrows), and (lower panel) the corresponding spin FET setup.

SO field was proposed but difficult to achieve in real materials. Here, on the basis of first-principles calculations and tight-binding model analysis, we report for the first time a unidirectional SO field in monolayer transition metal dichalcogenides (TMDs, MX₂, M = Mo, W; and X = S, Se) induced by two parallel chalcogen vacancy lines. By changing the relative positions of the two vacancy lines, the direction of the SO field can be tuned from x- to y-axis. Moreover, using $k \cdot p$ perturbation theory and group theory analysis, we demonstrate that the emerging unidirectional SO field is subject to both the structural symmetry and 1D nature of such defects engineered in 2D TMDs. In particular, through transport calculations, we confirm that the predicted SO states carry highly coherent spin current. Our findings shed new light on creating PSH states for high-performance spintronic devices.

Future Plans

We plan to expand our current studies in the following areas:

- (a) Fractional quantum states, such as fractional quantum anomalous/spin Hall effect and fractional excitonic insulator state
- (b) Initiate a new research topic on pseudo-spin ice and quantum pseudo-spin glass
- (c) Flat-band-enabled excitonic insulator state
- (d) Amorphous topological materials
- (e) Topological flat band in line-graph lattices
- (f) Topological flat band in non-line-graph lattices
- (g) Non-Hermitian topology in line-graph lattices
- (h) Continue the efforts of experimental collaborations.

References

1. "A Unified View of Topological Phase Transition in Band Theory", H. Huang, and Feng Liu, *Research*, **2020**, 7832610 (2020).
2. "Realization of an Antiferromagnetic Superatomic Graphene: Dirac Mott Insulator and Circular Dichroism Hall Effect", Y. Zhou and Feng Liu, *Nano Lett.* <https://doi.org/10.1021/acs.nanolett.0c03579>, (2020).
3. "Electronic structures of a diagonally striped lattice: Multiple (N-1)-fold degenerate flat bands", X. Ni, J. Yan, and Feng Liu, *Phys. Rev. B* **102**, 235117 (2020).
4. " π -Orbital Yin–Yang Kagome bands in anilato-based metal–organic frameworks", X. Ni, Y. Zhou, G. Sethi, and Feng Liu, *Phys. Chem. Chem. Phys.* **22**, 25827 (2020).
5. "Fermionic Analogue of High Temperature Hawking Radiation in Black Phosphorus", H. Liu, J-T Sun, C. Song, H. Huang, Feng Liu, and S. Meng, *Chin. Phys. Lett.*, **37**, 067101 (2020).
6. "Honeycomb-Lattice Mott Insulator on Tantalum Disulphide", J. Lee, K-H Jin, A. Catuneanu, A. Go, J. Jung, C. Won, S-W Cheong, J. Kim, Feng Liu, H-Y Kee, and H. Yeom, *Phys. Rev. Lett.*, **125**, 096403 (2020).
7. "1D topological phases in transition-metal monochalcogenide nanowires", K-H Jin and Feng Liu, *Nanoscale*, **12**, 14661 (2020).
8. "Giant intrinsic circular dichroism of enantiomorphic flat Chern bands and flatband devices", Y. Zhou, G. Sethi, C. Zhang, X. Ni, and Feng Liu, *Phys. Rev. B*, **102**, 125115 (2020).
9. "Magneto-Optical Detection of Photoinduced Magnetism via Chirality-Induced Spin Selectivity in 2D Chiral Hybrid Organic-Inorganic Perovskites", Z. Huang, B. Bloom, X. Ni, Z. Georgieva, M. Marciesky, E. Vetter, Feng Liu, D. Waldeck, and D. Sun, *ACS Nano*, **14**, 10370 (2020).
10. "Prediction of room-temperature multiferroicity in strained MoCr₂S₆ monolayer", L-Z Liu, K-H Jin, and Feng Liu, *J. Appl. Phys.* **127**, 155302 (2020).
11. "Theory of Epitaxial Growth of Borophene on Layered Electride: Thermodynamic Stability and Kinetic Pathway", X. Ni, H. Huang, K-H Jin, Z. Wang and Feng Liu, *J. Phys. Chem. C*, **124**, 6063 (2020).
12. "Robustness of topological insulating phase against vacancy, vacancy cluster, and grain boundary bulk defects", X. Ni, H. Huang and Feng Liu, *Phys. Rev. B* **101**, 125114 (2020).
13. "Topological Band Engineering of Lieb Lattice in Phthalocyanine-Based Metal–Organic Frameworks", W. Jiang, S. Zhang, Z. wang, Feng Liu and T. Low, *Nano Lett.*, **20**, 3, 1959 (2020).
14. "Site-Controlled Uniform Ge/Si Hut Wires with Electrically Tunable Spin–Orbit Coupling", F. Gao, J-H Wang, H. Watzinger, H. Hu, M. J. Rančić, J-Y Zhang, T. Wang, Y. Yao, G-L Wang, J. Kukučka, L. Vukušić, C. Kloeffel, D. Loss, Feng Liu, G. Katsaros, J-J Zhang, *Adv. Mater.* **32**, 1906523 (2020).
15. "Doping-induced topological phase transition in Bi: The role of quantum electronic stress", K-H Jin, H. Yeom, and Feng Liu, *Phys. Rev. B* **101**, 035111 (2020).
16. "Aperiodic topological crystalline insulators", H. Huang, Y-S Wu, and Feng Liu, *Phys. Rev. B* **100**, 041103(R) (2020).
17. "A Lieb-like lattice in a covalent-organic framework and its Stoner ferromagnetism", W. Jiang, H. Huang and Feng Liu, *Nature Commun.*, **10**, 2207 (2019).

18. "Unidirectional Spin–Orbit Interaction Induced by the Line Defect in Monolayer Transition Metal Dichalcogenides for High-Performance Devices", X. Li, S. Zhang, H. Huang, L. Hu, Feng Liu and Q. Wang, *Nano Lett.*, **19**, 6005, (2019).
19. "Observation of topological surface states in the high-temperature superconductor MgB₂", X. Zhou, K. Gordon, K-H Jin, H. Li, D. Narayan, H. Zhao, H. Zheng, H. Huang, G. Gao, N. Zhigadlo, Feng Liu, and D. Dessau, *Phys. Rev. B* **100**, 184511 (2019).
20. "Orbital design of topological insulators from two-dimensional semiconductors", L. Gao, J. Sun, G. Sethi, Y. Zhang, S. Du, and Feng Liu, *Nanoscale*, **11**, 22743 (2019).
21. "Anomalous Dirac Plasmons in 1D Topological Electrides", J. Wang, X. Sun, S. Gao, W. Duan, Feng Liu, and B. Huang, *Phys. Rev. Lett.*, **123**, 206402 (2019).
22. "Energy barriers for Pb adatom diffusion on stepped ultrathin Pb(111) quantum nanofilms: First-principles calculations", Y. Han, J. W. Evans, and Feng Liu, *Phys. Rev. B* **100**, 195405 (2019).
23. "Enhancing superconductivity in bulk β-Bi₂Pd by negative pressure induced by quantum electronic stress", X. Zhang, M. Zhang and Feng Liu, *Phys. Rev. B* **100**, 104527 (2019).
24. "Comparison of quantum spin Hall states in quasicrystals and crystals", H. Huang and Feng Liu, *Phys. Rev. B.*, **100**, 085119 (2019).
25. "Polaronic Resistive Switching in Ceria-Based Memory Devices", L. Sun, X. Hao, Q. Meng, L. Wang, Feng Liu and M. Zhou, *Adv. Electron. Mater.*, 1900271 (2019).
26. "Weyl points created by a three-dimensional flat band", Y. Zhou, K-H Jin, H. Huang, Z. Wang and Feng Liu, *Phys. Rev. B*, **99**, 201105(R) (2019).
27. "Topological superconducting phase in high-T_c superconductor MgB₂ with Dirac–nodal-line fermions", K-H Jin, H. Huang, J-W Mei, Z. Liu, L-K Lim and Feng Liu, *npj Computational Materials*, **5**, 57 (2019).
28. "A 2D nonsymmorphic Dirac semimetal in a chemically modified group-VA monolayer with a black phosphorene structure", K-H Jin, H. Huang, Z. Wang and Feng Liu, *Nanoscale*, **11**, 7256 (2019).
29. "Valley splitting in the van der Waals heterostructure WSe₂/CrI₃: The role of atom superposition", Z. Zhang, X. Ni, H. Huang, L. Hu and Feng Liu, *Phys. Rev. B*, **99**, 115441 (2019).
30. "Topological band evolution between Lieb and kagome lattices", W. Jiang, M. Kang, H. Huang, H. Xu, T. Low and Feng Liu, *Phys. Rev. B*, **99**, 125131 (2019).
31. "Kagome bands disguised in a coloring-triangle lattice", S. Zhang, M. Kang, H. Huang, W. Jiang, X. Ni, L. Kang, S. Zhang, H. Xu, Z. Liu and Feng Liu, *Phys. Rev. B*, **99**, 100404(R) (2019).
32. "A 3D percolation model for multicomponent nanocarbon composites: the critical role of nematic transition", X. Ni, C. Hui, N. Su, R. Cutler and Feng Liu, *Nanotechnology*, **30**, 185302 (2019).
33. "Dichotomy between frustrated local spins and conjugated electrons in a two-dimensional metal-organic framework", W. Jiang, Z. Liu, J-W Mei, B. Cui and Feng Liu, *Nanoscale*, **11**, 955 (2019)

Quantifying exciton heterogeneities in metal halide perovskites

Luisa Whittaker-Brooks, University of Utah, Department of Chemistry, 315 South 1400 East, Salt Lake City, Utah, 84112

i) Program Scope

Metal halide perovskite (MHP) multiple quantum wells which consist of multilayers of alternate organic and inorganic layers exhibit large exciton binding energies due to the dielectric confinement between the inorganic and organic layers. These naturally formed multiple quantum wells have strong spin-orbit coupling (SOC) due to the presence of heavy elements in their crystal structures. Although the fundamental properties of 2D MHPs are far from being entirely understood, it is widely accepted that their band edge absorption coefficient results from strong exciton interactions. However, studies demonstrating how different exciton interactions and doping effects influence electronic traps and disorder on the band edge absorption coefficient of 2D MHPs have not been demonstrated. Understanding these interactions in MHPs will allow us to access low energy optical transitions for the fabrication of solution processable short-to-mid-wavelength IR photodetectors ($1 - 8 \mu\text{m}$). Moreover, upon doping, it is possible to move the Fermi energy into the conduction band (CB) to favorably promote the transport of charges in a working device. Herein, we study the development of 2D MHPs having strong SOC, high carrier mobility, and tunable quantum well structures. Our studies shed light on the design and modulation of fundamental physical phenomena by carefully elucidating the role of dopants (n-type and p-type), exciton heterogeneity, orientation, structure, and bias stress effects on the performance of MHPs as potential IR photodetectors.

ii) Recent progress

a. Quantifying exciton heterogeneities in mixed-phase organometal halide multiple quantum wells via Stark spectroscopy

2D MHP quantum wells naturally self-assemble through weak van der Waals forces. We investigate the structural and optoelectronic properties of 2D layered butylammonium ($\text{C}_4\text{H}_9\text{NH}_3^+$, BA $^+$) methylammonium (CH_3NH_3^+ , MA) lead iodide, $(\text{BA})_2(\text{MA})_{n-1}\text{Pb}_n\text{I}_{3n+1}$ quantum wells with varying n from 1 to 4. Through conventional structural characterization, $(\text{BA})_2(\text{MA})_{n-1}\text{Pb}_n\text{I}_{3n+1}$ thin films showcase high-quality phase (n) purity. However, while investigating the optoelectronic properties, it is clear that these van der Waals heterostructures consist of multiple quantum well thicknesses coexisting within a single thin film. We utilized electroabsorption spectroscopy and Liptay theory to develop an analytical tool capable of deconvoluting the excitonic features that arise from different quantum well thicknesses (n) in $(\text{BA})_2(\text{MA})_{n-1}\text{Pb}_n\text{I}_{3n+1}$ thin films. To obtain a quantitative assessment of exciton heterogeneities within a thin film comprising multiple quantum well structures, exciton resonances quantified by absorption spectroscopy were modeled as Gaussian features to yield various theory-generated electroabsorption spectra which were then fit to our experimental electroabsorption features. In addition to identifying the quantum well heterostructures present within a thin film, this novel analytical tool provides powerful insight into the exact exciton composition and can be utilized to analyze the optoelectronic properties of many other mixed-phase quantum well heterostructures beyond those formed by 2D MHPs. Our findings may help in designing more efficient and reproducible light emitting diodes based on 2D mixed-phase metal-organic multiple quantum wells.

Findings: Due to the convoluted optical composition of these mixed-phase $(\text{BA})_2(\text{MA})_{n-1}\text{Pb}_n\text{I}_{3n+1}$ quantum well thin films, we have utilized Stark spectroscopy, specifically electroabsorption (EA)

spectroscopy, in combination with absorption spectroscopy, to elucidate the true compositional phase distributions within thin films. We note that EA is a nonlinear optical spectroscopy method and as such it does not involve exciton funneling among the various quantum wells, in contrast to

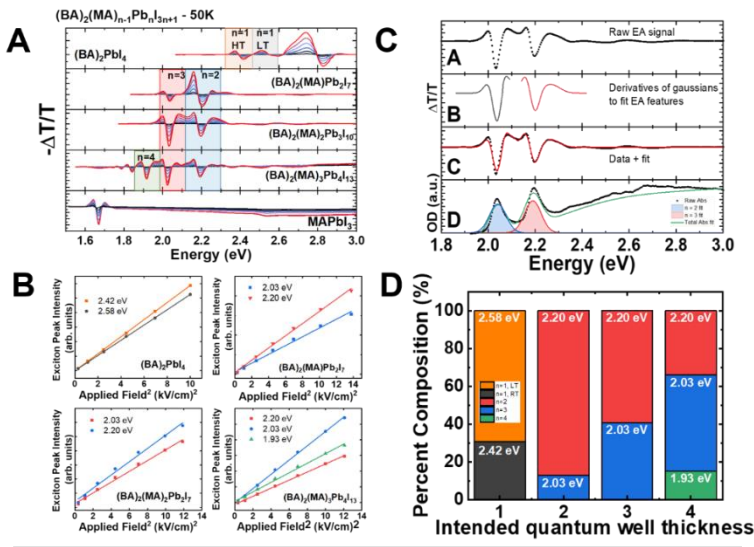


Figure 1. (A) EA spectra of $(BA)_2(MA)_{n-1}Pb_nI_{3n+1}$ thin films. Shaded boxes represent the exciton absorption of pure quantum well phases (LT = low temperature phase, HT = high temperature phase). (B) EA amplitude plotted against the applied field squared (F^2) for various 2D-MHPs. (C) Example of fitting routine used for investigating exciton compositions. (D) Pure phase quantum well distribution within each $(BA)_2(MA)_{n-1}Pb_nI_{3n+1}$ thin film derived from EA fitting parameters.

the quantum well present within a thin film and can be used to quantify sample heterogeneity. The percent distributions for all quantum well phases observed within a MHP thin film are summarized in **Figure 1D**. As we previously reported,¹ $(BA)_2PbI_4$ undergoes a structural phase change at 250 K. However, at temperatures below 250 K, we still observe remnants of the room-temperature phase indicating that $(BA)_2PbI_4$ undergoes a partial structural phase transition. From fitting all the excitonic features against the oscillator strength, we find that these films despite being structurally phase pure, they are very heterogeneous optically. As such, the realization of phase-pure $(BA)_2(MA)_{n-1}Pb_nI_{3n+1}$ quantum well heterostructures is a convoluted process that involves a close interplay between the kinetic and thermodynamic stabilities inherent to the stoichiometry of the structures upon increasing the layer thicknesses (n) and often do not correlate to their optical properties.

b. Dynamic structural disorder effects on the optical properties of 2D-MHPs

Unlike GaAs-based multiple quantum wells, the EA spectra of 2D MHPs do not agree closely with theory and have led to contradictory interpretations of the optical properties of these materials.¹⁻⁴ Furthermore, there are unexplained optical spectral features which challenge our fundamental understanding of the ground and excited states participating in the optical transitions of 2D MHPs. Subsequent EA studies on MHPs have been oddly rare considering the interest in this class of materials and the open questions regarding the nature of their excited states. In an effort to reconcile these differences and determine which EA features are universal to 2D MHPs, we fabricated EA devices with 2D MHP spanning multiple compositions, namely

PL spectroscopy. In the presence of an electric field, localized states (excitons) behave differently than delocalized states (band to band transitions); therefore, we can use this characteristic to our advantage when multiple spectroscopic features overlap in a multiple quantum well system. The EA spectra for $(BA)_2(MA)_{n-1}Pb_nI_{3n+1}$ quantum well thin films ($n = 1 - 4$) are shown in **Figure 1A**. As shown in **Figure 1B**, all the exciton features found in the EA spectra for each thin film depend linearly with F^2 , confirming that these features are in fact localized excitons, and do not originate from delocalized continuum states associated with the bandgap. **Figure 1C** displays an example of the fitting process for a $BA_2(MA)_2Pb_3I_{10}$ thin film. The Gaussian amplitudes represent the relative compositions of

phenethylammonium lead iodide (PEA_2PbI_4), phenethylammonium tin iodide (PEA_2SnI_4), butylammonium lead iodide (BA_2PbI_4), and butylammonium tin iodide (BA_2SnI_4). We discovered an anomalous temperature-dependence in the EA line shape, moving from 1st derivative (linear Stark Shift) at room temperature to 2nd-derivative (quadratic Stark shift) at 50 K which significantly affect the excitonic properties of 2D MHPs. Furthermore, the temperature-dependence in the EA line shape is highly sensitive to the morphology obtained for the 2D MHP thin films. These results contribute to the on-going conversation about dynamic disorder and local symmetry breaking that give rise to possible Rashba and polaronic effects in MHPs. While

previous time-domain studies have made progress on this important puzzle by probing the lattice's response to photoexciton, this study demonstrates EA is capable of probing the opposite side of the interaction by observing the lattice's influence on the character of the excited state *prior* to any lattice response.

Findings: In general, an external applied field can shift or broaden an exciton's absorption peak causing the electroabsorption ΔA to resemble a 1st or 2nd derivative line shape, respectively. The proportion of each effect is determined by the ratio of first-order quadratic Stark shift ΔE_Q and a second-order linear Stark shift ΔE_L^2 . We found that in each of the four 2D MHPs exciton's EA signal resembles a 2nd-derivative line shape at 300 K but transitions to 1st derivative shape at 50 K. The dotted lines in **Figure 2A-D** mark the exciton resonance energies and the line shape transition is qualitatively evident by noting the line's intersection point on the EA signal—it intersects a zero-crossing point (1st derivative) in the 50 K signal whereas for the 300 K signal it intersects a negative peak (2nd derivative). This trend is supported by numerical 1st and 2nd-derivative fits with the unperturbed absorbance spectrum, and the transition is more pronounced in the thin film exhibiting higher morphological order (**Figure 2C and 2D**). We showed through theoretical

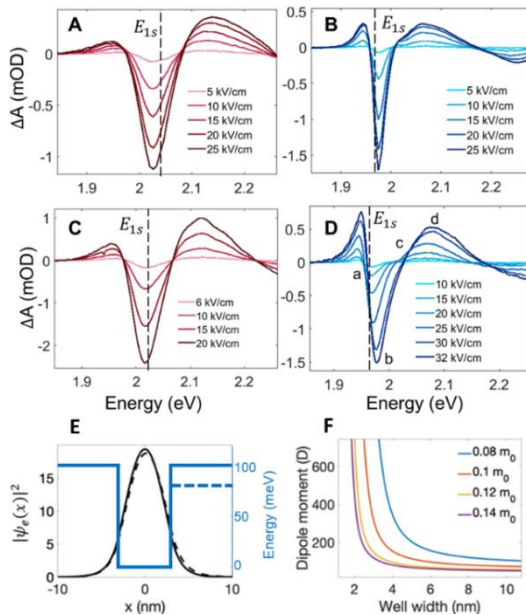


Figure 2. Voltage-dependent EA spectra of morphologically disordered PEA_2SnI_4 thin film at (A) 300 K and (B) 50 K. Morphologically ordered thin film at (C) 300 K and (D) 50 K. (E) An envelope wavefunction representation of the 2D MHP exciton in a symmetric (undotted) and asymmetric (dotted) finite potential well associated with local disorder. (F) Magnitude of disorder-induced dipole moments for various reduced effective masses.

calculations of the EA signal that ferroelectric polar nanodomains cannot explain the line shape transition. Rather, the ratio of $\Delta E_Q : \Delta E_L^2$ must change demonstrating a real effect on the exciton's properties as a function of temperature. We find that the anomalous line shape transition is due to a decrease in dipole moment μ_{ge} by a factor of $\sim \times 0.5$ between 300 K and 50 K for all tested 2D MHPs. Furthermore, we found significant sample-to-sample discrepancy (10 – 45 D) for μ_{ge} at 300 K which appears to be correlated to the morphological order of each thin film. Large discrepancies in μ_{ge} have previously been observed in conductive polymer films and the atypically large values, e.g. $\mu_{ge} = 48$ D, have been assigned to disorder-induced dipole moments originating from static disorder, i.e. inhomogeneous polymer lengths and orientation. In effect, asymmetric energy landscape associated with disorder can shift an excited state's charge density, resulting in a dipole moment relative to the symmetric case. To explore the extent to which this effect is present in our 2D MHPs, we simulated the charge density shift using a simple envelope wavefunction

approximation. As shown in **Figure 2E**, the x-axis projection of the 2D envelope wavefunction is subjected to asymmetric boundary conditions where the barrier lengths are set to roughly twice the exciton's diameter, $L_x = L_y = 6$ nm and the electron's effective mass $m_e = 0.12 m_0$ has been taken from band-structure calculations. A small reduction in two of the barriers from 100 to 80 meV results in a surprisingly large permanent dipole of 19 D which is within the correct range to explain the observed sample-to-sample variations in μ_{ge} . **Figure 2F** shows how this effect can increase substantially for smaller effective masses, such as those in the tin-based 2D MHPs. Our dynamic disorder induced dipole model not only explains the reduction of μ_{ge} with temperature, but also predicts an inverse relationship between $\Delta\mu_{ge}(300K - 50K)$ and binding energy that is observed in all samples. As expected, the disordered film exhibits higher μ_{ge} than its ordered counterpart and the overall morphological order correlates most strongly with μ_{ge} at 50 K where dynamic disorder is suppressed due to the reduction of acoustic phonons, but the effects of morphological 'static disorder' are still present. Only in highly ordered films at low temperature are the influences of both static and dynamic disorder suppressed. These results extend the capabilities of EA as a technique to probe for exciton-phonon interactions, as this analysis represents the first link between dynamic disorder and EA spectra. We can conclude that (1) dipolar organic cation is not a necessary ingredient of dynamic disorder, (2) thermal fluctuations alone are large enough to double the exciton's dipole moment and localize its wavefunction, and (3) tin-based MHPs are more affected by dynamic disorder due to lower effective masses and lower binding energies.

iii) Future plans: *Circularly polarized light detection through 1D metal halide perovskites*

Detection of circularly polarized light (CPL) can be used for object identification, quantum-based computing and information processing, and communication through polarized reflections. As well, materials sensitive to CPL can often have polarized emissive properties, making them excellent candidates for spin-polarized light-emitting diodes (LEDs). There is an enormous need for intrinsic CPL photodetectors. MHPs have the facile functionalization of small organic molecules but retain the high mobility of inorganic semiconductors, making them perfect candidates for CPL photodetection. As future work, we will be developing a series of MHPs with induced chirality that are based on μ -conjugated organic cations. We will use (R/S-) methylbenzylammonium (R/S-MBA) within a tin iodide lattice to make $(R/S\text{-MBA})_2\text{SnI}_4$ to investigate its CPL response. We

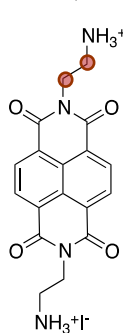


Figure 3. NDIC2 with highlighted locations for chiral center (red circles).

believe the chirality in this material will be actually induced onto the Sn-I octahedra through the distortion of the bond angles of the SnI_4 sheets. This transfer of chirality is quite unique and opens up many interesting fundamental questions about the optoelectronic properties of hybrid – chiral – MHPs. We will study the effect that adding a chiral center to NDIC2 has on the CPL response. The chirality can be added to the terminal ethylammonium groups (**Figure 3**); by adding here, the chiral center is close to the Pb_2I_6 wire and likely will induce a substantial degree of octahedra tilting. We will provide answers to the following questions: (1) Does the chiral center affect the molecular packing of the NDIC2 molecule? (2) Due to the strong conjugated

nature of NDIC2, is the "chiral transfer" less pronounced than in the $(R/S\text{-MBA})_2\text{PbI}_4$ example? (3) Is this MHP able to make successful photodetector devices (i.e. is the mobility and carrier diffusion length high enough for the realization of successful devices)?

iv) References: (1) *J. Phys. Chem. Lett.* **2017**, *8*, 4557-4564; (2) *Solid State Commun.* **2002**, *122*, 249-252; (3) *Sci. Adv.* **2017**, *3*, e1700704; (4) *J. Phys. Chem. C* **2018**, *122*, 26623-26634; (5) *PSSA physica status solidi (a)* **1973**, *18*, 347-359.

v) Publications supported by this award

1. K. Hansen and L. Whittaker-Brooks. Dynamic structural disorder effects on the optical properties of 2D-MHPs. *Submitted*
2. E. Amerling, Y. Zhai, B. W. Larson, B. Flugel, Z. Owczarczyk, H. Lu, L. Whittaker-Brooks, and J. Blackburn. Evidence of free carrier generation in 1D organolead iodide molecular heterostructures. *Submitted*
3. E. Amerling, K. Hansen, and L. Whittaker-Brooks. Electroabsorption spectroscopy as a tool to probe unique optoelectronic features in metal halide perovskites. *Submitted*
4. E. Amerling, H. Lu, B. W. Larson, A. E. Maughan, A. Phillips, E. Lafalce, L. Whittaker-Brooks, J. Berry, M. C. Beard, Z. V. Vardeny, and J. L. Blackburn. A multi-dimensional perspective on electronic doping in metal halide perovskites. *ACS Energy Lett.*, Accepted 2021.
5. L. Flannery, J. Ogle, D. Powell, C. J. Tassone, and L. Whittaker-Brooks. Voltage bias stress effects in organic-inorganic halide perovskites are strongly dependent on morphology and ion migration pathways. *J. Mater. Chem. A.*, 2020, 8, 25109-25119.
6. E. Amerling, S. Baniya, E. Lafalce, S., Blair, V. Vardeny, and L. Whittaker-Brooks. Quantifying exciton heterogeneities in mixed-phase organometal halide multiple quantum wells via Stark spectroscopy studies. *ACS Appl. Mater. Interfaces*, 2020, 12, 52538-52548.
7. M. T. Pham, E. Amerling, H. M. Luong, H. Dang, L. Whittaker-Brooks and T. D. Nguyen. Origin of Rashba spin-orbit coupling in 2D and 3D lead iodide perovskites. *Sci. Rep.*, 2020, 10, 4964.
8. C. G. Hawkins, A. Verma, W. Horbinski, R. Weeks, P. Mukherjee, and L. Whittaker-Brooks. Decreasing the ion diffusion pathways for the intercalation of multivalent cations in defect-tolerant TiS_{2-x} nanobelt cathode insertion hosts. *Appl. Mater. Interfaces*, 2020, 12, 21788–21798.

Unique optical excitations in topological insulators

PI: Stephanie Law

Department of Materials Science and Engineering, University of Delaware, Newark DE 19716

Program Scope

The overall goal of this project is to have a complete understanding of and control over Dirac plasmon polaritons in topological insulators (TIs). TIs are materials that exhibit a bulk bandgap crossed by surface states with linear dispersion and spin-momentum locking. Among other interesting properties, these surface states house exotic plasmonic excitations that are predicted to be two-dimensional, massless, and spin-polarized. The goal of this program is to explore the properties of Dirac plasmons in topological insulators (TIs), understand how these plasmons couple both to each other and to other excitations in the system, to investigate plasmons in topological insulator nanoparticles, and discover how this coupling in both single-layer and multi-layer systems modifies the photonic band structure of the TI system.

Recent Progress

The first phase of the research program focused on the excitation of plasmon polaritons in TI thin films. We have successfully completed this phase by exciting Dirac plasmon polaritons in single Bi_2Se_3 TI layers and mapping their dispersion [1]. We have demonstrated that these polaritons are comprised of Dirac surface state electrons and shown strong coupling between the Dirac plasmon polaritons and the α and β phonons in the Bi_2Se_3 layer. These polaritons exhibit high effective mode indices and long plasmon lifetimes, comparable to graphene plasmons. In addition, we have determined that the excess electrons in our films can be attributed to the poor interface between the Bi_2Se_3 and the sapphire substrate [2]. We have mitigated this issue through the use of lattice-matched buffer layers, which reduce the carrier density (moving the Fermi energy closer to the Dirac point) while simultaneously increasing the electron mobility [3]. Since the previous meeting, the project has focused on two thrusts: improved synthesis of TI thin films, heterostructures, and nanoparticles; and investigation of plasmon coupling in multilayer structures.

TI synthesis

One of the major hurdles impeding the progress of research into TIs is their persistent high unintentional doping density, their significant twinning, and the inability to use strain to modify the film properties due to the van der Waals (vdW) bonding between the TI layers. As noted above, we have significantly reduced the TI bulk doping through the use of lattice-matched buffer layers. Despite the vdW bonding between the film and the substrate, the film quality is still influenced by interactions with the substrate. The lattice-matched buffer layer improves the TI film quality and

can be used as the trivial band insulator (BI) component in a layered TI/BI superlattice. In addition to growth on sapphire substrates, we have also investigated TI growth on GaAs (001) substrates. Unlike sapphire, (001) GaAs has surface dangling bonds, a zincblende structure, and an anisotropic in-plane surface energy. These factors increase the interaction between the GaAs substrate and the Bi_2Se_3 TI film. By growing at very high substrate temperatures (close to the thermal degradation point of Bi_2Se_3) and using intermittent annealing cycles to increase adatom mobility, we have demonstrated the growth of (0015) oriented Bi_2Se_3 directly on GaAs, as shown in the top panel of Figure 1 [4]. This is the first demonstration of epitaxial Bi_2Se_3 on a substrate without prepatternning, demonstrating that vdW materials can exhibit traditional epitaxial growth under the correct conditions. We have also demonstrated the growth of self-assembled Bi_2Se_3 nano-columns on a BiInSe_3 buffer layer on GaAs, shown in the bottom panel of Figure 1 [5]. Unlike traditional epitaxial systems, this self-assembly is not driven by strain. Instead, it is caused by very long adatom diffusion lengths coupled with a high selenium overpressure, similar to the growth of catalyst-free GaN nanowires. This new morphology is important for two reasons: first, it can be used to investigate the unusual plasmonic behavior predicted in TIs confined to nanoscale dimensions [6], and second, it shows that the morphology of TI films can be controlled by controlling the growth parameters. TI thin films normally show a terraced “wedding-cake” morphology with triangular domains and substantial twinning. This result shows that TI film morphology can be controlled, opening the door to the growth of smooth films with fewer grain boundaries in the future.

TI plasmons

The second phase of the project leverages our ability to grow periodic layered structures comprising TIs and trivial band insulators (BIs) by molecular beam epitaxy (MBE). Plasmons are excited at each TI/BI interface and interact with each other through their evanescent electric fields. We first investigated five-layer films with the following structure: BI/TI/BI/TI/BI. In these structures, we have two TI layers resulting in four surface states that couple across the TI layers and the central BI layer [7]. We grew multiple films in which we varied the central BI layer thickness and the two TI layer thicknesses. Each film was fabricated into stripes to allow excitation of the localized plasmon polariton mode. For two films (A and B), multiple stripe widths were etched to map the polariton mode dispersion, shown in Figure 2. As we change the stripe width, the wavevector changes, and we can measure the extinction of the sample using Fourier transform infrared spectroscopy. In all spectra, we observe either two or three extinction peaks. One of these

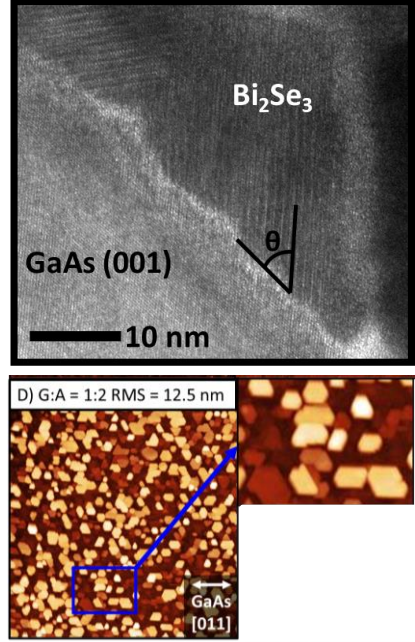


Figure 1. (top) Transmission electron micrograph of (0015) Bi_2Se_3 on (001) GaAs [4]. (bottom) Atomic force micrograph of self-assembled Bi_2Se_3 nano-columns on (001) GaAs [5].

peaks is identified as the epsilon near zero (ENZ) mode in the top BiInSe_3 band insulator layer. This identification is made due to its flat dispersion, narrow bandwidth, and from transfer matrix modeling, described later. The other two modes correspond to the middle and upper polariton branches arising from the strong coupling among the Dirac plasmon polariton and the α and β phonons at ~ 2 and ~ 4 THz, respectively, in the TI and BI layers. To clearly identify these modes, we built a transfer matrix modeling program. For successful modeling, we first had to determine the THz permittivity of the TI and BI layers. We did this by performing angle- and polarization-dependent FTIR transmission measurements on films of Bi_2Se_3 and BiInSe_3 . We

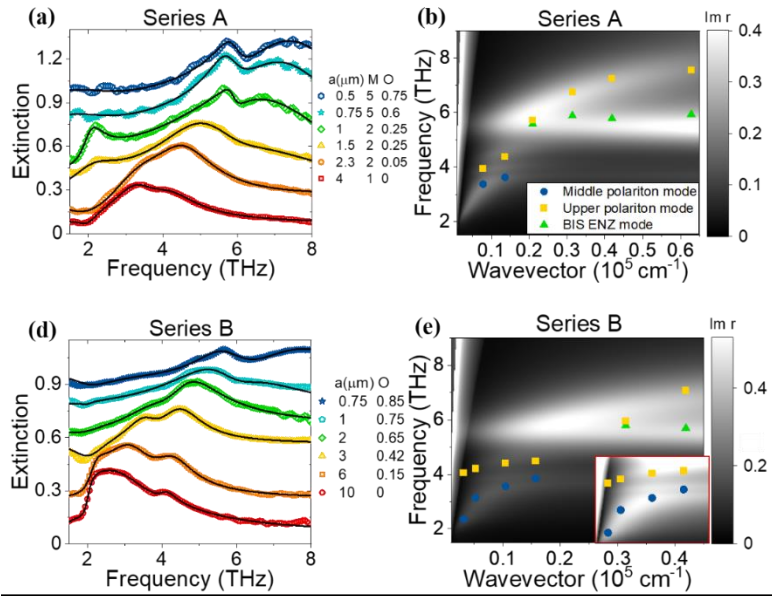


Figure 2. (a, d) Extinction spectra for Series A and B, respectively. Black solid curves are the three oscillator Fano resonance fitting of the experimental data (open symbols). Data multiplication (M) and offset (O) are used for better visualization. (b, e) Color plot: Transfer matrix model of Series A and B. The experimental upper polariton mode (yellow squares), middle polariton mode (blue circles), and BIS ENZ mode (green triangles) extracted from Fano resonance fitting are shown for comparison. Inset of (e) is a zoom-in at low wavevectors with adjusted color scale. Anti-crossing caused by plasmon phonon interaction is clearly seen. Figure adapted from [7].

fitted the data using the Drude-Lorentz model to extract the frequency-dependent permittivity for both materials. This permittivity was then used in the transfer matrix model along with the frequency-dependent conductivity of the topological surface states to model the extinction spectra of the entire structure as a function of wavevector and structural parameters. The T-matrix modeling for Series A and B is shown as the grayscale plots in Figure 2. It is clear that the T-matrix modeling reproduces the experimental data, shown as filled symbols, extremely well.

In addition to fabricating stripes of varying width in series A and B to map out the polariton dispersion relationship, we also fabricated series C in which the center BI layer thickness was varied, and series D, in which the TI layer thickness was varied. These experiments were done to understand how the plasmons couple across both the BI and the TI. In both cases, we observe a discrepancy between T-matrix modeling and experimental data when the BI or the TI layer is thin (Figure 3). For the case of the narrow spacer, we attribute this disagreement to penetration of the surface state wavefunction into the BI layer. Wavefunction penetration can lead to quantum mechanical coupling between the surface states, adding complexity to the optical response that is not captured by the T-matrix modeling. For the case of the thin TI layers, we attribute the disagreement between the modeling and experiment to strong coupling among the surface states as well as a shift in the beta phonon frequency. Overall, this project has resulted in expressions for

the permittivity of Bi_2Se_3 and BiInSe_3 in the THz, a T-matrix modeling program for layered TI structures, and an understanding of how the plasmon polariton behaves in a TI multilayer stack as a function of TI thickness, BI thickness, and wavevector. We have observed hybridization among the TI surface states as well as between the plasmon polariton and the phonons in the structure.

Future Plans

Future plans include investigating plasmon polaritons in structures with more than two TI layers to try to create a Dirac metamaterial. We plan to perform scanning near-field optical microscopy measurements to directly image the TI plasmon. We will measure the extinction spectra of TI nanoparticles to observe how the optical properties change in the quantum mechanical regime [6]. We will investigate in-plane coupling between TI plasmons in closely-spaced nanoribbons. Finally, we will investigate plasmons in TI films as the Fermi energy is moved through the Dirac point. At the end of the program, we anticipate having a complete understanding of the behavior of plasmon polaritons in TI thin films, superlattices, and nanostructures.

References

- [1] T. P. Ginley and S. Law, *Coupled Dirac Plasmons in Topological Insulators*, Adv. Opt. Mater. **6**, 1800113 (2018).
- [2] Y. Wang, T. P. Ginley, C. Zhang, and S. Law, *Transport Properties of $\text{Bi}_2(\text{Se}_{1-x}\text{Te}_x)_3$ Thin Films Grown by Molecular Beam Epitaxy*, J. Vac. Sci. Technol. B **35**, 02B106 (2017).
- [3] Y. Wang, T. P. Ginley, and S. Law, *Growth of High-Quality Bi_2Se_3 Topological Insulators Using $(\text{Bi}_{1-x}\text{In}_x)_2\text{Se}_3$ Buffer Layers*, J. Vac. Sci. Technol. B **36**, 02D101 (2018).
- [4] T. P. Ginley, Y. Zhang, C. Ni, and S. Law, *Epitaxial Growth of Bi_2Se_3 in the (0015) Orientation on GaAs (001)*, J. Vac. Sci. Technol. A **38**, 023404 (2020).
- [5] T. P. Ginley and S. Law, *Self-Assembled Nano-Columns in Bi_2Se_3 Grown by Molecular Beam Epitaxy*, J. Vac. Sci. Technol. A **accepted**, (2021).
- [6] G. Siroki, D. K. K. Lee, P. D. Haynes, and V. Giannini, *Single-Electron Induced Surface Plasmons on a Topological Nanoparticle*, Nat. Commun. **7**, 12375 (2016).
- [7] Z. Wang, T. P. Ginley, S. V. Mambakkam, G. Chandan, Y. Zhang, C. Ni, and S. Law, *Plasmon Coupling in Topological Insulator Multilayers*, Phys. Rev. Mater. **4**, 115202 (2020).

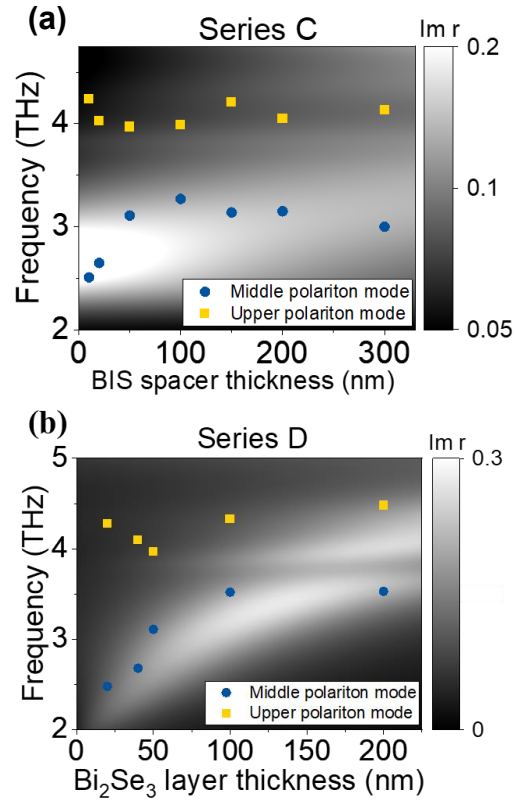


Figure 3. (a) Experimental data (symbols) and T-matrix modeling (grayscale) for Series C. (b) Experimental data (symbols) and T-matrix modeling (grayscale) for Series D. Figure adapted from [7].

Publications

1. T. P. Ginley, Y. Zhang, C. Ni, and S. Law, *Epitaxial Growth of Bi₂Se₃ in the (0015) Orientation on GaAs (001)*, J. Vac. Sci. Technol. A **38**, 023404 (2020).
2. Z. Wang, T. P. Ginley, S. V. Mambakkam, G. Chandan, Y. Zhang, C. Ni, and S. Law, *Plasmon Coupling in Topological Insulator Multilayers*, Phys. Rev. Mater. **4**, 115202 (2020).
3. T. P. Ginley and S. Law, *Self-assembled nano-columns in Bi₂Se₃ grown by molecular beam epitaxy*, J. Vac. Sci. Technol. A **in press** (2021).

Electron Spin Polarization in Large Electric Fields

Vanessa Sih, University of Michigan, Ann Arbor

Program Scope

This research program investigates the effect of large accelerating electric fields on electron spin polarization in semiconductors. The goals of this research are to understand the mechanisms that enable and limit the electrical generation of spin polarization in non-magnetic materials, the role of spin-orbit effects and spin scattering in a strongly driven regime, and to determine whether a high-electric field regime that preserves or even amplifies spin polarization that has been theoretically predicted can be realized experimentally. The experimental approach uses ultrafast optical techniques to monitor the motion and dynamics of spin-polarized electrons with sub-micron and sub-picosecond resolution using spatial- and time-resolved pump-probe optical spectroscopy and electrical device design and measurement techniques to produce large electric fields while minimizing excessive electrical heating. The expectation is that this research will improve our understanding of the fundamental processes that cause the electrical generation of spin polarization and contribute to spin dephasing. This knowledge will contribute to the development of robust spin-based devices for information processing, storage, and communication.

Recent Progress

Qi, Yu and Flatté predicted a “spin Gunn effect” that could enable the creation of large spin polarization in gallium arsenide (GaAs) and indium phosphide (InP) at room temperature [1]. The mechanism for this effect is amplification of spin polarization driven by a different mobility for spin-up and spin-down electrons, and this amplification occurs when a term proportional to the spatial derivative of the product of the charge density, electric field, and mobility exceeds the spin decay rate. They showed that this could occur near a Gunn domain, which is a dipole layer which forms in GaAs and InP at high electric fields due to the lower mobility of electrons in the L valley and results in a negative differential resistance (NDR) characteristic. The repeated process of Gunn domain nucleation at the cathode, transit through the device at the electron drift velocity, and domain annihilation at the anode causes current oscillations with a constant applied electric field, which is known as the Gunn effect. The threshold for nucleating a Gunn domain in gallium arsenide is 3.2 kV/cm, which poses practical challenges, including sample heating and breakdown.

In order to limit sample heating effects, measurements are performed using voltage pulses from a high-voltage source. The size and shape of the semiconductor channels can also be designed to reduce the dissipated power. Since the electric field required to sustain a Gunn domain is lower than the electric field required to nucleate a Gunn domain, a tapered wedge-shaped

geometry near the cathode connected to a rectangular region should lower the threshold voltage required to observe the Gunn effect. A schematic of the device geometry is shown in Fig. 1(a), and the expected electric field profile is shown in Fig. 1(b). In order to test this, we fabricated and performed experiments on twelve devices with different device dimensions, determining the threshold voltage with I-V characteristics to determine when the negative differential resistance (NDR) characteristic is observed and with oscilloscope traces of Gunn oscillations. We show that a wedge-shaped tapering results in a Gunn threshold voltage reduction when the wedge ratio is low enough in Ref. [P1].

In order to demonstrate the spin Gunn effect, we plan to use optical pump-probe techniques to monitor how the Gunn domain profile affects the electron spin polarization, as these techniques provide sensitivity to small changes in electron spin polarization with sub-micron spatial and sub-picosecond temporal resolution. In addition, the spin Gunn effect produces an amplification of spin polarization, so an optical pump pulse can be used to generate the initial spin polarization. In order to synchronize the spin polarization measurements with the Gunn effect, we are interested in whether optical pulses can be used to trigger the formation of Gunn domains.

In Ref. [P3], we illuminate a GaAs Gunn device and study the light-induced changes of Gunn oscillation properties. We performed measurements as a function of laser wavelength and illumination power and with the laser both mode-locked, producing picosecond duration pulses at a repetition rate of 76 MHz, and in continuous-wave output mode. We observe that illumination leads to the modulation of the Gunn threshold voltage, the Gunn oscillation magnitude, and the coherency of Gunn oscillation, with the nature of the modulation dependent on which part of the device was illuminated. For example, Fig. 2(a) shows that near-anode illumination increases the coherency of Gunn

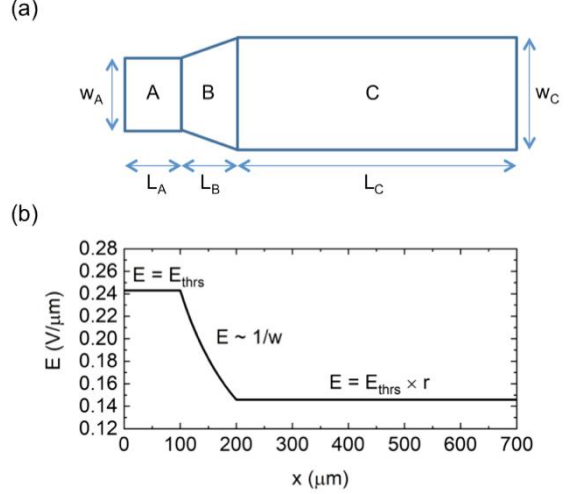


Figure 1. (a) Device schematic showing dimensions of the tapered region and channel. (b) Estimated electric field profile along the device. The wedge ratio r is defined to be $w_A:w_C$. Reproduced from Ref. [P1].

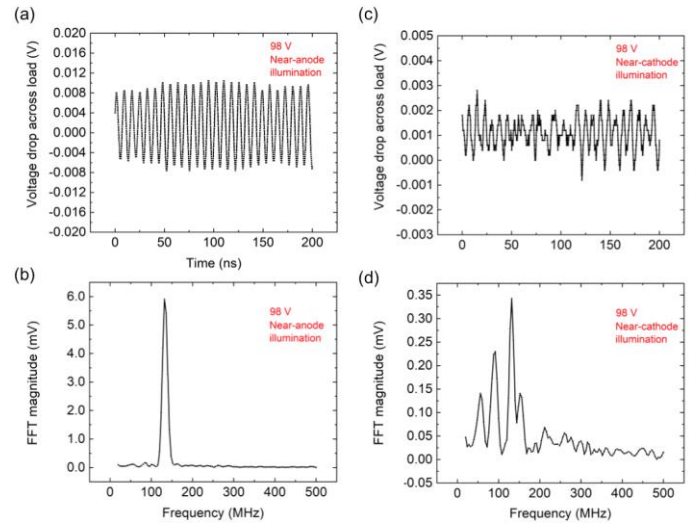


Figure 2. (a) Voltage drop across load when the device is illuminated near the anode. (b) FFT of spectrum shown in (a). (c) Voltage drop across load when the device is illuminated near the cathode. (d) FFT of spectrum shown in (c). [P3]

oscillations and increases the oscillation magnitude by a factor of 3 compared to no illumination, whereas Fig. 2(c) shows a voltage trace for near-cathode illumination, in which we observe that the coherency of Gunn oscillations decreases and that the oscillation magnitude is decreased by a factor of 2 compared to no illumination. We attribute these effects to the generation of optically-excited carriers, which produces a change in the conductivity and the electric field profile along the device.

In materials with significant spin-orbit coupling strength, the momentum-dependent spin-orbit field can be measured through its effects on electron spin precession and dephasing, and the in-plane carrier momentum can be changed with an in-plane electric field. In addition, the out-of-plane electric field can be changed with an applied gate voltage and affect the spatial inversion asymmetry and its corresponding spin-orbit field. In Ref. [P2], time-resolved Kerr rotation measurements were used to measure electron spin precession and dephasing in a two-dimensional electron gas confined in a wide quantum well as a function of applied in-plane and gate voltages. For in-plane voltages applied along the [110] crystallographic direction, the electron spin lifetime was observed to decrease with increasing drift velocity but not change with applied gate voltage. However, for in-plane voltages applied along the [1-10] direction, the electron spin lifetime was longer and exhibited a gate voltage dependence.

Future Plans

Our next steps are to utilize optical pump-probe techniques to monitor electron spin dynamics in the presence of Gunn domains to determine whether the predicted spin amplification produced by the spin Gunn effect is occurring and to determine the spin decay rate at high electric fields. We will also continue to work on electrical device design and fabrication and characterization in order to produce the devices needed for the experiments.

References

[1] Y. Qi, Z.-G. Yu, and M. E. Flatté, “Spin Gunn Effect,” Phys. Rev. Lett. **96**, 026602 (2006)

Publications supported by BES

[P1] Hua-Wei Hsu, Michael J. Dominguez, and Vanessa Sih, “Gunn threshold voltage characterization in GaAs devices with wedge-shaped tapering,” Journal of Applied Physics **128**, 074502 (2020)

[P2] F. G. G. Hernandez, G. J. Ferreira, M. Luengo-Kovac, V. Sih, N. M. Kawahala, G. M. Gusev, and A. K. Bakarov, “Electrical control of spin relaxation anisotropy during drift transport in a two-dimensional electron gas,” Physical Review B **102**, 125305 (2020)

[P3] Hua-Wei Hsu and Vanessa Sih, “Illumination-induced modulation of conductivity and Gunn oscillation properties in epitaxial GaAs,” Journal of Applied Physics, accepted and in production (2021)

Control of energy transfer and molecular transport via strong coupling

Stephen Forrest; Department of Electrical Engineering and Computer Science and Physics, University of Michigan, Ann Arbor, and Vinod Menon; Department of Physics, City University of New York, NY, NY. (Collaborator: Matthew Sfeir, Brookhaven Natl. Labs)

Program Scope

Control of energy transport and molecular excited states play key roles in the development of energy efficient technologies geared towards a sustainable future. Our research team has pursued a radically new concept for materials engineering based on coherently combining particular material excitations with light specifically in the context of energy harvesting systems and light emitters. We exploit the half-light/half-matter quasiparticles known as polaritons formed by strong light-matter interactions to develop revolutionary methods for controlling energy transport and molecular excited states. The polaritons take on beneficial properties of both light and matter: they have low mass of charges enabled by mixing of electronic excitations with photons; long range transport enabled by their optical character; and strong interactions provided by their electronic character. Specific goals and outcomes include:

- Demonstration of long-range transport of electronic excitations in disordered organic molecular systems through the formation of half-light/half-matter quasiparticles,
- Demonstration of an analog of photosynthesis for energy harvesting using a combination of molecular antennas, strongly coupled polaritons for long-range transport, and organic heterojunctions acting as reaction centers,
- Control of energetics of molecular systems through strong coupling resulting in modified light emission and absorption properties of solids, and
- Achieving strong coupling to vibrations in molecules as a route for engineering electronic transitions and chemical reactions.

The research program has a strong training component of postdoctoral researchers, graduate students and undergraduate students in the team laboratories, and is also a collaboration with The Center for Functional Nanomaterials at Brookhaven National Laboratories.

Recent Progress

There has been considerable progress made in our program during its last two years. Specifically, we have found that very long polariton transport is supported in amorphous organic thin films, and have developed tools for measuring this transport that have correspondingly led to a deep understanding of why this is possible. Furthermore, we have begun to exploit this transport in unique antenna/reaction center devices, whereas polaritons formed by optical excitation, transport over extremely long distances through the film to a heterojunction “reaction center” that generates an electron-hole pair that is subsequently detected in an external circuit. This “artificial photosynthesis” device was one of the primary goals of our research.

Besides enhancing transport, another intriguing question that has emerged recently is the possibility of hybrid polariton states to modify molecular dynamics. In this context, we investigated the ultrafast dynamics of polariton states formed in an archetypical organic singlet fission molecular system. The goal of these studies was to elucidate the role of dark states that form in cavity polariton systems of N molecules on the overall dynamics. In other words, the

question was to understand if polariton formation alone modifies dynamics. Our work reported in ACS Photonics (2020) showed the role of the long-lived dark states that form in the limit of ensemble (many molecule) strong coupling on the overall dynamics. Furthermore, our work also showed how to overcome the role of these dark states by utilizing systems in the ultrastrong coupling regime. This is an important step towards modifying chemical kinetics and molecular dynamics through cavity strong coupling and could have applications in energy harvesting and catalysis.

Another area of much interest is to utilize strongly coupled systems for ultrafast optical modulation of signals. We demonstrated the ultrafast modulation of strong coupling via thermal modification of the reflectivity of the metal mirrors used in the cavity (APL Photonics 2021). Such ultrafast modulation especially if transition between strong and weak coupling can be achieved will lead to optical switching with large extinction and ultralow switching energies.

In addition, using experimental methods developed in this program, we have examined polariton generation in 2D heterojunctions, and observed very large optical non-linearities. That is, in 2D van der Waals heterostructures, a tunable moiré lattice potential for electronic excitations may form, enabling the generation of correlated electron gases in the lattice potentials. Excitons confined in moiré lattices have also been reported, but no cooperative effects have been observed and interactions with light have remained perturbative. In our work, by integrating MoSe₂–WS₂ heterobilayers in a microcavity, we establish cooperative coupling between moiré-lattice excitons and microcavity photons, thereby integrating versatile control of both matter and light into one platform. The density dependence of the moiré polaritons reveals strong nonlinearity due to exciton blockade, suppressed exciton energy shift and suppressed excitation-induced dephasing, consistent with the quantum confined nature of the moiré excitons. Such a moiré polariton system combines strong nonlinearity and microscopic-scale tuning of matter excitations using cavity engineering and long-range light coherence, providing a platform with which to study collective phenomena from tunable arrays of quantum emitters. In addition, we have also recently studied long range propagation of polaritons in 2D materials using the Bloch surface polaritons.

Below we discuss two of the key results from the program:

1. Ultralong range transport: We demonstrated the use of ultrastrong coupling to achieve long range exciton transport in amorphous organic thin films. This is the result of the polariton lending significant photonic content to the excitonic state to which it is strongly coupled. We showed, for example, that Bloch surface waves (BSW) are excited at the interface between a distributed Bragg reflector (DBR) dielectric stack and an organic layer sitting on its surface using prism coupling. These ultrastrong coupled BSWs had Rabi splitting energies of >400 meV, making the polaritons propagating on the surface stable at room temperature, and immune to scattering or deexcitation at the many defects found in the vapor deposited organic thin films. Most importantly, however, was our observation of polariton propagation over distances of ~ 100 μm due to the very light, photon-like nature of the polaritonic state, even though the films are amorphous (see Fig. 1). That is, the photonic content of the polariton gives it a high propagation velocity, and at the same time it is stable when encountering defects in the film during transport. This brings up the intriguing prospect of employing polariton diffusion in solar energy harvesting. In this task, we investigated the prospects of using the concept of averaging of disorder via polariton formation for device applications. The idea is to mimic photosynthetic systems, whereby light is incident on the absorbing film within a microcavity over a wide collection area is transported efficiently to the reaction center as shown schematically in Fig. 1d.

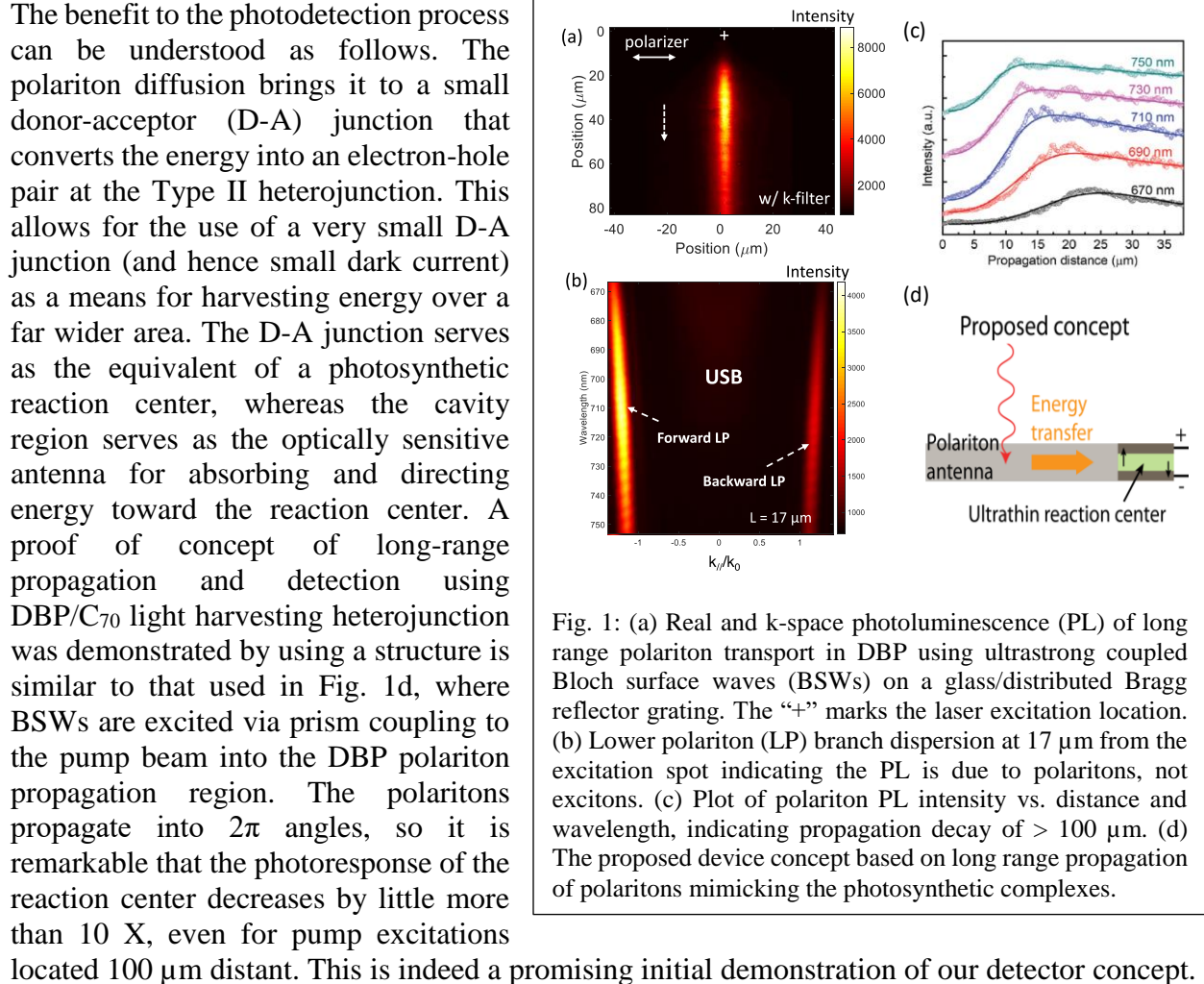


Fig. 1: (a) Real and k-space photoluminescence (PL) of long range polariton transport in DBP using ultrastrong coupled Bloch surface waves (BSWs) on a glass/distributed Bragg reflector grating. The “+” marks the laser excitation location. (b) Lower polariton (LP) branch dispersion at 17 μm from the excitation spot indicating the PL is due to polaritons, not excitons. (c) Plot of polariton PL intensity vs. distance and wavelength, indicating propagation decay of > 100 μm . (d) The proposed device concept based on long range propagation of polaritons mimicking the photosynthetic complexes.

2. Role of dark states in the dynamics of strongly coupled molecular systems: Initial studies integrating organic materials into optical cavities have led to controversies about the effect of strong-coupling on kinetic processes, including interactions with nominally “dark” exciton states, lifetimes of the polaritons themselves, and the strength of coupling between exciton-polaritons and other excitations in the system. For example, two recent experiments examining the effect of cavity polaritons on the reverse intersystem crossing process (energetically allowed conversion from triplet to singlet excitons) reach dramatically different conclusions regarding the conversion kinetics of triplet excitons to cavity polaritons. A central issue in this controversy is the presence of a large reservoir of localized “dark” exciton-polariton states (of order N-1, where N is the number of molecules coupled to the cavity) that have poor spatial coupling to small number (2) delocalized polariton states. Furthermore, there exist a sub-ensemble of molecules that are uncoupled to the cavity due to misaligned transition dipoles which can affect the relaxation dynamics.

Similarly, several recent reports have considered strong coupling using singlet exciton fission materials (SF), in which molecular singlet excitons rapidly convert into a triplet pair (biexciton) state followed by dephasing into two independent triplet excitons. However, before the energetics of a singlet fission microcavity system can be systematically controlled, fundamental scientific

questions need to be addressed, such as whether exciton-polaritons can directly decay to biexcitonic states, the role of reservoir states (including “dark” polaritons, excitons of higher spin multiplicity, and uncoupled molecules) in determining the relaxation dynamics, and the effect of excited state occupation on the strong coupling conditions.

Under this program we investigated the interconversion of excitons polaritons, singlet excitons and triplet excitons in a singlet fission material strongly coupled to an optical microcavity using transient optical spectroscopy (Fig. 2a). Despite prominent transient spectral features observed near the polariton resonances, the overall carrier dynamics are nearly identical between the uncoupled and strongly coupled singlet fission system due to weak electronic interactions between exciton-polaritons and reservoir states (Fig. 2b). Instead of indicating a polariton population, the prominent transient features near the cavity polariton resonances are attributed to changes in the population dynamics of the reservoir states, which in turn modify the exciton-photon coupling conditions. The transient absorption spectra of the full cavity system excited by 665nm pump (Figure 2b) shows several notable features, including a rise near the triplet fingerprint region wavelength (508 nm) and set of prominent dispersive spectral features corresponding to signatures of the cavity polaritons (620-680 nm) indicating strong coupling. The extracted rate constants from fits to these transient absorption data are nearly identical to those obtained for the control sample in the absence of cavity.

In summary, we demonstrated the role of dark states in controlling the overall dynamics. Weak interactions between cavity polaritons and reservoir states requires a carefully considered approach to the design of polariton systems for modified molecular dynamics. First and foremost, this means that systems must be identified in which extremely long-lived excited states are present (e.g., triplet excitons) or systems in which light-matter interactions can be further enhanced.

Note: This work was done in collaboration with **Sfeir** group - Brookhaven Natl. Labs (Now at CUNY Adv. Science Research center).

Future Plans: This is the last year of the current program.

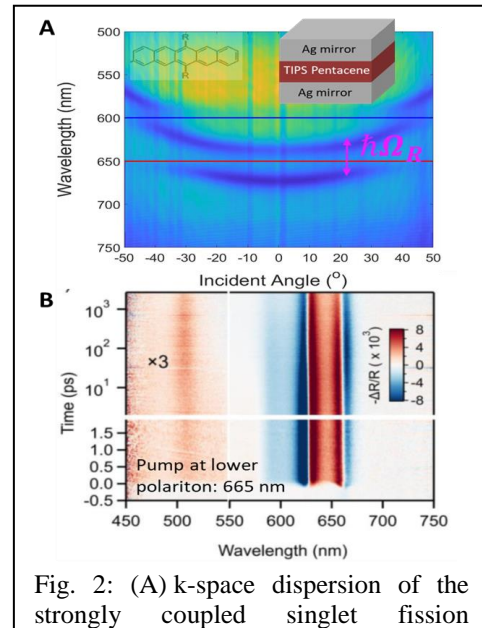


Fig. 2: (A) k-space dispersion of the strongly coupled singlet fission molecules in cavity. Inset shows the molecular structure and the cavity. (B) Transient Absorption spectrum under excitation at the lower polariton (665 nm) showing long-lived states ($>10^3$ ps).

Publications (last 24 months)

Van der Waals heterostructure polaritons with moiré-induced nonlinearity, L Zhang, F Wu, S Hou, Z Zhang, Y-H Chou, K Watanabe, T Taniguchi, S R Forrest¹, and H Deng, Nature, doi.org/10.1038/s41586-021-03228-5 (2021).

Ultrafast Thermal Modification of Strong Coupling in an Organic Microcavity, B. Liu, V.M Menon, M.Y Sfeir, APL Photonics 6, 016103 (2021)

Modifying the spectral weights of vibronic transitions via strong coupling to surface plasmons
R Deshmukh, P Marques, A Panda, MY Sfeir, S R Forrest, VM Menon, ACS Photonics, 7, 43-48. pubs.acs.org/journal/apchd5, (2020).

Moiré lattice-induced formation and tuning of hybrid dipolar excitons in twisted WS₂/MoSe₂ heterobilayers, L Zhang, Z Zhang, F Wu, D Wang, R Gogna, S Hou, K Watanabe, T Taniguchi, K Kulkarni, T Kuo, S R Forrest, H Deng, arXiv, arXiv:1911.10069 (2020).

Temperature dependence of an amorphous organic thin film polariton laser, Y Qu, S Hou, SR Forrest, ACS Photonics, 2020, 7, 4, 867-72 (2020)

Efficient Charge Generation via Hole Transfer in Dilute Organic Donor–Fullerene Blends, Y Song, A Schubert, X Liu, S Bhandari, S R Forrest, B D Dunietz, Eitan Geva, and Jennifer P. Ogilvie, Journal of Physical Chemistry Letters 11 (6), 2203-2210 (2020).

Ultralong-Range Energy Transport in a Disordered Organic Semiconductor at Room Temperature Via Coherent Exciton-Polariton Propagation, S Hou, M Khatoniar, K Ding, Y Qu, A Napolov, V M Menon, S R Forrest, Advanced Materials, 2002127, (2020), <https://doi.org/10.1002/adma.202002127>

Formation and tuning of moiré excitons in large-twist angle WS₂/MoSe₂ heterobilayers, L Zhang, Z Zhang, F Wu, D Wang, R Gogna, S Hou, K Watanabe, T Taniguchi, K Kulkarni, T Kuo, Stephen Forrest, H Deng, (2020), DOI: [10.21203/rs.3.rs-37553/v1](https://doi.org/10.21203/rs.3.rs-37553/v1)

Using Fourier-Plane Imaging Microscopy for Determining Transition-Dipole-Moment Orientations in Organic Light-Emitting Devices, J Kim, H Zhao, S Hou, M Khatoniar, V Menon, SR Forrest, Physical Review Applied 14 (3), 034048 (2020).

Nanoscale Mapping of Morphology of Organic Thin Films, J Kim, S Hou, H Zhao, SR Forrest Nano Letters <https://dx.doi.org/10.1021/acs.nanolett.0c03440>, 20, 8290 (2020).

Twist-angle dependence of moiré excitons in WS₂/MoSe₂ heterobilayers, L Zhang, Z Zhang, F Wu, D Wang, R Gogna, S Hou, K Watanabe, Nature Comm. 11, doi.org/10.1038/s41467-020-19466-6 (2020)

“The role of long-lived excitons in the dynamics of strongly coupled molecular polaritons,” B. Liu, V. M. Menon, and M. Y. Sfeir, ACS Photonics 7, 2292-2301 (2020)

Propagating hybrid Tamm exciton polaritons in organic microcavity," B. Liu, R. Wu, and V. M. Menon, J. Phys. Chem C 123, 26509 (2019)

"Polariton chemistry: Thinking inside the (photon) box," J. Yuen-Zhou, and V. M. Menon PNAS 116, 5214 (2019)

Ultrastrong coupling of vibrationally dressed organic Frenkel excitons with Bloch surface waves in a one-sided all-dielectric structure, S Hou, Y Qu, X Liu, SR Forrest, Physical Review B 100 (4), 045410 (2019).

Efficient Charge Generation Via Hole Transfer in Dilute Organic Donor-Fullerene Blends. Song, Yin; Schubert, Alexander; Liu, Xiao; Bhandari, Srijana; Forrest, Stephen R.; Dunietz, Barry D.; et al. ChemRxiv. Preprint. <https://doi.org/10.26434/chemrxiv.11328542.v1>, (2019)

DISCLOSURES

UM2020-082 Ultrahigh resolution R,G,B OLED Display Patterning
Disclosed 8/24/19, S.R. Forrest
US Patent Application No. 17/100,003 filed 11/20/20

UM2020-430 The Use of High Glass Transition Temperature Morphological Stabilizing Layer for Improved Thermal Stability of Organic Thin Films
Disclosed 4/16/20, S.R. Forrest and J. Kim
U.S. Provisional Application No. 63/126,676 filed 12/17/20

UM2021-013 Simple and Precise 3D Morphological Investigations Using Fourier Plane Microscopy of van der Waals Solids
Disclosed 7/6/20, S.R. Forrest and J. Kim

UM2021-192 Engineering Excited State Lifetimes via Strong Coupling
Disclosed 11/24/20, S.R. Forrest

UM2021-213 Transferable Dielectric Mirrors and Their Optical Applications
Disclosed 12/11/20, S.R. Forrest and S. Hou

UM2021-224 Artificial Photosynthetic Devices Utilizing Polariton Antennas
Disclosed 12/18/20, S.R. Forrest and S. Hou

PRESENTATIONS

Stephen Forrest, "Excitons and Exciton Confinement in Organic Heterojunctions" at the Physics and Chemistry of Surfaces and Interfaces-46 Conference in Santa Fe, NM, January 16-18, (2019).

Stephen Forrest, "Organic exciton-polaritons in the ultrastrong coupling regime" at the Department of Energy R&D Workshop in Gaithersburg, MD, March 18-19, (2019).

Vinod Menon, Exciton engineering in emerging semiconductors, Madrid, January 8-9 (2020)

Session V

Digital Synthesis: A pathway to create and control novel states of condensed matter

Anand Bhattacharya, Dillon Fong, Sam Jiang (Materials Science Division, Argonne National Laboratory)

Program Scope: ‘Digital Synthesis’ is a strategy for realizing novel states of condensed matter by creating materials in an atomic layer-by-layer fashion. With this approach, we are able to create artificial crystals, including cation-ordered and delta-doped analogs of known materials, and control charge transfer and band lineup in heterostructures. Thus, our program seeks to create new materials out of known ingredients to yield novel properties. We manipulate these properties with external fields and currents, and to develop new insights about how we might realize these properties ‘by design’. Our program focuses on correlated materials, which are mostly complex oxides, and topological semimetals and insulators, that are mostly intermetallics. The areas that we will explore include (*i*) a new interfacial superconductor that we discovered at the (111) interface of KTaO_3 , (*ii*) a new class of superconductors in the nickelates, (*iii*) using the spin Seebeck effect to probe the magnetic excitations in novel quantum magnets and (*iv*) creating and exploring epitaxial films of non-magnetic topological semimetals and insulators.

We synthesize our materials using molecular beam epitaxy (MBE), multi-target sputtering and pulsed laser deposition (PLD) techniques, and characterize them with tools that probe structural, electronic and magnetic degrees of freedom, including their spin and charge transport properties.

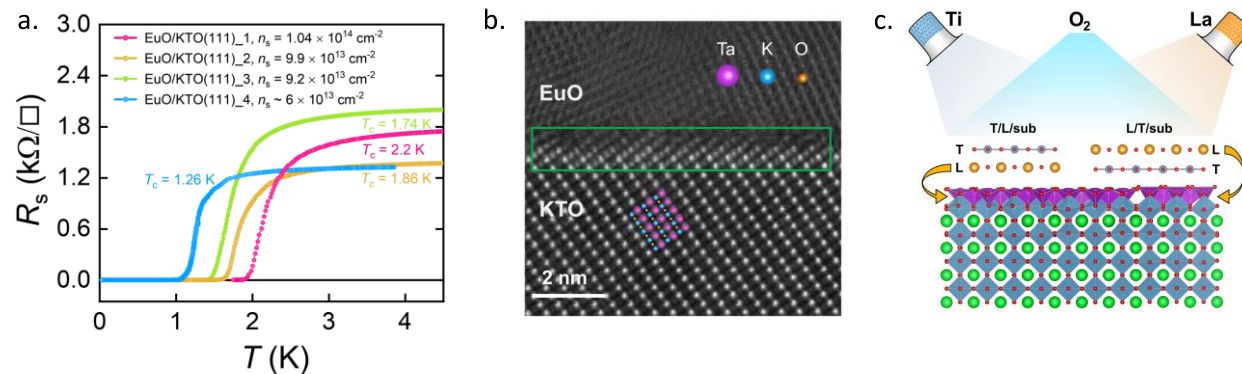


Fig. 1 a. Superconducting transitions in EuO/KTO (111) interfaces. **b.** Scanning transmission electron microscopy image of a EuO/KTO (111) interface. **c.** Schematic of atomic layer by layer deposition of LaTiO_3 in a sequence of TiO_2 - LaO - \dots - SrTiO_3 showing how a TiO_2 layer always floats to the top, as determined by in-situ x-ray scattering during MBE growth. Going forward, we will use this approach to tailor interfaces with KTO substrates.

Recent Progress

In this extended abstract, we describe progress and future plans related to objectives (*i*) and (*ii*) stated above, regarding superconductivity in oxide interfaces and thin films. Here we highlight a few significant developments that motivate our work, and seed our future plans:

(i) Discovery of Superconductivity in KTaO_3 (*Science* 2021): In recent work¹, we have discovered that a metallic electron gas formed at interfaces between (111) oriented KTaO_3 (KTO) and polycrystalline EuO (**Fig. 1b.**) or amorphous LaAlO_3 capping layers becomes superconducting with a transition temperature T_c as high as 2.2 K (**Fig. 1a.**)—far in excess of the 2DEG formed at $\text{LaAlO}_3/\text{SrTiO}_3$ interfaces, where T_c is limited to ~ 200 mK. Surprisingly, interfacial states on the

(001) surface of KTaO_3 at similar carrier densities remained normal down to 25 mK. The occurrence of superconductivity in the (111) orientation also occurs for an amorphous LaAlO_3 capping layer.

The two-dimensionality of the superconductivity is verified in the out-of-plane and in-plane upper critical field, where the extracted values of the thickness of the superconducting layer is smaller than the Ginzburg-Landau coherence length. Current-voltage measurements in the superconducting state are also found to be consistent with 2D superconductivity. We note that $B_{\text{c}\parallel}(0)$ is substantially larger than the paramagnetic pair-breaking field, which could be due to disorder but may also occur due to more intrinsic reasons, for example unconventional triplet pairing may be energetically stabilized in a magnetic field, as has been observed in bulk non-centrosymmetricⁱⁱ superconductors. Furthermore, in samples prepared with lower carrier concentrations and higher mobility, we observe a strong *in-plane* anisotropy in resistance (“stripe” phase) that forms spontaneously at $T \leq 2.2$ K. The behavior of the observed nematicity and its relation to superconductivity bears some similarity to those found in the cuprate and iron-based high-temperature superconductors and more recently in doped Bi_2Se_3 .ⁱⁱⁱ The orientational selective superconductivity and tunable electronic phases on the KTO (111) surface therefore provide a new platform for investigating unconventional superconductivity, which has long been a central theme in condensed matter physics. We should note that several groups have now confirmed that the KTO (111) interfaces superconduct^{iv}, and have found that the KTO (110) interface^v is also superconducting, though with a lower T_c .

(ii) *Understanding layer by layer growth of interfaces on SrTiO_3* (*Sci. Adv.* 2019): One of our goals is to tailor interfaces of KTaO_3 and similar oxides to create interfacial electron gases. The states found at these interfaces depend critically upon the first few layers in the immediate vicinity of the interface. In this light, we present recent results on another well studied and related d^0 oxide – SrTiO_3 .

In traditional models of heteroepitaxy, the substrate serves mainly as a crystalline template for the thin-film lattice, dictating the initial roughness of the film and the degree of coherency strain. The most common substrate used in the growth of complex oxide heterostructures is strontium titanate (SrTiO_3) partly due to the ability to consistently produce an atomically smooth, TiO_2 -terminated (001) surface. The atomic force microscopy image shows that the steps are approximate 0.4-nm-high. Since this is the size of one unit cell, researchers assume that the $\text{SrO}/\text{TiO}_2 \dots$ stacking sequence continues to the surface. However, using the molecular beam epitaxy (MBE) growth chamber we helped construct at Advanced Photon Source (APS)^{vi}, we find that the surface is not stoichiometric, regardless of how carefully the substrate is prepared. It instead exhibits excess TiO_2 such that the SrTiO_3 surface is terminated by a TiO_2 double layer.

In recent work^{vii}, we studied the implications of the TiO_2 double layer on heteroepitaxial growth. We deposited LaTiO_3 (LTO) on SrTiO_3 (001) in a layer-by-layer fashion, i.e., alternating between one monolayer of LaO and one monolayer of TiO_2 (**Fig. 1 c.**). We show that the traditional model of layer-by-layer growth on SrTiO_3 should be replaced with a dynamic model in which the TiO_2 adlayer from the substrate continuously “floats” to the surface of the growing film much like a surfactant, so that while the perovskite stacking sequence is maintained at the heterointerface, the TiO_2 adlayer is also maintained at the film surface. Aside from providing a better understanding of heteroepitaxial growth, our work shows that the ultrathin films are likely to be terminated by TiO_2 regardless of the nature of the film. Similar studies are planned for growth of LTO on KTO.

(iii) *LaNiO₃ is a quantum critical metal* (*Nat. Commun.* 2020): The nature of the electronic and magnetic properties of LaNiO₃ has been debated and studied for several decades^{viii}. It is the only member of the rare-earth perovskite nickelate *ReNiO₃* family that remains metallic, without developing long range magnetic order down to the lowest temperatures. We have discovered that LaNiO₃ is a ‘strange’ metal at low temperatures, where the resistivity as a function of temperature does not agree with Fermi liquid theory, where we expect $\rho(T) = \rho_0 + aT^2$. We synthesized very high mobility epitaxial thin films of LaNiO₃ using ozone assisted MBE, where the residual resistivity $\rho_0 < 4 \Omega\text{-cm}$, by careful control of cation stoichiometry and mitigation of oxygen vacancy formation. Over nearly a decade of temperature below 1.2 K, we find that $\rho(T) = \rho_0 + bT$.^{ix} Upon application of magnetic fields, a quadratic dependence in $\rho(T)$ is recovered, and Fermi-liquid behavior is restored. These findings are a signature of a metal whose transport properties are governed by antiferromagnetic quantum critical fluctuations, which are suppressed by magnetic fields. Furthermore, we find that the introduction of a small concentration of magnetic impurities qualitatively changes the magnetotransport properties of LNO. The magnetoresistance as a function of temperature is found to scale in a manner strongly resembling some heavy-fermion Kondo lattice systems in the vicinity of an antiferromagnetic quantum critical point.

(iv) *Understanding layer-by-layer growth of nickelates* (*APL Mater.* 2020): Reflection High Energy Electron Diffraction (RHEED) is often used to monitor the growth process during molecular beam epitaxy, as the minima / maxima indicate the completion of each monolayer. However, given the strong interaction between electrons and the surface, quantitative analysis with RHEED is difficult; furthermore, RHEED cannot be used to probe atomic-scale processes taking place below the surface.

For this reason, we constructed a new MBE chamber at the APS that allows both RHEED and surface X-ray diffraction studies during epitaxial thin film growth. This allows us to relate the growth oscillations observed during RHEED with those observed from X-ray scattering. In recent^x work, we studied the initial case of LaNiO₃ layer-by-layer growth on (La_{0.18}Sr_{0.82})(Al_{0.59}Ta_{0.41})O₃. We found that during the earliest stages of growth, the RHEED and X-ray signals are out-of-phase with each other before gradually becoming in-phase, demonstrating that while regular RHEED oscillations may imply high quality growth, the film-substrate interface can undergo significant changes during deposition due to the occurrence of interdiffusion at the growth temperature.

Future Plans

(i) *Superconductivity and electronic nematicity at KTaO₃ interfaces*: There are several key questions and opportunities that arise in this area of research building upon our findings thus far. Our effort will fall broadly into two categories – the first being materials development and understanding how to control the properties of the interfacial electron gases at KTO interfaces, and to also find other materials where such states may be found. Thus, we seek to find other overlayers on KTO that may give rise to an interesting interfacial electron gas. As an example, LaTiO₃ (LTO) is a Mott insulator and is known to give rise to an interfacial conductor on KTO (001) interfaces^{xi}, and we have already grown LTO with MBE on STO (see Recent Progress). We would also like to find ways to pattern our samples into mesoscale structures. We are collaborating with Prof. Jeremy Levy at the University of Pittsburgh to use his approach of writing nanoscale wires using a conducting AFM tip^{xii} that has been very successful in the LaAlO₃/SrTiO₃ interface. Furthermore, we’d like to understand how vacancy formation and cation diffusion using in-situ x-rays during growth of overlayers such as EuO or LTO on KTO. Ultimately, we’d like to grow KTaO₃ films

and dope them in a controlled manner. These and other aspects of materials development are being actively pursued

The second aspect of this research is to elucidate the nature of superconductivity and also the electronic nematicity that we observe. We are currently carrying out an extensive study of electric field-effect gating of superconductivity at the KTO (111) interface. Along with magnetotransport measurements currently in progress, we hope to develop a comprehensive picture of the nematic state that will constrain future theories. In all of these aspects we are collaborating with several theorists including Mike Norman, Peter Littlewood, and Ivar Martin at Argonne and Arun Paramekanti at Toronto. Two theory papers motivated by our work have appeared.^{xiii}

(ii) *Superconductivity in nickelates:* Superconductivity in nickelates was discovered in 2019, when a group at Stanford University reported that epitaxial thin films of the infinite layer ‘112’ compound $\text{Nd}_{1-x}\text{Sr}_x\text{NiO}_2$ ($x = 0.2$), with $\text{Ni}^{(1+x)+}$ in square-planar coordination with O, is a superconductor with T_c values reported as 9–15 K^{xiv}. Several follow-up results have also been reported.^{xv} The 112 phase is obtained from the perovskite (113) $\text{Nd}_{1-x}\text{Sr}_x\text{NiO}_3$ phase via topotactic reduction. The discovery of a such a closely related superconducting analog to the cuprates has aroused great interest in the quantum materials community.

Our research will be pursued along two lines – our first goal is to reproduce these results using MBE grown films using an approach similar to the Stanford group. We will use in-situ x-ray scattering to understand the reduction process. We also seek alternative strategies to doping, including delta doping, interfacial charge-transfer and ionic-liquid gating. We also seek alternative pathways to realize square planar Ni-O coordination, in collaboration with our colleagues at Argonne (John Mitchell, Mike Norman) who are actively pursuing this direction of research. We will use magnetotransport and thermogalvanic (Nernst effect) measurements to elucidate the nature of electronic states in these materials.

References

-
- ⁱ C. Liu et al., *Science* **371**, 716 (2021).
 - ⁱⁱ Y. Lu et al., *JPSJ* **83**, 023702 (2014).
 - ⁱⁱⁱ S. Yonezawa *Condens. Matter* **4**, 2 (2019); R.M. Fernandes et al., *Nat. Phys.* **10**, 97 (2014).
 - ^{iv} Y. Ma et al., *Chin. Phys. Lett.* **37**, 117401; Z. Chen et al., arXiv:2009.05689
 - ^v Z. Chen et al., *Phys. Rev. Lett.* **126**, 026802 (2021).
 - ^{vi} G. Eres et al., *Rev. Sci. Intrum.* **90**, 093902 (2019).
 - ^{vii} S. Y. Cook et al., *Sci. Adv.* **5**, eaav0764 (2019).
 - ^{viii} S. Catalano et al., *Rep. Prog. Phys.* **81**, 046501 (2018).
 - ^{ix} C. Liu et al., *Nat. Commun.* **11**, 1 (2020).
 - ^x Xi Yan et al., *APL Mater.* **8**, 101107 (2020).
 - ^{xi} K. Zou et al., *APL Mater.* **3**, 036104 (2015).
 - ^{xii} C. Cen et al., *Science* **323**, 1026 (2009).
 - ^{xiii} P. V. Arribi et al., *Phys. Rev. B* **103**, 035115 (2021); F. L. Buessen et al., arXiv:2101.03174.
 - ^{xiv} D. Li et al., *Nature* **572**, 624 (2019).
 - ^{xv} S. Zeng et al., arXiv:2004.11281; M. Osada et al., arXiv: 2006.133369.

Digital Synthesis FWP Publications, since March 2019.

1. “Breaking atomic-level ordering via biaxial strain in functional oxides: A DFT study”, K. Rawat, D. D. Fong, D. S. Aidhy (to appear in *J. Appl. Phys.*)
2. “Two-dimensional superconductivity and anisotropic transport at KTaO_3 (111) interfaces”, C. Liu, X. Yan, D. Jin, Y. Ma, H.-W. Hsiao, Y. Lin, T. M. Bretz-Sullivan, X. Zhou, J. Pearson, B. Fisher, J. S. Jiang, W. Han, J.-M. Zuo, J. Wen, D. D. Fong, J. Sun, H. Zhou, A. Bhattacharya, *Science* **371**, 716 (2021).
3. “Topological Hall Effect in a Topological Insulator Interfaced with a Magnetic Insulator”, Peng Li, Jinjun Ding, Steven S.-L. Zhang, James Kally, Timothy Pillsbury, Olle G. Heinonen, Gaurab Rimal, Chong Bi, August DeMann, Stuart B. Field, Weigang Wang, Jinke Tang, Jidong Samuel Jiang, Axel Hoffmann, Nitin Samarth, and Mingzhong Wu, *Nano Lett.* **21**, 84 (2021).
4. “Interface creation on a mixed-terminated perovskite surface”, Y. Li, F. Wrobel, X. Yan, A. Bhattacharya, J. Sun, H. Hong, H. Zhou, H. Wang, D. D. Fong, *Appl. Phys. Lett.* **118**, 061601 (2021).
5. “Amorphization mechanism of SrIrO_3 electrocatalyst: Amorphization mechanism of SrIrO_3 electrocatalyst: How oxygen redox initiates ionic diffusion and structural reorganization”, G. Wan, J. W. Freeland, J. Kloppenburg, G. Petretto, J. N. Nelson, D.-Y. Kuo, C.-J. Sun, J. Wen, J. T. Diulus, G. S. Herman, Y. Dong, R. Kou, J. Sun, S. Chen, K. Shen, D. Schlom, G.-M. Rignanese, G. Hautier, D. D. Fong, Z. Feng, H. Zhou, & J. Suntivich, *Science Advances* **7**, eabc7323 (2021).
6. “In situ X-ray and electron scattering studies of oxide molecular beam epitaxial growth”, Xi Yan, Friederike Wrobel, Yan Li, Hua Zhou, Huanhua Wang, Anand Bhattacharya, Jirong Sun, Hawoong Hong, and Dillon D. Fong, *APL Materials* **8**, 101107 (2020).
7. “Observation of an antiferromagnetic quantum critical point in high-purity LaNiO_3 ”, Changjiang Liu, Vincent FC Humbert, Terence M Bretz-Sullivan, Gensheng Wang, Deshun Hong, Friederike Wrobel, Jianjie Zhang, Jason D Hoffman, John E Pearson, J. Samuel Jiang, Clarence Chang, Alexey Suslov, Nadja Mason, MR Norman, Anand Bhattacharya, *Nature Communications* **11**, 1 (2020).
8. “Fermi surface topology and nontrivial Berry phase in the flat-band semimetal Pd_3Pb ”, Mojammel A Khan, Po-Hao Chang, Nirmal Ghimire, Terence M Bretz-Sullivan, Anand Bhattacharya, Jidong S. Jiang, John Singleton, John F Mitchell, *Phys. Rev. B* **101**, 245113 (2020).
9. “In situ X-ray studies of the incipient ZnO Atomic Layer Deposition on $\text{In}_{0.53}\text{Ga}_{0.47}\text{As}$ ”, E.V. Skopin, L. Rapenne, J.L. Deschanvres, E. Blanquet, G. Ciatto, L. Pithan, D. D. Fong, M.-I. Richard, and H. Renevier, *Phys. Rev. Mater.* **4**, 043403 (2020).
10. “Organismic materials for beyond von Neumann machines”, H.-T. Zhang, P. Panda, J. Lin, Y. Kalcheim, K. Wang, J. W. Freeland, D. D. Fong, S. Priya, I. K. Schuller, S. K. R. S. Sankaranarayanan, K. Roy, and S. Ramanathan, *Appl. Phys. Rev.* **7**, 011309 (2020).
11. “Ferroelectric domain wall motion in freestanding single-crystal complex oxide thin film”, S. R. Bakaul, J. Kim, S. Hong, M. J. Cherukara, T. Zhou, L. Stan, C. R. Serrao, S. Salahuddin, A. K. Petford-Long, D. D. Fong, M. V. Holt, *Adv. Mater.* **3**, 19007036 (2019).

12. "Counter-thermal flow of holes in high-mobility LaNiO₃ thin films", Chanjiang Liu, Friederike Wrobel, Jason D. Hoffman, Deshun Hong, John E. Pearson, Eva Benckiser and Anand Bhattacharya, *Phys. Rev. B (R)* **99**, 041114 (2019).
13. "Parameter transferability, self-doping, and metallicity in LaNiO₃/LaMnO₃ superlattices", A Lopez-Bezanilla, L. F. Arsenault, A. Bhattacharya, P. B. Littlewood, A. J. Millis, *Phys. Rev. B* **99**, 035133 (2019).
14. "Strongly Correlated Aromatic Molecular Conductor", Y. Hu, G. Zhong, Y.-S. Guan, J. N. Armstrong, C. Li, C. Liu, A. N'Diaye, A. Bhattacharya, S. Ren, *Small* **15**, 1900299 (2019).
15. "Experimental setup combining in situ hard X-ray photoelectron spectroscopy and real-time surface X-ray diffraction for characterizing atomic and electronic structure evolution during complex oxide heterostructure growth", G. Eres, C. M. Rouleau, Q. Lu, Z. Zhang, E. Benda, H. N. Lee, J. Z. Tischler, and D. D. Fong, *Rev. Sci. Instrum.* **90**, 093902 (2019).
16. "In operando studies of CO oxidation on epitaxial SrCoO_{2.5+d} thin films", C. M. Folkman, S. H. Chang, H. Jeen, E. Perret, P. M. Baldo, Carol Thompson, J. A. Eastman, H. N. Lee and D. D. Fong, *APL Mater.* **7**, 081126 (2019).
17. "Confined polaronic transport in (LaFeO₃)_n / (SrFeO₃)₁ superlattices", S. H. Chang, S. K. Kim, Y.-M. Kim, Y. Dong, C. M. Folkman, D. W. Jeong, W. S. Choi, A. Y. Borisevich, J. A. Eastman, A. Bhattacharya, and D. D. Fong, *APL Mater.* **7**, 071117 (2019).
18. "Interfacial Octahedral Manipulation Imparts Hysteresis-free Metal to Insulator Transition in Ultrathin Nickelate Heterostructure", Y. Dong, Z. Ma, Z. Luo, H. Zhou, D. D. Fong, W. Wu, C. and Gao, *Adv. Mater. Inter.* **6**, 1900644 (2019).
19. "Spin Seebeck effect in insulating SrFeO_{3-d} films", D. Hong, C. Liu, J. E. Pearson, A. Hoffmann, D. D. Fong, and A. Bhattacharya, *Appl. Phys. Lett.* **114**, 242403 (2019).
20. "Mixture domain states in PbTiO₃ film with potentials for functional application", Han Xu, Zhan Zhang, Yongqi Dong, Changgan Zeng, Dillon D. Fong, Zhenlin Luo, *Appl. Phys. Lett.* **114**, 242901 (2019).
21. "Seeded lateral solid-phase crystallization of the perovskite oxide SrTiO₃", Y. Chen, J. A. Tilka, Y. Ahn, J. Park, A. Pateras, T. Zhou, D. E. Savage, I. McNulty, M. V. Holt, D. M. Paskiewicz, D. D. Fong, T. F. Kuech, and P. G. Evans, *J. Phys. Chem. C* **123**, 7447 (2019).
22. "How heteroepitaxy occurs on strontium titanate", S. Y. Cook, K. Letchworth-Weaver, I.-C. Tung, T. K. Andersen, H. Hong, L. D. Marks, D. D. Fong, *Science Advances*, **5**, eaav0764 (2019).
23. Y. Zhu, J. G. Connell, S. Tepavcevic, P. Zapol, R. Garcia-Mendez, N. J. Taylor, J. Sakamoto, B. J. Ingram, L. A. Curtiss, J. W Freeland, D. D. Fong, and N. M. Markovic, Dopant-dependent stability of garnet solid electrolyte interfaces with lithium metal, *Advanced Energy Materials* **9**, 1803440 (2019).

Electronic Materials Program

Joel W. Ager,^{1,2} Daryl C. Chrzan,^{1,2} Oscar D. Dubon,^{1,2} Wladek Walukiewicz,^{1,2} Junqiao Wu,^{1,2} and Ali Javey^{1,3}

¹Materials Sciences Division, Lawrence Berkeley National Laboratory, Berkeley, CA

²Materials Science and Engineering, University of California, Berkeley, CA

³Electrical Engineering and Computer Science, University of California, Berkeley, CA

Program Scope

LBL's Electronic Material Program (EMAT) discovers and creates semiconductors of novel composition and morphology for energy applications by *removing chemical and physical constraints* that limit materials performance and growth. Emphasis is placed on exploration of single-crystalline semiconductors that are not epitaxially coupled with the underlying substrates, thus expanding the utility of semiconductors for new applications while enabling study of new material properties. In the case of monolayer semiconductors, elimination of the difference between the surface and the bulk allows us to control defects (including fixing/creating them) via surface treatments. In parallel, we utilize a toolbox of physical and chemical approaches to implement extreme control of band structures in both low dimensional and 3D materials using surface/interface effects. Finally, by exploiting new insights into the process of templated liquid-phase nucleation and growth, we synthesize high-quality single-crystal semiconductors on amorphous substrates.

Recent Progress

Discovery that chemical defect passivation of 2D semiconductor can produce near-unity photoluminescence quantum efficiency.

While there has been intense research interest in the optical properties of monolayer transition metal dichalcogenides (TMDs) such as MoS₂, their intrinsic optical properties had remained unknown. For example, the observed quantum efficiency for light emission for direct gap TMDs was low, on the order of 1% or less,^{1,2} which would rule out their use in important energy-related applications such as photovoltaics or light emitting diodes.^{3–5} *This limitation has been essentially eliminated* by our discovery that treatment of monolayers of MoS₂ with an organic superacid eliminates all defect related non-radiative recombination, resulting in near unity quantum efficiency at low pump powers, as shown in Fig. 1.⁶ The treatment is air-stable and the monolayers remain essentially opto-electronically perfect for weeks. Our ability to obtain optoelectronic monolayers with near-perfect properties opens the door for the development of highly efficient light-emitting diodes, lasers, and solar cells based on monolayer materials.

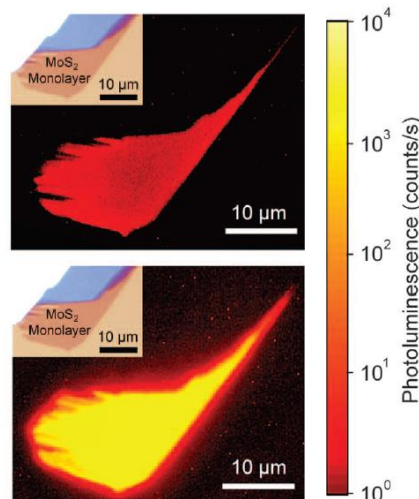


Figure 1. The photoluminescence from a monolayer of MoS₂ is increased by orders of magnitude by treatment with an organic superacid. The photoluminescence quantum efficiency is essentially 100% at low carrier generation rates. From Amani *et al.*, *Science*, 2015.⁶

Transistor with 1 nm gate length

Scaling of silicon (Si) transistors is predicted to fail below 5 nm gate lengths because of severe short channel effects. As an alternative to Si, certain 2D layered semiconductors are attractive because of their atomically uniform thickness down to a monolayer, lower dielectric constants, larger band gaps, and heavier carrier effective mass. Here, we demonstrate molybdenum disulfide (MoS_2) field effect transistors (FETs) with a 1-nm physical gate length using a 1D single-walled carbon nanotube (SWNT) as the gate electrode.⁷ The 1D2D FETs exhibit excellent switching characteristics with near ideal subthreshold swing of ~65 millivolts per decade and an On/Off current ratio of $\sim 10^6$ when the MoS_2 approaches 1 nm in thickness.

Grown of high-quality single-crystal III-V semiconductors on amorphous substrates.

The program has focused on controlling phase transitions at the nanoscale with an eye towards developing processing routes that enable the growth of a broad range of materials. The scientific genesis of this work is our discovery that control of nucleation can

allow III-V semiconductors to be grown with very large grain sizes on amorphous substrates.⁸ The key innovation is the use of a semi-permeable capping layer to control the flux of the group V in such a way as to control the nucleation rate. The growth mechanism can produce single crystalline materials if only a single nucleation site is allowed in a given volume. We have shown that templated liquid-phase crystal growth (TLP CG) is capable of growing high-quality (nominally) *single crystalline* III-V semiconductors on *amorphous* substrates.⁹ In the prototypical process we synthesized InP in (nominally) single-crystal form in a variety of shapes (Fig. 3). The approach has been demonstrated for GaP and InSb, and even extended to the synthesis of multilayers.

Fig. 3. Orientation image map of single crystal InP grown on an amorphous substrate (SiO_2) using TLP CG. Scale bar is 3 μm . Adapted from Chen *et al.*, *Nature Comm.*, 2016.⁹

Dopant-free heterojunction solar cells.

A salient characteristic of solar cells is their ability to subject photo-generated electrons and holes to pathways of asymmetrical conductivity—“assisting” them towards their respective contacts. All commercially available crystalline silicon (c-Si) solar cells achieve this by making use of doping in either near-surface regions or overlaying silicon-based films. Despite being commonplace, this approach is hindered by several optoelectronic losses and technological

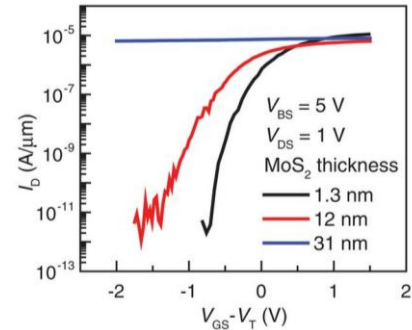
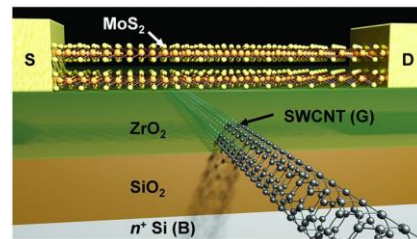
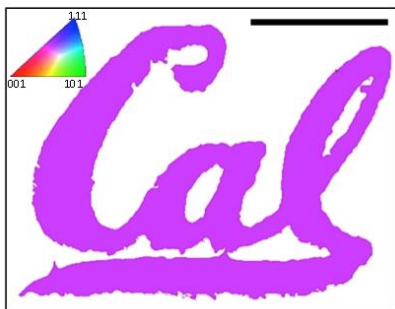


Fig. 2 (top) Schematic of 1D2D-FET with a MoS_2 channel and SWCNT gate. (bottom) For thin MoS_2 channels the subthreshold swing (SS) is near-ideal at ~65 mV per decade at room temperature Adapted from Desai *et al.*, *Science*, 2016.⁷



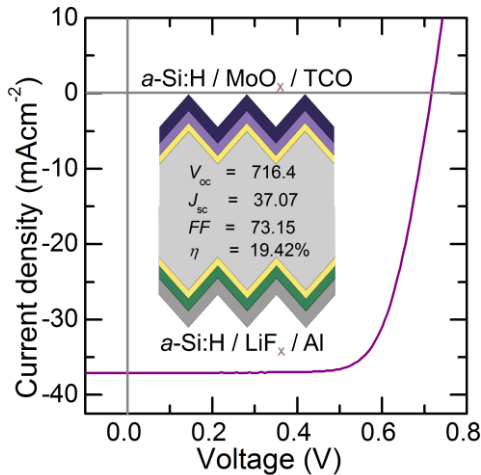


Fig. 4. Light JV characteristic and schematic of the dopant-free asymmetric heterocontact (DASH) silicon solar cell that uses molybdenum oxide and lithium fluoride as hole and electron-selective contacts, respectively. TCO refers to a Transparent Conductive Oxide stack. Adapted from Bullock *et al.*, *Nature Energy*, 2016.¹⁰

TMDs can be made to be optically “perfect,” with their luminescence dynamics appearing to be controlled only by intrinsic processes, allows us to use these materials as a starting point for incisive studies of intrinsic and extrinsic defects.^{6,11} The overall strategy will involve manipulation and chemical surface treatment of TMDs, controlled defect introduction, optical characterization, and electronic structure calculations. Initial work in this area is promising. We have discovered a method to retain the near-unity quantum efficiency of MoS₂ monolayers while they undergo exposure to conditions typical of semiconductor processing such as solvent and vacuum treatments.

In the next three years, we will employ a systematic and rational approach to engineer band structure of low-dimensional materials by modulating their interactions with the environment, and by doing so, we will stabilize new phase, states and properties needed for applications in energy production, conversion and transport. Two general approaches will be employed: physical modulation and chemical modulation. In an initial demonstration of the former approach, we have demonstrated strain engineering during the growth of WSe₂, showing that strains on the order of 1% can be achieved even in the case of non-epitaxial growth. For bilayer WSe₂, the strain can be sufficient to drive the indirect

limitations specific to doped silicon. EMAT made a major breakthrough in the discovery of alternative materials that can form “carrier-selective” interfaces on c-Si.¹⁰ The work successfully interfaced both dopant-free electron and hole carrier-selective heterocontacts using alkali metal fluorides and metal oxides, respectively (Fig. 4). Cells fabricated with this approach had high open circuit voltages over 710 mV, demonstrating the quality of the interfaces, and power conversion efficiencies approaching 20%. The new interface approach allows for a simplification in architecture and for lower temperature processing, both of which will improve the cost-to-performance ratio of c-Si photovoltaics.

Future Plans

Our discovery that certain monolayer

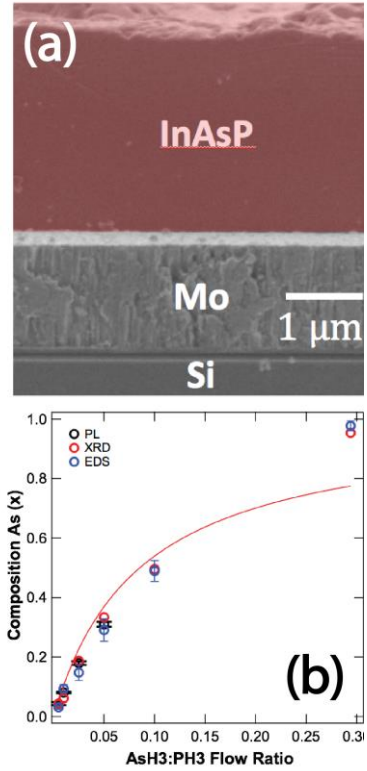


Fig. 5. Growth of single crystal InAs_{1-x}P_x using TLPBG. (a) SEM image of InAs_{1-x}P_x film. (b) Composition of the film as a function of growth conditions.

to direct phase transition which we had previously observed by the application of mechanical strain.¹²

It is clear that a broad range of semiconductor technologies would be impacted by the ability to inexpensively grow one material upon any other. Therefore we are continuing our efforts to grow high quality, single crystal semiconductor films of any desired thickness upon any substrate. At present, we have demonstrated non-epitaxial growth of high quality single crystal materials with lateral dimensions much larger than the film thickness. Recently, we have shown that growth of *ternary* III-V single crystal material is possible using TLPBG (Fig. 5). However, a remaining challenge is control of the orientation of the resultant single crystals grown via TLPBG. We are exploring a number of nucleation strategies to address this remaining challenge in non-epitaxial growth.

References

- (1) Yuan, L.; Huang, L. *Nanoscale* **2015**, *7* (16), 7402–7408.
- (2) Wang, H.; Zhang, C.; Rana, F. *Nano Lett.* **2015**, *15* (1), 339–345.
- (3) Miller, O. D.; Yablonovitch, E.; Kurtz, S. R. *IEEE J. Photovoltaics* **2012**, *2* (3), 303–311.
- (4) Tran, T.-T. D.; Sun, H.; Ng, K. W.; Ren, F.; Li, K.; Lu, F.; Yablonovitch, E.; Chang-Hasnain, C. J. *Nano Lett.* **2014**, *14* (6), 3235–3240.
- (5) Sutter-Fella, C. M.; Li, Y.; Amani, M.; Ager, J. W.; Toma, F. M.; Yablonovitch, E.; Sharp, I. D.; Javey, A. *Nano Lett.* **2016**, *16* (1), 800–806.
- (6) Amani, M.; Lien, D.-H.; Kiriya, D.; Xiao, J.; Azcatl, A.; Noh, J.; Madhvapathy, S. R.; Addou, R.; KC, S.; Dubey, M.; Cho, K.; Wallace, R. M.; Lee, S.-C.; He, J.-H.; Ager, J. W.; Zhang, X.; Yablonovitch, E.; Javey, A. *Science (80-.).* **2015**, *350* (6264), 1065–1068.
- (7) Desai, S. B.; Madhvapathy, S. R.; Sachid, A. B.; Llinas, J. P.; Wang, Q.; Ahn, G. H.; Pitner, G.; Kim, M. J.; Bokor, J.; Hu, C.; Wong, H.-S. P.; Javey, A. *Science (80-.).* **2016**, *354* (6308), 99–102.
- (8) Kapadia, R.; Yu, Z.; Wang, H.-H. H.; Zheng, M.; Battaglia, C.; Hettick, M.; Kiriya, D.; Takei, K.; Lobaccaro, P.; Beeman, J. W.; Ager, J. W.; Maboudian, R.; Chrzan, D. C.; Javey, A. *Sci. Rep.* **2013**, *3*, 2275.
- (9) Chen, K.; Kapadia, R.; Harker, A.; Desai, S.; Seuk Kang, J.; Chuang, S.; Tosun, M.; Sutter-Fella, C. M.; Tsang, M.; Zeng, Y.; Kiriya, D.; Hazra, J.; Madhvapathy, S. R.; Hettick, M.; Chen, Y.-Z.; Mastandrea, J.; Amani, M.; Cabrini, S.; Chueh, Y.-L.; Ager III, J. W.; Chrzan, D. C.; Javey, A. *Nat. Commun.* **2016**, *7*, 10502.
- (10) Bullock, J.; Hettick, M.; Geissbühler, J.; Ong, A. J.; Allen, T.; Sutter-Fella, C. M.; Chen, T.; Ota, H.; Wolf, S. De; Schaler, E. W.; Ballif, C.; Cuevas, A.; Javey, A. *Nat. Energy* **2016**, *1* (January), 15031.
- (11) Amani, M.; Taheri, P.; Addou, R.; Ahn, G. H.; Kiriya, D.; Lien, D.-H.; Ager, J. W.; Wallace, R. M.; Javey, A. *Nano Lett.* **2016**, *16* (4), 2786–2791.
- (12) Desai, S. B.; Seol, G.; Kang, J. S.; Fang, H.; Battaglia, C.; Kapadia, R.; Ager, J. W.; Guo, J.; Javey, A. *Nano Lett.* **2014**, *14* (8), 4592–4597.

Publications primarily supported by DOE Physical Behavior of Materials 2015-2017

- (1) Rembert, T.; Battaglia, C.; Anders, A.; Javey, A. Room Temperature Oxide Deposition Approach to Fully Transparent, All-Oxide Thin-Film Transistors. *Adv. Mater.* **2015**, *27*, 6090–6095.
- (2) García-Hemme, E.; Yu, K. M.; Wahnon, P.; González-Díaz, G.; Walukiewicz, W. Effects of the D-Donor Level of Vanadium on the Properties of $Zn_{1-x}V_xO$ Films. *Appl. Phys. Lett.* **2015**, *106*, 182101.
- (3) Welna, M.; Kudrawiec, R.; Nabetani, Y.; Tanaka, T.; Jaquez, M.; Dubon, O. D.; Yu, K. M.; Walukiewicz, W. Effects of a Semiconductor Matrix on the Band Anticrossing in Dilute Group II-VI Oxides. *Semicond. Sci. Technol.* **2015**, *30*, 85018.
- (4) Jaquez, M.; Yu, K. M.; Ting, M.; Hettick, M.; Sánchez-Royo, J. F.; Welna, M.; Javey, A.; Dubon, O. D.; Walukiewicz, W. Growth and Characterization of $ZnO_{1-x}S_x$ Highly Mismatched Alloys over the Entire Composition. *J. Appl. Phys.* **2015**, *118*, 215702.
- (5) Amani, M.; Lien, D.-H.; Kiriya, D.; Xiao, J.; Azcatl, A.; Noh, J.; Madhvapathy, S. R.; Addou, R.; KC, S.; Dubey, M.; Cho, K.; Wallace, R. M.; Lee, S.-C.; He, J.-H.; Ager, J. W.; Zhang, X.; Yablonovitch, E.; Javey, A. Near-Unity Photoluminescence Quantum Yield in MoS_2 . *Science* **2015**, *350*, 1065–1068.
- (6) Hsu, W.; Sutter-Fella, C. M.; Hettick, M.; Cheng, L.; Chan, S.; Chen, Y.; Zeng, Y.; Zheng, M.; Wang, H.-P.; Chiang, C.-C.; Javey, A. Electron-Selective TiO_2 Contact for $Cu(In,Ga)Se_2$ Solar Cells. *Sci. Rep.* **2015**, *5*, 16028.
- (7) Francis, C. A.; Detert, D. M.; Chen, G.; Dubon, O. D.; Yu, K. M.; Walukiewicz, W. $Ni_xCd_{1-x}O$: Semiconducting Alloys with Extreme Type III Band Offsets. *Appl. Phys. Lett.* **2015**, *106*, 22110.
- (8) López, N.; Yu, K. M.; Tanaka, T.; Walukiewicz, W. Multicolor Electroluminescence from Intermediate Band Solar Cell Structures. *Adv. Energy Mater.* **2015**, *1501820*.
- (9) Baranowski, M.; Kudrawiec, R.; Luce, A. V.; Latkowska, M.; Yu, K. M.; Misiewicz, J.; Tu, C. W.; Walukiewicz, W.; Kuang, Y. J. Temperature Evolution of Carrier Dynamics in GaN_xPyAs_{1-y-x} alloys. *J. Appl. Phys.* **2015**, *117*, 175702.
- (10) Liu, K.; Hsin, C.-L. L.; Fu, D.; Suh, J.; Tongay, S.; Chen, M.; Sun, Y.; Yan, A.; Park, J.; Yu, K. M.; Guo, W.; Zettl, A.; Zheng, H.; Chrzan, D. C.; Wu, J. Self-Passivation of Defects: Effects of High-Energy Particle Irradiation on the Elastic Modulus of Multilayer Graphene. *Adv. Mater.* **2015**, *27*, 6841–6847.
- (11) Ting, M.; dos Reis, R.; Jaquez, M.; Dubon, O. D.; Mao, S. S.; Yu, K. M.; Walukiewicz, W. Electronic Band Structure of ZnO-Rich Highly Mismatched $ZnO_{1-x}Te_x$ Alloys. *Appl. Phys. Lett.* **2015**, *106*, 92101.
- (12) Kiriya, D.; Zhou, Y.; Nelson, C.; Hettick, M.; Madhvapathy, S. R.; Chen, K.; Zhao, P.; Tosun, M.; Minor, A. M.; Chrzan, D. C.; Javey, A. Oriented Growth of Gold Nanowires on MoS_2 . *Adv. Funct. Mater.* **2015**, *25*, 6257–6264.
- (13) Roy, T.; Tosun, M.; Hettick, M.; Ahn, G. H.; Hu, C.; Javey, A. 2D-2D Tunneling Field-Effect Transistors Using $WSe_2/SnSe_2$ Heterostructures. *Appl. Phys. Lett.* **2016**, *108*, 83111.
- (14) Amani, M.; Taheri, P.; Addou, R.; Ahn, G. H.; Kiriya, D.; Lien, D.-H.; Ager, J. W.; Wallace, R. M.; Javey, A. Recombination Kinetics and Effects of Superacid Treatment in Sulfur- and Selenium-Based Transition Metal Dichalcogenides. *Nano Lett.* **2016**, *16*, 2786–2791.
- (15) Sutter-Fella, C. M.; Li, Y.; Amani, M.; Ager, J. W.; Toma, F. M.; Yablonovitch, E.; Sharp, I. D.; Javey, A. High Photoluminescence Quantum Yield in Band Gap Tunable Bromide Containing Mixed Halide Perovskites. *Nano Lett.* **2016**, *16*, 800–806.
- (16) Wang, H.-P.; Sutter-Fella, C. M.; Lobaccaro, P.; Hettick, M.; Zheng, M.; Lien, D.-H.; Miller, D. W.; Warren, C. W.; Roe, E. T.; Lonergan, M. C.; Guthrey, H. L.; Haegel, N. M.; Ager, J. W.; Carraro, C.; Maboudian, R.; He, J.-H.; Javey, A. Increased Optoelectronic Quality and Uniformity of Hydrogenated P-InP Thin Films. *Chem. Mater.* **2016**, *28*, 4602–4607.
- (17) Xu, X.; Bullock, J.; Schelhas, L. T.; Stutz, E. Z.; Fonseca, J. J.; Hettick, M.; Pool, V. L.; Tai, K. F.; Toney, M. F.; Fang, X.; Javey, A.; Wong, L. H.; Ager, J. W. Chemical Bath Deposition of P-Type Transparent, Highly Conducting $(CuS)_x:(ZnS)_{1-x}$ Nanocomposite Thin Films and Fabrication of Si Heterojunction Solar Cells. *Nano Lett.* **2016**, *16*, 1925–1932.
- (18) Alarcón-Lladó, E.; Brazzini, T.; Ager, J. W. Surface Origin and Control of Resonance Raman Scattering and Surface Band Gap in Indium Nitride. *J. Phys. D. Appl. Phys.* **2016**, *49*, 255102.

- (19) Tosun, M.; Chan, L.; Amani, M.; Roy, T.; Ahn, G. H.; Taheri, P.; Carraro, C.; Ager, J. W.; Maboudian, R.; Javey, A. Air-Stable N-Doping of WSe₂ by Anion Vacancy Formation with Mild Plasma Treatment. *ACS Nano* **2016**, *10*, 6853–6860.
- (20) Desai, S. B.; Madhvapathy, S. R.; Amani, M.; Kiriya, D.; Hettick, M.; Tosun, M.; Zhou, Y.; Dubey, M.; Ager, J. W.; Chrzan, D.; Javey, A. Gold-Mediated Exfoliation of Ultralarge Optoelectronically-Perfect Monolayers. *Adv. Mater.* **2016**, *28*, 4053–4058.
- (21) Amani, M.; Burke, R. A.; Ji, X.; Zhao, P.; Lien, D.-H.; Taheri, P.; Ahn, G. H.; Kiriya, D.; Ager, J. W.; Yablonovitch, E.; Kong, J.; Dubey, M.; Javey, A. High Luminescence Efficiency in MoS₂ Grown by Chemical Vapor Deposition. *ACS Nano* **2016**, *10*, 6535–6541.
- (22) Chen, K.; Kapadia, R.; Harker, A.; Desai, S.; Seuk Kang, J.; Chuang, S.; Tosun, M.; Sutter-Fella, C. M.; Tsang, M.; Zeng, Y.; Kiriya, D.; Hazra, J.; Madhvapathy, S. R.; Hettick, M.; Chen, Y.-Z.; Mastandrea, J.; Amani, M.; Cabrini, S.; Chueh, Y.-L.; Ager III, J. W.; Chrzan, D. C.; Javey, A. Direct Growth of Single-Crystalline III–V Semiconductors on Amorphous Substrates. *Nat. Commun.* **2016**, *7*, 10502.
- (23) Zhou, Y.; Kiriya, D.; Haller, E. E.; Ager, J. W.; Javey, A.; Chrzan, D. C. Compliant Substrate Epitaxy: Au on MoS₂. *Phys. Rev. B* **2016**, *93*, 54106.
- (24) Chen, Y.; Zhang, S.; Gao, W.; Ke, F.; Yan, J.; Saha, B.; Ko, C.; Suh, J.; Chen, B.; Ager, J. W.; Walukiewicz, W.; Jeanloz, R.; Wu, J. Pressure-Induced Structural Transition of Cd_xZn_{1-x}O Alloys. *Appl. Phys. Lett.* **2016**, *108*, 152105.
- (25) Kiriya, D.; Lobaccaro, P.; Nyein, H. Y. Y.; Taheri, P.; Hettick, M.; Shiraki, H.; Sutter-Fella, C. M.; Zhao, P.; Gao, W.; Maboudian, R.; Ager, J. W.; Javey, A. General Thermal Texturization Process of MoS₂ for Efficient Electrocatalytic Hydrogen Evolution Reaction. *Nano Lett.* **2016**, *16*, 4047–4053.
- (26) Bullock, J.; Hettick, M.; Geissbühler, J.; Ong, A. J.; Allen, T.; Sutter-Fella, C. M.; Chen, T.; Ota, H.; Schaler, E. W.; De Wolf, S.; Ballif, C.; Cuevas, A.; Javey, A. Efficient Silicon Solar Cells with Dopant-Free Asymmetric Heterocontacts. *Nat. Energy* **2016**, *1*, 15031.
- (27) Ristova, M. M.; Francis, C.; Toma, F. M.; Yu, K. M.; Walukiewicz, W. Electrochemical Modification of the Optical and Electrical Properties of Cd-Rich Ni_xCd_{1-x}O Alloys. *Sol. Energy Mater. Sol. Cells* **2016**, *147*, 127–133.
- (28) Roy, T.; Tosun, M.; Hettick, M.; Ahn, G. H.; Hu, C.; Javey, A. 2D-2D Tunneling Field-Effect Transistors Using WSe₂/SnSe₂ Heterostructures. *Appl. Phys. Lett.* **2016**, *108*, 83111.
- (29) Desai, S. B.; Madhvapathy, S. R.; Sachid, A. B.; Llinas, J. P.; Wang, Q.; Ahn, G. H.; Pitner, G.; Kim, M. J.; Bokor, J.; Hu, C.; Wong, H.-S. P.; Javey, A. MoS₂ Transistors with 1-Nanometer Gate Lengths. *Science* **2016**, *354*, 99–102.
- (30) Yu, K. M.; Detert, D. M.; Chen, G.; Zhu, W.; Liu, C.; Grankowska, S.; Hsu, L.; Dubon, O. D.; Walukiewicz, W. Defects and Properties of Cadmium Oxide Based Transparent Conductors. *J. Appl. Phys.* **2016**, *119*, 181501.
- (31) Ristova, M. M.; Zhu, W.; Yu, K. M.; Walukiewicz, W. Semiempirical Modeling of a Three Sublayer Photoanode for Highly Efficient Photoelectrochemical Water Splitting: Parameter and Electrolyte Optimizations. *Sol. Energy Mater. Sol. Cells* **2016**, *157*, 190–199.
- (32) Fonseca, J. J.; Tongay, S.; Topsakal, M.; Chew, A. R.; Lin, A. J.; Ko, C.; Luce, A. V.; Salleo, A.; Wu, J.; Dubon, O. D. Bandgap Restructuring of the Layered Semiconductor Gallium Telluride in Air. *Adv. Mater.* **2016**, *28*, 6465–6470.
- (33) Gao, W.; dos Reis, R.; Schelhas, L. T.; Pool, V. L.; Toney, M. F.; Yu, K. M.; Walukiewicz, W. Formation of Nanoscale Composites of Compound Semiconductors Driven by Charge Transfer. *Nano Lett.* **2016**, *16*, 5247–5254.
- (34) Chen, Y.; Ke, F.; Ci, P.; Ko, C.; Park, T.; Saremi, S.; Liu, H.; Lee, Y.; Suh, J.; Martin, L. W.; Ager, J. W.; Chen, B.; Wu, J. Pressurizing Field-Effect Transistors of Few-Layer MoS₂ in a Diamond Anvil Cell. *Nano Lett.* **2017**, *17*, 194–199.

Uncovering and surmounting loss mechanisms in light emitters

Principal Investigator: Chris G. Van de Walle, University of California, Santa Barbara

Program Scope

The aim of this project is twofold: to develop reliable first-principles methodologies for calculating loss mechanisms in optoelectronic devices, and to apply them to technologically important materials. One focus is on nitride semiconductors, the key materials for solid-state lighting, but we have broadened our investigations to also include small-bandgap materials used in infrared applications, and halide perovskites that excel in photovoltaics and are being considered for light emitting diodes (LEDs).

Our approach for calculating radiative and nonradiative recombination is based on advanced first-principles techniques, taking full account of accurate electronic structure and electron-phonon interactions without any fitting to experiment. We address Auger recombination as well as point-defect-assisted Shockley-Read-Hall (SRH) recombination. For Auger, we have drawn attention to the key role of phonon-assisted processes. For SRH, we identify point defects that detrimentally impact efficiency. Our overall goal is to generate the fundamental knowledge that is essential for improving efficiencies, and to provide guidelines for overcoming the limitations.

Recent Progress

Methodology

We have continued our development of accurate methodology, based on density functional theory, for radiative [P13] and nonradiative [P1, P6, S1] recombination processes.

The implementation of spin-orbit coupling in our methodology for Auger recombination has enabled us to produce accurate results for materials such as InAs and PbSe. These small-gap materials have important applications in infrared devices. For InAs, we found that the direct Auger process is dominant and is enhanced by the presence of strong spin-orbit coupling [P1]. Surprisingly, our calculations showed that recombination in PbSe is dominated by the phonon-assisted indirect process [P11], which goes against the conventional wisdom that direct Auger recombination dominates in narrow-band-gap semiconductors. Our results allowed us to explain the observed low Auger rate as well as its weak temperature dependence. These methodological developments were also crucial to our ability to study Auger processes in halide perovskites [P6].

For defect-assisted recombination, we have improved our approach for calculating nonradiative capture coefficients and made the code publicly available on a [Github repository](#) [S1].

We also developed advanced methodology in the area of polarization. Electric fields induced by spontaneous and piezoelectric polarization strongly impact device efficiencies, but can sometimes be employed for heterostructures engineering [P10]; they also complicate first-principles modeling

of surfaces or nanostructures. We have developed a novel approach for accurately accounting for polarization effects in slab calculations [S5].

Efficiency of nitride light emitters

The active layer of nitride LEDs and lasers consists of InGaN; identifying centers that cause non-radiative recombination in this alloy is thus of primary importance. We examined the charge-state transition levels of native point defects and impurities using explicit alloy calculations, and monitored the dependence of defect levels on In content and distribution of In atoms. We found that the relative shift of the charge-state transition levels of the different defects can be explained by the atomic character of the defect state and whether it is derived from valence-band or conduction-band states of the host material. We also found that defects on the nitrogen site lead to a larger spread in levels compared with defects on the cation site [P5].

Transition-metal impurities are known to strongly impact semiconductor performance. Iron is incorporated in group-III nitrides both intentionally (to produce semi-insulating buffer layers or to enable spintronics) and unintentionally as a trace impurity. We performed a comprehensive investigation of the role of iron in the electrical and optical properties of GaN, InN, and AlN [P2]. Substitutional Fe acts as a strong nonradiative recombination center, involving carrier capture in an unusual mechanism that involves excited states. Carrier capture can also lead to current collapse in high-electron-mobility transistors. Formation of complexes between Fe impurities and native defects, or hydrogen and oxygen impurities may occur as well (**Figure 1**).

We have also extended our investigations to other nitride semiconductors that have recently attracted attention, such as BGaN alloys [P3,P14] and II-IV-nitrides [P4,P10].

Loss mechanisms in halide perovskites

Hybrid perovskites, such as methylammonium lead iodide (MAPbI_3), have emerged as promising materials for highly efficient solar cells and light emitters. Despite the remarkable success, the fundamental mechanisms that are responsible for the high efficiency are still vigorously debated.

We previously identified Auger recombination as exceptionally strong in methylammonium-lead iodide (MAPbI_3), the prototypical hybrid perovskite. This could hamper the performance of solar cells, and is of particular concern for applications in light emitters. We have proposed that alloying can suppress the Auger process (**Figure 2**).

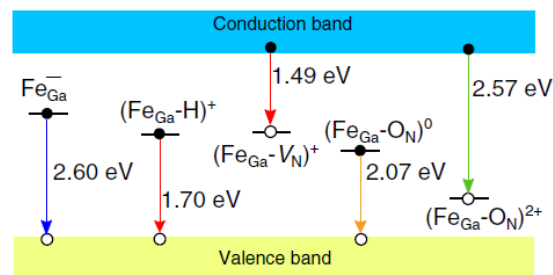


Figure 1. Peak energies for emission processes due to substitutional Fe and its complexes with hydrogen, oxygen, or nitrogen vacancies. The initial charge state for each optical transition is indicated.

In collaboration with experimental groups, we have investigated carrier dynamics and differences in recombination efficiency between surface and bulk regions [S4], and clarified that the strong anisotropy in optical transitions observed in layered hybrid perovskites stems from the orbital character of the band edges [P7].

Crucially, we have made substantial progress in understanding and quantifying the role of point defects in halide perovskites. In the literature, the notion of “defect tolerance” has often been invoked to explain the unexpectedly good performance of halide perovskites in optoelectronic applications. However, this concept has not been rigorously defined or assessed. A common interpretation is that none of the energetically favorable intrinsic defects have deep levels in the band gap.

We have conclusively shown that this is not the case [P8]. Point defects with levels deep in the bandgap can definitely form, but they do not cause detrimental nonradiative recombination because strong anharmonicity causes their capture rate to be low. Conversely, point defects that have states closer to the band edges and that traditionally would have been regarded harmless can actually act as strong recombination centers. In all cases, rigorous evaluation of capture coefficients based on configuration coordinate diagrams calculated with a hybrid functional is essential.

This leaves the question as to which centers *are* actually responsible for the experimentally observed defect-assisted nonradiative recombination rates. Employing our first-principles approaches to explicitly compute nonradiative recombination rates, we have quantitatively shown that the iodine interstitial is a dominant nonradiative recombination center in MAPbI₃ [P9] (**Figure 3**).

We have also addressed a hitherto overlooked type of defects, namely hydrogen vacancies, finding that they can have an extremely high carrier capture coefficient, three orders of magnitude larger than that of the iodine interstitial. A comparative study of hydrogen vacancies in MAPbI₃ and FAPbI₃ (FA: formamidinium) also reveals a fundamental difference: the hydrogen vacancies are much more difficult to form in FAPbI₃, and

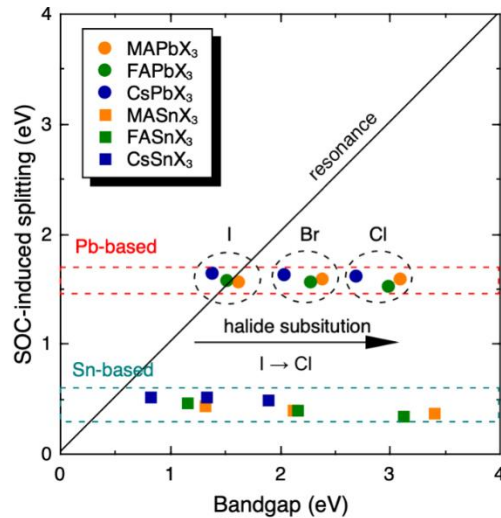


Figure 2. Relationship between the spin-orbit-coupling (SOC) induced splitting in the conduction band and the bandgap for halide perovskites. Avoiding the resonance suppresses Auger recombination.

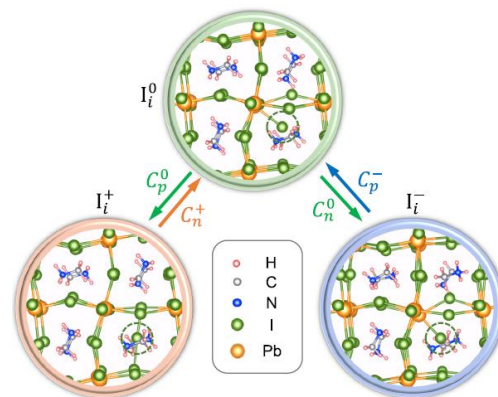


Figure 3. Local atomic structures of the iodine interstitial (I_i , dashed circles) in MAPbI₃, in the +, 0, and - charge states. Arrows show the relevant carrier capture processes. The subscript on the capture coefficients denotes the carrier being captured (n for electrons, p for holes) while the superscript denotes the charge state of the initial configuration.

they have substantially lower capture coefficients [S2]. To the best of our knowledge, this is the first time a rationale has been proposed as to why adding FA is essential for achieving high efficiency (as is empirically well established).

We have also emphasized the impact of impurities on recombination efficiencies, illustrated with the example of bismuth: Bi incorporates on Pb sites and introduces sub-bandgap states, but it is not an efficient recombination center [P12]. Instead, we found that Bi acts as a donor and pushes the Fermi level closer to the conduction band; this shift promotes the formation of iodine interstitials, which are the actual nonradiative recombination centers. Our insights provide a physically sound explanation for the detrimental effect of Bi on the photovoltaic performance of perovskite solar cells. These results focus attention on the detrimental role that unintentionally incorporated impurities can play, not necessarily by acting as nonradiative recombination centers themselves, but by shifting the Fermi level and thereby promoting the formation of efficiency-killing defects.

The bottom line is that point defects are an equally big concern for halide perovskites as they are for conventional semiconductors, and controlling them is essential for obtaining high efficiencies. The halide perovskites are therefore not really “defect tolerant”; a more accurate statement is that they can be grown with surprisingly high quality using low-cost deposition techniques. The insights obtained in our studies will not only help to establish a correct understanding of the defect physics in halide perovskites, but will also serve as a guide for experimentalists to further suppress the formation of strong recombination centers during synthesis, thus enabling optimal performance in both photovoltaic and light-emitting applications.

Future Plans

In terms of methodology, we are developing a multidimensional formalism for computing nonradiative capture, as well as an approach for impurity Auger recombination. We are also studying the impact of polarization fields near surfaces.

We will continue to explore efficiency-reducing defects, impurities, and complexes. For nitride semiconductors, this is currently particularly important at shorter wavelengths in AlGaN-based UV emitters. For halide perovskites, we will investigate chemical trends in the defect properties as a function of chemical composition of the host material.

Two-year Publication List

[P1] “Impact of phonons and spin-orbit coupling on Auger recombination in InAs”, J.-X. Shen, D. Steiauf, A. McAllister, G. Shi, E. Kioupakis, A. Janotti, and C. G. Van de Walle, Phys. Rev. B **100**, 155202 (2019). [doi: [10.1103/PhysRevB.100.155202](https://doi.org/10.1103/PhysRevB.100.155202)]

[P2] “Electrical and optical properties of iron in GaN, AlN, and InN”, D. Wickramaratne, J.-X. Shen, C. E. Dreyer, A. Alkauskas, and C. G. Van de Walle, Phys. Rev. B **99**, 205202 (2019). [doi: [10.1103/PhysRevB.99.205202](https://doi.org/10.1103/PhysRevB.99.205202)]

- [P3] “First-principles study of bandgap bowing in BGaN alloys”, M. E. Turiansky, J.-X. Shen, D. Wickramaratne, and C. G. Van de Walle, *J. Appl. Phys.* **126**, 095706 (2019). [doi: [10.1063/1.5111414](https://doi.org/10.1063/1.5111414)]
- [P4] “Optimizing *n*-type doping of ZnGeN₂ and ZnSiN₂”, N. L. Adamski, Z. Zhu, D. Wickramaratne, and C. G. Van de Walle, *Phys. Rev. B* **100**, 155206 (2019). [doi: [10.1103/PhysRevB.100.155206](https://doi.org/10.1103/PhysRevB.100.155206)]
- [P5] “Deep-level defects and impurities in InGaN alloys”, D. Wickramaratne, C. E. Dreyer, J.-X. Shen, J. L. Lyons, A. Alkauskas, and C. G. Van de Walle, *Phys. Status Solidi B* **257**, 1900534 (2019). [doi: [10.1002/pssb.201900534](https://doi.org/10.1002/pssb.201900534)]
- [P6] “First-principles simulation of carrier recombination mechanisms in halide perovskites”, X. Zhang, J.-X. Shen, and C. G. Van de Walle, *Adv. Energy Mater.* **10**, 19027830 (2019). [doi: [10.1002/aenm.201902830](https://doi.org/10.1002/aenm.201902830)]
- [P7] “Bright magnetic dipole radiation from two-dimensional lead-halide perovskites”, R. A. De-Crescent, N. R. Venkatesan, C. J. Dahlman, R. M. Kennard, X. Zhang, W. Li, X. Du, M. L. Chabinyc, R. Zia, J. A. Schuller, *Sci. Adv.* **6**, eaay4900 (2020). [doi: [10.1126/sciadv.aay4900](https://doi.org/10.1126/sciadv.aay4900)]
- [P8] “Correctly assessing defect tolerance in halide perovskites”, X. Zhang, M. E. Turiansky, and C. G. Van de Walle, *J. Phys. Chem. C* **124**, 6022 (2020). [doi: [10.1021/acs.jpcc.0c01324](https://doi.org/10.1021/acs.jpcc.0c01324)]
- [P9] “Iodine interstitials as a cause of nonradiative recombination in hybrid perovskites”, X. Zhang, M. E. Turiansky, J.-X. Shen, and C. G. Van de Walle, *Phys. Rev. B* **101**, 140101(R) (2020). [doi: [10.1103/PhysRevB.101.140101](https://doi.org/10.1103/PhysRevB.101.140101)]
- [P10] “Band alignments and polarization properties of the Zn-IV-nitrides”, N. L. Adamski, D. Wickramaratne, and C. G. Van de Walle, *J. Mater. Chem. C* **8**, 7890 (2020). [doi: [10.1039/d0tc01578d](https://doi.org/10.1039/d0tc01578d)]
- [P11] “Anomalous Auger recombination in PbSe”, X. Zhang, J.-X. Shen, and C. G. Van de Walle, *Phys. Rev. Lett.* **125**, 037401 (2020). [doi: [10.1103/PhysRevLett.125.037401](https://doi.org/10.1103/PhysRevLett.125.037401)]
- [P12] “Hidden role of Bi incorporation in nonradiative recombination in methylammonium lead iodide”, X. Zhang, J.-X. Shen, M. E. Turiansky, and C. G. Van de Walle, *J. Mater. Chem. A* **8**, 12964 (2020). [doi: [10.1039/d0ta04968a](https://doi.org/10.1039/d0ta04968a)]
- [P13] “Radiative capture rates at deep defects from electronic structure calculations”, C. E. Dreyer, A. Alkauskas, J. L. Lyons, and C. G. Van de Walle, *Phys. Rev. B* **102**, 085305 (2020). [doi: [10.1103/PhysRevB.102.085305](https://doi.org/10.1103/PhysRevB.102.085305)]
- [P14] “Thermodynamics of boron incorporation in BGaN”, J.-X. Shen, M. E. Turiansky, D. Wickramaratne, J. S. Speck, and C. G. Van de Walle (*Phys. Rev. Mater.*, in press)

Submitted

- [S1] “Nonrad: A Practical Implementation to Compute Nonradiative Capture Coefficients from First Principles”, M. E. Turiansky, A. Alkauskas, M. Engel, G. Kresse, D. Wickramaratne, J.-X. Shen, C. E. Dreyer, and C. G. Van de Walle (submitted to *Comput. Phys. Commun.*)
- [S2] “Minimizing hydrogen vacancies to enable highly efficient hybrid perovskites”, X. Zhang, J.-X. Shen, M. E. Turiansky, and C. G. Van de Walle (submitted to *Nature Mater.*)
- [S3] “Tutorial: A first-principles understanding of point defects and impurities in GaN”, J. L. Lyons, D. Wickramaratne, and C. G. Van de Walle (submitted to *J. Appl. Phys.*)

[S4] “Hidden carrier dynamics in the heterogeneous energy landscape of halide perovskites”, S. A. Bourelle, X. Zhang, S. Feldmann, A. Mathieson, L. Eyre, H. Abolins, C. G. Van de Walle, F. Deschler, T. Winkler (submitted to Science)

[S5] “Finite-size correction for slab supercell calculations of materials with spontaneous polarization”, S.H. Yoo, M. Todorova, D. Wickramaratne, L. Weston, C. G. Van de Walle, and J. Neugebauer (submitted to NPJ Comput. Mater.)

Lateral Heterostructures of Organic Charge Transfer Complexes and Inorganic Two-Dimensional Materials

Pengpeng Zhang, Department of Physics and Astronomy, Michigan State University

Program Scope

In this program, we focus on exploring lateral heterostructures constructed of dissimilar inorganic two-dimensional materials or organic charge transfer complexes using bottom-up approach. Formation of heterostructures not only allows the integration of different functionalities for device applications, but also enables new physical properties and behaviors that are not accessible in the individual pristine counterparts. The two recent studies to be discussed below, despite carried out on completely different systems, highlight the unique advantages of lateral heterostructures. First, heterointerfaces that are typically buried in the bulk are directly exposed on surface in lateral heterostructures, which enables spatially resolved studies to establish a microscopic understanding of structure-property relationship. Second, lateral heterostructures and the associated charge transfer and/or strain at the heterojunction can be utilized to tailor the properties of each individual constituents or even trigger phase transition.

Recent Progress

Spatially resolved investigation of mixed valence and insulator-to-metal transition in organic salt.

Charge transfer complex (CTC) molecular crystals with effective half-filled bands are correlated electron systems due to strong on-site Coulombic repulsion (U). When U is larger than bandwidth W , localization of electrons on respective molecules gives rise to Mott insulating state. These correlated CTC systems can undergo Mott insulator-to-metal transition (IMT) triggered by bandwidth-control via hydrostatic pressure or by electric/optical field. A very recent study further revealed a cooperative photoinduced hidden conducting phase, stable for over 400 days, in K-TCNQ (tetracyanoquinodimethane), a quasi-one-dimensional CTC with segregated-stacked TCNQ anions and alkali K cations bounded by ionic interaction.¹ In these systems, phase separation often occurs on macroscopic scale near the Mott transition, originating from the bistability of insulating Mott and correlated metal in free energy. Intriguingly, beyond phase separation, mixed valence of neutral TCNQ molecules (TCNQ^0) and TCNQ radical anions (TCNQ^{-1}) is also discovered in the high-conductance state of K-TCNQ. In inorganic Mott systems like oxides, it is known that such valence change involves the migration of oxygen vacancy or ions, resulting in local electronic inhomogeneity which plays a crucial role in IMT.² Does mixed valence and chemical composition variation give rise to any local inhomogeneity in the electronic structure of K-TCNQ? Furthermore, how does this local inhomogeneity relate to the phase separation that occurs on a much larger length scale? To address these questions, imaging and spectroscopy studies with molecular resolution are imperative.

In this work, we use the self-assembly bottom-up approach to create heterojunctions of mixed valence consisted of TCNQ (TCNQ^0) and K-TCNQ (TCNQ^{-1}) domains on the weakly interacting HOPG substrate (Fig. 1a). STM/STS is utilized to correlate the spatial distribution of electronic structures to the morphology of molecular heterojunction. Our results, as illustrated in Fig. 1b, show that pristine TCNQ and K-TCNQ assemblies are both insulating, while a continuum of density of states (DOS) across Fermi level arises in the TCNQ region near domain boundary (points 7-12 in Fig. 1c). Considering that molecules within this region, $\sim 1.5\text{nm}$ from the physical domain boundary, are as well packed as those in the deep interior of the TCNQ assembly, these

continuum states that emerge inside the molecular band gap cannot be attributed to localized defects states associated with disorders in the TCNQ structure. As discussed in our recent work, adding a K^+ vacancy in the bulk K-TCNQ unit cell introduces DOS within the bulk gap.¹ Thus, the continuum DOS observed in our experiment most likely originates from the abrupt valence change at the boundary, the electrostatic effects of which spreads a couple of nanometers into the interior of TCNQ assembly. Local electric fields are created as these

states reach equilibrium with the rest of the system including HOPG substrate via charge transfer. The strength of the electric fields can be estimated from the degree and width of the band bending (Fig. 1c), which amounts to the order of 10^7 - 10^8 V/m in both assemblies.

Nonetheless, current-induced phase segregation in bulk K-TCNQ has been reported to be highly periodic with stripe-like patterns of alternating carrier-rich and carrier-poor domains,³ whereas mixed valence, typically a consequence of electrochemical migration of metal ions in metal-TCNQ systems, represents a local phenomenon. Next, we discuss a possible scenario to associate these phenomena developed at different length scales. In macroscopic transport studies carried out in bulk K-TCNQ, the electrochemical migration of K^+ is expected to generate a gradient of mixed valence between the two electrodes. Microscopically, as K^+ ions migrate away from the positive terminal, leaving behind nano-puddles of K-TCNQ and TCNQ, local electric field will be built up in line with the STM/STS observation discussed above. IMT naturally starts from locations of the greatest local electric field and propagates towards the other electrode. Stripe-like alternating metallic and insulating domains are developed along this propagation direction, likely due to the Coulomb interaction between adjacent metallic domains which determines the overall periodicity of the pattern.

To summarize, our STM/STS investigation provides the first microscopic understanding of the crucial physics occurring near domain boundaries of mixed valence in K-TCNQ. Additionally, our study demonstrates that the ability to construct organic heterojunctions using bottom-up approach is vital for identifying the key physical processes empowered by interface.

B. Semiconductor to topological insulator transition in TMD core-shell lateral heterostructures.

Polymorphic phase transition is an important route for engineering the properties of two-dimensional materials. Heterostructure construction, on the other hand, not only allows the integration of different functionalities for device applications, but also enables the exploration of new physics arising from proximity coupling. Yet, implementing a design that incorporates the

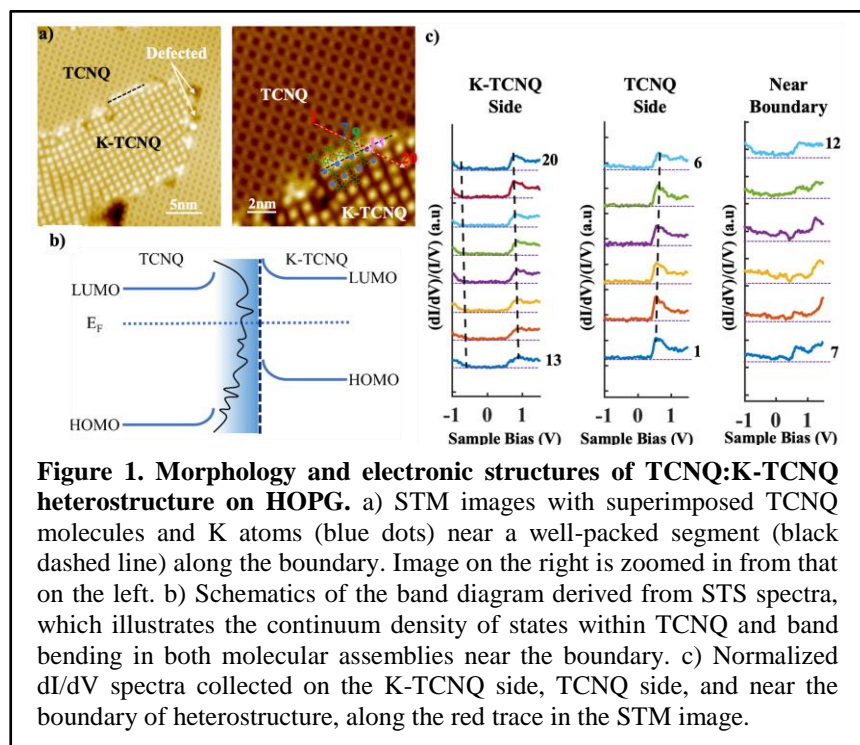
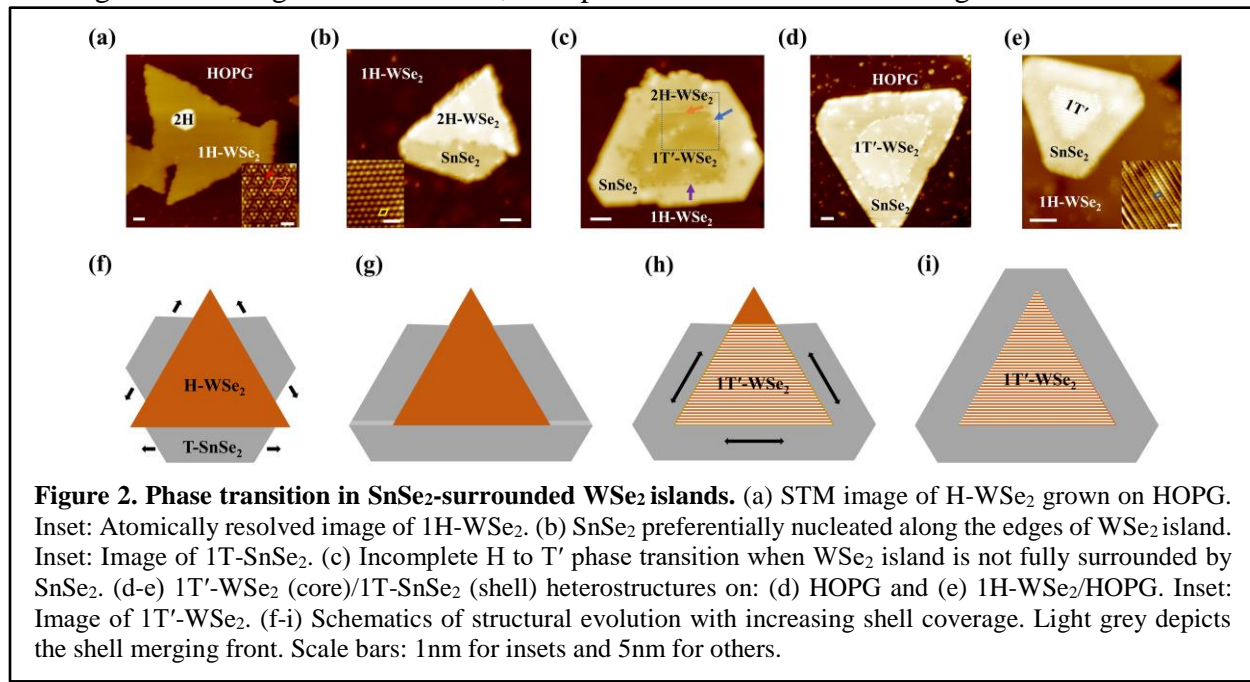


Figure 1. Morphology and electronic structures of TCNQ:K-TCNQ heterostructure on HOPG. a) STM images with superimposed TCNQ molecules and K atoms (blue dots) near a well-packed segment (black dashed line) along the boundary. Image on the right is zoomed in from that on the left. b) Schematics of the band diagram derived from STS spectra, which illustrates the continuum density of states within TCNQ and band bending in both molecular assemblies near the boundary. c) Normalized dI/dV spectra collected on the K-TCNQ side, TCNQ side, and near the boundary of heterostructure, along the red trace in the STM image.

advantages of both remains underexplored. In light of integrating heterostructure formation and phase engineering in one step, we demonstrate a novel phase transition technique based on the construction of lateral ($\text{WSe}_2/\text{SnSe}_2$) core-shell architecture, which is distinct from any of the known phase transition protocols.

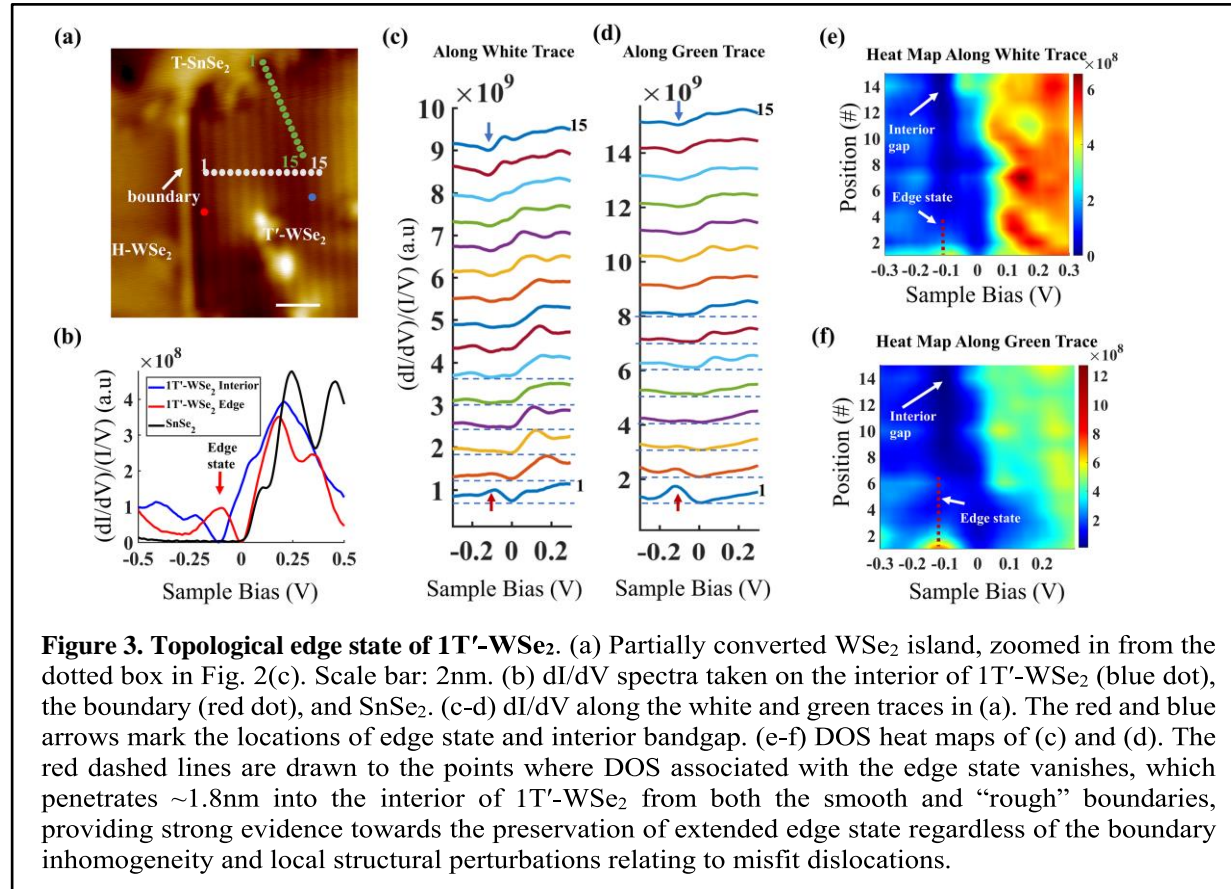
$\text{WSe}_2/\text{SnSe}_2$ core-shell architectures are grown on HOPG via sequential molecular beam epitaxy (MBE) deposition of WSe_2 and SnSe_2 . Thermodynamically stable H-phase of WSe_2 is formed initially, as confirmed by the lattice measurements shown in the inset of Fig. 2a. Inset of Fig. 2b reveals atomically resolved 1T- SnSe_2 that preferentially nucleates along the edges of existing WSe_2 islands. Intriguingly, approaching the formation of enclosed architecture, characteristic stripe-like features emerge on WSe_2 core (Fig. 2c-e). The striped phase with structure illustrated in the inset of Fig. 2e is commonly referred to as T'-phase, suggesting a H to T' phase transition in WSe_2 core. The observed phase transition is closely related to the degree of SnSe_2 coverage surrounding H- WSe_2 islands, as depicted in the schematics in Fig. 2f-i.



It is known that T'-phase of group VI transition metal dichalcogenides (TMDs) are metastable except for 1T'- WTe_2 .⁴⁻⁶ Direct synthesis is typically carried out at conditions away from equilibrium, whereas phase transition triggered by mechanical stress or electron doping might introduce structural damage and/or additional source of contamination. We employ STM/STS and first-principles calculations to reveal the semiconductor to topological insulator (TI) transition associated with the polymorphic change of WSe_2 core (Fig. 3) and exclude electron doping as the origin of phase transition. In addition to the observation of misfit dislocations which relax the epitaxial strain at heterojunctions, we propose a novel phase transition mechanism that involves the propagation of stress from shell to core mediated through the covalently bonded core-shell boundaries. Since the proposed mechanism only fundamentally requires a van der Waals interacting substrate and sufficient core-shell lattice mismatch, our approach could be potentially versatile towards other TMDs and chemical vapor deposition methods.

Most importantly, realization of phase transition on the template of heterostructures allows the rational design and integration of TMD functionalities. In the $\text{WSe}_2/\text{SnSe}_2$ core-shell architecture, the topological edge state originating from 1T'- WSe_2 remains intact and is robust to

periodic local perturbations at the core-shell boundary (Fig. 3e-f). Since SnSe₂ becomes superconducting at low temperatures,⁷ WSe₂/SnSe₂ lateral heterostructure with the directly exposed boundary on surface provides a valuable platform for future investigations into spatial extension of superconducting proximity effect and induced topological superconductivity at the edge of 2D TI.



Future Plans

For the benefit of device miniaturization and scalability when integrating the functionality and versatility of CTCs with inorganic electronic materials, there is a strong incentive to turn to CTC thin films with thickness at the nanometer or even molecular scale. This raises an important question: can substrate provide a means to engineer functionalities of CTCs? It demands thorough understanding of substrate influence on CTC properties. Additionally, superconducting proximity effect on the edge state of 2D topological insulator will continue to be explored utilizing lateral heterostructures of 1T'-WSe₂/1T-SnSe₂.

References:

1. Hu, Y.; et al., *Under Review* 2021.
2. Jeong, J.; et al., *Science* **339**, 1402 (2013).
3. Kumai, R.; Okimoto, Y.; Tokura, Y., *Science* **284**, 1645 (1999).
4. Duerloo, K.-A. N.; Li, Y.; Reed, E. J., *Nature Communications* **5**, 4214 (2014).
5. Chen, P.; et al., *Nature Communications* **9**, 2003 (2018).
6. Ugeda, M. M.; et al., *Nature Communications* **9**, 3401 (2018).
7. Zhang, Y.-M.; et al., *Physical Review B* **98**, 220508 (2018).

Publications:

1. Tan, A.; Zhang, P. P., Tailoring the Growth and Electronic Structures of Organic Molecular Thin Films. *Journal of Physics: Condensed Matter* **31**, 503001 (2019).
2. Tan, A.; Zhang, P. P., Interfacial Charge Transfer Enhancement via Formation of Binary Molecular Assemblies on Electronically Corrugated Boron Nitride. *Physical Chemistry Chemical Physics* **21**, 26146 (2019).
3. Dong, X.; Hu, Y.; Ren, S.; Zhang, P. P., Spatially Resolved Investigation of Mixed Valence and Insulator-to-Metal Transition in an Organic Salt. *The Journal of Physical Chemistry Letters* **11**, 8352 (2020).
4. Dong, X.; Lai, W.; Zhang, P. P., Semiconductor to Topological Insulator Transition Induced by Stress Propagation in Metal Dichalcogenide Core-Shell Lateral Heterostructures. *Materials Horizons* DOI: [10.1039/DOMH01688H](https://doi.org/10.1039/DOMH01688H) (2021).
5. Hu, Y.; Adhikari, D.; Tan, A.; Dong, X.; Zhu, T.; Wang, X.; Huang, Y.; Mitchell, T.; Tao, Z.; Dasenbrock-Gammon, N.; Snider, E.; Dias, R. P.; Huang, C.; Kim, R.; Neuhart, I.; Ali, A. H.; Zhang, J.; Bechtel, H.; Martin, M. C.; Gorder, S.; Hu, F.; Li, Z.; Armstrong, J. N.; Wang, J.; Liu, M.; Benedict, J.; Zurek, E.; Sambandamurthy, G.; Grossman, J. C.; Zhang, P. P.; Ren, S., Laser-Induced Cooperative Transition in Molecular Electronic Crystal. *Under Review* (2021).

Plasmon and Photon Excitations in Layered Heterostructures

Harry A. Atwater, California Institute of Technology

Program Scope

Two-dimensional and layered material structures have been the subject of widespread intensive scientific interest and investigation. Light-matter interactions in layered and two-dimensional materials represent a method to both achieve extreme optical confinement approaching the atomic scale, and a tool for observing and exploring new materials phenomena. Layered narrow bandgap and zero bandgap materials, such as black phosphorus and graphene, support unusual and intriguing quantum-confined electronic states in thin layers and surface electronic states. The incomplete screening of applied electrostatic fields in ultrathin materials permits the exploration of light-matter interactions at high electric fields and carrier densities, enabling interrogation of materials properties over a wide range of Fermi level conditions in a single sample. This enables us to explore the relationship between the electrochemical potential and the optical and plasmonic properties of ultrathin and layered materials. Our research project seeks to understand the nature of optical interband and intraband plasmon excitations in narrow bandgap layered semiconductors such as graphene and black phosphorus, and how strong electrostatic fields alter the band occupancy and electronic structure of thin narrow bandgap semiconductors. Gate control of the Fermi level in black phosphorus heterostructures may enable creation of materials with tunable birefringence at optical frequencies, and in-plane optical dispersion at infrared frequencies, including a tunable in-plane hyperbolic optical dispersion.

Recent Progress

A short summary of recent progress on investigation of interband and intraband plasmon excitations in narrow bandgap layered materials (graphene and black phosphorus) is given here:

- Realization of tunable ‘perfect’ (up to 97%) absorption in graphene plasmonic nanostructures. By variation of the graphene Fermi level, we were able to tune absorption in a patterned graphene layer with a coverage of 0.07 monolayers from 2.9% (the non-resonant interband absorption value) up to >95%. This was achieved using careful analysis of the impedance matching between the nanostructured graphene surface and free space (*Nano Letters*).
- Demonstration of mid-infrared phase modulation in resonant graphene/gold plasmonic antenna arrays; we observed phase modulation of up to 237° at an operating wavelength of 8.50 μm (*Nano Letters*; Web of Science Highly Cited paper).
- Demonstration of bright non-thermal mid-infrared emission, originating from spontaneous emission of non-equilibrium plasmons generated in graphene under ultrafast optical pumping. (in press, *Nature Materials*, 2021).
- Observation in few-layer black phosphorus of interband transitions from the mid-infrared to the visible, revealing Pauli-blocking of intersubband optical transitions (the Burstein–Moss effect); the quantum-confined Stark effect; and the modification of quantum well selection rules by a symmetry-breaking, applied electric field. These effects generate near-unity tuning of the BP oscillator strength for some material thicknesses and photon energies, along a single in-plane crystal axis, transforming absorption from highly anisotropic to nearly isotropic. The

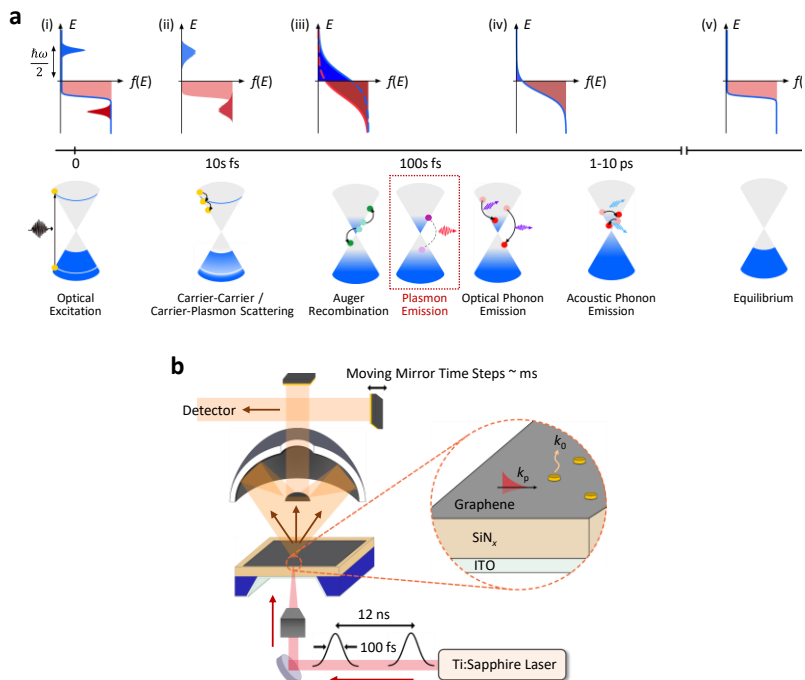
anisotropy of these electro-optical phenomena results in dynamic control of linear dichroism and birefringence, a promising concept for active control of the complex polarization state of light, and the propagation direction of surface waves (*Nano Letters*).

- Modulation of the intraband optical conductivity of black phosphorus (5 to 15 μm) by tuning the charge density in a two-dimensional electron gas, thereby modifying its free carrier-dominated intraband response. With a moderate doping density, we were able to observe a polarization-dependent epsilon-near-zero behavior in the dielectric permittivity of BP. The intraband polarization sensitivity is intimately linked to the difference in effective fermionic masses along the two crystallographic directions, as confirmed by our measurements (*Science Advances*).

1. Mid-Infrared Radiative Emission from Bright Hot Plasmons in Graphene

The decay dynamics of excited carriers in graphene have attracted wide scientific attention, and carrier relaxation occurs via several stages and decay channels. The promptly excited carriers with a non-Fermi distribution undergo carrier-carrier and carrier-plasmon scatterings on a 10-fs timescale, followed by Auger recombination and optical phonon emission. The excited carriers eventually reach a complete equilibrium with the lattice and environment through direct or disorder-assisted acoustic phonon emission processes, which occur on a picosecond timescale. These carrier relaxation processes in graphene upon optical pumping are depicted in Fig. 1a. Previous studies have predicted and revealed the strong interplay of plasmons and particle/hole excitations in graphene, which plays a significant role in reducing the lifetime of photoexcited charge carriers. Several theoretical studies report that plasmon emission rates are at least one order of magnitude larger than those of optical phonon emission. However, theorists had predicted that

Figure 1 | Carrier relaxation processes in graphene and experimental configuration. (a) Carrier relaxation processes in graphene under ultrafast optical excitation: (i) Sharply peaked distribution of photoexcited carriers upon optical pumping. (ii) Carriers with a non-Fermi-like distribution undergoing carrier-carrier scattering on a 10-fs timescale. (iii) Carriers in a quasi-equilibrium state. (iv) Carriers that have been thermalized under interband processes but are still hotter than the lattice. (v) Complete equilibrium between the carriers and the lattice. (b) Far-field infrared emission measurement setup.



a significant portion of the photoexcited carrier energy is released via a prompt flux of plasmon emission on a 100-fs timescale¹.

In 2020, we demonstrated Fermi-level-dependent mid-infrared emission in graphene originating from a previously unobserved decay channel: hot plasmon emission. Our observations of non-thermal contributions of Fermi-level-dependent radiation are first experimental demonstration of hot plasmon emission

arising from a photo-inverted carrier distribution in graphene achieved via ultrafast optical excitation. Results are shown in Figs. 2 d, e and f. Our calculations indicate that the reported plasmon emission process can be several orders of magnitude brighter than Planckian emission mechanisms in the mid-infrared spectral range. Evidence for bright hot plasmon emission is further supported by graphene decorated with gold nanodisks, which serve as out-coupling scatterers and promote localized plasmon excitation. These observations set a framework for exploration of ultrafast and ultrabright mid-infrared emission processes and light sources. Our recent work constitutes the first experimental observation of plasmon emission directly arising from a photo-inverted carrier distribution - the theoretically predicted but experimentally overlooked decay pathway in graphene - by measuring Fermi-level-dependent non-thermal emission contributions under ultrafast optical excitation.

2. Intraband and Interband Photonics in Black Phosphorus Heterostructures

The isolation of monolayer and ultrathin black phosphorus (BP) in recent years has opened scientific exploration of two-dimensional and layered materials with energy gaps between graphene and transition metal dichalcogenides, as black phosphorus is an emerging two-dimensional semiconductor material with an infrared energy gap and typical carrier mobilities between those of graphene and transition metal dichalcogenides. One of the most unusual features of BP is its large in-plane structural anisotropy, which generates a polarization-dependent optical response. This optical anisotropy corresponds to a large, broadband birefringence, wherein the distinct optical index of refraction along each axis leads to a phase delay between polarization

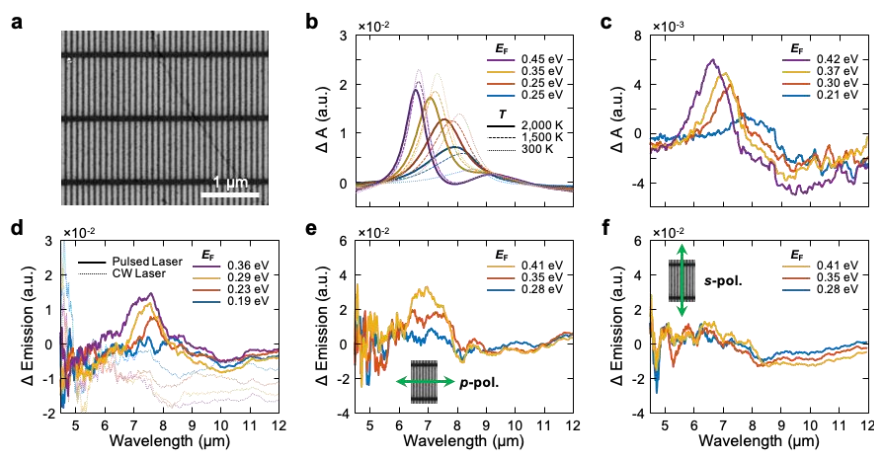


Figure 2 | Graphene-Fermi-level-dependent emission spectra from 35 nm graphene nanoribbon arrays (a) SEM image of 35 nm graphene nanoribbon arrays. (b) Calculated graphene-Fermi-level-dependent changes in absorptivity with varying carrier temperatures in graphene. (c) Measured graphene-Fermi-level-dependent changes in absorptivity at room temperature. (d) Measured gate-dependent changes in emission with respect to emission at CNP under pulsed (solid lines) and CW (dotted lines) laser excitations. (e-f) Measured polarization-dependent changes in emission with respect to emission at CNP under pulsed laser excitation at various graphene Fermi levels.

states of light. An additional constraint on optical absorption corresponds to the naturally occurring quantum well nature of the BP band structure, wherein optical transitions are only allowed between subbands of opposite parities, because photons carry parity -1. For low energy transitions, this corresponds to transitions between bands of equal quantum number (ie: v_1 to c_1 , v_2 to c_2).

Using field-effect device configurations like the ones depicted in Fig. 3, we can isolate and characterize three distinct, anisotropic electro-optic effects in BP: Pauli-blocking of intersubband optical transitions, the quantum confined Stark effect; and modification of quantum well selection rules by a symmetry-breaking electric field.

Future Plans

We are investigating the nature of hybridized photonic states at the interfaces of black phosphorus twisted bilayer heterostructures and twisted layer heterostructures between black phosphorus and molybdenum ditelluride. By creating heterostructures with small enough twist angle between layers whose constituent lattices are commensurate one expects atomic reconstruction; similarly, by forming superlattices between incommensurate systems one can develop highly strained Moiré potentials with strong pseudo-magnetic fields. These effects are expected to yield new optical properties associated with interband and intraband transitions and can be studied in BP/BP or bilayer-BP/MoTe₂ twisted bilayer systems.

References

1. F. Hamm, J. M., Page, A. F., Bravo-Abad, J., Garcia-Vidal, F. J. & Hess, O. Nonequilibrium plasmon emission drives ultrafast carrier relaxation dynamics in photoexcited graphene. *Phys. Rev. B* **93**, 041408 (2016).

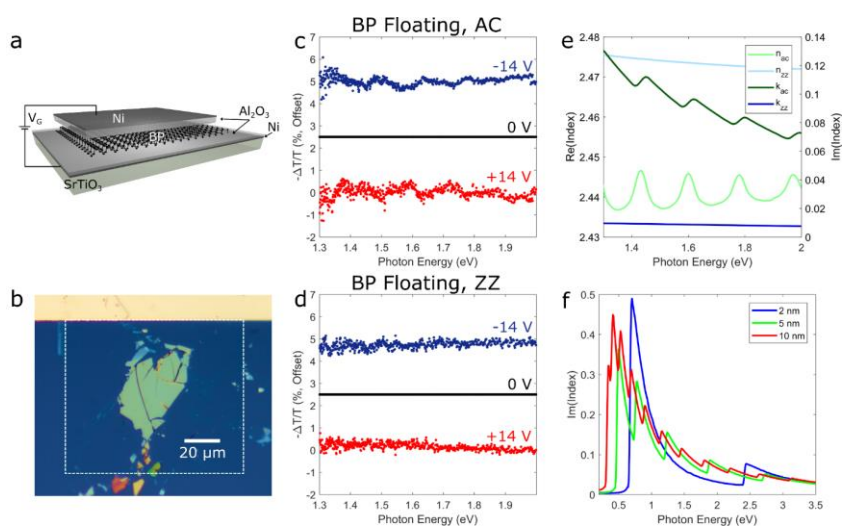


Figure 3. | Tunable visible interband transitions in BP. (a) Schematic figure of visible tuning device. Few-layer BP is mechanically exfoliated on 45 nm Al₂O₃/5 nm Ni on SrTiO₃ and then coated with 45 nm Al₂O₃. A 5 nm thick semitransparent Ni top contact is used. (b) Optical image of fabricated sample with 20 nm thick BP. Dashed white line indicates the boundary of the top Ni contact. (c) Tuning of extinction with field applied to floating device, for light polarized along the AC axis. (d) Corresponding tuning for light polarized along the ZZ axis. (e) Calculated index of refraction for 20 nm thick BP for the measured energies. (f) Calculated imaginary index of refraction of several thicknesses of BP from the infrared to visible.

Publications

1. Tunable intraband optical conductivity and polarization-dependent epsilon-near-zero behavior in black phosphorus, Souvik Biswas¹, William S. Whitney², Meir Y. Grajower¹, Kenji Watanabe³, Takashi Taniguchi³, Hans A. Bechtel⁴, George R. Rossman⁵, Harry A. Atwater¹, *Science Advances*, **7**: eabd4623 2021.
2. Mid-Infrared Radiative Emission from Bright Hot Plasmons in Graphene, L. Kim, S. Kim, P.K. Jha, V.W. Brar, and H.A. Atwater, in press, *Nature Materials* 2021; also arXiv:2001.11052.
3. “Experimental demonstration of tunable graphene-polaritonic hyperbolic metamaterial”, Jeremy Brouillet, G. T. Papadakis, and H.A. Atwater, *Optics Express*, **27** pp 30225-30232 (2020).
4. Phase Modulation with Electrically Tunable Vanadium Dioxide Phase-Change Metasurfaces Y. Kim, P.C. Wu, R. Sokhoyan, K. Mauser, R. Glaudell, G.K. Shirmanesh, *Nano Letters* **19**, pp. 3961-3968 (2019).
5. Probing the Band Structure of Topological Silicon Photonic Lattices in the Visible Spectrum, By: Peng, Siying; Schilder, Nick J.; Ni, Xiang; et al., *Physical Review Letters* **122**, Article Number: 117401(2019).
6. Mimicking surface polaritons for unpolarized light with high permittivity materials Papadakis, Georgia T.; Davoyan, Artur; Yeh, Pochi; et al. *Physical Review Materials* ,**3** Article Number: 015202 (2019).
7. Anisotropic Quantum Well Electro-Optics in Few-Layer Black Phosphorus, Sherrott, Michelle C.; Whitney, William S.; Jariwala, Deep; et al. *Nano Letters*, **19** 269-276 (2019).
8. Electronically Tunable Perfect Absorption in Graphene, Kim, Seyoon; Jang, Min Seok; Brar, Victor W.; et al. *Nano Letters*, **18**, 971-979 (2018).
9. Optical magnetism in planar metamaterial heterostructures Papadakis, Georgia T.; Fleischman, Dagny; Davoyan, Artur; et al. *Nature Communications* **9** Article Number: 296 (2018).

Session VI

Physical Mechanisms and Electric-Bias Control of Phase Transitions in Quasi-2D Charge-Density-Wave Quantum Materials

Alexander A. Balandin, Department of Electrical and Computer Engineering, University of California, Riverside, California 92521 USA

Program Scope

This DOE project (08/15/2020 to 08/14/2023) aims at understanding the physical mechanisms and developing methods for electric-bias control of phase transitions in quasi-two-dimensional (2D) charge-density-wave (CDW) quantum materials. The investigation mostly focuses on thin films of transition metal dichalcogenides (TMD), which reveal phase transitions at room temperature (RT) and above. The specific objectives of the project include (i) development of innovative approaches for investigation and controlling CDW phases with external stimuli; (ii) understanding the physical mechanisms behind the phase transitions in quasi-2D van der Waals materials; (iii) investigating the “hidden phases” at temperatures below the transition to commensurate CDW phase; and (iv) separating the electric field CDW switching from Joule heating induced switching. The physics of CDW phases in quasi-2D materials of TMD group is substantially different from, and much less understood than their bulk counterparts with quasi-1D crystal structure. In addition to the above RT phase transitions, 1T-TaS₂ reveals such intriguing properties as multiple step-like resistance changes and hysteresis, and surprising radiation hardness. The reports on de-pinning and sliding of CDWs in 2D material systems are scarce. The role of electric field and local heating on inducing the transitions in 2D CDW is not clear. The use of innovative characterization techniques such as low-frequency noise spectroscopy, Brillouin and Raman light scattering spectroscopy, nanoscale thermometry, ultra-fast current pulses are utilized to investigate and understand these phenomena. The physics insights gained on 2D van der Waals quantum materials’ properties will enable transformative changes in materials for electronics, potentially leading to new – DOE mission relevant – technologies for operation in high-radiation environments as well as in medical diagnostics. The CDW switching above RT can potentially be used in low-energy information processing. The strongly-correlated quantum 2D CDW materials are also relevant to developing quantum communication and computing technologies.

Recent Progress

During the first year of this project we worked to clarify the mechanism of the CDW phase transitions: electric field vs heat. The application of an electric field can trigger the CDW phase transition directly, by affecting the charged ions and electrons in the crystal. Alternatively, however, the electric current induced by the field is responsible for Joule heating, which, in turn, can also trigger CDW phase transitions [1-3]. The strength of the Joule heating should depend on details of the specific material, the device structure, and bias mode (DC *vs.* pulse) and duration. For these reasons, the mechanism of the different phase transitions that arise in different CDW devices or test structures is still the subject of intensive debate. Following the plan of this DOE

project, we investigated the RT switching of 1T-TaS₂ thin-film CDW devices, using nanosecond-duration electrical pulsing to construct their time-resolved current-voltage characteristics [4]. The switching action is based upon the nearly-commensurate to incommensurate CDW phase transition in this material, which has a characteristic temperature of 350 K near thermal equilibrium (measured at small bias). For sufficiently short pulses, with rise times in the nano-second range, self-heating of the devices is suppressed, and their current-voltage (I-V) characteristics are weakly non-linear and free of hysteresis. This changes as the pulse duration is increased to ~200 ns, where the current develops pronounced hysteresis that evolves non-monotonically with the pulse duration. To analyze the switching mechanism and estimate the speed of the switching, we developed a model for the time-dependent heat dissipation in the device by solving the transient heat-diffusion equation. Calculations were performed for the specific layered structure of the experimentally tested devices, using the finite-element method. For a quantitative comparison of the experimental and modeled trends, we define the width of the hysteresis ($V_C - V_M$) as the difference in the voltage values observed during the up and down ramps of the voltage at a constant current. This width is a meaningful parameter as it defines the operational range of voltages for CDW voltage-controlled oscillators and other types of switches [1].

Combining the results of our experiments with a numerical analysis of transient heat diffusion in these CDW devices on Si substrate, we have established the thermal origin of the switching. It is evident that both the experiment and simulations exhibit a peak at some particular value of the pulse duration, which should be defined by the interplay of the time constants for the generation and escape of heat (see Figure 1). The absolute values of the measured and simulated hysteresis windows are different due to the fact that not all experimental factors, *e.g.* the heat dissipated to environment, are accounted for in the simulation. The fine details of the position of the simulation data points, *i.e.* deviations from a smooth trend, are numerical due to the relatively coarse mesh used. What is interesting is that in spite of this thermal character, our modeling suggests that suitable reduction of the size of these devices and fine-tuning the thermal resistance of the device layered structure should allow their operation at GHz

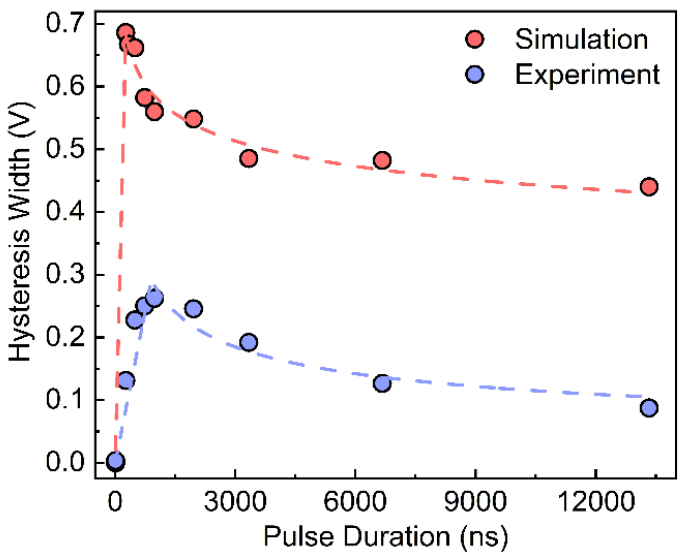


Figure 1: Experimental and simulated hysteresis window width ($V_C - V_H$) calculated at the constant current of 8 mA and as a function of pulse duration. The experimental and theoretical results both follow the same trend, exhibiting a peak at shorter pulse durations and approaching saturation at longer pulse times. The absolute values of the measured and simulated hysteresis windows are different due to the fact that not all experimental factors, *e.g.* actual thermal boundary resistance and heat dissipated to the environment, are accounted for in the simulation. The dash lines in the figure are guide for the eye. The data are after Ref. [4].

frequencies. We have used our experimentally validated physics-based model to simulate the I-V curves of a device with channel length, width and thickness of 1 μm , 2 μm , and 10 nm, respectively (see Figure 2). In this case, the hysteresis appears at substantially shorter pulses than in the measurements with the larger devices. For a pulse duration of 20 ns, the calculated channel temperature reaches \sim 360 K, which is already above the NC to IC-CDW transition temperature. The hysteresis in fact begins to develop for pulses as short as \sim 1 ns, which corresponds to a CDW device speed of \sim 1 GHz. The conducted experiments and modeling lead to an interesting conclusion that even if the CDW switching is of thermally induced nature, the devices based on this phase transitions can be made extremely fast.

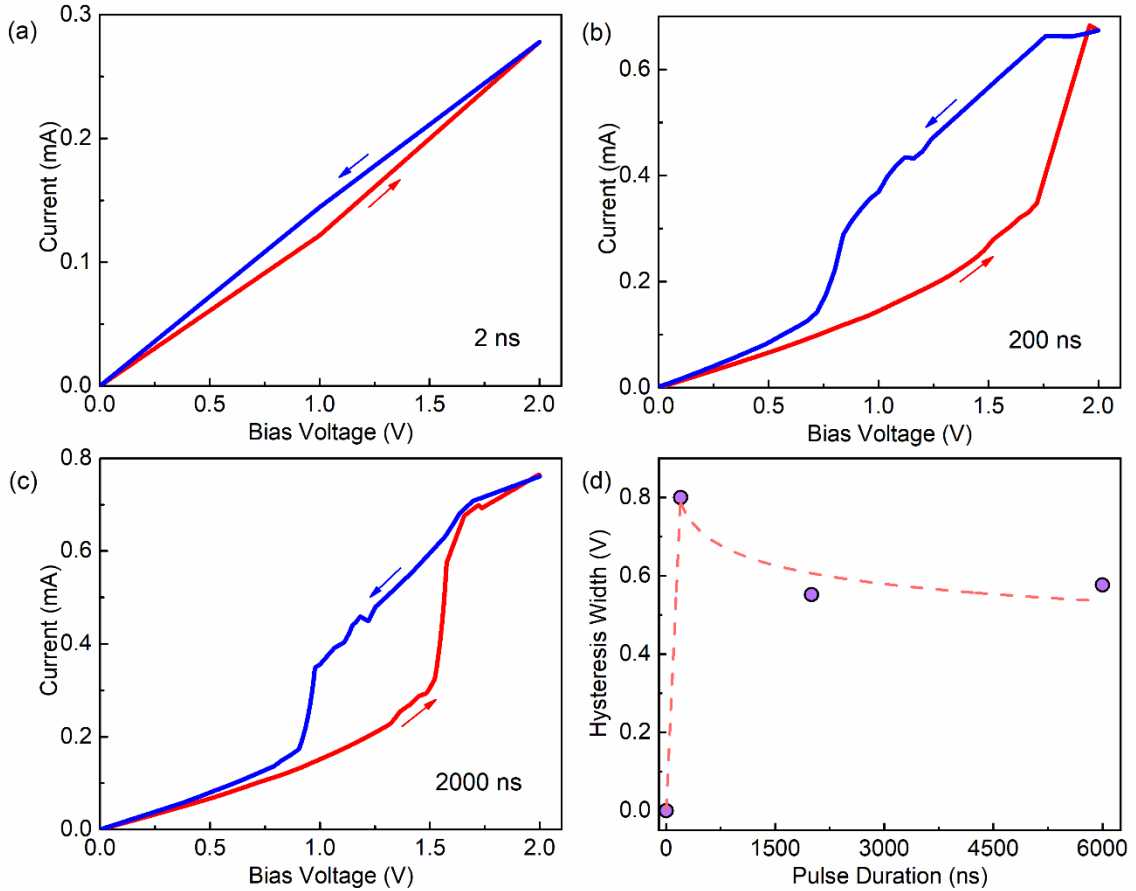


Figure 2: Simulated pulsed measurement results for the projected device with smaller dimensions (the device length, width and thickness are 1 μm , 2 μm , and 10 nm respectively), at various pulse durations: (a) 2 ns, (b) 200 ns, and (c) 2,000 ns. (d) Calculated hysteresis width for the same device as a function of pulse duration at constant current of 0.34 mA. The trend is similar to the experimental and simulation results obtained for the larger device structures. However, in this case, the hysteresis window can be observed even at smaller pulse durations. The hysteresis width has decreased compared to the larger devices. This confirms that, despite the dominant self-heating effect, careful tuning of the dimensions can lead to a device that can operate at GHz frequencies. The dash line in the figure is guide for the eye. The data are after Ref. [4].

Future Plans

The project's plan includes several approaches for distinguishing the pure electrical-field-driven phase changes from those resulting from local Joule heating by using the local thermometry, and ultra-fast current pulses. For this year, we plan to refine the model for simulating the CDW switching under ultra-fast pulses, and conduct the local thermometry study by measuring PL response of quantum dots placed in select locations on the device structure.

The low-frequency noise measurements will be employed to study the phase transitions and CDW sliding in quasi-2D TMD materials. Presently, these measurements are continued for 1T-TaS₂ structures. In addition, to verify that the noise spectroscopy is sensitive to a wide range of various phase transitions, we will perform measurements with another quasi-2D van der Waals material - FePS₃ – which is expected to have different type of phase transitions associated with the spin order.

The PI's team will use a combination of the Brillouin – Mandelstam and Raman spectroscopy for *in situ* observation of CDWs transitions in 2D materials under external electric and magnetic field stimuli. Getting Brillouin signal from opaque materials such as 1T-TaS₂ is challenging. We will attempt to observe the surface acoustic phonon modes.

References

- [1] G. Liu, B. Debnath, T. R. Pope, T. T. Salguero, R. K. Lake, and A. A. Balandin, "A charge-density-wave oscillator based on an integrated tantalum disulfide–boron nitride–graphene device operating at room temperature," *Nature Nano*, 11, 845–850 (2016).
- [2] G. Liu, S. Rumyantsev, M. A. Bloodgood, T. T. Salguero, and A. A. Balandin, "Low-frequency current fluctuations and sliding of the charge density waves in two-dimensional materials," *Nano Letters*, 18, 3630–3636 (2018).
- [3] A. K. Geremew, S. Rumyantsev, F. Kargar, B. Debnath, A. Nosek, M. A. Bloodgood, M. Bockrath, T. T. Salguero, R. K. Lake, and A. A. Balandin, "Bias-voltage driven switching of the charge-density-wave and normal metallic phases in 1T-TaS₂ thin-film devices," *ACS Nano*, 13, 7231–7240 (2019).
- [4] A. Mohammadzadeh, S. Baraghani, S. Yin, F. Kargar, J. P. Bird, and A. A. Balandin, Thermally-driven charge-density-wave transitions in 1T-TaS₂ thin-film devices: Prospects for GHz switching speed, *Applied Physics Letters* (in print, 2021) - chosen as an Editor's Pick.

Publications

- [1] A.A. Balandin, Invited Keynote Talk "Electronic properties and device applications of quasi-2D charge density wave materials," Session - 2D Atomic and Molecular Sheets—Electronic and Photonic Properties and Device Applications, Materials Research Society (MRS) Fall Meeting, 2020 – live presentation format; abstract available at MRS web-site.

[2] Amirmahdi Mohammadzadeh, Saba Baraghani, Shenchu Yin, Fariborz Kargar, Jonathan P. Bird, and Alexander A. Balandin, Thermally-driven charge-density-wave transitions in 1T-TaS₂ thin-film devices: Prospects for GHz switching speed, Applied Physics Letters (in print, 2021) - chosen as the APL Editor's Pick. The pre-print is available at <https://arxiv.org/abs/2101.06703> .

Singlet and Triplet Exciton Interaction and Dynamics in Molecular Crystals

Ivan Biaggio, Lehigh University, Bethlehem, PA 18018

Program Scope

We aim at fundamental investigations of excitonic effects in molecular crystals such as rubrene and related materials. Areas of focus are the triplet-pair state that is an intermediary to the fission process, how it is formed, how long the spin-correlation persists, and how and why it can efficiently separate into two independent triplet excitons. As part of this we seek to model and understand the diffusion process in the crystal lattice and the effects of its dimensionality on the fission process and the geminate fluorescence that can be emitted via triplet fusion. Other future aims are excitation spectroscopy of singlet fission, the investigation of how a triplet exciton created in a completed fission process diffuses, and its interaction with defects.

Recent Progress

We are reporting on a new project that got started last year towards the end of the summer (July 2020) in the midst of the covid crisis, which lead to delays.

However, it was still possible to work with data acquired very recently, in an effort that involved the PI and a senior undergraduate student who has now graduated. Here we will be reporting about those results.

We addressed how the geminate annihilation of two triplet excitons created by singlet exciton fission is affected by the dimensionality of triplet exciton transport. This dimensionality is determined by the typically anisotropic triplet exciton mobilities in organic molecular crystals. As an example, in many crystals there is a significant mobility along a close stacking direction of the molecules, but only weak mobility in other directions. The work had both a theoretical and an experimental aspect. From the theoretical side, we analyzed the exciton diffusion process using a random-walk model. In this model, the time-dynamics of the probability that two geminate triplet excitons meet again is a key factor determining the annihilation probability of the excitons. The

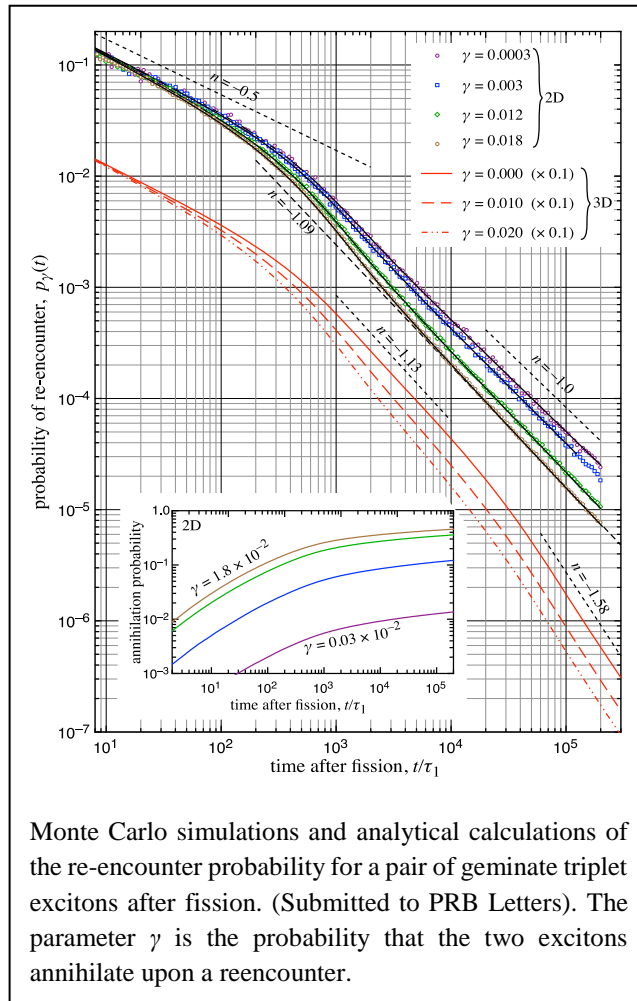
parameters that determine this probability are essentially only the average exciton hopping times along the crystallographic directions.

On the experimental side, we have been able to apply this random walk model to the geminate fluorescence dynamics in rubrene. This worked well in this material because in rubrene the main channel for triplet-triplet annihilation is via triplet fusion and subsequent photon emission [1]. From the dynamics of the geminate fluorescence we were then able investigate the time-scales over which triplet exciton transport undergoes transitions from being one-dimensional just after fission, two-dimensional a few nanoseconds later, and ultimately three-dimensional after microseconds.

The figure to the right shows some results of our modeling work, detailing the expected dynamics of the re-encounter probability, which determines the time-dependence of the overall annihilation probability as exciton diffusion progresses. The annihilation probability density has clearly identifiable power-law regimes with transitions from one to the other as the dimensionality of the triplet exciton transport changes with time from 1D, to 2D, to 3D.

Normally, the triplet excitons originating from fission will initially move in one dimension for a time determined by the average time it takes for an exciton to hop out of its original molecular column, and we show that the duration of the 1D regime is a key factor in determining fission efficiency (even if the annihilation probability for a single re-encounter— γ in the figure above—is low). This will be an important factor to consider for the development of materials with optimized exciton fission efficiency.

Our experimental tests in rubrene single crystals have confirmed the essential features of the model presented above. We used 513 nm, 150 fs excitation pulses at a low repetition rate of 5kHz to allow for a significant decay of the triplet exciton population between illumination pulses, and a low excitation density of the order of 10^{19} m^{-3} . This was necessary in order to guarantee that the fluorescence signal we were detecting was exclusively due to triplet fusion events between geminate pairs. We used time-correlated single photon counting, processing on average one photon per cycle and accumulating data over a few hours.

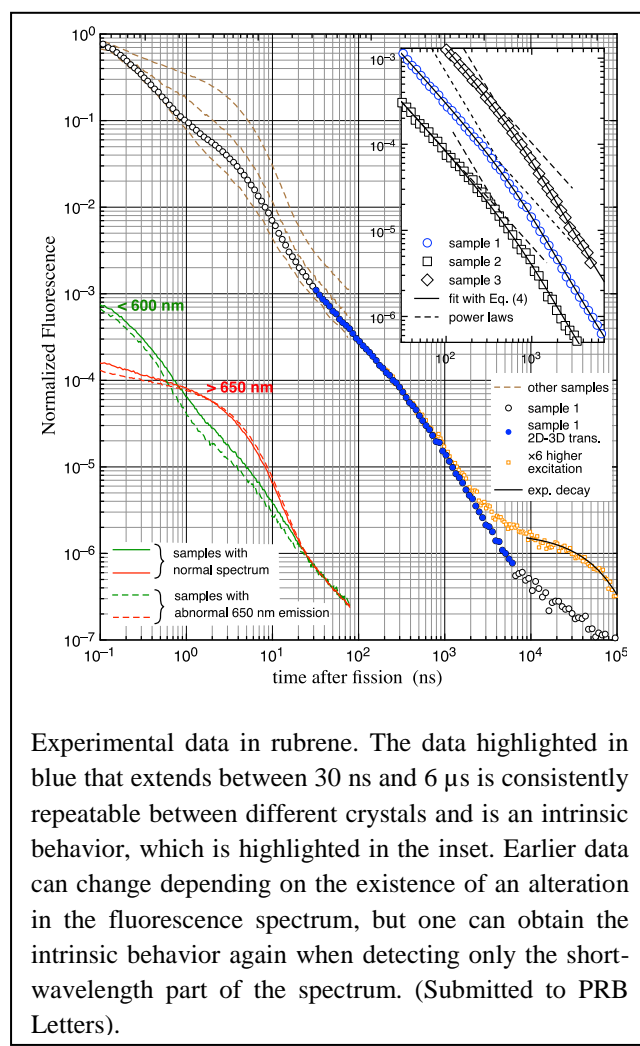


We found a sample-dependence that correlated to an alteration of the fluorescence spectrum of some samples, but it only existed in the initial time interval, up to 10-20 ns. At later times we observed a very consistent power law behavior where the exponent of the power law changed around 1 μ s after excitation, which we have been able to assign to a change in the dimensionality of transport from 2D diffusion to 3D diffusion. This change occurs in coincidence to the average hopping time of a triplet exciton in the lowest probability direction in the crystal, which can be determined from a theoretical fit to the data. One could argue that measuring the longest hopping time into the lowest mobility direction is somewhat academic, but the fact that it can be done demonstrates the viability of this method for characterizing triplet exciton transport in molecular crystals.

Both our theoretical analysis and experimental data, and the fact that the predicted behaviors are reproduced over several decades of time and intensity, show that the measurement of fluorescence dynamics in this geminate-fusion limit can be a valuable method to obtain information on the behavior of the triplet excitons after fission. We believe that we have now demonstrated that the photons emitted during geminate fusion can be effectively used as a probe of triplet exciton transport. While we demonstrated these ideas in rubrene, the sensitivity of single-photon counting means that the model and approach are applicable to any singlet-fission material in which triplet-triplet annihilation is accompanied by some probability of photon emission.

Future Plans

The work presented above opens the door to the general use of geminate-fusion fluorescence as an investigative tool to, *e.g.*, disentangle the effect of variations in the fusion probability and of variations in the triplet transport that determine the probability of re-encounter. Therefore, we plan to extend the use of this type of experiment to lower temperatures, and to also investigate the effect of a magnetic field.



But this project is in its early stages, and this is just one of the experimental tools that we plan to use. Future plans include continuing our excitation spectroscopy studies of singlet exciton fusion under different photoexcitation conditions. Our early results [2] have shown an unexpected dependence of fission time upon the photon energy used for photoexcitation. The observed change could be related either to the fact of exciting to higher vibrational levels, or to the presence of different triplet species, which could have affected our data because we were constrained in the choice of the wavelength used to probe the triplet population [2]. Our plan is now to change our detection scheme so that we can control both the excitation and the detection wavelength. We will do so in a transient grating configuration that allows for much flexibility in terms of being able to perform this singlet fission experiment in a low perturbation limit.

Finally, we are planning further experiments on the fluorescence quantum beats that can be observed in rubrene [3], their long lifetime, and how this relates to how the geminate pair evolves in the crystal lattice because of diffusion and hopping transport.

References

- [1] I. Biaggio, P. Irkhin, “Extremely efficient exciton fission and fusion and its dominant contribution to the photoluminescence yield in rubrene single crystals,” *Appl. Phys. Lett.* **103**(26), 263301 (2013).
- [2] D.M. Finton, E.A. Wolf, V.S. Zoutenbier, K.A. Ward, I. Biaggio, “Routes to singlet exciton fission in rubrene crystals and amorphous films,” *AIP Advances* **9** (9), 095027 (2019).
- [3] Eric A. Wolf, Drew M. Finton, Vincent Zoutenbier, Ivan Biaggio, “Quantum beats of a multiexciton state in rubrene single crystals,” *Appl. Phys. Lett.* **112**, 083301 (2018).

Publications

Eric A. Wolf and Ivan Biaggio, “Geminate Exciton Fusion Fluorescence to Probe Triplet Exciton Transport after Singlet Fission,” Submitted to *Phys. Rev. B Letters*, December 31, 2020.

Discovery of Goniopolar Metals with Zero-field Hall and Nernst Effects

Joseph P. Heremans, Ohio State University

Program Scope

This project is about discovering new goniopolar materials, a recently discovered [H19] genus of materials that simultaneously have *p*-type conduction along some crystallographic directions and *n*-type conduction along others (**Fig. 1**). Two classes of uniform materials show this behavior, metals or degenerately-doped semiconductors with a Fermi surface of a particular topology; and semiconductors with conduction (CB) and valence bands (VB) that have strongly anisotropic effective masses, and in which that anisotropy is different in the CB and VB. Besides uniform materials, layered composites can have similar behavior (labeled *pxn*) via an effective medium effect [G18]. In appropriately-cut goniopolar materials or layered composites, the electrical conductivity and thermopower tensors can have off-diagonal components. This confers to the samples properties like zero-field Nernst-Ettingshausen and Hall effects, relevant in many transport applications requiring the current in the sample to be at an angle vis-à-vis the applied electric field or thermal gradient. There are several examples of such applications. First, transverse thermoelectrics [G10] allow a complete thermoelectric (TE) generator or cooler to be fabricated from one material. This decreases the number of interfacial contacts in series with the TE material, and decreases the effects of contact resistances, bringing the device ZT much closer to the material zT. Transverse thermoelectric generators (TEGs) also avoid the need to have electrical contacts at high temperatures, greatly simplifying the metallurgical demands on the contacts. Second, single-crystal gyrators [V14] can be made from Hall plates or goniopolar materials. They are passive non-reciprocal circuit elements where the input current is connected to the output voltage and vice versa. The project is to analyze theoretically what material properties lead to goniopolarity, to synthesize, measure and optimize such materials for specific classes of applications, namely transverse thermoelectric devices (Nernst generators, Ettingshausen coolers) and gyrators.

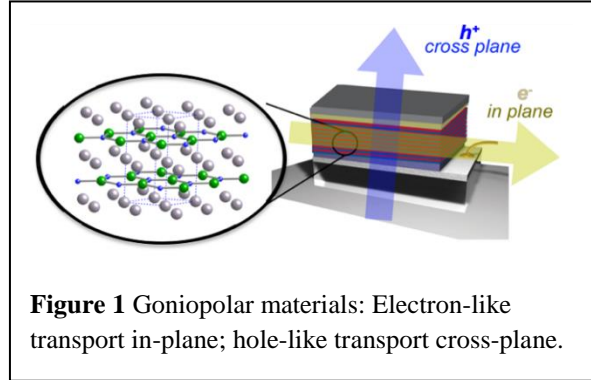


Figure 1 Goniopolar materials: Electron-like transport in-plane; hole-like transport cross-plane.

Recent Progress

During this first seven-month period, we have obtained three new results.

1. We demonstrated a zero-field Nernst effect in Re_4Si_7 that gives a transverse thermoelectric figure of merit $z_{xy}T \sim 0.7$, the highest ever achieved to date. We built a transverse TEG that demonstrates a thermal efficiency commensurate with the material $z_{xy}T$ measured.

The principal challenges in current TEGs are the losses associated with contact resistances and the need for highly stable diffusion-resistant semiconductor/metal contacts at the hot end.

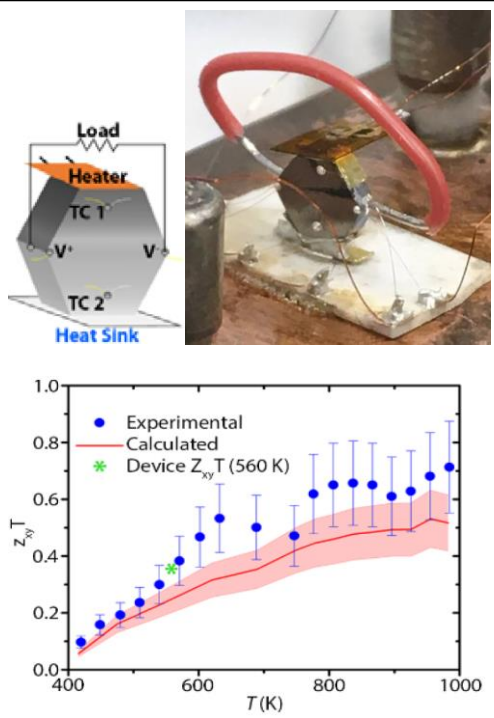


Figure 2. (top) Transverse thermoelectric generator (TEG) made from a Re_4Si_7 single crystal cut so that the heat flux forms an angle of 52° in the plane defined by the in-plane and cross-plane crystallographic directions. Thermocouples (TC) and voltage wires are shown. The load resistor of $90 \text{ m}\Omega$ is the constantan wire with red insulation. (bottom) Transverse figure of merit: the red lines are calculated from the materials parameter along the crystallographic axes; the blue dots are the material $Z_{xy}T$ derived from the measured zero-field Nernst voltage and the thermal and electrical conductivities. The green star is the device $Z_{xy}T$ derived from the measured thermal efficiency of the TEG. The agreement between $Z_{xy}T$ and $z_{xy}T$ is proof of the assertion that transverse TEGs have low parasitic losses due to contact resistances.

Transverse TEGs, in which a thermal gradient in a single material with two cold end contacts induces a perpendicular voltage, promise to overcome both problems. Transverse TEG's are constructed from a single slab of material, and do not require multiple *n* and *p* elements connected in series electrically, each with its own electrical and thermal contact resistance at both hot and cold end; the parasitic losses are thus much reduced, bringing the device $Z_{xy}T$ much closer to the material $z_{xy}T$. Having the electrical contacts at the cold end also eliminates the need for high-temperature stable contact metallurgy that are critical in conventional TEG's. However, the measured transverse thermoelectric efficiencies, $z_{xy}T$, have until now been far too low for practical implementation. The results from this study period show that single crystals of Re_4Si_7 , an air-stable, thermally robust, layered compound, have a $z_{xy}T$ of 0.7 ± 0.15 at 980 K , a value that is on par with existing commercial technologies today. Through a complete experimental investigation of the angle-dependent transport properties, we show that this excellent transverse thermoelectric performance is a consequence of the large, oppositely signed in-plane *p*-type and cross-plane *n*-type thermopowers. A combination of measurements, density functional theory calculations, and analytical models establish that these large anisotropic thermopowers arise from the population of the highly anisotropic VB and isotropic CB. We constructed a transverse TEG and tested its thermal efficiency on a load resistor (see Fig. 2 top). The device $Z_{xy}T$ was calculated from the

measured thermal efficiency, and found to be equal to the material $z_{xy}T$ (see Fig. 2 bottom), thus providing experimental proof for the statement made above about the role of contact resistance. Overall, this finding of an efficient, robust transverse thermoelectric single crystal will enable the exploration of unique devices for waste heat recovery and establishes how to identify other materials with this phenomenon. A manuscript is submitted.

2. We have identified, synthesized and measured a new class of goniopolar materials, NaSnAs (publication accepted in *Chemistry of Materials*, 2021). We calculated the layered semiconductor NaSnAs to have a lower electron m^* in-plane than cross-plane, and a very high hole m^* in-plane and low hole m^* cross-plane. We established the growth of >3 mm-sized NaSnAs crystals via Sn flux, and confirmed the band gap to be 0.65 eV, in agreement with theory. NaSnAs exhibits *p*-type thermopowers cross-plane and *n*-type thermopowers in-plane (Fig. 3), confirming that the large anisotropy in the effective mass at the band edges is an excellent indicator for axis-dependent conduction polarity. Overall, this work shows that the discovery of semiconductors with such a phenomenon can be accelerated by computationally evaluating the anisotropic curvatures of the band edges, paving the way for their future discovery and application

3. We developed a ferromagnet/semimetal MnBi/Bi composite in which the ferromagnet forms aligned needles in the Bi matrix (published in *Nanomaterials*). This first publication on this material describes the new metallurgical process to obtain precipitates of the hard ferromagnet MnBi in a Bi matrix. By performing an anneal in magnetic field, the MnBi forms needles that are aligned along the direction of the applied field (see photo Fig. 4). MnBi is a hexagonal crystal (NiAs structure). The precipitates are single crystals with their c-axis oriented along the length of the needles, and the c-axis is the magnetic easy axis at room temperature. The work further shows how the straight composite can be used to generate an extraordinarily large anomalous Nernst coefficient, by combining the spin-Seebeck effect due to the Bi/MnBi interfaces with the Nernst coefficient of Bi (see Fig. 5). In future work, the transport properties of that composite, cut diagonally and magnetized, is expected to show very large zero-field Hall and Nernst effects, based on the same principle as multilayer *pxn* materials.

Future Plans

Scientifically, the future plan mostly follows the plan in the proposal. The search of materials includes delafossites, starting with PdCoO₂ and PtCoO₂.and expanding to chromium-containing compounds, e.g. PdCrO₂. The work on layered intermetallics (e.g. NaSn₂As₂ [H19]

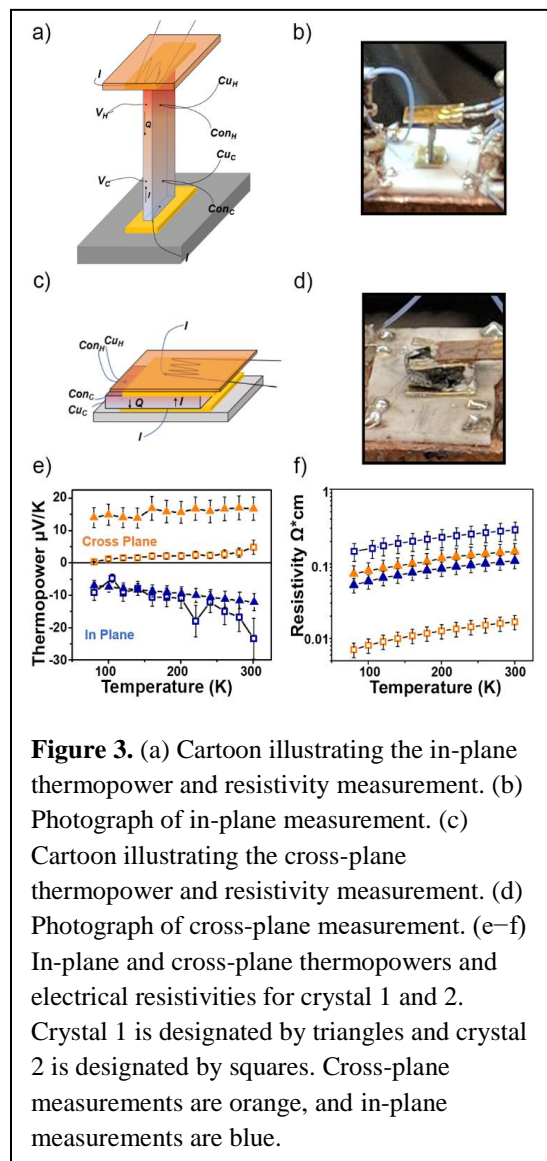


Figure 3. (a) Cartoon illustrating the in-plane thermopower and resistivity measurement. (b) Photograph of in-plane measurement. (c) Cartoon illustrating the cross-plane thermopower and resistivity measurement. (d) Photograph of cross-plane measurement. (e–f) In-plane and cross-plane thermopowers and electrical resistivities for crystal 1 and 2. Crystal 1 is designated by triangles and crystal 2 is designated by squares. Cross-plane measurements are orange, and in-plane measurements are blue.

and now NaSnAs) will continue, expanding to CaGaGe, Ti₂PTe₂, Zr₂PTe₂ and others. Third, we will expand the work on transition metal di-silicides (e.g. Re₄Si₇) to materials that contain no expensive elements like Re.

New opportunities have opened. First, we will investigate the theoretical possibility that by doping the semimetal bismuth p-type, one can obtain goniopolar behavior because the CB and VB of Bi have strong and different anisotropies. If true, p-type Bi would be a good candidate material for transverse cryogenic thermoelectric coolers. Higher figures of merit can probably be reached by alloying Sb in the Bi, lowering the lattice thermal conductivity and giving a field-induced Weyl band. With NSF funding (DMR-2011876), we identified the thermal chiral anomaly in undoped Bi₈₉Sb₁₁ [V21]. P-type doping will lead the chemical potential away from the Weyl points, and populate the trivial VB maximum. This will make the material goniopolar but with the CB a Weyl band in magnetic field, with hitherto unexplored effects.

The MnBi/Bi composites described above are also new. They combine a hard ferromagnet with the material, Bi, that has the highest spin-orbit coupling and an enormous Landé factor tensor (-75 along the trigonal direction). Skew-cut composites are expected to have giant zero-field Hall, Nernst and thermal Hall signals.

References

- [G10] H. J. Goldsmid, Thermoelectricity, Springer Verlag, Berlin (2010)
- [G18] M. Grayson, Q. Shao, B. Cui, Y. Tang, X. Yan, and C. Zhou, “Introduction to (p × n)-Type Transverse Thermoelectrics,” in Bringing Thermoelectricity into Reality, Patricia Aranguren, (ed.), Intech Open, (2018) [DOI: 10.5772/intechopen.78718].
- [H19] B. He & al. “The Fermi Surface Geometrical Origin of Axis-Dependent Conduction Polarity in Layered Materials,” *Nature Materials* **18**, 568-572 (2019).
- [V14] G. Viola and D. P. DiVincenzo, “Hall Effect Gyrotors and Circulators,” *Phys. Rev. X* **4**, 021019 (2014).
- [V21] D. Vu et al., “Thermal chiral anomaly in the magnetic-field induced ideal Weyl phase of Bi_{1-x}Sb_x topological insulators”, arXiv:1906.02248 *Nature Materials* (2021, accepted).

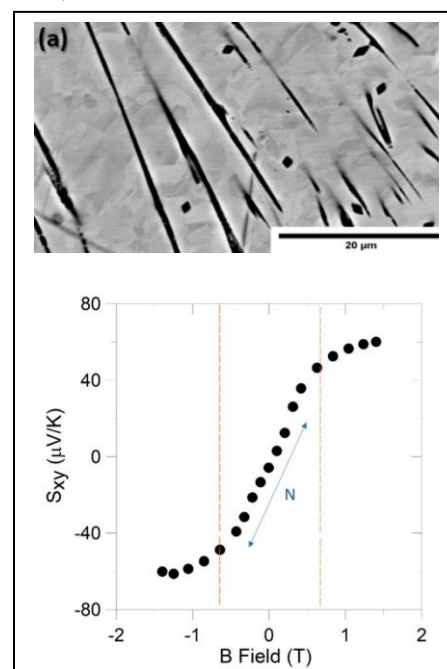


Figure 4. (a) Representative backscatter electron image of a Bi/BiMn composite with 1% MnBi. (b) The enormous anomalous Nernst coefficient at 80K of a 50% MnBi / 50% Bi composite, shown as function for field, is the sum of the spin-Seebeck effect at the Bi/MnBi interfaces and the Nernst coefficient of Bi.

Publications (7 months)

1. Wooten, Brandi L.; Vandaele, Koen; Boona, Stephen R., and Heremans, Joseph P. "Combining Spin-Seebeck and Nernst Effects in Aligned MnBi/Bi Composites", *Nanomaterials*, **10**:10 2083 (2020) DOI:10.3390/nano10102083
2. Ochs, Andrew; Gorai, Prashun; Wang, Yaxian; Scudder, Michael; Koster, Karl; Moore, Curtis; Stevanović, Vladan; Heremans, Joseph; Windl, Wolfgang; Toberer, Eric; Goldberger, Joshua, "Computationally-Guided Discovery of Axis-Dependent Conduction Polarity in NaSnAs Crystals", *Chemistry of Materials* (Accepted, Jan 8, 2021) DOI:10.1021/acs.chemmater.0c04030

Elucidating Chirality-induced Magnetism and Magnetoelectric Functionalities in Layered Chiral Hybrid Metal Halide Perovskites

Dali Sun, North Carolina State University

Program Scope

2D layered Hybrid Metal Halides (2D-HMHs) are a new class of synthetic semiconductors prepared by low-temperature solution processing with a large chemical and structural ‘universe’ benefiting from their synthetic versatility. By implanting chiral organic cations into the HMH superstructure, the 2D-chiral-HMH would simultaneously exhibit ferromagnetic, ferroelectric, and magnetoelectric functionalities stemming from a Chirality-Induced Spin Selectivity (CISS) effect that may not be subject to thermal fluctuations. The goal of this program is to elucidate the fundamental origins of chirality-induced magnetism via the CISS effect and their electrical tunability in 2D layered Hybrid Metal Halides material systems. To date, we focused our efforts on developing two ultrasensitive detection themes based on spin-orbitronics and magneto-optics to probe the CISS-induced magnetism and magnetoelectric functionalities in this hybrid material. Specific research activities include preparation and structural characterization of the chiral 2D-HMHs, development of the magneto-optical detection under light illumination, and theoretical modeling.

Recent Progress

Designing a novel magnetically ordered system at a low-dimensional limit beyond the current 2D layered magnets would offer an alternative route for understanding the 2D magnonic excitation and their rich interactions between microwave photons, optical photons, and phonons. The CISS effect, the unique ‘spin filtering’ effect arising from the chirality of low-cost non-magnetic organic materials and their assemblies that lack inversion symmetry, suggests a promising pathway to study the low-dimensional magnetism and their spin-wave excitation in a hybrid organic-inorganic quantum system.

Preparation, structural, optical, and magnetic characterization of the chiral 2D-HMH films: To study the emergent chirality-induced magnetism in the 2D layered HMH structure, here we firstly focus on studying the CISS-induced magnetism in R-/S-Methylphenethylamine lead iodide, R/S-(MePEA)₂PbI₄, one of the prototypical layered chiral HMH materials. The synthesis of chiral-HOIPs was performed following previously published protocols [1]. The chiral-HOIP thin film was spin-coated onto pre-cleaned Indium Tin Oxide (ITO) or SiO₂/Si substrates. An optimized thickness (~ 300nm) was chosen to maintain the homogeneity of the thin film which is crucial to enable forthcoming device characterizations. A top SiO₂ capping layer (100nm) has been deposited to prevent the 2D-HMH film from degradation. The scheme in Figure 1a depicts the layered structure of the HOIP and illustrates how the chiral S- or R- phenylethylammonium

(S/R-MePEA) ligands separate the lead halide octahedral layers. The orientation of the prepared thin film was examined by XRD as shown in Figure 1(b), indicating the layered structure with the c axis normal to the film plane. The chirality of the chiral-HOIP films originates from the implanted chiral organic ligands inserted between the inorganic layers, validated by circular dichroism spectrums as shown in Figure 1(c). The circular dichroism spectra of the HOIPs using S- (red, $(S\text{-MePEA})_2\text{PbI}_4$) and R- phenylethylammonium (black, $(R\text{-MePEA})_2\text{PbI}_4$) films exhibit an approximate mirror image symmetry spanning the 250 nm -500 nm wavelength range. The magnetic properties of the prepared chiral-HMH thin films and their single crystals have been studied using SQUID magnetometer. Due to the lack of magnetic elements in the molecular structure, no clear evidence of ferromagnetic ordering has been observed except for a pronounced paramagnetic background. The absence of magnetic hysteresis loops at low temperatures confirms our hypothesis that the CISS-induced net magnetization would be only activated upon external stimuli, as demonstrated below.

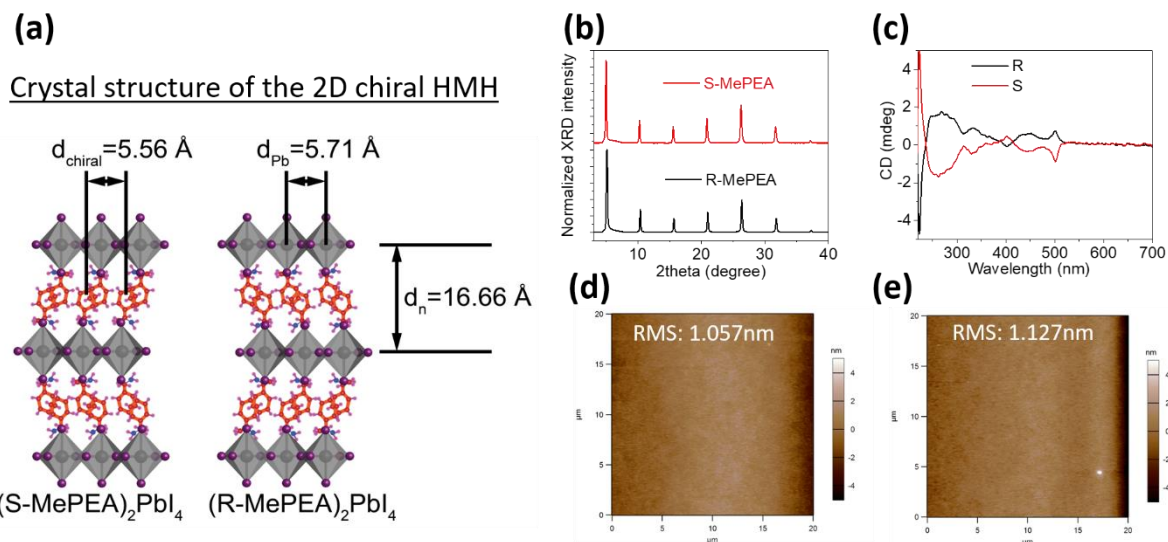


Figure 1. (a) Schematic molecular structures of 2D R(S)-(MePEA)₂PbI₄ in the current study. (b) and (c) show the measured XRD pattern and circular dichroism (CD) spectra in the prepared (R/S-MePEA)₂PbI₄ thin films. (d) and (e) show the obtained AFM images of these two films, respectively.

Sagnac magneto-optical detection of net magnetization induced by photocarriers in 2D chiral HMH/NiFe heterostructures: Collaborated with Prof. David Waldeck's group (University of Pittsburgh), we have shown the experimental observation of the CISS-induced spin (magnetic) signals in the 2D-chiral-HMH/ferromagnet interface under photoexcitation using an ultrasensitive magneto-optical Kerr effect (MOKE) detection scheme called a Sagnac interferometer [2]. Compared to the conventional steady-state MOKE tool that has a Kerr rotation angle resolution of microRadians, a modified fiber Sagnac interferometer is employed based on the design conceived by J. Xia et al [2] with dramatically enhanced sensitivity. It is therefore reasonable that such a non-invasive spatially resolved Sagnac MOKE approach can locally probe the CISS-induced magnetic signals at the molecular level, providing a direct readout to monitor and convert light signals into a magnetic response.

Under light illumination, photo-excited charge carriers become spin-polarized by the CISS effect as they propagate through the chiral cations in the structure [3]. The direction of spin polarization is determined by the chirality, resulting in a change of local magnetization at the 2D-chiralHMH/ferromagnet interface [see Fig. 2(a), Ref. 3]. The sample area was illuminated through the transparent ITO substrate by 405 nm light from a diode laser. At this wavelength, the CD signal is most pronounced as shown in Figure 2(b), implying an efficient CISS process when the photocarriers transmit through the chiral molecules. The sample was illuminated at a low laser intensity (≤ 0.6 mW) to suppress laser-induced heating. Figure 2(c) shows the successful observation of light-driven CISS-induced magnetism in the 2D-chiralHMH/NiFe bilayer detected by Sagnac MOKE [3]. By applying a positive out-of-plane magnetic field ($B_z: +210$ mT), the Kerr signal in the ITO/(S-PEA)₂PbI₄/NiFe sample shows a decrease in the order of microRadians ($\Delta\theta_{\text{Kerr}} \approx -0.8$ μrad), supporting our statement that an ultrasensitive detection tool is required to probe this Kerr signal. In contrast, the R-chiral-HMH sample exhibits a surprising increase of the Kerr signal under the same illumination. By reversing the magnetic field, the sign of $\Delta\theta_{\text{Kerr}}$ is inverted depending on the chirality, mimicking the nature of magnetization in typical ferromagnets.

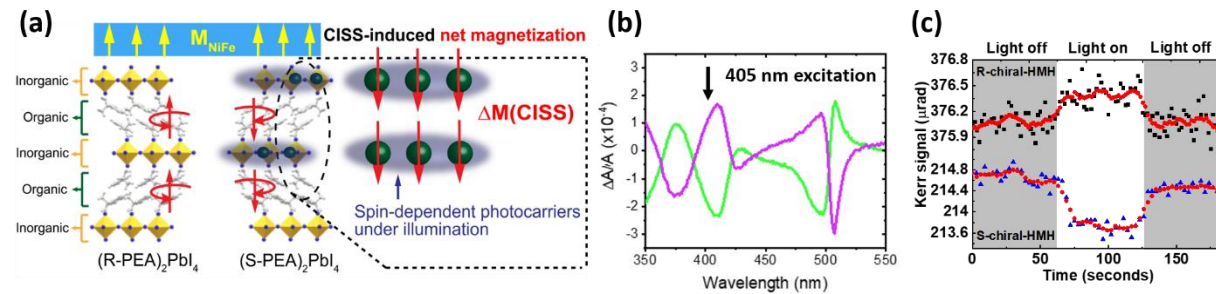


Figure 2. (a) Schematic illustration of the proposed photoinduced magnetism at the ferromagnet/chiral-HOIP interface. The generation of a net magnetization mediated by spin-dependent photocarriers via the CISS effect is formed in the chiral-HMH structure next to the NiFe layer under the light illumination. (b) Measured typical CD spectra for S-HOIP (green) and R-HOIP (purple) thin films. (c) Time trace of measured Kerr (t) signal upon the illumination in the S- and R-chiral-HMH/NiFe heterostructure, respectively. The red line is an adjacent average smoothing of the data. Taken from Ref. [3,4].

DFT calculations and theory modeling: Collaborate with Prof. Feng Liu's group (University of Utah), we have shown the electrical dipole moment of R(S)-PEA to be ~ 1.575 Debye, as indicated by the molecular electronic potential distribution, which provides one factor contributing to the spin-selective molecular adsorption, i.e., circular dichroism (CD) [3]. However, the HOMO-LUMO gaps of R- and S-PEA are 6.12 and 5.85 eV, respectively, which is much bigger than the laser energy used (405 nm). Therefore, the magnetic dipole moment that can only arise upon photoexcitation is absent, such that no CD effect is expected from the chiral molecules alone, nor the net contribution via the CISS effect. Thus, we hypothesize that the inorganic perovskite framework in combination with the chiral molecules is necessary to account for the observed photoinduced magnetism via the CISS effect. It is possible that the CISS effect in chiral-HOIPs not only generates spin-polarized current, but also forms 'local' magnetic states

which may be coupled or mediated by polarons or delocalized carriers that are formed in the metal–halogen framework under photoexcitation. We anticipate that the generation of carriers/polarons is crucial in determining the amplitude of the CISS effect, exchange couplings, and resulting interfacial magnetization, which requires further studies to understand sufficiently.

Future Plans

The goal of future work is to perform temperature and field orientation dependent magnetotransport and magneto-optical studies of the prepared 2D chiral HMH films interfaced with ferromagnet and nonmagnetic materials. We plan to conduct the Sagnac MOKE measurement in the ferromagnet/2D-HMH heterostructure as a function of laser wavelength to test whether the generated magnetization signal matches the change in the measured CD spectra. This will help to unravel rich synergistic effects from the junction of quantum chemistry, materials design, spintronics, and emergent chiral magnetism. We anticipate launching a promising testbed to encompass a variety of chiral-HMHs for multiferroic spintronic studies. These tools, and the HMH materials characterized within, are expected to impact other research areas where HMHs are being explored, such as spin-optoelectronics and Terahertz emission, etc.

References

- [1] “A Layered Hybrid Perovskite Solar-Cell Absorber with Enhanced Moisture Stability” I. C. Smith, E. T. Hoke, D. Solis-Ibarra, and M. D. McGehee, H. I. Karunadasa, *Angewandte Chemie*, 126 (42), 11414–11417 (2014). <https://doi.org/10.1002/anie.201406466>
- [2] “Modified Sagnac interferometer for high-sensitivity magneto-optic measurements at cryogenic temperatures”. J. Xia, P. T. Beyersdorf, M. M. Fejer, and A. Kapitulnik, *Applied Physics Letters* 89, 62508 (2006). <https://doi.org/10.1063/1.2336620>
- [3] “Magneto-Optical Detection of Photoinduced Magnetism via Chirality-Induced Spin Selectivity in 2D Chiral Hybrid Organic–Inorganic Perovskites”. Z. Huang, B. P. Bloom, X. Ni, Z. N. Georgieva, M. Marciesky, E. Vetter, F. Liu, D. H. Waldeck, and D. Sun, *ACS Nano* 14, 10370–10375 (2020). <https://doi.org/10.1021/acsnano.0c04017>
- [4] “Quantum engineering with hybrid magnonics systems and materials”. D. D. Awschalom, C. H. R. Du, R. He, F. J. Heremans, A. Hoffmann, J. T. Hou, H. Kurebayashi, Y. Li, L. Liu, V. Novosad, J. Sklenar, S. E. Sullivan, D. Sun, H. Tang, V. Tiberkevich, C. Trevillian, A. W. Tsai, L. R. Weiss, W. Zhang, X. Zhang, L. Zhao, C. W. Zollitsch. “Quantum engineering with hybrid magnonics systems and materials”. *IEEE Transactions on Quantum Engineering* (In press). <https://arxiv.org/abs/2102.03222>

Publications

There are no publications to report because this is a new award with a start date of Sep. 1, 2020.

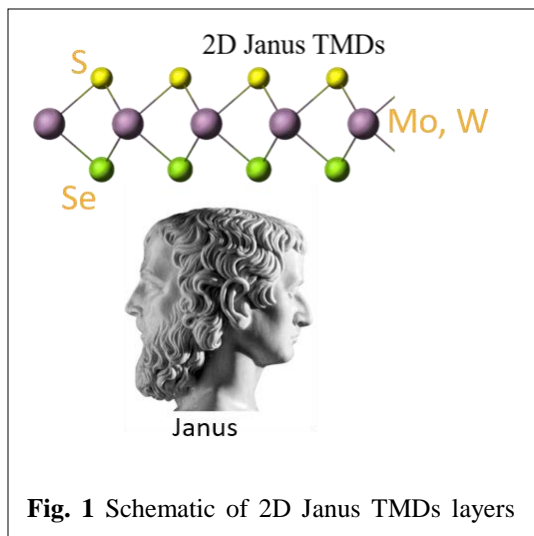
The synthesis 2D Janus vdW crystals and novel quantum phenomena arising from mirror-symmetry breaking

Associate Prof. Dr. Sefaattin Tongay

Materials Science and Engineering, Arizona State University, Tempe, AZ, USA

Program Scope (Year 1)

Named after the two-faced Roman god, Janus crystals are a new class of two-dimensional (2D) quantum materials that contain different atoms on each face, breaking their mirror symmetry.



It is well known that broken symmetry can change the physical behavior of 2D solids. To date, broken inversion symmetry has already led to the discovery of many novel quantum properties. Now the question arises, what new quantum phenomena could be realized when mirror symmetry, the last degree of freedom, is broken in these 2D Janus layers? This remains an unanswered question. Theory suggests that broken mirror symmetry induces a colossal intrinsic vertical polarization field and could show high T_c ferromagnetic order, giant Rashba splitting, and exotic excitonic phases and valleytronic physics. This is just the tip-of-the-iceberg and many exciting quantum effects are waiting to be discovered. However, due to

limitations in sample preparation, there are no experimental studies to date.

Considering these opportunities, the **objective** of this proposal is to discover, investigate, and establish a fundamental understanding of the electronic, excitonic, and magnetic phenomena arising from the strong polarization field and broken mirror-symmetry in 2D Janus transition metal dichalcogenides (TMDs) and their vdW junctions. This will be accomplished in three tasks, outlined below;

Task 1: Synthesize a variety of new epitaxial grade 2D excitonic and magnetic Janus TMDs layers for the first time and establish their excitonic properties in the 2D limit.

Task 2: Probe the excitonic interactions in 2D Janus vdW junctions under different polarization architecture, polarization strength, stacking order, and interlayer inaction strength (high pressure).

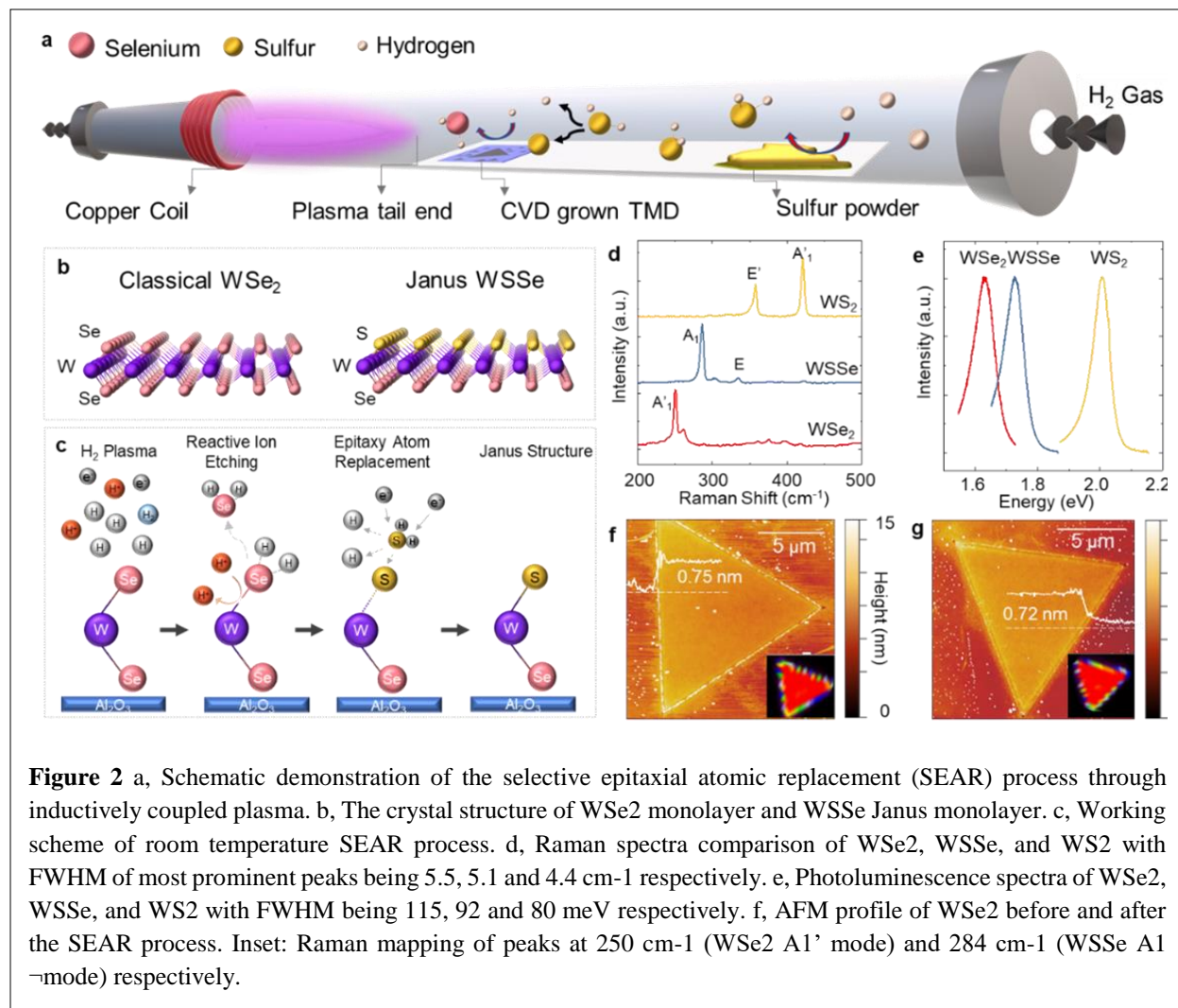
Task 3: Shed the first light on polarization induced Rashba splitting, magnetism, and skyrmion formation mechanisms in 2D Janus layers.

Recent Progress

Within the **first year** of this DOE-BES project, we have mainly focused on Task 1 and Task 2 activities. Within Task 1, we have successfully synthesized 2D Janus TMDs and introduced completely a new technique in the literature for the first time. We have focused on establishing their emergent excitonic behavior (excitonic series, exciton binding, dipolar-dipolar excitons, and lifetimes) in 2D Janus MoSSe and WSSe samples. These studies have resulted in 7 publications and 1 manuscript submission.

World's first large area synthesis of 2D Janus crystals

Named after the two-faced Roman god, Janus crystals are a new class of two-dimensional (2D) materials that contain different atoms/composition on each side of their unit cell and thus break the mirror symmetry (Fig. 2 above) Due to the large electronegativity difference across their unit-cells, these materials are expected to host substantial vertical polarization fields. Considering the discoveries made by the effects of electric field and broken crystal symmetry in the past, there is significant scientific interest in these materials.



Despite these exciting theoretical predictions, there are limited experimental studies to date, mainly due to the challenges in 2D Janus synthesis, sample preparation, and limited material quality. The prime difficulty presented in the synthesis of these Janus materials is that they are thermodynamically unstable in their bulk form, except for the BiTeI family. While the creation of thermodynamically stable 2D alloys is easier, Janus layers, unlike their alloy counterparts, must be produced at unit cell level with atomic precision.

In our project, we have accomplished the room temperature synthesis method of 2D Janus transition metal dichalcogenides (TMDs) and the **vertical** and **lateral** heterostructures of these 2D Janus TMDs by a Selective Epitaxy Atomic Replacement (SEAR) process. The growth starts with chemical vapor deposited (CVD) MSe₂ (M = W, Mo), and the operation relies on the formation of selenium vacancies (VSe) by hydrogen radicals created through inductively coupled plasma (ICP), and substitution by sulfur atoms in the presence of low-energy reactive sulfur radicals. The present technique differs in that the replacement process is driven kinetically not thermally: the chalcogen vacancies are created and low energy chalcogen radicals are utilized to decorate different chalcogen atoms on the surface to form 2D Janus layers. Some of our exciting datasets are listed below in figure 2.

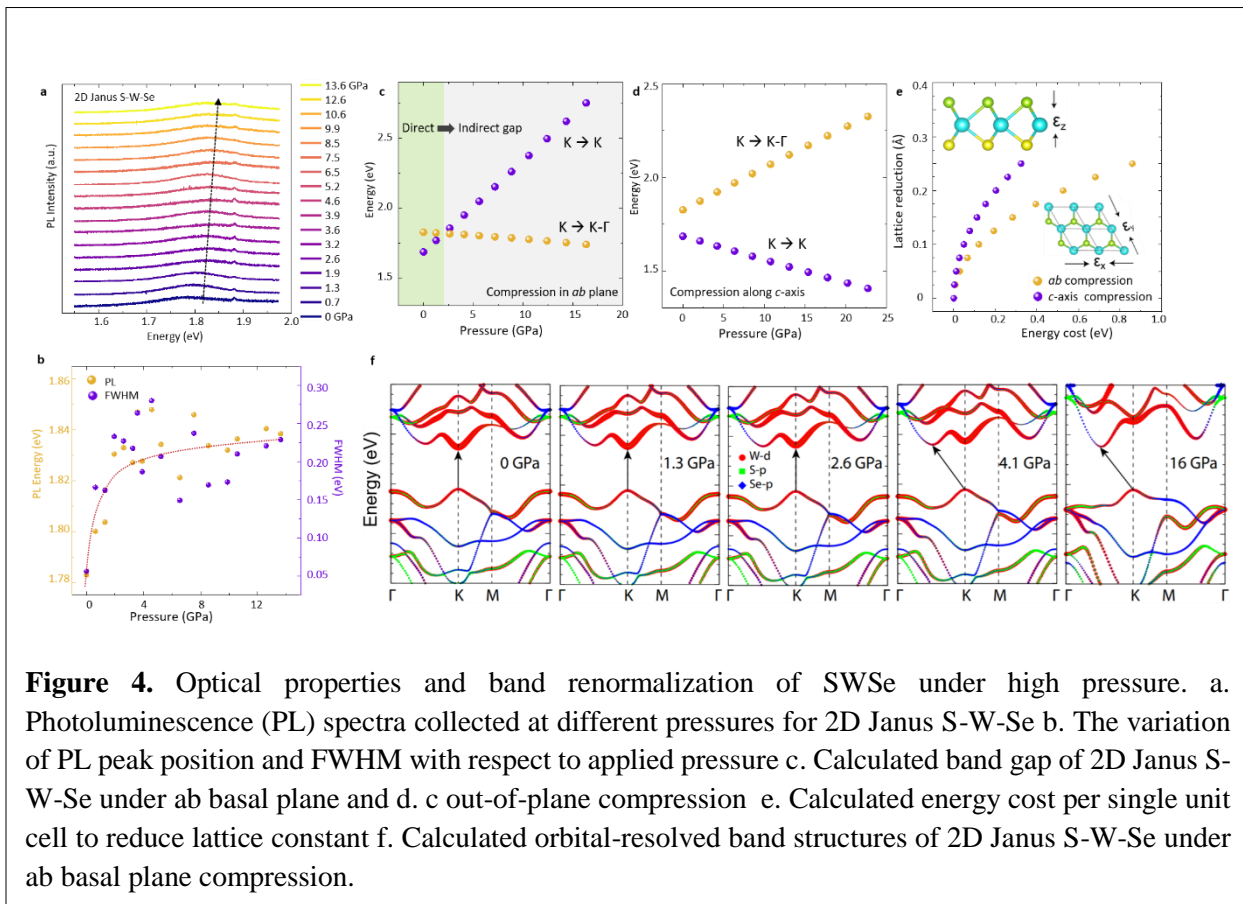
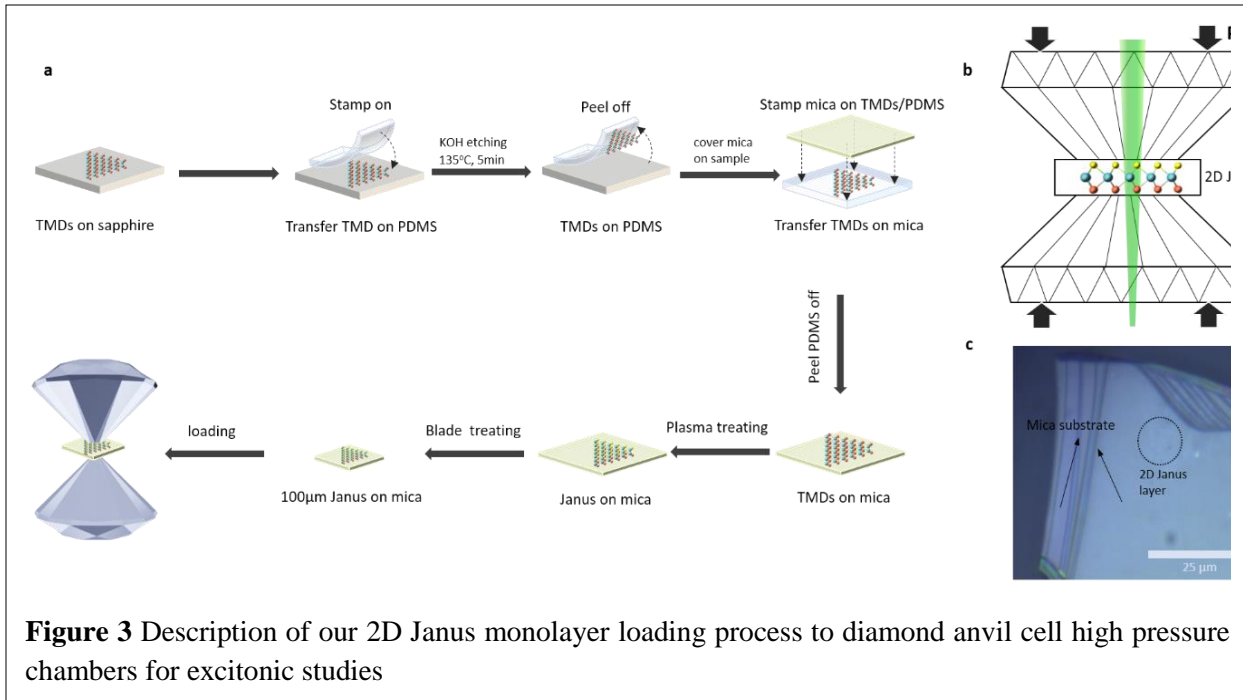
Work based on: Room-Temperature Synthesis of 2D Janus Crystals and their Heterostructures

Dipesh B Trivedi, Guven Turgut, Ying Qin, Mohammed Y Sayyad, Debarati Hajra, Madeleine Howell, Lei Liu, Sijie Yang, Naim Hossain Patoary, Han Li, Marko M Petrić, Moritz Meyer, Malte Kremser, Matteo Barbone, Giancarlo Soavi, Andreas V Stier, Kai Müller, Shize Yang, Ivan Sanchez Esqueda, Houlong Zhuang, Jonathan J Finley, Sefaattin Tongay;
Advanced Materials, 2006320 (2020) In press

Unusual excitonic behavior in 2D Janus layers under extreme pressures

With our established growth techniques, we were able to collect the very first datasets on these 2D Janus systems. This includes high-pressure studies which offer a unique way to probe the material behavior when lattice constant is varied by the applied pressure in diamond anvil cell (DAC). While there are a few high-pressure studies on bulk, few-layered, and monolayer thick classical TMDs, the behavior of 2D Janus layers under pressure is not established due to difficulties in sample preparation and integration with the DAC chamber.

Based on our established knowledge on DAC technologies, we have marked the first high-pressure studies in 2D Janus S-Mo-Se and S-W-Se monolayers from 0 up to 15 GPa. In our studies, we find that the induced colossal field creates added difficulties in transferring 2D Janus layers into only 500 µm culet size DAC. Thus, it was imperative to adopt two-step fabrication techniques inspired by studies on classical TMDs. In this method, classical TMDs are synthesized and transferred onto 2D mica templates using dry-polymer assisted technique, next converted to 2D Janus monolayers, and lastly, 2D Janus/mica heterolayers were transferred into our DAC chamber. In-situ Raman and photoluminescence (PL) spectroscopy techniques were used to investigate their vibrational and optical properties under high pressures. Our experimental and theoretical findings revealed unique excitonic and vibrational responses from 2D Janus layers at high pressures and offer fundamental insights to these material systems. Some of the exciting datasets are below below



Work based on: Anomalous Behavior of 2D Janus Excitonic Layers under Extreme Pressures

Han Li Ying Qin Byeongkwan Ko Dipesh B. Trivedi Debarati Hajra Mohammed Yasir Sayyad Lei Liu Sang-Heon Shim Houlong Zhuang Sefaattin Tongay

Advanced Materials DOI:10.1002/adma.202002401 (2020)

Future Plans

Currently, the team is working towards the following goals;

In-situ synthesis of CVD and exfoliated Janus dichalcogenide materials: My team is currently developing new in-situ Jansu conversion technique that allows us to collect spectroscopic data during the course of the growth process. This will allow us to yield excitonic quality Janus layers to take aggressive directions towards the excitonic physics of 2D Janus materials. In parallel, we will take steps towards converting exfoliated monolayers into Janus crystals to eliminate defects that are commonly found in CVD samples. This will also enable us to eliminate bound exciton emissions arising from point defects (vacancies) and probe the neutral excitons more clearly.

Excitonic physics of 2D Janus layers. Once in-situ growth methods are established, the team will take steps to probe excitonic properties of 2D Janus dichalcogenides and make comparison to their classical counterparts. We will probe the exciton levels, exciton wavefunction size, exciton lifetime, and excitons valleytronic response in the presence of colossal Janus fields present in 2D Janus layers.

2D Magnetic Janus layers and Skyrmionic physics. Our team is currently in the process to access 2D Janus layers if dihalides and triahlides. Once the growth strategy of these 2D magnet systems and 2D Janus magnetic layers are established, we will investigate the effect of colossal Janus field on the formation of Skyrmiions, change in the Tc, and magnetic ordering. Our focus systems will be NiI₂, NiBr₂, and 2D Janus NiBrI systems.

Resulting Publications

1. Imaging moiré flat bands in three-dimensional reconstructed WSe₂/WS₂ superlattices
Hongyuan Li, Shaowei Li, Mit H Naik, Jingxu Xie, Xinyu Li, Jiayin Wang, Emma Regan, Danqing Wang, Wenyu Zhao, Sihan Zhao, Salman Kahn, Kentaro Yumigeta, Mark Blei, Takashi Taniguchi, Kenji Watanabe, Sefaattin Tongay, Alex Zettl, Steven G Louie, Feng Wang, Michael F Crommie
Nature Materials, 2021 <https://doi.org/10.1038/s41563-021-00923-6>
2. Room-Temperature Synthesis of 2D Janus Crystals and their Heterostructures
Dipesh B Trivedi, Guven Turgut, Ying Qin, Mohammed Y Sayyad, Debarati Hajra, Madeleine Howell, Lei Liu, Sijie Yang, Naim Hossain Patoary, Han Li, Marko M Petrić, Moritz Meyer, Malte Kremser, Matteo Barbone, Giancarlo Soavi, Andreas V Stier, Kai Müller, Shize Yang, Ivan Sanchez Esqueda, Houlong Zhuang, Jonathan J Finley, Sefaattin Tongay; **Advanced Materials**, 2006320 (2020) In press

3. Epitaxial Synthesis of Highly Oriented 2D Janus Rashba Semiconductor BiTeCl and BiTeBr Layers
Debarati Hajra, Renee Sailus, Mark Blei, Kentaro Yumigeta, Yuxia Shen, Sefaattin Tongay
ACS Nano DOI:10.1021/acsnano.0c06434 (2020)
4. Anomalous Behavior of 2D Janus Excitonic Layers under Extreme Pressures
Han Li Ying Qin Byeongkwan Ko Dipesh B. Trivedi Debarati Hajra Mohammed Yasir Sayyad Lei Liu Sang-Heon Shim Houlong Zhuang Sefaattin Tongay
Advanced Materials DOI:10.1002/adma.202002401 (2020)
5. "Nanoscale Conductivity Imaging of Correlated Electronic States in WSe₂/WS₂ Moire Superlattices"; Zhaodong Chu, Emma C Regan, Xuejian Ma, Danqing Wang, Zifan Xu, M. Iqbal Bakti Utama, Kentaro Yumigeta, Mark Blei, Kenji Watanabe, Takashi Taniguchi, Sefaattin Tongay, Feng Wang, Keji Lai
Phys. Rev. Lett. 125, 186803 (2020)
6. "Harnessing biological applications of quantum materials: opportunities and precautions"; Mani Modayil Korah, Tejaswi Nori, Sefaattin Tongay, and Matthew D. Green
J. Mater. Chem. C, 2020,8, 10498-10525 (2020)
7. "Anisotropic band structure of TiS₃ nanoribbon revealed by polarized photocurrent spectroscopy"; Zhen Lian, Zeyu Jiang, Tianmeng Wang, Mark Blei, Ying Qin, Morris Washington, Toh-Ming Lu, Sefaattin Tongay, Shengbai Zhang, and Su-Fei Shi
Appl. Phys. Lett. 117, 073101 (2020)
8. "Manipulation of room-temperature valley-coherent exciton-polaritons in atomically thin crystals by real and artificial magnetic fields" Christoph Rupprecht, Evgeny Sedov, Martin Klaas, Heiko Knopf, Mark Blei, Nils Lundt, Sefaattin Tongay, Takashi Taniguchi, Kenji Watanabe, and Ulrike Schulz
2D Materials 7 035025 (2020)
9. The Raman Spectrum of Janus Transition Metal Dichalcogenide Monolayers WS₂ and MoS₂
Marko M. Petrić, Malte Kremser, Matteo Barbone, Ying Qin, Yasir Sayyad, Yuxia Shen, Sefaattin Tongay, Jonathan J. Finley, Andrés R. Botello-Méndez, Kai Müller
Phys. Rev. B 103, 035414 (2021)

Session VII

Physical Chemistry of Inorganic Nanostructures

A. Paul Alivisatos, Department of Chemistry, UC Berkeley; Materials Sciences Division, Lawrence Berkeley National Laboratory

Peidong Yang, Department of Chemistry, UC Berkeley; Materials Sciences Division, Lawrence Berkeley National Laboratory

Stephen R. Leone, Department of Chemistry, UC Berkeley; Materials Sciences Division, Lawrence Berkeley National Laboratory

Eran Rabani, Department of Chemistry, UC Berkeley; Materials Sciences Division, Lawrence Berkeley National Laboratory

David T. Limmer, Department of Chemistry, UC Berkeley; Materials Sciences Division, Lawrence Berkeley National Laboratory

Program Scope

The properties of inorganic nanostructures depend critically on the structures of individual nanoscale building blocks as well as their assembled superstructures. The controlled synthesis, advanced structural characterization, and theoretical modeling of optical and electronic properties of inorganic semiconductor nanostructures will enable the design and control of nanoscale energy conversion systems with great precision. Herein, our program focuses on three interconnecting themes: 1) rationalized synthesis and assembly of colloidal nanoscale building blocks, 2) *in situ* observation of structural dynamics and transformations, and 3) excited state dynamics of inorganic nanostructures and the development of new spectroscopic methods. With the three efforts combined, we aim to develop a holistic understanding that both imparts fundamental knowledge of inorganic nanostructures and guides the design of their advanced applications.

Recent Progress

1. Rationalized Synthesis and Assembly of Nanoscale Building Blocks: Rationalized synthesis and assembly of nanoscale building blocks are key to tailoring nanomaterials for applications. High-throughput synthesis offers a unique opportunity for understanding the reaction networks using a data-driven approach with the aim of achieving rationalized synthesis of nanocrystals. We explored the synthesis space of cesium lead bromide perovskite species using a robotic high-throughput synthesis and characterization platform. Machine learning algorithm was deployed to de-convolute the absorption spectra of multiple lead-containing species and obtain their relative concentrations. This combined approach has allowed us to create a map of the cesium lead bromide perovskite synthesis space (Figure 1), which elucidates the interconversion between various distinct species.¹ By parameterizing a chemical model to reproduce this map using machine-learning algorithms, we can reveal the best routes for reaching synthesis targets.

In addition to the synthesis of building blocks, we aim to understand and engineer the interactions between nanoparticles and rationalize the design of nanocrystal assemblies. Using *in situ* TEM, we illuminated the annealing and defects removal pathways of assembled CdSe QDs.² Knowledge of such pathways has allowed us to design and synthesize atomically attached QD superlattices with precise control of crystallographic alignment and long-range translational order, opening the door to a new dimension of control in engineering the properties of nanoscale materials.³ The synthetic diversity and flexible assembly of perovskite building blocks have brought new opportunities and challenges on the nanoscale control and manipulation of colloidal nanocrystals. We have harnessed the synthetic control of CsPbBr₃ to produce uniform size distribution of 0D QDs, 1D nanowires,⁴ and 2D nanoplates.⁵ Their self-assembly processes were probed *in situ* with optical spectroscopy and synchrotron small-angle x-ray scattering technique.

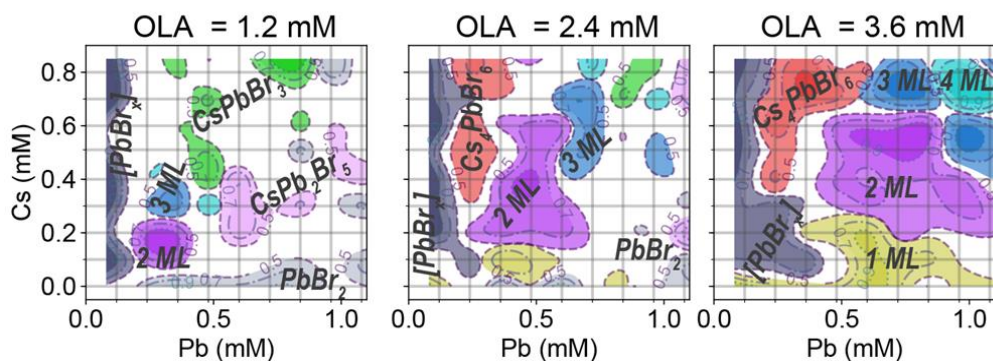


Figure 1. Example maps for the synthesis space of cesium lead bromide perovskite species.

2. *In situ* Observation of Nanoscale Structural Transformation: Observing the structural transformation and dynamics of semiconductors under different environmental conditions can greatly enhance our prediction and control of their physical behaviors. In this program, *in situ* techniques were utilized to tackle the structural transformation with not only high spatial resolution, but also high time resolution.

The halide perovskite materials with soft ionic lattices have a library of structural polymorphs. However, the transformation kinetics and mechanism among different species are difficult to probe directly by electron microscopy due to the fragility of perovskite under electron bombardment. Recently, direct, non-invasive imaging techniques such as photoluminescence (PL) microscopy,⁶ cathodoluminescence (CL) microscopy, and high-pressure Raman spectroscopy were utilized to probe the structural transformation of halide perovskite nanostructures. In particular, through *in situ* dynamic CL imaging and multiscale modeling of the LT-CsPbIBr₂ to HT-CsPbIBr₂ structural phase transition, we have uncovered the mechanism in which liquid-like interface mediates structural transformation in cesium lead halides (Figure 2).⁷ The liquid-like dynamics arise from the low cohesive energy of their ionic bonds, in sharp contrast to traditional covalent semiconductors such as CdSe. The phase transition of charge-ordered halide perovskite Cs₂In(I)In(III)Cl₆ was another demonstration of the importance of the reconfigurable halide

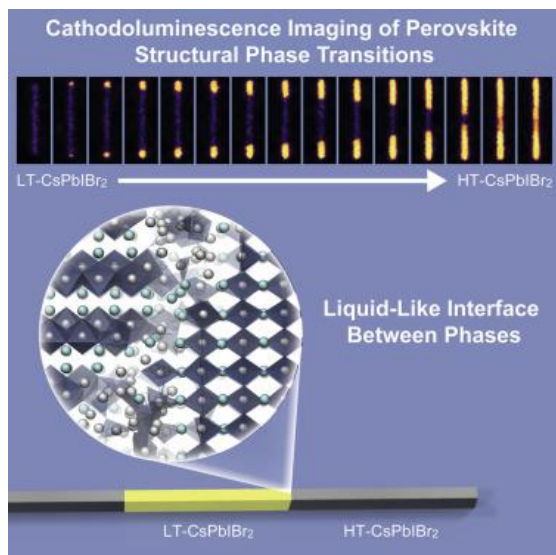


Figure 2. Phase transition modulated by the liquid-like interface between halide perovskite lattices.

we have recently crossed the threshold of investigating the etching dynamics of semiconductor colloidal nanocrystals such as PbSe and CdSe QDs. Preliminary results revealed that the etching trajectories depend on the faceting conditions of these nanocrystals. Extensive studies of structure-property relationships in II-VI semiconducting nanostructures conducted within this program can inform the identification of the most suitable candidates for single particle *in situ* etching studies, which often yield valuable insights into the inverse process of growth. In addition to the graphene encapsulation, carbon nanotubes as a reaction tube were also utilized in TEM experiments to visualize the structural dynamics of halide perovskite with atomic spatial resolution and high temporal resolution.

3. Excited State Dynamics of Inorganic Nanostructures:

Thin film and nanoscale junctions have driven recent progress across the photovoltaic and photoelectrochemical fields. However, the transport in nanoscale junctions is still measured as a bulk-averaged quantity by measuring the transport or kinetics across an entire junction. In this program, we developed a transient extreme ultraviolet (XUV) technique for measuring the layer-specific carrier transport simultaneously in each layer of a junction. We first developed a theoretical model which extracts detailed carrier and lattice dynamics from the Si L_{2,3} edge.⁹ The carrier population and temperature, as well as the excited state lattice deformations (optical and acoustic phonons), are obtained in a single measurement, and their scattering processes are compared over time following excitation into different valleys in the Si band structure.¹⁰ The insight gained from these studies allowed us

perovskite nanostructures.⁸ This charge disproportioned material is a semiconductor at ambient condition, but behaves like metal under high pressure. The In-based charge-ordered structure may provide a platform for future discovery of exotic electronic phenomena such as high-TC superconductivity in halide perovskite compounds.

With the advancement of liquid-cell transmission electron microscopy (TEM) technique, we are probing the structural and chemical dynamics of colloidal nanocrystals with high spatial resolution. We have developed new methods to introduce user-defined chemical potentials in graphene liquid cells with redox additives. This approach has allowed us to regulate the etching dynamics of noble metals. Furthermore,

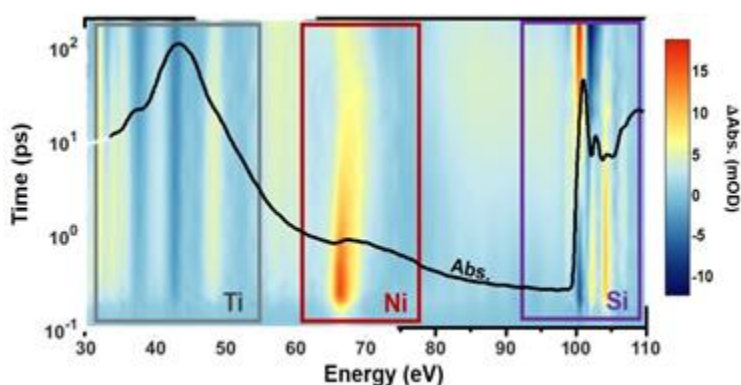


Figure 3. The XUV ground state spectrum (black line) and the transient XUV spectrum (colormap) of the Si-TiO₂-Ni junction, with the energy region of each elemental edge labeled. The transient spectrum is shown in a logarithmic time axis for visual clarity.

to address the debated case of how hole transport occurs in the amorphous oxide layer of a metal-oxide-semiconductor junction (Figure 3).¹¹ The photoexcited holes on Si are measured to tunnel rapidly through the TiO₂ to the Ni while the photoexcited electrons on Si do not transport. Our findings represent the first element-specific, all-optical, ultrafast quantification of the hole dynamics in a multi-layer nanoscale junction, advancing the element-specific technique of XUV spectroscopy.

The excitonic and charge transfer dynamics of semiconductor nanostructures were also investigated using a combination of visible wavelength transient absorption (TA) spectroscopy, classical simulation and quantum dynamical theory. We have achieved the transfer of multiple holes (~3) from multi-excitonic II-VI QDs to customized molecular acceptors.¹² A broad photo-induced absorption feature, assigned based on atomistic modeling to surface trapped holes,¹³ revealed stark differences between the surface trap states on native QDs and those on QDs modified with molecular acceptors. Modeling of the TA data shows that a reservoir of long-lived trapped holes on surface-modified QDs may continue to transfer to molecular acceptors over a timescale significantly beyond the Auger recombination lifetime, increasing the transfer efficiency. In a related study, TA was used to characterize the phonon dephasing process in Ruddlesden-Popper layered lead halide perovskites, which couples strongly to excitonic dynamics and hence influences charge carrier lifetimes. It was found that the choice of organic cation to separate the lead halide sheets has a strong effect on dephasing rates: flexible alkyl-amines give faster dephasing than aryl amines, with a smaller temperature dependence. Atomistic classical simulations of the two materials suggest that dephasing is driven largely by anharmonic coupling of optical modes in the ligand and lead halide layers, particularly significant for flexible alkyl groups with high dynamic disorder. This work lays the foundations for a more detailed study of exciton-phonon coupling in Ruddlesden-Popper phases, leading ultimately to design principles for optoelectronic devices. The two studies above highlight the important impacts of molecular components on the excited state dynamics of inorganic semiconductor nanostructures.

Future Plans

In the future, we will continue to advance the rationalized synthesis of new colloidal nanoscale building blocks and their assemblies. Such efforts will leverage on the large datasets of automated synthesis and advanced machine learning methods. Furthermore, machine learning algorithms are being developed to enable new structural analysis methods using data such as electron microscopy images; this will accelerate the feedback loop to inform precise synthesis. Single particle optical microscopies as well as *in situ* electron microscopies will continue to be developed and applied to yield powerful insights on the structural transformation and reactivity of inorganic nanostructures. In addition, measurements of lead halide perovskite nanostructures using advanced time-resolved spectroscopic methods such as the XUV spectroscopy are underway, along with the development of theoretical tools for modeling the observed excited state dynamics.

References

1. JC Dahl, WT Osowiecki, Y Cai, JK Swabeck, Y Bekenstein, M Asta, EM Chan, and AP Alivisatos. “Probing the Stability and Band Gaps of Cs₂AgInCl₆ and Cs₂AgSbCl₆ Lead-Free Double Perovskite Nanocrystals”, *Chem. Mater.*, 2019, 31, 3134–3143.

2. JC Ondry, JP Philbin, M Lostica, **E Rabani**, and **AP Alivisatos**. “Resilient Pathways to Atomic Attachment of Quantum Dot Dimers and Artificial Solids from Faceted CdSe Quantum Dot Building Blocks,” *ACS Nano*, 2019, 13, 12322-12344.
3. JC Ondry, JP Philbin, M Lostica, **E Rabani**, and **AP Alivisatos**. “Colloidal Synthesis Path to 2D Crystalline Quantum Dot Superlattices”, *ACS Nano*, 2020, DOI: 10.1021/acsnano.0c07202.
4. M Gao, H Liu, S Yu, S Louisia, Y Zhang, DP Nenon, **AP Alivisatos** and **P Yang**. “Scaling Laws of Exciton Recombination Kinetics in Low Dimensional Halide Perovskite Nanostructures”, *J. Am. Chem. Soc.*, 2020, 142, 8871-8879.
5. Y Liu, M Siron, D Lu, J Yang, R Reis, F Cui, M Gao, M Lai, J Lin, Q Kong, T Lei, J Kang, J Jin, J Ciston, and **P Yang**. “Self-Assembly of Two-Dimensional Perovskite Nanosheet Building Blocks into Ordered Ruddlesden–Popper Perovskite Phase,” *J. Am. Chem. Soc.*, 2019, 141, 13028-13032.
6. Y Zhang, D Lu, M Gao, M Lai, J Lin, T Lei, Z Lin, L Quan, and **P Yang**. “Quantitative imaging of anion exchange kinetics in halide perovskites,” *Proc. Natl. Acad. Sci. USA*, 2019, 116, 12648–12653.
7. CG Bischak, M Lai, Z Fan, D Lu, P David, D Dong, H Chen, AS Etman, T Lei, J Sun, M Grünwald, **DT Limmer**, **P Yang**, and NS Ginsberg. “Liquid-like Interfaces Mediate Structural Phase Transitions in Lead Halide Perovskites”, *Matter*, 2020, 3, 534-545.
8. J Lin, H Chen, Y Gao, Y Cai, J Jin, AS Etman, J Kang, T Lei, Z Lin, MC Folgueras, LN Quan, Q Kong, M Sherburne, M Asta, J Sun, MF Toney, J Wu and **P Yang**. “Pressure Induced Semiconductor to Metal Phase Transition of a Charge-Ordered Indium Halide Perovskite”, *Proc. Natl. Acad. Sci. USA*, 2019, 116, 23404-23409.
9. SK Cushing, M Zurch, PM Kraus, LM Carneiro, A Lee, HT Chang, CJ Kaplan, and **SR Leone**. “Hot phonon and carrier relaxation in Si(100) determined by transient extreme ultraviolet spectroscopy,” *Struct. Dyn.*, 2018 5, 054302.
10. SK Cushing, A Lee, IJ Porter, LM Carneiro, HT Chang, M Zuerch, and **SR Leone**. “Differentiating Photoexcited Carrier and Phonon Dynamics in the D, L, and G Valleys of Si(100) with Transient Extreme Ultraviolet Spectroscopy,” *J. Phys. Chem. C*, 2019, 123, 3343–3352.
11. SK Cushing, IJ Porter, BR de Roulet, A Lee, BM Marsh, S Szoke, ME Vaida, and **SR Leone**. “Layer-Resolved Ultrafast Extreme Ultraviolet Measurement of Hole Transport in a Ni-TiO₂-Si Photoanode,” *Sci. Adv.*, 2020, 6(14), eaay6650.
12. C Yan, D Weinberg, D Jasrasaria, MA Kolaczkowski, Z Liu, JP Philbin, AD Balan, Y Liu, AM Schwartzberg, **E Rabani**, and **AP Alivisatos**. “Uncovering the Role of Hole Traps in Promoting Hole Transfer from Multiexcitonic Quantum Dots to Molecular Acceptors”, *ACS Nano*, 2020, DOI: 10.1021/acsnano.0c08158.
13. D Jasrasaria, JP Philbin, C Yan, D Weinberg, **AP Alivisatos**, and **E Rabani**. “Sub-Bandgap Photoinduced Transient Absorption Features in CdSe Nanostructures: The Role of Trapped Holes”, *J. Phys. Chem. C*, 2020, 124, 17372–17378.

Publications

A. Publications primarily funded and intellectually led by this FWP

1. MR Hauwiller, LB Frechette, MR Jones, JC Ondry, GM Rotskoff, P Geissler, and **AP Alivisatos**. “Unravelling Kinetically-Driven Mechanisms of Gold Nanocrystal Shape Transformations using Graphene Liquid Cell Electron Microscopy,” *Nano Lett.*, 2018, 18 (9), 5731-5737.
2. SK Cushing, M Zurich, PM Kraus, LM Carneiro, A Lee, HT Chang, CJ Kaplan, and **SR Leone**. “Hot phonon and carrier relaxation in Si(100) determined by transient extreme ultraviolet spectroscopy,” *Struct. Dyn.*, 2018, 5, 054302.
3. D Lu, Y Zhang, M Lai, A Lee, C Xie, J Lin, T Lei, Z Lin, CS Kley, J Huang, **E Rabani**, and **P Yang**. “Giant Light-Emission Enhancement in Lead Halide Perovskites by Surface Oxygen Passivation,” *Nano Lett.*, 2018, 18, 6967-6973.
4. M Lai, A Obliger, D Lu, CS Kley, CG Bischak, Q Kong, T Lei, L Dou, NS Ginsberg, **DT Limmer**, and **P Yang**. “Intrinsic anion diffusivity in lead halide perovskites is facilitated by a soft lattice,” *Proc. Natl. Acad. Sci. USA*, 2018, 115, 11929-11934.
5. DP Nenon, K Pressler, J Kang, BA Koscher, JH Olshansky, WT Osowiecki, MA Koc, LW Wang, and **AP Alivisatos**. “Design Principles for Trap-Free CsPbX₃ Nanocrystals: Enumerating and Eliminating Surface Halide Vacancies with Softer Lewis Bases,” *J. Am. Chem. Soc.*, 2018, 140, 17660-17772.
6. SK Cushing, A Lee, IJ Porter, LM Carneiro, HT Chang, M Zuerch, and **SR Leone**. “Differentiating Photoexcited Carrier and Phonon Dynamics in the D, L, and G Valleys of Si(100) with Transient Extreme Ultraviolet Spectroscopy,” *J. Phys. Chem. C*, 2019, 123, 3343–3352.
7. MR Hauwiller, JC Ondry, CM Chan, P Khandekar, J Yu, and **AP Alivisatos**. “Gold Nanocrystal Etching as a Means of Probing the Dynamic Chemical Environment in Graphene Liquid Cell Electron Microscopy,” *J. Am. Chem. Soc.*, 141, 4428-4437 (2019).
8. J Gao, L Kidon, **E Rabani**, and **AP Alivisatos**. “Ultrahigh Hot Carrier Transient Photocurrent in Nanocrystal Arrays by Auger Recombination,” *Nano Lett.*, 2019, 19, 4804-4810.
9. Y Zhang, D Lu, M Gao, M Lai, J Lin, T Lei, Z Lin, L Quan, and **P Yang**. “Quantitative imaging of anion exchange kinetics in halide perovskites,” *Proc. Natl. Acad. Sci. USA*, 2019, 116, 12648–12653.
10. Y Liu, M Siron, D Lu, J Yang, R Reis, F Cui, M Gao, M Lai, J Lin, Q Kong, T Lei, J Kang, J Jin, J Ciston, and **P Yang**. “Self-Assembly of Two-Dimensional Perovskite Nanosheet Building Blocks into Ordered Ruddlesden–Popper Perovskite Phase,” *J. Am. Chem. Soc.*, 2019, 141, 13028-13032.
11. J Lin, H Chen, J Kang, L Quan, Z Lin, Q Kong, M Lai, S Yu, L Wang, LW Wang, M Toney, and **P Yang**. “Copper(I) Based Highly Emissive All-Inorganic Rare-Earth Halide Clusters,” *Matter*, 2019, 1, 180-191.

12. A Levy, W Dou, **E Rabani** and **DT Limmer**. A complete quasiclassical map for the dynamics of interacting fermions. *J. Chem. Phys.*, 2019, 150, 234112.
13. A Levy, L Kidon, J Bätge, J Okamoto, M Thoss, **DT Limmer**, and **E Rabani**. Absence of Coulomb blockade in the Anderson impurity model at the symmetric point. *J. Phys. Chem. C*, 2019, 123, 13538–13544.
14. JC Ondry, JP Philbin, M Lostica, **E Rabani**, and **AP Alivisatos**. “Resilient Pathways to Atomic Attachment of Quantum Dot Dimers and Artificial Solids from Faceted CdSe Quantum Dot Building Blocks,” *ACS Nano*, 2019, 13, 12322–12344.
15. JC Dahl, WT Osowiecki, Y Cai, JK Swabeck, Y Bekenstein, M Asta, EM Chan, and **AP Alivisatos**. “Probing the Stability and Band Gaps of $\text{Cs}_2\text{AgInCl}_6$ and $\text{Cs}_2\text{AgSbCl}_6$ Lead-Free Double Perovskite Nanocrystals”, *Chem. Mater.*, 2019, 31, 3134–3143.
16. LN Quan, J Kang, CZ Ning, and **P Yang**. “Nanowires for Photonics”, *Chem. Rev.*, 2019, 119, 9153–9169.
17. BA Koscher, Z Nett, and **AP Alivisatos**. “The Underlying Chemical Mechanism of Selective Chemical Etching in CsPbBr_3 Nanocrystals for Reliably Accessing Near-Unity Emitters”, *ACS Nano*, 2019, 13, 11825–11833.
18. AD Balan, JH Olshansky, Y Horowitz, HL Han, EA O’Brien, L Tang, GA Somorjai, and **AP Alivisatos**. “Unsaturated Ligands Seed an Order to Disorder Transition in Mixed Ligand Shells of CdSe/CdS Quantum Dots”, *ACS Nano*, 2019, 13, 13784–13796.
19. J Lin, H Chen, Y Gao, Y Cai, J Jin, AS Etman, J Kang, T Lei, Z Lin, MC Folgueras, LN Quan, Q Kong, M Sherburne, M Asta, J Sun, MF Toney, J Wu and **P Yang**. “Pressure Induced Semiconductor to Metal Phase Transition of a Charge-Ordered Indium Halide Perovskite”, *Proc. Natl. Acad. Sci. USA*, 2019, 116, 23404–23409.
20. H Chen, J Lin, J Kang, Q Kong, D Lu, J Kang, M Lai, LN Quan, Z Lin, J Jin, LW Wang, MF Toney and **P Yang**. “Structural and Spectral Dynamics of Single-Crystalline Ruddlesden-Popper Phase Halide Perovskite Blue Light-Emitting Diodes”, *Sci. Adv.*, 2020, 6, eaay4045.
21. CK Lin, Q Zhao, Y Zhang, S Cestellos-Blanco, Q Kong, M Lai, J Kang, and **P Yang**. “Two-Step Patterning of Scalable All-Inorganic Halide Perovskite Arrays”, *ACS Nano*, 2020, 14, 3500–3508.
22. SK Cushing, IJ Porter, BR de Roulet, A Lee, BM Marsh, S Szoke, ME Vaida, and **SR Leone**. “Layer-Resolved Ultrafast Extreme Ultraviolet Measurement of Hole Transport in a Ni-TiO₂-Si Photoanode”, *Sci. Adv.*, 2020, 6, eaay6650.
23. H Liu, M Siron, M Gao, D Lu, Y Bekenstein, D Zhang, L Dou, **AP Alivisatos**, and **P Yang**. “Lead Halide Perovskite Nanowires Stabilized by Block Copolymers for Langmuir-Blodgett Assembly”, *Nano Res.*, 2020, 5, 5404.

24. M Gao, H Liu, S Yu, S Louisia, Y Zhang, DP Nenon, **AP Alivisatos** and **P Yang**. “Scaling Laws of Exciton Recombination Kinetics in Low Dimensional Halide Perovskite Nanostructures”, *J. Am. Chem. Soc.*, 2020, 142, 8871–8879.
25. V Jamali, F Niroui, LW Taylor, OS Dewey, BA Koscher, M Pasquali, and **AP Alivisatos**. “Perovskite-Carbon Nanotube Light-Emitting Fibers”, *Nano Lett.*, 2020, 20(5), 3178–3184.
26. GA Kamat, C Yan, WT Osowiecki, IA Moreno-Hernandez, M Ledendecker, and **AP Alivisatos**. “Self-Limiting Shell Formation in Cu@Ag Core–Shell Nanocrystals during Galvanic Replacement”, *J. Phys. Chem. Lett.*, 2020, 11(13), 5318–5323.
27. JC Dahl, X Wang, X Huang, EM Chan, and **AP Alivisatos**. “Elucidating the Weakly Reversible Cs–Pb–Br Perovskite Nanocrystal Reaction Network with High-Throughput Maps and Transformations”, *J. Am. Chem. Soc.*, 2020, 142, 11915–11926.
28. **DT Limmer**, NS Ginsberg. “Photoinduced phase separation in the lead halides is a polaronic effect”, *J. Chem. Phys.*, 2020, 152, 230901.
29. D Jasrasaria, JP Philbin, C Yan, D Weinberg, **AP Alivisatos**, and **E Rabani**. “Sub-Bandgap Photoinduced Transient Absorption Features in CdSe Nanostructures: The Role of Trapped Holes”, *J. Phys. Chem. C*, 2020, 124, 17372–17378.
30. CG Bischak, M Lai, Z Fan, D Lu, P David, D Dong, H Chen, AS Etman, T Lei, J Sun, M Grünwald, **DT Limmer**, and **P Yang**, and NS Ginsberg. “Liquid-like Interfaces Mediate Structural Phase Transitions in Lead Halide Perovskites”, *Matter*, 2020, 3, 534–545.
31. C Yan, D Weinberg, D Jasrasaria, MA Kolaczkowski, Z Liu, JP Philbin, AD Balan, Y Liu, AM Schwartzberg, **E Rabani**, and **AP Alivisatos**. “Uncovering the Role of Hole Traps in Promoting Hole Transfer from Multiexcitonic Quantum Dots to Molecular Acceptors”, *ACS Nano*, 2020, DOI: 10.1021/acsnano.0c08158.
32. JC Ondry, JP Philbin, M Lostica, **E Rabani**, and **AP Alivisatos**. “Colloidal Synthesis Path to 2D Crystalline Quantum Dot Superlattices”, *ACS Nano*, 2020, DOI: 10.1021/acsnano.0c07202.

B. Collaborative publications

1. MD Fabian, B Shapiro, **E Rabani**, D Neuhauser and R Baer. Stochastic density functional theory. *WIREs Computational Molecular Science* 2019, e1412.
2. L Kidon, H Wang, M Thoss and **E Rabani**. “On the memory kernel and the reduced system propagator,” *J. Chem. Phys.*, 2018, 149, 104105.
3. J Deng, Y Su, D Liu, **P Yang**, B Liu, and C Liu. “Nanowire Photoelectrochemistry”, *Chem. Rev.*, 2019, 119, 9221–9259.
4. MH Oh, MG Cho, DY Chung, I Park, YP Kwon, C Ophus, D Kim, MG Kim, B Jeong, XW Gu, J Jo, JM Yoo, J Hong, S McMains, K Kang, YE Sung, **AP Alivisatos**, and T Hyeon.

“Design and Synthesis of Multigrain Nanocrystal via Geometric Misfit Strain”, *Nature*, 2020, 577, 359-363.

5. BD Folie, JA Tan, J Huang, PC Sercel, M Delor, M Lai, JL Lyons, N Bernstein, A Efros, **P Yang**, NS Ginsberg. “Effect of Anisotropic Confinement on Electronic Structure and Dynamics of Band Edge Excitons in Inorganic Perovskite Nanowires”, *J. Phys. Chem. A*, 2020, 124, 1867-1876.
6. BH Kim, J Heo, S Kim, CF Reboul, H Chun, D Kang, H Bae, H Hyun, J Lim, H Lee, B Han, T Hyeon, **AP Alivisatos**, P Ercius, H Elmlund, and J Park “Critical Differences in 3D Atomic Structure of Individual Ligand-Protected Nanocrystals in Solution”, *Science*, 2020, 368, 60-67.
7. E Shi, B Yuan, SB Shiring, Y Gao, Akriti, Y Guo, C Su, M Lai, **P Yang**, J Kong, BM Savoie, Y Yu, L Dou. “Two-Dimensional Halide Perovskite Lateral Epitaxial Heterostructures”, *Nature*, 2020, 580, 614-620.

Characterization of Functional Nanomachines

PI: Michael F. Crommie

Co-Investig.: A.P. Alivisatos, C. Bustamante, M.L. Cohen, F.R. Fischer, S.G. Louie, A. Zettl

UC Berkeley, Physics Department, 366 LeConte Hall #7300, Berkeley, CA 94720

Materials Sciences Division, Lawrence Berkeley National Laboratory

e-mail: crommie@berkeley.edu

Program Scope: The overarching goal of this program is to explore the fundamental behavior of nanomachines that are engineered at the atomic scale and that can control energy and information through mechanical transduction processes. We are following two paths toward this goal: first, we are exploring naturally occurring biomotors that take advantage of the molecular mechanisms provided by Nature and, second, we are purposefully designing new synthetic molecular machines in a molecule-by-molecule fashion. This research helps to clarify the mechanisms by which nanomachines convert different forms of energy into directed mechanical activity as well as how these processes are affected by different environmental dissipation mechanisms. This program is aimed at creating new categories of functional nanomachines, such as bottom-up fabricated synthetic molecular machines that operate on surfaces, top-down fabricated carbon-based nanomachines that exploit the electromechanical properties of nanotubes and graphene, and hybrid nanomachines composed of integrated synthetic and biological components. This program has seven co-investigators whose expertise span physics, chemistry, and biology. The experimental tools utilized by our collaboration range from synthetic chemistry, electron microscopy, and scanned probe techniques (**Alivisatos, Fischer, and Crommie**), to photolithography, wet biology, and laser tweezers (**Zettl and Bustamante**). **Cohen and Louie** provide theoretical support through the use of *ab initio* density functional techniques and molecular dynamics calculations.

Recent Progress: Here we highlight our activities in the subtask entitled *Imaging Molecular Actuation in Nanodevices*. We will highlight three thrusts within this subtask: (1) Gate-induced surface molecular control, (2) Current-induced molecular diffusion and electromigration, and (3) Charge-patterning in 1D molecular arrays.

(1) Gate-induced surface molecular control: We have demonstrated reversible nanoscale control over the microscopic geometry of molecular surface ions by applying current and voltage signals to a graphene field-effect transistor (FET) in the absence of electrochemical solvents (Fig. 1). Reversible control over the surface concentration of charged F₄TCNQ molecules was accomplished by simultaneously applying a source-drain current and an electrostatic back-gate voltage to graphene FET devices at cryogenic temperature. Under these conditions the primary effect of the source-drain current is to heat the graphene surface and promote molecular diffusion. When an electrostatic back-gate is simultaneously applied with the

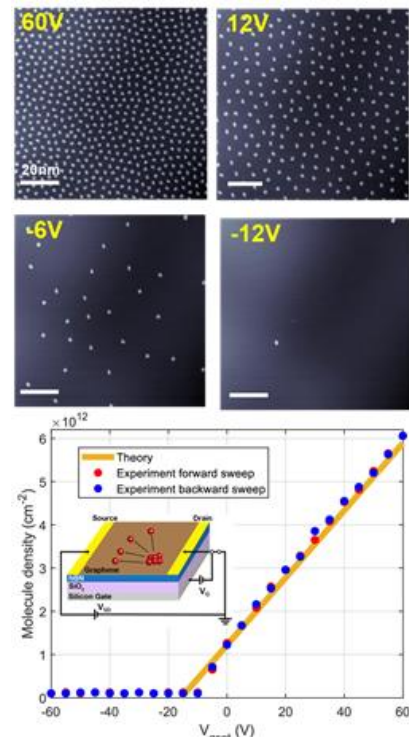


Fig. 1: **Top:** four STM images of the same patch of an F₄TCNQ-covered graphene FET demonstrate control over molecular concentration by tuning gate-voltage. **Bottom:** plot of molecular coverage vs. gate voltage compared to model calculation.

source-drain current, the diffusing molecules adjust their inter-particle surface density in response to the gate voltage. Setting the source-drain current to zero causes the molecules to freeze in place so that their gate-adjusted density can be measured directly via STM imaging. This “freeze-frame” imaging technique allows us to directly visualize the effects of molecular motion in response to electrical signals applied to our devices (Fig. 1). We observe that the molecular surface density varies linearly with applied back-gate voltage, thus suggesting that the molecules contribute to the screening of the gate electric field. The graphene Fermi level is also observed to be pinned by the F₄TCNQ lowest unoccupied molecular orbital (LUMO) energy level (E_L) as the gate voltage is changed during the surface concentration manipulation process. This implies that the molecules on the FET surface are charged and dynamically change their concentration in order to suppress energetically unfavorable filling of graphene band states.

We are able to quantitatively predict the concentration of molecules on the graphene surface for a given gate voltage by assuming that the lowest-energy electronic configuration (under diffusive conditions) occurs when the Fermi energy is pinned at E_L . For a given gate voltage the total charge density on the molecule-decorated FET surface divides itself between charge carried by the molecules and charge carried by the graphene Dirac band. Because E_F is pinned at E_L , the graphene band charge can be found by integrating charge density from the Dirac point (E_D) up to E_L , resulting in the following expression relating molecular density to back gate voltage:

$$N_M = CV_{G-set} + \frac{|E_D - E_L|^2}{\pi \hbar^2 v_F^2}$$

As seen from the solid line in Fig. 1, this expression fits our data well for a value of $|E_D - E_L| = 142 \pm 23$ meV which matches spectroscopic data obtained from completely different measurements. The connection established here between molecular electronic structure and molecular surface concentration provides a completely new technique for quantitatively determining molecular energy levels by simply counting the number of molecules on a surface.

(2) Current-induced molecular diffusion and electromigration: We have succeeded in observing controlled electromigration of individual molecules at the surface of a graphene FET. This has enabled us to use scanning tunneling microscopy to disentangle the electromigration “wind” force (which arises from electron momentum transfer to a scattering defect) from the “direct” force (which is exerted directly on a charged defect by the background electric field) for individual charged molecules for the first time.

Electromigration was observed in the same adsorbate/graphene FET set-up described above. F₄TCNQ molecules were deposited onto graphene FETs held at room temperature in UHV before transferring the device to the STM and cooling down to $T = 4$ K for measurement. Electromigration was found to occur only for molecules in a neutral charge state and not for charged ions (this is quite different from the molecular concentration-control protocol described in the section above, which occurs only for molecules in a charged ionic state).

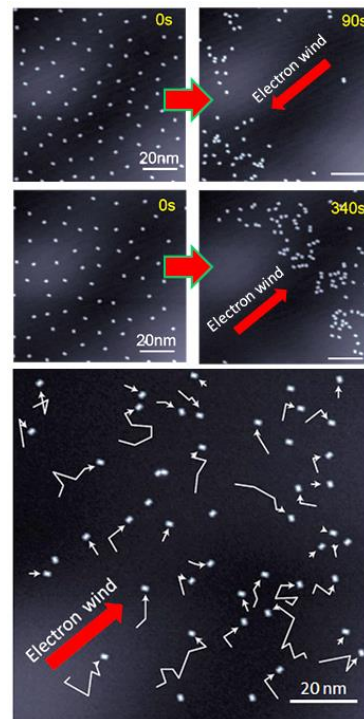


Fig. 2: Top: demonstration of electromigration of F₄TCNQ molecules at the surface of a graphene FET. Before and after images are shown for current flowing in different directions (electromigrating molecules follow the direction of current flow). **Bottom:** time-series of images shows trajectory of electromigrating molecules.

To observe electromigration we first imposed a uniform molecular concentration across the surface using the control protocol described above. Current densities higher than 5 A/m were then passed through the sample for 30 second time increments, after which the current was stopped and the surface imaged in a “frozen state” via STM. Fig. 2 shows the results of this electromigration protocol for current flowing in opposite directions. The molecules are clearly seen to move in the direction of current flow (the “wind” direction). Electromigration is also seen to have a diffusive character, as shown by the time-lapse image at the bottom of Fig. 2 where the positions of different molecules are observed to exhibit biased diffusion under the influence of transport current.

In order to quantitatively analyze the observed electromigration behavior we had to determine the local electric field and the molecular surface diffusion barrier. The local electric field was determined from scanning tunneling potentiometry measurements, whereas the diffusion barrier was extracted from the temperature dependence of molecular diffusion characteristics. Application of a standard model of defect electromigration suggests that the electron wind force for our molecules is 200 times stronger than the direct force. One possible explanation for why *charged* molecules don’t undergo electromigration in our system is that the Coulomb potential is not “sharp” enough to induce high-momentum-transfer scattering, unlike the neutral molecule which exhibits higher multipole components in its scattering potential.

(3) Charge-patterning in 1D molecular arrays: The ability to tune the electronic properties of molecular arrays is important for developing new molecule-scale electromechanical devices. However, controlling internal device charge distributions within molecular arrays has proved challenging. We have succeeded in performing gate-tunable charge patterning of precise 1D molecular arrays on a graphene FET. 1D molecular arrays were fabricated using an edge-templated self-assembly process that allows F₄TCNQ molecules to be precisely positioned on graphene devices. The charge configuration of the molecular arrays were reversibly switched between different collective charge states by tuning the graphene E_F via a back-gate electrode (Fig. 3a). Charge-pinning at the ends of the molecular arrays enabled the charge state of the entire array to be controlled by adding or removing an edge molecule and changing the total number of molecules between an odd and an even integer. Charge patterns altered in this way propagate down the array in a cascade, allowing the array to function as a charge-based molecular shift register. An extended multi-site theoretical Anderson impurity model was used to quantitatively explain this behavior.

At a gate-voltage of $V_G = 0 \text{ V}$ the LUMO orbital of every F₄TCNQ molecule in our 1D arrays was observed to lie above E_F , indicating that the molecules are all charge-neutral (that is, the LUMO states are all empty). By contrast, when the gate voltage was raised to $V_G = 60 \text{ V}$ the LUMO orbitals all fell below E_F and became filled with charge (one electron per LUMO). The most

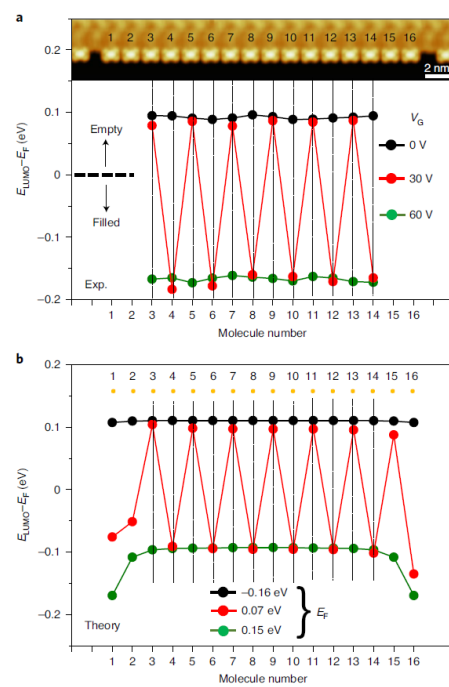


Fig. 3: (a) STM image of a 1D array of F₄TCNQ molecules as well as a plot of the measured spatially alternating LUMO energy level at intermediate gate voltage. (b) Result of theoretical model simulating 1D array behavior at the intermediate gate voltage in (a). Excellent agreement is seen between the simulation in (b) and the data shown in (a).

interesting doping regime, however, was the intermediate regime, $V_G = 30$ V, which moved the LUMO energy level closer to E_F . In this regime the LUMO states adopted an unusual electronic structure where their energies aligned alternately above and below E_F for adjacent molecules within the array, thus exhibiting an alternating charge pattern with negatively charged molecules sitting adjacent to neutral molecules, as seen in Fig. 3a.

We can understand the gate-dependent charging behavior of close-packed F₄TCNQ arrays using a modified Anderson impurity model where each molecule is described by an impurity state (i.e., the LUMO level) and a Hamiltonian that includes the molecular charging energy as well as electronic hopping to the graphene substrate. As shown in Fig. 3b, this model results in the LUMO states for all molecules being unoccupied for a Fermi level at $E_F = -0.16$ eV, while they are all occupied by one electron each when the Fermi level is aligned to $E_F = +0.15$ eV. At an intermediate Fermi level of $E_F = +0.07$ eV, however, the model predicts that the LUMO occupancies spatially alternate along the molecular array, yielding a periodic charging pattern in Fig. 3b identical to what is seen experimentally in Fig. 3a. The observed charge alternation can be interpreted as a nearest-neighbor Coulomb blockade: if an electron occupies a molecule in the array then it is unfavorable for electrons to occupy the two adjacent molecules because the Coulomb potential raises their LUMO energies. The difference in energy between neighboring LUMO states thus provides a direct measure of the strength of the screened Coulomb interaction between molecules on graphene. Our calculation yields a value of 0.19 eV for this difference, which is in reasonable agreement with the measured value of 0.28 eV.

Future Plans: An important future direction for this project is to create more complex molecular structures whose internal degrees of freedom can be mechanically actuated *remotely* (i.e., by electrostatic gating or optical excitation) and imaged *locally* at the single-molecule level. This is a grand challenge that has not yet been accomplished and that would open significant new research avenues. We are pursuing this goal along three different fronts: (i) Development of electronically improved device substrates, (ii) Development of more effective molecular deposition techniques, and (iii) Development of new time-resolved local characterization techniques, as follows:

(i) **Substrates:** Two key issues relevant for molecular actuation are gate-tunability and optical compatibility. In the past we used metal crystal substrates which were bad on both fronts. Currently we use graphene FETs, which have the advantage of providing gate-tunability. In the future we plan to use single-layer TMD FET substrates. TMDs (such as MoSe₂, WSe₂, etc.) have a 2 eV bandgap and clean, inert surfaces. They are harder to work with than graphene, but could provide revolutionary new capabilities for gating and optically exciting new molecular systems.

(ii) **Molecular deposition:** Up to now we have been limited to studying molecular structures that can be vacuum deposited onto surfaces and imaged either singly or after surface reaction. For the future we are developing new “matrix assisted deposition” techniques involving “direct contact transfer” that will allow us to *cleanly* deposit large molecular structures from solution phase onto a surface. This will be highly enabling since it will allow local probe characterization of new, complex solution-synthesized molecular structures.

(iii) **Time-resolved characterization:** Currently we have no time resolution in our experiments beyond “before excitation” / “after excitation” measurement (where time resolution is on the order of seconds). We are currently developing new pump-probe STM techniques that should give us picosecond time resolution with atomic-scale spatial resolution. This capability will be extremely useful for better determining the dynamical properties of nanomachine systems.

Publications resulting from work supported by DOE grant over previous two years:

1. J. Lu, H.-Z. Tsai, A. N. Tatan, S. Wickenburg, A. A. Omrani, D. Wong, A. Riss, E. Piatti, K. Watanabe, T. Taniguchi, A. Zettl, V. M. Pereira, M. F. Crommie. Frustrated supercritical collapse in tunable charge arrays on graphene. *Nature Communications* **10**, 477 (2019).
2. S. Oh, M. F. Crommie, M. L. Cohen. Simulating the Nanomechanical Response of Cyclooctatetraene Molecules on a Graphene Device. *ACS Nano* **13**, 1713 (2019).
3. Thang Pham, Alex Zettl. Electrically Driven Dynamics of Few-Chain NbSe₃. *Phys. Stat. Solidi B* 1900241 (2019).
4. S. Tafoya, S. J. Large, S. Liu, C. Bustamante, and D. A. Sivak,. Using a system's equilibrium behavior to reduce its energy dissipation in nonequilibrium processes. *Proc. Natl. Acad. Sci (USA)* **116**, 5920 (2019).
5. T. Joshi, C. Chen, H. Li, C. S. Diercks, G. Wang, P.J. Waller, H. Li, J. L. Bredas, O. M. Yaghi, M. F. Crommie. Local Electronic Structure of Molecular Heterojunctions in a Single-Layer 2D Covalent Organic Framework. *Advanced Materials* **31**, 1805941 (2019).
6. D. J. Rizzo, M. Wu, H.-Z. Tsai, T. Marangoni, R. Durr, A. A. Omrani, F. Liou, C. Bronner, T. Joshi, G. D. Nguyen, G. F. Rodgers, W.-W. Choi, J. H. Jørgensen, F. R. Fischer, S. G. Louie, M. F. Crommie. Length-dependent Evolution of Type II Heterojunctions in Bottom-Up-Synthesized Graphene Nanoribbons. *Nano Lett.* **19**, 3221 (2019).
7. J. Schöneberg, M. R. Pavlin, S. Yan, M. Righini, I.-H. Lee, L.-A. Carlson, A. H. Bahrami, D. H. Goldman, X. Ren, G. Hummer, C. Bustamante, J. H. Hurley.. ATP-dependent force generation and membrane scission by ESCRT-III and Vps4. *Science* **362**, 1423 (2018).
8. L. M. Alexander, D. H. Goldman, L. M. Wee, C. Bustamante. Non-equilibrium Dynamics of a Nascent Polypeptide During Translation Suppress its Misfolding. *Nature Communications* **10**, 2709 (2019).
9. Z. Chen, R. Gabizon, A. I. Brown, A. Lee, A. Song, C. D. Diaz, A. Kaplan, E. Koslover, T. Yao, C. Bustamante. High-resolution and high-accuracy topographic and transcriptional maps of the nucleosome barrier. *eLife*.:e48281 (2019).
10. V. P. Desai, F. Frank, A. Lee, M. Righini, L. Lancaster, H. F. Noller, I. Tinoco Jr., and C. Bustamante,. Co-temporal force and fluorescence measurements reveal a ribosomal gear shift mechanism of translation regulation by structured mRNAs. *Mol. Cell* **75**, 1007 (2019).
11. H. D. Ha, C. Yan, G. Katsoukis, G. A. Kamat, I. A. Moreno-Hernandez, H. Frei, A. P Alivisatos, Precise Colloidal Plasmonic Photocatalysts Constructed by Multistep Photodepositions, *Nano Lett.* **20**, 8661 (2020).
12. H. Cho, I. A. Moreno-Hernandez, V. Jamali, M. H. Oh, and A. P. Alivisatos. In Situ Quantification of Interactions between Charged Nanorods in a Predefined Potential Energy Landscape, *Nano Lett.* **21**, 628 (2021).
13. Hsin-Zon Tsai, Johannes Lischner, Arash A. Omrani, Franklin Liou, Andrew S. Aikawa, Christoph Karrasch, Sebastian Wickenburg, Alexander Riss, Kyler C. Natividad, Jin Chen, Won-Woo Choi, Kenji Watanabe, Takashi Taniguchi, Chenliang Su, Steven G. Louie, Alex Zettl, Jiong Lu, and Michael F. Crommie. A molecular shift register made using tunable

- charge patterns in one-dimensional molecular arrays on graphene. *Nature Electronics* **3**, 598 (2020).
- 14. Gabriel Dunn, Vivekananda P. Adiga, Thang Pham, Christopher Bryant, Donez J. Horton-Bailey, Jason N. Belling, Ben LaFrance, Jonathan A. Jackson, Hamid Reza Barzegar, Jong Min Yuk, Shaul Aloni, Michael F. Crommie, and Alex Zettl. Graphene-Sealed Flow Cells for In-Situ Transmission Electron Microscopy of Liquid Samples, *ACS Nano* **14**, 9637 (2020).
 - 15. C. Bustamante, L. Alexander, K. Maciuba, and C. M. Kaiser. Single-molecule studies of protein folding with optical tweezers. *Annual review of biochemistry* **89**, 443 (2020).
 - 16. S. Fukuda, S. Yan, Y. Komi, M. Sun, R. Gabizon, and C. Bustamante. The Biogenesis of SRP RNA Is Modulated by an RNA Folding Intermediate Attained during Transcription. *Molecular Cell* **77**, 241 (2020).
 - 17. Z. Chen, A. Shaw, H. Wilson, M. Woringer, X. Darzacq, S. Marqusee, Q. Wang, and C. Bustamante. Single-molecule diffusometry reveals no catalysis-induced diffusion enhancement of alkaline phosphatase as proposed by FCS experiments. *Proc. Natl. Acad. Sci.* **117**, 21328 (2020).
 - 18. Daniel J. Rizzo, Gregory Veber, Jingwei Jiang, Ryan McCurdy, Ting Cao, Christopher Bronner, Ting Chen, Steven G. Louie, Felix R. Fischer, Michael F. Crommie. Inducing Metallicity in Graphene Nanoribbons via Zero-Mode Superlattices, *Science* **369**, 1597 (2020).
 - 20. Peter H. Jacobse, Ryan D. McCurdy, Jingwei Jiang, Daniel J. Rizzo, Gregory Veber, Paul Butler, Rafa Zuzak, Steven G. Louie, Felix R. Fischer, Michael F. Crommie. Bottom-up Assembly of Nanoporous Graphene with Emergent Electronic States. *J. Am. Chem. Soc.* **142**, 13507 (2020).
 - 21. Mustafa Caglar, Inese Silkina, Bertram T. Brown, Alice L. Thorneywork, Oliver J. Burton, Vitaliy Babenko, Stephen Matthew Gilbert, Alex Zettl, Stephen Hofman and Ulrich F. Keyser. Tunable Anion-Selective Transport through Monolayer Graphene and Hexagonal Boron Nitride, *ACS Nano* **14**, 2729 (2020).
 - 22. Daniel J. Rizzo, Qingqing Dai, Christopher Bronner, Gregory Veber, Brian J. Smith, Michio Matsumoto, Simil Thomas, Giang D. Nguyen, Patrick R. Forrester, William Zhao, Jakob H. Jørgensen, William R. Dichtel, Felix R. Fischer, Hong Li, Jean-Luc Bredas, Michael F. Crommie. Revealing the Local Electronic Structure of a Single-layer Covalent Organic Framework Through Electronic Decoupling, *Nano Letters* **20**, 963 (2020).
 - 23. F. Wang, Y. Hao, Q. Li, J. Li, H. Zhang, X. Zhang, L. Wang, C. Bustamante, and C. Fan. Programming PAM antennae for efficient CRISPR-Cas9 DNA editing. *Science Advances* **6**, eaay9948 (2020).
 - 24. B. Feng, R. P. Sosa, A. K. Mårtensson, K. Jiang, A. Tong, K. D. Dorfman, M. Takahashi, P. Lincoln, C. J. Bustamante, F. Westerlund, and B. Nordén. Hydrophobic catalysis and a potential biological role of DNA unstacking induced by environment effects. *Proceedings of the National Academy of Sciences* **116**, 17169 (2019).

Abstract

PROJECT TITLE: Superatomic Clusters and Cluster-Based materials – Structure, Stability, and Applications

PI: Jena, Purusottam

Department of Physics, Virginia Commonwealth University, Richmond, VA 23284-2000
pjena@vcu.edu

Program Scope:

The objective of our project is to provide a fundamental understanding of the structure-property relationships of a novel class of superatomic clusters mimicking the chemistry of atoms and to explore their potential for enabling unusual reactions as well as serving as building blocks of new materials. Working closely with experimental groups, our goal is not only to validate our theoretical predictions but also to guide experiments in focused discovery of energy and magnetic materials.

The project exploits the unique size and composition-specific properties of isolated clusters and explores their potential as building blocks of functional materials. Using first-principles theory, our approach is an atom-by-atom rational design of a new class of superatomic clusters, such as superalkalis and superhalogens that not only mimic the chemistry of alkali and halogen atoms, respectively, but also are suitable for forming supersalts with unusual properties. The project deals with three interrelated thematic areas: (1) *Superions as building blocks of energy materials*: Realizing that hybrid solar cells and electrolytes in metal-ion batteries are salts composed of metal cations and anions, we study a wide range of superalkalis and superhalogens as building blocks of energy materials. These include perovskite solar cells and solid-state electrolytes in Na/K-ion batteries whose properties are tailored by choosing the size and composition of the superions. (2) *Ligand assisted rational design of highly reactive clusters and their interaction with chemically inert species*: Design and realization of stable, yet highly reactive agents, capable of converting saturated hydrocarbons and chemically inert waste into valuable products at room temperature have considerable economic and environmental importance and remain as one of the outstanding challenges in modern cluster science. We study the potential of a new class of *superelectrophilic (supernucleophilic) clusters* based on *closo*-borate structures $B_nX_{n-1}^-$ ($BeB_{n-1}X_{n-1}^{2-}$) ($n=6-12$, $X=CN, BO, SCN$) that can bind noble gas atom Ar and activate inert molecules like N_2 at room temperature (activate CO_2). The uniqueness of these species is that the open B (Be) site, carrying a positive charge, is highly reactive, while being protected by the strong borate scaffold. (3) *In search of realizable metastable phases of carbon and silicon*: Knowing that metastable phases of matter may have properties far superior to those of their ground state (a case in point is diamond *vs* graphite), our focus is to develop a scheme for rational design of metastable phases of matter that can be experimentally realized by using molecular precursors. We apply this paradigm shift in materials synthesis to study new phases of carbon and silicon-based cage clusters and explore their potential for forming magnetic materials and synthesizing diamond under milder conditions. These studies not only complement recent experiments but also are aimed at guiding them in discovery of new materials.

The complexity of the above systems necessitates the use of a multi-scale approach - from molecular orbital theory to supercell band structure theory and *ab-initio* molecular dynamics. Although most studies are carried out using density functional theory (DFT) with a variety of hybrid exchange-

correlation functionals, post-Hartree-Fock methods are used, when needed, to validate the accuracy of the DFT-based results. Efficient search algorithms and methodology are developed for rational design of metastable phases of cluster-based matter.

Exploration of new frontiers of superatomic clusters as building blocks of energy and magnetic materials can have the potential for advanced technologies. The project lies at the interface between physics, chemistry, and materials science and is ideal to train graduate and undergraduate students as well as postdoctoral fellows in multi-disciplinary research.

Recent Progress:

Research over the past two years has resulted in 40 publications of which 32 papers are published and two papers are in press in peer-reviewed journals. Some of these papers are published in high-impact journals such as *Angew. Chem. Int. Ed.*, *Physical Review Letters*, *Nature Communication*, *Journal of Physical Chemistry Letters*, *Small*, *Journal of Materials Chemistry A*, *Nanoscale*, etc. We have edited a book on *Superatoms: Principles, Synthesis, and Applications*” in which we authored five chapters. The book is expected to be published by Wiley in summer of 2021.

The papers cover a wide range of topics dealing with structure-property relationships of zero-dimensional systems (clusters), one-dimensional systems (nano-tubes), two-dimensional systems (topological materials, van der Waals Ferroelectrics, transition-metal dichalcogenide monolayers, graphene, and penta-graphene), and three-dimensional materials with clusters as building blocks for Li- and Na-ion batteries, ferroelectric, fereroelastic, and tri-ferroic materials. The works on clusters involve superhalogens as building blocks of super Lewis acids, stable tetra- and penta-anions in the gas phase, design of stable di-anionic clusters mimicking the properties of chalcogens, ligand stabilization of negatively charged clusters in defiance of the 18-electron rule, record-high stability of multiply-charged clusters aided by selected terminal group, superatomic clusters as building blocks of materials, and design and synthesis of metal-chalcogenide nanoclusters through atom-by-atom substitution. We showed that N-doped peanut-shaped carbon nanotubes can be used for efficient CO₂ electrocatalytic reduction. Potential of a number of nanostructured materials for electrolytes in Li-, Na-, and K-ion batteries were explored. These include: tetragonal C₂₄ (a topological nodal-surface semimetal) as an anode material for Na-ion batteries, high-pressure induced stable phase of Li₂MnSiO₄ as high-performance poly-anion cathode material, hydrogenated C₆₀ as high-capacity stable anode materials for Li-ion batteries, porous nodal-line semi metallic carbon for K-ion battery anode, yttrium-sodium halides as solid-state electrolytes for Na-ion battery, 3D porous honeycomb carbon as Na-ion battery anode material, Si₂BN nanoribbons assembly in a 3D porous structure as a universal anode material for both Li- and Na-ion batteries, and 2D g-GeC monolayer as an anode material for Li/Na-ion batteries. Clusters when used as building blocks of materials were shown to render promising properties in superionic conductors and multi-ferroic materials. We also studied two-dimensional metal-free boron chalcogenides B₂X₃ (X=Se and Te) and MIL-100(Fe)/TiO₂ composites as photocatalysts. We also studied the magnetic properties of 2D penta-silicene, semiconducting CrI₃, boronated holey graphene, and type-I multiferroic double-metal trihalides. Work on 2D materials further included interfacial properties of penta-graphene-metal contact, twin orbital-order phases in ferromagnetic semiconducting VI₃ monolayer, and penta-BCN (a new ternary pentagonal monolayer with intrinsic piezoelectricity).

Five of the papers published are jointly with experimentalists [1-5]. Four of these papers [6-9] were featured on the cover of journals [Fig. 1]. Recently, an experiment [10] confirmed one of our important predictions dealing with the stability of a doubly charged negative ion [11]. We had shown that the second electron in B₁₂(CN)₁₂²⁻ cluster is bound by 5.3 eV, making it the most stable di-anion known in nature. Experimentally measured value of 5.5 eV for the second electron binding energy confirmed our prediction.

The discovery of this ultra-stable dianion has important implications for chemistry. For example, the authors [10] showed that once one of the CN ligands is removed, the positive charge on the naked B-atom is protected by the extra electron in the $B_{12}(CN)_{11}^-$ cluster. The strong electric field generated as a result is able to bind a noble gas atom Ar at room temperature! This opens a new field not only in noble gas chemistry but also the activation of inert molecules.



Ref. 6 **Ref. 7** **Ref. 8** **Ref. 9**

Fig. 1. Cover images of papers published during 2019-2020.

Future Plans:

Our future projects will include design of cluster-based materials for energy harvesting, conversion, and storage; design of highly stable multiply charged negative ions and their use in promoting unusual chemical reactions, developing new algorithm to search for metastable phases of materials based on carbon and silicon; and understanding the evolution of the structure and properties of clusters. We plan to work with experimentalists for focused discovery of new cluster-based materials for Li, Na-, and K-ion batteries and ligated transition metal clusters. We will also study the potential of cluster-based materials for a new generation of ferroelastic, ferroelectric, and multi-ferroic materials.

References:

1. Boateng, D. A., Word, M. D., Gutsev, L. G., Jena, P., and Tibbetts, K. M.: “Conserved Vibrational Coherence in the Ultrafast Rearrangement of 2-Nitrotoluene Radical Cation”, *J. Phys. Chem. A* **123**, 1140 (2019)
2. He, X., Fang, H., Gosztola, D. J., Jiang, Z., Jena, P., and Wang, W.: “Mechanistic insight of Photocatalysis using MIL-100(Fe)/TiO₂ Composites”, *ACS Appl. Mat. and Interfaces* **11**, 12516 (2019)
3. Teprovich Jr., J. A., Ward, P. A., Weeks, J. A., Tinkey, S. C., Huang, C., Zhou, J., Zidan, R., Jena, P.: “Hydrogenated C₆₀ as high-capacity stable anode materials for Li-ion batteries”, *ACS Applied Energy Materials* **2**, 6453 (2019)

4. Gutsev, L. G., Gutsev, G. L., Tibbetts, K. M., and Jena, P.: “Homocoupling and Heterocoupling of Grignard Perfluorobenzene Reagents via Aryne Intermediates: A DFT Study”, *J. Phys. Chem. A* **123**, 9693 (2019)
5. Ghoilpour-Ranjbar, H., Fang, H., Guan, J., Peters, D., Seifert, A., Jena, P., Laskin, J.: “Designing New Metal Chalcogenide Nanoclusters Through Atom-by-Atom Substitution”, *Small* (in press)
6. Fang, H. and Jena, P.: “Stable Tetra- and Penta-Anions in the Gas Phase”, *Angew. Chem. Int. Ed.* **58**, 11248 (2019)
7. Reddy, G. N., Parida, R., Rivera, R. I., Chakraborty, A., Jena, P., and Giri, S.: “Unique Reactivity of Boron in B@(Ge_9Y_3)₃ [Y = H, CH₃, BO, CN]: Formation of a Lewis Base”, *Phys. Chem. Chem. Phys.* **21**, 23301 (2019)
8. Yadav, M., Fang, H., Giri, S., Jena, P.: “Ligand Stabilization of Manganocene Dianion – In Defiance of the 18 Electron Rule”, *Phys. Chem. Chem. Phys.* **21**, 24300 (2019) (**cover page**)
9. Zhong, M., Fang, H., and Jena, P.: “Record-High Stability and Compactness of Multiply-Charged Clusters Aided by Selected Terminal Group”, *Phys. Chem. Chem. Phys.* **22**, 4880 (2020)
10. Mayer, M. et. al. “Rational design of an argon-binding superelectrophilic anion”, *Proc. Nat. Acad. Sci.* **116**, 8167 (2019)
11. Zhao, H., Zhou, J., and Jena, P.: “Stability of B₁₂(CN)₁₂²⁻: Implications for Lithium and Magnesium Ion Batteries”, *Angew. Chem. Int. Ed. (VIP)* **55**, 3704 (2016)

Publications (2019-21):

1. Fang, H. and Jena, P.: “Sodium Superionic Conductors Based on Clusters”, *ACS Appl. Mat. and Interfaces* **11**, 963 (2019)
2. Boateng, D. A., Word, M. D., Gutsev, L. G., Jena, P., and Tibbetts, K. M.: “Conserved Vibrational Coherence in the Ultrafast Rearrangement of 2-Nitrotoluene Radical Cation”, *J. Phys. Chem. A* **123**, 1140 (2019)
3. Hassan, A., Guo, Y., Wang, Q., Kawazoe, Y., and Jena, P.: “Interfacial properties of penta-graphene-metal contacts”, *J. Appl. Physics* **125**, 065308 (2019)
4. Qie, Y., Liu, J., Wang, S., Sun, Q., and Jena, P.: “Tetragonal C₂₄: A Topological Nodal-surface Semimetal with Potential as an Anode Material for Sodium Ion Batteries”, *J. Mat. Chem. A* **7**, 5733 (2019)
5. He, X., Fang, H., Gosztola, D. J., Jiang, Z., Jena, P., and Wang, W.: “Mechanistic insight of Photocatalysis using MIL-100(Fe)/TiO₂ Composites”, *ACS Appl. Mat. and Interfaces* **11**, 12516 (2019)
6. Reddy, G. N., Parida, R., Jena, P., and Giri, S.: “Superhalogens as Building Blocks of Super Lewis Acids”, *Chem. Phys. Chem.* **20**, 1 (2019)
7. Zhou, W., Shen, H., Wang, Q., Kawazoe, Y., and Jena P.: “N-doped Peanut-Shaped Carbon Nanotubes for Efficient CO₂ Electrocatalytic Reduction, *Carbon* **152**, 241 (2019)
8. Halsey-Moore, C., Jena, P., McLeskey, Jr., J. T.: “Range-separated DFT functionals for orbital energy modeling of MEH-PPV polymer”, *J. Comp. Theo. Chem.* **1162**, 112506 (2019)
9. Fang, H. and Jena, P.: “Stable Tetra- and Penta-Anions in the Gas Phase”, *Angew. Chem. Int. Ed.* **58**, 11248 (2019) (**cover page**)
10. Chen, G., Zhao, T., Wang, Q. and Jena, P.: “Rational Design of Stable Di-anions and The Concept of Super-Chalcogens,” *J. Phys. Chem. A* **123**, 5753 (2019)
11. Wang, S., Liu, J., Qie, Y., Gong, S., Sun, Q., Jena, P.: “High-pressure induced stable phase of LiMnSiO₄ as high-performance poly-anion cathode material”, *J. Mat. Chem. A* **7**, 16406 (2019)

12. Guo, Y., Zhang, C., Zhou, J., Wang, Q., Jena, P.: "Lattice dynamic and instability in penta silicene: A light single-element ferroelectric material with high Curie temperature", *Phys. Rev. Applied* **11**, 064063 (2019)
13. Chen, S., Huang, C., Sun, H., Ding, J., Jena, P., Kan, E.: "Boosting the Curie Temperature of Twodimensional Semiconducting CrI₃ Monolayer through van der Waals Heterostructures", *J. Phys. Chem. C* **123**, 17987 (2019)
14. Nafday, D., Fang, Ho., Jena, P., Saha-Dasgupta, T.: "Boronated Holey Graphene: A case of 2D Ferromagnetic Metal", *Phys. Chem. Chem. Phys.* **21**, 21128 (2019)
15. Teprovich Jr., J. A., Ward, P. A., Weeks, J. A., Tinkey, S. C., Huang, C., Zhou, J., Zidan, R., Jena, P.: "Hydrogenated C₆₀ as high-capacity stable anode materials for Li-ion batteries", *ACS Applied Energy Materials* **2**, 6453 (2019)
16. Li, X., Liu, J., Wang, F. Q., Wang, Q., and Jena, P.: "Rational design of porous nodal-line semi metallic carbon for K-ion battery anode material", *J. Phys. Chem. Letters* **10**, 6360 (2019)
17. Reddy, G. N., Parida, R., Rivera, R. I., Chakraborty, A., Jena, P., and Giri, S.: "Unique Reactivity of Boron in B@(Ge_9Y_3)₃ [Y = H, CH₃, BO, CN]: Formation of a Lewis Base", *Phys. Chem. Chem. Phys.* **21**, 23301 (2019) (**cover page**)
18. Yadav, M., Fang, H., Giri, S., Jena, P.: "Ligand Stabilization of Manganocene Dianion – In Defiance of the 18 Electron Rule", *Phys. Chem. Chem. Phys.* **21**, 24300 (2019) (**cover page**)
19. Gutsev, L. G., Gutsev, G. L., Tibbetts, K. M., and Jena, P.: "Homocoupling and Heterocoupling of Grignard Perfluorobenzene Reagents via Aryne Intermediates: A DFT Study", *J. Phys. Chem. A* **123**, 9693 (2019)
20. Huang, C., Wu, F., Yu, S., Jena, P., and Kan, E.: "Discovery of twin orbital-order phases in ferromagnetic semiconducting VI₃ monolayer: Driven by electronic correlation and Inter-atomic Exchange", *Phys. Chem. Chem. Phys.* **22**, 512 (2020)
21. Xu, M., Huang, C., Li, Y., Liu, S., Zhong, X., Jena, P., Kan, E., and Wang, Y.: "Electrical Control of Magnetic Phase Transition in a Type-I Multiferroic Double-metal Trihalides Monolayer", *Phys. Rev. Lett.* **124**, 067602 (2020)
22. Zhong, M., Fang, H., and Jena, P.: "Record-High Stability and Compactness of Multiply-Charged Clusters Aided by Selected Terminal Group", *Phys. Chem. Chem. Phys.* **22**, 4880 (2020) (**cover page**)
23. Erakulan, E. S., Mathan Kumar, E., Jena, Puru, and Thapa, R.: "B₂H₆ splitting on catalytic surfaces and role of BH₃ towards hydrogen spillover", *J. Power Sources* **455**, 227973 (2020)
24. Qie, Y., Wang, S., Xie, H., Fu, S., Sun, Q., and Jena, P.: "Yttrium-Sodium Halides as Promising Solid-State Electrolytes with High Ionic Conductivity and Stability for Na Ion Battery", *J. Phys. Chem. Lett.* **11**, 3376 (2020)
25. Huang, C., Fang, H., Whetten, R. and Jena, P.: "Robustness of Superatomic Clusters and Their Potential as Building Blocks of Materials", *J. Phys. Chem. C* **124**, 6435 (2020)
26. Zhao, K., Guo, Y., Shen, Y., Wang, Q., Kawazoe, Y., and Jena, P.: "Penta-BCN: A New Ternary Pentagonal Monolayer with Intrinsic Piezoelectricity", *J. Phys. Chem. Letters* **11**, 3501 (2020)
27. Shen, Y., Wang, Q., Kawazoe, Y., Jena, P.: "Potential of porous nodal-line semi-metallic carbon for sodium-ion battery anode", *J. Power Sources* **478**, 228746 (2020)
28. Zhou, W., Xie, H., Qie, Y., Wang, S., Wang, Q., Jena, P. "3D porous honeycomb carbon as Na-ion battery anode material achieving high capacity, excellent rate performance with long-term cycle life", *Carbon* **168**, 163 (2020)
29. Younis, U.; Muhammad, I.; Wu, W.; Ahmad, S.; Sun, Q.; Jena, P. "Assembling Si₂BN nanoribbons to a 3D porous structure as a universal anode material for both Li- and Na-ion batteries with high performance", *Nanoscale* **12**, 19367 (2020)
30. Khossossi, N., Banerjee, A., Essaoudi, I., Ainane, A., Jena, P., Ahuja, R. "Thermodynamics and kinetics of 2D g-GeC monolayer as an anode material for Li/Na-ion batteries", *J. Power Sources* **485**, 229318(2021)

31. Guan, J., Zhang, X., Deng, K., Jena, P., and Kan, E.: "Two-dimensional Metal-free Boron Chalcogenides B_2X_3 (X=Se and Te) as Photocatalysts for Water Splitting Under Visible Light", *Nanoscale* DOI: 10.1039/d0nr08203a
32. Ghoilpour-Ranjbar, H., Fang, H., Guan, J., Peters, D, Seifert, A., Jena, P., Laskin, J.: "Designing New Metal Chalcogenide Nanoclusters Through Atom-by-Atom Substitution", *Small* (in press)
33. Gao, Y., Wu, M., Jena, P.: "A Family of Ionic Supersalts with Covalent-like Directionality and Unconventional Multiferroicity", *Nature Commun.* (in press)
34. Jena, P. and Sun, Q., Editors, "*Superatoms: Principles, Synthesis, and Applications*", Wiley (in press)
35. Jena, P., Fang, H., Sun, Q.: "Rational Design of Superatoms using Electron-Counting Rules" in *Superatoms: Principles, Synthesis, and Applications*, Edited by P. Jena and Q. Sun, Wiley (in press)
36. Wu, M. and Jena, P.: "Superatom-based Ferroelectrics" in *Superatoms: Principles, Synthesis, and Applications*, Edited by P. Jena and Q. Sun, Wiley (in press)
37. Jena, P., Fang, H., and Sun, Q.: "Cluster-based Materials for Energy Harvesting and Storage" in *Superatoms: Principles, Synthesis, and Applications*, Edited by P. Jena and Q. Sun, Wiley (in press)
38. Li. T. Sun, Q., and Jena, P.: "Thermal and thermoelectric properties of cluster-based materials" in *Superatoms: Principles, Synthesis, and Applications*, Edited by P. Jena and Q. Sun, Wiley (in press)
39. Sheng, H., Sun, Q., and Jena P.: "Clusters for CO_2 Activation and Conversion" in *Superatoms: Principles, Synthesis, and Applications*, Edited by P. Jena and Q. Sun (in press)
40. Jena, P and Sun, Q.: "Conclusions and Future Outlook" in *Superatoms: Principles, Synthesis, and Applications*, Edited by P. Jena and Q. Sun (in press)

Stimuli-Responsive Mesostructured Hybrid Materials

Ivan I. Smalyukh, University of Colorado at Boulder

Program Scope.

The main objective of this project is to explore self-organization of pre-engineered anisotropic functional units into colloidal composites with ordered mesoscopic structures that can be tuned and switched by weak external stimuli, such as light and low-voltage electric fields. Tunable composite materials with interesting physical behavior are designed through integrating unique properties of solid nanostructures with the facile responses of soft matter to weak external stimuli. The research focuses on understanding and control of self-assembly of metal and semiconductor nanoparticles, as well as on material behavior arising from their ordered self-organization and alignment. The design and realization of desired physical properties in these composites are based on the following three strategies: (1) discovery of new condensed matter phases of hybrid molecular-colloidal systems enriched by diversity of colloidal particle's geometric shapes, surface charging, boundary conditions for molecular alignment and chirality; (2) topology of continuous & singular field configurations in the molecular-colloidal systems; (3) effective medium behavior and plasmon-exciton interactions in colloidal assemblies formed by different types of nanoparticles co-assembled at the mesoscopic scales. The fundamental studies of interactions and ordering of nanoparticles reveal underpinning physical mechanisms that guide mesoscale morphology and ultimately determine material properties of the self-assembled composites. PI explores mesoscale self-assembly of anisotropic nanoparticles dispersed in responsive liquid crystalline host media that will enable new composites with properties controlled by applying fields, changing temperature, and using other external stimuli. The focus is on fundamental understanding and control of nanoscale self-assembly and alignment of metal and semiconductor nanoparticles that enable new material behavior arising from orientationally and positionally ordered self-organization of anisotropic molecules and nanoparticles into tunable long-range structures. Electrical realignment of the liquid crystal host, like that used in displays, allows for rearrangement and reorientation of anisotropic nanoparticles, leading to an unprecedented control over self-assembled nanostructures and to dramatic changes in the material emergent behavior and properties. The effective-medium optical properties are characterized and correlated with the hierarchical structure and composition of self-assembled configurations, as well as with plasmon-excitation and other interactions separately studied at the level of individual nanoparticles. Experiments are conducted in parallel with analytical and numerical modeling of interactions and effective-medium optical properties, which provide important insights. PI explores how the ensuing novel composite materials can be used to control transmission and directional scattering of light, as needed for applications in smart windows, displays and electro-optic devices. This research transcends traditional disciplinary boundaries of physics, topology, chemistry, engineering, and materials science. The research in this project broadly advances our knowledge of the nanoscale self-organization phenomena and the ensuing physical behavior.

Recent Progress.

The main recent progress in our research includes the discoveries of monoclinic nematics (Nature 2021) [1], elastic colloidal monopoles (Nature 2019) [2] and high-order multipoles (Nat. Comm. 2020) [3], magnetic and nematic skyrmion bags (Nat Phys 2019) [4], heliknotons and hopfions [5], electrostatically controlled anchoring [6] & interactions [7], & many other (see the 2-year publication list). As an example, in [2] PI developed nematic colloids with strong elastic monopole moments and demonstrated switching of these colloidal atoms by unstructured light, which echoed the common ability of driving the conventional atoms between the ground and various excited states. PI also demonstrated out-of-equilibrium dynamic assembly of the colloidal particles, as well as explained this diverse and surprising behavior using a model that considers the balance of optical and elastic torques responsible for the excited-state elastic monopoles [2]. Below, PI briefly summarizes the recent research finding that just appeared in Nature and introduced a new mesomorphic state of matter that combines monoclinic orientational order and fluidity [1].

Deep relations are believed to exist between symmetries of building blocks and condensed matter phases they form. For example, constituent molecular and colloidal rods and discs impart their uniaxial symmetry onto nematic liquid crystals, like the ones used in displays. Low-symmetry organizations could hypothetically form in mixtures of rods and discs, but entropy tends to phase-separate them at molecular and colloidal scales whereas strong elasticity-mediated interactions drive formation of chains and crystals in nematic colloids. To have a structure with few or no symmetry operations apart from the trivial ones has so far been demonstrated to be a property of solids alone, but not of their fully fluid condensed matter counterparts, even though such symmetries have been considered theoretically and observed in magnetic colloids. PI recently showed [1] that dispersing highly anisotropic charged colloidal discs in a nematic host composed of molecular rods provides a platform for observing many low-symmetry mesomorphic phases. Depending on temperature, concentration and surface charge of the discs, researchers found nematic, smectic and columnar organizations with symmetries ranging from axisymmetric uniaxial to orthorhombic and monoclinic. With increasing temperature, PI and his team observe unusual transitions from less to more ordered states and re-entrant phases. Most importantly, they demonstrate the presence of monoclinic colloidal nematic order as well as the possibility of thermal and magnetic control of low-symmetry self-assembly. These experimental findings are supported by theoretical and numerical modelling of the colloidal interactions between discs in the nematic host and may provide a route towards realizing myriads of new condensed matter phases in systems with dissimilar shapes and sizes of building blocks, as well as their technological applications. Since the works of Einstein and Perrin showed how particles in colloidal dispersions obey the same statistical thermodynamics as atoms and molecules, the colloidal atom paradigm has provided insights into physics of atomic and molecular systems through probing dynamics of colloidal crystals and glasses. This colloidal atom paradigm has inspired the development of colloidal self-assembly to reproduce the diversity of atomic systems, but this PI's recent work [1] demonstrates monoclinic nematic

colloidal fluids that have not been demonstrated in molecular systems to date, potentially inspiring future discoveries of counterparts of these colloidal fluids in molecular, polymeric, micellar and other systems. Importantly, the phase behavior of this molecular-colloidal composite of molecular rods and colloidal discs is readily controlled by changing temperature, surface charging of discs and number density of discs within the molecular nematic host medium (Fig. 1). The structural organization can be further controlled by weak external fields; for example, magnetic fields of \sim 50–100 mT readily reconfigure self-assembled colloidal structures.

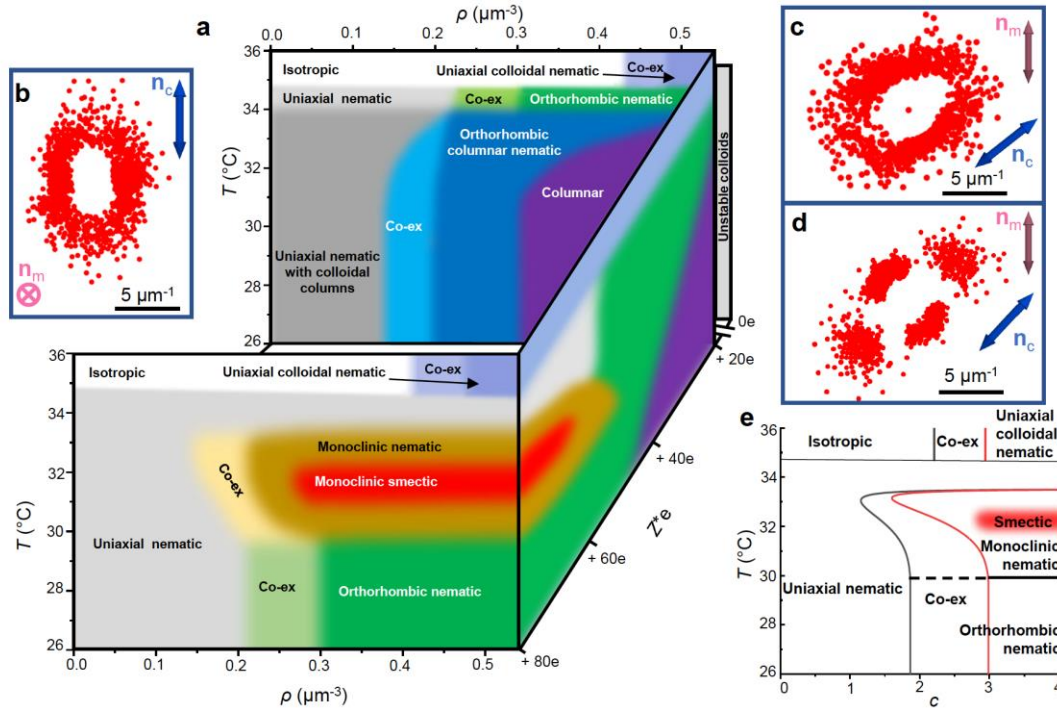


Fig. 1. Phase diagrams and characterisation of phases in a system of molecular rods and colloidal discs.

Diagram shows the hybrid liquid crystal phases emerging upon variation of the number density ρ , temperature T and effective colloidal surface charge $Z^* e$. “Co-ex” refers to co-existence regions between neighbouring phases. Discs aggregate at $Z^* e < +10e$ when nemato-elastic attractions overpower electrostatic repulsions; Wigner-type crystals form at $Z^* e > +100e$. Formation of colloidal columns within the uniaxial nematic at $Z^* e = +20e$ becomes progressively slower with decreasing ρ , but dimers and short columns are found starting from $\rho \approx 0.01\mu\text{m}^{-3}$ at room temperature. T is measured with an error of $\pm 0.1^{\circ}\text{C}$; relative errors of estimating ρ and $Z^* e$ are $\pm 5\%$ and $\pm 1\%$, respectively. (b-d) Fourier analysis of pairwise colloidal positions in an orthorhombic nematic at $\rho = 0.34\mu\text{m}^{-3}$, $T = 27.0 \pm 0.1^{\circ}\text{C}$ (b), monoclinic nematic at $\rho = 0.31\mu\text{m}^{-3}$, $T = 30.7 \pm 0.1^{\circ}\text{C}$ (c), and monoclinic smectic at $\rho = 0.29\mu\text{m}^{-3}$, $T = 31.7 \pm 0.1^{\circ}\text{C}$ (d). The Fourier analysis is based on 3D imaging (based on photon-upconverting luminescence excited by infrared femtosecond laser light) and tracking of disc positions with an error $< 50\text{nm}$. (e) Theoretical T versus dimensionless concentration $c = \rho D^3 \pi^2 / 16$ phase diagram for $Z^* e \approx +80e$, corresponding to its experimental counterpart in (a); D is the disk diameter. The diagram is obtained analytically by considering steric, screened electrostatic and weak elastic interactions between the colloidal disks. For more details, see Ref. [1].

The newly discovered composite soft matter system exhibits orientational fluid order with the lowest monoclinic symmetry demonstrated so far, which emerges from the oblique mutual self-alignment of uniaxial colloidal and molecular building blocks at the mesoscale. Monoclinic order is unambiguously revealed through the direct imaging of discs that exhibit a skewed orientational

distribution and by the oblique relative alignment of the molecular and colloidal directors. While many solid substances, like the common painkiller paracetamol, can inter-transform between monoclinic and orthorhombic states, our work demonstrates that the plurality of low symmetries of orientational order can also be achieved in colloidal LC fluids. Low-symmetry nematic, smectic and columnar states of LC colloids may find important uses in applications ranging from displays to biodetectors and studies of nonabelian topological defects near orthorhombic-monoclinic nematic phase transitions. Being made of organic molecular soft matter medium and solid photon-upconverting discs, the system serves as an example of how the combination of soft and hard material systems at the mesoscale can result in emergent behaviour and highly tunable physical properties that can be controlled by weak thermal, magnetic, electric and other stimuli.

Future Plans. PI will continue developing mesostructured stimuli-responsive materials that combine unique properties of solid nanostructures (quantum dots and plasmonic nanoparticles) and facile responses of soft matter, along with emergent new behavior enabled by various aspects of topology of order parameter fields. Using twist-bend nematics of CB7CB and its mixtures doped with magnetically monodomain colloidal platelets, PI will explore topological transformations between heliknotons & hopfions in response to low voltages & weak magnetic fields. In-depth studies will reveal how mesoscale self-organization, which can yield centimeter-large monocrystals of colloidal nanoparticles with tunable center-to-center separations, leads to new physical behavior and material properties arising from a combination of unique properties of nanoparticles and structural organization at nanometer to macroscopic scales. Co-dispersions of quantum wells and plasmonic nanoparticles will be developed. In these systems, the PI will probe how plasmon-exciton interactions can lead to new physical behavior when the nanoparticle-scale interactions are combined with different forms of long-range orientational and positional ordering that can be tuned by weak external stimuli. Effective medium properties of these pre-engineered metamaterials will be studied. By exploiting unique properties of solid nanostructures, PI intends to develop a new breed of composites with novel physical behavior, pre-engineered properties, and facile response to external fields. For example, PI's preliminary studies show that mesostructured composites made of perovskite quantum nanoparticles dispersed in thermotropic chiral nematics can exhibit ultra-strong responses to light and electric fields; PI will study how luminescence lifetime of these dispersed nanoparticles can be tuned with the help of gold nanorod co-located with them in a single nematic medium in various geometries controlled by boundary conditions on nanorod surfaces.

References

1. H. Mundoor, J.-S. Wu, H. Wensink and **I.I. Smalyukh**. *Nature* **590**, 268-274 (2021).
2. Y. Yuan, Q. Liu, B. Senyuk and **I.I. Smalyukh**. *Nature* **570**, 214-218 (2019).
3. Y. Yuan, M. Tasinkevych and **I.I. Smalyukh**. *Nature Commun* **11**, 1-14 (2020).
4. D. Foster, C. Kind, P. J. Ackerman, J.-S. Tai, M. R. Dennis and **I. I. Smalyukh**. *Nature Physics* **15**, 655-659 (2019).
5. R. Voinescu, J.-S. B. Tai and **I. I. Smalyukh**. *Phys Rev Lett* **125**, 057201 (2020).

6. H. Mundoor, B. Senyuk, S. Park, B. Fleury and **I.I. Smalyukh**. *Science Advances* **5**, eaax4257 (2019).
7. J. Everts, B. Senyuk, H. Mundoor, M. Ravnik and **I.I. Smalyukh**. *Science Advances* **7**, eabd0662 (2021).

Publications within 2 years (DE-SC0019293):

1. H. Mundoor, J.-S. Wu, H. Wensink and **I.I. Smalyukh**. Thermally reconfigurable monoclinic nematic colloidal fluids. *Nature* **590**, 268-274 (2021).
2. J. Everts, B. Senyuk, H. Mundoor, M. Ravnik and **I.I. Smalyukh**. "Anisotropic electrostatic screening of charged colloids in nematic solvents." *Science Advances* **7**, eabd0662 (2021).
3. Y. Yuan, P. Keller and **I. I. Smalyukh**. Elastomeric Nematic Colloids, Colloidal Crystals and Microstructures with Complex Topology. *Soft Matter*, doi:10.1039/D0SM02135K (2021).
4. Y. Yuan, M. Tasinkevych and **I.I. Smalyukh**. From monopoles to high-order elastic multipoles in nematic colloids formed by gold mesoflowers. *Nature Commun* **11**, 1-14 (2020).
5. R. Voinescu, J.-S. B. Tai and **I. I. Smalyukh**. Hopf solitons in helical and conical backgrounds of chiral magnetic solids. *Phys Rev Lett* **125**, 057201 (2020).
6. B. Fleury, B. Senyuk, M. Tasinkevych and **I.I. Smalyukh**. Ferroelectric colloidal dipoles in liquid crystals. *Nano Lett.* **20**, 7835-7843 (2020).
7. I. I. Smalyukh. Knots and other new topological effects in liquid crystals and colloids. *Rep. Prog. Phys.* **83**, 106601 (2020).
8. M. Chekini, E. Prince, L. Zhao, H. Mundoor, **I. I. Smalyukh** and E. Kumacheva. Chiral carbon dots synthesized on cellulose nanocrystals. *Advanced Optical Materials* **8**, 1901911 (2020).
9. B. Senyuk, J. Aplinc, M. Ravnik and I.I. Smalyukh. High-order elastic multipoles as colloidal atoms. *Nature Commun.* **10**, 1825 (2019).
10. Q. Liu, A. Kuzyk, M. Endo and **I. I. Smalyukh**. Plasmonic colloidal origami with photo-switchable chirality in liquid crystals. *Opt. Lett.* **44**, 2831-2834 (2019).
11. J.-S. B. Tai and I. I. Smalyukh. Static Hopf solitons and knotted emergent fields in solid-state chiral ferromagnetic nanostructures. *Phys Rev Lett* **121**, 187201 (2019).
12. Y. Yuan, Q. Liu, B. Senyuk and **I.I. Smalyukh**. Elastic colloidal monopoles and out of equilibrium interactions in liquid crystals. *Nature* **570**, 214-218 (2019).
13. D. Foster, C. Kind, P. J. Ackerman, J.-S. Tai, M. R. Dennis and **I. I. Smalyukh**. Two-dimensional skyrmion bags in liquid crystals and ferromagnets. *Nature Physics* **15**, 655-659 (2019).
14. H. Mundoor, B. Senyuk, S. Park, B. Fleury and **I.I. Smalyukh**. Electrostatically controlled surface boundary conditions in nematic liquid crystals and colloids. *Science Advances* **5**, eaax4257 (2019).

15. B. Senyuk, K. Crust, A. Mozaffari, Y. Zhou, R. Zhang, J. de Pablo and **I.I. Smalyukh**.
Elastic colloidal octupoles and transformations of multipoles in nematic colloidal emulsions.
Science Advances, in press (2021).

Session VIII

DOE Award # DE-FG02-07ER46426
Light-Matter Interactions in Nanoscale Systems for Energy Applications

PI: Shanhui Fan,
 Department of Electrical Engineering, Stanford University. Email: shanhui@stanford.edu.

Co-PI: Prof. Mark Brongersma,
 Department of Material Science and Engineering, Stanford University, Email: markb29@stanford.edu.

Program Scope

The overall emphasis of the program is to develop a fundamental understanding of light-matter interaction at nanoscale, in the context of renewable energy harvesting, including enhancing the efficiency of solar cells. Towards this goal, we are undertaking substantial efforts on developing novel thermal radiators based on two-dimensional materials, on exploring the implications of time-dependent refractive index modulations in the control of thermal radiations, and on demonstrating various consequences of radiative cooling, including the radiative cooling of solar cells.

Below we review some of the major progresses made in this report period.

Recent Progress

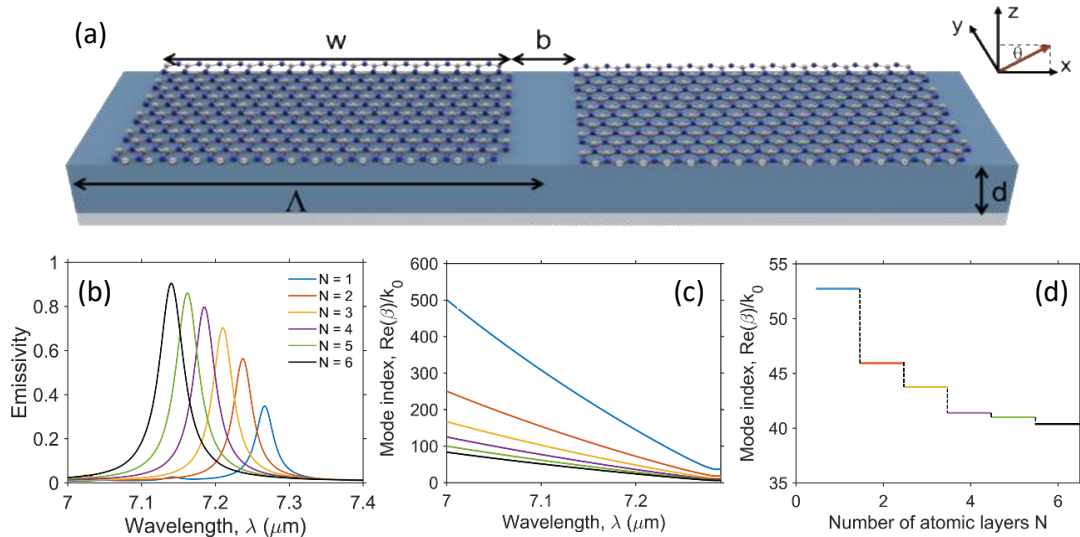


Figure 1 (a) Schematic of the considered thermal emitter with an atomically-thin hBN top layer. The middle layer (light blue) and the substrate (silvery) are MgF₂ and Ag films, respectively. (b) Emissivity spectra in the normal direction for the thermal emitters with different number of hBN atomic layers (N). (c) Mode index of the phonon polaritons in thin hBN film with different numbers of atomic layers. (d) Mode index of the ribbon mode at the peak emissivity for emitters with different numbers of atomic layers.

Atomic-Scale Control of Coherent Thermal Radiation. Originating from random charge fluctuations, thermal radiation is usually incoherent in both the spatial and temporal domains. However, the coherence of thermal radiation, especially the temporal coherence, can be significantly improved using judiciously patterned nanostructures. This can be utilized to improve the performance of energy harvesting and thermal management systems that harness thermal radiation for energy transport. The spectral and angular properties of thermal radiation are typically

controlled by bulk emitters with feature sizes comparable or somewhat smaller than the relevant thermal wavelengths, such as photonic crystals and multilayer structures. While such bulk thermal emitters provide plentiful bulk modes for thermal radiation control, low-dimension emitters such as those constructed with two-dimensional (2D) materials can often leverage a high modal density around strong materials resonances. They also offer new degrees of freedom to dynamically control thermal radiation, including the use of strain and electrical gating.

In this collaborative work between the Brongersma and Fan groups, we explore the control of temporally coherent thermal radiation at the atomic scale with 2D materials (Figure 1). In particular, we focus on using hexagonal boron nitride (hBN), which has a strong high-temperature phonon-polaritonic response in the mid-infrared spectral range. We show that, despite its atomic-scale thickness, thermal emitters made from single or a few atomic layers of hBN can generate a coherent emissivity spectrum with a peak emissivity comparable to bulk materials. The spectral emissivity peak of phononic 2D-material emitters exhibits a much higher quality factor compared to the emissivity peak from emitters based on plasmonic 2D materials like graphene. We show that the radiative properties of the considered hBN thermal emitters depend sensitively on the number of atomic layers. Thus this system provides a pathway to achieve atomic-scale control of thermal radiation.

This work has been accepted for publication in ACS Photonics.

Photonic refrigeration from time-modulated thermal emission. For a static structure maintained at a fixed thermodynamic temperature, its thermal radiation property is subject to a set of fundamental constraints, including the Stephan-Boltzmann law that constrains the emission power at every frequency, and the Kirchhoff law that requires the detailed balance between emission and absorption.

In this project, we systematically explored the thermal emission properties of dynamically modulated structure. Our results indicated that both the Stephan-Boltzmann law, and the Kirchhoff's law, can be overcome with a structure undergoes dynamic modulation.

Our results also pointed to a new possibility for constructing a photon-based heat engine. Active photonic cooling is of significant importance with the potential to realize robust, compact, vibration-free, all-solid-state refrigeration. To date, the proposed photonic cooling approaches, including laser cooling and electroluminescent cooling, are all based on luminescence and impose stringent requirements on luminescence efficiency. Recent advances in nanophotonic control of thermal emission have offered a promising approach to manipulate photon emission without the luminescence process. In this project, we proposed a photonic refrigeration technique based on time-modulation of thermal emission (Fig. 2). This technique results in a mechanism of

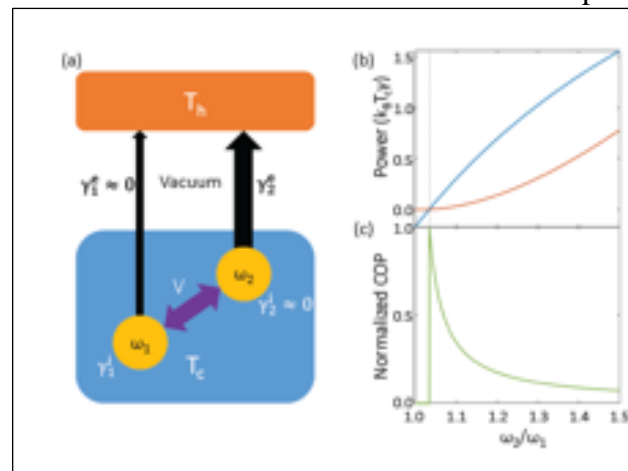


Figure 2: A photonic heat engine. (a) Basic setup. The cold side consists of two modes undergoing refractive index modulation. Such a time modulated thermal radiator can be used as a cooling device. (b) The power density and (c) the Coefficient of performance (COP) as a function of frequency ratio between the two modes on the cold side, as the structure undergoes refractive index modulation.

refrigeration with a significantly higher performance than laser cooling of solids, while also overcoming the stringent quantum efficiency requirements of electroluminescent cooling. Our work opens exciting new avenues in active, time-modulated control of thermal emission for active cooling and energy harvesting applications.

This work has been published in [Physical Review Letters](#). The paper was featured in Physics, the news outlet associated with the Physical Review journals.

Nighttime radiative cooling for water harvesting from solar panels. The sun is the most important and easily accessible thermodynamic resource for human beings. Photovoltaics nowadays has played a significant and increasingly important role in renewable energy. However, due to the lack of sun as a thermodynamic resource at night, photovoltaic systems, or in general any solar energy harvesting devices, which typically occupy large land areas, only work during the day and do not provide useful functionalities over a significant fraction of time.

On the other hand, at night there does exist a ubiquitous thermodynamic resource that has been largely underexplored: the low temperature outer space at 3K. Remarkably, the cold outer space can indeed be accessed through a process known as radiative cooling: Any sky facing objects can emit a significant fraction of thermal radiation into outer space through the atmosphere transparent window in the mid-

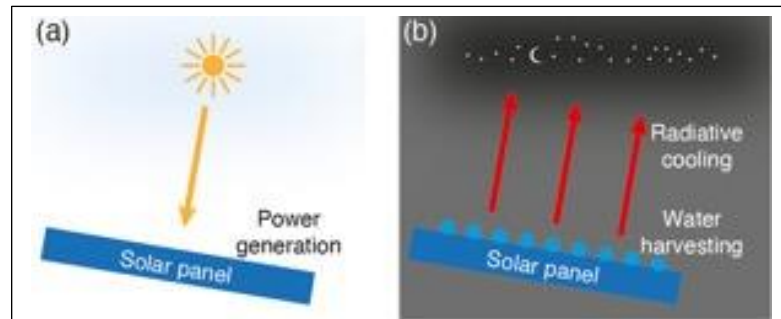


Figure 3: Solar panel for nighttime water harvesting. (a), Typical solar panels only work in the daytime with photovoltaic power generation. (b), Proposal of using solar panels at night for water harvesting from the air using radiative cooling.

infrared wavelength range. With recent advances in nanophotonics and materials innovation, radiative cooling has become a frontier of renewable energy research and with possible applications including enhancing efficiencies of air conditioning and solar energy systems, thermal management, and direct renewable power generation. Moreover, using radiative cooling to reach below the dew point for water harvesting from the air has also been demonstrated as a promising clean water generation approach. Due to its underlying mechanisms, radiative cooling works best in locations with good sky access. Interestingly, these coincide with locations where photovoltaic panels are typically installed. Therefore, it is of interest to explore the use of existing photovoltaic panels at night to perform radiative cooling. Such a process may enable a wide range of new functionalities for existing solar panels, which to date only work during the day.

In this paper, we propose to extend the functionality of solar panels into nighttime to perform water harvesting, using nighttime radiative cooling (Fig. 3). Such a process, if possible, could serve as a cost-effective, sustainable, and widely applicable approach for immediate applications including dust cleaning on solar panels for reducing photovoltaic power loss, agrophotovoltaic by a synergistic combination of both photovoltaics and agriculture using the same area, as well as evaporative cooling of solar panel during the day for reduced temperature and improved efficiency of solar panels. With theoretical analysis, we identified the suitable temperature and humidity range for nighttime water harvesting from solar panels, and outlined the water harvesting potential under various conditions. We further show that through photonic thermal emissivity engineering, both the amount of water production and the suitable temperature and humidity range can be

significantly improved. Our results point to new avenues to explore the nighttime utilization of a wide range of existing sky-facing solar energy harvesting systems, which were thought to work only during the day, and highlight the opportunities to use both the sun and the outer space as energy resources.

This work has been published in ACS Photonics.

Future Plans

In the near future (the coming year) we plan to focus on continued efforts towards understanding light-matter interaction in nanophotonic structures in the context of energy applications. In particular, building upon the theoretical works as discussed above on atomic scale control of thermal radiation, Fan and Brongersma's groups will collaborate towards experimental demonstration of such capability. We will also continue our efforts in the study of radiative cooling, focusing in particular on the improvement of nighttime power generation based on radiative cooling.

Journal Publications of DOE Sponsored Research in 2019-2021

1. Y. Li, K.-J. Zhu, Y.-G. Peng, W. Li, T. Yang, H.-X. Xu, H. Chen, X.-F. Zhu, S. Fan, and C.-W. Qiu, "Thermal meta-device in analogue of zero-index photonics," *Nature Materials*, vol. 18, pp. 48–54 (2019).
2. Z. Zhao, C. Guo, and S. Fan, "Connection of temporal coupled-mode-theory formalisms for a resonant optical system and its time-reversal conjugate," *Physical Review A*, vol. 99, art. No. 033839 (2019).
3. C. Chang, Z. Zhao, D. Li, A. J. Taylor, S. Fan, and H. Chen, "Broadband Linear-to-Circular Polarization Conversion Enabled by Birefringent Off-Resonance Reflective Metasurfaces," *Physical Review Letters*, vol. 123, art. No. 237401 (2019).
4. A. P. Raman, W. Li, and S. Fan, "Generating Light from Darkness," *Joule*, vol. 3, pp. 2679–2686 (2019).
5. A. Cordaro, J. van de Groep, S. Raza, E. F. Pecora, F. Priolo, M. L. Brongersma, "Antireflection High-Index Metasurfaces Combining Mie and Fabry-Perot Resonances," *ACS Photonics*, vol. 6, pp. 453-459 (2019).
6. M. Dong, N. Chen, X. Zhao, S. Fan, and Z. Chen, "Nighttime radiative cooling in hot and humid climates," *Optics Express*, vol. 27, pp. 31587-31598 (2019).
7. S. Peng, N. J. Schilder, X. Ni, J. van de Groep, M. L. Brongersma, A. Alù, A. B. Khanikaev, H. A. Atwater, and A. Polman, "Probing the Band Structure of Topological Silicon Photonic Lattices in the Visible Spectrum," *Physical Review Letters*, vol. 122, art. No. 117401 (2019).
8. K. X. Wang, Y. Guo, and S. Fan, "Wave optics light-trapping theory: mathematical justification and ultimate limit on enhancement," *Journal of Optical Society of America*, vol. 36, pp. 2414-2422 (2019).
9. W. Li and S. Fan. "Radiative cooling: harvesting the coldness of the universe," *Optics and Photonics News*, vol. 30, pp. 32-39 (2019).
10. X. Huang, W. Li, H. Fu, D. Li, C. Zhang, H. Chen, Y. Fang, K. Fu, S. P. DenBaars, S. Nakamura, S. M. Goodnick, C. Ning, S. Fan, and Y. Zhao. "High-Temperature Polarization-Free III-Nitride Solar Cells with Self-Cooling Effects," *ACS Photonics*, vol. 6, pp. 2096-2103 (2019).

11. M. Ono, P. Santhanam, W. Li, B. Zhao, and S. Fan, "Experimental demonstration energy harvesting from the sky using the negative illumination effect of a semiconductor photodiode," *Applied Physics Letters*, vol. 114, art. No. 161102 (2019)
12. S. Buddhiraju, W. Li, and S. Fan, "Photonic Refrigeration from Time-Modulated Thermal Emission," *Physical Review Letters*, vol. 124, art. No. 077402 (2020).
13. W. Li, S. Buddhiraju, and S. Fan, "Thermodynamic limits for simultaneous energy harvesting from the hot sun and cold outer space," *Light: Science and Applications*, vol. 9, art. No. 68 (2020).
14. M. Xue, K. Nassiri, Z. Lyu, J. Jiang, C. Ying, N. Lee, K. Zang, Y. Chen, T. Zheng, T. I. Kamins, M. L. Brongersma, K. C. Saraswat, J. S. Harris, "Free-standing 2.7 μm thick ultrathin crystalline silicon solar cell with efficiency above 12.0%," *Nano Energy*, vol. 70, art. No. 104466 (2020).
15. M. Dong, Z. Zhang, Y. Shi, X. Zhao, S. Fan, and Z. Chen, "Fundamental Limits of the Dew-Harvesting Technology," *Nanoscale and Microscale Thermophysics and Engineering*, vol. 24, pp. 43–52 (2020).
16. J. W. Stewart, J. H. Vella, W. Li, S. Fan, and M. H. Mikkelsen, "Ultrafast pyroelectric photodetection with on-chip spectral filters," *Nature Materials*, vol. 19, pp. 158–162 (2020).
17. L. Fan, W. Li, W. Jin, M. Orenstein, and S. Fan, "Maximal nighttime electrical power generation via optimal radiative cooling," *Optics Express*, vol. 28, pp. 25460-25470 (2020).
18. W. Li, M. Dong, L. Fan, J. J. John, Z. Chen, and S. Fan, "Nighttime Radiative Cooling for Water Harvesting from Solar Panels," *ACS Photonics*, vol. 8, pp. 269–275 (2021).
19. D. Li, X. Liu, W. Li, Z. Lin, B. Zhu, Z. Li, J. Li, B. Li, S. Fan, J. Xie, and J. Zhu, "Scalable and hierarchically designed polymer film as a selective thermal emitter for high performance all-day radiative cooling", *Nature Nanotechnology*, vol. 16, pp. 153-158 (2021).
20. K. Zhou, W. Li, B. B. Patel, R. Tao, Y. Chang, S. Fan, Y. Diao and L. Cai, "3D printable nanoporous polymer matrix composites for daytime radiative cooling", *Nano Letters*, vol. 21, pp. 1493-1499 (2021).
21. B. Zhao, J. Song, M. Brongersma, and S. Fan, "Atomic-scale control of coherent thermal radiation", *ACS Photonics* (accepted, 2021).

Metamaterials

Costas M. Soukoulis, Thomas Koschny, Jigang Wang
Ames Laboratory, Iowa State University, Ames, Iowa

Program Scope

Metamaterials are novel artificial materials that enable the realization of innovative properties unattainable in naturally existing materials. We exploit coherence in light and matter and significantly advance the photonic technologies our modern societies so vitally rely on. This will be accomplished through fundamental theoretical understanding, analysis, development, fabrication, and experimental characterization of metamaterials and investigate their feasibility for various applications. Our work targets current, fundamental problems and opportunities in controlling light with matter and matter with light. We expand the control afforded by metasurfaces over the radiative vacuum and radiation damping of resonant nanoparticles and enable new, fundamental improvements to metasurface-based difference-frequency generations for coherent THz sources as well as photon energy-conversion. We demonstrate constructive ways to increase the operational bandwidth of metasurfaces, explore non-trivial optical forces and novel avenues for implementing opto-mechanical coupling and coherent manipulation of mechanical state of matter with light.

Recent Progress

Dark-state surface lasers: Incorporating gain in metamaterials can balance losses, but must be performed properly, as a reduced or even eliminated absorption does not guarantee loss compensation. We have studied the possible regimes of interaction of a gain material with a passive metamaterial and show that background amplification and loss compensation are two opposite extremal behaviors, and that both of which can lead to lasing [1a]. The quest for subwavelength coherent light sources has led to the exploration of dark-mode based surface lasers, which allow for independent adjustment of the lasing state and its coherent radiation output. We further developed our theory of novel dark dielectric surface-state based lasing meta-surfaces (SMASER). Here, lasing, i.e. stimulated emission into a macroscopically populated dark electromagnetic surface state, constitutes a dielectric analog of lasing into dark plasmon-polaritons (SPASER) and allows to design ultra-thin, large-aperture lasing dielectric surfaces, with control over directionality and shape of the out-coupled laser beam. We found that to understand the observed lasing emissions in preliminary experiments, it was necessary to consider and quantify finite-size effects. We developed a theory for experimentally relevant finite-size effects and finite emitting apertures, which does explain the interplay between lasing mode structure, intended out-coupling of radiation and edge leakage. Depending on the size of the system, distinct and even counterintuitive behavior

of the lasing state is possible, determined by a balanced competition between multiple loss channels, including dissipation, intentional out-coupling of coherent radiation, and leakage from the edges of the finite system. Our results provide important guidance for ongoing experimental implementations and are crucial for the design of future experiments that will enable the realization of ultra-thin coherent light sources and [1b]. Building on the concept of dark-mode resonant metasurfaces weakly coupled to radiation, we also proposed and demonstrated a sub-wavelength dark-state-based metasurface, which enables configurable, simultaneous electric and magnetic responses with low loss [1c].

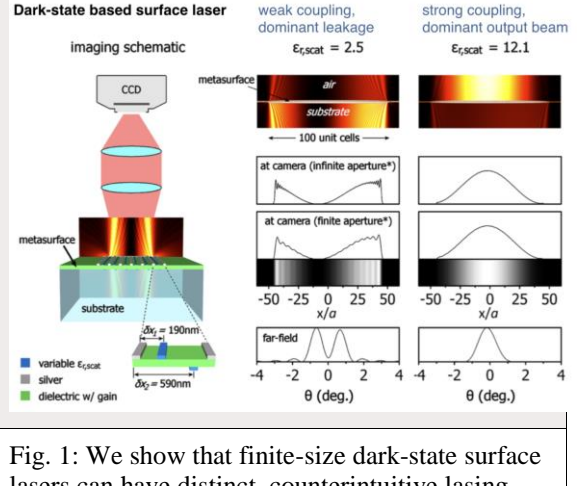


Fig. 1: We show that finite-size dark-state surface lasers can have distinct, counterintuitive lasing behavior, determined by competition between dissipation, coherent out-coupling, and leakage from the edges.

Radiation-controlled nonlinear metasurfaces for highly efficient THz generation: Optical, plasmonic metasurfaces offer new opportunities for developing high performance terahertz emitters and detectors beyond the limitations of conventional nonlinear bulk materials like ZnSe or LiNbO₃. However, optical nano-structures suffer from radiative damping that can outweigh dissipative loss. Simple meta-atoms for second-order nonlinear conversion encounter a fundamental trade-off in the necessary local symmetry breaking and local-field enhancement due to radiation damping that is inherent to the operating resonant mode and cannot be controlled separately. We have developed a novel theoretical concept for the suppression of radiative damping that enables strongly enhanced nonlinear light-matter interaction. Dark resonant metasurfaces could all but eliminate linear scattering and, therefore, remove this restriction to the improvement of terahertz generation efficiency. This can be achieved by combining a resonant dark-state metasurface, which locally drives nonlinear nano-resonators in the near field, with a specific spatial symmetry that enables destructive interference of the radiating linear moments of the meta-atoms, and perfect absorption via simultaneous electric and magnetic critical coupling of the pump radiation to the dark mode. This allows eliminating linear radiation damping while maintaining constructive interference and effective radiation of the nonlinear components. We numerically demonstrate a giant second-order nonlinear susceptibility of about 10^{-11} m/V, a one order of magnitude improvement compared with previously reported split-ring-resonator metasurfaces, leading to two orders of magnitude higher terahertz output power. Our study offers a new paradigm of high-efficiency, tunable nonlinear meta-devices and enables more energy efficient terahertz technologies and optoelectronic nano-circuitry [2].

Metallized-DNA templated meta-atoms can be insensitive to morphological disorder: Bottom-up fabrication of bio-templated nanostructures to form specific plasmonic nano-resonators that can implement meta-atoms holds promise as a means of achieving large-scale optical metamaterials. However, in contrast to top-down methods, the stochastic growth of these self-assembled meta-atoms is prone to significant disorder and surface roughness, which raises concerns about the robustness of their resonant optical response. We performed extensive numerical studies to demonstrate the robustness of optical response for self-assembled plasmonic metamaterials with morphological disorder, and the corresponding surface roughness, to answer the question as to what extent the disorder in meta-atom morphology must be controlled experimentally. Using the common split-ring-resonator (SRR) motif as an example, we developed an aggregated-random-spheres model that mimics the nucleated growth of metallized DNA origami templates to simulate realistic, experimentally observed levels of disorder and surface roughness of the self-assembled meta-atoms. We find that SRRs, even with significant level of roughness, show distinct and clean resonance features comparable to the ideal smooth SRR. Despite broadening line-shapes, the expected SRR resonances are observed even if dramatic disorder is introduced, demonstrating a high level of robustness of the optical responses of these deeply subwavelength meta-atoms. Only for extreme disorder, which causes drastic segmentation of the SRRs, does the resonant response disappear. Our results are very encouraging for the prospects of bottom-up fabrication towards functional metamaterials and meta-devices. [3].

Theory of multi-resonant metasurfaces: Metasurfaces derive their properties from the collective average response of typically resonant, sub-wavelength electric and/or magnetic scatterers. A major draw-back of these resonant meta-atoms is their inherently narrow operating bandwidth. Practical signals and applications almost always require a finite bandwidth of operation. Previously, we established a theory for multi-resonant meta-surfaces, which enable broad-band, arbitrarily large monotonic phase manipulation, solving a long-standing problem of broadband response from narrow metasurface resonances, and enabling arbitrary time-shift modulation of pulsed signals, with applications for broadband communication technology [4a]. We proposed practical designs suitable for future fabrication and experimental characterization in our lab. Our solution has consequences for the general spatial phase- and group-delay manipulations of radiation with metasurfaces, which promise to replace bulky prisms and lenses with 2D surfaces. We developed theoretical fundamentals of emulating bulk

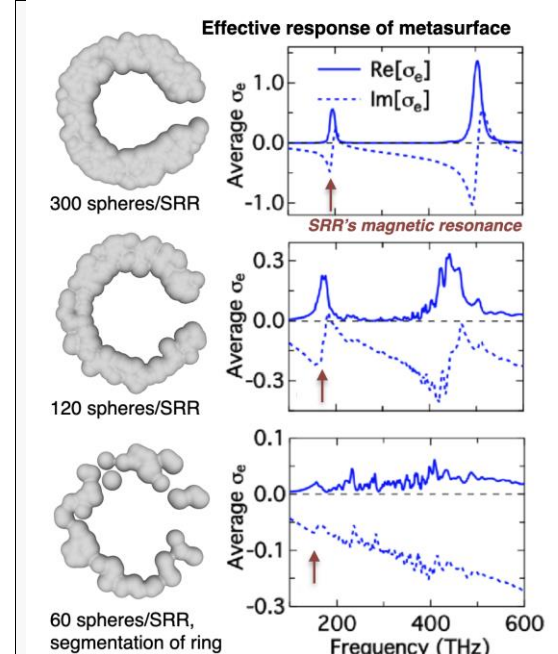


Fig. 2: We demonstrate that robust optical response is possible for metallized-DNA meta-atoms with realistic morphological disorder and surface roughness.

optics with achromatic metasurfaces based on multi-resonant broadband metasurfaces, which allows emulating bulk optics elements like slabs, lenses, prisms, etc. in a sub-wavelength thickness metasurface [4b].

Future Plans

Enhance nanoscale light-matter interactions at wavelengths orders of magnitude larger: Manipulating deeply subwavelength THz light-matter interaction, radiation damping, and local near-field with metasurfaces as a means to enhance nonlinearity and coupling to quantum processes in materials, enabling next-generation technology for sensing and THz generation.

Avoid or control radiation damping in resonant nanostructures, manipulate the electromagnetic vacuum seen by quantum emitters in metasurfaces: Develop dark-state surface lasers and active metasurfaces, understanding light-matter interaction in complex, dressed electromagnetic states coupled to quantum-gain to counter dissipative loss and enable novel functionalities in coherent optical radiation and near-field sources.

Breaking the bandwidth limit with multi-resonant metasurfaces: Implementing and demonstrating achromatic, multi-resonant metasurfaces to enable broadband group delay, refraction and lensing by a surface.

How can we take advantage of the tight integration of macromolecular mechanical and resonant electromagnetic states in metallized DNA-templated meta-molecules? Generate non-trivial optical forces at the nanoscale for control of matter with light; create and exploit coherent opto-mechanical coupling mediated light-matter interaction. Explore non-periodic metasurfaces, understanding limitations and benefits arising from spatial and morphological disorder, taking advantage of synergies with bio-inspired metamaterial fabrication.

References

1. (a) Nanomater. Nanotechnol. 9, 1 (2019); (b) ACS Photonics 5, 3788 (2018);
(c) ACS Photonics 7, 241 (2020).
2. PRL 122, 027401 (2019).
3. Adv. Opt. Mater. 8, 1901794 (2020).
4. (a) ACS Photonics, 5, 1101 (2018); (b) Adv. Opt. Mater. 2000942 (2020).

Publications

1. Tsilipakos, O., Koschny, T., Soukoulis, C.M. 2018. Metasurfaces with interleaved electric and magnetic resonances for broadband arbitrary group delay in reflection. 2018 12th International Congress on Artificial Materials for Novel Wave Phenomena. art. no. 8534076, pp. 389-391. <https://doi.org/10.1109/MetaMaterials.2018.8534076>
2. Fang, M., Shen, N.H., Sha, W.E.I., Huang, Z.X., Koschny, T., Soukoulis, C.M. 2019. Nonlinearity in the dark: Broadband terahertz generation with extremely high efficiency. *Physical Review Letters.* 122(2), art. no. 027401.
<https://doi.org/10.1103/PhysRevLett.122.027401>
3. Droulias, S., Koschny, T., Kafesaki, M., Soukoulis, C.M. 2019. On loss compensation, amplification and lasing in metallic metamaterials. *Nanomaterials and Nanotechnology.* 9, art. no. 1847980418817947. <https://doi.org/10.1177/1847980418817947>
4. Peng, B., Xu, K., Zhang, H., Ning, Z.Y., Shao, H.Z., Ni, G., Li, J., Zhu, Y.Y., Zhu, H.Y., Soukoulis, C.M. 2018. 1D SbSeI, SbSI, and SbSBr with high stability and novel properties for microelectronic, optoelectronic, and thermoelectric applications. *Advanced Theory and Simulations.* 1(1), art. no. 1700005. <https://doi.org/10.1002/adts.201700005>
5. Zheng, B., Yang, Y., Shao, Z., Yan, Q., Shen, N.H., Shen, L., Wang, H., Li, E., Soukoulis, C.M., Chen, H. 2019. Experimental realization of an extreme-parameter omnidirectional cloak. *Research.* art. no. 8282641.
<https://doi.org/10.34133/2019/8282641>
6. Fan, Y., Shen, N.H., Zhang, F., Zhao, Q., Wu, H., Fu, Q., Wei, Z., Li, H., Soukoulis, C.M. 2018. Graphene plasmonics: A Platform for 2D optics. *Advanced Optical Materials.* 7(3), art. no. 1800537. <https://doi.org/10.1002/adom.201800537>
7. Peng, B., Mei, H., Zhang, H., Shao, H., Xu, K., Ni, G., Jin, Q., Soukoulis, C.M., Zhu, H. 2019. High thermoelectric efficiency in monolayer PbI₂ from 300 K to 900 K. *Inorganic Chemistry Frontiers.* 6(4), pp. 920-928. <https://doi.org/10.1039/c8qi01297k>
8. Liu, F., Tsilipakos, O., Pitilakis, A., Tasolamprou, A.C., Mirmoosa, M.S., Kantartzis, N.V., Kwon, D.H., Kafesaki, M., Soukoulis, C.M., Tretyakov, S.A. 2019. Intelligent metasurfaces with continuously tunable local surface impedance for multiple reconfigurable functions. *Physical Review Applied.* 11(4), art. no. 044024.
<https://doi.org/10.1103/PhysRevApplied.11.044024>
9. Tsilipakos, O., Tasolamprou, A.C., Koschny, T., Kafesaki, M., Economou, E.N., Soukoulis, C.M. 2018. Pairing toroidal and magnetic dipole resonances in elliptic dielectric rod metasurfaces for reconfigurable wavefront manipulation in reflection. *Advanced Optical Materials.* 6(22), art. no. 1800633.
<https://doi.org/10.1002/adom.201800633>
10. Xu, K., Xu, Y., Zhang, H., Peng, B., Shao, H., Ni, G., Li, J., Yao, M., Lu, H., Zhu, H., Soukoulis, C.M. 2018. The role of Anderson's rule in determining electronic, optical and transport properties of transition metal dichalcogenide heterostructures. *Physical*

- Chemistry Chemical Physics. 20(48), pp. 30351-30364.
<https://doi.org/10.1039/c8cp05522j>
11. Shen, N., Hossen, M., Hillier, A.C., Koschny, T., Soukoulis, C.M. 2020. Robustness of optical response for self-assembled plasmonic metamaterials with morphological disorder and surface roughness. Advanced Optical Materials. 8, art. no. 1901794.
<https://doi.org/10.1002/adom.201901794>.
 12. Jain, A., James, A.R., Nogan, J., Luk, T.S., Subramania, G., Liu, S., Brener, I., Shen, N.H., Koschny, T., Soukoulis, C.M. 2020. Dark-state-based low-loss metasurfaces with simultaneous electric and magnetic resonant response. ACS Photonics. 7(1), pp. 241-248.
<https://doi.org/10.1021/acsphotonics.9b01480>.
 13. Tasolamprou, A.C., Zhang, L., Economou, E.N., Soukoulis, C.M., Koschny, T. 2020. Surface states on photonic crystals as hybrid dielectric metasurface bound states of the termination layer. ACS Photonics. 7(10), pp. 2842–2849.
<https://doi.org/10.1021/acsphotonics.0c01083>.
 14. Mavidis, C.P., Tasolamprou, A.C., Hasan, S.B., Koschny, T., Economou, E.N., Kafesaki, M., Soukoulis, C.M., Vos, W.L. 2020. Local density of optical states in the three-dimensional band gap of a finite photonic crystal. Physical Review B. 101(23), art. no. 235309. <https://doi.org/10.1103/PhysRevB.101.235309>
 15. Tsilipakos, O., Kafesaki, M., Economou, E.N., Soukoulis, C.M., Koschny, T., 2020. Squeezing a Prism into a Surface: Emulating Bulk Optics with Achromatic Metasurfaces. Adv. Opt. Mater. 2000942 (2020). <https://doi.org/10.1002/adom.202000942>

Light-matter interaction phenomena using subwavelength engineering of material properties

PI: Igal Brener

Team members: Michael B. Sinclair, Willie Luk, John Klem, Jayson Briscoe, Raktim Sarma

Sandia National Laboratories, Albuquerque, NM 87185, USA

Program Scope

Nanostructured materials offer new opportunities to rewrite the laws of light–matter interaction as they are customarily applied to bulk materials. This project focuses on such emergent behavior, with an emphasis on metamaterials coupled to semiconductors. Our hypothesis is that nanostructured “meta-atoms” that tailor electromagnetic fields for desired interactions with judiciously chosen materials can lead to metamaterials and metasurfaces with new types of optical behaviors or with improved behavior for optical emission, nonlinearities, or response to external stimuli. Our long-term objective is to uncover new optical and material behaviors that will expand our fundamental understanding of nanoscale materials, and eventually lead to technologically relevant applications. For the upcoming period of performance, we focus our efforts on two main topics. *Novel Light-Matter Interactions at the Nanoscale for Next Generation Nonlinear Metasurfaces* will investigate the rich nonlinear optical physics that can be obtained when the unique electromagnetic behaviors of metasurfaces are combined with nonlinear semiconductor materials, 2D materials, spintronic materials, or topological materials. *Ultrafast Spatiotemporal Phenomena in Metamaterials* will explore novel transient behavior such as non-reciprocity and frequency conversion that can be achieved through ultrafast spatial and temporal modulation of the meta-atom optical properties. To achieve these goals, our program combines state-of-the-art capabilities in: III-V semiconductor growth; semiconductor physics; electromagnetic theory and simulation; micro- and nano-lithography; and spectroscopic and ultrafast characterization.

Recent Progress

1. Spatial Temporal Phenomena: Frequency Conversion in a Time-Variant Dielectric Metasurface

Based on previous studies of the ultrafast optical behavior of semiconductor metasurfaces [1] along with our studies of high quality-factor (Q) metasurfaces [2], we explored all-optical tuning of the confined resonant modes through carrier induced refractive index modulation [3]. In this work, we demonstrated a spectral shift of 10 nm, at a pump fluence of $89 \mu\text{J cm}^{-2}$. This represents more than a linewidth of spectral tuning which could be applied to optical switching or rapidly varying spectral filtering. An absolute reflectance change of 0.31 is achieved using a pump fluence of $150 \mu\text{J cm}^{-2}$, limited by the fabrication quality.

Building on these encouraging results, we embarked on an investigation of a new type of temporal phenomena: optical frequency conversion in an optically pumped metasurface [4]. While traditional methods of frequency conversion rely on nonlinear processes such as harmonic generation, our approach

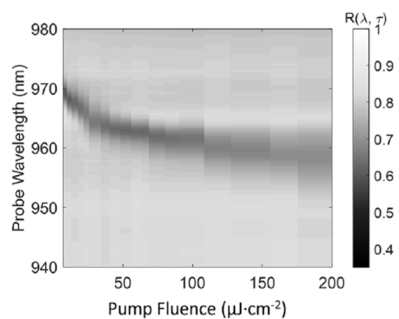


Figure 1: Reflectance of a high-Q metasurface as a function of pump fluence measured at a probe delay of 1 ps. More than one linewidth of tuning is achieved for fluences less than $100 \mu\text{J}\cdot\text{cm}^{-2}$.

exploits the modification of the frequency spectrum that occurs when an optical wave propagates through a medium with a rapidly varying refractive index. Specifically, we utilized a GaAs-based, broken-symmetry metasurface design [2] that exhibits a high-Q (~ 500) confined optical mode at 970 nm. Photons are injected into the high-Q mode using an ultrafast probe pulse (see Fig. 2a). While the probe photons are circulating within the nanoresonator cavity, a pump pulse is used to rapidly create a large population of free carriers that cause a near instantaneous change of the resonator's refractive index. This, in turn, causes a spectral shift of the cavity mode, leading to a rapid variation of the instantaneous phase of the confined pulse, and a concomitant shift of its optical frequency [4]. Fig. 2b shows the measured reflectance spectra of the probe pulse as a function of the pump-probe delay, while Fig. 2c shows individual spectra of the reflectance from the metasurface at different values of pump probe delay. The fringes observed in the experimental results are caused by optical interference between the frequency converted light and the portion of the probe that is not resonant with the cavity mode and are direct evidence of frequency conversion occurring in the time-variant metasurface.

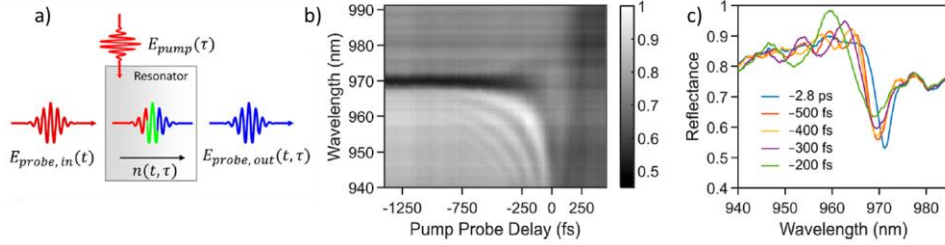


Figure 2: From reference 4. a) A schematic showing the principle of frequency conversion in a time-variant resonator. b) Experimental transient reflectance spectra measured at a pump fluence of $740 \mu\text{J cm}^{-2}$ c) Individual spectra of the reflectance from the metasurface at different values of pump probe delay.

2. Nonlinear Phenomena: High Harmonic Generation using Epsilon-Near-Zero Media

The epsilon-near-zero (ENZ) modes of nanoscale plasmonic films possess many beneficial attributes for the study of light-matter interactions, such as extremely large local field enhancements [5], and the ability to readily achieve perfect absorption in a simple geometry [6]. To capitalize on these properties, we studied harmonic generation from a nanoscale CdO film [7]. Here, we anticipated that the large resonant enhancement of the driving laser field would greatly boost the harmonic output. Utilizing 60 fs optical pulses centered at $2.08 \mu\text{m}$ to pump the sample using the same perfect absorption configuration as in [8], we observe odd-order harmonics from the third to the ninth order, corresponding to a shortest harmonic wavelength of $\sim 250 \text{ nm}$ (see Fig. 3). Interestingly, we find that ENZ-assisted harmonics exhibit a pronounced spectral redshift as well as linewidth broadening, that we attribute to photo-induced electron heating and the consequent time-dependent ENZ wavelength of the material. Due to the resonant field enhancements of the ENZ mode, this high harmonic generation is observed at much lower input laser intensities than other dielectrics that don't support ENZ modes such as zinc oxide and silicon [7].

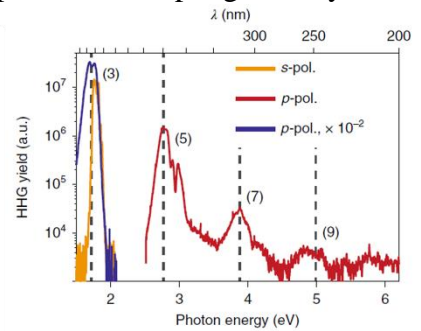


Figure 3: From reference 6. High-harmonic spectrum of the CdO-based structure. For p-polarized illumination, the spectrum extends from the third to the ninth order (blue and red line).

3. Second-Harmonic Generation from a Hybrid Dielectric Metasurface/Semiconductor Quantum-Well Structure

Building on previous studies of second harmonic generation (SHG) in semiconductor metasurfaces, we designed and demonstrated a hybrid approach for realizing efficient SHG in an ultrathin nonlinear structure that combines the attributes of low losses, high damage thresholds, large bandwidths, wavelength scalability, monolithic integrability, and ease of fabrication [9]. The new design employs high-Q leaky mode resonances in germanium dielectric metasurfaces that are coupled to highly nonlinear quantum well intersubband transitions (see Fig 4). Using this sample, we demonstrate SHG at pump wavelengths ranging from 8.5 to 11 μm , with a maximum second-harmonic nonlinear conversion factor of 1.1 mW/W^2 and maximum second-harmonic conversion efficiency of 2.5×10^{-5} at modest pump intensities of $10 \text{ kW}\cdot\text{cm}^{-2}$. These results open a new direction for designing low loss, broadband, and efficient ultrathin nonlinear optical devices.

3. Dielectric Metasurfaces for THz applications

Previously, we had demonstrated ultrafast optoelectronic switching with sub-picosecond switching times and extremely high ON/OFF conductivity contrast in all-dielectric photoconductive metasurfaces [10]. These studies opened possibilities for utilizing these metasurfaces for THz applications [11]. Our recent research on the metasurface design and the use of an alternative configuration of degenerate Mie modes expanded this new dimension in metasurface design, where not only optical but also electronic properties can be designed for non-linear effects and novel functionalities [12]. An example of a perfectly-absorbing photoconductive metasurface based on two magnetic dipole modes is shown in Fig. 5. This metasurface is designed to support degenerate magnetic dipole modes with the dipole moment *in* and *out* of the metasurfaces plane. The degeneracy of the Mie modes of opposite symmetry allows us to achieve perfect absorption of incident light within an optically thin metasurface. By combining near-IR excitation of this metasurface with THz waves, we detect photocurrent within the metasurface proportional to the amplitude to the THz electric field, enabling detection of THz waves with high efficiency. Our studies of photoconductive metasurfaces for detection of THz radiation opened doors to a wider range of investigations, where photoconductive metasurfaces can be explored also for non-linear generation of THz waves.

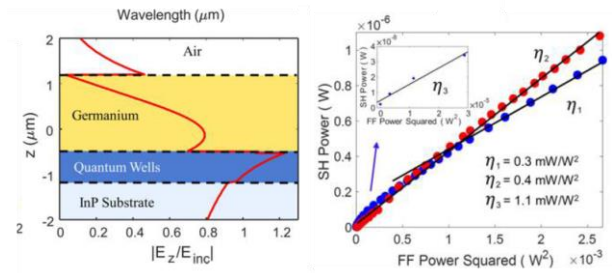


Figure 4. (left) A schematic cross-section of our SHG structure showing large field overlap between the germanium metasurface and the nonlinear quantum wells. (right) SHG power versus input power showing a maximum conversion efficiency of $1.1 \text{ mW}\cdot\text{W}^{-2}$

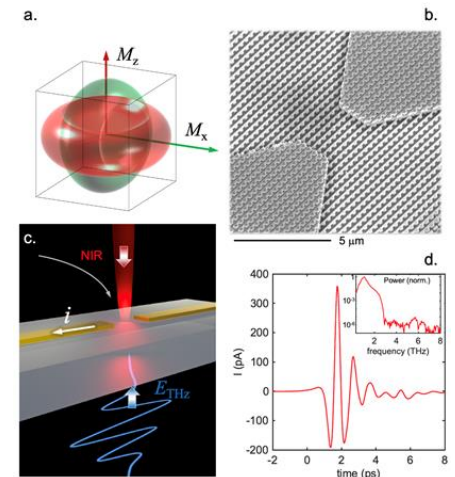


Figure 5: (a) Schematic diagram of a rectangular GaAs resonator supporting two magnetic dipole modes, M_x and M_z . (b) SEM of the photoconductive metasurface integrated with electrical contacts. (c) Schematic diagram showing the principle of THz wave detection where the NIR optical pulses are combined with a THz waves leading to photocurrent generation. (d) Example of THz pulse detection using a photoconductive metasurface [12].

Future Plans

Our activities will proceed along the following directions:

- i) *Novel Light-Matter Interactions at the Nanoscale for Next Generation Nonlinear Metasurfaces*: We will explore the “matter” aspect of nonlinear metasurfaces and study: 1) all-dielectric metasurfaces that employ new types of nonlinear optical materials including III-Sb semiconductor heterostructures; and 2) the integration of dielectric metasurfaces with other exotic material systems such as two-dimensional materials and Weyl semimetals.
- ii) *Non-Hermitian Physics and Exceptional Points of Coupled Nanoresonators*: We will fabricate two-layer Fano metasurfaces and study the evolution of the non-Hermitian physics as the coupling coefficient between adjacent nanoresonators is varied. Our initial efforts will be directed towards static metasurfaces and will be later followed by dynamic tuning of system through the exceptional points.
- iii) *Topological Photonic Metasurfaces*: We will collaborate with Alexander Cerjan, a recently hired theoretician at Sandia, to demonstrate semiconductor-based topological photonic structures exhibiting higher order topology such as corner states.
- iv) *Ultrafast and Spatiotemporal Phenomena in Metamaterials*: We will explore new semiconductor platforms such as InAs as well as new metasurface designs to maximize the refractive index modulation achievable using free carriers. We will develop optical means for repetitively modulating the metasurfaces and combine them with spatially structured illumination to study new spatial temporal effects such as enhanced frequency conversion.
- v) *Photoconductive metasurfaces THz wave generation*: we plan to explore all-dielectric perfectly absorbing ultrafast photoconductive metasurfaces for generation of THz waves.

References

- [1] M. R. Shcherbakov, S. Liu, V. V. Zubyuk, A. Vaskin, P. P. Vabishchevich, G. Keeler, T. Pertsch, T. V. Dolgova, I. Staude, I. Brener and A. A. Fedyanin, “Ultrafast all-optical tuning of direct-gap semiconductor metasurfaces”, Nat Commun **8**, 17 (2017).
- [2] S. Campione, S. Liu, L.I. Basilio, L.K. Warne, W.L. Langston, T.S. Luk, J.R. Wendt, J.L. Reno, G.A. Keeler, I. Brener, M.B. Sinclair, ACS Photonics 3, 2362-2367 (2016)
- [3] N. Karl, P.P. Vabishchevich, S. Liu, M.B. Sinclair, G.A. Keeler, G.M. Peake and I. Brener, Applied Physics Letters 115, 141103 (2019).
- [4] N. Karl, P.P. Vabishchevich, M.R. Shcherbakov, S. Liu, M.B. Sinclair, G. Shvets, and I. Brener, Nano Lett. 20, 7052–7058 (2020)
- [5] S. Campione, I. Brener, F. Marquier, Physical Review B 91, 121408 (2015)
- [6] T.S. Luk, S. Campione, I. Kim, S. Feng, Y.C. Jun, S. Liu, J.B. Wright, I. Brener, P. B. Catrysse, S. Fan, M. B. Sinclair, Physical Review B 90, 085411 (2014)
- [7] Y. M. Yang, J. Lu, A. Manjavacas, T.S. Luk, H. Z. Liu, K. Kelley, J. P. Maria, E. L. Runnerstrom, M.B. Sinclair, S. Ghimire, I. Brener, Nature Physics 15, 1022 (2019)
- [8] Y.M. Yang, K. Kelley, E. Sachet, S. Campione, T. S. Luk, J. P. Maria, M. B. Sinclair, I. Brener, Nature Photonics 11, 390 (2017)
- [9] R. Sarma, D. de Ceglia, N. Nookala, M.A. Vincenti, S. Campione, O. Wolf, M. Scalora, M.B. Sinclair, M.A. Belkin, and I. Brener, ACS Photonics 6, 1458 (2019)
- [10] T. Siday et al., “Terahertz Detection with Perfectly-Absorbing Photoconductive Metasurface,” Nano Lett. 19, 2888 (2019).
- [11]. O. Mitrofanov and I. Brener, “All-dielectric Photoconductive Metasurfaces for Terahertz Applications” Photoniques 101, 47 (2020).
- [12]. O. Mitrofanov et al., “Perfectly absorbing dielectric metasurfaces for photodetection,” APL Photonics 5, 101304 (2020).

Two-year list of publications supported by BES

1. H. Abudayyeh, B. Lubotzky, S. Majumder, J. A. Hollingsworth and R. Rapaport, "Purification of Single Photons by Temporal Heraldng of Quantum Dot Sources", *ACS Photonics* 6, 446 (2019).
2. S. Campione, J. F. Klem, S. Liu, I. Montano, M. B. Sinclair and T. S. Luk, "Experimental Evidence of the Lorentz-Like Effective Medium Resonance in Semiconductor Hyperbolic Metamaterials Using Strong Coupling to Plasmonic Metasurfaces", *IEEE Transactions on Antennas and Propagation* 68, 1748 (2020).
3. A. Jain, A. R. James, J. Nogan, T. S. Luk, G. Subramania, S. Liu, I. Brener, N.-H. Shen, T. Koschny and C. M. Soukoulis, "Dark-State-Based Low-Loss Metasurfaces with Simultaneous Electric and Magnetic Resonant Response", *ACS Photonics* 7, 241 (2019).
4. N. Karl, P. P. Vabishchevich, S. Liu, M. B. Sinclair, G. A. Keeler, G. M. Peake and I. Brener, "All-optical tuning of symmetry protected quasi bound states in the continuum", *Applied Physics Letters* 115, 141103 (2019).
5. O. Mitrofanov, T. Siday, P. Vabishchevich, L. Hale, T. Harris, T. S. Luk, J. L. Reno and I. Brener, in *Terahertz Emitters, Receivers, and Applications X*, edited by M. Razeghi, A. N. Baranov and M. S. Vitiello (SPIE, 2019), Vol. 11124, pp. 36.
6. R. Sarma, D. de Ceglia, N. Nookala, M. A. Vincenti, S. Campione, O. Wolf, M. Scalora, M. B. Sinclair, M. A. Belkin and I. Brener, "Broadband and Efficient Second-Harmonic Generation from a Hybrid Dielectric Metasurface/Semiconductor Quantum-Well Structure", *ACS Photonics* 6, 1458 (2019).
7. T. Siday, P. P. Vabishchevich, L. Hale, C. T. Harris, T. S. Luk, J. L. Reno, I. Brener and O. Mitrofanov, "Terahertz Detection with Perfectly-Absorbing Photoconductive Metasurface", *Nano Lett* 19, 2888 (2019).
8. C. F. Wang, T. G. Habteyes, T. S. Luk, J. F. Klem, I. Brener, H. T. Chen and O. Mitrofanov, "Observation of Intersubband Polaritons in a Single Nanoantenna Using Nano-FTIR Spectroscopy", *Nano Lett* 19, 4620 (2019).
9. M. Woerner, C. Somma, K. Reimann, T. Elsaesser, P. Q. Liu, Y. Yang, J. L. Reno and I. Brener, "Terahertz Driven Amplification of Coherent Optical Phonons in GaAs Coupled to a Metasurface", *Phys Rev Lett* 122, 107402 (2019).
10. Y. M. Yang, J. Lu, A. Manjavacas, T. S. Luk, H. Z. Liu, K. Kelley, J. P. Maria, E. L. Runnerstrom, M. B. Sinclair, S. Ghimire and I. Brener, "High-harmonic generation from an epsilon-near-zero material", *Nature Physics* 15, 1022 (2019).
11. V. V. Zubuk, P. P. Vabishchevich, M. R. Shcherbakov, A. S. Shorokhov, A. N. Fedotova, S. Liu, G. Keeler, T. V. Dolgova, I. Staude, I. Brener and A. A. Fedyanin, "Low-Power Absorption Saturation in Semiconductor Metasurfaces", *ACS Photonics* 6, 2797 (2019).
12. L. L. Hale, J. Keller, T. Siday, R. I. Hermans, J. Haase, J. L. Reno, I. Brener, G. Scalari, J. Faist and O. Mitrofanov, "Noninvasive Near-Field Spectroscopy of Single Subwavelength Complementary Resonators", *Laser & Photonics Reviews* 14, 1900254 (2020).
13. L. L. Hale, P. P. Vabishchevich, T. Siday, C. T. Harris, T. S. Luk, S. J. Addamane, J. L. Reno, I. Brener and O. Mitrofanov, "Perfect absorption in GaAs metasurfaces near the bandgap edge", *Opt Express* 28, 35284 (2020).
14. O. Mitrofanov and I. Brener, "All-dielectric photoconductive metasurfaces for terahertz applications", *Photoniques*, 47 (2020).
15. O. Mitrofanov, L. L. Hale, P. P. Vabishchevich, T. S. Luk, S. J. Addamane, J. L. Reno and I. Brener, "Perfectly absorbing dielectric metasurfaces for photodetection", *Applied Photonics* 5, 1 (2020).

16. O. Mitrofanov, C.-F. Wang, T. Habteyes, T. S. Luk, J. Klem, I. Brener, H.-T. Chen, M. Razeghi and A. N. Baranov, in *Terahertz Emitters, Receivers, and Applications XI*, edited by M. Razeghi and A. N. Baranov (SPIE, 2020), pp. 9.
17. N. Karl, P. P. Vabishchevich, M. R. Shcherbakov, S. Liu, M. B. Sinclair, G. Shvets and I. Brener, “Frequency Conversion in a Time-Variant Dielectric Metasurface”, *Nano Lett* 20, 7052 (2020).
18. R. Sarma, M. Goldflam, E. Donahue, A. Pribisova, S. Gennaro, J. Wright, I. Brener and J. Briscoe, “Optimization and Prediction of Spectral Response of Metasurfaces Using Artificial Intelligence”, *Crystals* 10, 1114 (2020).
19. R. Sarma, N. Nookala, K. J. Reilly, S. Liu, D. de Ceglia, L. Carletti, M. D. Goldflam, S. Campione, K. Sapkota, H. Green, G. T. Wang, J. Klem, M. B. Sinclair, M. A. Belkin and I. Brener, “Strong Coupling in All-Dielectric Intersubband Polaritonic Metasurfaces”, *Nano Lett* 21, 367 (2021).
20. A. Vaskin, S. Liu, S. Addamane, P. P. Vabishchevich, Y. Yang, G. Balarishnan, M. B. Sinclair, T. Pertsch, I. Brener and I. Staude, “Manipulation of quantum dot emission with semiconductor metasurfaces exhibiting magnetic quadrupole resonances”, *Optics Express* 29, 5567 (2021).
21. J. Bohn, T. S. Luk, C. Tollerton, S. W. Hutchings, I. Brener, S. Horsley, W. L. Barnes and E. Hendry, “All-optical switching of an epsilon-near-zero plasmon resonance in indium tin oxide”, *Nature Communications* **12**, 1017 (2021).

Opening New Frontiers of Near-Zero-Index (NZI) Optics: from Photonic Time Crystals to Non-Reciprocity and Novel Localization Regimes

PI: Alexandra Boltasseva, Purdue University

Program Scope

Our goals are to explore new optical phenomena and applications enabled by photonic materials that support the so-called near-zero index (NZI) or epsilon-near-zero (ENZ) regime, as well as to predict and control fundamental physical properties of optical materials. Specifically, our objectives are to (i) explore NZI materials behavior for the realization of photonic time-crystals; (ii) conduct the foundational studies of disorder, localization effects, and non-reciprocity in the NZI regime; and (iii) demonstrate ultrafast control over parity-time (PT) symmetry states in NZI media. The near-zero optical response of homogeneous media proposed in this project can potentially transform the research fields of nonlinear optics, photonic crystals, optical metamaterials, on-chip waveguide circuitry, lasers, enhanced sensitivity sensors, advanced light modulators as well as emerging quantum photonics.

Recent Progress

In the first period of this effort, we pursued our goals in three parallel thrusts. Towards the realization of photonic time crystals, we investigated both the modulation depth and speed in emerging photonic materials, specifically, titanium nitride (TiN), zirconium nitride (ZrN), cadmium oxide (CdO), zinc oxide (ZnO), and aluminum-doped zinc oxide (AZO). We showed that TiN and ZrN show large modulations of 15% and 50% in their ENZ regimes^[1], with sub-picosecond electron-phonon response times and nanosecond lattice cooling times. Another candidate material, under interband pumping, zinc oxide showed a sub-picosecond rise time and a fall time of 20ps^[2]. For cadmium oxide, the relaxation time was found to be around 100ps^[3]. Importantly, for CdO the dynamic response can be controlled/varied by the doping levels. Among the studied materials, AZO with a sub-10-fs rise time and a 500fs fall time exhibits the most suitable dynamic response and was selected as the material of choice for this effort. The comprehensive analysis, development and characterization of these materials form the solid foundation for the next thrust of the proposed work, where we will employ the fast, time-varying permittivity modulation in the NZI medium to realize non-reciprocal optical devices, photonic time crystals^[4] and other functionalities.

Near-zero-index materials open up new frontiers for nonlinear optics. We explored the usage of the proposed NZI media for demonstrating enhanced nonlinear optical effects. We demonstrated optical time reversal, adiabatic frequency shifts^[5], and broadband coherent absorption^[6] in time-varying ENZ media. We further showed that by strongly-coupled plasmonic antennae mounted on NZI media, nonlinear effects such as negative refraction^[7] can be enhanced by several orders of magnitude.

The realm of NZI materials and other media with unusual optical properties also includes metamaterials. Towards our second objective, we explored via simulation the thermal spin photonics in the near-field of nonreciprocal media and investigated polaritonic fluctuations in natural hyperbolic media. We also extended our exploration of different types of resonators and metasurfaces to augment optical switching, lasing, and quantum optics. We explored hybrid plasmonic resonators for ultrafast switching applications, and bound-states-in continuum structures for lasing applications^[8]. With MXenes, an emerging plasmonic material, we have demonstrated dynamically controlled random lasing^[9].

We further explored how machine learning can advance nanophotonic applications including the rapid classification of quantum emitters^[10] and the rapid design of nanocomposites^[11]. We demonstrated far-field, bright emission of single-photons from nitrogen vacancy centers coupled to plasmonic nano patch antennae^[12]. We also demonstrated a chip-compatible plasmonic launcher^[13], which provide an efficient way to couple single-photons into plasmonic devices on a chip.

Future Plans

Utilizing our discovery of the permittivity modulation limits, and the relaxation times in various oxides and nitrides, we plan on extending our efforts in the first demonstration of photonic time crystals. We also seek to employ our fast-acting NZI materials to demonstrate on-chip nonreciprocal devices for a wide array of optical device applications spanning optical switching, PT-symmetry studies, and lasing.

References

- [1] B. T. Diroll, S. Saha, V. M. Shalaev, A. Boltasseva, R. D. Schaller, *Adv. Opt. Mater.* **2020**, *8*, 2000652.
- [2] S. Saha, A. Dutta, C. DeVault, B. T. Diroll, R. D. Schaller, Z. Kudyshev, X. Xu, A. Kildishev, V. M. Shalaev, A. Boltasseva, *Mater. Today* **2020**, DOI 10.1016/j.mattod.2020.10.023.
- [3] S. Saha, B. T. Diroll, J. Shank, Z. Kudyshev, A. Dutta, S. N. Chowdhury, T. S. Luk, S. Campione, R. D. Schaller, V. M. Shalaev, A. Boltasseva, M. G. Wood, *Adv. Funct. Mater.* **2020**, *30*, 1908377.
- [4] E. Lustig, Y. Sharabi, M. Segev, *Optica* **2018**, *5*, 1390.
- [5] J. B. Khurgin, M. Clerici, V. Bruno, L. Caspani, C. DeVault, J. Kim, A. Shaltout, A. Boltasseva, V. M. Shalaev, M. Ferrera, D. Faccio, N. Kinsey, *Optica* **2020**, *7*, 226.
- [6] V. Bruno, S. Vezzoli, C. DeVault, T. Roger, M. Ferrera, A. Boltasseva, V. M. Shalaev, D. Faccio, *Micromachines* **2020**, *11*, 110.
- [7] V. Bruno, C. DeVault, S. Vezzoli, Z. Kudyshev, T. Huq, S. Mignuzzi, A. Jacassi, S. Saha,

- Y. D. Shah, S. A. Maier, D. R. S. Cumming, A. Boltasseva, M. Ferrera, M. Clerici, D. Faccio, R. Sapienza, V. M. Shalaev, *Phys. Rev. Lett.* **2020**, *124*, 043902.
- [8] S. I. Azzam, K. Chaudhuri, A. Lagutchev, Z. Jacob, Y. L. Kim, V. M. Shalaev, A. Boltasseva, A. V Kildishev, *Laser Photon. Rev.* **2021**, 2000411.
 - [9] Z. Wang, S. I. Azzam, X. Meng, M. Alhabeb, K. Chaudhuri, K. Maleski, Y. L. Kim, A. V. Kildishev, V. M. Shalaev, Y. Gogotsi, A. Boltasseva, *Opt. Mater. Express* **2020**, *10*, 2304.
 - [10] Z. A. Kudyshev, S. I. Bogdanov, T. Isacsson, A. V. Kildishev, A. Boltasseva, V. M. Shalaev, *Adv. Quantum Technol.* **2020**, *3*, 2000067.
 - [11] A. K. Boddeti, A. Alabassi, V. Aggarwal, Z. Jacob, *arXiv* **2019**, DOI 10.1364/ome.9.004765.
 - [12] S. I. Bogdanov, O. A. Makarova, X. Xu, Z. O. Martin, A. S. Lagutchev, M. Olinde, D. Shah, S. N. Chowdhury, A. R. Gabidullin, I. A. Ryzhikov, I. A. Rodionov, A. V. Kildishev, S. I. Bozhevolnyi, A. Boltasseva, V. M. Shalaev, J. B. Khurgin, *Optica* **2020**, *7*, 463.
 - [13] C. Chiang, S. I. Bogdanov, O. A. Makarova, X. Xu, S. Saha, D. Shah, Z. O. Martin, D. Wang, A. S. Lagutchev, A. V. Kildishev, A. Boltasseva, V. M. Shalaev, *Adv. Opt. Mater.* **2020**, 2000889.

Publications

Journals:

- [1] Z. A. Kudyshev, S. I. Bogdanov, T. Isacsson, A. V Kildishev, A. Boltasseva, and V. M. Shalaev, “Rapid Classification of Quantum Sources Enabled by Machine Learning,” *Adv. Quantum Technol.*, vol. 3, no. 10, p. 2000067, Oct. 2020.
- [2] S. I. Bogdanov et al., “Ultrafast quantum photonics enabled by coupling plasmonic nanocavities to strongly radiative antennas,” *Optica*, vol. 7, no. 5, p. 463, May 2020.
- [3] S. I. Azzam et al., “Single and Multi-Mode Directional Lasing from Arrays of Dielectric Nanoresonators,” *Laser Photon. Rev.*, p. 2000411, Jan. 2021.
- [4] Z. Wang et al., “Dynamically controlled random lasing with colloidal titanium carbide MXene,” *Opt. Mater. Express*, vol. 10, no. 9, p. 2304, Sep. 2020.
- [5] B. T. Diroll, S. Saha, V. M. Shalaev, A. Boltasseva, and R. D. Schaller, “Broadband Ultrafast Dynamics of Refractory Metals: TiN and ZrN,” *Adv. Opt. Mater.*, vol. 8, no. 19, p. 2000652, Oct. 2020.

- [6] C. Chiang et al., “Chip-Compatible Quantum Plasmonic Launcher,” *Adv. Opt. Mater.*, vol. 8, no. 20, p. 2000889, Oct. 2020.
- [7] S. Saha et al., “Extraordinarily large permittivity modulation in zinc oxide for dynamic nanophotonics,” *Mater. Today*, Nov. 2020.
- [8] J. B. Khurgin et al., “Adiabatic frequency shifting in epsilon-near-zero materials: the role of group velocity,” *Optica*, vol. 7, no. 3, p. 226, Mar. 2020.
- [9] S. Saha et al., “Broadband, High-Speed, and Large-Amplitude Dynamic Optical Switching with Yttrium-Doped Cadmium Oxide,” *Adv. Funct. Mater.*, vol. 30, no. 7, p. 1908377, Feb. 2020.
- [10] V. Bruno et al., “Negative Refraction in Time-Varying Strongly Coupled Plasmonic-Antenna-Epsilon-Near-Zero Systems,” *Phys. Rev. Lett.*, vol. 124, no. 4, p. 043902, Jan. 2020.
- [11] V. Bruno et al., “Broad Frequency Shift of Parametric Processes in Epsilon-Near-Zero Time-Varying Media,” *Appl. Sci.*, vol. 10, no. 4, p. 1318, Feb. 2020.
- [12] V. Bruno et al., “Dynamical Control of Broadband Coherent Absorption in ENZ Films,” *Micromachines*, vol. 11, no. 1, p. 110, Jan. 2020.
- [13] Khandekar, Chinmay, and Zubin Jacob.; Thermal spin photonics in the near-field of nonreciprocal media; *New Journal of Physics* 21, no. 10 (2019): 103030.
- [14] Khandekar, Chinmay, and Zubin Jacob ; Circularly polarized thermal radiation from nonequilibrium coupled antennas.; *Physical Review Applied* 12, no. 1 (2019): 014053.
- [15] Boddeti, Ashwin K., Abubakr Alabassi, Vaneet Aggarwal, and Zubin Jacob.; Spectral domain inverse design for accelerating nanocomposite metamaterials discovery,; *Optical Materials Express* 9, no. 12 (2019): 4765-4771.
- [16] Molesky, Sean, and Zubin Jacob. ; Definition of polaritonic fluctuations in natural hyperbolic media; *Physical Review A* 99, no. 3 (2019): 033833.
- [17] Jahani, Saman, Hangqi Zhao, and Zubin Jacob.; Switching Purcell effect with nonlinear epsilon-near-zero media; *Applied Physics Letters* 113, no. 2 (2018): 021103.

Conferences:

- [1] S. I. Bogdanov et al., “Enhancing the performance of coupled cavity-antenna plasmonic nanostructures for ultrafast quantum photonics,” in Conference on Lasers and Electro-Optics, 2020, vol. Part F182-, p. FM4C.3.
- [2] Z. A. Kudyshev, A. V. Kildishev, V. M. Shalaev, and A. Boltasseva, “Deep learning assisted photonics,” in Active Photonic Platforms XII, 2020, vol. 11461, p. 8.

- [3] S. Bogdanov et al., “Optical electron spin relaxometry in diamond nitrogen-vacancy centers for applications in quantum and nanoscale photonics,” in Spintronics XIII, 2020, vol. 11470, p. 70.
- [4] S. Bogdanov et al., “Plasmonic nanostructures from crystalline silver for ultrafast quantum photonics,” in Plasmonics: Design, Materials, Fabrication, Characterization, and Applications XVIII, 2020, vol. 11462, p. 16.
- [5] S. Bogdanov et al., “Assembly and integration of plasmon-enhanced single-photon sources,” in Active Photonic Platforms XII, 2020, vol. 11461, p. 56.
- [6] P. D. Terekhov et al., “Thermally controlled bound states in the continuum in Si₃N₄ photonic crystals,” in Metamaterials, Metadevices, and Metasystems 2020, 2020, vol. 11460, p. 37.
- [7] S. I. Bogdanov et al., “Optical modification of cavity-antenna plasmonic nanostructures for brighter and faster single-photon emission,” in OSA Quantum 2.0 Conference, 2020, p. QM4B.5.
- [8] Z. A. Kudyshev, S. I. Bogdanov, T. Isacsson, A. V. Kildishev, A. Boltasseva, and V. M. Shalaev, “Rapid Classification of Quantum Sources Enabled by Machine Learning,” *Adv. Quantum Technol.*, vol. 3, no. 10, p. 2000067, Oct. 2020.
- [9] S. Saha et al., “Broadband, high-speed, and extraordinarily large all-optical switching with yttrium-doped cadmium oxide,” in Optics InfoBase Conference Papers, 2020, vol. Part F181-, p. 1128123.
- [10] V. Shalaev, “From early random metamaterials to metasurfaces and quantum photonics,” APS Mar Meeting 2019. 2020.
- [11] S. I. Azzam et al., “Room-Temperature Lasing Action from All-dielectric Metasurfaces Near Bound States in the Continuum,” in Conference on Lasers and Electro-Optics, 2020, p. FTh1C.4.
- [12] Z. A. Kudyshev, S. Bogdanov, T. Isacsson, A. V. Kildishev, A. Boltasseva, and V. M. Shalaev, “Machine learning-assisted classification of quantum emitters (Conference Presentation),” in Advanced Optical Techniques for Quantum Information, Sensing, and Metrology, 2020, vol. 11295, p. 21.
- [13] Khandekar, C., and Z. Jacob. "Thermal Spin Photonics In Nonequilibrium And Nonreciprocal Systems." In 2020 Fourteenth International Congress on Artificial Materials for Novel Wave Phenomena (Metamaterials), pp. 441-443. IEEE.
- [14] Khandekar, C., L. Yang, A. W. Rodriguez, and Z. Jacob. "Thermal Radiation Engineering Via Quantum Nonlinear Mixing Of Photons." In 2020 Fourteenth International Congress on Artificial Materials for Novel Wave Phenomena (Metamaterials), pp. 115-117. IEEE.

[15] Khandekar, Chinmay, Liping Yang, Alejandro W. Rodriguez, and Zubin Jacob. "Nonlinear frequency mixing of photons for thermal-radiation engineering." In *Frontiers in Optics*, pp. JM6A-27. Optical Society of America, 2020

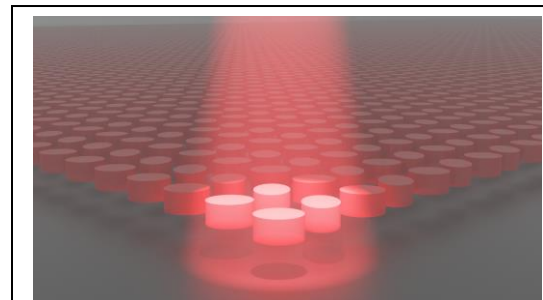
[16] Cortes, Cristian L., Ward Newman, Ashwin K. Boddeti, Tyler Sentz, and Zubin Jacob. Fundamental figure of merit for engineering dipole-dipole interactions; Conference on Lasers and Electro-Optics (CLEO), pp. 1-2. IEEE, 2019.

Metamaterials as a Platform for the Development of Novel Materials for Energy Applications

Willie J. Padilla, Duke University

Program Scope

We propose to explore the fundamental properties of metamaterials and metasurfaces and their potential for control of energy at the sub-wavelength scale in support of the mission of the Department of Energy and the office of Basic Energy Sciences. Electromagnetic metasurfaces fashioned from dielectrics provide a new platform for the discovery and design of materials with novel structures, functions, and properties. The assembled team proposes to advance the knowledge base of these materials through fundamental investigations of the experimental and theoretical properties of metamaterials for the discovery, prediction and design of new materials with novel structures, functions, and properties. The proposed research activities are synergistic, and emphasize a complete basic research program including the conceptual / computational design, machine learning, fabrication / synthesis of the materials, and the characterization and analysis of their electromagnetic properties.



Depiction of an all-dielectric metasurface consisting of elliptical resonators. The metasurface geometry necessary to match its emission to that of the external quantum efficiency of GaSb was determined using an inverse method developed in the program, termed the neural adjoint.

The proposed project uses machine learning to explore the fundamental properties of metamaterials / metasurfaces and their potential for energy applications. There are four main objectives: 1) Machine Learning the Interactions of Light and Matter, 2) Zero Rank and Coherent Perfect Absorbers, 3) Bound States in the Continuum, and 4) Spatial—Temporal Metasurfaces.

The program implements a complete basic research program consisting of theory, machine learning, modeling, characterization, and analysis, in order to fully characterize metamaterials and metasurfaces, while minimizing iterations necessary to achieve the proposal goals.

Recent Progress

We have recently shown metasurfaces which may operate as both coherent perfect absorbers and perfect absorbers. [1,2] We used waveguide theory to analytically solve for the

resonance frequency of electric and magnetic modes, as well as their dependence on geometrical parameters. [3] Coupled mode theory [4] was used to determine the scattering matrices of each state, and it was found that the perfect absorber realized a null scattering matrix, while the coherent perfect absorber state has nullity a matrix of rank 1. This means that the perfect absorber will absorb any state of incoming light, whereas the coherent perfect absorber needs incoming light of equal amplitude and a particular phase combination. None-the-less, the single metasurface system we present can realize both of these states with only a change in height of the resonator. The key results of this study were demonstration that any combination of opposite symmetry modes may be used to fashion a perfect absorber, and here we used an EH₁₂₁ even mode and a HE₁₁₁ mode. This was the first study, to our knowledge, which showed coherent perfect absorption in a system with significant loss, as well as the first study to show all-dielectric metasurface absorbers using higher order modes for absorption.

All-dielectric low loss metasurfaces may support high quality factor (Q-factor) modes, termed bound-states-in-the-continuum (BIC). [5] Although there are many reasons why BICs may occur, we specifically have been studying BICs produced by symmetry breaking. We fashioned an all-dielectric metasurface (ADM) which consisted of cylindrical resonators in a square array. The sample was fashioned such that it had interconnect in-between unit-cells, such that it could be free standing, i.e. no substrate was necessary, and thus no additional loss. The symmetry in our ADM was broken by adding a flat to the perimeter of the cylinder, and we investigated the dependence of Q on the strength of the symmetry breaking. Ultimately, the Q-factor is limited by the size of the array, and scales as $Q \propto N^2$, where N is the number of resonators in the sample, and material loss. [6] In order to avoid standing modes which may exist on our metasurface, we fabricated a free-standing ADM with 19 x 19 unit cells, i.e. a prime number to avoid any potential resonances between the size of the array and the unit-cell periodicity. We found a high-Q mode on the metasurface, and determined that its quality factor was limited not by the size of our array, but rather by material loss. Our results are currently being written up and will be submitted soon for publication in a referred journal.

We have completed three separate studies on deep learning the electromagnetic properties of metamaterials - two have been published and one has been accepted for publication. The first work was focused on development of a forward neural network that was capable of determining the underlying physics which described the scattering response of metasurfaces given only its geometry. Here we used a 2x2 array of all-dielectric metasurfaces and allowed the height and radius to vary independently. It is important to detail that the system here possessed an underlying complexity that made design of a specific scattering state impossible to find with the standard approach, i.e. numerical simulation and optimization. We were thus led to deep learning naturally to solve this challenging problem. Our neural network was indeed able to solve for the function relating metasurface geometry to scattering. We also used our forward model to find every single possible permutation of geometry to build a database of possible scattering

states. This enabled us to perform a type of inverse method, where we drew by hand a desired scattering, and then searched our database to find the best possible solution.

Another study was focused on inverse modelling and we developed a method which we termed neural adjoint (NA). The approach of NA is to first develop an accurate forward model, after which the weights and biases of the neural network (NN) are locked. Then, the NN is run “backwards” where a desired output (in one case this is a spectra) is put in and the NA varies the input in order to find a good solution. We compared our inverse method to five other well known state-of-the-art inverse approaches and demonstrated that our NA inverse method performed as well or better than all. Results were published in the premiere machine learning conference NeurIPS.

In another study, we used NA to find the metasurface geometry necessary to give a desired scattering state. We took a specific example of looking for a metasurface that would yield a match to the external quantum efficiency of gallium antimonide (GaSb). Our NA inverse method is only as accurate as our forward model, and thus we performed 60,000 numerical simulations for a training dataset. Here our metasurface had over 1 trillion possible permutations of the geometry, but none-the-less, we were able to develop an accurate forward network which predicted the transmission with an accuracy of 1×10^{-3} . We then use NA to find inverse solutions to two problems, a well-posed and an ill-posed problem, and the NA performed well on both. We further developed an active learning approach where, for ill-posed inverse problems, we used Uniform Manifold Approximation and Projection (UMAP), [7] which is a type of dimensionality reduction method permitting us to visualize the direction to move in the geometry space for better solutions.

Future Plans

All-dielectric metasurfaces which function as coherent perfect absorbers should be capable of determining the state of coherence of incoming light, since absorption in these structures is dependent on a balance of power on each side of the ADM, as well as the phase. We plan to fabricate a coherent perfect absorber operating at terahertz frequencies in order to study the extent to which ADMs can detect varying degrees of coherence. In one instance, we will use light which has the same phase that is incident on both sides of the CPA, which should yield a maximum absorption. The power ratio of the two beams will be varied as well as the phase, and we will investigate the sensitivity of detection.

We will use deep learning in order to “learn” the physics of metamaterials. For example, researchers have had good success in finding forward mappings which relate the geometry of metamaterials to spectra. However, it may be possible to use neural networks to determine the parameters of response functions from the metamaterial geometry, and from these determine the scattering state. Although this ultimately has the same result of determining the scattering, a

Lorentz oscillator response function, for example, can then indicate how many charges are involved in a particular resonance, and their effective masses, since the Lorentz oscillator model is causal. Thus we will use deep learning to understand more about the physics involved in the resonant modes which lead to specific scattering states.

We will continue to study BICs through symmetry breaking. At present it is unknown how the specific type of break (geometrical defect) that is used affects different modes supported by the ADM. Further, the number of defects used, and their spatial dependence is unknown and will be investigated. It may be possible to form quasi-infinite systems of BICs through making ring type structures, where resonators form units on the ring. Thus the quality factor will be quite high, and only limited by the material loss, but not by array size.

References

1. W. Wan, Y. Chong, L. Ge, H. Noh, A. D. Stone, H. Cao, “Time-Reversed Lasing and Interferometric Control of Absorption,” *Science* **331**, 889 (2011).
2. D. G. Baranov, A. Krasnok, T. Shegai, A Alù, Y. Chong, “Coherent perfect absorbers: linear control of light with light,” *Nat. Rev. Mater.* **2**, 17064 (2017).
3. X. Ming, X. Liu, L. Sun, W. J. Padilla, “Degenerate critical coupling in all-dielectric metasurface absorbers,” *Opt. Express* **25**, 24658 (2017).
4. H. A. Haus, W. P. Huang. “Coupled Mode Theory,” *Proceedings of the IEEE* **19**, 10, (1991).
5. C. W. Hsu, B. Zhen, A. D. Stone, J. D. Joannopoulos, and M. Soljačić, “Bound states in the continuum,” *Nat. Rev. Mater.* **1**, 16048 (2016).
6. M. A. Belyakov, M. A. Balezin, Z. F. Sadrieva, P. V. Kapitanova, E. A. Nenasheva, A. F. Sadreev, and A. A. Bogdanov, “Experimental observation of symmetry protected bound state in the continuum in a chain of dielectric disks,” *Phys. Rev. A* **99**, 053804 (2019).
7. L. McInnes, J. Healy, and J. Melville, “Umap: Uniform manifold approximation and projection for dimension reduction,” *arXiv preprint arXiv:1802.03426* (2018).

Publications

1. Yang Deng, Simiao Ren, Kebin Fan, Jordan M. Malof, and Willie J. Padilla, Neural-adjoint method for the inverse design of all-dielectric metasurfaces, *Optics Express* Accepted for publication (2021).
2. Simiao Ren, Willie Padilla, and Jordan Malof, Benchmarking deep inverse models over time, and the neural-adjoint method. In H. Larochelle, M. Ranzato, R. Hadsell, M. F. Balcan, and H. Lin, editors, *Advances in Neural Information Processing Systems*, 33, 38–48. Curran Associates, Inc., 2020.
3. Christian C. Nadell, Bohao Huang, Jordan M. Malof, and Willie J. Padilla, Deep learning for accelerated all-dielectric metasurface design, *Optics Express* 27, 27523 (2019).
doi:10.1364/OE.27.027523
4. Jonathan Y. Suen, Kebin Fan, and W.J. Padilla, A Zero-Rank, Maximum Nullity Perfect Electromagnetic Wave Absorber, *Advanced Optical Materials* 7, 1801632 (2019).
doi:10.1002/adom.201801632
5. Kebin Fan, Ilya V. Shadrivov, and W.J. Padilla, Dynamic bound states in the continuum, *Optica* 6, 169 (2019). doi:10.1364/OPTICA.6.000169

Semiconductor excitonic nanoshells for energy conversion applications.

Mikhail Zamkov

The Center for Photochemical Sciences, Department of Physics, Bowling Green State University, Bowling Green, Ohio 43403. zamkovm@bgsu.edu

Program Scope

The project focuses on developing a novel class of colloidal inorganic nanocrystals that facilitate multi-exciton processes,^{1,2} by relaxing the quantum confinement of charges. Currently, this is achieved through two nanoscale geometries: (1) – nanoshell quantum dots (QDs), and (2) - quantum dots molecules. Nanoshell QDs are engineered to have a radial energy gradient, which promotes the two-dimensional, shell-localization of photoinduced charges (Fig. 1b). As a result, the 2D quantum confinement is achieved in the surface layer of a semiconductor colloid, for which all three dimensions exceed its corresponding exciton Bohr radius. A large exciton volume of a nanoshell (Fig. 1a) suppresses non-radiative decay of multiple excitons.

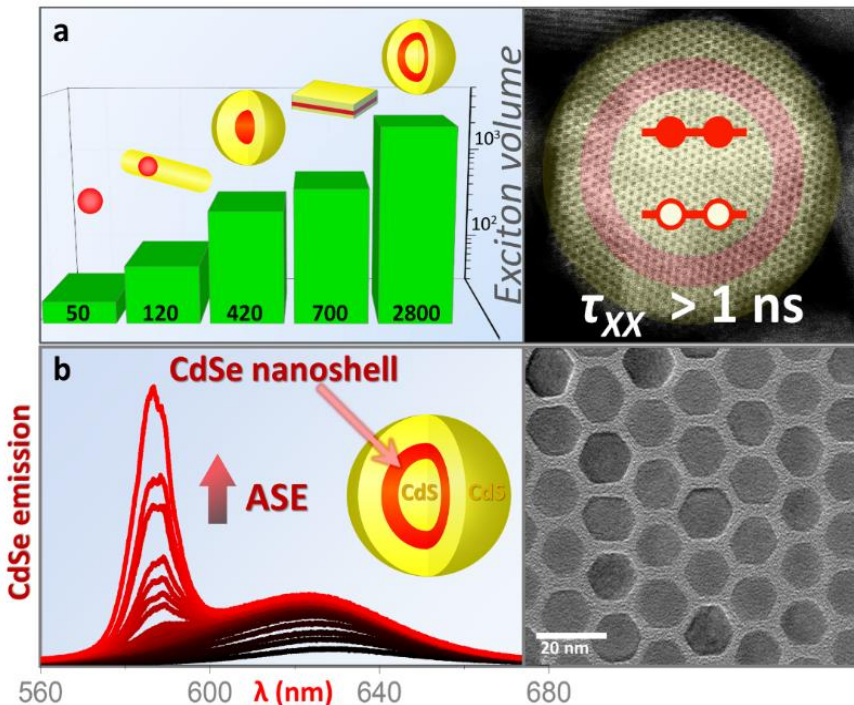
In the process of developing nanoshell quantum dots, we have discovered a novel strategy for building composite assemblies of inorganic nanocrystals, known as ***nanocrystal or quantum dot molecules***. These composite nanomaterials consist of inorganically coupled domains, assembled from pre-fabricated colloidal nanocrystals. Such nanocrystal molecules allow several reaction steps to progress at the same site with minimal mass and energy transfer distances. Their multi-component architecture can also be used to render dual functionalities in composite nanostructures consisting of plasmonic, magnetic, light-emitting, or light-harvesting domains.

Recent Progress

Our research efforts in the last two years of the DOE project were focused on: (i) - the chemical synthesis and ultrafast spectroscopy of semiconductor colloids exhibiting the quantum confinement in the surface layer (nanoshell quantum dots); (ii) – building colloidal assemblies of inorganic nanoparticles, known as nanocrystal molecules. Coupling between different components in such nanoparticle assemblies was shown to foster unique collective properties that find application in photocatalysis, quantum computing (exciton qubits), and photovoltaics.

Low-threshold Laser Medium Utilizing Nanoshell Quantum Dots. Nanoshell QDs comprising a CdSe quantum-well layer were found to be a promising nanoscale morphology for the development of lasing applications (publication #7). A unique combination of a large exciton volume and a smoothed potential gradient across interfaces of the reported CdS_{bulk}/CdSe/CdS_{shell} (core/shell/shell) nanoshell QDs causes the suppression of Auger processes (publication #3), which was manifested in our recent work though the observation of stable amplified stimulated emission (ASE) at low pump fluences. Overall, present findings demonstrate unique advantages

of the nanoshell QD architecture as a promising optical gain medium in solid-state lighting and lasing applications.



Energy transport in CsPbX_3 nanocrystals solids. Artificial solids of CsPbX_3 perovskite nanocrystals (NCs) are well known for their promising charge transport characteristics. In our recent study (publication #10), we have shown that the same set of electronic properties allows CsPbBr_3 NC solids to act as superior energy transport materials, which support a long-range diffusion of electrically neutral excitons.

By performing time-resolved bulk quenching measurements on halide-treated CsPbBr_3 NC films, we observed average exciton diffusion lengths of 52 nm and 71 nm for I and Cl^- treated solids, respectively. Steady-state fluorescence quenching studies have been employed to explain such a large diffusion length as due to a high defect tolerance and a low disorder of exciton energies in CsPbBr_3 NC solids. We expect that the demonstrated ability of halide-treated CsPbBr_3 NC solids to support a long-range exciton transport could be beneficial for applications in light energy concentration, as was demonstrated in this work through energy transfer measurements in assemblies of perovskite NC donors and CdSe quantum dot acceptors.

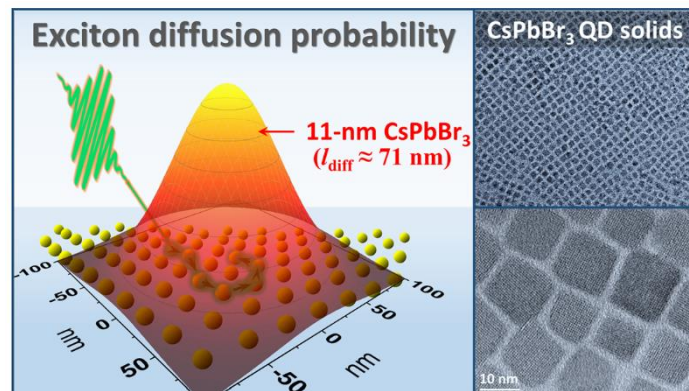


Figure 2. Long-range energy transport in solids of CsPbBr_3 nanocrystals. Our recent study (publication #10) shows that exciton diffusion in halide-treated CsPbBr_3 NC solids is 50-70 nm, which exceeds that of chalcogenide nanocrystals by an order of magnitude.

Building Artificial Molecules from Colloidal Nanocrystals. Building artificial molecules from colloidal nanocrystals paves the way to unique multi-particle properties and interactions. Our most recent study (publication #12) demonstrates a synthetic strategy for the assembly of colloidal nanocrystal molecules via the molten-surface adhesion of semiconductor nanocrystals at hybrid interfaces (Fig. 3). The present method was demonstrated by constructing both homogenous (e.g. CdS-CdS, PbS-PbS, CdSe-CdSe) and heterogeneous (e.g. PbS-CdS, CdS-CdSe) nanocrystal assemblies featuring a well-defined number of domains coupled through charge- and energy-transfer interactions.

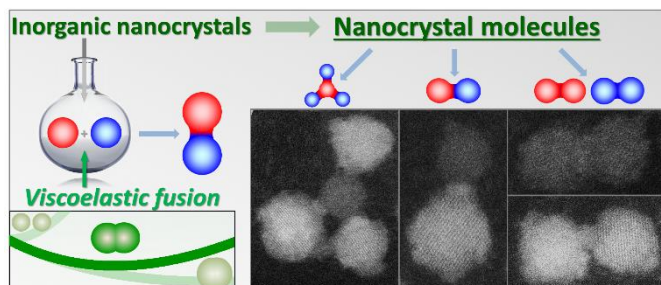


Figure 3. Assembly of nanocrystal molecules via molten layer adhesion.

The observed assembly process was explained within the viscoelastic interaction theory adapted for molten-surface colloids (Fig. 4). We hope that the present work will provide a synergy of synthetic and theoretical tools needed for building artificial molecules of many other inorganic nanocrystals.

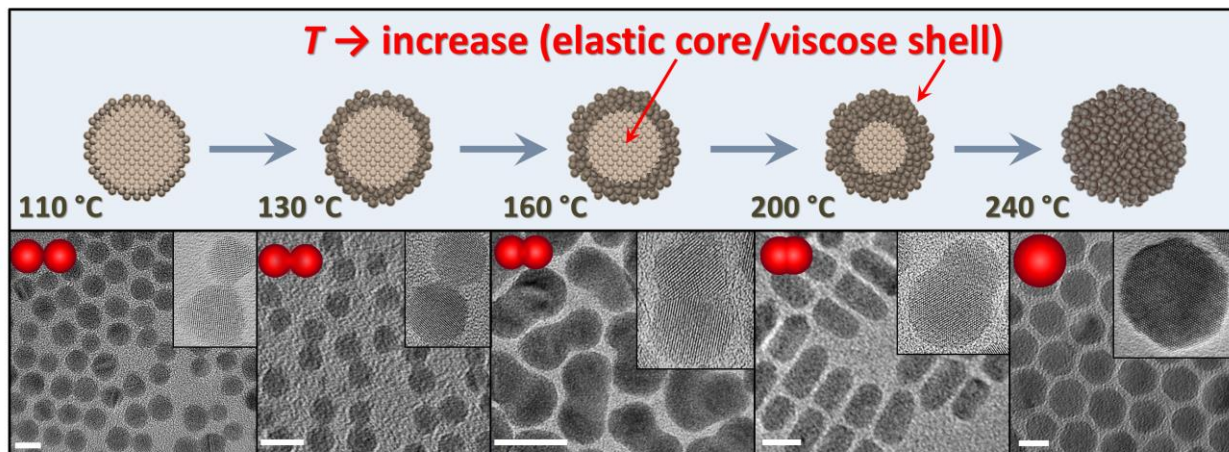


Figure 4. Illustration of the viscoelastic assembly approach. Formation of a molten layer in heated colloidal NCs enables bonding of nanoparticles at hybrid interfaces. The driving force for the assembly process is controlled by nanoparticle surfactants, while the degree of inter-particle fusion is tunable via the solvent temperature.

Future Plans

The general direction for the future development of our research program will focus on (1) – expanding the nanoshell synthesis to other semiconductor combinations, and (2) – building artificial molecules from inorganic nanocrystals. Our recent discovery of molten surfaces in colloidal semiconductor nanocrystals (Fig. 4) is expected to advance both of these research directions (1 & 2).

References

- 1) Razgoniaeva, N.; Moroz, P.; Yang, M.; Budkina, D. S.; Eckard, H.; Augspurger, M.; Khon, D.; Tarnovsky, A. N.; Zamkov, M. *J. Am. Chem. Soc.*, **2017**, *139*, 7815-7822.
- 2) Zamkov, M. "Solar Hydrogen Generation: Exceeding 100% Efficiency." *Nat. Energy*, **2017**, *2*, 17072.

Publications from DOE-sponsored research (last 2 years)

- 1) Yang, M.; Moroz, P.; Jin, Z.; Budkina, D. S.; Sundrani, N.; Porotnikov, D.; Cassidy, J.; Sugiyama, Y.; Tarnovsky, A. N.; Mattoussi, H.; Zamkov, M., "Delayed Photoluminescence in Metal-Conjugated Fluorophores." *J. Am. Chem. Soc.* **2019**, *141*, 11286-11297. <https://doi.org/10.1021/jacs.9b04697>
- 2) Grzelak, D.; Parzyszek, S.; Moroz, P.; Szustakiewicz, P.; Zamkov, M.; Lewandowski, W., "Self-Assembled PbS/CdS Quantum Dot Films with Switchable Symmetry and Emission." *Chem. Mater.* **2019**, *31*, 7855-7863. <https://doi.org/10.1021/acs.chemmater.9b01767>
- 3) Kholmicheva, N.; Budkina, D. S.; Cassidy, J.; Porotnikov, D.; Harankahage, D.; Boddy, A.; Galindo, M.; Khon, D.; Tarnovsky, A. N.; Zamkov, M., "Sustained Biexciton Populations in Nanoshell Quantum Dots." *ACS Photonics* **2019**, *6*, 1041-1050. <https://doi.org/10.1021/acspophotonics.9b00068>
- 4) Moroz, P.; Romero, L. R.; Zamkov, M., "Colloidal Semiconductor Nanocrystals in Energy Transfer Reactions." *Chem. Commun.* **2019**, *55*, 3033-3048. <https://doi.org/10.1039/C9CC00162J>
- 5) Kholmicheva, N.; Romero, L. R.; Cassidy, J.; Zamkov, M., "Prospects and Applications of Plasmon-Exciton Interactions in the Near-Field Regime." *Nanophotonics* **2019**, *8*, 613-628. <https://doi.org/10.1515/nanoph-2018-0143>
- 6) Cassidy, J.; Ellison, C.; Bettinger, J.; Yang, M.; Moroz, P.; Zamkov, M. "Enabling Narrow Emission Linewidths in Colloidal Nanocrystals through Coalescence Growth." *Chem. Mater.* **2020**, *32*, 7524-7534. <https://doi.org/10.1021/acs.chemmater.0c02874>
- 7) Porotnikov, D.; Diroll, B. T.; Harankahage, D.; Obloy, L.; Yang, M.; Cassidy, J.; Ellison, C.; Miller, E.; Rogers, S.; Tarnovsky, A. N.; Schaller, R. D.; Zamkov, M. "Low-threshold laser medium utilizing semiconductor nanoshell quantum dots." *Nanoscale* **2020**, *12*, 17426-17436. <https://doi.org/10.1039/D0NR03582C>
- 8) Porotnikov, D.; Zamkov, M., "Progress and Prospects of Solution-Processed Two-Dimensional Semiconductor Nanocrystals." *J. Phys. Chem. C* **2020**, *40*, 21895-21908. <https://doi.org/10.1021/acs.jpcc.0c06868>
- 9) Cassidy, J.; Zamkov, M., "Nanoshell Quantum Dots: Quantum Confinement Beyond the Exciton Bohr Radius." *J. Chem. Phys.* **2020**, *152*, 110902. <https://doi.org/10.1063/1.5126423>

- 10)** Yang, M.; Moroz, P.; Miller, E.; Porotnikov, D.; Cassidy, J.; Ellison, C.; Medvedeva, X.; Klinkova, A.; Zamkov, M. "Energy Transport in CsPbBr₃ Perovskite Nanocrystal Solids." *ACS Photonics* **2020**, 7, 154-164. <https://doi.org/10.1021/acspophotonics.9b01316>
- 11)** Porotnikov, D.; Yang, M.; Cassidy, J.; Harankahage, D.; Ellison, C.; Zamkov, M. "Photoinduced Alignment of Electric Dipoles in Colloidal Semiconductor Nanocrystals." **2021**, *Under review (ACS Nano)*.
- 12)** Cassidy, J.; Yang, M.; Porotnikov, D.; Harankahage, D.; Moroz, P.; Razgoniaeva, N.; Ellison, C.; Bettinger, J.; Khon, D.; Zamkov, M. "Building Artificial Molecules from Colloidal Nanocrystals." **2021**, *Submitted*.

Wavelength Conversion through Plasmon-Coupled Surface States

Mona Jarrahi, University of California Los Angeles

Program Scope

The scope of this research program is to conduct fundamental physical studies on interaction of optical waves with plasmonic photoconductive nanostructures for high power terahertz wave generation. Toward this goal, we have investigated physical characteristics of plasmon-coupled surface states for wavelength conversion. Surface states generally degrade semiconductor device performance by raising the charge injection barrier height, introducing localized trap states, inducing surface leakage current, and altering the electric potential. Therefore, there has been an endless effort to use various surface passivation treatments to suppress the undesirable impacts of the surface states. We show that the giant built-in electric field created by the surface states can be harnessed to enable passive wavelength conversion with unprecedented efficiencies without utilizing any nonlinear optical phenomena. Photo-excited surface plasmons are coupled to the surface states to generate an electron gas, which is routed to a nanoantenna array through the giant electric field created by the surface states. The induced current on the nanoantennas, which contains mixing product of different optical frequency components, generates radiation at the beat frequencies of the incident photons. We utilize the unprecedented functionalities of plasmon-coupled surface states to demonstrate passive wavelength conversion of nanojoule optical pulses at a 1550 nm center wavelength to terahertz regime with record-high efficiencies that exceed nonlinear optical methods by 4-orders of magnitude. The presented scheme can be used for optical wavelength conversion to different parts of the electromagnetic spectrum ranging from microwave to far-infrared regimes by using appropriate optical beat frequencies.

Recent Progress

When a semiconductor lattice is terminated on the surface, the periodicity of the lattice is broken since the surface atoms do not have sufficient number of atoms that they can bond to, leaving behind incomplete chemical bonds. These so called dangling bonds produce localized surface states with energy levels that are located within the bandgap of the semiconductor [1-4]. The Fermi energy level at the surface of a semiconductor is pinned to the energy level at which the surface state density peaks, while the Fermi energy level away from the semiconductor surface is determined by the semiconductor doping. Therefore, the presence of the surface states takes away a very important degree of freedom for engineering semiconductor devices by altering the electric potential profile and is generally a major source of degradation in semiconductor devices. Despite the endless efforts to suppress the surface semiconductor states, they have unique electrochemical properties that are not provided by bulk semiconductors and could enable unprecedented device functionalities. Figure 1a illustrates how the presence of surface states induces a giant built-in electric field at the surface of a p-doped InAs

semiconductor, which exceeds the breakdown field of bulk InAs. The energy level at which the surface state density of InAs peaks is located above its direct bandgap because there is a large difference between the direct and indirect bandgap energies of InAs [2, 3]. Since the electrons that occupy the surface states have an average total energy higher than the bulk InAs, they migrate from the surface states to the bulk InAs to reach equilibrium, leaving behind immobile charge of uncompensated donor ions, which produces a giant built-in electric field. Ideally, wavelength conversion can be achieved by accelerating photoabsorbed charges through this giant built-in electric field with very high mobility. However, efficient wavelength conversion was not possible before due to the very shallow band bending at the surface of the semiconductor, which severely limits the interaction between the giant built-in electric field and optical beam.

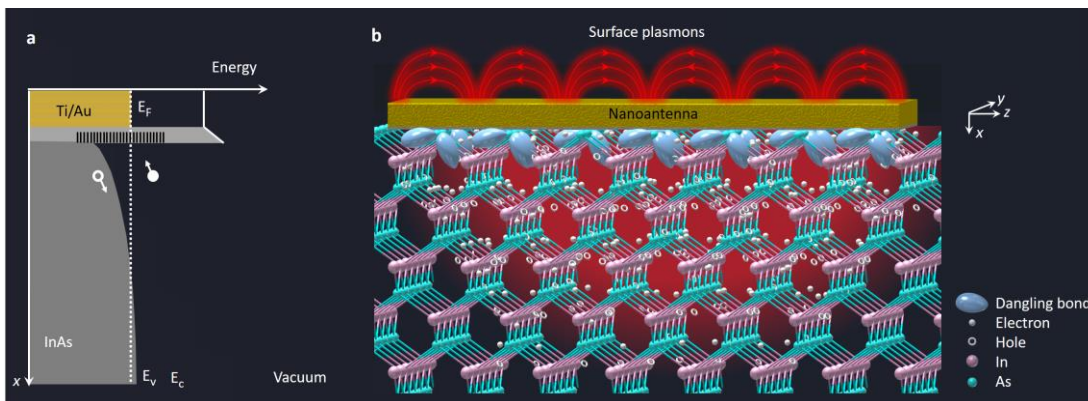


Fig. 1. Energy band bending caused by the InAs surface states. a, Energy band diagram of a highly p-doped InAs substrate in contact with Ti/Au. The energy level at which the surface state density of InAs peaks is located above its direct (0.36 eV) and indirect bandgap energies (1.21 eV) of InAs. Electrons in these surface states recombine with the holes in the valence band and occupy a part of the conduction band to minimize their total energy. As a result, the Fermi energy level (E_F) is pinned above the conduction band minimum (E_c). Free electrons in the conduction band then migrate to the p-doped InAs layer to minimize their energy further, resulting in a steep band bending and a giant built-in electric field induced at the InAs surface. b, Schematic of the InAs lattice in contact with a nanoantenna that couples photo-excited surface plasmons to the surface states.

To effectively utilize this built-in electric field for optical wavelength conversion, optical photons excite a nanoantenna array to couple photo-excited surface plasmons to the surface states (Fig. 1b). Excitation of surface plasmons enhances the optical intensity and photoabsorption near the InAs surface, where the strength of the built-in electric field is maximized. The absorbed photons generate a tightly confined electron gas under the nanoantenna contacts with an electron concentration that resonates at the mixing product of different optical frequency components. This electron gas swiftly drifts to the nanoantennas through the built-in electric field. The induced current on the nanoantennas generates radiation at the beat frequencies of the optical photons. Figure 2a shows a nanoantenna array designed to couple photo-excited surface plasmons to the InAs surface states where a built-in electric field drifts the photo-induced electron gas to the nanoantennas to generate radiation at the optical beat frequencies. Unlike the bulky and complex nonlinear optical setups that require high-energy lasers, tight optical focus, and/or tilted beam to provide high optical pump intensity and phase

matching for efficient wavelength conversion, wavelength conversion through plasmon-coupled surface states does not require a complex optical setup and is not sensitive to optical focus and alignment. Figure 2b shows a fabricated nanoantenna array on InAs that is simply glued at the tip of an optical fiber without using any intermediate optical component and can be pumped by a compact fiber laser.

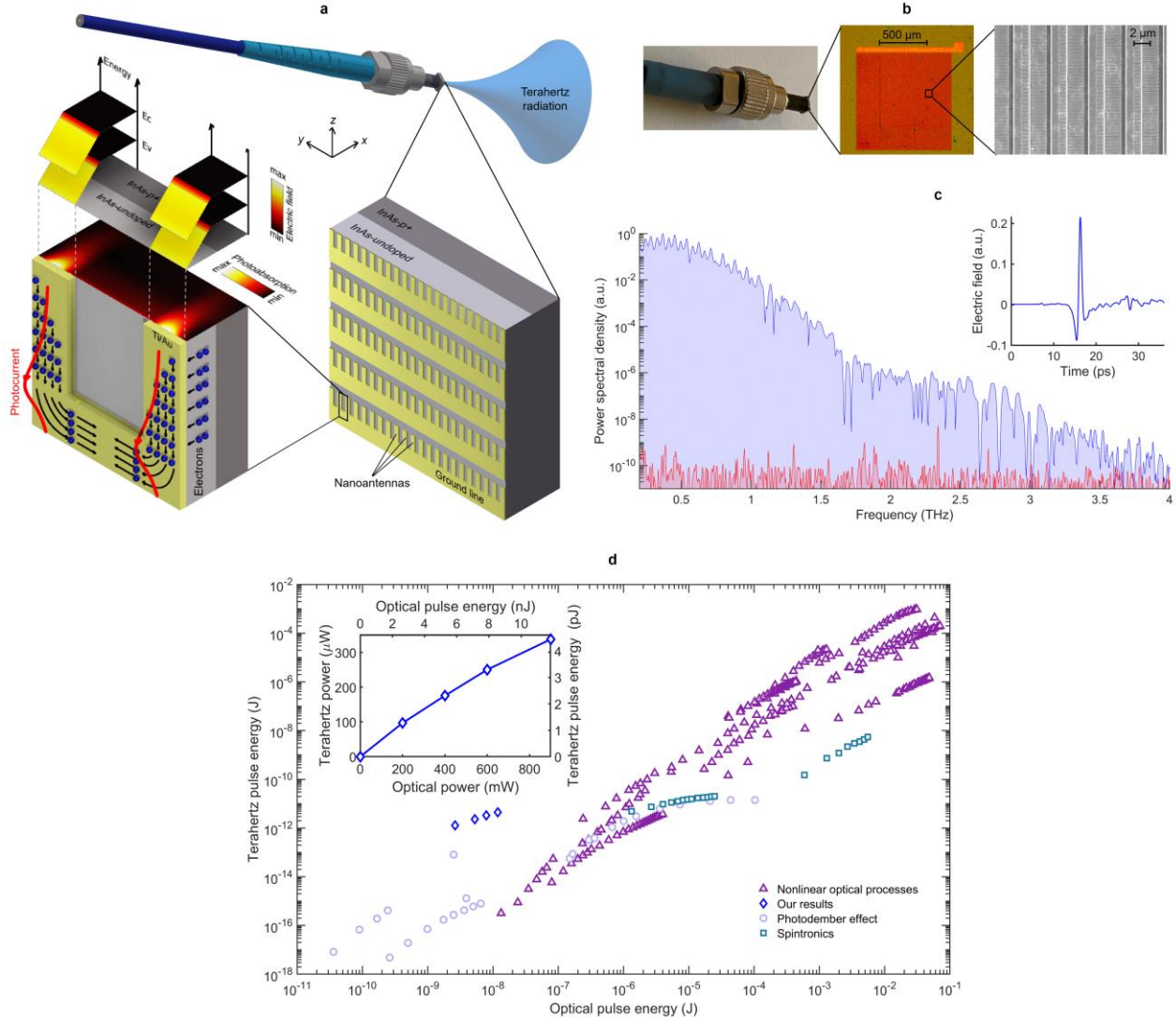


Fig. 2. Wavelength conversion through plasmon-coupled surface states. a, Schematic of a nanoantenna array on an InAs semiconductor substrate, which is designed to couple photo-excited surface plasmons to the surface states where a built-in electric field drifts the photo-induced electron gas to the nanoantennas to generate radiation at the optical beat frequencies. The nanoantenna geometry and semiconductor structure are chosen to maximize the spatial overlap between the built-in electric field and photoabsorption profiles. b, Photograph, microscopy, and scanning electron microscopy images of a fabricated nanoantenna array on a substrate consisting of a 100-nm-thick undoped InAs layer grown on a 500-nm-thick InAs epilayer with a p-type doping of 10^{19} cm^{-3} grown on a semi-insulating GaAs substrate. c, Measured terahertz radiation (in blue) and noise (in red) spectra generated from the nanoantenna array when pumped by 3.68 nanojoule optical pulses at a 1550 nm center wavelength. The time-domain radiated terahertz pulse is shown in the inset. d, Measured terahertz pulse energy/power from the fabricated nanoantenna array as a function of the optical pulse energy/power (inset) in comparison with other passive optical-to-terahertz converters reported in the literature.

We experimentally demonstrate conversion of 3.68 nanojoule optical pulses with a 150 fs pulsedwidth coupled to the fiber at a 1550 nm center wavelength to 1.78 picojoule terahertz pulses radiated from the nanoantenna array [5] with more than a 4 THz bandwidth and 105 dB dynamic range (Fig. 2c). Broader radiation bandwidths exceeding 6 THz and higher dynamic ranges exceeding 110 dB are achieved when using optical pulses with shorter pulsedwidth and higher power. The measured terahertz pulse energy/power from the fabricated nanoantenna array as a function of the optical pulse energy/power (Fig. 2d inset) is compared with other passive optical-to-terahertz converters reported in the literature, which utilize nonlinear optical processes, spintronics, and the photo-Dember effect. The comparison indicates record-high efficiency of the plasmon-coupled surface states in passive wavelength conversion of nanojoule optical pulses to terahertz regime with efficiencies that exceed nonlinear optical methods by 4-orders of magnitude (Fig. 2d).

Future Plans

The presented wavelength conversion scheme via plasmon-coupled surface states can be used for optical wavelength conversion to different parts of the electromagnetic spectrum ranging from microwave to far-infrared regimes in both pulsed and continuous wave operation. We plan to explore enhancing the wavelength conversion efficiency by boosting the built-in electric field at the semiconductor surface and increasing the spatial overlap between the built-in electric field and photoabsorption profiles. Using alternative semiconductors with a larger number of surface states above the conduction band, introducing higher p-type doping levels, and incorporating a gradient composition semiconductor ($\text{In}_{1-x}\text{Ga}_x\text{As}$ with x increasing as a function of depth in the substrate) would introduce a steeper band-bending at the semiconductor surface and, therefore, would further enhance the built-in electric field. In addition, by growing the semiconductor active layer on a distributed Bragg reflector and an appropriate choice of nanoantenna geometry, most of the excited surface plasmons would be trapped in the semiconductor active layer and, therefore, a much stronger spatial overlap between the built-in electric field and photoabsorption profiles can be achieved.

References

1. Mönch, W. On the physics of metal-semiconductor interfaces. *Reports Prog. Phys.* **53**, 221–278 (1990).
2. Tersoff, J. Schottky barriers and semiconductor band structures. *Phys. Rev. B* **32**, 6968–6971 (1985).
3. Piper, L. F. J., Veal, T. D., Lowe, M. J. & McConville, C. F. Electron depletion at InAs free surfaces: Doping-induced acceptorlike gap states. *Phys. Rev. B* **73**, 195321 (2006).
4. Mönch, W. *Semiconductor Surfaces and Interfaces*. (Springer-Verlag, 1993).
5. Turan, D., Lu, P. K., Yardimci, N. T., Liu, Z., Luo, L., Park, J.-M., Nandi, U., Wang, J., Preu, S. & Jarrahi, M. Wavelength conversion through plasmon-coupled surface states. arXiv:2012.03179, 2020

Publications (resulting from work supported by the DOE grant over the past two years)

1. D. Turan, P. K. Lu, N. T. Yardimci, Z. Liu, L. Luo, J.-M. Park, U. Nandi, J. Wang, S. Preu, M. Jarrahi, "Wavelength conversion through plasmon-coupled surface states," arXiv:2012.03179
2. M. Veli, D. Mengua, N. T. Yardimci, Y. Luoa, J. Li, Y. Rivenson, M. Jarrahi, A. Ozcan, "Terahertz Pulse Shaping Using Diffractive Surfaces," *Nature Communications*, 37, 2021
3. J. Li, D. Mengua, N. T. Yardimci, Y. Luo, X. Li, M. Veli, Y. Rivenson, M. Jarrahi, A. Ozcan, "Spectrally-Encoded Single-Pixel Machine Vision Using Diffractive Networks," *Science Advances*, 2021
4. P. K. Lu, D. Turan, M. Jarrahi, "High-sensitivity telecommunication-compatible photoconductive terahertz detection through carrier transit time reduction," *Optics Express*, 28, 26324-26335, 2020
5. F. Kuwashima, M. Jarrahi, S. Cakmakyapan, T. Shirao, K. Iwao, K. Kurihara, O. Morikawa, H. Kitahara, T. Furuya, K. Wada, M. Nakajima, M. Tani, "Evaluation of High-Stability Optical Beats in Laser Chaos by Plasmonic Photomixing," *Optics Express*, 28, 24833-24844, 2020
6. N. Wang, M. Jarrahi, "High-precision millimeter-wave frequency determination through plasmonic photomixing," *Optics Express*, 28, 24900-24907, 2020
7. S.-H. Yang, M. Jarrahi, "Navigating Terahertz Spectrum via Photomixing," *Optics & Photonics News Magazine*, 31, 36-43, 2020 (Invited)
8. Y.-J. Lin, M. Jarrahi, "Heterodyne Terahertz Detection through Electronic and Optoelectronic Mixers," *Reports on Progress in Physics*, 83, 066101, 2020
9. D. Turan, N. T. Yardimci, M. Jarrahi, "Plasmonics-enhanced photoconductive terahertz detector pumped by Ytterbium-doped fiber laser," *Optics Express*, 28, 3835-3845, 2020
10. Y. Luo, D. Mengua, N. T. Yardimci, Y. Rivenson, M. Jarrahi, A. Ozcan, "Design of Task-Specific Optical Systems Using Broadband Diffractive Neural Networks," *Light: Science & Applications*, 8, 112, 2019
11. Y.-J. Lin, S. Cakmakyapan, N. Wang, D. Lee, M. Spearrin, M. Jarrahi, "Plasmonic Heterodyne Spectrometry for Resolving the Spectral Signatures of Ammonia over a 1-4.5 THz Frequency Range," *Optics Express*, 27, 36838-36845, 2019
12. N. Wang, S. Cakmakyapan, Y.-J. Lin, H. Javadi, M. Jarrahi, "Room-temperature heterodyne terahertz detection with quantum-level sensitivity," *Nature Astronomy*, 3, 977–982, 2019

Defects in gallium oxide

Matthew D. McCluskey, Washington State University (WSU), Pullman, WA

Leah Bergman, University of Idaho (UI), Moscow, ID

Program Scope

This project investigates fundamental defect properties of gallium oxide. Monoclinic β - Ga_2O_3 is an excellent candidate for next-generation power electronics due to its large band gap, which results in a high breakdown field estimated at 8 MV/cm. β - Ga_2O_3 also benefits from being relatively cheap to produce and easy to grow in single crystals. Experimentally, there are basic questions about the microscopic origin of electrical breakdown in β - Ga_2O_3 . Understanding the fundamental properties of dopants and defects in this material could enable significant improvements in device performance.

Unintentional impurities and deliberately introduced dopants are characterized by IR, UV/visible, and photoluminescence (PL) spectroscopy. Spatially resolved PL measurements provide maps of optical properties over μm -to-mm length scales. The effect of dopants on electrical properties are studied by Hall-effect and current-voltage measurements. Our investigation of dopants and defects encompasses acceptors, hydrogen, and transition metals.

Recent Progress

Thin-film bandgap: To address the significant interest in using β - Ga_2O_3 for high-temperature device technologies, we have initiated a study on the temperature response of the optical bandgap of β - Ga_2O_3 films. The thin films were grown via the magnetron sputtering technique. Figure 1 presents a characteristic scanning electron microscope (SEM) image of the film showing its nano-crystalline morphology.

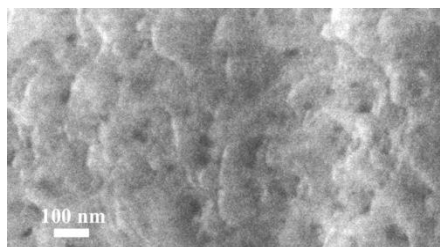
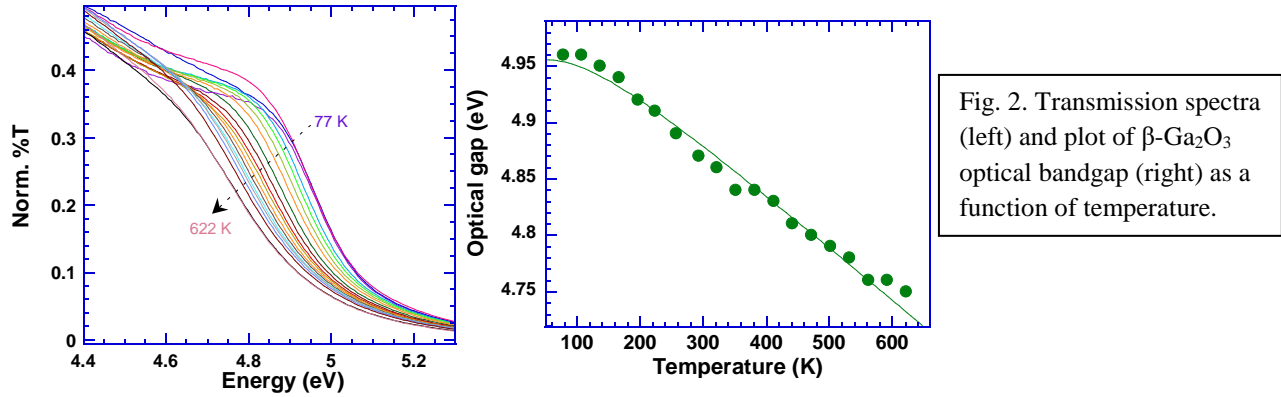


Fig. 1. SEM image of β - Ga_2O_3 film showing nanocrystalline morphology.

Figure 2 presents the transmission spectra as a function of temperature in the range of 77 to 622 K. The derivative of the transmission (not shown) is a good measure for analyzing optical gaps in semiconductors and was used to generate the plot on the right. As can be seen in Fig. 2, the β - Ga_2O_3 bandgap exhibits a redshift with increasing temperature, a behavior that can be modeled in terms of the electron-phonon (e-p) interaction. The Bose-Einstein type empirical model for the e-p interaction is used [1]:

$$E(T) = E(0) - \frac{2\alpha}{\exp(\frac{\theta}{T}) - 1} \quad (1)$$

where $E(0)$ is the optical gap at absolute zero, $\omega_p = k_B\Theta$ corresponds to the average phonon energy involved in the interaction, and α is the strength of the e-p coupling. As can be inferred from Fig. 2, the optical gap at 77 K is ~ 4.96 eV and that at 620 K is ~ 4.74 eV, which constitutes a redshift of ~ 220 meV.



The bandgaps of single crystals were found previously to be systematically smaller than those of thin films [2 and references therein]. In that work, it was found that the bandgaps at room temperature of single crystals are in the range of 4.52 – 4.6 eV, while those of thin films are 4.75 – 5.0 eV. The different energy ranges for single crystals and films were discussed in terms of the band-structure of β -Ga₂O₃, where several allowed transition can occur due to the valence band ordering. For randomly oriented thin films and unpolarized transmission measurements, deeper transitions become preferred [2]. Our room-temperature value of the optical gap (4.86 eV) falls in the range expected from a thin film.

The fit of Eq. (1) to the data in Fig. 2 resulted in $E(0) = 4.96$ eV, $\alpha = 80$ meV, and $\omega_p = 29$ meV. Previous studies on electronic transport properties of β -Ga₂O₃ found that low energy phonons were involved and dominate the electronic scattering at room temperature [3-5]. Polar optical phonons at 21 meV and 29 meV, and non-polar optical modes at 30 meV, were established to provide the main coupling mechanisms [3-5]. Our result of low energy phonons is consistent with those found from the transport studies.

Thin film PL: A laser with a line in the deep-UV (5.1 eV, 244 nm) was used to generate bandgap excitation. Figure 3 shows a high-resolution PL spectrum of our film from 3 to 5 eV. The PL emission at 3.56 eV (Fig. 3) of our β -Ga₂O₃ is attributed to the self-trapped hole (STH) recombination mechanism. The basic mechanism of forming STH requires the creation of free electron-hole (e-h) pairs, which can be accomplished via laser excitation above the bandgap. Consequently, the holes in the valence band are trapped by the crystal distortion.

To confirm that the emission at 3.56 eV is indeed due to STH, a laser with energy below the bandgap was used that should not result in the creation of free e-h pairs. Figure 3 shows the PL of the film using the 3.81 eV laser. As can be seen in the figure, the 3.56 eV PL was totally diminished, as expected for sub-bandgap excitation. Additionally, an emission line in the range of ~ 3.14 eV is present in the spectrum, attributed to native defects in β -Ga₂O₃ that result in donor-acceptor recombination. The other emission lines in Fig. 3, at 4.08 eV and 4.60 eV, are currently under investigation. A key point is that the bandgap recombination emission at ~4.85 eV is very weak, as predicted theoretically [6]. Moreover, the Stokes shift, defined to be the energy difference between the STH emission and the optical gap, is ~ 1.29 eV. This is a large value which is characteristic of STH [6].

Localized emission centers: Optical and structural imaging methods revealed the presence of localized surface defects that emit in the near-UV (3.27 eV, 380 nm) when excited by sub-bandgap light. Figure 4 shows a PL map of a bulk, hydrogenated sample. The defect emission was observed everywhere, but especially bright regions were detected as well. Some emitters are so bright, low laser power (<0.6 mW delivered to the sample) and short integration times (10 ms) had to be used to avoid saturating the spectrometer. To obtain a useful benchmark comparison, we collected PL maps of hydrogenated Ga₂O₃ and hydrothermal bulk ZnO under the same experimental conditions. From this comparison, we found that the Ga₂O₃ emitters have an intensity *50 times* that of ZnO. We are currently performing experiments to determine the identity of these very bright centers.

Iridium electronic transitions: Bulk Mg-doped β -Ga₂O₃ samples show a strong IR absorption peak at 5148 cm⁻¹ and a large number of smaller neighboring peaks from 5090-5190 cm⁻¹ (Fig. 5). The small peaks are attributed to IrMg pairs. Undoped β -Ga₂O₃ samples that have similar concentrations of iridium do not show evidence of these features, presumably because the iridium is in the form of Ir³⁺, which is not IR active.

Magnesium accepts an electron from the iridium donor, creating the IR-active Ir⁴⁺. Further supporting this idea, the magnesium acceptors can be passivated to be neutral through hydrogen annealing. The neutral complexes can no longer be compensated by iridium donors, and so the majority of iridium in the crystal has the form of Ir³⁺. As a result, hydrogen annealing Ga₂O₃:Mg greatly suppresses the Ir⁴⁺ peak (Fig. 5).

Zn acceptors: A major problem in Ga₂O₃ research is producing semi-insulating substrates for device epilayer growth. We have investigated the Zn acceptor as a possible dopant for semi-

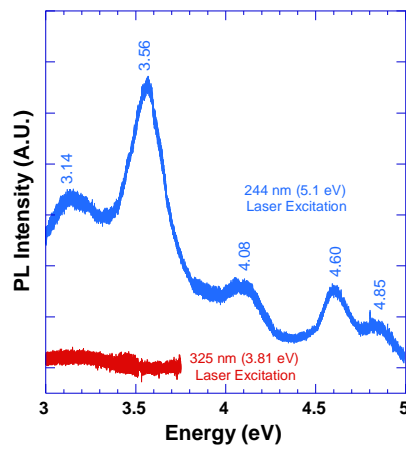


Fig. 3. Room-temperature PL spectra, above bandgap excitation (5.1 eV laser) and sub-bandgap excitation (3.81 eV laser).

insulating material. We find that high-quality $\text{Ga}_2\text{O}_3:\text{Zn}$ crystals can be grown with high ($>10^{18} \text{ cm}^{-3}$) densities of Zn, resulting in very large resistance ($\sim 1 \text{ T}\Omega$). By comparing with Mg-doped samples, we verified that the sidebands in Fig. 5 are indeed due to iridium-acceptor pairs. Furthermore, Zn can be passivated by hydrogen, resulting in a characteristic O-H vibrational mode.

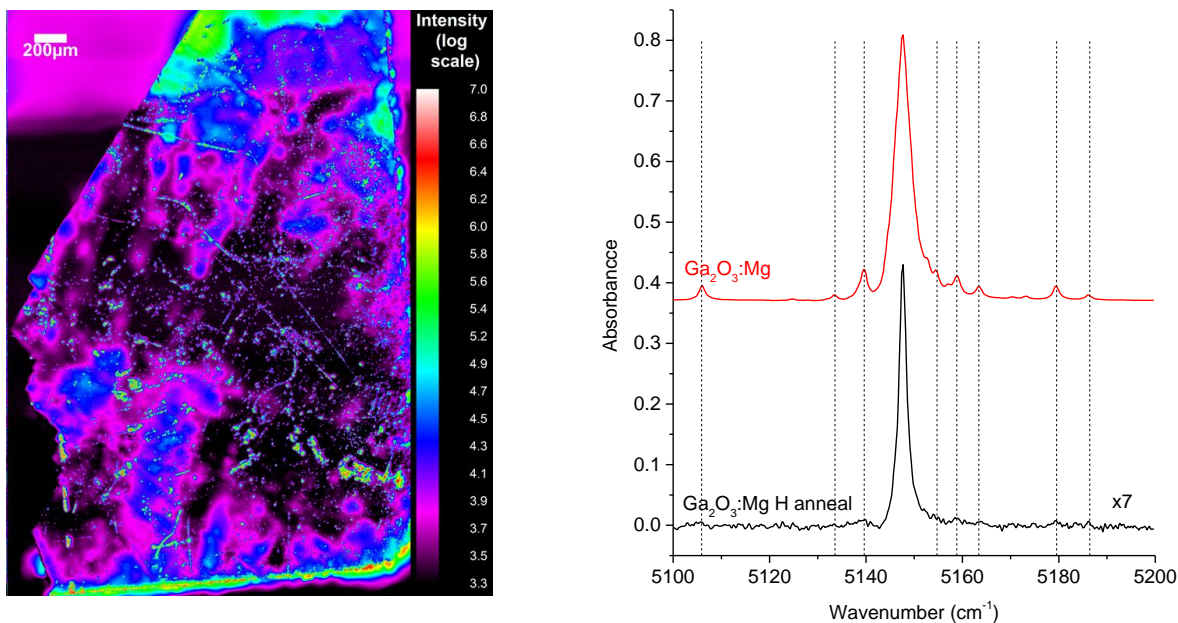


Fig. 4. Map of the PL intensity of bright emitters (3.27 eV) in hydrogenated Ga_2O_3 .

Fig. 5. IR spectra of Mg-doped gallium oxide, as-grown and hydrogen-annealed. The peak at 5148 cm^{-1} is due to Ir^{4+} while the smaller peaks arise from IrMg pairs.

Future Plans

Manuscripts describing the thin-film and Zn acceptor work are under preparation and will be submitted in 1-2 months. Spatially resolved PL experiments are being performed on Fe-doped samples and a manuscript will be submitted in the next year.

References

1. C. F. Li and Y.S. Huang, *Phys. Rev. B* **55**, 9251 (1997).
2. T. Onuma et al., *Japanese Journal of Applied Physics* **54**, 112601 (2015).
3. K. Ghosh and U. Singisetti, *Appl. Phys. Lett.* **109**, 072102 (2016).
4. K.A. Mengle and E. Kioupakis, *AIP Advances* **9**, 015313 (2019).
5. A. Parisini, and R. Fornari, *Semicond. Sci. Technol.* **31**, 035023 (2016).
6. J.B. Varley, A. Janotti, C. Franchini, and C.G. Van de Walle, *Phys. Rev. B* **85**, 081109 (2012).

Publications

J. Huso, M.D. McCluskey, Y. Yu, Md. M. Islam, and F. Selim, “Localized UV emitters on the surface of Ga_2O_3 ,” *Scientific Reports* **10**, 21022:1-7 (2020).

J.R. Ritter, M.J. Caldas, T.J. da Silva, A. Calzolari, and M.D. McCluskey, “Surface effects on pyrene luminescence excitation,” *ACS Applied Electronic Materials* **2**, 2806-2812 (2020).

J. Lapp, D. Thapa, J. Huso, A.J. Canul, M.G. Norton, M.D. McCluskey, and L. Bergman, “Enhancement of the ultraviolet photoluminescence of ZnO films: Coatings, annealing, and environmental exposure studies,” *AIP Advances* **10**, 085217:1-8 (2020).

A. Canul, D. Thapa, J. Huso, L. Bergman, R.V. Williams, and R. Machleidt, “Mixed-strategy approach to band-edge analysis and modeling in semiconductors,” *Phys. Rev. B* **101**, 195308:1-15 (2020).

M.D. McCluskey and A. Janotti, “Defects in semiconductors,” *J. Appl. Phys.* **127**, 190401:1-3 (2020).

M.D. McCluskey, “Point defects in Ga_2O_3 ,” *J. Appl. Phys.* **127**, 101101:1-13 (2020).

J.R. Ritter, K.G. Lynn, and M.D. McCluskey, “Iridium-related complexes in Czochralski-grown β - Ga_2O_3 ,” *J. Appl. Phys.* **126**, 225705:1-6 (2019).

J.R. Ritter, K.G. Lynn, and M.D. McCluskey, “Hydrogen passivation of calcium and magnesium doped β - Ga_2O_3 ,” *Proc. SPIE* **10919**, 109190Z (2019); DOI: 10.1117/12.2507187.

J. Huso, J.R. Ritter, L. Bergman, and M.D. McCluskey, “High order oxygen local vibrational modes in $\text{ZnS}_{1-x}\text{O}_x$,” *Phys. Stat. Solidi B* **2019**, 1800607:1-9 (2019).

J. Huso, L. Bergman, and M.D. McCluskey, “Bandgap of cubic $\text{ZnS}_{1-x}\text{O}_x$ from optical transmission spectroscopy,” *J. Appl. Phys.* **125**, 075704:1-5 (2019).

M.D. McCluskey, “Vibrational spectroscopy,” in *Characterisation and Control of Defects in Semiconductors*, ed. F. Tuomisto (IET, United Kingdom, 2019), Ch. 3.

Establishing microscopic photophysics of local cation and anion phase segregation in hybrid perovskite solar cells

Masaru Kuno, Prashant Kamat

University of Notre Dame, Department of Chemistry and Biochemistry

Program Scope

Alloyed lead halide perovskites have taken a dominant role in the quest to develop low cost, third generation solar cells. This is due to their optimal light harvesting properties, which can be tuned across the visible spectrum by mixing halide anions (i.e. Cl^- , Br^- , and I^-) as well as A^+ cations (i.e. FA^+ , MA^+ , and Cs^+). Unfortunately, stability issues related to ion migration/photosegregation impede their large-scale commercialization. Uniformly-mixed halide perovskites [e.g. $\text{APb}(\text{I}_{1-x}\text{Br}_x)_3$] reversibly segregate into narrow bandgap I-rich and wide bandgap Br-rich domains during continuous, visible wavelength illumination. Produced I-rich inclusions reduce local open circuit voltages and decrease mixed halide perovskite solar cell power conversion efficiencies. For mixed cation systems, bias-induced cation migration/segregation similarly degrades perovskite solar cell performance and is likely the origin of their hysteretic behavior. A fundamental need therefore exists to better understand the origin of anion and cation instabilities in hybrid perovskites.

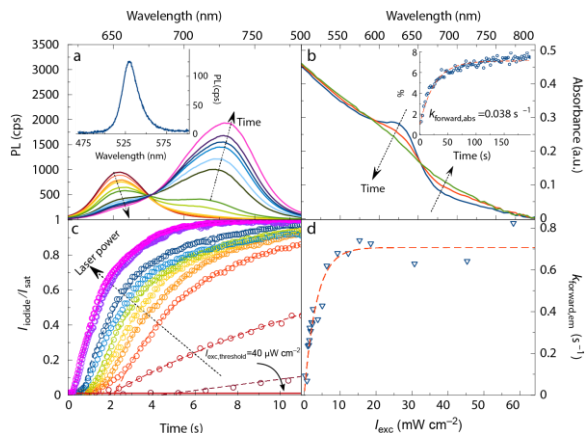


Figure 1. (a) Emission redshift of $\text{MAPb}(\text{I}_{0.5}\text{Br}_{0.5})$ under CW illumination. (b) Absorption changes of the same film. (c) I_{exc} -dependent emission-based forward photosegregation rate. (d) I_{exc} -dependent forward photosegregation rate constant.

in the absorption (**Figures 1a, 1b**). It further explains unusual excitation intensity (I_{exc})-dependent photosegregation rates (**Figure 1c**), rate constants (**Figure 1d**), and the existence of an excitation intensity threshold for halide photosegregation (**solid red line, Figure 1c**). Most relevantly, the model invokes a thermodynamic, bandgap-based origin for halide segregation under illumination.

In tandem, we have begun addressing bias-induced cation migration.[2] This is a second, intrinsic instability of hybrid perovskites and is thought to be the origin of current-voltage hysteresis in perovskite solar cells. Even though this instability is now well recognized, few studies have probed or developed microscopic models of cation instabilities, let alone ones that jointly consider light-induced anion instabilities. Our program thus aims to conduct comprehensive investigations of hybrid perovskite anion *and* cation instabilities.

Recent Progress

During the current funding period, we have successfully deployed a new superresolution infrared absorption technique, called infrared photothermal heterodyne imaging (IR-PHI) to visualize cation migration in mixed cation hybrid perovskites.[2] These IR-PHI studies reveal cation compositional heterogeneities in solution-processed mixed cation films such as $\text{FA}_x\text{MA}_{1-x}\text{PbI}_3$ and show bias-induced cation migration in $\text{FA}_{1-x}\text{Cs}_x\text{PbI}_3$, and $\text{FA}_x\text{MA}_y\text{Cs}_{1-x-y}\text{PbI}_3$ films. The latter IR-PHI results have been independently validated using time-of-flight secondary ion mass spectrometry.

We have, in tandem, discovered that $\text{FA}_x\text{MA}_y\text{Cs}_{1-x-y}\text{PbI}_3$ active layers with orthorhombic, post-perovskite (δ)-phase inclusions exhibit improved stability against bias-induced cation segregation. This enhanced stability is rationalized as δ -phase inclusions within parent alloys acting as barriers to inhibit cation migration. This, in turn, raises prospects for applying compositional microstructuring of mixed cation/mixed anion perovskites to suppress their bias and possibly light-induced cation/anion instabilities.

Future Plans

We propose to continue probing the microscopic origin of anion and cation instabilities in hybrid perovskites. We identify three areas where more detailed investigations should be conducted to refine our understanding of $\text{APb}(\text{I}_{1-x}\text{Br}_x)_3$ photosegregation -the end goal being to develop a universal, predictive model of anion *and* cation instabilities in hybrid perovskites. The **first** involves evaluating whether a thermodynamic or a polaron model holds more merit in explaining mixed halide perovskite photosegregation. This involves directly testing predictables from each model class and, more broadly, establishing how well they rationalize photosegregation in other mixed anion systems beyond $\text{MAPb}(\text{I}_{1-x}\text{Br}_x)_3$. The **second** involves better understanding the high carrier density response of mixed halide perovskites and specifically how carrier density impacts halide photosegregation. Of note here is that most studies have probed $\text{APb}(\text{I}_{1-x}\text{Br}_x)_3$ photosegregation under relatively low excitation intensities. Our **third** area focuses on cation instabilities in hybrid perovskites and specifically cation migration under bias. This entails concerted experimental and theoretical studies to develop a microscopic picture of bias-induced cation migration/segregation. In this way, we propose to conceptually tie together hybrid perovskite cation and anion instabilities, which exist under normal solar cell operating conditions (i.e. built in bias and light).

References

- [1] *Rationalizing the light-induced phase separation of mixed halide organic-inorganic perovskites*, S. Draguta, O. Sharia, S. Yoon, M. Brennan, Y. V. Morozov, J. Manser, P. Kamat, W. F. Schneider, M. Kuno, *Nature Commun.* **2017**, 8, 200. DOI: 10.1038/s41467-017-00284-2
- [2] *Suppressing cation migration in triple-cation lead halide perovskites*, I. M. Pavlovec, M. C. Brennan, S. Draguta, A. Ruth, T. Moot, J. A. Christians, K. Aleshire, S. P. Harvey, S. Toso, S. U. Nanayakkara, J. Messinger, J. M. Luther, M. Kuno, *ACS Energy Lett.* **2020**, 5, 9, 2802-2810. DOI: 10.1021/acsenergylett.0c01207

Publications

1. To exchange or not to exchange. Suppressing anion exchange in lead halide perovskites with PbSO_4 -oleate capping, V. K. Ravi, R. A. Scheidt, A. Nag, M. Kuno, P. V. Kamat, *ACS Energy Lett.* **2018**, 3, 1049–1055.

2. Vacancy-mediated anion photosegregation kinetics in mixed halide hybrid perovskites: Coupled kinetic Monte Carlo and optical measurements, A. Ruth, M. C. Brennan, S. Draguta, Y. V. Morozov, M. Zhukovskyi, B. Janko, P. Zapol, M. Kuno, *ACS Energy Lett.* **2018**, 3, 2321-2328.
3. Crystal structure of individual CsPbBr₃ perovskite nanocubes, M. C. Brennan, M. Kuno, S. Rouvimov, *Inorg. Chem.* **2019**, 58, 1555–1560.
4. Tracking transformative transitions: From CsPbBr₃ nanocrystals to bulk perovskite films, R. A. Scheidt, C. Atwell, P. V. Kamat, *ACS Mater. Lett.* **2019**, 1, 8-13.
5. Interplay between photo and thermal activation dictates halide ion segregation in mixed halide perovskites, T. Elmelund, B. Seger, M. Kuno, P. V. Kamat, *ACS Energy Lett.* **2020**, 5, 56-63.
6. What exactly causes light-induced halide segregation in mixed-halide perovskites?, M. Kuno, M. C. Brennan, *Matter*, **2020**, 2, 21-23.
7. Photoinduced anion segregation in mixed halide perovskites, M. C. Brennan, A. Ruth, P. V. Kamat, M. Kuno, *Trends in Chem.* **2020**, 2, 282-301.
8. Superlattices are greener on the other side: How light transforms self-assembled mixed halide perovskite nanocrystals, M. C. Brennan, S. Toso, I. M. Pavlovec, M. Zhukovskyi, S. Marras, M. Kuno, L. Manna, D. Baranov, *ACS Energy Lett.* **2020**, 5, 1465-1473.
9. Universal size-dependent Stokes shifts in lead halide perovskite nanocrystals, M. C. Brennan, A. Forde, J. E. Herr, K. J. Koh, M. Zhukovskyii, A. Baublis, Y. V. Morozov, S. Zhang, Z. Zhang, D. S. Kilin, M. Kuno, *J. Phys. Chem. Lett.* **2020**, 11, 4937-4944.
10. Suppressing cation migration in triple-cation lead halide perovskites, I. M. Pavlovec, M. C. Brennan, S. Draguta, A. Ruth, T. Moot, J. A. Christians, K. Aleshire, S. P. Harvey, S. U. Nanayakkara, J. Messinger, J. M. Luther, M. Kuno, *ACS Energy Lett.* **2020**, 5, 2802-2810.
11. Thermal decoherence of the superfluorescent response in lead halide perovskite nanocrystal superlattices, F. Mattiotti, M. Kuno, F. Borgonovi, B. Janko, G. L. Celardo, *Nano Lett.* **2020**, 20, 7382-7388.
12. Iodine (I) expulsion at photoirradiated mixed halide perovskite interface. Should I stay or should I go? P. S. Mathew, G. F. Samu, C. Janáky, P. V. Kamat, *ACS Energy Lett.* **2020**, 5, 6, 1872-1880.
13. Shining new light on photoinduced halide segregation in mixed-halide, hybrid perovskites, M. Kuno, *Nature Mater.* **2021**, 20, 6-7.
14. Halide ion migration in perovskite nanocrystals and nanostructures, P. V. Kamat, M. Kuno, *Accts. Chem. Res.* **2021** (ASAP).
15. Modulation of photo induced iodine expulsion in mixed halide perovskites with electrochemical bias, J. T. DuBose, P. S. Mathew, J. Cho, M. Kuno, P. V. Kamat (submitted **2021**).
16. Terminal halide stoichiometries following photosegregation of mixed halide hybrid perovskites, I. M. Pavlovec, A. Ruth, I. Gushchina, S. Zhang, M. Kuno (in preparation **2021**).

Nanocrystal-based Dyads for Solar to Electric Energy Conversion

David H. Waldeck, Department of Chemistry, University of Pittsburgh

David N. Beratan, Department of Chemistry, Duke University

Ron Naaman, Department of Chemical and Biological Physics, Weizmann Institute of Science

Program Scope

This project explores design features, at the molecular and nanoscales, that promote efficient charge and spin transfer in self-assembling, nanostructured materials. Chiral molecules and nanostructures can exhibit unusual electronic and magnetic properties, including electron spin filtering and vectorial charge transfer; a phenomenon referred to as the chiral induced spin selectivity (CISS) effect. These effects include the magnetization dependence of chiral molecule and chiral organic-inorganic material interactions with ferromagnetic surfaces. The underlying mechanism(s) giving rise to these properties are poorly understood; however, experiments imply that exchange interactions are important and indicate that the magnitude of the spin selectivity correlates with the chiro-optical response of the chiral molecules and materials. A major theme of the team's current effort is to reveal the underlying electronic interactions through which chiral molecules imprint a chiro-optical response on the electronic properties of materials, with the aim of revealing features of the CISS mechanism through its correlation with the chiro-optical responses. The team is exploring the properties of chiral materials along three interrelated thrusts: elucidation of mechanisms to imprint electronic chirality on semiconductor nanoparticles, vectorial charge transfer in chiral structures, and spin transfer in chiral structures that select the electron's spin orientation.

Recent Progress

Recent work by the team has emphasized studies into the electrical and magnetic properties of interfaces between chiral molecules (and materials) and magnetic substrates (and nanoparticles). The four vignettes described below proceed from fundamental investigations into spin dependent tunneling at chiral molecule/ferromagnetic interfaces to the demonstration of chiral materials for applications, e.g., memory device structures and electrocatalysis.

Spin dependent tunneling. We have used Kelvin-probe and Kelvin-probe microscopy measurements to study the extent of electron tunneling into chiral self-assembled monolayers films that coat a Co/Au substrate [1] We studied the response as a function of the magnetization strength, the magnetization direction, and the handedness and length of the chiral molecules. The data show that the electron penetration from the metal electrode into the chiral molecules depends on the ferromagnet's magnetization direction; one spin orientation of electrons from the ferromagnet

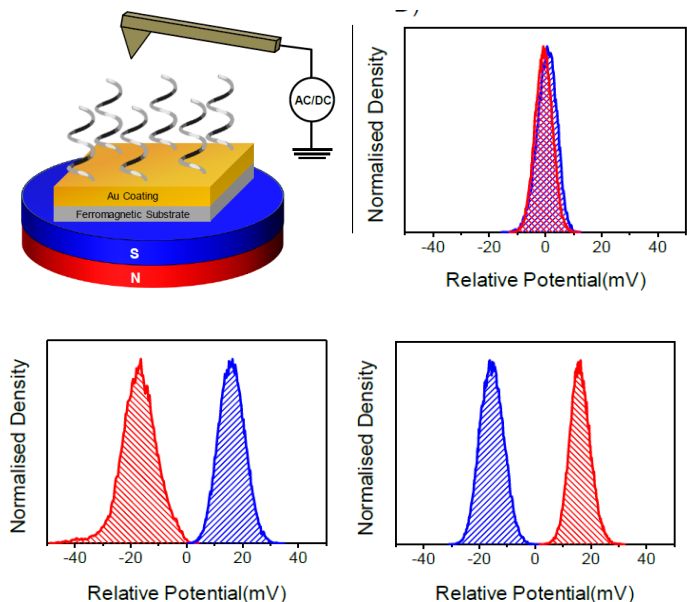


Figure 1. Kelvin probe microscopy measurements show how the surface electrostatic potential changes with an electrode's magnetization (South (blue) to North (red)) and film chirality. For an achiral film the magnet does not change the surface electrostatic potential, but for chiral films it changes by tens of millivolts (case of a left-handed film is shown on the left and that for a right-handed film is shown on the right).

penetrates more easily into a chiral molecule than does the other orientation. The measurements are performed at room temperature and generate electrostatic potential changes as high as 100 mV. See Figure 1.

We have examined the dependence of spin polarization in conduction and in electric field-induced polarization on molecular length by using double-stranded DNA oligonucleotides and oligopeptides. Through a combination of different measurement methods we have shown that the CISS response of chiral molecules scales linearly with oligomer length (for lengths below 10 nm) and that the spin-currents, measured in magnetic conducting probe-AFM, depend nonlinearly on the applied potential. These findings and the correlation of the CISS response with a molecule's chiro-optical response suggests the importance of a molecule's polarizability in CISS.

Optically-generated magnetism: We have used the magneto-optic Kerr effect (MOKE) to study photogenerated magnetization at the interface of two-dimensional, chiral hybrid organic–inorganic perovskites (chiral-HOIPs) and a permalloy substrate [2]. These materials are analogous to traditional HOIPs, but they are endowed with chirality by the incorporation of phenylethylamine ligands which break the degeneracy of the electron spin in charge transport. Illumination of the chiral-HOIPs generates a Kerr signal (measured via a Sagnac interferometer) at the chiral-HOIP/NiFe interface, which indicates an optical modulation of the magnetization. The MOKE signal shows a linear dependence of the response on the magnetic field and its sign is controlled by the chirality of the HOIPs; *i.e.*, the incident light generates an enantiospecific magnetization at the permalloy interface. These results demonstrate one approach for using chiral semiconductor materials in opto-spintronic applications.

10 nm Memory Architecture: We are investigating how chiral materials can address the demand for new magnetic memory architectures. Current magnetic memory sizes are limited to 30–50 nm,

because the magnetization and magnetic orientation become susceptible to thermal fluctuations and stray magnetic fields for smaller size domains. By creating assemblies of 10 nm superparamagnetic iron-oxide nanoparticles (SPIONS) on chiral films, we have demonstrated 10 nm single domain ferromagnetism [3]. The asymmetric adsorption of chiral molecules on SPIONS causes them to exhibit an enantiospecific ferromagnetism with an average coercive field of ≈ 80 Oe and stabilizes their magnetization direction at room temperature. More recently we showed how chiral quantum dots (QDs), manifesting the CISS effect, can be used to create a 9-state flash memory [4]. By assembling a double QD architecture on the active area of a Hall sensor we demonstrated an optical nine-state readout which arises from the modulation of the electron transfer rate by the QD chirality and the light polarization. These studies show how the use of chiral materials and chiral environments around active materials can be used to stabilize magnetization.

Chiral Electrocatalysts: We have developed a procedure for electrodepositing chiral cobalt oxide thin film electrocatalysts and shown that they display an improved performance in water electrolysis, as compared to their achiral analogues [5]. We showed that chiral cobalt oxide electrocatalysts reduce the reaction overpotential by 65 mV at 10 mA/cm², increase the oxygen yield by 1.4-fold at a fixed current density at pH 10, and decrease the production of hydrogen peroxide by 4-fold. We attribute the improved performance of the chiral catalysts to an improved reaction selectivity that arises because the spin polarized current through the electrocatalyst generates spin-polarized intermediates on the electrode surface which facilitate the generation of triplet oxygen over competing singlet pathways.

Future Plans

Electron transfer in linked nanoparticles. Because nanoparticle diameters can be large on the scale of chemical bonds, the tunneling mechanism involves a tunable mix of through-bond, through-space, and through-solvent tunneling. We are using quantum mechanical modeling to examine how the combination of distance, nanoparticle (NP) diameters, and intervening medium structure influence the tunneling between NPs (see Fig. 2). For larger diameter NPs, solvent mediated tunneling dominates, while through-bond and through-solvent tunneling dominates for smaller QDs. Currently we are exploring how to predict the diameter at which the transition occurs between tunneling mechanisms for NPs. These calculations are being performed with CdSe and CdTe parameters for comparisons with experiment, and future studies will include the treatment of chiral linkers.

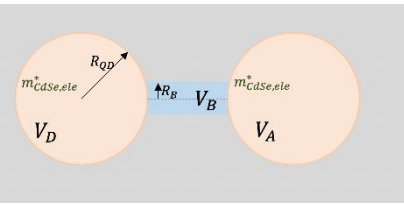


Figure 2 The orange spheres denote donor and acceptor NPs, the blue cylinder represents the bridge, and the gray region represents the solvent.

Chiral Imprinting on Perovskite NPs Chiral ligands imprint chirality and induce circular dichroism (CD) on perovskite NPs and nanoplates (NPLs), and we are using a combined theoretical and experimental approach to examine how the electrostatic field of a chiral ligand (e.g.,

phenylethylamine) induces chirality onto the exciton transitions of a structurally achiral NP. We have implemented a new synthetic strategy that promises to improve size focusing and lower the average CsPbBr_3 NP diameter for NPs with a number of different chiral ligands. This new synthetic strategy allows us to perform chiral imprinting and study chiral symmetry constraints on electron transfer and energy transfer in the same systems. We are developing assays to quantify the ligand coverage on the NP and NPL surfaces and quantify its impact on the CD signal strengths. We have computed the absorption spectra and CD spectra for perovskite clusters and are correlating the bisignate CD signals at 500 nm and 300 nm with those observed experimentally. Given that the spin-filtering in chiral materials correlates with the CD signal strengths, understanding the electronic origins of the CD signal strengths should help elucidate the mechanism underlying CISS.

Chiral Metal Oxide Filters: Spin injection into solid state spintronics devices is generally achieved by using a fixed ferromagnetic material and another free ferromagnetic layer which can create significant engineering challenges in miniaturization. We are exploring the use of chiral metal-oxide thin films as efficient spin filters and spin-valve functions. Methods to create chiral metal oxide films by electrodeposition and by atomic layer deposition are being developed. Chiro-optical spectra of the chiral oxide films will be measured and compared with the film's spin filtering properties. The realization of this new material platform promises to simplify the engineering challenges for spintronics devices and reduce costs.

References

1. S. Ghosh, et al. *J. Phys. Chem. Letters* **11** (2020) 1550-1557.
2. Z. Huang, et al. *ACS Nano* **14** (2020) 10370–10375.
3. G. Koplovitz, et al. *Small* **15** (2019) 1804557.
4. H. Al-Bustami, et al. *Letters* **20** (2020) 8675-8681.
5. S. Ghosh, et al. *J. Phys. Chem. C* **124** (2020) 22610–22618.

Publications

X. Xu, Y. Guo, B. P. Bloom, J. J. Wei, H.Y. Li, H. L. Li, Y. K. Du, Z. Zeng, L.Q. Li, and D. H. Waldeck, *Elemental Core Level Shift in High Entropy Alloy Nanoparticles via X-ray Photoelectron Spectroscopy Analysis and First-Principles Calculation* *ACS Nano* **2020**, *14*, 17704-17712.

R. Naaman, Y. Paltiel, and D. H. Waldeck *Chiral Induced Spin Selectivity Gives a New Twist on Spin-Control in Chemistry* *Accounts of Chemical Research* **53** (2020) 2659-2667.

H. Al-Bustami, B. P. Bloom, S. Goldring, S. Yochelis, R. Naaman, D. H. Waldeck, Y. Paltiel *Optical Multilevel Spin Bit Device using Chiral Quantum Dots* *Nano Letters* **20** (2020) 8675-8681.

G. H. Debnath, P. Mukherjee, and D. H. Waldeck *Optimizing the Key Variables to Generate Host Sensitized Lanthanide Doped Semiconductor Nanoparticle Luminophores* *J. Phys. Chem. C* **124** (2020) 26495-26517.

S. Ghosh, B. P. Bloom, Y. Lu, D. Lamont, and D. H. Waldeck *Increasing the Efficiency of Water Splitting through Spin Polarization using Cobalt Oxide Thin Film Catalysts* J. Phys. Chem. C **124** (2020) 22610–22618.

Z. Huang, B. P. Bloom, X. Ni, Z. N. Georgieva, M. Marciesky, E. Vetter, F. Liu, D. H. Waldeck, and D. Sun *Magneto-optical Detection of Photoinduced Magnetism via Chirality Induced Spin Selectivity in 2D Chiral Hybrid Organic-Inorganic Perovskites* ACS Nano **14** (2020) 10370–10375.

R. Naaman, Y. Paltiel, and D. H. Waldeck *Chiral Molecules and the Spin Selectivity Effect* J. Phys. Chem. Letters **11** (2020) 3660-3666.

S. Ghosh, S. Mishra, E. Avigad, B. P. Bloom, L. T. Baczewski, S. Yochelis, Y. Paltiel, R. Naaman, D.H. Waldeck *Effect of Chiral Molecules on the Electron's Spin Wavefunction at Interfaces* J. Phys. Chem. Letters **11** (2020) 1550-1557.

J. M. Abendroth, D. M. Stemer, B.P. Bloom, P. Roy, R. Naaman, D. H. Waldeck, P. S. Weiss, and P. Chandra Mondal *Spin Selectivity in Photoinduced Charge-Transfer Mediated by Chiral Molecules* ACS Nano **13** (2019) 4928-4946.

K. Michaeli, D. N. Beratan, D. H. Waldeck, and R. Naaman *Voltage-induced long-range coherent electron transfer through organic molecules* Proceedings of the National Academy of Sciences **116** (2019) 5931-5936.

R. Naaman, Y. Paltiel, and D. H. Waldeck *Chiral Molecules and the Electron Spin* Nature Reviews, **3** (2019) 250-260.

G. Koplovitz, G. Leitus, S. Ghosh, B. P. Bloom, S. Yochelis, D. Rotem, F. Vischio, M. Striccoli, E. Fanizza, R. Naaman, D. H. Waldeck, D. Porath and Y. Paltiel *Single Domain 10 nm Ferromagnetism Imprinted on Superparamagnetic Nanoparticles Using Chiral Molecules* Small **15** (2019) 1804557.

Exploring the impact of the local environment on charge transfer states at molecular donor-acceptor heterojunctions

Barry P. Rand,^{1,2} Antoine Kahn,¹ and Noel C. Giebink³

¹ Department of Electrical Engineering, Princeton University, Princeton, NJ 08544

² Andlinger Center for Energy and the Environment, Princeton University, Princeton, NJ 08544

³ Department of Electrical Engineering, The Pennsylvania State University, University Park, PA 16802

Program Scope

Charge transfer from a donor-type to an acceptor-type system forms the basis for the photovoltaic effect observed within excitonic systems. The charge transfer (CT) state is a bound geminate charge pair that defines an intermediate state in both charge generation and recombination processes. As such, the CT state possesses a binding energy ($\sim 10k_bT$) that still needs to be overcome in order to produce a free charge pair. While some important realizations have been made concerning CT states recently regarding their role in limiting open-circuit voltage, there still remains a lack of fundamental knowledge regarding what controls CT state energy and the efficiency by which they may be dissociated, and whether or not Frenkel excitons become free charge via the formation of CT states. This research program sets out to comprehensively investigate the various nanoscale environmental factors that determine CT state behavior (dielectric, structural, dynamic, and energetic), as well as to quantify their spatial extent and density of states (DOS) energetic distribution.

We will utilize sensitive spectral response measurements, impedance spectroscopy, X-ray scattering, and spectroscopic ellipsometry to probe the structure and optical response of thin films, as well as to extract dielectric properties. Surface-sensitive techniques such as ultraviolet photoelectron spectroscopy (UPS), inverse photoelectron spectroscopy (IPES), and X-ray photoelectron spectroscopy (XPS) will be utilized to probe energy levels. Finally, time-resolved and steady-state photoluminescence (PL), electroluminescence (EL), electroabsorption, and pump-probe spectroscopy measurements will be used to probe CT state energetics and dynamics. In this way, the PIs assembled in this collaborative proposal represent a complementary team uniquely suited with the ability to transform our understanding of CT states.

Recent Progress

Molecular doping of an organic semiconductor, whether molecular or polymer, involves a charge exchange between dopant and host. N-type doping implies reduction of the host upon electron transfer from the highest occupied molecular orbital (HOMO) of the dopant to the lowest

unoccupied molecular orbital (LUMO) of the host. The relative magnitudes of the ionization energy (IE) of the dopant and the electron affinity (EA) of the host are therefore at play. The host:dopant system studied here, i.e. the polymer poly[(9,9-dioctylfluorene-2,7-diyl)-*alt*-(benzo[2,1,3]thiadiazol-4,7-diyl)] (F8BT) and the dopant (pentamethylcyclopentadienyl) (1,3,5-trimethylbenzene)ruthenium dimer ($[\text{RuCp}^*\text{Mes}]_2$), offers an opportunity to investigate a donor-to-acceptor CT state. The electron affinity of the acceptor, F8BT, measured via inverse photoemission spectroscopy is 2.8 eV, a value that reflects the difficulty of reducing this polymer. The thermodynamic reducing strength of the donor, the $[\text{RuCp}^*\text{Mes}]_2$ dimer, is insufficient for a direct reduction of F8BT and, without additional external stimulus, prevents the dopant-to-host electron transfer. This situation is reminiscent of that observed with the molecular host phenyldi(pyren-2-yl)phosphine oxide (POPY_2), EA= 2.1 eV, for which a $[\text{RuCp}^*\text{Mes}]_2$ -to- POPY_2 CT states was observed.[DOI: 10.1038/nmat5027] EQE measurements on ITO/F8BT/bathocuproine(BCP)/Al stacks, where the polymer is either undoped or 15 wt% doped, are shown in Fig. 1. The undoped F8BT device shows two main features centered at 2.6 and 3.7 eV attributed to optical absorption by F8BT alone. However, the doped F8BT device exhibit a broad feature below the polymer optical gap (scans 1 and 2), attributed to CT states, presumably involving the F8BT LUMO (~ 2.8 eV below vacuum level) and the $[\text{RuCp}^*\text{Mes}]_2$ neutral dimer HOMO (nominally ~ 4.0 eV below vacuum level). The breadth of this feature owes to the highly disordered nature of the polymer and the broad distribution of polymer chain:dimer interface configurations. Scans 3-5, taken following device exposure to light of a solar simulator, show an order of magnitude reduction in the CT state signal attributed to a comparable reduction in the concentration of neutral dimers via cleavage upon photoactivation of the doping process: Excitation above the F8BT gap (solar simulator) enables a first electron transfer from the dimer HOMO to the singly occupied F8BT HOMO, followed by immediate cleavage of the dimer and release of the two highly reducing $[\text{RuCp}^*\text{Mes}]$ monomers.[DOI: 10.1038/nmat5027; 10.1002/adma.201103238] The CT state is eliminated. Confirmation of n-doping concomitant to the cleavage of the dimers and elimination of the CT states was obtained via current-voltage and EQE measurements on a green OLED (emitter TPBi:Ir(ppy)₃) in which the doped F8BT served as electron injection layer (not shown here).

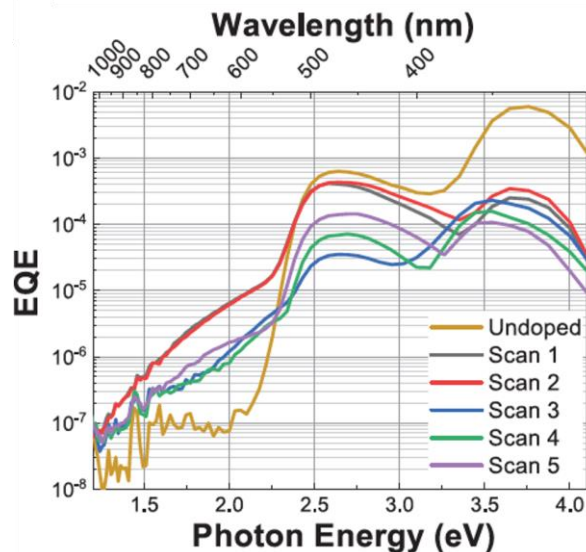


Figure 1: EQE scans of the ITO/F8BT (undoped or doped)/BCP/Al device. Scans 3-5 follow irradiation of the device to photoactivate doping.

where the polymer is either undoped or 15 wt% doped, are shown in Fig. 1. The undoped F8BT device shows two main features centered at 2.6 and 3.7 eV attributed to optical absorption by F8BT alone. However, the doped F8BT device exhibit a broad feature below the polymer optical gap (scans 1 and 2), attributed to CT states, presumably involving the F8BT LUMO (~ 2.8 eV below vacuum level) and the $[\text{RuCp}^*\text{Mes}]_2$ neutral dimer HOMO (nominally ~ 4.0 eV below vacuum level). The breadth of this feature owes to the highly disordered nature of the polymer and the broad distribution of polymer chain:dimer interface configurations. Scans 3-5, taken following device exposure to light of a solar simulator, show an order of magnitude reduction in the CT state signal attributed to a comparable reduction in the concentration of neutral dimers via cleavage upon photoactivation of the doping process: Excitation above the F8BT gap (solar simulator) enables a first electron transfer from the dimer HOMO to the singly occupied F8BT HOMO, followed by immediate cleavage of the dimer and release of the two highly reducing $[\text{RuCp}^*\text{Mes}]$ monomers.[DOI: 10.1038/nmat5027; 10.1002/adma.201103238] The CT state is eliminated. Confirmation of n-doping concomitant to the cleavage of the dimers and elimination of the CT states was obtained via current-voltage and EQE measurements on a green OLED (emitter TPBi:Ir(ppy)₃) in which the doped F8BT served as electron injection layer (not shown here).

In another work, we have identified six organic small molecules and polymer D-A systems with large frontier orbital energy offsets that display unprecedented, more than 2 eV broad, CT state features. Figure 2(a) show the external quantum efficiencies (EQE) of these D-A systems. All donor molecules here have optical gaps greater than 3 eV, while the acceptor molecules have approximately 4 eV optical gap and large electron affinity. The energy gap between the highest occupied molecular orbital (HOMO) of the donor and lowest unoccupied molecular orbital (LUMO) of the acceptor is therefore significantly smaller than in typical high-performing organic solar cells. In-depth experimental and computational analysis on one of the systems, NPB-HAT-CN (NPB is N,N'-di(1-naphthyl)-N,N'-diphenyl-(1,1'-biphenyl)-4,4'-diamine and HAT-CN is 1,4,5,8,9,11-hexaazatriphenylenehexacarbonitrile), revealed that the broad feature is associated with multiple electronic CT states originating from intermolecular interactions between the frontier molecular orbitals. In this work, we established that internal conversion between electronic CT levels is not efficient and emission does not happen from the lowest possible electronic states (Figure 2(b) [top]), implying these states do not fully obey Kasha's rule for electronically excited molecules. We were also able to show that dissociation efficiency of the NPB-HAT-CN CT-excitons are photon energy dependent and excitation to higher energy CT states is more likely to create photocurrent, revealing an example of non-constant internal conversion efficiency (Figure 2(b) [bottom]). An important consequence of this observation was that there are low energy states present in OPVs that are not revealed by the EQE measurement, which was later confirmed by our ultra-sensitive photothermal deflection spectroscopy measurement of the NPB-HAT-CN thin film (Figure 2(b) [bottom]). Although not

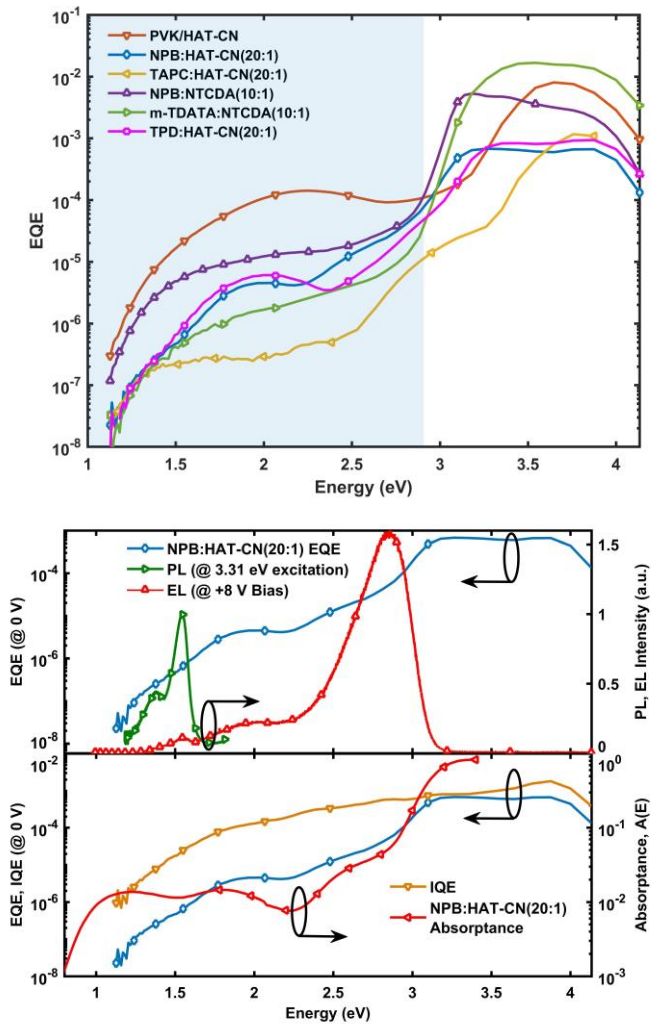


Figure 2: (a) External quantum efficiency (EQE) spectra of organic bulk and planar heterojunction solar cells, exhibiting broad CT spectra extending to approximately 1.1 eV. (b) [top] PL spectrum of an NPB:HAT-CN(20:1) film excited at 3.31 eV (green solid line). The purple and red dashed lines show two distinct peaks in the PL spectra, located at 1.55 eV and 1.38 eV. [bottom] Absorptance of a 20:1 NPB:HAT-CN film measured via PDS (red). Estimated IQE (gold) and EQE spectra of an NPB:HAT-CN(20:1) device (blue). The IQE exhibits two order of magnitude drop from 2.0 to 1.1 eV.

contributing to the photocurrent, these hidden states can still influence key photophysical processes like recombination and transport, and thus deserve careful examination.

Future Plans

From our work on large frontier orbital offset heterojunction OPVs, we discovered that the low energy EQE tails of these devices have a common cut-off around 1.1 eV (Figure 2(a)), despite considerable variations in their CT energy gap. This unique phenomenon could potentially be explained in terms of the resonant energy transfer from the low-lying CT state to polaron (cation) states, which successfully neutralizes a CT exciton and creates an excited polaron, thus abruptly quenching EQE. Most small molecule donor materials considered in our work have low energy polaron transition at ~ 1 eV, which strengthens our hypothesis about the cut-off energy, which we will pursue in the next period.

In terms of energy loss, Marcus theory of electron transfer, which only considers Franck-Condon vibrational broadening, cannot completely interpret the experimental CT state luminescence and absorption data, especially in the case of highly disordered donor-acceptor blends. Several attempts have been made to extract the effects of energetic disorder utilizing standard CT state characterization techniques. In the future, we plan to build on such an approach demonstrated by Burke et al. [*Adv. Energy Mater.*, 5, 1500123, (2015)], where a Gaussian energetic distribution of CT states has been considered. As a starting point, we have extracted the CT state energetic distributions for several fullerene acceptor based archetypal planar and bulk heterojunction devices. As donors, we explored small molecule organic materials that form thin films with varying degrees of order. For example, the donors pentacene and zinc phthalocyanine exhibit broad CT energy distribution, owing to the coexistence of amorphous and nano-crystalline domains. On the other hand, amorphous donors such as rubrene show much narrower energetic distributions, owing to their ability to form completely amorphous, and thus homogeneous, films. In the future, we plan to estimate the energy losses and energetic disorders for a series of state-of-the-art high-efficiency organic solar cells. Utilizing the enhanced understanding of the CT energetic distribution from this proposed work, we aim to redefine energy loss as the difference between the peak of the CT distribution and the room temperature open-circuit voltage, a general approach that allows to also incorporate the effect of disorder.

Finally, our work will expand our exploration of hybrid charge transfer states to organic-2D transition metal dichalcogenide material systems, where preliminary data have shown very large CT oscillator strengths and correspondingly high second order nonlinear optical susceptibility. We also plan to investigate the efficiency of photocurrent generation in large offset donor-acceptor systems where the donor HOMO and acceptor LUMO hybridize to form new optical excitations in the infrared spectral region.

2-Year Publications Supported by this BES Award

"Morphological requirements for nanoscale electric field buildup in a bulk heterojunction solar cell," K.N. Schwarz, V.D. Mitchell, S.-U.-Z. Khan, C. Lee, A. Reinhold, T.A. Smith, K.P. Ghiggino, D.J. Jones, B.P. Rand, G.D. Scholes, *J. Phys. Chem. Lett.*, **12**, 537 (2021).

"Image-enhanced bipolaron formation at organic semiconductor/electrode interfaces", J. Schrecengost, S. Mukhopadhyay, N.C. Giebink, *Phys. Rev. B*, **102**, 165311 (2020).

"Fate of low-lying charge-transfer excited states in a donor:acceptor blend with a large energy offset," G. Londi, S.-U.-Z. Khan, L. Muccioli, G. D'Avino, B.P. Rand, D. Beljonne, *J. Phys. Chem. Lett.*, **11**, 10219 (2020).

"Polariton transitions in femtosecond transient absorption studies of ultrastrong light-molecule coupling," C.A. DelPo, B. Kudisch, K.H. Park, S.-U.-Z. Khan, F. Fassoli, D. Fausti, B.P. Rand, G.D. Scholes, *J. Phys. Chem. Lett.*, **11**, 2667 (2020).

"n-Doping of a low-electron-affinity polymer used as an electron-transport layer in organic light-emitting diodes," H.L. Smith, J.T. Dull, E. Longhi, S. Barlow, B.P. Rand, S.R. Marder, A. Kahn, *Adv. Funct. Mater.*, **30**, 2000328 (2020).

"Reduced recombination and capacitor-like charge buildup in an organic heterojunction," K.N. Schwarz, P.B. Geraghty, V.D. Mitchell, S.-U.-Z. Khan, O.J. Sandberg, N. Zarrabi, B. Kudisch, J. Subbiah, T.A. Smith, B.P. Rand, A. Armin, G.D. Scholes, D.J. Jones, K.P. Ghiggino, *J. Am. Chem. Soc.*, **142**, 2562 (2020).

"Sensitization of silicon by singlet exciton fission in tetracene", T.C. Wu, M. Einzinger, J. Kompalla, H. Smith, C. Perkins, L. Nienhaus, S. Wieghold, D. Congreve, N. Thompson, A. Kahn, M. Bawendi, M.A. Baldo, *Proc. of SPIE* Vol. 11464 1146416-1-7 (2020).

"High-voltage photogeneration exclusively via aggregation-induced triplet states in a heavy-atom-free nonplanar organic semiconductor," N.C. Davy, M. Koch, G.O. Ngongang Ndjawa, X. Lin, G.J. Man, Y.L. Lin, J.C. Sorli, B.P. Rand, A. Kahn, G.D. Scholes, Y.-L. Loo, *Adv. Energy Mater.*, **9**, 1901649 (2019).

"Engineering charge-transfer states for efficient, low-energy-loss organic photovoltaics," X. Liu, B.P. Rand, S.R. Forrest, *Trends Chem.*, **1**, 815 (2019).

"Multiple charge transfer states in donor-acceptor heterojunctions with large frontier orbital energy offsets," S.-U.-Z. Khan, G. Londi, X. Liu, M.A. Fusella, G. D'Avino, L. Muccioli, A.N. Brigeman, B. Niesen, T.C.-J. Yang, Y. Olivier, J.T. Dull, N.C. Giebink, D. Beljonne, B.P. Rand, *Chem. Mater.*, **31**, 6808 (2019).

“Sensitization of silicon by singlet exciton fission in tetracene”, M. Einzinger, T. Wu, H.L. Smith, C.F. Perkinson, L. Nienhaus, S. Wieghold, D.N. Congreve, A. Kahn, M.G. Bawendi, M.A. Baldo, *Nature*, **571**, 90 (2019).

Tuning Organic Semiconductor Packing and Morphology through Non-equilibrium Solution Processing

Zhenan Bao, Stanford University

Program Scope

Electronic devices based on organic molecules provide remarkable opportunities for applications in organic field effect transistors (OFETs), electronic paper, RFID, photovoltaics (OPV), and sensors. Previously, little work has been devoted to the understanding of how the morphology and molecular packing are affected by the solution processing conditions. Our research group has developed the *solution shearing (SS) method* as a versatile method to prepare high performance OTFTs, especially from highly crystalline small molecule OSCs. We discovered for the first time that it was possible to reduce the π - π stacking distance between organic semiconductor molecules using the SS method [1]. We observed *an order of magnitude increase in charge carrier mobility* by simply changing the processing conditions. We subsequently were able to perform further investigations to understand the mechanism for trapping the metastable strained packing structures, by real time X-ray diffraction experiments or by engineering the fluid field during the OSC crystallization [2-3]. More importantly, SS provides us many ‘knobs’ to tune during processing to allow us to trap metastable non-equilibrium molecular assembly and morphology that are not easily accessible by typical film formation methods, such as spin coating. Understanding the effects of various solution processing conditions on molecular packing and morphology is essential for unprecedented charge transport and future large-scale production of organic electronics. Our long-term goal is to develop a systematic understanding of various important parameters that impact organic electronic material crystallization and morphology. Based on the obtained various structures achieved by non-equilibrium processing, we hope to correlate the charge transport with morphology. Non-equilibrium processing provides unprecedented access of a range of diverse morphologies that are not easily accessible by other methods. This will allow us to gain new fundamental understanding that may facilitate the development of novel organic materials that are currently unrealized or unexpected.

The goal for this project is to understand factors impact polymer semiconductor alignment and morphology formation during solution coating. Polymer semiconductors are widely used in flexible and stretchable electronics and energy applications. Despite some recent studies, there is still a lack of detailed solution-state characterization of polymer semiconductors in terms of their conformation, degree of entanglement, shear stress-induced aggregation and chain relaxation dynamics under shear flow. These characteristics will directly impact the response of the polymer semiconductor solution to solution coating conditions and the resulting polymer alignment and morphology. Furthermore, the rigidity of the polymer structure and molecular weight will impact their solution-state properties. In this project, we investigate approaches to reduce entanglements in polymer semiconductor solutions in order to investigate their impact on the resulting thin film morphology and charge transport. On the other hand, we also study ways to control polymer semiconductor pre-aggregation in solution again to achieve desired morphology. These materials have been fully characterized using DOE-supported synchrotron X-ray scattering facilities in the Stanford Synchrotron Radiation Lightsource (SSRL) to determine the alignment and morphology.

Recent Progress

1. Effects of pre-aggregates in solution.

Efficient charge transport favors ordered structures across multiple length scales from the single chain conformation to the macroscale alignment. At the single-chain level, the intrachain transport can be improved by reducing kinks and bending, which can extend π -electron delocalization along the backbone. At the nano- to mesoscale, the interchain charge hopping through the overlapping of π -orbitals can be facilitated by forming short-range ordered polymer aggregates. At the macroscale, the overall charge transport across device channels can be boosted by further aligning polymer chains and aggregations throughout the entire film. To achieve multiscale morphological ordering in a semiconducting film, generating straight and strong flow field during solution deposition is primarily needed for achieving directional orientation of polymer chains in the printing solution. A coating blade with micro-trenches was designed to effectively generate an intensive unidirectional flow field to align and elongate polymer chains in the solution beneath the blade (Figures 1). However, it remains challenging to prevent chain relaxation from the extended conformation and aligned orientation during film drying.

Here, we investigated a way to induce conjugated polymer nanofibril structure formation from conjugated polymer/elastomer phase separation that confines the conjugated polymer chains with an extended chain conformation. The relaxation of these larger aligned nanofibers in the elastomer matrix compared to that of a single polymer chain should be much slower kinetically at time scales relevant to drying. Indeed, we show that semiconducting polymer films with aligned nanoconfined morphology could be fabricated through the conjugated-polymer/elastomer phase-separation-induced elasticity (termed CONPHINE) methodology, which achieves morphological ordering at multiple length scales in a single coating step.

A high mobility semiconducting polymer poly-[2,5-bis(7-decylnonadecyl)pyrrolo[3,4-c]pyrrole-1,4-(2H,5H)-dione-(E)-(1,2-bis(5-(thiophen-2-yl)selenophen-2-yl)ethene) (DPPDTSE) and a elastomer polystyrene-block-poly(ethylene-ran-butylene)-block-polystyrene (SEBS) were chosen as the two components in the CONPHINE film to demonstrate the concept. In order to maximize the macroscopic alignment in the CONPHINE films, it is crucial to use high shear stress to pre-align the polymer chains before drying and to minimize the drying time to “freeze in” the aligned orientation of the phase-separated nanofibrils. From AFM phase images, aligned nanofibers along the shearing direction were observed on the bottom interface of the SS-CONPHINE film (**Figure 1**), while the SC-CONPHINE film exhibited a randomly oriented nanofiber network. The SS-CONPHINE films, the alignment of nanofibers reduce the morphological boundaries that are unfavorable for charge transport, leading to the lowest E_A and

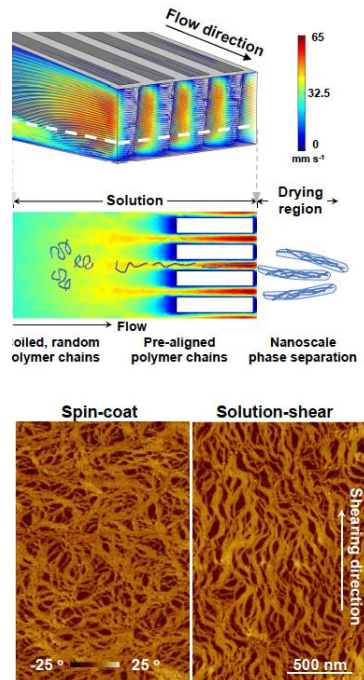


Figure 1. Top: Calculated 3D and 2D velocity fields (stream-line representation) of the solution between the coating blade and the substrate. Bottom: AFM images showing aligned nanofibers coated by rationally designed blade vs. random orientation for spin-coated.

therefore the highest charge carrier mobility in the best aligned SS-CONPHINE film. As a result, we observed significant increase in charge carrier mobility by 5x for the aligned nanofiber film.

2. Inducing molecular aggregation by modifying polymer molecular weight/rigidity.

Based on the above exciting initial findings, we further investigate the impact of molecular weight on molecular aggregation formation in solution state. Flory-Huggins solution theory describes the phenomenon of miscibility in multi-component polymer systems. Within this framework, free energy of mixing increases with molecular weight via entropic contributions, and the dependence of the free energy on molecular weight can be further elevated in systems where higher molecular weight polymers possess significantly lower solubility, as is generally the case for conjugated PSCs. Here, a secondary insulating component, SEBS, is blended with a conjugated diketopyrrolopyrrole (DPP)-based PSC (P2TDPP2TFT4) with number-averaged molecular weights of 50 (P-50k) and 97 kDa (P-97k). The high molecular weight PSC exhibited greater induced interchain aggregation of the PSC,

We used absorption spectroscopy and rheological measurement to characterize solution states of polymer aggregation. We show for the first time that depending on the molecular weight of the semiconducting component, the matrix-PSC interactions can be used to improve charge transport. The high molecular weight PSC (P-97k) undergoes greater molecular ordering and becomes more edge-on in the film with SEBS elastomeric matrix, resulting in remarkable increases in charge carrier mobility. On the macroscopic scale, charge transport can be improved by aligning polymer chains or aggregates across the whole conductive channel. Moreover, an extensional flow-driven solution shearing (SS) method, which can induce polymer chain alignment and improve the charge carrier mobility of polymer blends, is used to guide P-97k/SEBS solution during film deposition. This work suggests blending polymer semiconductors with a suitable insulating matrix can overcome the previous reported issues with high molecular weight PSCs, in terms of lower crystallinity, lack of alignment, and significantly lower FET performance. The low (P-50k) and high (P-97k) molecular weight polymers both possess crystalline and amorphous structures, while the crystallinity of P-97k is lower than P-50k due to increased entanglements between polymer chains. By introducing the secondary SEBS matrix, the aggregation state of the semiconducting component will be modulated owing to the phase separation and confinement effect in nano-scale. Such a modification of polymer chain organization is expected to impact charge transport of P-50k and P-97k polymers, respectively.

Future Plans

We will perform studies to further understand how the solution-phase aggregate, which are likely differ in size and shape of molecular additives may affect PSC aggregation. Bulky molecules and nanoparticles are known to impact polymer dynamics, entanglement and free volume. However, such effects have been less investigated with conjugated polymers, especially on how these additives may be used in a synergistic way to allow tuning of crystallinity and alignment. We will investigate controlling solution state disentanglement using additives combined with extensional fluid flow generated using patterned blade and how they affect alignment and potentially the crystallinity and charge transport.

References

- [1] G. Giri, E. Verploegen, S. C. B. Mannsfeld, S. Atahan-Evrenk, D. H. Kim, S. Y. Lee, H. a Becerril, A. Aspuru-Guzik, M. F. Toney, and Z. Bao, “Tuning charge transport in solution-sheared organic semiconductors using lattice strain,” *Nature*, 480, 504–8, 2011.
- [2] G. Giri, R. Li, D.-M. Smilgies, E. Q. Li, Y. Diao, K. M. Lenn, M. Chiu, D. W. Lin, R. Allen, J. Reinschach, S. C. B. Mannsfeld, S. T. Thoroddsen, P. Clancy, Z. Bao, and A. Amassian, “One-dimensional self-confinement promotes polymorph selection in large-area organic semiconductor thin films.,” *Nat. Commun.*, 5, 3573, 2014.
- [3] Y. Diao, B. C.-K. Tee, G. Giri, J. Xu, D. H. Kim, H. a Becerril, R. M. Stoltenberg, T. H. Lee, G. Xue, S. C. B. Mannsfeld, and Z. Bao, “Solution coating of large-area organic semiconductor thin films with aligned single-crystalline domains.,” *Nat. Mater.*, 12, 665–71, 2013.

Publications

1. S. Nikzad, H.-C. Wu, J. Kim, C. M. Mahoney, J. R. Matthews, W. Niu, Y., Li, H. Wang, W.-C. Chen, M. F. Toney, M. He, Z. Bao, Inducing Molecular Aggregation of Polymer Semiconductors in a Secondary Insulating Polymer Matrix to Enhance Charge Transport, **Chemistry of Materials** (2020), 32, 2, 897-905.
2. S. Nikzad, H.-C. Wu, G.-J. N. Wang, H. Yan, S. A. Schneider, M. F. Toney, Z. Bao, Effect of Extensional Flow on the Evaporative Assembly of a Donor-Acceptor Semiconducting Polymer, **ACS Applied Electronic Material** (2019), 1, 11, 2445-2454.
3. J. Xu, H.-C. Wu, C. Zhu, A. Ehrlich, L. Shaw, M. Nikolka, S. Wang, F. Molina-Lopez, X. Gu, S. Luo, D. Zhou, Y.-H. Kim, G.-J. N. Wang, K. Gu, V. R. Feig, S. Chen, Y. Kim, T. Katsumata, Y.-Q. Zheng, He. Yan, J. W. Chung, J. Lopez, B. Murmann, Z. Bao, Multi-scale ordering in highly stretchable polymer semiconducting films, **Nature Materials** (2019), 18, 594-601.
4. G. Chen, R. Rastak, Y. Wang, H. Yan, V. Feig, Y. Liu, Y. Jiang, S. Chen F. Lian, F. Molina-Lopez, L. Jin, K. Cui, J. W. Chung, E. Pop, C. Linder, Z. Bao, Strain- an Strain-Rate-Invariant Conductance in a Stretchable and Compressible 3D Conducting Polymer Foam, **Matter** (2019), 1, 1, 24-25.
6. L. Shaw, Y. Diao, G. Martin-Noble, H. Yan, P. Hayoz, T. R. Weitz, D. Kalblein, M. F. Toney, Z. Bao, Manipulation of Statistical Analysis of the Fluid Flow of Polymer Semiconductor Solutions During Meniscus-Guided Coating, **MRS. Bull. Impact Article**, doi:10.1557/mrs.2020.306, 2020.
7. A. C. Hinckley, S. C. Andrews, M. Dunham, A. Snood, M. Barako, S. A. Schneider, M. F. Toney, K. Goodson, Z. Bao, Achieving High Thermoelectric Performance and Metallic Transport in Solvent-Sheared PEDOT:PSS, **Adv. Elect. Mater.**, doi.org/10.1002/aelm.202001190, 2021.

Exploring the design principles of low-dimensional organometal halide perovskites assisted by machine learning

Yiying Wu, Department of Chemistry & Biochemistry, The Ohio State University

Program Scope

The objectives of this project include (1) applying machine learning to understand how the structural features of small organic molecules influence the dimensionality and stability of organometal halide perovskites, (2) utilizing our newly installed near-ambient-pressure XPS to investigate the surface evolution of perovskite films under *in operando* conditions, and (3) controlling the perovskite/electrolyte interfaces for stable photoelectrochemistry.

Recent Progress

- (1) Exploring the design principles of low-dimensional organometal halide perovskites assisted by machine learning.

Organic-inorganic halide perovskites have amazing structural tunability: the metal halide octahedra can be controlled to form zero- (0D), one- (1D), two- (2D), or three-dimensional (3D) inorganic frameworks by choosing appropriate organic amines to direct the dimensionality. The structure stability of the widely studied 3D perovskites can be predicted by the Goldschmidt tolerance factor. However, there is not a reliable model for predicting the structure-directing effect of amines on the low-dimensional cases. Recently, we have carried out a study that uses a machine learning-assisted strategy to predict the dimensionality of lead iodide-based perovskites.

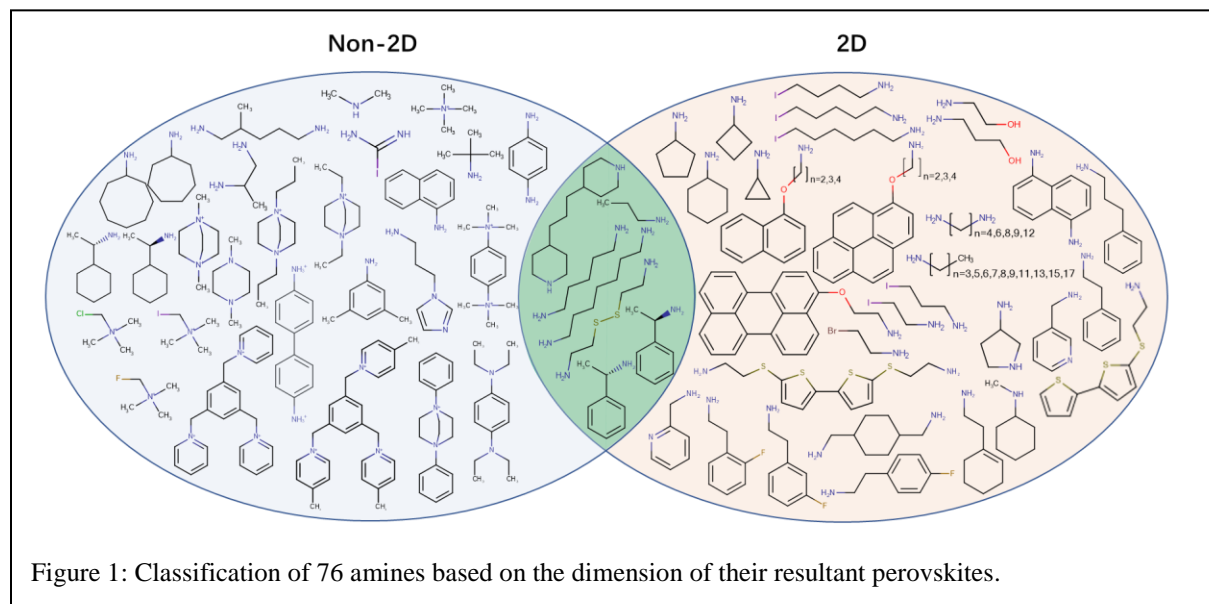


Figure 1: Classification of 76 amines based on the dimension of their resultant perovskites.

Literature survey has identified 76 amines reported to form low dimensional Pb-I based perovskites. Due to very limited number of 0D PbI_3 -based perovskites, we have combined 0D and 1D into one group named as “non-2D”, and thus classify the collection of amines into “2D” and “non-2D” (see Figure 1). Machine learning models were trained and tested based on the classification and the structural features of these amines. A testing accuracy of 85% was achieved by the fitted model to predict whether an amine can form a 2D perovskite or not. Coefficient analysis in the logistic regression model reveals heavy contributions from geometric and topological features such as steric effect and eccentricity. Importantly, a quantitative model is created to calculate the probability of forming 2D perovskite for a selected amine. This model has also been applied to several unreported amines to verify the prediction capability. This work demonstrates the application of machine learning for gaining the design principle for low dimensional hybrid halide perovskites. This work will be submitted soon.

(2) Ambient Pressure XPS Investigation of Thermally Stable Halide Perovskite Solar Cells Post-treated with Small Molecules (ACS Appl. Mater. Interfaces 2020, 12 (39), 43705–43713)

Long-term thermal stability impedes the applications of perovskite solar cell and optoelectronics. Inspired by our prior results from machine learning (ACS Energy Letters, (2019) 397-404.), we discover that coating a thin layer of 4,4'-dibromotriphenylamine (DBTPA) on top of a $\text{CH}_3\text{NH}_3\text{PbI}_3$ (MAPbI_3) thin film can improve the stability of the resultant perovskite solar cells. The passivated perovskite solar cells retained more than 98% of their initial power conversion efficiency over 800 h at 85 °C in N_2 atmosphere without encapsulation. Near-ambient pressure x-ray photoelectron spectroscopy (NAP-XPS) was employed to investigate the evolution of composition and evaluate thermal and moisture stability by in-situ studies. A comparison between pristine MAPbI_3 films and DBTPA-treated films shows the DBTPA treatment suppresses the escape of iodide and methylamine up to 150 °C under 5 mbar humidity. Furthermore, we have used ATR-FTIR and XPS to probe the interactions between DBTPA and MAPbI_3 surface. The results prove that DBTPA coordinate with perovskite by Lewis acid-base and cation- π interaction. Compared with the 19.9% efficiency of pristine sample, the efficiency of passivated sample reaches 20.6%. Our results reveal DBTPA as a new post-treating molecule that not only leads to the improvement of photovoltaic efficiency but also thermal and moisture stability. This work has been written as a manuscript and will be submitted for publication soon.

(3) Anthraquinone Redox Relay for Dye-Sensitized Photo-electrochemical H_2O_2 Production (Angew. Chem. Int. Ed. 2020, 59, 10904 –10908)

Solar-to-fuel conversion through semiconductor photoelectrochemistry (PEC) is regarded as a cost-effective way to make use of abundant solar energy. A PEC system for water splitting has been widely investigated but less attention has been paid to other worthwhile redox reactions, like HBr oxidation, H_2O_2 production, and N_2 fixation, etc. Hydrogen peroxide (H_2O_2), is an important green oxidant in industry. A PEC system allows on-site production of H_2O_2 which can be directly utilized on small scale without unsafe transportation and chemical contamination.

In our work, anthraquinone (AQ) redox mediators are introduced to metal-free organic dye sensitized photo-electrochemical cells (DSPECs) for the generation of H_2O_2 . Instead of

directly reducing O_2 to produce H_2O_2 , visible-light-driven AQ reduction occurs in the DSPEC and the following autoxidation with O_2 allows H_2O_2 accumulation and AQ regeneration. In an aqueous electrolyte, under 1 sun conditions, a water-soluble AQ salt is employed with the highest photocurrent of up to 0.4 mA cm^{-2} and near-quantitative faradaic efficiency for producing H_2O_2 . In a non-aqueous electrolyte, under 1 sun illumination, an organic-soluble AQ is applied and the photocurrent reaches 1.8 mA cm^{-2} with faradaic efficiency up to 95% for H_2O_2 production. This AQ-relay DSPEC exhibits the highest photocurrent so far in non-aqueous electrolytes for H_2O_2 production and excellent acid stability in aqueous electrolytes, thus providing a practical and efficient strategy for visible-light-driven H_2O_2 production. This work has been published in *Angewandte Chemie International Edition* (<https://doi.org/10.1002/anie.202003745>).

In addition to the above proposed activities, this project is further expanded to probe the electrode/electrolyte interfacial reactions and stability in batteries, especially in the superoxide-based K-O₂ battery that my lab invented in 2013. This invention used the reversible oxygen/superoxide redox chemistry to solve the challenges in metal-air batteries.

Future Plans

1. **Apply localized high concentrated electrolyte (LHCE) concept to photoelectrochemistry system based on halide perovskite photocathode:** Most of the halide perovskites (ex. MAPbI_3 or CsPbI_3) are not stable inside polar solvent while many photoelectrochemistry processes prefer polar environment. Consider the advantage of the LHCE in which there are almost no free solvent, we propose the usage of LHCE for halide perovskite-based photoelectrochemistry system. Start from ether (such as DME) as solvent, we plan to use high/per-fluorinated compound (such as 1,1,2,2-tetrafluoro-1-(2,2,2-trifluoroethoxy) ethane) as diluent and the salt with the same cation in the perovskite as the electrolyte (such as CsMPSA for CsPbI_3) which is supposed to further passivate the decomposition of the perovskite photocathode. The solvent can be changed to more polar compounds such as alcohols or even water if possible. The tolerance against trace/limited amount of water which can be a proton source inside the LHCE electrolyte is also a potential highlight for this project.
2. **Constructing low dimensional perovskite with functionalized ammonium:** 2D perovskites have been widely used to improve the stability of 3D perovskites for solar cell application. The same concept may also be useful for photoelectrochemistry system. Therefore, we propose a 2D halide perovskite structure on the surface of traditional 3D perovskite (MAPbI_3) with functionalized ammonium for photoelectrolysis. 1,6-diaminohexane functionalized with an Anthraquinone group will be used to construct a 2D

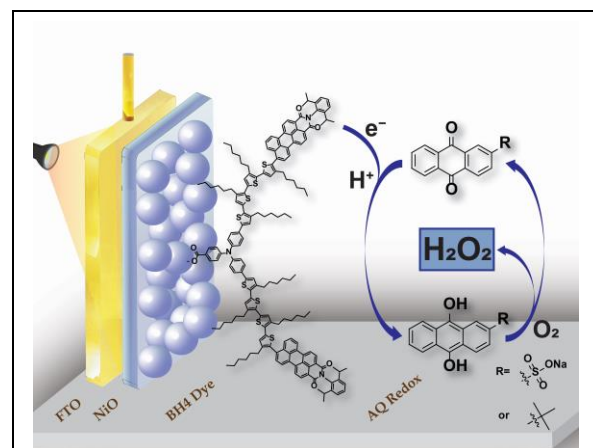


Figure 2: Illustration of the working principle of dye-sensitized photoelectrochemistry (DSPEC) for H_2O_2 production by using AQ redox mediators.

perovskite layer on the MAPbI₃ cathode surface which can protect the 3D perovskite and at the same time, accept photoelectrons for electrolysis based on Anthraquinone. Furthermore, the high conjugated Anthraquinone molecule may improve the out-of-plane charge transport which may allow the use of only 2D perovskite for the photoelectrolysis.

3. **Synthesis of multi-ammonium halide perovskites to understand the design principle for low dimensional perovskites:** Quasi-2D perovskites have been synthesized and widely studied for solar cell and other photoelectronic application. The combination of 3D spacer (typically methylammonium) and 2D spacer (such as larger ammonium with long carbon chain) results in the formation of multilayered 3D structure separated by 2D ammoniums which has both the advantages of 2D and 3D perovskites. Therefore, we propose the synthesis of halide perovskites with multiple ammoniums. By combining both the 2D and 1D spacers as well as 1D and 0D spacers, we expected to see the formation of quasi-1D and quasi-0D structures respectively. Quasi-1D perovskites should contain separated 2D layers that provide ribbon-like structures while quasi-0D perovskites may have separated 1D chains which look like sticks. Properties like broad-band emission and ferro/piezoelectricity can be further studied and modified by tuning the types of ammoniums.

References

None.

Publications

- (1) Qin, L.; Xiao, N.; Zheng, J.; Lei, Y.; Zhai, D.; Wu, Y. Localized High-Concentration Electrolytes Boost Potassium Storage in High-Loading Graphite. *Adv. Energy Mater.* **2019**, *9* (44), 1902618. <https://doi.org/10.1002/aenm.201902618>.
- (2) Liang, H.; Hu, Y. C.; Tao, Y.; Wu, B.; Wu, Y.; Cao, J. Existence of Ligands within Sol-Gel-Derived ZnO Films and Their Effect on Perovskite Solar Cells. *ACS Appl. Mater. Interfaces* **2019**, *11* (46), 43116–43121. <https://doi.org/10.1021/acsami.9b13278>.
- (3) Yu, Y.; Chien, S. C.; Sun, J.; Hettiaratchy, E. C.; Myers, R. C.; Lin, L. C.; Wu, Y. Excimer-Mediated Intermolecular Charge Transfer in Self-Assembled Donor-Acceptor Dyes on Metal Oxides. *J. Am. Chem. Soc.* **2019**, *141* (22), 8727–8731. <https://doi.org/10.1021/jacs.9b03729>.
- (4) Sun, J.; Yu, Y.; Curtze, A. E.; Liang, X.; Wu, Y. Dye-Sensitized Photocathodes for Oxygen Reduction: Efficient H₂O₂ Production and Aprotic Redox Reactions. *Chem. Sci.* **2019**, *10* (21), 5519–5527. <https://doi.org/10.1039/c9sc01626k>.
- (5) Yu, Y.; Click, K. A.; Chien, S. C.; Sun, J.; Curtze, A.; Lin, L. C.; Wu, Y. Decoupling PH Dependence of Flat Band Potential in Aqueous Dye-Sensitized Electrodes. *J. Phys. Chem. C* **2019**, *123* (14), 8681–8687. <https://doi.org/10.1021/acs.jpcc.9b00710>.

- (6) Yu, Y.; Tan, X.; Ning, S.; Wu, Y. Machine Learning for Understanding Compatibility of Organic-Inorganic Hybrid Perovskites with Post-Treatment Amines. *ACS Energy Lett.* **2019**, *4* (2), 397–404. <https://doi.org/10.1021/acsenergylett.8b02451>.
- (7) Sun, J.; Wu, Y. Anthraquinone Redox Relay for Dye-Sensitized Photoelectrochemical H₂O₂ Production. *Angew. Chemie Int. Ed.* **2020**, *anie.202003745*. <https://doi.org/10.1002/anie.202003745>.
- (8) Hu, K.; Qin, L.; Zhang, S.; Zheng, J.; Sun, J.; Ito, Y.; Wu, Y. Building a Reactive Armor Using S-Doped Graphene for Protecting Potassium Metal Anodes from Oxygen Crossover in K–O₂ Batteries. *ACS Energy Lett.* **2020**, 1788–1793. <https://doi.org/10.1021/acsenergylett.0c00715>.
- (9) Li, X.; Li, C.; Wu, Y.; Cao, J.; Tang, Y. A Reaction-and-Assembly Approach Using Monoamine Zinc Porphyrin for Highly Stable Large-Area Perovskite Solar Cells. *Sci. China Chem.* **2020**, 1–8. <https://doi.org/10.1007/s11426-020-9710-7>.
- (10) Qin, L.; Xiao, N.; Zhang, S.; Chen, X.; Wu, Y. From K-O₂ to K-Air Batteries: Realizing Superoxide Batteries on the Basis of Dry Ambient Air. *Angew. Chemie Int. Ed.* **2020**, *anie.202003481*. <https://doi.org/10.1002/anie.202003481>.
- (11) Qin, L.; Zhang, S.; Zheng, J.; Lei, Y.; Zhai, D.; Wu, Y. Pursuing Graphite-Based K-Ion O₂batteries: A Lesson from Li-Ion Batteries. *Energy Environ. Sci.* **2020**, *13* (10), 3656–3662. <https://doi.org/10.1039/d0ee01361g>.
- (12) Ning, S.; Zhang, S.; Sun, J.; Li, C.; Zheng, J.; Khalifa, Y. M.; Zhou, S.; Cao, J.; Wu, Y. Ambient Pressure X-Ray Photoelectron Spectroscopy Investigation of Thermally Stable Halide Perovskite Solar Cells via Post-Treatment. *ACS Appl. Mater. Interfaces* **2020**, *12* (39), 43705–43713. <https://doi.org/10.1021/acsami.0c12044>.
- (13) Schkeryantz, L. A.; Zheng, J.; McCulloch, W. D.; Qin, L.; Zhang, S.; Moore, C. E.; Wu, Y. Designing Potassium Battery Salts through a Solvent-in-Anion Concept for Concentrated Electrolytes and Mimicking Solvation Structures. *Chem. Mater.* **2020**, *32* (24), 10423–10434. <https://doi.org/10.1021/acs.chemmater.0c02983>.
- (14) Sun, J.; Zhang, S.; Schkeryantz, L.; Wu, Y. Photoelectrochemical H₂O₂Production from Oxygen Reduction. In *ACS Symposium Series*; American Chemical Society, 2020; Vol. 1364, pp 93–109. <https://doi.org/10.1021/bk-2020-1364.ch003>.
- (15) Qin, L.; Schkeryantz, L.; Zheng, J.; Xiao, N.; Wu, Y. Superoxide-Based K-O₂Batteries: Highly Reversible Oxygen Redox Solves Challenges in Air Electrodes. *Journal of the American Chemical Society*. American Chemical Society July 8, 2020, pp 11629–11640. <https://doi.org/10.1021/jacs.0c05141>.

- (16) Xiao, G.-B.; Wang, L.-Y.; Mu, X.-J.; Zou, X.-X.; Wu, Y.-Y.; Cao, J. Lead and Iodide Fixation by Thiol Copper(II) Porphyrin for Stable and Environmental-Friendly Perovskite Solar Cells. *CCS Chem.* **2021**, 25–36. <https://doi.org/10.31635/ccschem.021.202000516>.
- (17) Yu, Z.; Wang, L.; Mu, X.; Chen, C.; Wu, Y.; Cao, J.; Tang, Y. Intramolecular Electric Field Construction in Metal Phthalocyanine as Dopant-Free Hole Transporting Material for Stable Perovskite Solar Cells with >21 % Efficiency. *Angew. Chemie* **2021**, 133, ange.202016087. <https://doi.org/10.1002/ange.202016087>.

Interfaces in Electronic and Structural Materials

Yuri Mishin, PI

Department of Physics and Astronomy
George Mason University, MSN 3F3
4400 University Drive, Fairfax, VA

Phone: 703-993-3984
Fax: 703-993-1269
Email: ymishin@gmu.edu

Program Scope

The Program pursues the following goals: (1) Conduct a systematic atomistic-scale simulation study of a large set of grain boundaries and other interfaces in structural and functional materials. (2) Determine the equilibrium structures of the interfaces as a function of bicrystallography, temperature and chemical composition. (3) Identify a set of interface phases, investigate their reversible phase transformations, and construct grain boundary phase diagrams. (4) Calculate the Kapitza resistance of the grain boundaries and establish relationships between the Kapitza resistance and the grain boundary crystallographic characteristics, atomic structure, temperature and chemical composition. (5) Develop a fundamental understanding of phonon scattering at grain boundaries.

These goals will be achieved by atomistic computer simulations using molecular dynamics and a variety of Monte Carlo techniques. The Kapitza resistance of the grain boundaries will be calculated by non-equilibrium molecular dynamics, combined in some cases with the wave-packet method. To ensure the accuracy of the predictions, a new machine-learning (neural-network) interatomic potential will be constructed for the relevant systems by training the potential parameters on a massive database of first-principles energies. The project is expected to significantly impact the state of knowledge in interface science by improving the fundamental understanding of structure and thermal resistance of interfaces in metallic and semiconductor materials. It is relevant to the BES mission and is aligned with DOE's Grand Challenge of controlling matter away from equilibrium and the Basic Research Needs for solar energy utilization and electrical energy storage.

Recent Progress

1. We have constructed a new machine-learning interatomic potential has been constructed for Si using the recently proposed Physically-Informed Neural Network (PINN) format [1]. PINN is a new type of machine-learning potentials that drastically improves their transferability by informing them of the physical nature of interatomic bonding in the material. The integration with physics is achieved by combining a physics-based analytical bond-order potential (BOP) with a neural-network regression. The neural network adjusts the BOP parameters on the fly during the simulations according to the local environment of every individual atoms. This approach has recently been demonstrated by developing accurate and reliable general-purpose PINN potentials for Al [2] and Ta [3].

To construct a PINN potential for Si, a massive DFT database has been generated. It includes supercells representing over a dozen crystal structures of Si, point defects such as vacancies and interstitials, surfaces with different crystallographic orientations and reconstructions, gamma-surfaces representing generalized stacking faults on different fault planes, a set of clusters containing from two atoms (dimer) to about a hundred atoms, and single-layer and double-layer 2D structures

(silicenes). Each supercell was computed for a large set of volumes and various shape distortions. For most of the supercells, ab initio MD simulations were run at several different temperatures and densities. Multiple snapshots of such simulations were included in the training database, along with static structures. In total, the DFT database represents over 500,000 different atomic environments. The neural network parameters were optimized to achieve the root-mean-square deviation from the DFT data of about 3 meV/atom, which is essentially the DFT accuracy. The new potential has been tested against additional DFT data that were not included in the training set.

The Si PINN potential obtained accurately reproduces a broad range of physical properties of Si on the DFT level, including the phonon dispersion relations, thermal expansion, phononic thermal conductivity, point and extended defect formation energies, all 2D structures, and the isolated clusters. The new potential enables DFT-level simulations of mechanical behavior and thermodynamic properties of Si. We believe that it will be extensively used for Si simulations by us and many other groups in the future.

2. We have studied the Kapitza resistance of a series of [001] tilt GBs in Si has been studied using the new potential and the non-equilibrium MD method. The Kapitza conductance \square_K was found to decrease with the misorientation angle and slightly increase with temperature. For high-angle GBs, \square_K is much lower than the bulk conductivity at low temperatures but the two tend to converge at high temperatures. An interesting effect was found wherein \square_K suddenly decreases when the GB dislocations become disordered due to premelting. Structural phase transformations in GBs have a significant effect on their thermal conductivity. One of the fundamental issues in nano-scale thermal conductivity is the definition, or even existence, of the local temperature. This issue has been addressed in two previous publications under this project.

3. We have recently started a new direction within this project, which focuses on metal-ceramic interfaces. Metal-ceramic interfaces are critical elements of the microstructure of many technological materials, including metal-matrix composites. The creep resistance of many metal-matrix composites degrades at temperatures above 0.7 of the melting temperature of the matrix. The degradation effect is attributed to the loss of slip resistance of the metal-ceramic interfaces and to the fast diffusion of the metallic element along these interfaces. The microscopic mechanisms of the high-temperature interfacial creep and interface diffusion remain unknown. Our goal is to provide a fundamental understanding and develop new methods for computational prediction of the atomic structure, thermodynamics, kinetics, and mechanical responses of metal-ceramic interfaces at high temperatures. As a starting point, we have chosen Al-Si composites as a model system. Al-Si alloys possess prototypical properties of metal-matrix composites, with Al being ductile (matrix) and Si being hard and brittle (reinforcer).

Figure 1 shows that the interface structure is significantly disordered and contains a mixture of Al and Si atoms within a ~ 1 nm layer. Diffusion of both Al and Si atoms within this layer can be readily detected by the MD simulations, with Si atoms diffusing significantly slower than Al. To demonstrate the capability of the proposed methodology to study the interface slip process, we joined two crystals of Al and Si with a cube-on-cube orientation. The Si surface layer was fixed, while the Al surface layer was translated in the [100] direction parallel to the interface with a constant velocity (Fig. 2), imposing a constant shear rate on the system. The interface sliding process occurs partially inside the

~1 nm interface layer and partially between this layer and the Al lattice. The process is accompanied by more extensive intermixing of the Al and Si atoms within the interface layer than due to the interface diffusion alone. The shear stress arising in the system plotted as a function time (and thus displacement) shows a saw-tooth behavior known from previous studies of grain boundary sliding and shear-coupled grain boundary motion. While the precise mechanism responsible for this stick-slip behavior is yet to be understood, we hypothesize that the sliding occurs by nucleation-controlled shear transitions. Namely, at a critical value of the stress, a local shear island of a critical size nucleates and quickly spread along the entire interface.

Further work is required to probe the dependence of this process on the interface cross-section, temperature, time, and most importantly, on the shear rate. The present simulations implemented a relatively high velocity of 0.1 m/s. In the future, it will be necessary to reduce this rate as much as possible within the computational capabilities of the MD method. These goals will be pursued by our group under a different support.

Future Plans

No future plans as this program will not be continued past February 28, 2021.

References

- G. P. Purja Pun, R. Batra, R. Ramprasad and Y. Mishin, "Physically informed artificial neural networks for atomistic modeling of materials", *Nature Communications* **10**, 2339 (2019).
- G. P. Purja Pun, V. Yamakov, J. Hickman, E. H. Glaessgen, and Y. Mishin, "Development of a general-purpose machine-learning interatomic potential for aluminum by the physically informed neural network method", *Physical Review Materials* **4**, 113807 (2020).
- Y.-S. Lin, G. P. Purja Pun and Y. Mishin, Development of a physically-informed neural network interatomic potential for tantalum, *Nature Communications*, in review (preprint: arXiv:2101.06540).

Publications of DOE sponsored research

1. D. L. Medlin, N. Yang, C. D. Spataru, L. M. Hale and Y. Mishin: Unraveling the dislocation core structure at a van der Waals gap: Bismuth telluride as a prototype, *Nature Communications* **10**, 1820 (2019).
2. J. Hickman and Y. Mishin: Thermal resistance of tilt grain boundaries in silicon, *Physical Review Materials* **4**, 033405 (2020).
3. J. Hickman, G. P. Purja Pun, V. Yamakov and Y. Mishin: Physically-informed artificial neural network potential for silicon, *npj Computational Materials*, in review.

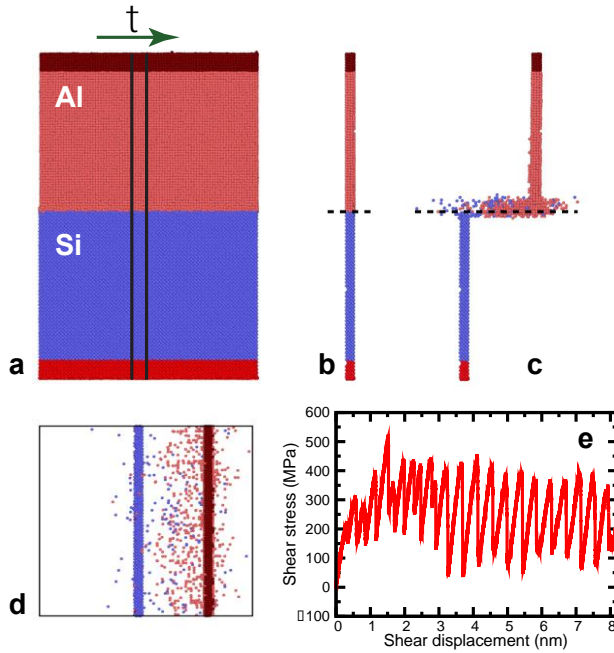


Figure 1: Preliminary results: **a** is the initial state of the Al-Si system. **b** is a zoom into the white box after a 60 ns anneal at 650 K. Note the local disordering and mixing at the interface. **c** is the initial and **d** the final structures of the thin stripe shown in **a**. The dashed line marks the initial interface position. The zooms into the encircled interface region shown in **e** (Al atoms) and **f** (Si atoms) reveal the spreading of the atoms caused by interface diffusion. Note that Si diffuses slower than Al.

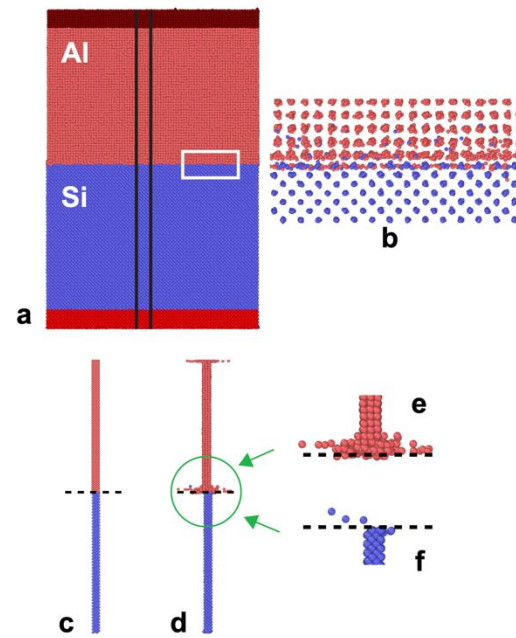


Figure 2: Preliminary results: **a** is the initial state of the Al-Si system subject to applied shear by translating the Al crystal relative to Si at 650 K. The vertical stripe between the lines was selected to visualize the atomic motion in the interface. **b** is the stripe's initial state, **c** the final state, and **d** the top view of the final state. The dashed line marks the initial interface position. Note the intermixing of Al and Si atoms caused by the shearing. **e** is the shear stress as a function of the relative displacement of the Al and Si crystals. The serrated shape of the plot is a signature of stick-slip dynamics.

Session IX

Excitons in Low-Dimensional Perovskites

William A. Tisdale, Massachusetts Institute of Technology

Program Scope

The goal of this research effort is to obtain a deeper understanding of strongly bound excitonic states in low-dimensional halide perovskites. Experiments will address how excitons in these quantum-confined materials move, how they interact with the polar lattice, and how their behavior can be manipulated through chemical or structural modification. Specific research activities include synthesis and structural characterization of 2D perovskite quantum wells, direct imaging of exciton and charge carrier transport, and ultrafast electronic and vibrational spectroscopy.

Recent Progress

Carrier diffusion imaging in multi-cation perovskites. In pursuit of increasing the power conversion efficiency (PCE) of photovoltaic devices, perovskite materials have been optimized using mixed halide (Br, I) and multi-cation compositions of Cs, methylammonium (MA), and formamidinium (FA)—though the explicit role each component plays in increasing PCE remains unknown. To aid in this effort, we performed transient photoluminescence microscopy on a variety of perovskite compositions (MA, CsFA, and CsMAFA) in single crystal and polycrystalline thin film architectures (Fig. 1).

Diffusivity values extracted via TPLM showed an invariance with material composition in single crystal perovskites. When cast into polycrystalline thin films, however, we observed a marked difference across the same material compositions. We reported a diffusivity of $0.047 \text{ cm}^2/\text{s}$ for MA-based thin films—an order of magnitude higher than that found for MA-free CsFA films ($0.005 \text{ cm}^2/\text{s}$). Angle-dependent x-ray and depth-profile ultraviolet photoemission spectroscopy revealed a gradient in the Br content of the mixed halide perovskites resulting in an energetic barrier at grain boundaries which

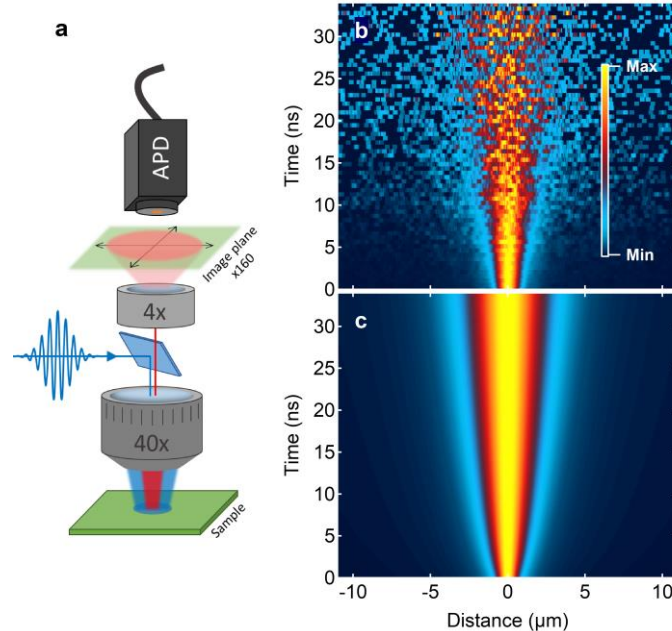


Figure 1. Carrier diffusion imaging. (a) Setup with (b) normalized diffusion data and (c) modeling results. *Published work from this award (Saidaminov et al., Nature. Mater. (2020)).*

hinders the diffusion of free charge carriers. This effect is exacerbated in the MA-free film. Introducing MA into the composition (CsMAFA) flattens the gradient observed and results in a significant increase of the thin film diffusivity ($0.034 \text{ cm}^2/\text{s}$). These findings open the possibility of removing MA while retaining the benefits to PCE through additives and solvent systems which uniformly crystallize the Br-containing components.

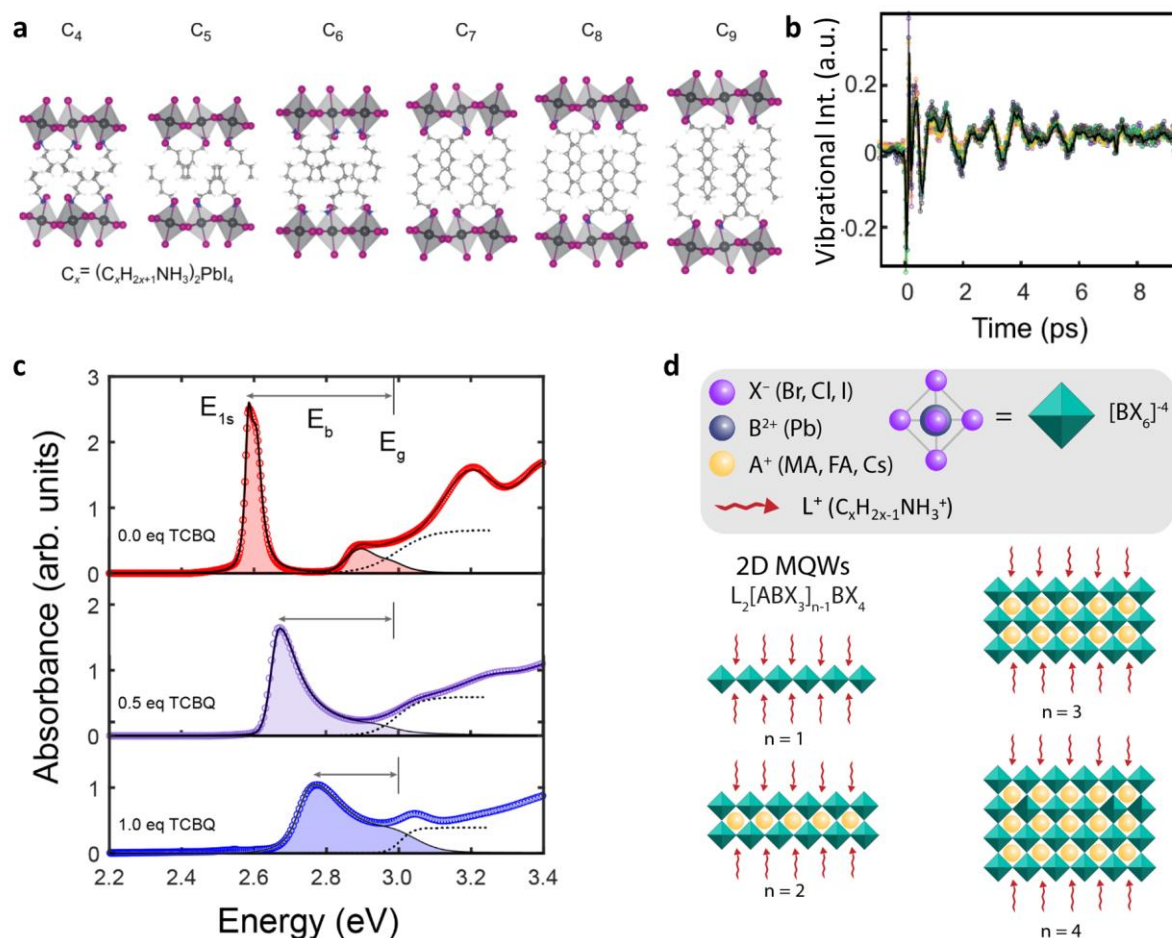


Figure 2. (a) Structure of 2D layered perovskites with increasing organic chain length. (b) Vibrational spectra from impulsive Raman. (c) Absorbance spectra showing shifting exciton binding energy with increasing dopant concentration. (d) Structure of 2D layered perovskite with increasing layer thickness. *Published work from this award* (Mauck *et al.*, *JPCC* (2019); Mauck & Tisdale, *Trends in Chem.* (2019); Passarelli *et al.*, *Nature Chem.* (2020)).

Exciton-phonon coupling in 2D perovskites. We investigated the extent to which the organic cation length influences the coupling between the tightly bound excitons and the phonons modes of the polar inorganic-organic lattice using resonant impulsive-stimulated Raman scattering and temperature-dependent photoluminescence with density functional theory (DFT). Using a series of structurally similar, 2D lead iodide perovskites ($C_xH_{2x+1}NH_3)_2PbI_4$, with organic chain lengths ranging from four to nine carbons ($x = 4 - 9$, Fig. 2a), we observed that the dominant vibrational

frequencies of the Raman spectra align with the phonon modes of the inorganic Pb-I cages calculated from DFT. The frequency of these modes also remains unchanged with increasing chain length as the coherence of the organic cation motion, driven by Coulombic interaction with heavy iodide ions and hydrogen bonding, does not extend beyond the fourth carbon in the cation chain. The lack of influence on the exciton-phonon coupling suggests that the exciton is highly confined to the 2D Pb-I layers and that the organic cations serve to function as a dielectric spacer between these layers.

Tunable exciton binding energy in 2D perovskites. The ability to tune the exciton binding energy (E_b), independent of the band gap (E_g), is highly desirable for these materials. In this effort, we were able to introduce a molecular dopant, tetrachloro-1,2 benzoquinone (TCBQ), into the organic sublayer of the layered crystal structure to continuously tune the binding energy of the 1s exciton by up to 200 meV, Fig. 2c. This represents a 50% reduction in the binding energy compared to the undoped perovskite. The interaction between the cationic organic donor and TCBQ acceptor cause an electrostatic screening of the exciton, through an increased polarizability of the organic sublattice, and a subsequent reduction in the binding energy. Temperature dependent absorption and photoluminescence measurements also showed the electronic bandgap, and thus the inorganic lattice, is minimally impacted by the incorporation of the dopant into the organic sublayer.

Future Plans

Future plans include use of high-magnetic field spectroscopy for accurate determination of exciton mass, binding energy, and spatial extent and investigation of the spatiotemporal dynamics of excitons in perovskite nanocrystal assemblies.

Publications

Publications citing support from DOE BES award DE-SC0019345 (past 2 years):

1. “Towards Stable Deep-Blue Luminescent Colloidal Lead Halide Perovskite Nanoplatelets: Systematic Photostability Investigation” S.K. Ha, C.M. Mauck, W.A. Tisdale; *Chem. Mater.* 31, 2486-2496 (2019).
2. “Markov Chain Monte Carlo Sampling for Target Analysis of Transient Absorption Spectra” M.N. Ashner, S.W. Winslow, J.W. Swan, W.A. Tisdale; *J. Phys. Chem. A* 123, 3893-3902 (2019).
3. “Melting Transitions of the Organic Subphase in Layered Two-Dimensional Halide Perovskites”

- N.S. Dahod, W. Paritmongkol, A. Stollmann, C. Settens, S.-L. Zheng, W.A. Tisdale; **J. Phys. Chem. Lett.** 10, 2924-2930 (2019).
4. “Excitons in 2D Organic-Inorganic Halide Perovskites” C.M Mauck & W.A. Tisdale; **Trends in Chemistry** 1, 380-393 (2019).
 5. “Epitaxial Dimers and Auger-Assisted Detrapping in PbS Quantum Dot Solids” R.H. Gilmore, Y. Liu, W. Shcherbakov-Wu, N.S. Dahod, E.M.Y. Lee, M.C. Weidman, H. Li, J. Jean, V. Bulović, A.P. Willard, J.C. Grossman, W.A. Tisdale; **Matter** 1, 250-265 (2019).
 6. “Synthetic Variation and Structural Trends in Layered Two-Dimensional Alkylammonium Lead Halide Perovskites” W. Paritmongkol, N.S. Dahod, A. Stollmann, N. Mao, C. Settens, S.-L. Zheng, W.A. Tisdale; **Chem. Mater.** 31, 5592-5607 (2019).
 7. “Setting an Upper Bound to the Exciton Binding Energy in CsPbBr₃ Perovskite Nanocrystals” K.E. Shulenberger, M.N. Ashner, S.K. Ha, F. Krieg, M.V. Kovalenko, W.A. Tisdale,[†] M.G. Bawendi;[†] **J. Phys. Chem. Lett.** 10, 5680-5686 (2019).
 8. “Facile Synthesis of Colloidal Lead Halide Perovskite Nanoplatelets *via* Ligand-Assisted Reprecipitation” S.K. Ha & W.A. Tisdale; **J. Vis. Exp.** 152, e60114 (2019).
 9. “Size-Dependent Biexciton Spectrum in CsPbBr₃ Perovskite Nanocrystals” M.N. Ashner, K.E. Shulenberger, F. Krieg, E.R. Powers, M.V. Kovalenko, M.G. Bawendi[†], W.A. Tisdale,[†] **ACS Energy Lett.** 4, 2639-2645 (2019).
 10. “Inorganic Cage Motion Dominates Excited State Dynamics in 2D Layered Perovskites (C_xH_{2x+1}NH₃)₂PbI₄ (x = 4-9)” C.M. Mauck, A. France-Lenord, A.C. Hernandez Oendra, N.S. Dahod, J.C. Grossman, W.A. Tisdale; **J. Phys. Chem. C** 123, 27904-27916 (2019).
 11. “Multi-Cation Perovskites Prevent Carrier Reflection from Grain Surfaces” M.I. Saidaminov, K. Williams, M. Wei, A. Johnston, R. Quintero-Bermudez, M. Vafaei, J.M. Pina, A.H. Proppe, Y. Hou, G. Walters, S.O. Kelley, W.A. Tisdale[†], E.H. Sargent[†]; **Nature Mater.** 19, 412-418 (2020).
 12. “Spatially Resolved Photogenerated Exciton and Charge Transport in Emerging Semiconductors” N.S. Ginsberg[†] & W.A. Tisdale[†]; **Ann. Rev. Phys. Chem.** 71, 1-30 (2020).
 13. “Substrate-Dependent Exciton Diffusion and Annihilation in Chemically Treated MoS₂ and WS₂” A.J. Goodman, D.H. Lien, G.H. Ahn, L.L. Spiegel, M. Amani, A.P. Willard, A.

Javey,* W.A. Tisdale.*

J. Phys. Chem. C 124, 12175-12184 (2020).

14. “Tunable Exciton Binding Energy in 2D Hybrid Layered Perovskites through Donor-Acceptor Interactions within the Organic Layer” J.V. Passarelli, C.M. Mauck, S.W. Winslow, C.F. Perkinson, J.C. Bard, H. Sai, K.W. Williams, A. Narayanan, D.J. Fairfield, M.P. Hendricks, W.A. Tisdale[†], S.I. Stupp[†];
Nature Chem. 12, 672-682 (2020).
15. “Low-Frequency Raman Spectrum of 2D Layered Perovskites: Local Atomistic Motion or Superlattice Modes?” N.S. Dahod, A. France-Lanord, W. Paritmongkol, J.C. Grossman, W. Tisdale;
J. Chem. Phys. 153, 044710 (2020).
16. “Two Origins of Broadband Emission in Multilayered 2D Lead Iodide Perovskites” W. Paritmongkol, E.R. Powers, N.S. Dahod, W.A. Tisdale;
J. Phys. Chem. Lett. 11, 8565-8572 (2020).
17. “Tuning the Excitonic Properties of the 2D $(\text{PEA})_2(\text{MA})_{n-1}\text{Pb}_n\text{I}_{3n+1}$ Perovskite Family via Quantum Confinement” M. Dyksik, S. Wang, W. Paritmongkol, D.K. Maude, W.A. Tisdale,* M. Baranowski,* P. Plochocka;*
J. Phys. Chem. Lett. 12, 1638-1643 (2021).

Control of light-matter interactions in hybrid structured environments with novel nanomaterials of different dimensionalities (Project # DE-SC0010697)

PI: A. V. Malko (UTD), co-PIs: Y. N. Gartstein (UTD), J. A. Robinson (Penn State University)

Program Scope

The rich photophysics of novel semiconductors like transition metal dichalcogenides (TMDs), lead halide perovskites (LHPs) as well as nanocrystal quantum dots (NQDs) can be gainfully exploited in integrated photonic structures alongside conventional semiconducting and dielectric materials. Realization of the prospects of such hybrid structures crucially depends on the ability to fabricate these “designer” assemblies while preserving and enhancing the optoelectronic properties of individual components. We study encapsulation and passivation methods together with relevant intrinsic photophysical properties of the materials in order to minimize energy losses and facilitate their judicious integration *via* control of energy flows and photon-exciton interconversions.

Recent Progress

Modified metal oxide deposition proves more versatile. Although atomic layer deposition (ALD) of metal oxides is well known as one of the common encapsulation methods, its application ordinarily results in severe losses of the emission efficiency. We, however, found earlier that a modified gas-phase technique with the room temperature co-deposition of both precursors trimethylaluminum (TMA) and water did not deteriorate the emission of traditional inorganic NQDs. We have now demonstrated that this approach can work well for various perovskite

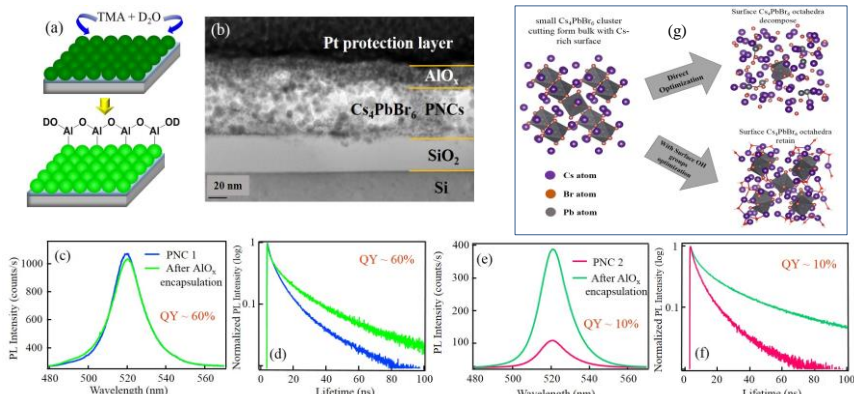


Figure 1: (a) Schematic of alumina encapsulation of PNCs by simultaneous exposure to TMA and D₂O. (b) TEM cross-sectional image of alumina encapsulated 0D PNC film. AlO_x layer thickness was ~ 20 nm for better visualization. PL intensity and lifetime of the high PLQY (c-d) and low PLQY (e-f) 0D Cs₄PbBr₆ PNCs thin film, respectively, before and after ALD. (g) DFT optimized crystal structures of small Cs₄PbBr₆ cluster cut-off from the bulk without (right, top) and with (right, bottom) surface OH group modifications.

materials, including dramatic enhancement of the PL emission in zero-dimensional (0D) Cs₄PbBr₆ and three-dimensional (3D) CsPbBr₃ nanocrystals (PNCs) as well as single crystal perovskites achieved *via* alumina encapsulation. Our studies unveil the pivotal role of the PNC surface composition and treatment in the process of its interaction with metal oxide precursors to control the PL properties and stability of PNCs. XPS analysis of Cs₄PbBr₆ films reveals the deposition process to be accompanied by the elemental composition changes, particularly by the reduction of the excessive cesium content. Our experiments agree with DFT simulations showing decomposition of structural [PbBr₆] octahedra in 0D perovskite lattice that would occur in the presence of excess Cs but which can be passivated by added hydroxyl groups.^{1, 2, 6, 9} Preservation and improvement of PNCs’ optical properties observed both on thin films and at the individual

particle level make our modified ALD a promising approach to integrate fragile perovskite materials into hybrid optoelectronic and photonic structures.

Excitons and their radiative transport in layered perovskites. Another type of highly emissive

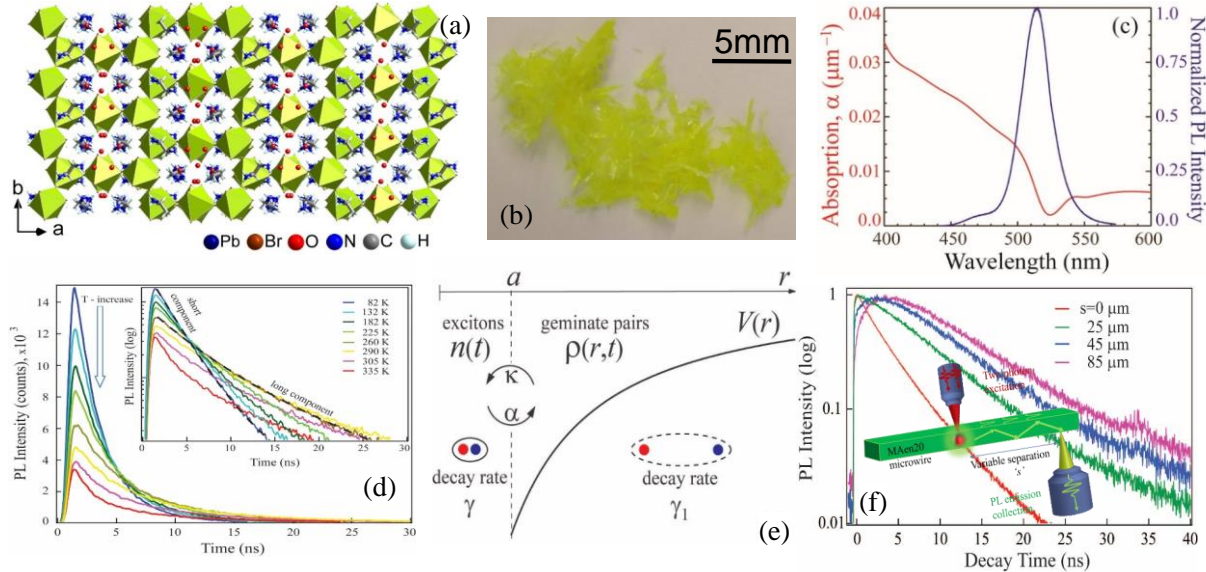


Figure 2: (a) Crystal structure of the MAen₂₀ compound. (b) Optical microphotograph of the flakes. (c) Linear absorption and PL spectra of an individual MAen₂₀ microwire. (d) PL dynamics taken in the temperature range 77-335 K recorded at the maxima of PL spectra. Inset: Same traces plotted on the log scale. (e) Model schematics of the interconversion between excitons (emissive species) and geminate pairs (non-emissive species). (f) Photon recycling in 2D microwires, PL decay traces at different excitation/collection separation distances. Inset: Schematics of the two-objectives setup with variable distance s between PL excitation and collection spots.

perovskites are recently developed 2D (layered) compounds. We explored the temperature T dependence of the photoexcitation dynamics in highly emissive layered perovskite (en)₄Pb₂Br_{9.3}Br with the ethylene diammonium (en) as a spacer between the layers, **Figure 2 (a-c)**. While the PL kinetics has been found to be substantially T -dependent over the whole range of $T \sim 77 - 350$ K, the PL quantum yield remains remarkably nearly T -independent, decreasing only at higher temperatures, **Figure 2(d)**. Numerical solutions of Onsager-Braun-type kinetic-diffusion equations show that our observations are consistent with the picture of a T -dependent dynamic interplay between tightly bound emissive excitons and larger-size, loosely bound, non-emissive geminate charge pairs arising already at earlier relaxation times, **Figure 2(e)**. The geminate pairs play the role of “reservoir” states providing delayed feeding into the emitting excitons.⁴ We formed the samples with a microwire morphology to decisively demonstrate the phenomenon of photon recycling. We tracked the evolution of PL signals as a function of the lateral separation between excitation and collection spots, **Figure 2(f)**. The delayed PL, representing photon recycling, was observed at distances >100 μm with characteristic distance-dependent rise time patterns. The experimental data was rationalized within a modeling framework accounting for recombination, emission and light propagation processes. Modeled intrinsic radiative efficiency of elementary recombination events $\sim 50\%$ agrees with the room- T PL data, rendering the material promising for light-emitting applications, including in structures exploiting photon management.⁷

Photon emission from semiconductor nanocrystals at telecom wavelengths and in photonic microcavities. In collaboration with Dr. Hollingsworth at LANL, we studied PbS/CdS core/shell

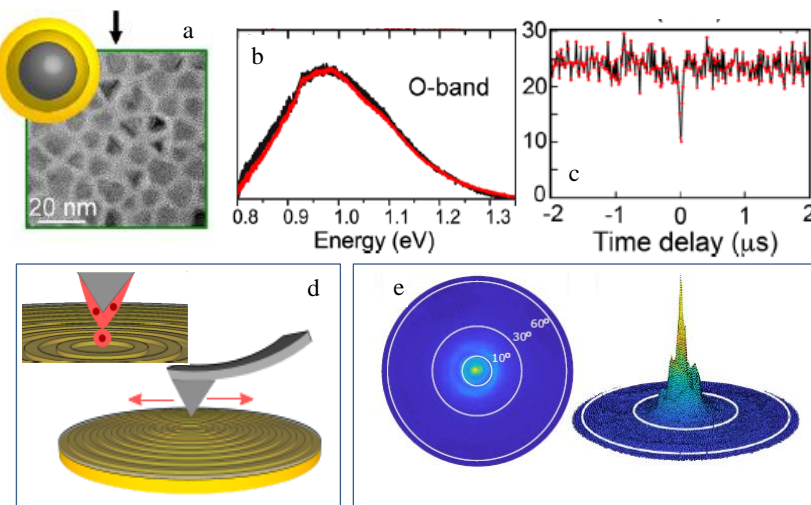


Figure 3. (a) TEM image and shell structure of PbS/CdS NQD. (b,c) PL spectra and photon antibunching of an individual PbS/CdS NQD. (d) Sketch of the wavelength-size, metal-dielectric bullseye antenna structure. Inset: individual NQD placement by dip-pen technique. (e) Directionality of the emission from CdSe/CdS NOD placed in the bullseye nanoantennae.

emitting in the O-band a second-order correlation function showed strong photon antibunching, important steps toward demonstrating the utility of lead chalcogenide QDs as single-photon emitters (SPEs), **Figure 3(a-c)**. We demonstrated that shell engineering and the use of lower laser-excitation powers can afford significantly suppressed blinking and photobleaching. Using dip-pen deposition technology, we presented a method for directly locating single free-standing NQD SPE with high spatial accuracy at the center of highly directional bullseye metal-dielectric nanoantennas. We employed non-blinking, high quantum yield CdSe/CdS NQDs for on-demand single-photon emission that is uncompromised by instabilities or non-radiative exciton recombination processes. Taken together this approach results in a record-high collection efficiency of 85% of the single photons into a low NA= 0.5, setting the stage for efficient coupling between on-chip, room temperature nanoantenna-emitter devices and a fiber or a remote free-space node without the need for additional optics.¹⁰

Engineering defects and improving PL efficiency of two-dimensional TMD layers.

Working with co-PI Robinson at Penn State University, we study defect formation in TMD monolayers. In order to investigate methods for controlling or creating optically active defects in TMDs, MoS₂ and WS₂ flakes are synthesized *via* scalable chemical vapor deposition (CVD) or powder vaporization (PV) processes, and subsequently annealed (either under H₂S or vacuum) under a range of temperatures and chemical environments meant to induce/heal sulfur vacancies in the as-grown material. PL and X-ray photoelectron spectroscopy (XPS) are then used to examine the samples' optical properties and films' stoichiometries, **Figure 4(a-d)**. PL studies of annealed MoS₂ with and without H₂S show drastic changes in position and intensity for the defect bound exciton peak and the free A-exciton peak, in addition to changes in overall intensity, **Figure 4(e,f)**. Intensity for H₂S-annealed samples increases by a factor of ~4X compared to as-grown MoS₂, whereas intensity decreases ~5X in vacuum-annealed samples. The defect-bound exciton peak is

NQDs as functional single-photon emitters for room temperature, solid-state operation in the telecom O and S bands.^{3, 8} Two shell-growth methods (cation exchange and successive ionic layer adsorption and reaction (SILAR)) were employed to prepare PbS-core/CdS-shell NQD heterostructures with shells of 2–16 monolayers. NQDs were bright and stable to resolve PL spectra representing both bands from single nanocrystals using standard detection methods, and for a NQD

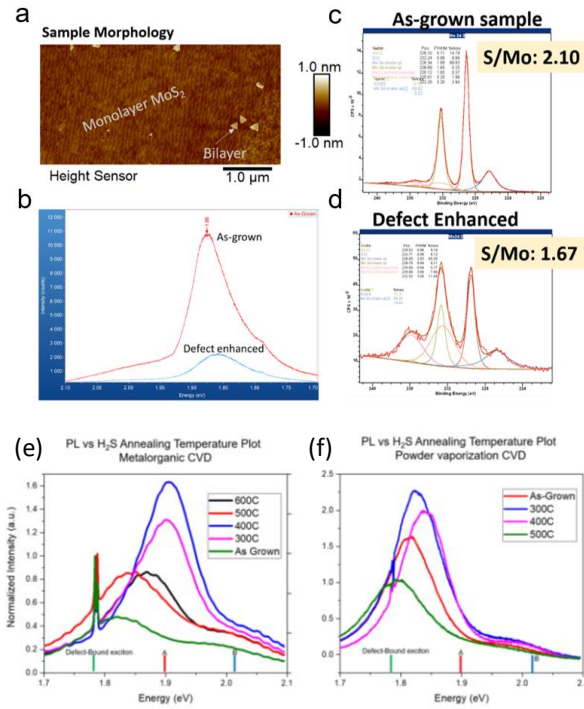


Figure 4. (a) AFM micrograph of continuous monolayer MoS₂ grown *via* MOCVD, (b) PL of the same, showing intensity difference between as-grown and defect-induced samples, (c,d) XPS of as-grown and defect-induced samples, respectively, including the S/Mo ratio for each, showing sub-stoichiometry in the defect-induced sample. (e,f) PL of as-grown and H₂S-annealed MoS₂ samples grown *via* (e) MOCVD and (f) PV.

quenched after sulfur annealing, with an associated blue shift of the A-exciton peak, while the intensity of the defect-bound exciton peak increased when samples are annealed in the absence of H₂S, along with a red shift of the A-exciton peak. Annealing the material in sulfur to heal defects also had varying degrees of effectiveness at the varied temperatures. The most vacancies are healed (leading to the highest PL intensity) at 400°C in the MOCVD samples, and 300°C in the PV samples, **Figure 4(e,f)**. Below these temperatures, it is assumed that not enough vacancies underwent the healing process. Above these temperatures, the competing effects of vacancy healing and vacancy generation by thermal dissociation are dominated by vacancy formation; in the extreme, this led to a higher number of vacancies (and lower PL intensity) in the 500°C H₂S-annealed PV MoS₂ than in its as-grown, unannealed counterpart. Investigation of film stoichiometry *via* XPS revealed that H₂S anneals also increased the sulfur-to-molybdenum content, providing further evidence of vacancy healing. In a similar trend to that seen for PL, the most sulfur-rich films are those annealed at more moderate temperatures, rather than the upper and lower bounds of the range tested.

Future Plans

Guided by our progress in ALD encapsulation of perovskites, we are planning to study blue-emitting perovskite materials that are known to be especially unstable and in need of encapsulation. In parallel, we are developing lead-free, bismuth-based perovskite nanoparticles with enhanced stability *via* ALD encapsulation. We will continue to fabricate well-ordered perovskite nanocrystals solids and use conformal deposition strategy to passivate, protect and stabilize the layers. With LANL, we will continue synthesis and development of nanocrystals of different dimensionalities and spectral signatures, in particular gNQDs for the near-IR range. The progress described above enables us to make inroads towards building more involved hybrid and photonic structures that could take advantage of enhanced near-field interactions in waveguiding and microcavity configurations with the longer-term goal of achieving effective control of light-matter coupling in such systems. Our TMD studies will be expanded; we will continue to explore annealing/defect healing options and corresponding improvements of PL efficiency. We will incorporate nanoparticles and TMD materials into photonic structures and provide insights into methods to control photonic and excitonic conversions.

Project publications within past 2 years, chronological order (2019-2021)

1. Y. Zhang, T. Guo, H. Yang, R. Bose, L. Liu, J. Yin, Y. Han, O. M. Bakr, O. F. Mohammed and A. V. Malko, “*Emergence of Multiple Fluorophores in Individual Cesium Lead Bromide Nanocrystals*”, *Nat. Comm.* **10**, 2930 (2019); doi:10.1038/s41467-019-10870-1
2. T. Guo, R. Bose, X. Zhou, Y. N. Gartstein, H. Yang, S. Kwon, M. J. Kim, M. Lutfullin, L. Sinatra, I. Gereige, A. Al-Saggaf, O. M. Bakr, O. F. Mohammed, and A. V. Malko, “*Delayed Photoluminescence and Modified Blinking Statistics in Alumina Encapsulated Zero-Dimensional Inorganic Perovskite Nanocrystals*”, *J. Phys. Chem. Lett.* **10**, 6780-6787 (2019); doi:/10.1021/acs.jpclett.9b02594
3. Z. Hu, Y. Kim, S. Krishnamurthy, I. D. Avdeev, M. O. Nestoklon, A. Singh, A. V. Malko, S. V. Goupalov, J. A. Hollingsworth, H. Htoon, “*Intrinsic Exciton Photophysics of PbS Quantum Dots Revealed by Low-Temperature Single Nanocrystal Spectroscopy*”, *Nano Lett.* **19**, 8519-8525 (2019); doi: 10.1021/acs.nanolett.9b02937
4. N. Mondal, R. Naphade, X. Zhou, Y. Zheng, K. Lee, I. Gereige, A. Al-Saggaf, O. Bakr, O. Mohammed, Y. Gartstein, A. V. Malko, “*Dynamical Interconversion between Excitons and Geminate Charge Pairs in Two-Dimensional Perovskite Layers Described by Onsager-Braun Model*”, *J. Phys. Chem. Lett.* **11**, 1112-1119 (2020); doi:10.1021/acs.jpclett.9b03709
5. J. Li, S. Yuan, J.-S. Qin, L. Huang, R. Bose, J. Pang, P. Zhang, Z. Xiao, K. Tan, A. V. Malko, T. Cagin, H.-C. Zhou, “*Fluorescence Enhancement in Solid State by Isolating Perylene Fluorophores in Metal-Organic Frameworks*”, *ACS Appl. Mater. Interfaces* **12**(23), 26727-26732 (2020); doi: 10.1021/acsami.0c05512
6. R. Bose, Y. Zheng, T. Guo, J. Yin, M. N. Hedhili, X. Zhou, J.-F. Veyan, I. Gereige, A. Al-Saggaf, Y. N. Gartstein, O. M. Bakr, O. F. Mohammed, A. V. Malko, “*Interface Matters: Enhanced Photoluminescence and Long Term Stability of Zero-Dimensional Cesium Lead Bromide Nanocrystals via Gas-Phase Aluminum Oxide Encapsulation*”, *ACS Appl. Mater. Interfaces* **12**(31), 35598-35605 (2020); doi: 10.1021/acsami.0c07694
7. Y. Zheng, R. Naphade, N. Mondal, O. M. Bakr, O. F. Mohammed, Y. N. Gartstein, A. V. Malko, “*Light Propagation and Radiative Exciton Transport in Two-Dimensional Layered Perovskite Microwires*”, *ACS Photonics* (2020); doi: 10.1021/acsphotonics.0c01479
8. S. Krishnamurthy, A. Singh, Z. Hu, A. V. Blake, Y. Kim, A. Sing, E. Dolgopolova, D. J. Williams, A. Piryatinski, A. V. Malko, H. Htoon, M. Sykora, and J. A. Hollingsworth, “*PbS/CdS Quantum Dot Room Temperature Single-Emitter Spectroscopy Reaches the Telecom O and S Bands via an Engineered Stability*”, *ACS Nano* (2020); doi: 10.1021/acsnano.0c05907
9. R. Bose, J. Yin, Y. Zheng, C. Yang, Y. N. Gartstein, O. M. Bakr, A. V. Malko, O. F. Mohammed, “*Gentle Materials Need Gentle Fabrication: Encapsulation of Perovskites Using Gas-Phase Alumina Oxides*”, accepted as a Perspective Article in *J. Phys. Chem. Lett.*
10. H. Abudayyeh, B. Lubotzky, A. Blake, J. Wang, S. Majumder, Z. Hu, Y. Kim, H. Htoon, R. Bose, A. V. Malko, J. A. Hollingsworth, R. Rapaport, “*High Purity Single Photon Sources with Near Unity Collection Efficiencies by Deterministic Placement of Quantum Dots in Nanoantennas*”, submitted

Describing Light-Matter Interaction at the Nanoscale Through Coupled Simulation of Quantum Electronic Transport and Electrodynamics

I. Knezevic, University of Wisconsin-Madison, iknezevic@wisc.edu

Program Scope

The control of light-matter interaction at the nanoscale is a grand challenge that cuts across modern photonics, plasmonics, and optoelectronics, and it requires predictive modeling to successfully tackle. The objective of this project is to develop and deploy a suite of simulation tools based on the density-matrix framework for quantum electronic transport which also incorporates light-matter interaction. We showcase the versatility of the density-matrix approach for this purpose, and present our recent advances in developing a fully self-consistent coupled quantum transport and electrodynamics simulation framework.

Recent Progress

- **Density-Matrix Model for Photon-Driven Transport in Quantum Cascade Lasers [1]**

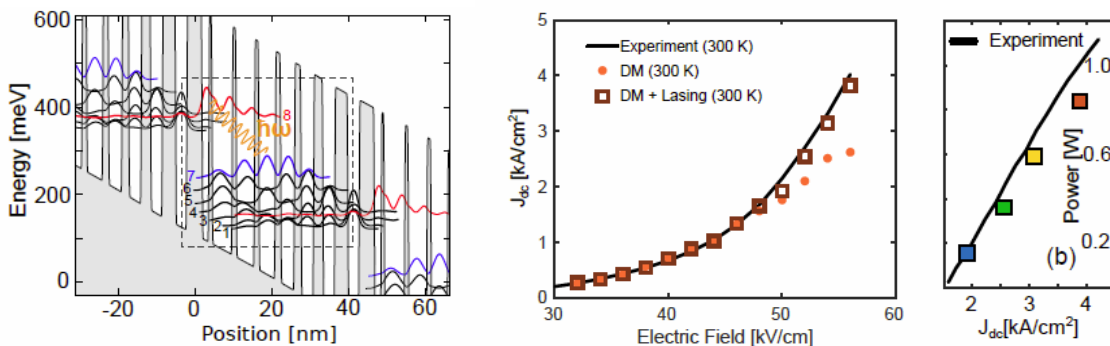


Fig. 1. (Left) Conduction-band edge and probability densities for the eight eigenstates used in calculations (bold curves). The states that belong to neighboring periods are denoted by thin gray curves and the dashed box indicates a single stage, starting with the injection barrier. The bias electric field is 50 kV/cm. The states are numbered in the order of increasing energy, starting with the ground state. The radiative transition occurs from state 8 to state 7. **(Middle)** Calculated dc current density as a function of the applied bias electric field at 300 K, with (open squares) and without (solid circles) the influence of photon-assisted tunneling. **(Right)** Measured and calculated output power as a function of the current density.

Quantum cascade lasers (QCLs) are unipolar sources of coherent radiation emitting in the terahertz and infrared portions of the electromagnetic spectrum, and also excellent model systems for far-from-equilibrium quantum transport in the presence of electromagnetic fields. The gain medium of a QCL is a periodic stack of compound-semiconductor heterostructures. The resulting multi-quantum-well electron band structure in the growth direction has discrete energy levels, and the associated wave functions are quasibound. While lasing stems from radiative electron transitions between specific states, nonradiative transitions mediated by various scattering mechanisms also play important roles in device operation. In particular, photon-assisted (PA) transport in terahertz and midinfrared QCLs is significant at and above lasing threshold, and appears particularly prominent in devices with diagonal design. There is a need for a computationally efficient quantum-transport treatment of PA tunneling in QCLs that does

not require phenomenological parameters and that employs broadly adopted intuitive concepts.

In this work, we present a quantum-mechanical model for photon-driven transport in QCLs that is computationally inexpensive, requires no phenomenological parameters, and is conducive to intuition building. The model stems from a rigorous theoretical framework with a positivity-preserving Markovian master equation of motion for the density matrix. The model is employed to characterize the steady-state and frequency response of a previously grown midinfrared QCL. Our results show that the inclusion of PA tunneling leads to substantial changes in electron transport around and above lasing threshold. Specifically, a significant increase in the current density is observed upon inclusion of PA tunneling, which allows for a significantly better agreement with experimental findings than the models that neglect this phenomenon. In particular, we show that, in quantum cascade lasers with diagonal design, photon resonances have a pronounced effect on electron dynamics around and above lasing threshold. This effect stems from a large spatial separation of the upper and lower lasing states.

- **Dielectric waveguides with embedded graphene nanoribbons for all-optical broadband modulation [2]**

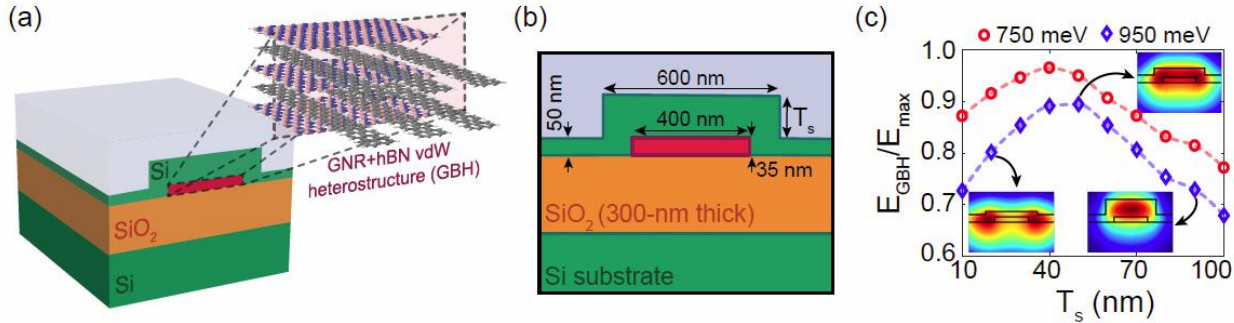


Fig. 2. (a) Schematic of a GBNH-embedded rib silicon waveguide. The zoomed-in heterostructure consists of graphene nanoribbons (gray) encased in hBN (pink). (b) The cross-section view of the waveguide. (c) $E_{\text{GBNH}}/E_{\text{max}}$ as a function of Si strip thickness, T_s . E_{GBNH} denotes the electric field at the center of the GBNH and E_{max} is the maximal electric field across the device. The closer the ratio is to 1, the more concentrated the optical field is near the GBNH. $T_s \sim 45$ nm yields optimal optical confinement. Insets show electric-field profile across waveguide for narrow (20 nm), optimal (45 nm), and thick (100 nm) Si strips at 950 meV.

All-optical processing offers low power consumption and fast operation speed and is a promising approach to high-bit-rate communication. Realization of all-optical integrated photonics requires core materials which strongly mediate photon–photon interaction. Recently, it was shown that, in the long-wavelength limit, graphene nanoribbons (GNRs) have a very strong Kerr optical nonlinearity at the telecom wavelength range (1.3–1.6 μm). We proposed a dielectric waveguide with embedded GNRs for all-optical self-amplitude-modulation applications. By implanting a van der Waals (vdW) heterostructure consisting of GNRs and hexagonal boron nitride into a rib silicon waveguide, we maximize the optical concentration near the GNRs and enhance nonlinear optical effects. Different-width GNRs incorporated in the vdW heterostructure provide strong self-sustaining broadband modulation over the telecom frequency range, without a need for dynamical tuning. The compact footprint and self-sustaining, broad-bandwidth saturable absorption make the proposed device a suitable component for ultrafast nanophotonic applications.

- Tunable plasmon-enhanced second-order optical nonlinearity in transition-metal dichalcogenide nanotriangles [3]

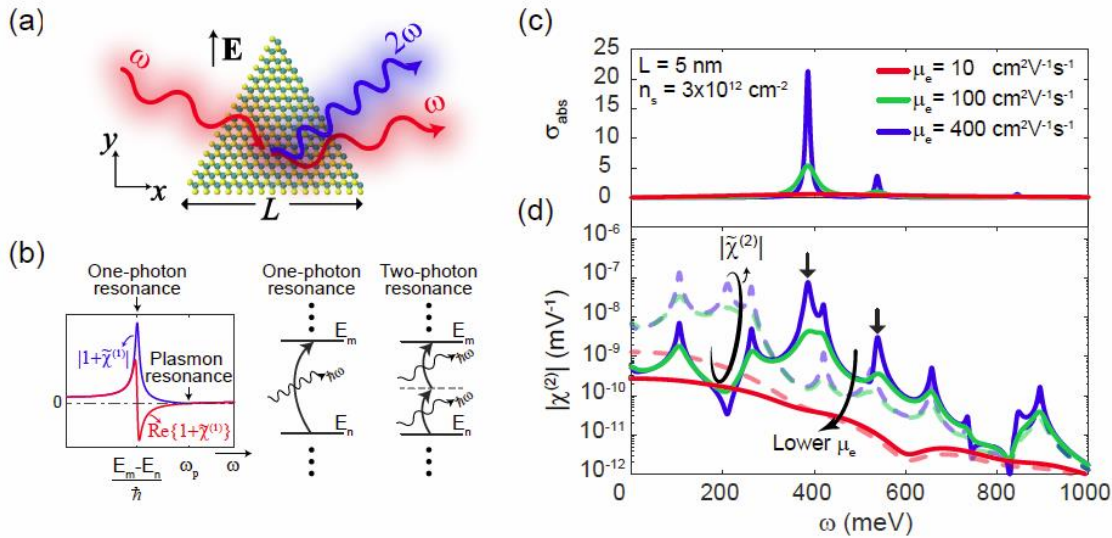


Fig. 3. (a) Schematic of an equilateral TMD nanotriangle with the side length L . TM-polarized incident light causes linear and second-order nonlinear optical response. (b) One-photon, two-photon, and plasmon resonances. One- and two-photon resonances are due to intersubband optical transitions, whereas plasmon resonances are due to collective oscillations of electrons. (c) Loss function and (d) second-order susceptibility in response to external field (solid) and total field (dashed) of a 5-nm TMD nanotriangle with sheet density $3 \times 10^{12} \text{ cm}^{-2}$ for different values of the electron mobility. Arrow-marked peaks are two different plasmon resonances.

The development of nanomaterials with a large nonlinear susceptibility is essential for nonlinear nanophotonics. In this paper, we show that equilateral nanotriangles made of single-layer TMDs such as MoS₂, WS₂, and WSe₂, whose growth has already been demonstrated, have a strong and electrically tunable second-order nonlinear optical response at midinfrared (mid-IR) to near-infrared (near-IR) frequencies. We calculate the second-order nonlinear optical response of these systems within the density-matrix quantum-transport framework that accounts for dissipative processes and screening in detail (excitonic effects are not considered). We show that the second-order susceptibility $\chi^{(2)}$ peaks in the vicinity of both two-photon intersubband resonances (whose positions are fixed by the nanotriangle geometry) and plasmon resonances (dynamically tunable by the carrier density). By tuning the carrier density to bring the plasmon and two-photon resonances into alignment, $\chi^{(2)}$ can become as high as 10^{-6} m/V , orders of magnitude higher than the intrinsic SHG of single-layer TMDs ($\sim 10^{-9} \text{ m/V}$) or the $\chi^{(2)}$ of bulk LiNbO₃ ($\sim 10^{-11} \text{ m/V}$) at near-IR frequencies. $\chi^{(2)}$ increases as the triangle size decreases. These findings underscore the suitability of single-layer TMD nanotriangles for nonlinear nanophotonics.

Future Plans

We have successfully integrated approximate electrodynamics into both vertical and lateral quantum transport of electrons described using the density matrix. Future plans involve full self-consistent integration of electrodynamics solvers (classical and quantum) with quantum electronic transport, most immediately for classical electrodynamics. To that end, we have been developing and will soon publish our work on two new computational electrodynamics

algorithms that calculate scalar electric and vector magnetic. The first is the field-potential finite-difference time-domain (FiPo FDTD) algorithm, already implemented with efficient convolutional perfectly matched layer (CMPL) boundary conditions and in the Lorenz gauge. Preliminary data in Fig. 4 is for a differentiated Gaussian current source in the z-direction (normal to the screen) and with a bandwidth of 6 GHz. The source is at the center of each panel.

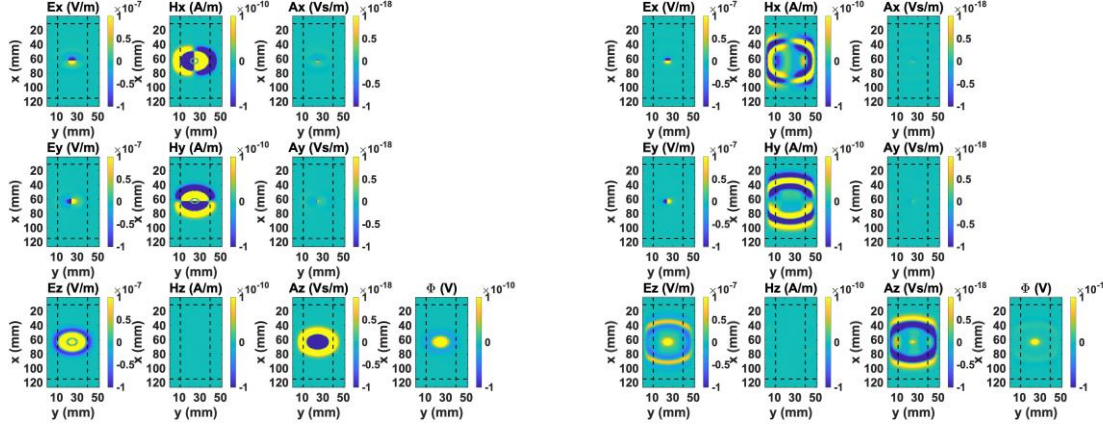


Fig. 4. Snapshot of fields and potentials for FiPo FDTD at 0.32 ns (**left**) and 0.49 ns (**right**) for a differentiated Gaussian source. The latter shows the efficiency of the CMPL absorbing boundary conditions.

In the second approach, we cast Maxwell's equations in terms of dual potentials, where, in addition to the well-known vector magnetic and scalar electric potentials we also introduce their duals (vector electric and scalar magnetic potentials). This form of Maxwell's equations is particularly useful when employed with the Coulomb gauge and offers exciting opportunities for the simulation of currents that carry angular momentum, such as electron beam vortices (Fig. 5).

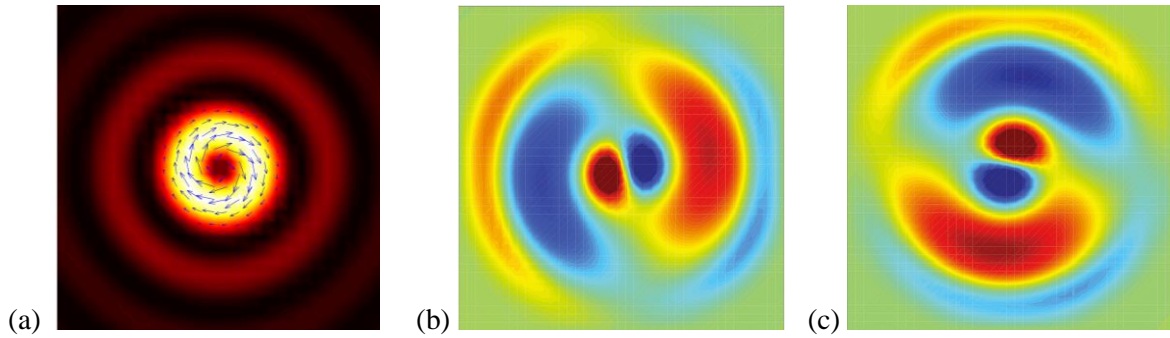


Fig. 5. (a) Top-down view of quiver plot showing current density in a vortex beam. The current density swirls around the propagation axis, which points into the page. The quiver plot is overlaid on a slice of $|\Psi|^2$. (b) and (c) Snapshot of the components A_x (b) and A_y (c) of the magnetic vector potential \mathbf{A} in the Coulomb gauge for the current source being the electron vortex beam from the left panel, which carries nonzero angular momentum.

References

- [1] S. Soleimanikahnoj, M. L. King, and I. Knezevic, *Phys. Rev. Applied*, in press (2021). arXiv:2012.14491
- [2] F. Karimi and I. Knezevic, *Opt. Mater. Express* 9, 4456-4463 (2019).
- [3] F. Karimi, S. Soleimanikahnoj, and I. Knezevic, submitted (2021). arXiv:2102.06325

Publications

S. W. Belling, Y. C. Li, A. H. Davoody, A. J. Gabourie, I. Knezevic, “DECaNT: Simulation Tool for Diffusion of Excitons in Carbon Nanotube Films,” *J. Appl. Phys.*, in press (2021). Preprint: <https://arxiv.org/abs/2010.11992>

S. Soleimanikahnoj, M. L. King, and I. Knezevic, “Density-Matrix Model for Photon-Driven Transport in Quantum Cascade Lasers,” *Phys. Rev. Applied*, in press (2021). Preprint: <https://arxiv.org/abs/2012.14491>

S. Soleimanikahnoj, O. Jonasson, F. Karimi, I. Knezevic, “Numerically efficient density-matrix technique for modeling electronic transport in mid-infrared quantum cascade lasers,” *J. Comput. Electron.*, published online first (2021). <https://doi.org/10.1007/s10825-020-01627-x>

M. L. King, F. Karimi, S. Soleimanikahnoj, S. Suri, S. Mei, Y.B. Shi, O. Jonasson, and I. Knezevic, “Coupled simulation of quantum electronic transport and thermal transport in midinfrared quantum cascade lasers,” in *Mid-Infrared and Terahertz Quantum Cascade Lasers*, edited by Dan Botez and Mikhail Belkin, Cambridge University Press, forthcoming (2021).

F. Karimi and I. Knezevic, “Dielectric waveguides with embedded graphene nanoribbons for all-optical broadband modulation,” *Opt. Mater. Express* 9(11), 4456-4463 (2019).

G. R. Jaffe, S. Mei, C. Boyle, J. D. Kirch, D. E. Savage, D. Botez, L. J. Mawst, I. Knezevic, M. G. Lagally, and M. A. Eriksson, “Measurements of the thermal resistivity of InAlAs, InGaAs and InAlAs/InGaAs Superlattices,” *ACS Appl. Mater. Interfaces* 11, 11970-11975 (2019).

F. Karimi, A.H. Davoody, and I. Knezevic, “Nonlinear optical response in graphene nanoribbons: The critical role of electron scattering,” *Phys. Rev. B* 97, 245403 (2018).

S. Mei and I. Knezevic, “Thermal conductivity of ternary III-V semiconductor alloys: mass-difference scattering versus long-range order,” *J. Appl. Phys.* 123, 125103 (2018).

W. Peng, M. Zamiri, S. A. Scott, F. Cavallo, J. J. Endres, I. Knezevic, M. A. Eriksson, and M. G. Lagally, “Electronic Transport in Hydrogen-Terminated Si(001) Nanomembranes,” *Phys. Rev. Applied* 9, 024037 (2018).

Hot Carrier Dynamics in Low-Dimensional Systems

Ian R. Sellers, Department of Physics & Astronomy, University of Oklahoma

Program Scope

This research is focused on the physics of hot carrier dynamics in confined semiconductor structures, more specifically: the role of polarons, carrier lifetime, and carrier-carrier interactions in the hot carrier dynamics of type-I and type-II quantum wells (QW) in III-V's, as well as metal-halide perovskites. While these two systems are quite different in terms of structure, constituent materials, and synthesis, they share several unique but similar properties. These include evidence of inhibited carrier relaxation and robust hot carrier effects upon high energy photoexcitation, along with interesting carrier-phonon dynamics. Here, the role of crystal structure, chemical composition, carrier-phonon interactions in hot carrier generation is assessed in a range of metal-halide perovskites using a suite of optical techniques. These include continuous wave (CW) photoluminescence and absorption, using resonant and non-resonant excitation, along with complementary transient absorption (TA) spectroscopy. Also investigated are InAs/AlAsSb quantum wells in which the type-II band structure allows for assessment of hot carrier relaxation in strongly confined heterostructures that has already demonstrated unusual hot carrier dynamics and phonon bottleneck effects. These systems also provide a potential III-V system for the demonstration of carrier multiplication (CM) and the ability to study Auger effects upon CM by design. Here, recent progress is presented along with results for the potential to inhibit carrier thermalization using multi-QW (MQW) and superlattices.

Recent Progress

Initial work on perovskite systems in this program was focused on the interaction of excitonic complexes and phonons (polarons) in 2D Ruddlesden-Popper films and compared to conventional bulk MAPbI_3 .¹ It is shown that the complex structure observed at low temperature is the product of a series of intrinsic and extrinsic excitons, within which carrier redistribution is evident with increasing temperature. At higher temperatures, two dominate excitons were evident whose origin are intrinsic to the perovskite structure. However, these excitons interacted quite differently with phonons: through processes mediated by the binding energy or in other words, the extension of the exciton wavelength within the lattice. The role of polarons in these systems along with their effect on carrier relaxation and the role of phonons in these materials have been investigated, along with several additional and complementary perovskite systems. Temperature dependent photoluminescence (PL) and transmission spectra have been used to analyze the effect of changing the components of various perovskite compounds, which is focused

here for brevity on four systems: FAMAPbSnI₃, FAPbI₃, FAMAPbI₃, and FAPbBr₃.² Low temperature measurements highlight subtle differences in the properties of these systems, which are screened at room temperature. Specifically, samples with the double cation FAMA display more complicated low temperature spectra than those synthesized with only FA, as the A-site organic cation. Figure 1 shows the temperature dependent Stokes shift extracted from PL and absorption spectra for the four materials under discussion. Insets to each figure show comparisons of the 4.2 K and 300 K absorption and PL spectra. The behavior of the three pure Pb-based perovskites show similar magnitude at room temperature. This work² shows that this is governed on one hand, by the Fröhlich coupling parameter, ionicity, and phonon energy (*ELO*) – the greater the interaction corresponds to larger Stokes shift; and on the other hand, the exciton binding energy of the specific system, which corresponds to fewer free carriers – therefore, lower carrier-phonon interaction which results in a smaller Stokes shift, or delayed temperature response. The behavior of the Sn-based (FAMA)PbSnI₃ film is considerably different from that of the pure Pb-based systems, in all measurements made. Specifically, in the case of Figure 1, the mixed Sn-Pb system displays a marked absence of a Stokes shift between the absorption and photoluminescence. This is attributed to the role of a high background impurity concentration in (FAMA)PbSnI₃, resulting in considerable broadening in the PL and significant sub bandgap free carrier absorption in these materials. TA further supports the trends observed in CW measurements; the three Pb-based films all show the convolution of an excitonic feature within 20 meV of the bandgap as a contributing factor to the photo bleach along with a region of high energy photoinduced absorption (PIA). However, once again, the behavior for the Sn-based perovskite is notably different with an unusual low energy PIA and a lack of high energy PIA. The large unusual low energy PIA is further evidence of the role of the contribution of significant sub bandgap absorption as seen in the CW measurements. An initial rapid cooling of hot carriers in the first few picoseconds displayed

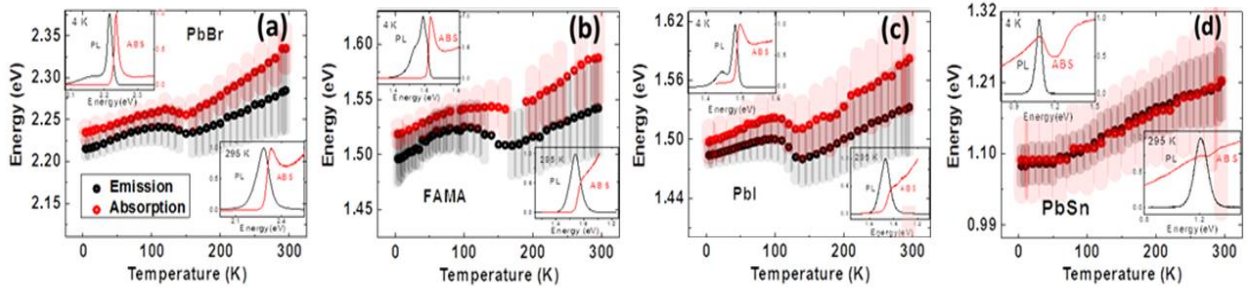


Figure 1: (a) Comparison of the temperature dependence of the peak PL energy (black circles) and the energy from the transmission spectra (red circles) for FAPbBr₃ (a), FAMAPbI₃ (b), FAPbI₃ (c), and FAMAPbSnI₃ (d) from 4.2 K to 300 K. Shaded regions correspond to the extent of FWHM. The insets show PL (black) and absorbance (red) spectra for 4.2 K (upper) and 295 K (lower).

in all the systems studied is attributed to efficient hot carrier-LO phonon coupling likely mediated by Klemens and more importantly, Ridley processes. In all cases, a longer-lived carrier relaxation

regime is evident that is apparently ubiquitous to metal-halide perovskites. This longer-lived cooling of carriers is attributed to phonon bottlenecks associated not only with LO phonons but, the intrinsic low thermal conductivity of perovskites limiting the dissipation of acoustic phonons, something also proposed in earlier InAs structures.³

In the *second thrust* of the program, deep InAs/AlAsSb quantum well structures are considered. These systems, which have a type-II band alignment, have been shown to produce hot carrier effects via inhibited hot carrier relaxation. The type-II InAs system displays a number of unusual properties such as low hot carrier thresholds, evidence of intervalley scattering, and the presence of a strong phononic band gap indicating a suppression of the Klemens mechanism in this system. As such, here the effects of electron phonon interaction and more specifically the LO-phonon relaxation pathways are the focus: can losses be controlled or engineered using the large phononic mismatch of the superlattices under investigation. A series of 2.1 nm type-II

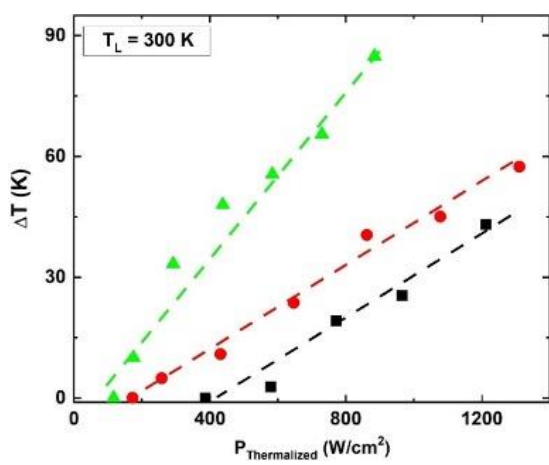


Figure 2: Temperature difference (ΔT) as a function of thermalized power for the type-II InAs MQWs with 2 nm (black), 5 nm (red), and 10 nm (green) barrier thickness at 300 K. The dashed lines indicate the results of linear fitting.

InAs/AlAs_{0.16}Sb_{0.84} quantum wells with increasing barrier thickness have been investigated. In this study, the carrier temperature is extracted through applying a PL ratio method, which considers the reference CW PL spectrum at thermal equilibrium with the lattice. Figure 2 shows the temperature difference (ΔT : difference between hot carriers and the lattice temperature) as a function of thermalized power (the excess kinetic energy of the electrons in the conduction band per time unit) at 300 K. It is observed that when the AlAs_{0.16}Sb_{0.84} barrier thickness is increased from 2 nm - through 5 nm - to 10 nm the hot carrier temperature increases, while the thermalization coefficient (efficiency of hot carrier relaxation, not shown for brevity) decreases. This is attributed to the increasing

role of phonon channels related to the AlAsSb barrier, which has a significantly larger phononic band gap than that of InAs. The consequence of this is to reduce Klemens relaxation pathways in the MQWs with larger AlAsSb barrier contributions.³ Monte Carlo simulations support this hypothesis with a significant decrease in the density of available InAs phonon states in the system as the contribution of the AlAsSb based barrier increase to 90 %, decoupling the Klemens channel in the InAs and increasing the phonon scattering time in the system considerably.⁴

Future Plans

Hot carriers are currently being assessed in CsFAPbI₃ based heterostructures, which are the most stable and structurally pure metal-halide perovskites systems we have investigated. This has enabled not only the assessment of hot carriers in transient absorption, but assessment of any evidence of “hot” photocurrent in electrical measurements. Simultaneous monochromatic-current-voltage (excitation at 532 nm) and photoluminescence measurements are also underway on MQW and SL structures in the InAs/AlAsSb system to investigate the presence of hot carriers on the extracted photocurrent and voltage in these heterostructures. In addition, a new generation of optical structures with band gaps of ~ 0.5 eV have also been designed and grown by MBE in this (InAs/AlAsSb) system. These samples have ground state (InAs) absorption energy that is approximately three times smaller than the (AlAsSb) QW barriers. Thus, these samples are relevant for a major goal of this program – studying the effects of Auger processes carrier multiplication in III-V quantum wells.

References

1. H. Esmaelpour, V. R. Whiteside, S. Sourabh, G. E. Eperon, J. T. Precht, M. C. Beard, H. Lu, B. K. Durant, and I. R. Sellers, *ACS Journal of Physical Chemistry C* **124**, 9496 (2020)
2. S. Sourabh, V. R. Whiteside, Y. Zhai, K. Wang, D. Y. Kim, M. C. Beard, and I. R. Sellers. *Physical Review Materials* (2021) *under review*
3. J. Garg & I. R. Sellers, *Semiconductor Science & Technology* **35**, 044001 (2020)

Publications

1. H. Esmaelpour, V. R. Whiteside, S. Sourabh, G. E. Eperon, J. T. Precht, M. C. Beard, H. Lu, B. K. Durant, and I. R. Sellers, *ACS Journal of Physical Chemistry C* **124**, 9496 (2020)
2. J. Garg and I. R. Sellers, *Semiconductor Science & Technology* **34**, 044001 (2020)
3. S. Sourabh, V. R. Whiteside, Y. Zhai, K. Wang, D. Y. Kim, M. C. Beard, and I. R. Sellers. *Physical Review Materials* (2021) *under review*
4. H. Esmaelpour, B. K. Durant, K. R. Dorman, V. R. Whiteside, J. Garg, T. D. Mishima, M. B. Santos, I. R. Sellers, J-F. Guillemoles and D. Suchet. *Applied Physics Letters, Special Issue: under review February* (2021)

Session X

Disorder in Topological Semimetals

Kirstin Alberi¹, Brian Fluegel¹, Anthony Rice¹, Stephan Lany¹, Mark van Schilfgaarde¹, Matt Beard¹ and Daniel Dessau²

¹National Renewable Energy Laboratory, ²University of Colorado, Boulder

Program Scope

Three dimensional (3D) topological semimetals offer exciting opportunities for controlling and exploiting exotic states of matter for the next generation of energy-relevant technologies. The topological phase and many of the unique properties these materials display are deeply connected to the underlying symmetry and disorder within the system, presenting opportunities to broadly tailor them. This project investigates the complex relationships between the properties of topological semimetals and disorder in the prototypical and technologically relevant 3D Dirac semimetal Cd₃As₂. We deliberately manipulate defects, impurities and interfaces in epitaxial layers to understand how they influence the optical and transport properties as well as the topological phase. The fundamental insights gained from the Cd₃As₂ material system are expected to set the stage for utilizing disorder within topological semimetals to design them for specific applications.

Recent Progress

Our ability to manipulate disorder in Cd₃As₂ is based on the degrees of freedom afforded by molecular beam epitaxy (MBE). We have the ability to control the crystallographic orientation, extended and point defects, and the composition and thickness of the Cd₃As₂ epilayers based on the choice of substrate, atomic flux ratios, growth temperature and growth time. We have previously developed the ability to grow Cd₃As₂ on GaAs substrates in the (001), (110) and (111) orientations by inserting a Zn_xCd_{1-x}Te buffer to control strain relaxation. We also use separate elemental arsenic and cadmium sources for growth, which allows us to manipulate point defect populations through selection of the arsenic overpressure. Our high-quality material (with room temperature electron mobilities as high as 18,700 cm²/V-s) provides a platform for targeted studies of specific types of disorder.

Understanding the response of topological semimetals to impurities and defects

Although the topological protection endowed by the inversion and time reversal symmetries in Cd₃As₂ prevent against carrier backscattering, point and extended defects can alter other material properties. One important example is the strong n-type doping of as-grown crystals through the incorporation of V_{As} defects [1,2]. High electron concentrations ($\sim 10^{18}$ cm⁻³) move the Fermi level 100-200 meV into the conduction band, obscuring measurements of electronic structure near the Dirac point and limiting the versatility of Cd₃As₂ for some applications [3]. We are currently investigating the extent to which control of the As/Cd flux ratio during molecular beam epitaxy can alter the V_{As} and free electron concentrations. Early results indicate that higher

As overpressures can be used to lower the electron concentration by an order of magnitude in epilayers grown in the (112) orientation (Fig. 1). Interestingly, we also find the choice of crystallographic growth direction affects the electron concentration. For example, growth in the (001) orientation results in lower overall electron concentrations and decreased dependence on the As/Cd flux ratio (Fig 1). We are currently investigating the mechanisms that lead to these different behaviors through a series of growth studies in combination with magneto-transport and positron annihilation spectroscopy measurements. In tandem, we are setting up supercell defect calculations for an inclusive set of potential dopant atoms and including lattice defects that can often form in response to doping. Based on this data we will predict the range of Fermi level positions achievable with doping under realistic growth conditions. The ability to lower the free electron concentration in as-grown material simply by altering the orientation of the growth surface presents exciting new opportunities to further study the material properties near the Dirac point and design epitaxial layers for device applications.

Extended defects are also known to affect the electron mobilities of Cd₃As₂ [4,5]. Dislocations, stacking faults and twin defects all form in epitaxial layers grown on lattice-mismatched substrates, and we use Zn_xCd_{1-x}Te buffer structures with varying lattice constants and miscuts to control their densities. Raman measurements offer a sensitive probe of twin defects in samples grown in the (112) orientation. Minimally twinned samples show contrasting polarization between light oriented parallel and orthogonal to the c-axis projection, whereas spectra from fully twinned samples have contributions from a mixture of domains having the three (112) variants.

Although Cd₃As₂ has previously been alloyed with Zn and P [1,6,7], we do not have a comprehensive view of how scalar potentials of isovalent impurities or charged centers influence its electronic, optical and transport properties. A goal of this project is to understand chemical trends in how different types of impurities influence Cd₃As₂, including the topological phase. We have started our investigation with Zn (isoelectronic) and Te (charged) impurities. Adding Zn at concentrations of just a few atomic percent causes a moderate drop in the electron mobility (Fig. 2). It is also interesting to note that the electron concentration drops as well. By comparing epilayers grown under different As/Cd flux ratios, we have obtained hints that Zn may slightly aid the incorporation of As into the lattice, especially for low As overpressures, thereby driving down the free electron concentration in this doping range. Further investigation is needed to verify this mechanism. At higher Zn concentrations > 15%, an additional small reduction of the electron concentration is linked to the total shift toward a p-type trivial semiconductor in Zn-rich alloys (> 25% Zn) [1,7]. However, the electron mobility continues to drop, commensurate with our

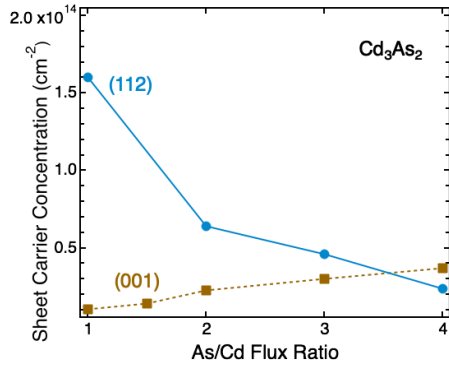


Figure 1. Electron sheet concentration in Cd₃As₂ epilayers grown with varying As/Cd flux ratios in the (112) or (001) orientation. All epilayers have roughly the same thickness.

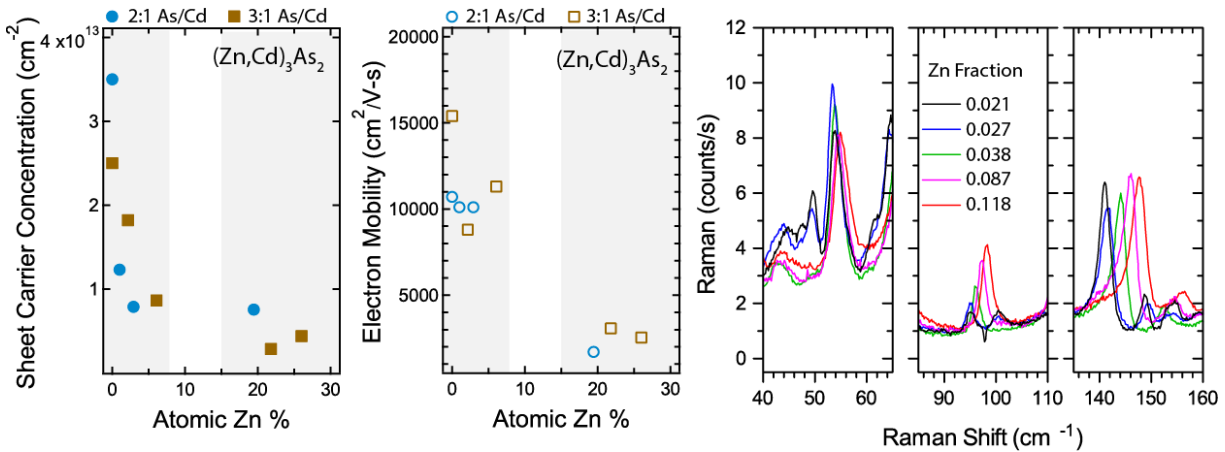


Figure 2. Electron sheet concentration (left) and mobility (center) in $(\text{Zn},\text{Cd})_3\text{As}_2$ epilayers as a function of Zn concentration and As/Cd flux ratio. Behaviors are distinguished between low-doped (< 10%) and moderately doped (> 15%) regimes. All epilayers have roughly the same thickness. (right) Raman spectra as a function of Zn doping. Scattering amplitude and frequency are affected to different degrees by the cation mass and binding, ranging from little dependence at the 54 cm^{-1} mode to a rapid frequency dependence at the 141 cm^{-1} mode.

expectation that Zn acts as a small angle scattering center and facilitates the generation of extended defects [2]. Alloying Cd_3As_2 also influences the Raman modes, but to different degrees (Fig. 2). These results provide a starting point from which to evaluate how other isoelectronic impurities affect carrier concentrations, scattering and other structural and optical properties.

Probing relationships between symmetry and topological phase

The Cd_3As_2 lattice is derived from the fluorite (CaF_2) lattice, where As occupies the 4a site (Ca) and Cd occupies the 8c (F) site, but with $\frac{1}{4}$ of sites being empty. In the ground state (GS), the empty sites are ordered, giving rise to a tetragonal space group symmetry (# 142) with 80 atoms in the primitive cell. Each As site is coordinated by eight 8c sites, and in the GS the arrangement of empty sites is such that each As site has 6 Cd neighbors and two empty sites. This observation suggested that short range order (SRO, i.e., exclusive As-Cd6 coordination) could play an important role. Recent research in ternary nitrides has identified cases where SRO is dominating the energetics of disorder [8]. Therefore, to better understand the role of ordering of the empty Cd sites, we performed DFT-SCAN supercell calculations with disordered configurations. Figure 3 shows that SRO reduces to a certain extend the energy, but the energies remain comparable to those of random disorder. From this data, the ordered-to-random phase transition can be estimated to occur around 1300K, considerably higher than crystal growth temperatures and even higher than the stability range of Cd_3As_2 . SRO does not reduce the energies enough to significantly reduce the disorder temperature. Thus, pure Cd_3As_2 can be viewed as an ordered vacancy compound [9], with a relatively strong ordering tendency. As a conclusion of these results, we will focus our near-term efforts on the ordered Cd_3As_2 structure. We will potentially revisit the role of empty-site disorder in the context of doping and alloy since the interaction between dopants and empty sites can induce disorder of the latter even when it is absent in the undoped material.

Manipulating Disorder at Interfaces

Epitaxially incorporating Cd_3As_2 and its alloys into heterostructures will ultimately support its use in a variety of applications. We have grown Cd_3As_2 epilayers directly on $\text{Zn}_x\text{Cd}_{1-x}\text{Te}$, Zn_3As_2 and GaAs surfaces. Band alignments determined through capacitance-voltage and x-ray photoemission spectroscopy, in addition to transport measurements, provide information on which interfaces will act as Ohmic contacts or Schottky barriers. By altering the interface initiation growth conditions, we can further explore how disorder at the interface influences carrier transport across it in both instances.

Future Plans

We intend to continue the studies outlined above to uncover the impact of disorder from defects and impurities as well as ways to control it. This includes the manipulation of V_{Cd} defects and the influence of impurities on the properties of the topological surface states. In addition to the transport and Raman measurements, we will also investigate how these various forms of disorder affect hot carrier cooling through optical-pump, THz-probe time-resolved spectroscopy methods. In the area of material computation, we plan to utilize the Quasiparticle Self-Consistent GW approximation to reliably model the bandstructure and gain further insight into transport and optical properties. Finally, we are in the process of building a portable ultra-high vacuum chamber for transporting samples from our MBE system at NREL to the angle-resolved photoemission spectroscopy (ARPES) instrument at the University of Colorado, Boulder. These measurement capabilities, combined with our ability to grow epilayers in various crystallographic orientations and thicknesses will allow us to probe the electronic structure of the bulk and surface states as a function of free carrier concentration and alloy composition.

References

- [1] S. Nishihaya, Sci. Adv. 4, eaar5668 (2018)
- [2] S. Jeon, *et al.*, Nat. Mater. 13, 851 (2014)
- [3] I. Crassee, *et al.*, Phys. Rev. Mater. 2, 120302 (2018)
- [4] T. Schumann, *et al.*, APL Mater. 4, 126110 (2016)
- [5] A. Rice, *et al.*, Phys. Rev. Mater. 3, 121201(R) (2019)
- [6] S. Thirupathaiah, *et al.*, Phys. Rev. B 98, 085145 (2018)
- [7] H. Lu, *et al.*, Sci. Rep. 7, 3148 (2017)
- [8] J. Pan, *et al.*, NPJ Comp. Mater. 6, 63 (2020)
- [9] J.E. Bernard and A. Zunger, Phys. Rev. B 37, 6835 (1988).

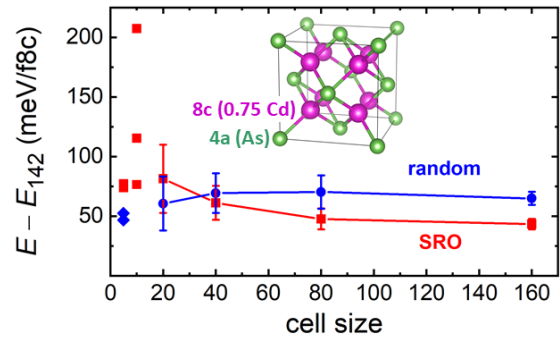


Figure 3. Energetics of empty-site disorder in Cd_3As_2 obtained from DFT supercell calculations. The energy is given per 8c site of the underlying fluorite lattice (insert), which is $\frac{3}{4}$ occupied with Cd. Data for short range ordered configurations in which As is exclusively coordinated by 6 Cd is shown in red. The energies of non-SRO structures (blue) approach the limit for a random distribution in the larger cells.

Overcoming Optical Selection Rules in Materials by Extreme Localization of Light

Hayk Harutyunyan, Department of Physics, Emory University, Atlanta, GA 30322

Program Scope

The main scope of this program is to study the new physical phenomena in light matter-interactions that arise due to the nanoscale confinement. Typically, the optical interactions in nanoscale materials are determined by the material composition of and the geometric properties nanostructures. In this conventional approach, the quantum transitions and carrier dynamics are governed by the electronic structure of the constituent materials. Nanoscale modification of the material structure and geometry can add a new way of controlling electronic transitions due to e.g. carrier confinement or carrier injection across heterogeneous interfaces. However, typically, the role of the specific properties of the optical modes are overlooked when studying the mechanisms of photo-assisted transitions.

The goal of this program is to study the optical absorption adopting a different approach and try to control the light-matter interactions by manipulating the properties of the excitation light itself. To this end, we use nanostructured materials to design special interfaces and nanocavities with desired optical properties. These structures support optical modes with tunable spatial and temporal parameters such as field enhancement and localization, field gradients and quality factors. By using optical spectroscopic methods we engineer and study fundamentally novel types of optical interactions at the nanoscale.

Recent Progress

Strong modification of light-matter interaction can be achieved in **ultrathin metallic films**. In such structures, the surface bound plasmonic modes feature very large field gradients that can dramatically modify the light absorption in the metal [1]. The main novel mechanism of such modified optical absorption is thought to be due to the resonantly enhanced Landau damping in metals, which leads to efficient free carrier absorption. The main obstacle for observing these new effects is the availability of high quality ultrathin (sub 10 nm) plasmonic continuous films. Typically, fabrication of such films is a challenge, because metal grows in the Volmer –Weber (three-dimensional) mode on common substrates such as fused-silica or silicon. In the initial stage of film growth, the deposited metal atoms cluster together and form isolated islands. As the deposition continues, these isolated islands increase in size, and eventually merge

to form a percolated conductive thin film. Such a three-dimensional (3D) growth mode leads to a minimum thickness value, commonly referred to as the “percolation threshold”, below which the deposited plasmonic metal (Au, Ag) layer is discontinuous and exhibits a rough surface morphology. To reduce the percolation threshold of thin films and improve their surface morphology, a thin wetting layer of a different material is generally utilized before metal deposition, however this also introduces additional optical losses.

Recently, we have demonstrated that wetting layer-free, ultrathin and plasmonic Au films can be fabricated by deposition directly on fused-silica substrates cooled to cryogenic temperatures. Cooling down the substrate decreases the diffusion rate of the metal atoms, thus, enabling the formation of stable metal nanoclusters of smaller sizes, thus lowering the percolation threshold. This suppresses the 3D clustering and favors the formation of percolated ultrathin metal films (Fig. 1). Using this approach, we showed wetting layer-free, plasmonic Au films down to the measured layer thickness of 3 nm.

Another approach for achieving unprecedented control over the light-matter interactions is centered on the idea of **time-varying metasurfaces** [2]. In a recent work, we used amorphous Ge to fabricate semiconductor metasurfaces comprising of an array of sub-wavelength resonators. These structures form cavities trapping the excitation light with a resonant peak in the mid-infrared spectral region at $\sim 3.3 \mu\text{m}$. Typically, the light matter interaction in the cavities are controlled by their geometric and material properties such the mode volume, cavity losses etc. However, using our approach of modifying the optical interaction by controlling the properties of the light itself, we introduce time-dependent losses in such cavities which drastically affect the nature of the light-matter interaction. We use a femtosecond laser pulse at above-bandgap energies to modify the refractive index of the cavity by generating electron-hole plasma via single photon absorption. This dramatically changes the quality factor of the resonator on an ultrafast time scale resulting in unusual and seemingly non-intuitive physical effects, such as negative extinction (Fig. 2). This is a direct result of the ultrafast Q-switching of the mode through time-dependent damping rate. The temporal profile of the fields trapped in the cavity no longer resemble an exponential decay as in static resonators but

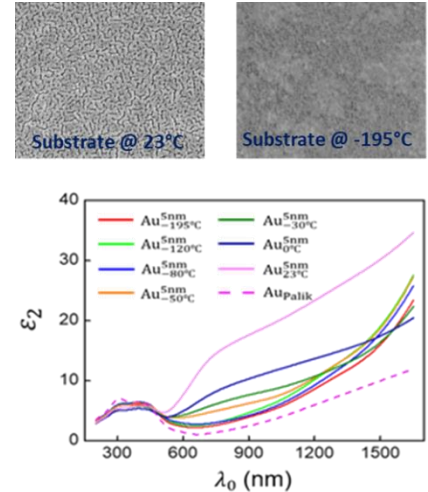


Fig. 1. SEM of 5 nm thick Au films deposited at room temperature and cryogenic temperature (top panels). The imaginary part of the dielectric constant decreases as a function of substrate temperature indicating formation of continuous films (bottom panel).

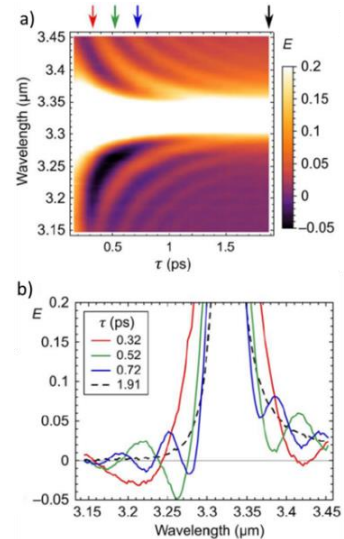


Fig. 2. a) Experimental extinction for different pump-probe delay times τ . (b) Extinction spectra for $\tau = 0.32$ ps (red), 0.52 ps (green), 0.72 ps (blue), and 1.92 ps (black dashed)

rather show an abrupt disappearance. This leads to a redistribution of spectral components, which manifests itself in tunable bands of negative extinction. More intuitively, negative extinction originates from spectral broadening of the captured (resonant) photons caused by the dynamic Q-switching and their subsequent constructive interference with the non-resonant photons present in the broadband incident pulse. We believe that this time-varying metasurfaces will find use in novel light sources, pulse shaping schemes, amplifiers, and wavelength-division multiplexing strategies.

One important research direction pursued in this program is studying the effect of electromagnetic field localization of the nature of light-matter interaction. To this end, we have explored **the interaction of magnons** (quanta of spin waves in magnetic materials) **with nano-confined light**. Typically, micro-focus Brillouin light scattering is used for the spectroscopic and spatial characterization of these elementary excitations in materials [3]. However, the small momentum of light limits the accessible excitations to the center of the Brillouin zone. By utilizing a metallic nanoantenna fabricated on ferromagnetic materials, we explore Brillouin light scattering from large-wavevector, high-frequency spin wave excitations that are inaccessible with free-space light.

Our results show that a nanoscale metallic antenna generate large-momentum components of optical field, and simultaneously increase its local intensity due to a combination of enhanced reflection and constructive interference. This leads to inelastic light scattering by spin-wave excitations with large wavevectors, inaccessible to free-space optical techniques due to momentum conservation (Fig.3). The spectral limitations associated with the small momentum of light, as well as the presented approach to large-momentum generation, are quite general. Thus, we expect that our approach can be extended to the optical studies of other types of excitations, such as phonons, excitons, and electronic transitions. The latter can facilitate more efficient optical detectors and photovoltaics based on indirect-bandgap semiconductors, where large momentum of electron-hole pairs results in an optical absorption bottleneck.

In the next research direction we explore **the nonlinear optical interactions in strongly-coupled 2-dimensional semiconductors** facilitated by the nanoscale confinement of light. In this case, the nano-confined optical modes give rise to strong coupling between the electromagnetic fields of the plasmonic nanoparticles and atomic layers of transition metal dichalcogenides. The coupling leads to the formation of polaritonic bands with

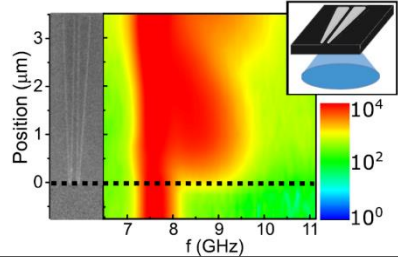


Fig. 3. Maps of the μ -BLS spectra of thermal spin waves at 295 K, as a function of the position of the probing laser spot along the biwire antenna.

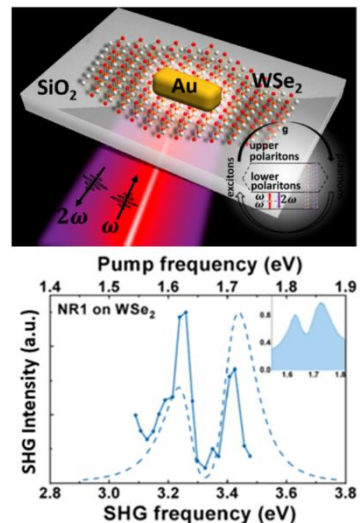


Fig. 4: Nonlinear Rabi splitting in a single Au nanocavity strongly coupled to a WSe₂ monolayer.

characteristic Rabi splitting [4]. In this work we exploit nonlinear-optical response of the system in the non-perturbative regime. Typically, the nonlinear optical effects such as frequency conversion are treated as small perturbations to the linear optical effects. This is because the nonlinear optical susceptibilities are very small compared to their linear counterparts. However, the strongly coupled system opens up a regime of interaction where the nonlinear effects can be strongly enhanced. The platforms with nanoscale confinement of light used in our project are an ideal testbed for exploring these interactions. Our results show that second harmonic generation can be strongly enhanced at polaritonic resonances (Fig. 4). We believe that these efforts will lay the groundwork for practical, scalable, and compact nonlinear sources and entangled photons generation for integrated room temperature quantum platforms.

Finally, we contributed to an invited review article on **hot carrier dynamics in nanostructures**. The PI has authored several seminal papers on this topic in the recent years. Typically, optical absorption in noble metals produces excited carriers near the Fermi level. However, the nanoscale confinement of fields leads to the breakdown of the dipole approximation resulting in resonant intraband absorption [5]. Hot carrier processes are of a great importance for various application in photocatalysis, photodetection, and photovoltaics. The article draws on the expertise and published research of our lab and reviews the recent literature on this topic.

Future Plans

In our future research, we will explore the light-induced ultrafast modulation of the optical properties of materials. We will study how trapping of light in semiconductor microresonators leads to the modification of their dielectric constant. In typical materials it is hard to achieve ultrafast modulation of the optical properties with large amplitudes at low excitation powers, which hampers viable application in photonics [6]. We aim develop metamaterials that can exhibit strong Kerr nonlinearities at modest switching powers based on the excitation of transient hot carriers.

References

- [1] T. Heilpern *et al.*, *Nat. Commun.*, 9, 1853, (2018)
- [2] A.M. Shaltout, V.M. Shalaev, M.L. Brongersma, *Science* 364, 648, (2019)
- [3] V. E. Demidov *et al.*, *Phys. Rev. Lett.*, 107, 107204, (2011)
- [4] G. Khitrova *et al.*, *Nat. Phys.*, 81, (2006)
- [5] H. Harutyunyan et al., *Nat. Nanotechnol.*, 10, 770, (2015)
- [6] M. Taghinejad *et al.*, *ACS Photonics.*, 6, 1082, (2019)

Publications

1. Second Harmonic Generation from a Single Plasmonic Nanorod Strongly Coupled to a WSe₂ Monolayer C. Li, X. Lu, A. Srivastava, S. D. Storm, R. Gelfand, M. Pelton, M. Sukharev, and H. Harutyunyan, *Nano Lett.*, <https://doi.org/10.1021/acs.nanolett.0c03757>, (2021)
2. Brillouin light scattering of spin waves inaccessible with free-space light R. Freeman, R. Lemasters, T. Kalejaiye, F. Wang, G. Chen, J. Ding, M. Wu, V. E. Demidov, S. O. Demokritov, H. Harutyunyan, and S. Urazhdin, *Phys. Rev. Research*, 2, 033427, (2020)
3. Hot-carrier dynamics in catalysis H. Harutyunyan, F. Suchanek, R. Lemasters, J. J. Foley, *MRS Bulletin*, 45, 32 - 36, (2020)
4. Time-variant metasurfaces enable tunable spectral bands of negative extinction M. R. Shcherbakov, R. Lemasters, Z. Fan, J. Song, T. Lian, H. Harutyunyan, and G. Shvets, *Optica*, 6, 1441-1442 (2019)
5. Ultrathin Wetting Layer-Free Plasmonic Gold Films R. Lemasters, C. Zhang, M. Manjare, W. Zhu, J. Song, S. Urazhdin, H. Lezec, A. Agrawal, and H. Harutyunyan, *ACS Photonics*, 6, 2600, (2019)

Weyl Semimetals for High-Thermopower Transverse Thermoelectric Transport

Sarah J. Watzman

Department of Mechanical and Materials Engineering, University of Cincinnati

Program Scope

Recently discovered Weyl semimetals (WSMs) have inspired considerable excitement due to their unique surface states and high-mobility charge carriers.^{1,2} These attributes make WSMs potentially transformative materials for thermoelectric energy conversion^{3,4,5} and viable candidates for transverse thermoelectric devices such as Nernst generators and Ettingshausen coolers. However, the unique transport mechanisms present in WSMs are not well understood. Determining which fundamental transport mechanisms contribute to and enhance thermoelectric transport in WSMs would enable focused materials development, paving the way toward dramatically more efficient solid-state energy conversion devices.

The long-term goal of this project is to determine, and be able to manipulate and enhance, the transport mechanisms present in WSMs, making these materials viable as solid-state energy conversion materials. This work seeks to determine the relationship between thermal transport, the tilting of a WSM's Dirac bands (symmetric = Type I or asymmetric = Type II), and the type of broken symmetry (inversion symmetry or time-reversal symmetry). Single-crystalline materials in all four categories of Table 1 will be systematically evaluated by investigating coupled thermal, electrical, and magnetic transport measurements. The effects of grain size on transport in WSMs will also be determined by comparing thermoelectric transport coefficients in polycrystalline samples to that of single-crystalline samples. Through this study, a foundational understanding of WSM transport will be gained, with the ultimate goal of transforming the field of thermoelectrics to viably include WSMs and the Nernst effect.

Table 1: Classification of WSMs with examples of candidate materials listed. In this work, comparisons will be made across rows and along columns.

	Type I (Symmetric Dirac Bands)	Type II (Tilted Dirac Bands)
Breaks Inversion Symmetry	(Ta, Nb)(As, P)	(Mo, W)(Te ₂ , P ₂)
Breaks Time-Reversal Symmetry	HgCr ₂ Se ₄	YbMnBi ₂

Recent Progress

Our research efforts in the first 1.5 years of this project have focused on (i) implementing an experimental setup for measuring the Nernst effect and (ii) studying the grain-size dependence of transport in polycrystalline NbP.

Experimental Setup for Measuring the Nernst Effect

A Quantum Design DynaCool Physical Property Measurement System (PPMS) was installed in the PI's lab prior to the beginning of this project. Although the PPMS comes equipped to measure longitudinal transport (Seebeck effect, electrical resistivity, thermal conductivity), it must be modified to measure the Nernst effect. We have built an electrical breakout box for the PPMS which allows us to control the PPMS chamber (and associated temperature and magnetic field) while using our own external electronics (nanovoltmeter and precision current source). LabVIEW

controls code has been developed for specialized measurements necessary in this project, including that of the Nernst effect.

Grain-Size Dependence of Transport in NbP

Table 2: NbP samples and their associated average grain sizes

Sample	Annealing Time, Temperature	Avg. Grain Size
Sample 1	n/a	2.1 micron
Sample 2	1 week, 1000°C	3.17 micron
Sample 3	2.5 weeks, 1100°C	4.55 micron
Sample 4	5 weeks, 1100°C	in progress
Ref. [6] EES 11, 2813 (2018)	n/a	2 micron
Ref. [7] PRB 97, 161404(R) (2018)	n/a	n/a (single-crystalline)

We have obtained polycrystalline samples of NbP, synthesized in Prof. Dr. Claudia Felser's group at the Max Planck Institute for Chemical Physics of Solids in Dresden, Germany, using methods similar to those in ref. [6]. In order to study the grain-size dependence of transport, samples have been annealed for varying amounts of time to promote grain growth, as indicated in Table 2. The average grain size of the samples has been determined from electron backscatter diffraction. Results from polycrystalline samples in this work (Samples 1-4) are compared to published data on polycrystalline NbP in ref. [6] and single-crystalline NbP in ref. [7].

Figure 1a shows results of the Nernst thermopower as a function of magnetic field in Sample 1. The maximum Nernst thermopower is found to be

43.4 $\mu\text{V K}^{-1}$ at 200.9 K at +9 T and -60.6 $\mu\text{V K}^{-1}$ at 110.6 K at -9 T. The Nernst thermopower is unsaturated at $|9 \text{ T}|$ for all temperatures measured. The Nernst thermopower is an odd function of magnetic field, and the slight asymmetry in this result is currently being resolved. Although the Nernst thermopower for Sample 1 is substantially large, it is still significantly smaller than that of the single crystal from ref. [7], as shown in Figure 1b. Furthermore, for both Sample 1 and the polycrystalline sample of ref. [6], the temperature at which the maximum Nernst thermopower occurs is increased from that of the single crystal in ref. [7].

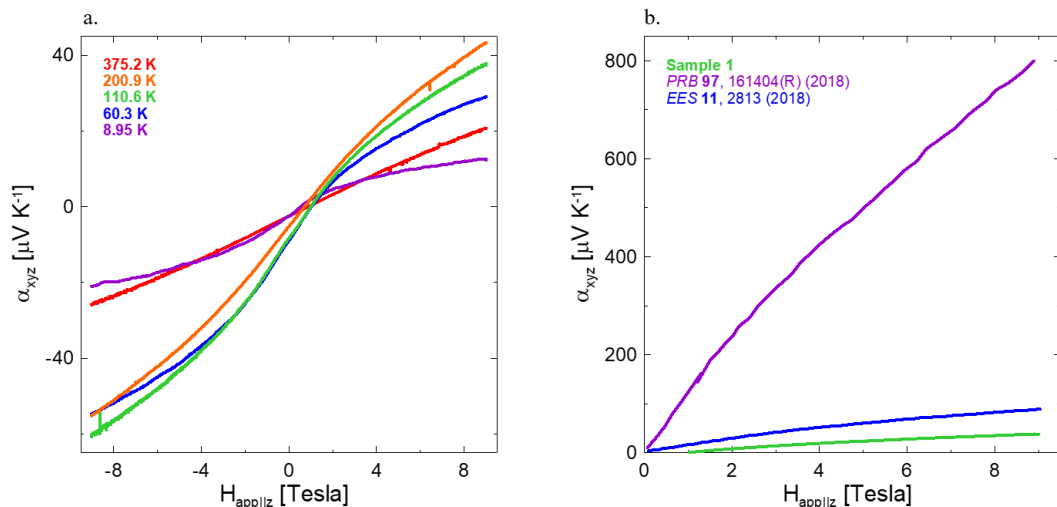


Figure 1: a. Nernst thermopower as a function of applied magnetic field in Sample 1. b. Comparison of Nernst thermopower as a function of applied magnetic field at $\sim 110 \text{ K}$.

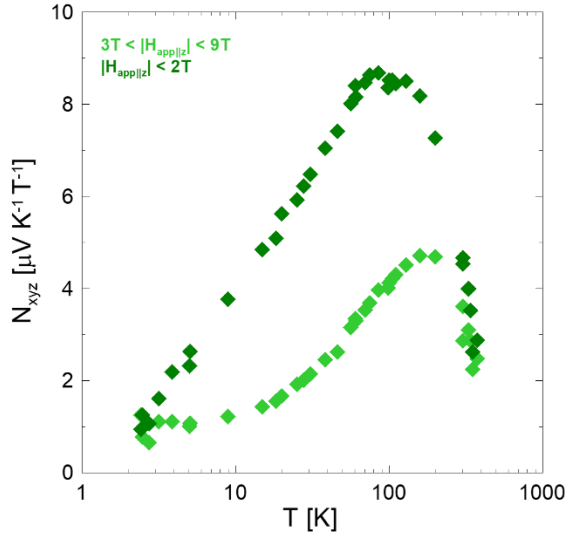


Figure 2: Temperature dependence of the Nernst coefficients in Sample 1.

increases with increasing grain size. Especially noteworthy is the order of magnitude decrease in thermal conductivity when moving from single-crystalline to polycrystalline NbP. Thermoelectric materials are characterized by the thermoelectric figure of merit, $zT = (\sigma\alpha^2/\kappa)T$, where σ is the electrical conductivity, α is the thermopower, and κ is the thermal conductivity. A transverse thermoelectric figure of merit, $zT_{xyz} = (\sigma_{yyz}\alpha_{xyz}^2/\kappa_{xxz})T$, can also be defined using the Nernst thermopower, α_{xyz} . Although the decrease in grain size from single-crystalline to polycrystalline NbP sufficiently decreases the Nernst thermopower, the significant decrease in thermal conductivity offers potential for NbP exhibiting a promising zT_{xyz} . Ongoing work in Samples 1 and 2 is considering the magneto-resistivity, magneto-thermal conductivity, and Hall effect in order to determine the temperature dependence of zT_{xyz} . Also noteworthy is the significant increase in thermopower (Figure 3a) in Samples 1 and 2. Single-crystalline NbP exhibits a maximum thermopower of $-8 \mu\text{V K}^{-1}$ at 90 K, while Sample 1 has a maximum of $-43.25 \mu\text{V K}^{-1}$ at 64.5 K and Sample 2 has a maximum of $-67.14 \mu\text{V K}^{-1}$ at 68.5 K. Underlying reasoning for this unexpected increase in thermopower with a decrease in grain size is currently ongoing. Additionally, chemical analysis of Samples 1-3 using ICP-OES is currently ongoing.

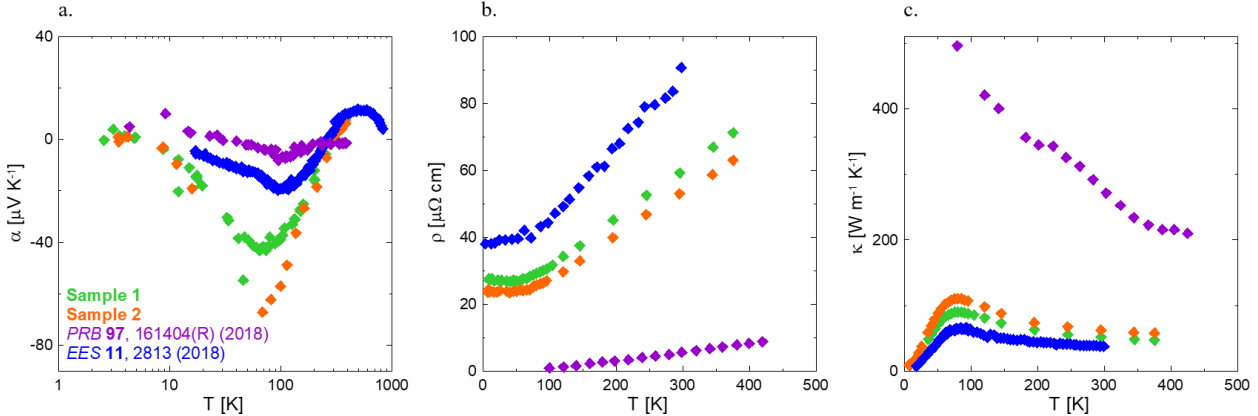


Figure 3: Sample comparison of **a.** thermopower, **b.** electrical resistivity, and **c.** thermal conductivity.

Future Plans

We will finish the full transport characterization of the polycrystalline samples of NbP, Samples 1-4, completing data sets such that both zT and zT_{xyz} can be determined as functions of temperature. Results will be analyzed and compared to the published work. The overarching goal of this project is to determine a balance between a large thermopower/Nernst thermopower, typically associated with larger grain sizes, and a small thermal conductivity, typically associated with smaller grain sizes, such as to maximize zT and zT_{xyz} . Single-crystalline WSMs are challenging to synthesize and small in size, while polycrystalline samples are significantly larger and therefore more reasonable for use in engineering applications. Determining this balance will help further the viability of WSMs for thermoelectric devices. We are also beginning a similar polycrystalline study in MoP, a triple point fermion material recently determined to have an extremely high electrical conductivity.⁸

We will next determine the effects of Dirac band tilting on transport in WSMs that break inversion symmetry by characterizing transport in WTe₂, a Type II WSM. Previous work in NbP determined that its large Nernst effect could be attributed to Dirac band-dominated transport, with a maximum Nernst thermopower occurring at the temperature where the chemical potential reached the energy of the Weyl points;⁷ the density of states (DOS) is zero here in a Type I WSM, and the carriers are compensated due to the symmetry of the bands. This is not the case in a Type II WSM like WTe₂, which could have a finite DOS at the energy of the Weyl points and is not compensated due to asymmetry in the Dirac bands. The main experimental conclusions will stem from the temperature dependence of thermopower and the magnetic field dependence of Nernst thermopower. We will start with bulk, single-crystalline WTe₂ then move to polycrystalline WTe₂. From here, we will continue following the proposed research plan.

References

- ¹ M. Z. Hasan, S.-Y. Xu, I. Belopolski, S.-M. Huang. Discovery of Weyl fermion semimetals and topological Fermi arc states. *Annu. Rev. Condens. Matter Phys.* **8**, 289-309 (2017).
- ² B. Yan, C. Felser. Topological materials: Weyl semimetals. *Annu. Rev. Condens. Matter Phys.* **8**, 337-354 (2017).
- ³ R. Lundgren, P. Laurell, G. A. Fiete. Thermoelectric properties of Weyl and Dirac semimetals. *Phys. Rev. B* **90**, 165115 (2014).
- ⁴ G. Sharma, P. Goswami, S. Tewari. Nernst and magnetothermal conductivity in a lattice model of Weyl fermions. *Phys. Rev. B* **93**, 035116 (2016).
- ⁵ J. Hu, S.-Y. Xu, N. Ni, Z. Mao. Transport of topological semimetals. *Annu. Rev. Mater. Res.* **49**, 11.1-11.46 (2019).
- ⁶ C. Fu, S. N. Guin, S. J. Watzman, et al. Large Nernst power factor over a broad temperature range in polycrystalline Weyl semimetal NbP. *Energy Environ. Sci.* **11**, 2813-2820 (2018).
- ⁷ S. J. Watzman, T. M. McCormick, et al. Dirac dispersion generates unusually large Nernst effect in Weyl semimetals. *Phys. Rev. B* **97**, 161404 (2018).
- ⁸ N. Kumar, Y. Sun, M. Nicklas, S. J. Watzman, et al. Extremely high conductivity observed in the triple point topological metal MoP. *Nat. Commun.* **10**, 2475 (2019).

Publications

- A. Saini, S. J. Watzman, J.-H. Bahk. Cost-performance trade-off in thermoelectric air conditioning system with graded and constant material properties. *arXiv:2011.02585* (2020).

Orienting Strained Interfaces designed to Direct Energy Flow

Dongkyu Lee, University of South Carolina

Program Scope

Achieving fast ion transport at reduced temperatures is a key requirement to develop advanced oxide-based energy applications. This research program aims to develop a new paradigm for oxide heterostructures with an exceptionally large number of strained interfaces that are designed to direct energy flow by controlling the orientation of interfaces for fast ion transport along the interfaces, and to explore the key role of interfacial strain in oxygen ion migration. On the synthesis side, pulsed laser deposition (PLD) of oxide multilayer films and vertical heteroepitaxial nanostructures will play an important role. In combination with electrochemical impedance spectroscopy (EIS) and electrical conductivity relaxation (ECR), real-time temperature-dependent high-resolution X-ray diffraction (HRXRD) and atom probe tomography (APT) will be utilized to understand the effect of interfacial strain on oxygen ion migration. The central challenge of this program is to create, understand, utilize self-assembled vertical heteroepitaxial nanostructures with the goal of obtaining and understanding fast ion transport properties by modulating interfacial strain. The specific objectives of this research program are: (1) to synthesize multilayer thin films and vertical heteroepitaxial nanostructures with fluorite Gd-doped CeO₂ (GDC) and bixbyite RE₂O₃ (RE = Y and Sm), (2) to evaluate the interfacial strain states under various temperature and ambient conditions, (3) to understand the effect of interfacial strain on ionic conductivity of the proposed nanostructures, (4) to understand the three-dimensional (3D) atomic structure of the proposed material design and interface phenomena at the atomic scale. The success of this program will provide a foundation of essential data and understanding for fast ionic conducting materials design. Beyond understanding the interfacial phenomena on the strain-enhanced ion transport properties, this research will also help facilitate the implementation of oxide heterostructures for practical applications.

Recent Progress

The grant commenced on 09/01/2020. One graduate student and one postdoctoral research associate have been fully supported by this DOE project. For the first part of our project, we have focused primarily on the effect of interfacial strain on the ionic conductivity of single-layer and multilayer thin films.

Single-layer GDC and RE₂O₃ films

A single-layer thin film can be considered as a heterostructure at the interface with the substrate, and indeed, the first evidence of interfacial effects on ionic conductivity of oxide electrolytes was derived from the study of ultra-thin films [1]. Furthermore, prior to the synthesis of multilayer thin

films, the growth of single-layer films is generally required for optimizing growth conditions for each layer. Therefore, single-layer GDC, Y_2O_3 , and Sm_2O_3 thin films were grown by PLD on single crystalline Al_2O_3 substrates as Al_2O_3 can eliminate the contribution to the in-plane conductivity of the films. PLD was performed using a KrF excimer laser at $\lambda = 248$ nm, 10 Hz pulse rate, and 50 mJ pulse energy under an oxygen partial pressure, $p(\text{O}_2)$, of 50~100 mTorr at 700 °C. After completing the film deposition, the samples were cooled down to room temperature in the PLD chamber for ~1 h under the same $p(\text{O}_2)$ as the film growth condition. As shown in Figure 1, all films were highly epitaxial and (111)-oriented. Off-normal phi-scan analysis confirmed that all films were the six-fold symmetry with respect to the [103] axis of the substrate (not shown here). The observation of six-fold symmetry may suggest the presence of twinned in-plane alignments but further investigations are needed. In order to investigate the out-of-plane ionic conductivity of GDC, single-layer GDC, Y_2O_3 , and Sm_2O_3 thin films were also deposited on (001) SrTiO_3 (STO) substrates. All films were grown epitaxially along (001) direction.

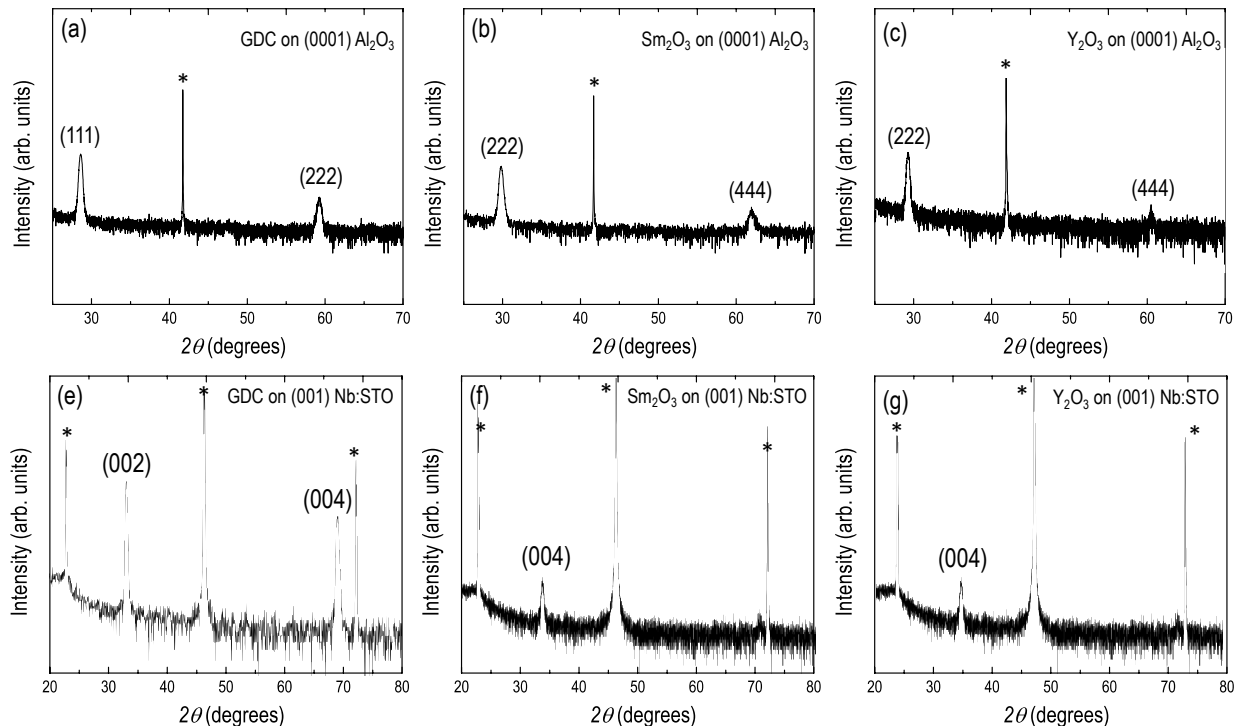


Figure 1. XRD θ - 2θ patterns of (a) GDC, (b) Sm_2O_3 , and (c) Y_2O_3 thin films on (0001) Al_2O_3 and (e) GDC, (f) Sm_2O_3 , and (g) Y_2O_3 thin films on (001) Nb:STO substrates. The substrate peaks are indicated with *.

To evaluate the ionic conductivity of the samples, *in-situ* EIS was employed. To assess the ion transport property of the single-layer thin films, we fabricated electrochemical cells of Pt/single-layer film/Nb:STO/Pt. The EIS measurements were conducted in the frequency range of 1 mHz to 1 MHz with AC amplitude of 10 mV and zero DC bias at temperatures between RT and 700 °C, using the Frequency Response Analyzer module (FRA, Solartron 1260). The out-of-plane ionic conductivity for the single-layer thin films was extracted from the real impedance of the

semicircles in the Nyquist plot, which can be modelled by an equivalent circuit with two serial elements each containing a resistor and a constant phase element. We confirmed that the conductivity of the single-layer thin films is independent of an oxygen partial pressure, indicating that the contribution of electronic conductivity to the total conductivity can be negligible under our experimental conditions. We also investigated the in-plane ion transport properties of the films. As expected, both RE_2O_3 films show extremely low ionic conductivity values, which indicates that RE_2O_3 can be used to avoid their contribution to the measured conductivity in multilayer thin films. At high temperatures, the out-of-plane ionic conductivity of the GDC film is similar to the in-plane ionic conductivity. However, the activation energies for the out-of-plane and in-plane ionic conductivity were found to be different, which might be attributed to different growth orientations of the GDC films or different ion flow directions.

Lateral GDC- RE_2O_3 multilayer films

Careful materials selection must first be taken into account to deconvolute the strain contribution from multiple factors to the interfacial ionic conductivity in multilayer thin films. First of all, two materials should be composed of an ionic conductor with abundant oxygen vacancies and an insulator to exclude the space charge effect and the contribution to the ionic conductivity, respectively. In addition, to form the coherent interface the lattice mismatch between two materials should be in the range of $\sim \pm 2\%$. In this context, a combination of fluorite GDC and bixbyite RE_2O_3 ($\text{RE} = \text{Y}$ and Sm) can be one of the best material combinations. As confirmed in Figure 2, Y_2O_3 and Sm_2O_3 can be considered as an insulator, which can prevent their contribution to the measured conductivity. Indeed, Y_2O_3 and Sm_2O_3 can theoretically introduce $\sim -2.1\%$ compressive and $\sim 1\%$ tensile strain, respectively, into GDC [2,3], which is expected to create the coherent interfaces enabling the investigation of the sole effect of interfacial strain on ion conduction (Figure 3). As shown in Figure 4, we successfully synthesized lateral GDC- RE_2O_3 multilayer thin films by PLD. All films were highly epitaxial. As expected, GDC films were found to be tensile strained with Sm_2O_3 and compressively strained with Y_2O_3 . Off-normal phi-scan analysis using

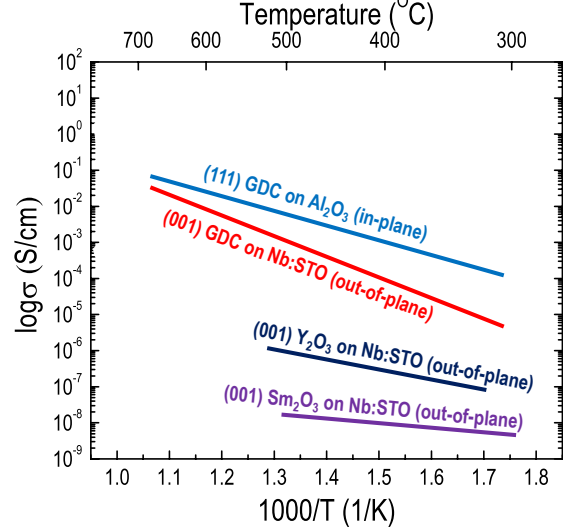


Figure 2. Ionic conductivity of GDC, Y_2O_3 , and Sm_2O_3 films obtained from EIS.

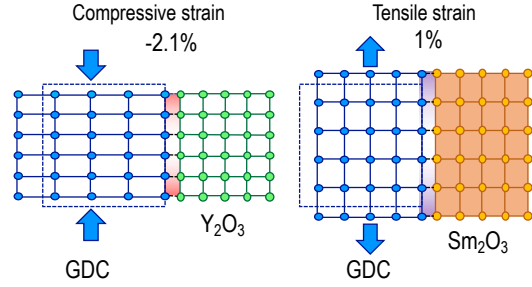


Figure 3. Epitaxy and strain generation by lattice mismatch in GDC- Y_2O_3 and GDC- Sm_2O_3 .

(200) and (103) reflection confirmed that GDC and RE₂O₃ films were rotated by 30° with respect to the [103] Al₂O₃.

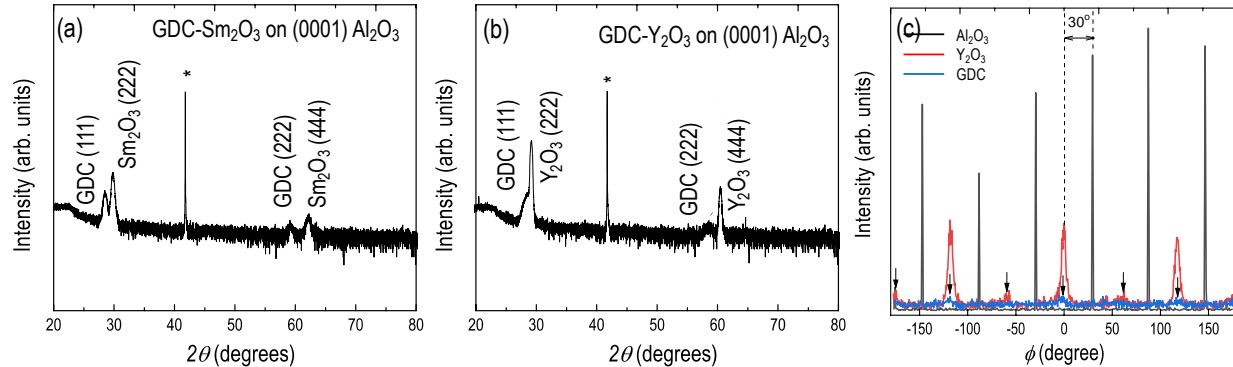


Figure 4. XRD θ -2 θ patterns of (a) GDC-Sm₂O₃ and (b) GDC-Y₂O₃ thin films on (0001) Al₂O₃ substrates. The substrate peaks are indicated with *. (c) In-plane phi scans of the (200), (400), and (103) reflection of GDC, Y₂O₃, and Al₂O₃, respectively.

Future Plans

The next step is to assess the interfacial strain and the in-plane ionic conductivity of GDC in the multilayer thin films. At the compressively strained interface between GDC and Y₂O₃, a decrease in the ionic conductivity of GDC is expected by increasing the vacancy formation energy and the vacancy migration barrier. In contrast to the compressively strained interfaces, the tensile strained interface between GDC and Sm₂O₃ is anticipated to enhance the ionic conductivity of GDC despite the relatively small tensile strain state. After the investigation of the multilayer thin films, we will move to the synthesis of vertical heteroepitaxial thin films (Figure 5).

References

- [1] Kosacki, I.; Rouleau, C.M.; Becher, P.F.; Bentley, J.; Lowndes, D.H. Surface/interface-related conductivity in nanometer thick YSZ films. *Electrochim. Solid-State Lett.* 2004, 7, A459.
- [2] Matovic, B.; Boskovic, S.; Zivkovic, L.; Vlajic, M.; Krstic, V. Lattice parameters of Gd-doped ceria electrolytes. *Mater. Sci. Forum* 2005, 494, 175-180.
- [3] Adachi, G. Y.; Imanaka, N. The binary rare earth oxides. *Chem. Rev.* 1998, 98, 1479-1514.

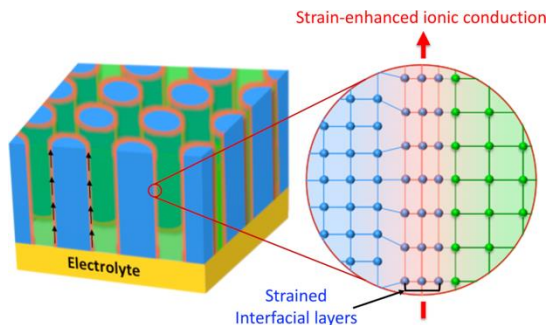


Figure 5. A schematic of a self-assembled vertical heteroepitaxial nanostructure.

Publications

Dongkyu Lee*, Gene Yang, Yuxi Ma, Evan Helfrick, “Influence of Stoichiometric Surface Changes on Surface Reconstructions in Epitaxial ABO_3 Perovskite Thin Films”, In revision, *Curr. Opin. Solid State Mater. Sci.* (2021)

Tailoring Photophysical Energy Transfer for Selective Separations of Critical Lanthanides

Andrew Ferguson, Christopher Chang, Mark Steger

Materials, Chemical, and Computational Science Directorate, National Renewable Energy Laboratory

Mark Jensen, Alan Sellinger, Thomas Mallos, Anastasia Kuvayskaya
Chemistry Department, Colorado School of Mines

Eric Schelter, Kevin Ruoff
Department of Chemistry, University of Pennsylvania

Program Scope

To overcome limitations of cation-size based separations of critical lanthanide elements,¹ or rare earths (REs), we aim to develop a novel approach that exploits the *unique and discontinuous electronic structures* of well-shielded 4f orbitals of the individual lanthanide ions,²⁻³ via *dynamic and element specific photo-induced modifications of the chemical environment* surrounding the metal ions. This concept is built on synthesis of ligands with the desired chemical and physical motifs⁴⁻⁷ that will ultimately enable demonstration of efficient solution-phase separations *via* control of (i) large, dynamic excited-state perturbations of the photophysical properties of the complexes or (ii) sensitization of ligand-centered photo-chemical reactions.⁸⁻⁹ This work will expand our understanding and control of excited-state energy flow in lanthanide complexes by:

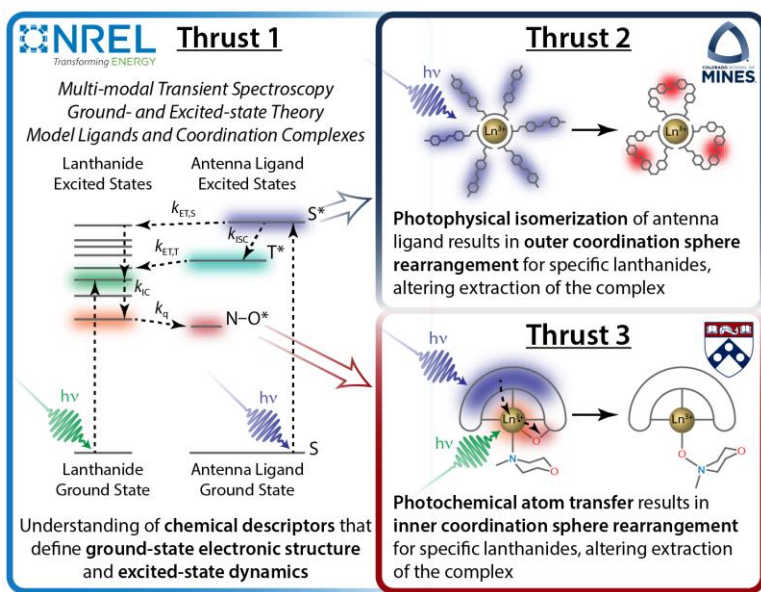


Fig. 1. Schematic illustrating the combined experimental-theoretical approach that will yield fundamental understanding to enable novel photophysical and photochemical lanthanide separations.

- Developing chemical descriptors of ground-state electronic structure & excited-state dynamics
- Probing energy transfer between lanthanide ions and surrounding coordination ligands
- Inducing lanthanide-selective photophysical/photochemical changes in the coordination sphere

Recent Progress

1. Development of Organophosphorous Ligands and Complexes

The premise of our work is that direct or indirect photo-excitation of organophosphorous ligands in the complexes of REs can change the intraligand steric effects in those complexes thereby altering the solubility and separations behavior of particular rare earths. To accomplish this for mixtures of a range of rare earths, the intrinsic thermodynamic size selectivity of the current generation of the ground state organophosphorous ligands used for the separation needs to be minimized so sufficient selectivity for particular rare earths can be generated in those excited complexes. This is contrary to years of work focused on increasing the selectivity for adjacent rare earths across the series.

We have begun this work by experimentally studying the intra-rare earth selectivity of organophosphonate ligands to understand how steric bulk and ground state dipole in the extracting ligands specifically creates selectivity for rare earths. Our hypothesis is that increased steric bulk will systematically quench rare earth size selectivity, while control of the ligand dipole will alter the acidity of the phosphonic acids⁵ and asymmetry between the two phosphonic acid substituents (phenyl-vinyl and OR groups in Fig. 2) will counter the effect of increased bulk. As we probe this hypothesis, the principles uncovered will be designed into photo-switchable ligands with variable interligand interactions.

The Sellinger group at Colorado School of Mines has prepared selected phenyl-vinylphosphonic acids with varying dipole extremes as shown in Figure 2. These reactions involve the palladium catalyzed Heck reaction of vinyl phosphonic acid with various bromo and iodo functionalized benzene derivatives.

The phenyl-vinyl phosphonic acids have been purified and initial reactions to prepare the monoethylhexyl-acid target products are in progress (dashed arrows; Fig. 2). These initial monoalkylation reactions have been challenging to isolate the products of interest and we are looking at various synthetic pathways to achieve the desired products.

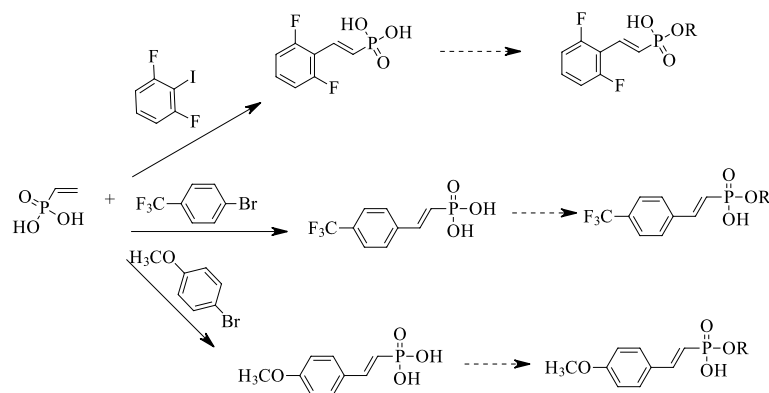


Fig. 2. Synthetic scheme for target phenyl-vinylphosphonic acid ligands with tuned ground state dipoles.

2. Development of Oxygen-atom Transfer Ligands and Complexes

For our initial efforts towards the goal of developing light-driven separations of rare earth elements, the Schelter group at University of Pennsylvania we have been pursuing air- and moisture-stable dysprosium (Dy) and (Y) and yttrium tris-hexafluoroacetylacetone (hfac) complexes appended with nitroxide antenna ligands for sensitization (Fig. 3a). The complexes comprising the tert-butyl 2-pyridyl nitroxide (2pyNO) ligand,¹⁰ $\text{RE}(\text{hfac})_3(2\text{pyNO})$ $\text{RE} = \text{Y, Dy}$,

have successfully been isolated as orange solids (Fig. 3b). They were characterized by ^1H and ^{19}F NMR spectroscopy and analyzed by UV/Vis/NIR absorption and luminescence spectroscopies. The spectra both display strong features in the UV region (250–350 nm) owing to absorption by the hfac ligands, with weaker transitions at ca. 500 nm and 700 nm due to the 2pyNO ligand, and even weaker transitions due to the Dy(III) ion (Fig. 3c). The photoluminescence (PL) spectra, as expected, differ in the presence of characteristic f-f PL peaks for the Dy analogue around 475 and 575 nm.

We have begun computational studies on an oxygen atom transfer reaction in the model $\text{Dy}(\text{hfac})_3(2\text{pyNO})$ complex, and the Yttrium transition metal analog. The oxygen atom transfer to transform a nitroxide donor reactant to a pyridyl-N-oxide product complex is predicted to occur in the chemically reduced anionic form of these complexes. The anions serve as a convenient ground-state ligand proxy for targeted MLCT lanthanide complex excited states. Preliminary DFT studies with relativistic core potentials show the anticipated difference in numerical behavior between the Y analog (with no d or f electrons and simple SCF convergence) and the Dy complex (with a partially filled f shell and difficult SCF convergence). In addition, a transition state structure for the Y complex has not been found, lending some support to the idea of a stepwise reaction mechanism. These preliminary studies illustrate the complexity that may be found once investigations move into the excited manifold of the target rare earth complexes.

More recently we have been pursuing the synthesis of analogous RE complexes where the 2pyNO ligand is replaced with tert-butyl 6-bipyridine nitroxide (6bpyNO). The precursor hydroxylamine, 6bpyNOH has been isolated as a mixture with the oxidized 6bpyNO and will be used to synthesize $\text{RE}(\text{hfac})_3(6\text{bpyNO})$ for follow-on characterization. In parallel, we have begun to investigate N-oxide ligands as singlet state alternatives to the doublet state nitroxides for similar purposes. This effort pursues an intermolecular rather than an intramolecular oxygen-atom transfer utilizing triphenylphosphine as the oxygen-atom acceptor, motivated by demonstrations that both 4-methylmorpholine N-oxide (NMMO) and 2,2'-bipyridyl N-oxide (bpyO) react with triphenylphosphine thermally and photochemically (470 nm light) to undergo slow, intermolecular oxygen-atom transfer to form triphenylphosphine oxide (monitored by ^{31}P NMR).

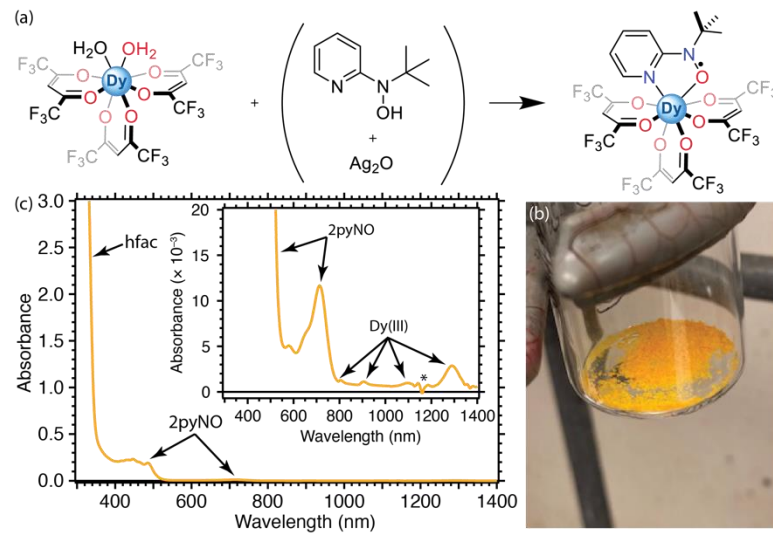


Fig. 3. (a) Synthetic scheme for $\text{Dy}(\text{hfac})_3(2\text{pyNO})$ complex. (b) Digital photograph showing orange product. (c) Absorbance spectra highlighting the dominant ligand absorption bands. Inset shows the weak low-energy 2pyNO absorption bands and Dy(III) transitions. * indicates artifacts due to imperfect background subtraction.

Future Plans

- Work is underway to provide baseline excited state spectroscopy (steady-state and transient photoluminescence and electronic and vibrational transient absorption measurements) of the complexes with the organophosphorous (CSM) and nitroxide antenna ligands (UPenn).
- Complete synthesis and characterization of oxygen atom transfer rates for:
 - RE(hfac)₃(6bpyNO) and comparison with 2pyNO analogues.
 - Dy/Y(hfac)₃(NMMO) and Dy/Y(hfac)₃(bpyO) complexes.
- Preliminary exploration of the photostability of Y(hfac)₃(2pyNO) has been investigated by irradiation with 470 nm light. Noticeable changes were observed in the NMR spectra. The process of identifying the products by investigation of the NMR and ESI-MS spectra is ongoing. This will be expanded to all oxygen-atom transfer complexes.
- Expand computational modeling of oxygen-atom transfer complexes

References

- (1) Xie, F.; Zhang, T.A.; Dreisinger, D.; Doyle, F., A critical review on solvent extraction of rare earths from aqueous solutions, *Miner. Eng.* **2014**, *56*, 10-28.
- (2) Mancino, G.; Ferguson, A.J.; Beeby, A.; Long, N.J.; Jones, T.S., Dramatic Increases in the Lifetime of the Er³⁺ Ion in a Molecular Complex Using a Perfluorinated Imidodiphosphinate Sensitizing Ligand, *J. Am. Chem. Soc.* **2005**, *127*, 524-525.
- (3) Liu, G.K.; Jensen, M.P.; Almond, P.M., Systematic Behavior of Charge-Transfer Transitions and Energy Level Variation in Soft Donor Complexes of the Trivalent Lanthanides, *J. Phys. Chem. A* **2006**, *110*, 2081-2088.
- (4) Jensen, M.P.; Chiarizia, R.; Ulicki, J.S.; Spindler, B.D.; Murphy, D.J.; Hossain, M.; Roca-Sabio, A.; de Blas, A.; Rodríguez-Blas, T., Solvent Extraction Separation of Trivalent Americium from Curium and the Lanthanides, *Solvent Extr. Ion Exch.* **2015**, *33*, 329-345.
- (5) Koldemir, U.; Braid, J.L.; Morgenstern, A.; Eberhart, M.; Collins, R.T.; Olson, D.C.; Sellinger, A., Molecular Design for Tuning Work Functions of Transparent Conducting Electrodes, *J. Phys. Chem. Lett.* **2015**, *6*, 2269-2276.
- (6) Cole, B.E.; Falcons, I.B.; Cheisson, T.; Manor, B.C.; Carroll, P.J.; Schelter, E.J., A molecular basis to rare earth separations for recycling: tuning the TriNOx ligand properties for improved performance, *Chem. Commun.* **2018**, *54*, 10276-10279.
- (7) Cheisson, T.; Cole, B.E.; Manor, B.C.; Carroll, P.J.; Schelter, E.J., Phosphoryl-Ligand Adducts of Rare Earth-TriNOx Complexes: Systematic Studies and Implications for Separations Chemistry, *ACS Sustainable Chem. Eng.* **2019**, *7*, 4993-5001.
- (8) Qiao, Y.; Sergentu, D.-C.; Yin, H.; Zabula, A.V.; Cheisson, T.; McSkimming, A.; Manor, B.C.; Carroll, P.J.; Anna, J.M.; Autschbach, J.; Schelter, E.J., Understanding and Controlling the Emission Brightness and Color of Molecular Cerium Luminophores, *J. Am. Chem. Soc.* **2018**, *140*, 4588-4595.
- (9) Wang, N.; Wang, J.; Zhao, D.; Mellerup, S.K.; Peng, T.; Wang, H.; Wang, S., Lanthanide Complexes with Photochromic Organoboron Ligand: Synthesis and Luminescence Study, *Inorg. Chem.* **2018**, *57*, 10040-10049.
- (10) Bogart, J.A.; Lee, H.B.; Boreen, M.A.; Jun, M.; Schelter, E.J., Fine-Tuning the Oxidative Ability of Persistent Radicals: Electrochemical and Computational Studies of Substituted 2-Pyridylhydroxylamines, *J. Org. Chem.* **2013**, *78*, 6344-6349.

Publications

Project initiated in September 2020, no publications to report.

Project Title: Design, Synthesis, and Atomic Scale Characterization of Rare-Earth Based Supramolecular Nano-graphene and Nanoribbons

Investigators: Saw Wai Hla¹ (PI), Larry A. Curtiss², Xuedan Ma¹, Eric Masson³, Anh T. Ngo^{2,4}, Volker Rose⁵, Tijana Rajh¹, Sergio E. Ulloa⁶

Affiliations:

¹ Nanoscience & Technology Division, Argonne National Laboratory, 9700 S. Cass Ave., Lemont, IL 60439

² Materials Science Division, Argonne National Laboratory, 9700 S. Cass Ave., Lemont, IL 60439

³Department of Chemistry and Biochemistry, Ohio University, Athens, OH 45701

⁴Department of Chemical Engineering, University of Illinois at Chicago, Chicago, IL 60608

⁵Advanced Photon Source, Argonne National Laboratory, 9700 S. Cass Ave., Lemont, IL 60439

⁶Department of Physics & Astronomy, Ohio University, Athens, OH 45701

Program Scope

This project seeks to advance fundamental understanding on the physics and chemistry of rare earths in well controlled environments and development of novel materials using molecular design and new synthetic approaches. We aim to develop novel two dimensional rare earth based supramolecular structures with well-defined sizes and shapes such as nano-graphene and nanoribbon structures for emission applications. In these structures, rare earth ions are caged in two dimensional networks containing organic linkers whose electronic properties can be tuned by an external stimulus. This electronic tuning should allow the emission of certain rare earth cations to be turned on or turned off, thereby effectively controlling the optical properties of the supramolecular structure as a whole. Atomic scale characterization of individual rare earth ions in the proposed structures are performed with the most advanced and one-of-a-kind instrumentation: The elemental, chemical, and magnetic properties of rare earth ions in the network are determined simultaneously using synchrotron X-ray scanning tunneling microscopy, while tunneling spectroscopy is used to measure the electronic structure of the caged rare earths on one ion-at-a-time basis. Low temperature electron paramagnetic resonance methods are used to probe the spin structures of the 4f electrons while excitation and energy conversion studies are carried out using advanced magneto-optical spectroscopy techniques. Taken in concert, these experiments provide unparalleled atomic level information of the rare earth ion environment within these novel structures. This, in turn, will be used to develop theoretical frameworks to describe accurately the electronic properties of the constituent 4f rare earth cations and develop rational blueprints for the design and synthesis of new structures with improved functions.

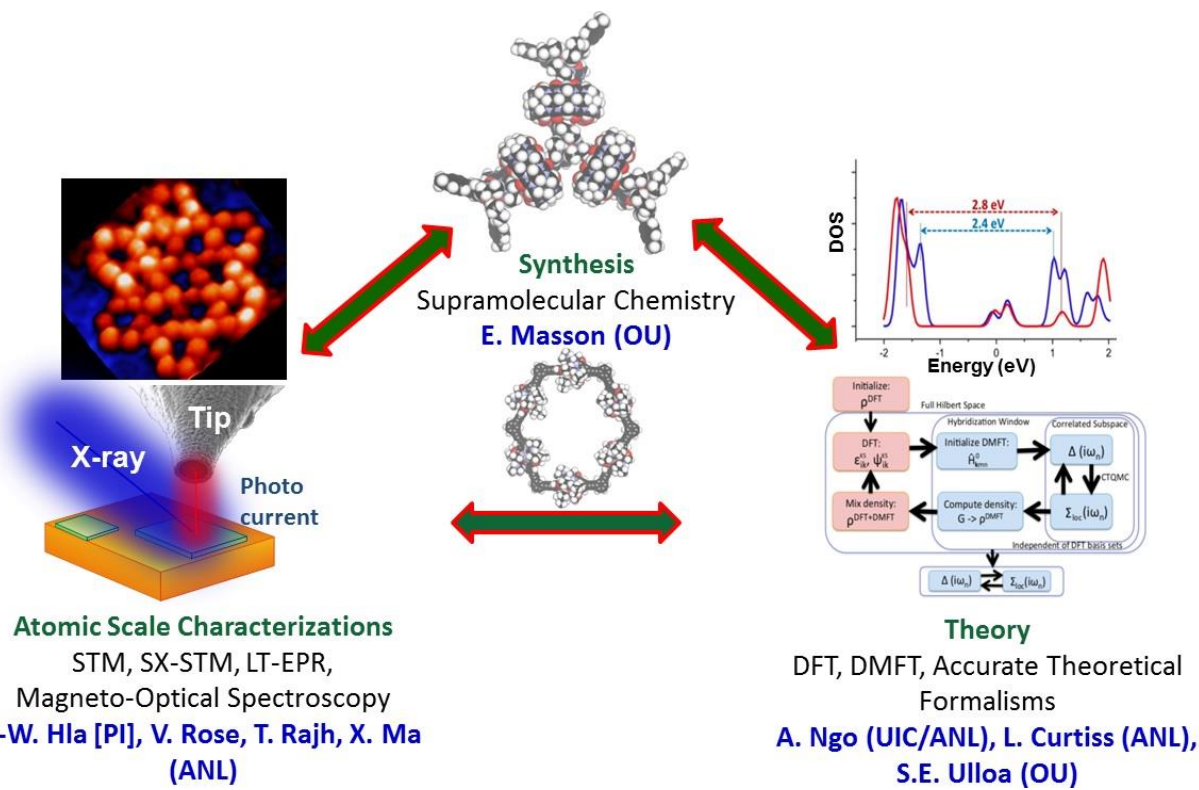


Fig. 1. Project organization.

Recent Progress

This project has started in October 2020 and thus it is less than 5 months old at the time of this report preparation. Although the project has commenced under limited operation status due to COVID-19 pandemic, we have made a significant progress in synthesis, atomic level characterizations and theoretical frameworks. In particular, we have successfully synthesized rare earth (RE) based planar molecules suitable for the investigations on materials surfaces, as well as performed atomic level characterizations and theoretical simulations on these RE molecules.

An important part of our project is to develop planar RE based supramolecular structures that can be deposited onto atomically clean materials surfaces intact under an ultrahigh vacuum (UHV) environment. Such molecular structures should allow atomic level investigations of individual RE ions caged inside the molecules on one-ion-at-a-time basis. The first step in this direction is to build basic molecular building blocks containing RE ions that can be linked to form larger 2D molecular structures on materials surfaces. For the initial part of the project, we have designed and synthesized a RE-bisamide molecular structure (Fig. 2). Here the RE atom is caged at the center of three equivalent molecular arms in a planar configuration (Fig. 2a, 2b). In this structure, the caged RE ion ($\text{RE} = \text{La, Eu, Lu}$) is well protected by the molecular ligands and the arms allow further extension of the structure into extended molecular networks by chemical design. Moreover, by changing the local chemical environment of the RE ion, its electronic and spintronic properties can be tuned to get desired outcomes.

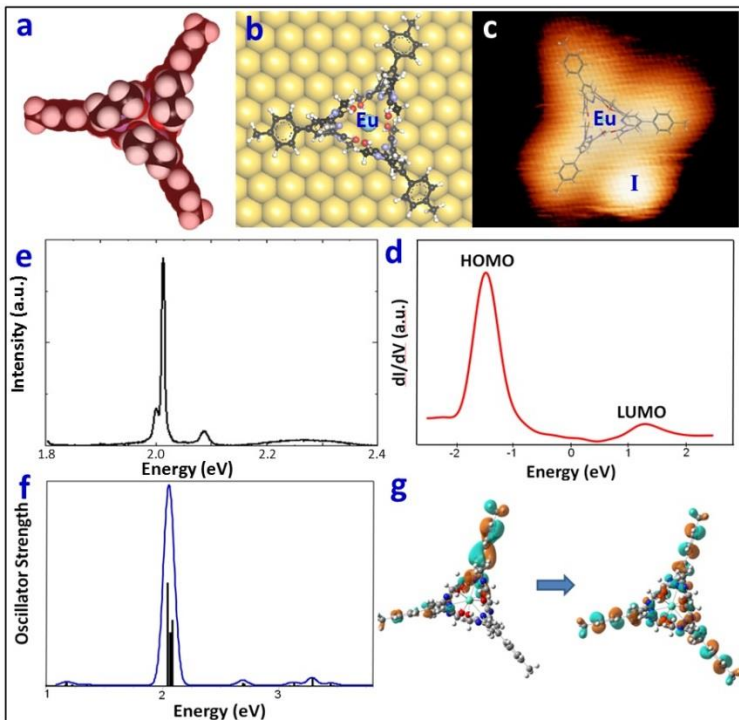


Fig. 2. **a)** ball model of Eu-bisamide molecule. **b)** DFT calculated adsorption configuration of Eu-bisamide on Au(111). **c)** An STM image of Eu-bisamide. Here ‘I’ is an anion. **d)** dI/dV tunneling spectroscopy data of a single Eu ion caged inside the molecule. **e)** PL spectrum of Eu-bisamide. **f)** TDDFT calculated spectrum shows agreement with (e). **g)** Excited state orbitals indicating transition for (f).

and +1.3 eV, respectively. Thus, the HOMO-LUMO gap of Eu-bisamide is measured as 2.8 eV. The photoluminescence spectra of the Eu-bisamide (Fig. 2e) show a strong peak around 2.1 eV, which is in agreement with the time dependent DFT (TDDFT) calculated results (Fig. 2f, 2g).

The RE-bisamide molecules were deposited onto atomically clean Au(111) surface via thermal evaporation under UHV and their structural and electronic properties were investigated using low temperature scanning tunneling microscopy (STM) and tunneling spectroscopy (Fig. 2c, 2d). STM images of RE-bisamide clearly show the expected triangular shape of the molecules on Au(111) surface while dI/dV-V tunneling spectroscopy measured on individual molecules reveal the electronic environment of the RE ions in the molecules. An example is shown in Fig. 2d, where the tunneling spectroscopy data recorded on individual Eu-bisamide molecules provide the energetic locations of the highest occupied and lowest unoccupied molecular orbitals (HOMO and LUMO) as -1.5 eV

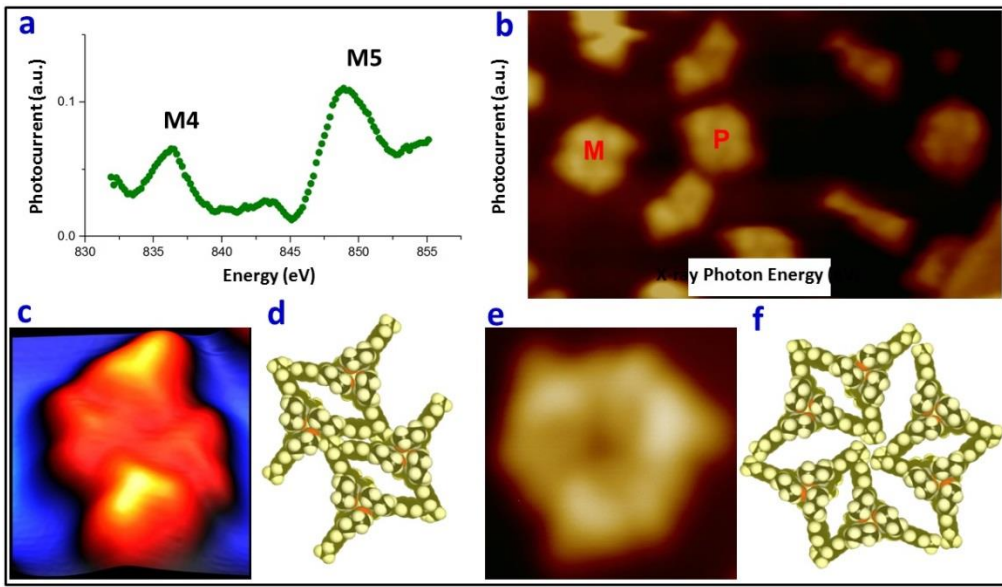


Fig. 3. **a)** STM-XAS spectrum of La-Bisamide. **b)** STM image of chiral La-Bisamide clusters on Au(111). ‘M’ and ‘P’ indicate chiral clusters. **c)** A 3-D STM image of 4-molecule cluster, **d)** a corresponding model. **e)** STM image of a 6-molecule cluster, and **f)** a corresponding model.

Although RE-bisamide molecules can be imaged on Au(111) surface, it is difficult to directly identify the existence of RE ions inside the molecules. In order to confirm that the RE atoms are intact in the molecules after thermal deposition we have performed elemental analysis using synchrotron X-ray scanning tunneling microscopy (SX-STM). In SX-STM, a synchrotron X-ray beam is incident to the STM tip-sample junction and X-ray excitations of core level electrons occur [1]. The resultant X-ray excited photo-electrons are then collected by an STM tip. This nascent technique enables detecting X-ray signals potentially down to the atomic limit [2]. The X-ray absorption spectroscopy (XAS) spectra of La-bisamide on Au(111) surface are acquired in the recently commissioned XTIP beamline at the sector 4-ID-E in Advanced Photon Source at Argonne National Laboratory [3]. The XAS spectra reveal the expected La M4 and M5 edges providing the first ever SX-STM measurement on the X-ray signals of individual RE ions.

On Au(111) surface, La-bisamide forms stable clusters composed of 2, 4, or 6 molecules (Fig. 3c to 3f). Interestingly, a careful analysis unveils the chiral nature of the clusters (Fig. 3b). Therefore our finding opens an exciting research direction to explore the relationship between the cluster chirality and the electronic and magnetic properties of RE atoms on solid surfaces.

Future Plans

Following our initial success on synthesis of RE-bisamide molecules (RE = La, Eu, Lu), we plan to extend the molecular synthesis with other RE elements such as Tb, Er, Sm, and Cs. Then we will perform atomic level characterizations of molecules containing different RE ions to compare their electronic, and magnetic structures. Using atomic level information of the rare earth ions as input, we will explore theoretical frameworks to describe accurately their electronic and magnetic properties. Then by changing the ligand environment via computation guided chemical synthesis the properties of the RE ions in the molecules will be fine tuned. We are also designing and synthesizing 2D molecular networks reminiscent of the graphene to explore and to control their emission properties.

References

- [1] V. Rose, K. Wang, T.U. Chien, J. Hiller, D. Rosenmann, J.W. Freeland, C. Preissner & S.-W. Hla. *Synchrotron x-ray scanning tunneling microscopy: Fingerprinting near to far field transitions on Cu(111) induced by synchrotron radiation.* *Adv. Funct. Mater.* **23**, 2646-2652 (2013).
- [2] H. Chang, N. Shirato, Y. Zhang, J. Hoffman, D. Rosenmann, J.W. Freeland, A. Bhattacharya, V. Rose, & S.-W. Hla. *X-ray magnetic circular dichroism and near-edge x-ray absorption fine structure of buried interfacial magnetism measured by using a scanning tunneling microscope tip.* *Appl. Phys. Lett.* **113**, 061602 (2018)
- [3] V. Rose, N. Shirato, M. Bartlein, A. Deriy, T. Ajayi, D. Rosenmann, S.-W. Hla, M. Fisher, and R. Reininger. *XTIP – the world's first beamline dedicated to the synchrotron X-ray scanning tunneling microscopy technique.* *J. Synchrotron Rad.* **27**, 836-843 (2020).

Publications

T.M. Ajayi, D.J. Trainer, S. Sarkar, Y. Li, T. Rojas⁴, N. Shirato, D. Rosenmann, Y. Liu, S. Wang, A.T. Ngo, V. Rose, X. Li, S.-W. Hla. *Tracing a Single Atom using Synchrotron X-rays.* Submitted.

Session XI

Understanding and Probing Phonon Transport in Emerging Quantum Materials

Bolin Liao

Department of Mechanical Engineering, University of California, Santa Barbara

Program Scope

The overarching goal of this project is to understand how the phase coherence of phonons and the interaction of phonons with other microscopic degrees of freedom in emerging quantum materials, such as topological and 2D materials, can affect the energy transport properties and eventually lead to control of energy transport by manipulating phonon interference and phonon scatterings. On the theory and computation side, in the past two years, we have focused on understanding phonon properties and thermal transport in emerging topological materials. Combining first-principles simulation and theory, we demonstrated the existence of ultrasoft phonons in topological Dirac/Weyl semimetals and dynamic phonon softening near topological phase transitions. These findings suggest that topological materials can be a promising new class of materials for thermoelectric and solid-state thermal switching applications. On the experimental side, we continue to develop the scanning ultrafast electron microscopy (SUEM) to directly probe the coherent phonon transport and phonon-electron interaction processes in emerging quantum materials. In the past two years, we have made significant progress in the SUEM instrumentation, including realizing and characterizing photoemission from the field-emission gun and understanding the SUEM contrast resulting from the surface photovoltage (SPV) effect in doped semiconductors. Our program will not only provide new insights into the microscopic transport and interaction processes of fundamental energy carriers in emerging quantum materials, but also open new venue towards energy-relevant applications such as thermal switches and coherent energy harvesters.

Recent Progress

1. Ultrasoft Phonons in Topological Semimetals due to Singular Electron-phonon Interaction and Kohn Anomaly

Emerging topological materials, including topological insulators and semimetals, have been one of the central themes of condensed matter physics and materials science in the past decade. Although their electrical and optical properties have been intensively studied, their phonon and thermal transport properties have remained less explored. One of our main focuses within the past two years is to identify and understand novel phonon physics in emerging topological semimetals. In particular, combining first-principles simulation and high-resolution Raman spectroscopy, we identified the existence of ultrasoft phonon modes in a class of topological Dirac

semimetals^{1,2} (Cd_3As_2 , Na_3Bi and ZrTe_5 under hydrostatic pressure) related to strong Kohn anomalies caused by their linear Dirac electronic bands. The Dirac nodes and the associated Kohn anomalies in Cd_3As_2 are shown in Figure 1. These soft phonon modes lead to strong phonon-phonon scattering and abnormally low lattice thermal conductivity of these materials. This is a significant finding because this may help resolve the long-standing mystery of the connection between topological materials and good thermoelectric materials. Our result suggests that the linear or close-to-linear electronic bands in topological insulators and semimetals are directly responsible for the lattice instability and the low lattice thermal conductivity of these materials. More importantly, since the Fermi surface geometry of these Dirac band materials can be sensitively controlled by external fields, we envision that this finding can potentially enable efficient thermal switches that can be controlled by external electric fields. This hypothesis has been verified by our first-principles simulations of the evolution of phonon dispersions across topological phase transitions. We find that ZrTe_5 undergoes a pressure-driven topological phase transition near 5 GPa, where significant phonon softening emerges in association with the topological phase transition². Similar effect is also observed near a chemical-composition-driven topological phase transition in $\text{Hg}_{1-x}\text{Cd}_x\text{Te}$ ². We propose that this phonon softening effect near topological phase transitions can be used to realize sensitive solid-state thermal switches whose thermal conductivity can be controlled by external means. In the case of ZrTe_5 , we find that ~10% modulation of its thermal conductivity can be realized across the pressure-driven topological phase transition. We will continue searching for other topological materials where this effect can be more prominent. To continue along this direction, we have requested using the inelastic x-ray scattering facility at Argonne National Lab (Advanced Photon Source) and Brookhaven National Lab (NSLS-II) to directly map out the phonon dispersions of topological Dirac semimetals across topological phase transitions. In addition, we have also requested and received computing time allocation from NERSC to continue our first-principles simulations of topological materials.

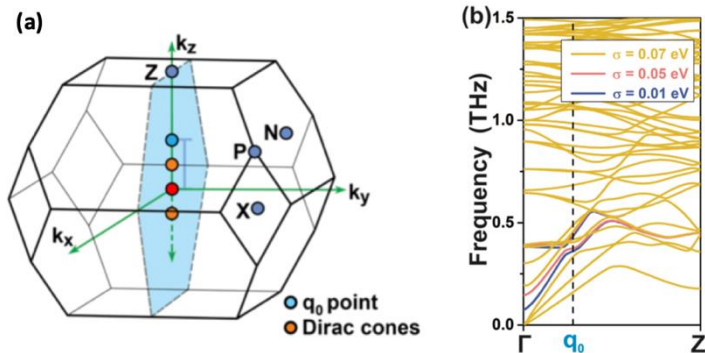


Figure 1 Phonon softening due to strong Kohn anomaly in topological Dirac semimetal Cd_3As_2 . (a) Brillouin zone of Cd_3As_2 showing the Dirac nodes locations. (b) Ultrasoft phonons in Cd_3As_2 due to strong Kohn anomalies.

2. Continued Development of Scanning Ultrafast Electron Microscope

A key step in developing time-resolved measurements with SUEM is to obtain pulsed electron beams by illuminating the electron gun tip (tungsten tip coated with zirconium oxide to reduce the work function to ~3.3 eV) with the pulsed UV laser beam (343 nm). The major challenge is the small size of the electron tip (~200 nm diameter at the apex) and the lack of feedback signal when attempting the alignment of the focus of the optical beam on the apex of the

electron tip. To overcome this challenge, we developed a method of modulating the UV optical beam with a mechanical chopper (at 1 kHz) and using a lock-in amplifier to directly read the secondary-electron detector. When the UV optical beam is near the electron tip, we can detect a small increase of the secondary-electron emission signal from the lock-in detector and then we can further adjust the alignment until we maximize the signal. This lock-in detection scheme provides a feedback signal that can be conveniently used to steer the optical alignment step that mainly relied on trial and error previously.

With this new alignment method, we managed to align the optical probe beam onto the electron gun tip, as shown in Fig. 2. Electrons emitted from the electron gun tip due to the illumination of the pulsed UV optical beam can be used to generate high-quality secondary electron images (Fig. 2), which can be instantaneously shut off by blocking the laser beam, confirming the photoemission nature (if the electrons are emitted due to thermal effect, then it takes a certain amount of delay time for the image to disappear before the tip cools down).

After finding photoemission from the electron gun tip, we were able to fully characterize the photoemission characteristics of the electron gun. Using a Faraday cup and a picoammeter, we were able to measure the photoemission current and the photoemitted electron number per pulse as a function of the incident optical UV pulse energy, as shown in Fig. 3. At 5 MHz laser repetition rate, we can reliably generate a photoemission current ~ 40 pA, corresponding to up to 50 electrons per pulse. Our results compare well to previous reports, indicating the photoemission current we achieved is sufficient for time-resolved SUEM measurements. To further enhance the photocurrent emitted from the electron gun, we tested using even shorter wavelength for the UV optical pulse (257 nm, 4th harmonic of the laser base frequency). We demonstrated that 4th harmonic (257 nm) optical excitation is much more efficient

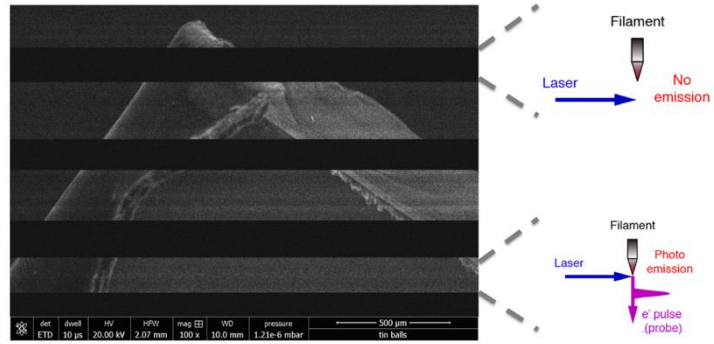


Figure 2. Secondary electron image generated by photoemitted electrons from the electron tip.

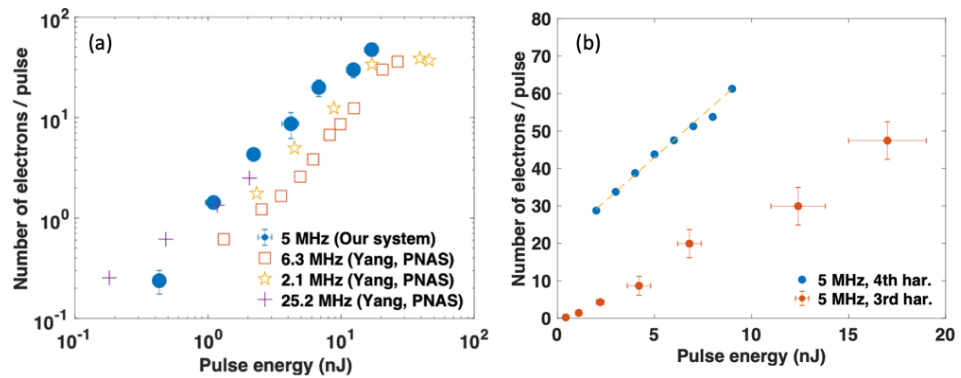


Figure 3. Photoemission characterization. (a) Number of emitted photoelectrons as a function of optical pulse energy (343 nm) as compared to previous reports. (b) Comparison of photoemission using 4th harmonic (257 nm) and 3rd harmonic optical excitation (343 nm).

in producing photoelectrons compared to 3rd harmonic (343 nm), as shown in Fig. 3b. With the newly operational SUEM setup, we recently characterized the impact of the surface photovoltaic (SPV) effect on the SEM contrast of surfaces of heavily-doped semiconductors³.

Future Plans

We will continue to develop computational and experimental capabilities to probe and understand novel phonon physics in emerging quantum materials. On the computational side, we believe our recent discovery of phonon softening in topological semimetals is only a "tip of the iceberg". We will aim to establish a direct and systematic connection among chemical bonds, electronic band topology, and phonon/lattice properties, which will help with material design and search for energy harvesting and thermal switching applications. On the experimental side, with the SUEM now operational, we plan to directly image photocarrier dynamics on the surface of topological materials, particularly examining the contributions of the surface electronic and phononic states. We will first focus on topological semimetals, including Cd₃As₂ and TaP, aiming to directly image the photoresponse of their surface Fermi arc states.

References

1. Yue, S. *et al.* Soft phonons and ultralow lattice thermal conductivity in the Dirac semimetal Cd₃As₂. *Phys. Rev. Research* **1**, 033101 (2019).
2. Yue, S. *et al.* Phonon softening near topological phase transitions. *Phys. Rev. B* **102**, 235428 (2020).
3. Li, Y., Choudhry, U., Ranasinghe, J., Ackerman, A. & Liao, B. Probing Surface Photovoltaic Effect Using Photoassisted Secondary Electron Emission. *J. Phys. Chem. A* **124**, 5246–5252 (2020).

Publications

Usama Choudhry, Sheng-Ying Yue and Bolin Liao, Origins of significant reduction of lattice thermal conductivity in graphene allotropes, Physical Review B, **100**, 165401, 2019

Sheng-Ying Yue, Hamid T. Chorsi, Manik Goyal, Timo Schumann, Runqing Yang, Tashi Xu, Bowen Deng, Susanne Stemmer, Jon A. Schuller and Bolin Liao, Soft phonons and ultralow lattice thermal conductivity in the Dirac semimetal Cd₃As₂, Physical Review Research, **1**, 033101, 2019

Hamid T. Chorsi, Sheng-Ying Yue, Prasad P. Iyer, Manik Goyal, Timo Schumann, Susanne Stemmer, Bolin Liao and Jon A. Schuller, Widely tunable optical and thermal properties of Dirac semimetal Cd₃As₂, Advanced Optical Materials, **8**, 1901192, 2020

Sheng-Ying Yue, Bowen Deng, Yanming Liu, Yujie Quan, Runqing Yang and Bolin Liao, Phonon softening near topological phase transitions, Physical Review B, **102**, 235428, 2020

Ebrahim Najafi, Amir Jafari and Bolin Liao, Carrier density oscillation in the photoexcited semiconductor, Journal of Physics D: Applied Physics, **54**, 125102, 2020

Spin-Mediated Heat Conduction and Thermoelectric Effects in Novel Materials

PI: Joshua L. Cohn, Department of Physics, University of Miami,

P.O. Box 248046, Coral Gables, FL 33124

Contact: (305) 284-7123; jcohn@miami.edu

Program Scope

This program involves experimental transport studies of spin-mediated heat transport and thermoelectric effects in novel materials (oxide conductors, magnetic insulators). Recent work focuses on magnon heat transport and spin-thermoelectric studies (Spin Seebeck, spin Peltier) of insulating helimagnets (CuOSeO_3 , ZnCr_2Se_4) at $T \leq 20$ K. Prior work in this program revealed, for CuOSeO_3 near $T=5$ K, the largest known magnon thermal conductivity for any ferromagnet.

Recent Progress

Low-temperature Spin Seebeck Effect in Cu_2OSeO_3 and New Test of Spin Current Theory
[Phys. Rev. B **101**, 100407 (2020), *Rapid Commun.*]

This recent study built on the work from our two prior papers on this compound [Phys. Rev. B **99**, 020403, *Rapid Communications* (2019); Phys. Rev. B **95**, 224407 (2017) (Editor's Suggestion)]. Most significantly, we put existing spin current theory to stringent tests that were not possible previously: Cu_2OSeO_3 remains the only material for which the magnon thermal conductivity and spin Seebeck effect can be measured directly.

The measurements themselves deploy 10-nm thick Pt films deposited on the polished heater end face of mm-sized single-crystal specimens [inset, Fig. 1 (a)] and low-T thermometers attached along their length. The remainder of Fig. 1 shows the H-T phase diagram for Cu_2OSeO_3 , spin Seebeck signal, $V_{LSSE} = \frac{[V_{Pt}(H) - V_{Pt}(-H)]}{2}$, and magnon thermal conductivity as functions of H, T.

Using Boltzmann theory expressions for S_{LSSE} and κ_m and spin wave dispersion from inelastic neutron scattering we were able to simultaneously fit the T -dependence of both coefficients using magnon scattering parameters from a simple continuum model employed in our prior work [Fig. 2 (a)] to model only the magnon thermal conductivity. A more fundamental test of the theory, independent of the model relaxation times – is its prediction that the two transport coefficients are directly related through their integral expressions. We identified a *sublinear* relationship between S_{LSSE} and κ_m [Fig. 2 (b)] for all specimens when the spin Seebeck coefficients were re-scaled by the product of their Pt film resistance and spin-mixing conductance (parameters from the theory that set the scale of the spin-Seebeck signal). A power law relationship, $(S_{LSSE})^n \propto \kappa_m$ with $n = 1.15$ provides the best fit to experiment, in excellent agreement with $n = 1.17$ predicted by theory. These confirmations of theory, heretofore inaccessible for any other material, highlight this compound as a model system for the study of magnon interactions and their role in the transport of spin and heat.

Novel spin-wave dispersion and thermal conductivity in ZnCr_2Se_4
[Phys. Rev. B **102**, 184431 (2020).]

Neutron scattering studies^{1,2} of our collaborator (Dmytro Inosov, TU Dresden) revealed unusual pseudo-Goldstone helimagnon modes in the magnon spectrum of the insulating Heisenberg helimagnet ZnCr_2Se_4 . This compound has an antiferromagnetic, helimagnetic phase tran-

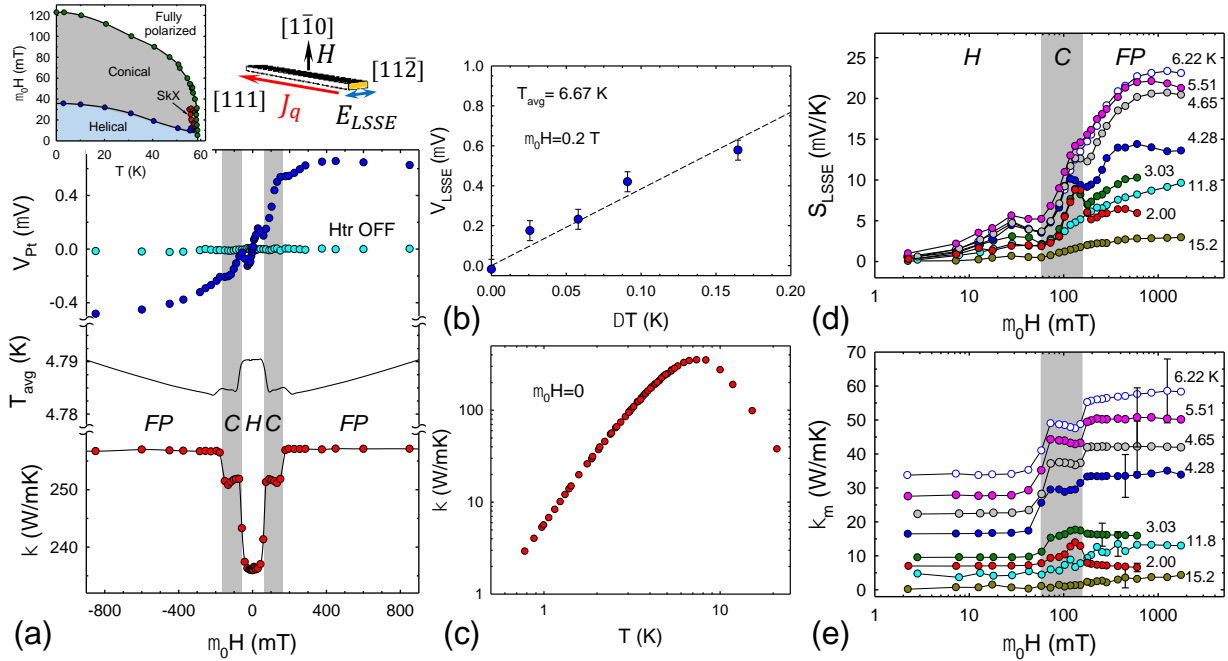


Fig. 1 (a) From top to bottom: longitudinal Spin Seebeck effect (LSSE) voltage (for heater on and off), average temperature, and thermal conductivity *vs.* field at $T_{avg} = 4.79\text{ K}$. Left inset: magnetic phase diagram, right inset: orientation of heat flow and fields, (b) LSSE voltage *vs.* ΔT at 6.67 K , (c) zero-field $\kappa(T)$, (d) LSSE coefficient and (e) magnon thermal conductivity *vs.* field for various temperatures. The shading in (a), (d), (e) distinguishes the conical (C) spin phase from helical (*H*) and fully polarized (*FP*) phases.

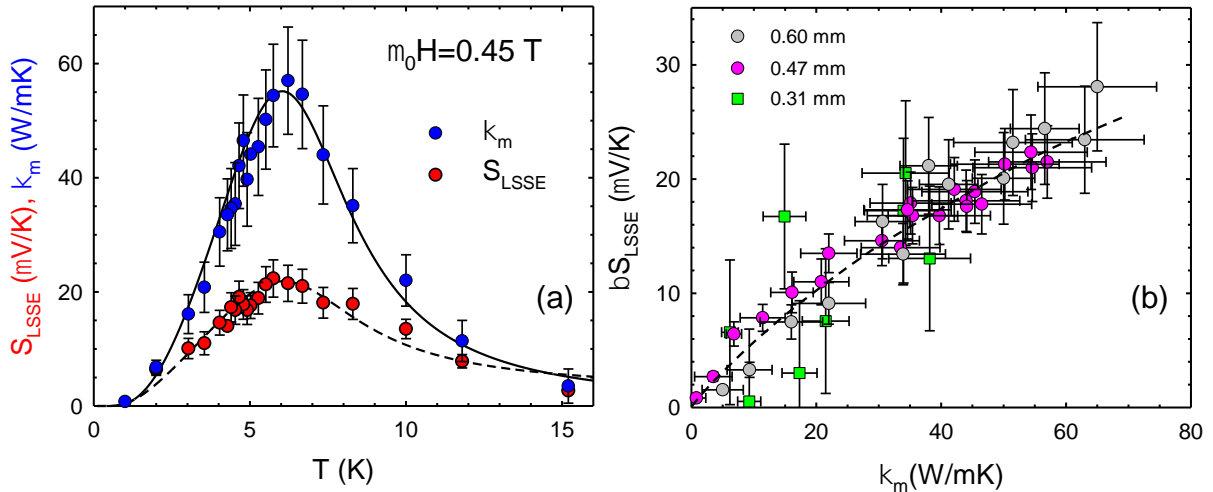


Fig. 2 (a) $\kappa_m(T)$ and $S_{LSSE}(T)$ in the fully polarized phase at $\mu_0H = 0.45\text{ T}$. Solid and dashed curves are best fits to theory. (b) Correlation between S_{LSSE} and κ_m in the fully polarized phase specimens with spin-mixing conductances varying by more than an order of magnitude (and accounted for in the scaling factor β).

sition at $T_N = 21\text{ K}$ [Fig. 3 (a)] that coincides with a cubic-tetragonal structural transition. The magnetic sublattice comprises frustrated $S = \frac{3}{2}\text{ Cr}^{2+}$ ions arranged on a pyrochlore lattice, a magnetic structure similar to that of Cu_2OSeO_3 . The spin-wave spectrum has, in addition to the usual Goldstone mode propagating along the spin helix [defined by the direction of applied field,

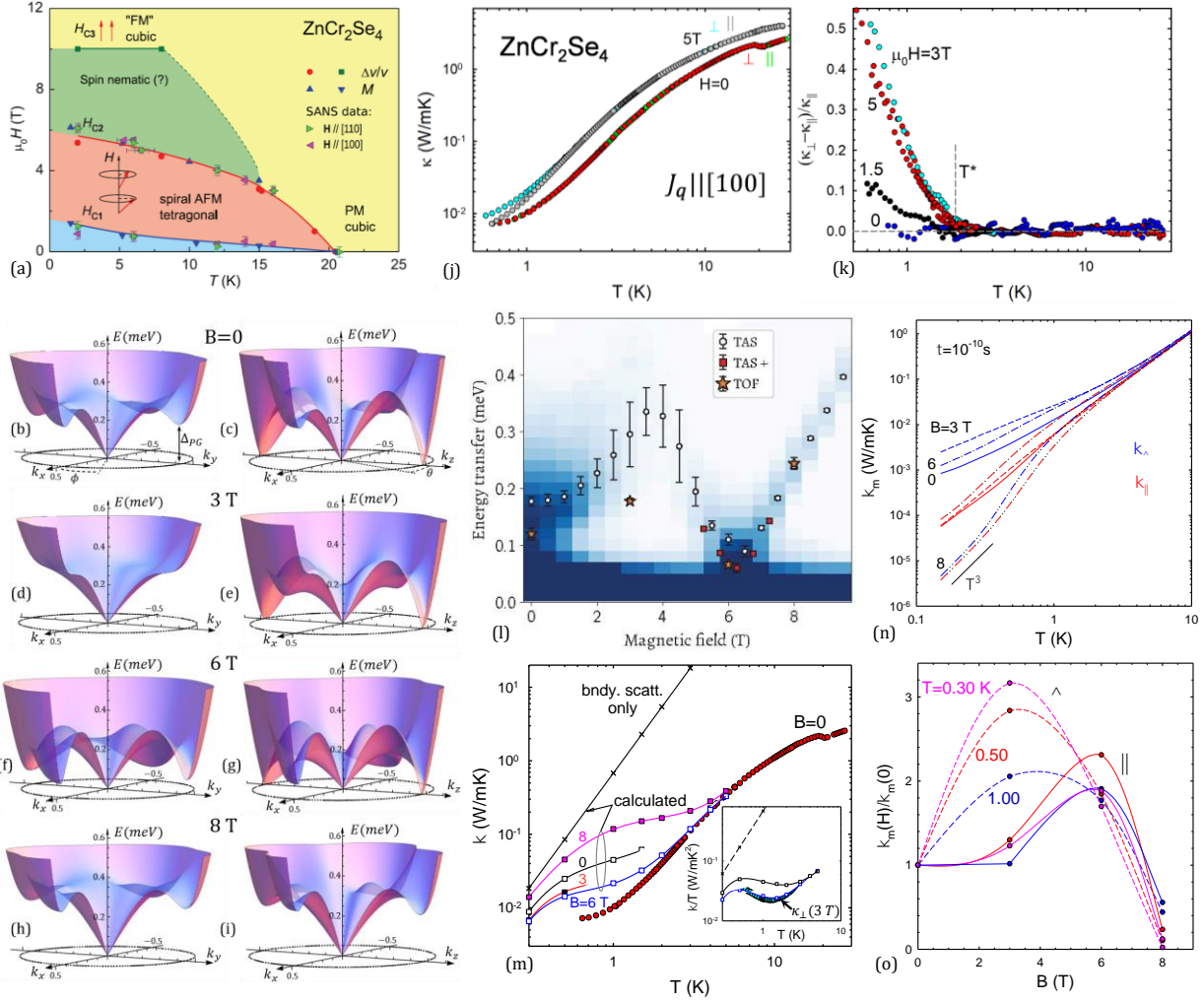


Fig. 3 (a) Magnetic phase diagram of ZnCr_2Se_4 (from Ref. 1). (b)-(i) Three-dimensional magnon dispersions, shown in the $k_x - k_y$ (left) and $k_x - k_z$ (right) planes for four values of magnetic field. Wave numbers are in units of $2\pi/a$. The polar and azimuthal angles (θ, ϕ) and pseudogap (Δ_{PG}) are labeled in the plots for $B = 0$. (j) Thermal conductivity vs temperature at fixed magnetic fields perpendicular and parallel to the heat flow along [100], (k) Normalized anisotropy, $(\kappa_\perp - \kappa_\parallel)/\kappa_\parallel$, vs. T at various applied fields demonstrating the onset of anisotropy at $T < T^* \approx 1.9 \text{ K}$. (l) Neutron scattering determinations of Δ_{PG} [at $(q_h, 0, 0)$] vs. magnetic field. (m) Computed $\kappa_L(T)$ (squares; $\kappa_{L,\perp} = \kappa_{L,\parallel} \text{ to } 1\%$) at various fields compared to the experimental $B = 0$ data (filled circles). The magnetoelastic constant was set so that the computed $T = 5 \text{ K}$ conductivities matched experimental data. Also shown is the computed thermal conductivity with only the boundary scattering term included (x's). Inset: Computed κ_L/T for the boundary scattering and $B = 0, 3\text{-T}$ curves from the main panel and corresponding experimental 3-T data (filled circles). (n), (o) calculated magnon conductivities as functions of T, B .

$\mathbf{q}_h \parallel \hat{k}_z$ in Fig. 3 (b)-(i)], modes with small spin gap ($\Delta_{PG} \sim 0.17 \text{ meV}$) propagating transverse to \mathbf{q}_h [along \hat{k}_x and \hat{k}_y in Fig. 3] that are attributed to quantum fluctuations.²

Such an unusual dispersion should have signatures in thermodynamic and transport properties.³ Thermal conductivity (κ) offers an elegant means to potentially separate magnetic effects from those arising entirely from the phonon dispersion: the difference in κ measured with ΔT parallel (κ_\parallel) and perpendicular (κ_\perp) to \mathbf{q}_h . Our measurements [Fig. 3 (j), (k)] reveal anisotropy that emerges only below $T^* \approx 1.9 \text{ K}$ and has a nonmonotonic dependence on magnetic field.

Separating magnonic (κ_m) and lattice (κ_L) contributions to the measured κ in this compound is challenging given its complex temperature and field dependencies. Note that Cu₂OSeO₃ [Fig. 1 (c)] has $\kappa \approx 300 - 400$ W/mK at 5 K [while $\kappa_L \approx (5 - 10)\kappa_m$], three orders of magnitude larger than that of ZnCr₂Se₄. This dramatic difference is clearly related to the stronger coupling between the spin and lattice systems in ZnCr₂Se₄, as manifested in, e.g., giant magnetostriction.^{4,5}

To better understand $\kappa(B, T)$ for ZnCr₂Se₄, we calculated κ_L and κ_m using analytic forms of the three-dimensional magnon dispersion. We found that although the appearance of a plateau or shoulder in $\kappa_L(T)$ and a maximum in κ_L/T [inset, Fig. 3 (m)] may be partially associated with κ_L , the anisotropy and its nonmonotonic behavior with field at $T < T^*$ are unlikely to be. On the other hand, the unusual magnon dispersion and its evolution with applied field suggest that magnon heat conduction is a plausible source for both the anisotropy and nonmonotonic field dependence of $\kappa(B, T)$. The calculated $\kappa_m(B, T)$, assuming a constant scattering time $\tau_m = 10^{-10}$ s [Fig. 3 (n)], captures some of the key features in the data, including $\kappa_{m,\perp} > \kappa_{m,\parallel}$ and nonmonotonic $\kappa_m(B)$ at low T . Not surprisingly, these features arise primarily from low-energy magnon states with momenta at small angles to \mathbf{q}_h .

Future Plans

We hope to exploit the large magnon spin current of Cu₂OSeO₃ crystals for spin injection in interfacial superconductor films (e.g. Nb). Discrepancies between experiment and the calculated κ_m for ZnCr₂Se₄ motivate a new hypothesis to be explored regarding the role of different chiralities of the spin helix within single magnetic domains and their possible manipulation with applied electric field.

References

1. A. S. Cameron, Y. V. Tymoshenko, P. Y. Portnichenko, J. Gavilano, V. Tsurkan, V. Felea, A. Loidl, S. Zherlitsyn, J. Wosnitza and D. S. Inosov, *Magnetic phase diagram of the helimagnetic spinel compound ZnCr₂Se₄ revisited by small-angle neutron scattering*, J. Phys.: Condens. Matter **28** 146001 (2016).
2. Y. V. Tymoshenko, Y. A. Onykiienko, T. Müller, R. Thomale, S. Rachel, A. S. Cameron, P. Y. Portnichenko, D. V. Efremov, V. Tsurkan, D. L. Abernathy, J. Ollivier, A. Schneidewind, A. Piovano, V. Felea, A. Loidl, and D. S. Inosov, *Pseudo-Goldstone magnons in the frustrated S=3/2 Heisenberg helimagnet ZnCr₂Se₄ with a pyrochlore magnetic sublattice*, Phys. Rev. X **7**, 041049 (2017).
3. C. C. Gu, Z. Y. Zhao, X. L. Chen, M. Lee, E. S. Choi, Y. Y. Han, L. S. Ling, L. Pi, Y. H. Zhang, G. Chen, Z. R. Yang, H. D. Zhou, and X. F. Sun, *Field-driven quantum criticality in the spinel magnet ZnCr₂Se₄*, Phys. Rev. Lett. **120**, 147204 (2018).
4. J. Hemberger, H.-A. Krug von Nidda, V. Tsurkan, and A. Loidl, *Large Magnetostriction and Negative Thermal Expansion in the Frustrated Antiferromagnet ZnCr₂Se₄*, Phys. Rev. Lett. **98**, 147203 (2007).
5. V. Felea, S. Yasin, A. Günther, J. Deisenhofer, H.-A. Krug von Nidda, S. Zherlitsyn, V. Tsurkan, P. Lemmens, J. Wosnitza, and A. Loidl, *Spin-lattice coupling in the frustrated antiferromagnet ZnCr₂Se₄ probed by ultrasound*, Phys. Rev. B **86**, 104420 (2012).

Publications 2019-2021

1. D. S. Inosov, Y. O. Onykiienko, Y. V. Tymoshenko, A. Akopyan, D. Shukla, N. Prasai, M. Doerr, S. Zherlitsyn, D. Voneshen M. Boehm, V. Tsurkan, V. Felea, A. Loidl, and J. L. Cohn, *Magnetic-field dependence of low-energy magnons, anisotropic heat conduction, and spontaneous relaxation of magnetic domains in the cubic helimagnet ZnCr₂Se₄*, Phys. Rev. B **102**, 184431 (2020).
2. A. Akopyan, N. Prasai, B. A. Trump, G. G. Marcus, T. M. McQueen, and J. L. Cohn, *Spin Seebeck Effect in Cu₂OSeO₃: Test of Bulk Magnon Spin-Current Theory*, Phys. Rev. B **101**, 100407 (Rapid Commun.) (2020).
3. D. Shukla, N. Prasai, T. M. Carlino, M. M. A. Mazza, A. M. Scott, and J. L. Cohn, *Anisotropic Heat Conduction in the Metal Organic Framework Perovskites [C(NH₂)₃]X(HCOO)₃ (X=Cu, Zn)*, Appl. Phys. Lett. **114**, 081907 (2019).
4. N. Prasai, A. Akopyan, B. A. Trump, G. G. Marcus, S. X. Huang, T. M. McQueen, and J. L. Cohn, *Spin phases of the helimagnetic insulator Cu₂OSeO₃ probed by magnon heat conduction*, Phys. Rev. B **99**, 020403 (Rapid Commun.) (2019).
5. C. J. Munro, E. C. Bell, M. O. Olagunju, J. L. Cohn, E. M. Zahran, L. G. Bachas, and M. R. Knecht, *Amino Acids for Sustainable Production of Cu₂O Materials: Effects on Morphology and Photocatalytic Reactivity*, ACS Sustain. Chem. Eng. **7**, 17055-17064 (2019).

Tuning anisotropic bonding via chemistry and pressure in layered pnictides and chalcogenides

Alexandra Zevalkink, Chemical Engineering and Materials Science, Michigan State University, East Lansing, MI

Olivier Delaire, Department of Mechanical Engineering and Materials Science, Duke University, Durham, NC

Program Scope

The overarching goal of this research program is to develop a predictive, chemistry-driven understanding of the impact of strongly anisotropic bonding on the phonon behavior and thermal properties of bulk layered materials. At finite temperatures, atomic vibrations (phonons) strongly impact the thermodynamics, thermal and electrical transport, and phase-switching properties of functional materials. In particular, soft phonon modes and strongly anharmonic potentials can have spectacular consequences, including structural phase transitions (for example in ferroelectrics and phase-change memory materials), metal-insulator transitions, and extreme thermal resistance preventing heat propagation.

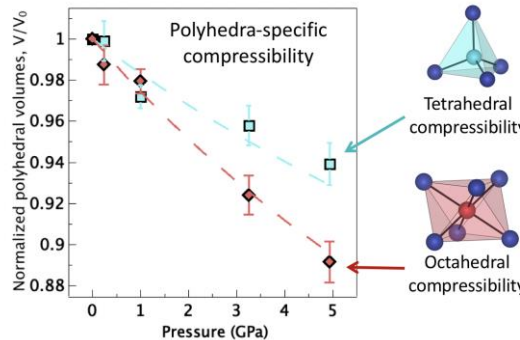
Bulk materials with highly-anisotropic bonding may provide unique strategies to induce soft-phonon modes and lattice instabilities. Recently, increasingly detailed investigations of the lattice dynamics in layered materials have been made possible by the advent of first-principles phonon calculations and advanced characterization techniques based on neutron and X-ray scattering. However, due to the lack of studies in which composition and bonding character are systematically varied, there are still fundamental questions regarding the impacts of anisotropic bonding and anharmonicity on lattice stability and thermal transport. Coherently tuning bonding anisotropy and anharmonicity across a family of related compounds would address this gap and could reveal new strategies for exploiting structural anisotropy in quasi-1D and 2D bulk materials to obtain tailored functional properties.

This project will systematically explore the lattice dynamics, phase stability, and transport properties in bulk layered and quasi-1D materials by using both composition and applied pressure to tune the degree of bonding anisotropy and anharmonicity. To accomplish this work, we will combine i) single-crystal growth of key material systems with tunable anisotropy, ii) in-situ high-temperature/high-pressure characterization of structure and phonons to probe bonding anisotropy and anharmonicity, including state-of-the-art inelastic X-ray scattering (IXS) and inelastic neutron scattering (INS), and iii) first-principles simulations leveraging large-scale computing to identify the fundamental origins of the observed effects, by relating atomic structure and dynamics to electronic orbital interactions. Finally, we will model and verify the impact of the phonon behavior on thermal transport to identify new strategies for a-priori design of thermal conductivity. Our integrated collaborative approach will systematically unravel the effects of anisotropy and bonding

anharmonicity on phonon transport, thermodynamics, and thermal properties and will provide new fundamental understanding to control properties of complex anisotropic materials.

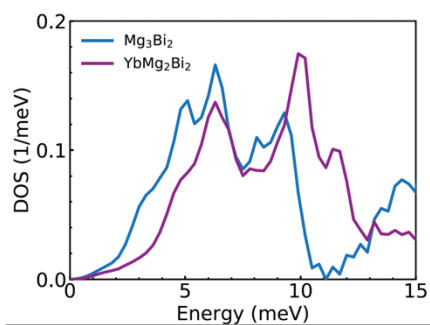
Recent Progress

Investigation of Mg₃Pn₂ at high-pressure: Alloys between Mg₃Sb₂ and Mg₃Bi₂ have recently been shown to be exceptional thermoelectric materials due in part to their anomalously low thermal conductivity. In the present study, in-situ high-pressure synchrotron X-ray diffraction was used to investigate the structure and bonding in Mg₃Sb₂ and Mg₃Bi₂ at pressures up to 50 GPa. Our results confirm prior predictions of isotropic in-plane and out-of-plane compressibility, but reveal large disparities between the bond strength of the two distinct Mg sites. Using single crystal diffraction, we show that the octahedral Mg-Sb bonds are significantly more compressible than the tetrahedral Mg-Sb bonds in Mg₃Sb₂, which lends support to arguments that the weaker octahedral Mg bonds are responsible for the anomalous thermal properties of Mg₃Sb₂ and Mg₃Bi₂. Further, we reported the discovery of a displacive and reversible phase transition in both Mg₃Sb₂ and Mg₃Bi₂ above 7.8 GPa and 4.0 GPa, respectively. The transition to the high-pressure structure involves a highly anisotropic volume collapse, in which the out-of-plane axis compresses significantly more than the in-plane axes. Single crystal diffraction at high pressure was used to solve the monoclinic high-pressure structure (*C*2/*m*), which is a distorted variant of the ambient-pressure structure containing four unique Mg coordination environments. This work was published in 2020 in Chemistry of Materials [1].



Octahedral Mg–Sb bonds are significantly more compressible than the tetrahedral Mg–Sb bonds in Mg₃Sb₂

Phonons and origin of ultralow thermal conductivity in Mg₃Pn₂: Mg₃Sb₂ and Mg₃Bi₂ exhibit an anomalously low thermal conductivity, comparable to those of much heavier compounds PbTe or Bi₂Te₃. Contrary to common mass-trend expectations, replacing Mg with much heavier Ca or Yb yields a threefold increase in thermal conductivity in ternary CaMg₂Sb₂ and YbMg₂Bi₂. We performed a comprehensive analysis of phonons in the series AMg₂X₂ (A = Mg, Ca, Yb, X = Bi, Sb) based on inelastic neutron and x-ray scattering, complemented with first-principles simulations, and show for the first time that the anomalously low lattice thermal conductivity of Mg₃X₂ has an inherent phononic origin. We uncover a large phonon softening and flattening of low-energy transverse acoustic phonons in Mg₃Bi₂ and Mg₃Sb₂ compared to the ternary analogues (A = Ca, Yb). Our first-principles simulations reveal how this is traced to a weak Mg-X chemical

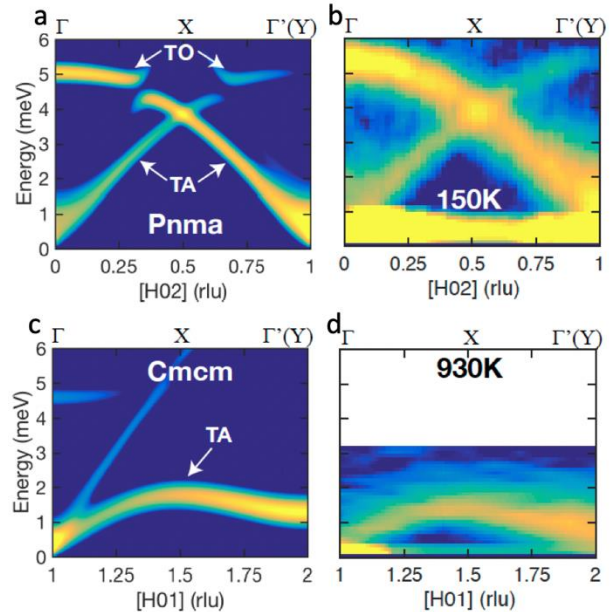


Low-energy phonon density of states of Mg₃Bi₂ and YbMg₂Bi₂ measured with neutron scattering.

bond, which softens low-energy transverse acoustic phonons. While the suppression in group velocity reduces κ_{lat} by a modest 20%, the soft anharmonic dispersion enables a threefold increase in phonon scattering primarily by enhancing the scattering phase-space. These findings rationalize the microscopic origins of the outstanding thermal properties of AMg_2X_2 compounds, and provide fundamental insights on means to control thermal transport properties, by manipulating phonon scattering without the traditional reliance on heavy elements or disorder. A manuscript was submitted (under review in Science Advances) [4].

Anisotropic bonding, phonon anharmonicity and ultralow thermal conductivity in SnS: The lattice dynamics and high-temperature structural transition in SnS and SnSe were investigated via inelastic neutron scattering, high-resolution Raman spectroscopy and first-principles simulations. The results revealed a spectacular, extreme softening and reconstruction of an entire manifold of low-energy acoustic and optic branches across a structural transition, reflecting strong directionality in bonding strength and anharmonicity. Further, our results solve a prior controversy by revealing the soft-mode mechanism of the phase transition that impacts thermal transport and thermoelectric efficiency. Our simulations of anharmonic phonon renormalization capture these striking effects, showing that the large phonon shifts directly affect the thermal conductivity by altering both the phonon scattering phase space and the group velocities. These results provide a new level of microscopic understanding of phase stability and thermal transport in technologically important materials, providing further insights on ways to control phonon propagation in thermoelectrics, photovoltaics, and other materials requiring thermal management. The results were published in Nature Communications [5].

Anharmonic lattice dynamics and superionic transition in layered chalcogenide $AgCrSe_2$: Unveiling the unusual atomic dynamics in superionic conductors is critical for the design of energy conversion and storage materials, for example to rationalize their thermal transport properties in thermoelectric applications or their fast ionic conductivity in solid-state electrolytes. Intrinsically low lattice thermal conductivity (κ_{lat}) in superionic conductors is of great interest for energy conversion applications in thermoelectrics. Yet, the complex atomic dynamics leading to



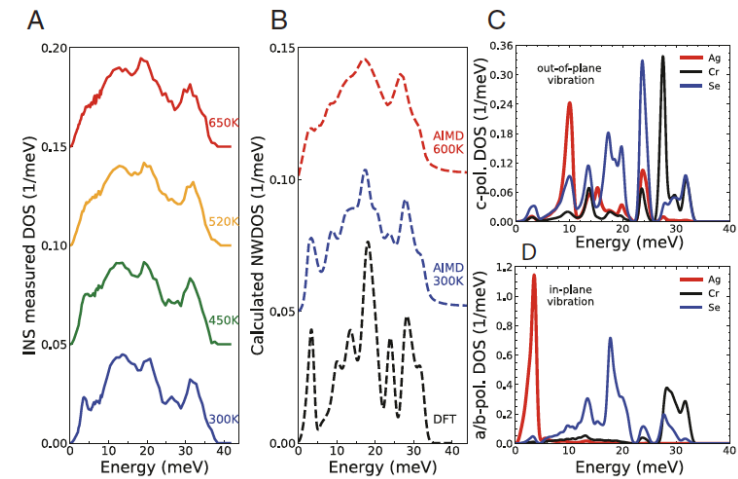
Phonon dispersions of the Pnma low-temperature phase (a,b) and Cmcm high-temperature phase (c,d) of thermoelectric compound SnS. Panels (a,c) are first-principles simulations, and (b,d) are inelastic neutron scattering data. A strong renormalization is seen, leading to flat, low-energy dispersions at high temperature, favoring low thermal conductivity.

superionicity and ultralow thermal conductivity have remained poorly understood. We performed a comprehensive study of the lattice dynamics and superionic diffusion in AgCrSe₂ from energy- and momentum-resolved neutron and X-ray scattering techniques, combined with first-principles calculations. Our results settle unresolved questions about the lattice dynamics and thermal conduction mechanism in AgCrSe₂. We find that the heat-carrying long-wavelength transverse acoustic (TA) phonons coexist with the ultrafast diffusion of Ag ions in the superionic phase, while the short-wavelength nondispersive TA phonons break down. Strong scattering of phonon quasiparticles by anharmonicity and Ag disorder are the origin of intrinsically low κ_{lat} .

The breakdown of short-wavelength TA phonons is directly related to the Ag diffusion, with the vibrational spectral weight associated to Ag oscillations evolving into stochastic decaying fluctuations. Furthermore, the origin of fast ionic diffusion is shown to arise from extended flat basins in the energy landscape and collective hopping behavior facilitated by strong repulsion between Ag ions. These results provide fundamental insights into the complex atomic dynamics of superionic conductors. The results were published in PNAS [6].

Future Plans

Single crystals of GeTe-SnTe and GeTe- Sb₂Te₃ alloys have been grown using the Bridgman technique. We plan to investigate the anisotropic electronic, thermal, and elastic transport properties of GeTe- Sb₂Te₃ crystals to determine the impact of the irregularly spaced van der Waal layers in this system. INS experiments and transport measurements will be performed on GeTe-SnTe crystals to investigate the effect of the rhombohedral to cubic phase transition on the phonons and thermal properties. We have performed preliminary measurements of phonons as a function of pressure in SnSe and we plan to finalize our measurements and first-principles modeling for publication. We plan to investigate anharmonic phonons and thermal transport in pseudo-binaries PbTe-PbSe and GeSe-AgBiSe₂ to probe phonon disorder scattering. We will use a combination of INS, IXS and first-principles simulations.



Phonon DOS from experiments and simulations. (A) INS powder measurements at the ARCS with $E_i = 20$ and 80 meV to get fine resolution at the low-energy portion and the whole spectrum. Data are stitched together at 9 meV. Blue, green, orange, and red lines are measured at 300, 450, 520, and 650 K, respectively. (B) Calculated neutron-weighted DOS. Black dashed line is labeled as DFT, and AIMD at 300 and 600 K are blue and red dashed lines, respectively. (C and D) Site-projected DOS from DFT for the c-axis polarized (C) and in-plane (D) motions in the a–b plane. Ag motions mainly contribute the strong peak around 3.5 meV for the in-plane vibration and a weaker peak near 10 meV for c-axis.

Publications

1. M. Calderon-Cueva, W. Peng, S. M. Clarke, J. Ding, B. Brugman, G. Levental, A. Balodhi, M. Rylko, O. Delaire, J. P. S. Walsh, S. M. Dorfman, and A. Zevalkink, Anisotropic structural collapse of Mg₃Sb₂ and Mg₃Bi₂ at high pressure, *Chem. Mater.* 33, 567–573 (2021).
2. A. Balodhi, K. Chang, K. T. Stevens, S. K. Chakrapani, S. M. Ennaceur, A. Migliori, A. Zevalkink, Determination of single crystal elastic moduli of KTb₃F₁₀ by resonant ultrasound spectroscopy, *J. Appl. Phys.*, 128, 165104 (2020).
3. W. Peng, D. M. Smiadak, M. G. Boehlert, S. Mather, J.B. Williams, D.T. Morelli, A. Zevalkink, Lattice hardening due to vacancy diffusion in (GeTe)_mSb₂Te₃ alloys, *J. Appl. Phys.* 126, 055106, (2019).
4. J. Ding, T. Lanigan-Atkins, M. Calderon-Cueva, A. Banerjee, D. L. Abernathy, A. Said, A. Zevalkink, and O. Delaire, “Anharmonic phonons and origin of ultralow thermal conductivity in Mg₃Sb₂ and Mg₃Bi₂” *under review (with referees) in Science Advances*.
5. T. Lanigan-Atkins*, S. Yang*, J. L. Niedziela, D. Bansal, A. F. May, A. A. Puretzky, J.Y.Y. Lin, D. Pajerowski, T. Hong, S. Chi, G. Ehlers, and O.Delaire. "Extended anharmonic collapse of phonon dispersions in SnS and SnSe", *Nature Communications* 11 (1), 1-9 (2020).
6. Jingxuan Ding, Jennifer L. Niedziela, Dipanshu Bansal, Jiuling Wang, Xing He, Andrew F. May, Georg Ehlers, Douglas L. Abernathy, Ayman Said, Ahmet Alatas, Yang Ren, Gaurav Arya, and Olivier Delaire, “Anharmonic lattice dynamics and superionic transition in AgCrSe₂”, *PNAS* 117 (8) 3930-3937 (2020).
7. Xing Tan, Jingxuan Ding, Huifang Luo, Olivier Delaire, Jiong Yang, Zhifang Zhou, Jinle Lan, Yuanhua Lin, Cewen Nan, “High thermoelectric performance of AgSb_{1-x}Pb_xSe₂ prepared by fast non-equilibrium synthesis”, *ACS Applied Materials & Interfaces*, 12, 37, 41333–41341 (2020).
8. T. Lanigan-Atkins *, X. He *, M. J. Krogstad, D. M. Pajerowski, D. L. Abernathy, Guangyong NMN Xu, Zhijun Xu, D.-Y. Chung, M. G. Kanatzidis, S. Rosenkranz, R. Osborn, and O. Delaire, “Two-dimensional overdamped fluctuations of soft perovskite lattice in CsPbBr₃”, *Nature Materials (accepted for publication)*.

Generating Metastable Magnetostructural Phases in Solid-State Caloric Systems

Shane Stadler, Louisiana State University, Department of Physics and Astronomy

Naushad Ali and Saikat Talapatra, Southern Illinois University, Department of Physics

Program Scope

The objective of this project is to discover and explore new solid-state caloric materials, and to understand the origins of their physical behaviors including magnetocaloric effects, barocaloric effects, and transport properties. Materials that exhibit extreme changes in magnetostructural and transport properties linked to magnetostructural phase transitions near room temperature are relatively rare, and often lead to multifunctional properties important for modern technologies. In this project, we explore new materials that exhibit magnetostructural transitions near room temperature that form as a result of doping, thermal quenching, or the application of pressure during synthesis, leading to metastable magnetostructural phases.

Recent Progress

One goal of this project is to induce coupled magnetostructural transitions near room temperature by creating metastable phases through thermal quenching or by applying pressure during synthesis. Such processes can permanently alter the behaviors of the phase transitions and physical properties of the materials. The application of hydrostatic pressure during measurement (i.e., not during synthesis), however, provides a method to alter the magnetocaloric and barocaloric properties after synthesis, and can also induce magnetostructural transformations.

Some Mn T X-based (T = Co, Ni, Fe; X = Ge, Si) intermetallic compounds exhibit pressure- and field-induced magnetostructural transitions (MSTs) that lead to shape-memory phenomena, magnetocaloric effects (MCEs), and volume anomalies near room temperature.¹⁻³ The isostructurally-substituted system, (MnNiSi)_{0.62}(FeCoGe)_{0.38}, has been shown to exhibit both large magnetocaloric and barocaloric effects near room temperature⁴, and has therefore been chosen for additional investigations focusing on the effects of quenching and pressure on the magnetostructural transitions, and on the magnetocaloric and barocaloric properties in this material system. The magnetization curves ($H = 100$ Oe) of the annealed samples are shown in Fig. 1 as a function of temperature, pressure, and the temperatures from which the samples were quenched (into ice water).⁵ The samples were annealed and quenched from temperatures that ranged from 700 °C (AQ700 in Fig. 1) to 1050 °C (AQ1050). Two trends have been observed with increasing quenching temperature: first, the transition shifts to lower temperature and, second, the thermal hysteresis decreases until the transition becomes quasi-second-order for AQ1050. The former can

be explained as the metastable high-temperature structure being frozen in by quenching from high temperature. The latter may be a result of the structural transition approaching the Curie temperature of the low temperature phase as the quenching temperature increases, and subsequent conversion of the coupled transition to second order.

Magnetization measurements under applied hydrostatic pressure (i.e., during the magnetization measurements) were carried out using a CuBe pressure cell (by Quantum Design). Pressure shifts the transitions to lower temperatures (dashed lines in Fig. 1), consistent with the previously reported behavior of this system.⁶ However, for all but AQ700, the transition becomes second order for applied pressures on the order of ~1 GPa (or less). The entropy changes remain relatively large from 35 J kg⁻¹K⁻¹ for AQ700 to ~22 J kg⁻¹K⁻¹ for AQ1050, despite the latter being nearly a second order transition.

The previous work on $(\text{MnNiSi})_{1-x}(\text{FeCoGe})_x$ prompted the study of the effects of pressure and quenching on the related stoichiometric MnTX system, MnCoGe. A series of samples were RF-melted and then subjected to various thermal treatments that included slow-cooling from 1100 °C (SC1100) and quenching from temperatures that ranged from 700 °C (AQ700) to 1150 °C (AQ1150). The slow-cooled sample (SC1100) undergoes a structural transition at about 490 K (from DSC data) and a second-order magnetic transition at about 350 K (see Fig 2).⁸ Referring to the calorimetric (DSC) curves in the upper right of Figure 2, quenching at 700 °C (AQ700) shifts the structural transition by over 50 K to lower temperature (relative to SC1100), however the magnetic transition remains unchanged. This indicates that, not only does quenching tend to stabilize the high-temperature phase, which is not unexpected, but also that quenching from higher temperatures might further shift the structural transition to lower temperature, and possibly couple the magnetic and structural transitions. This is precisely what occurs in the sample quenched at 800 °C (AQ800),

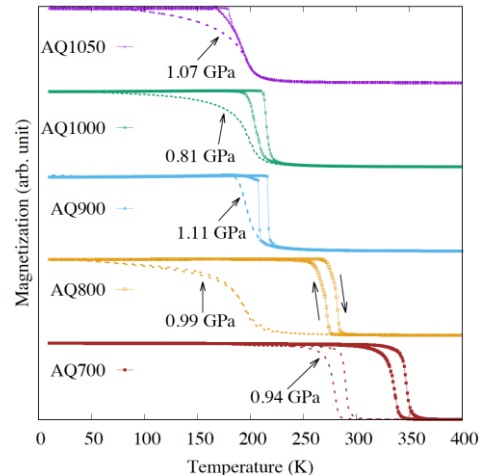


Fig. 1. Magnetization of as a function of temperature, pressure, and quenching temperature of $(\text{MnNiSi})_{0.62}(\text{FeCoGe})_{0.38}$.

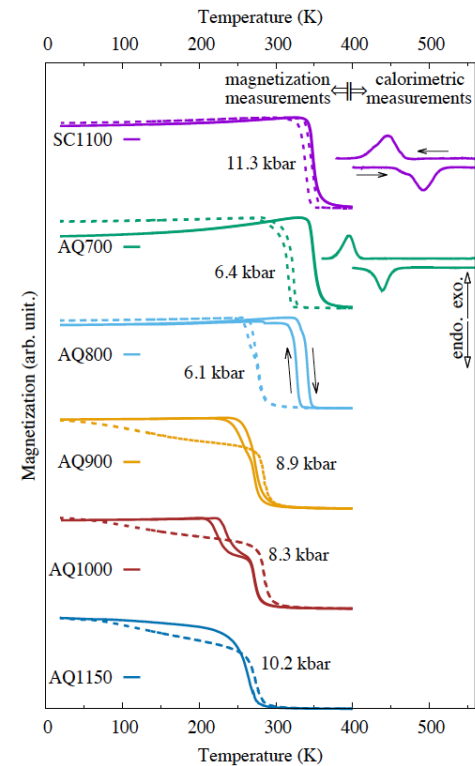


Fig. 2 Magnetization ($H = 100$ Oe) and DSC (upper right) data of MnCoGe as a function of temperature, quenching temperature, and applied pressure. The dashed lines indicate magnetization data measured at the specified pressures.

and possibly couple the magnetic and structural transitions.

and this sample exhibits a large magnetic entropy change $\Delta S_M = 34 \text{ J/kgK}$ at the magnetostructural transition temperature ($T_M = 330 \text{ K}$).⁸

Referring to the top two curves of Figure 2, which explicitly show both the structural (DSC) and magnetic transitions separated, it is clear that the application of pressure (dashed lines in Fig. 2) shifts the structural transition to lower temperature and that the magnetic transition follows it, indicating that the coupled transition observed in AQ800 is dominated by the structural transition. In addition, the large pressure-induced shift in AQ800 of nearly -10 K/kbar suggest that this material may exhibit large barocaloric effects. A phase diagram that relates the annealing/quenching temperatures of MnCoGe to the transition temperatures is shown in Figure 3.

As the quenching temperature exceeds 800 °C in Figure 2, the structural transition continues on to lower temperatures and decouples from the magnetic transition until the sample undergoes a single, second-order transition for AQ1150. It is interesting to note that, in samples AQ900 through AQ1150, that the application of hydrostatic pressure *increases* the magnetic transition temperature, an observation that is currently unexplained.

In conclusion, it was shown that thermal quenching can be used to stabilize high-temperature structural phases at lower temperatures such that they couple with magnetic transitions to form magnetostructural transitions. This was shown for the specific case of MnCoGe, and the result was the generation of a new system that exhibits large magnetocaloric effects. In addition, due to its high sensitivity to applied hydrostatic pressure, this same system may also exhibit large barocaloric effects, making it a promising multicaloric material to be explored for potential applications in future multicaloric devices.

We have also explored the effects of pressure during the synthesis of magnetocaloric materials including $\text{Ni}_2\text{Mn}_{1-x}\text{Cu}_x\text{Ga}$ and $\text{MnNi}_{1-x}\text{Co}_x\text{Ge}$ since they both have known magnetostructural transitions. Shown in Figure 4 is the apparatus that was used to synthesize the

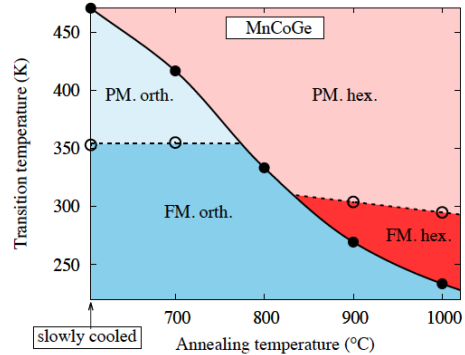


Fig. 3. An annealing/quenching temperature phase diagram of MnCoGe at ambient pressure.

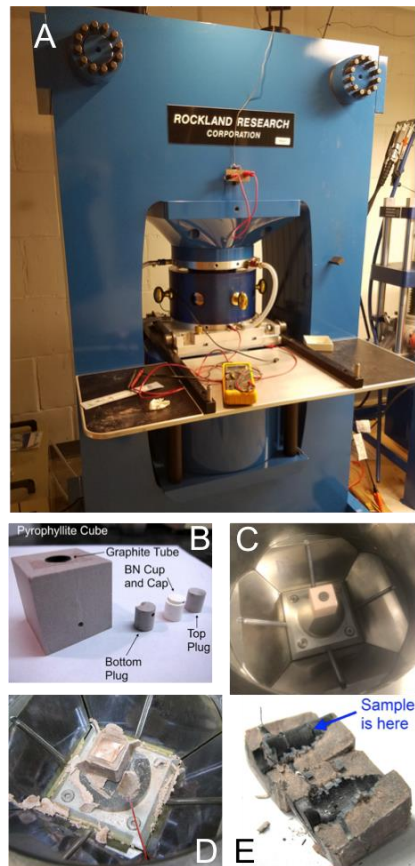


Fig. 4. The press with multi-anvil components as described in the text.

samples made at high pressure (and temperature). It is a multi-anvil (cubic) high-pressure furnace from Rockland Research Corporation that can apply pressures up to 10 GPa at temperatures up to 2000 °C. The materials were first RF melted, then ground, pressed into pellets, and inserted into a boron nitride crucible (Fig. 4B). The crucible was then loaded into a graphite sleeve, which serves as the furnace (current is passed through it during growth) and then placed inside a pyrophyllite cube, which acts as the pressure transmitting medium (Fig. 4C). Six symmetrically configured tungsten carbide anvils compress the cube inside a hardened-steel containment ring, resulting the extruded pyrophyllite and pressure-synthesized sample as shown, respectively, in Fig. 4(D and E).

A MnNi_{0.92}Co_{0.08}Ge sample was first synthesized by RF melting and broken into pieces. One was annealed at 800 °C and the other ground and synthesized in the high-pressure furnace at T = 800 °C and P = 5.5 GPa. As seen in Fig. 5(A), the RF sample had a magnetostructural transition at T = 300 °C (indicated by arrow A in the figure).⁹ When subjected to a 11-kbar hydrostatic pressure during the measurement, this transition shifts 50 K to lower temperature (arrow B). Arrow A in Fig. 5(B) is the same transition in the RF sample, however, arrow B* indicates the shifted transition observed in the sample synthesized at high pressure. Note that the shift to B* is not due to pressure applied during the measurement as in Fig 5(A) but rather pressure during synthesis, effectively locking in the high-pressure phase and maintaining the large magnetocaloric effects ($\Delta S_M \sim 80 \text{ J/kgK}$) at this metastable transition. The physical origins of this effect are currently being explored.⁹

Future Plans

We are starting many new projects including: (1) synthesizing magnetic high-entropy alloys (HEAs) under high pressure and exploring their physical properties, (2) studying the magnetocaloric properties of Heusler-type Mn_{2-x}Fe_{1+x}Ge melt-spun ribbons, (3) investigating Ni-Mn-Co/carbon nanotube composites, and (4) exploring the magneto- and barocaloric properties and metastable phases of new MnTX systems synthesized under high pressure.

References

- ¹E. Liu *et al.*, Nature Commun. **3**, 873 (2012).
- ²T. Samanta *et al.*, Appl. Phys. Lett. **100**, 052404 (2012).
- ³C. L. Zhang *et al.*, Appl. Phys. Lett. **103**, 132411 (2013).
- ⁴P. Lloveras *et al.*, APL Materials **7** (6), 061106 (2019).
- ⁵T. Samanta *et al.*, Appl. Phys. Lett. **112**, 021907 (2018).
- ⁶J.-H. Chen *et al.*, Intermetallics **112**, 106547 (2019).
- ⁷T. Samanta *et al.*, J. Appl. Phys. **117** (12), 123911 (2015).
- ⁸J.-H. Chen *et al.*, (Under review)
- ⁹T. Chhetri *et al.*, (Submitted for publication)

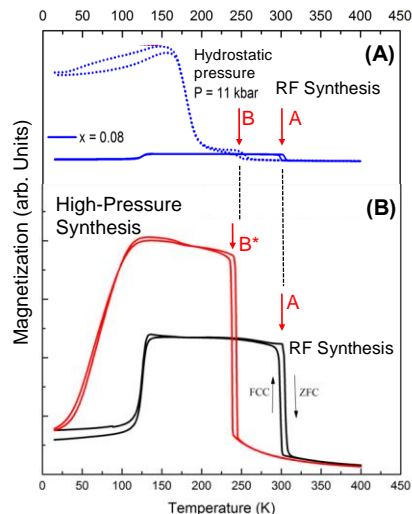


Fig. 5. MnNi_{0.92}Co_{0.08}Ge synthesized (A) in an RF furnace at ambient pressure and (B) at high pressure (5.5 GPa).

Publications (2019 – present)

Pol Lloveras, Tapas Samanta, María Barrio, Igor Dubenko, Naushad Alid, Josep-Lluís Tamarit, and Shane Stadler, *Giant reversible barocaloric response of $(MnNiSi)_{1-x}(FeCoGe)_x$ ($x = 0.39, 0.40, 0.41$)*, APL Materials **7** (6), 061106 (2019). [doi.org/10.1063/1.5097959]

Anil Aryal, Sudip Pandey, Igor Dubenko, Dipanjan Mazumdar, Shane Stadler, and Naushad Ali, *Effects of Rare-Earth ($R = Pr, Gd, Ho, Er$) Doping on Magnetostructural Phase Transitions and Magnetocaloric Properties in $Ni_{43-x}R_xMn_{46}Sn_{11}$ Shape Memory Alloys*, IEEE Trans. Mag. **55** (2), 2500505 (2019). [doi.org/10.1109/TMAG.2018.2868134]

Sudip Pandey, Mikhail Blinov, Anil Aryal, Igor Dubenko, Valerii Prudnikov, E. Lähderanta, Alexander Granovsky, Nina Pristinskaya, Shane Stadler, and Naushad Ali *Drastic violation of correlation between the anomalous Hall effect coefficient and resistivity in the Heusler alloy $Ni_{45}Cr_5Mn_{37}In_{13}$* , J. Magn. Magn. Mater. **481**, 25 (2019). [DOI: 10.1016/j.jmmm.2019.02.086]

Anil Aryal, Yuri Koshkid'ko, Igor Dubenko, CF Sánchez-Valdés, JL Sánchez Llamazares, E Lähderanta, Sudip Pandey, Alexander Granovsky, Jacek Cwik, Shane Stadler, and Naushad Ali, *Direct and indirect measurements of the magnetic and magnetocaloric properties of $Ni_{0.895}Cr_{0.105}MnGe_{1.05}$ melt-spun ribbons in high magnetic fields*, J. Magn. Magn. Mater. **488**, 165359 (2019). [doi.org/10.1016/j.jmmm.2019.165359]

Kuei-Chung Cheng, Jing-Han Chen, Shane Stadler, and Shih-Hsun Chen, *Properties of atomized $AlCoCrFeNi$ high-entropy alloy powders and their phase-adjustable coatings prepared via plasma spray process*, Appl. Surf. Sci. **478**, 478 (2019). [DOI: 10.1016/j.apsusc.2019.01.203]

Jing-Han Chen, Tej Poudel Chhetri, Ahmad Us Saleheen, David P. Young, Igor Dubenko, Naushad Ali, and Shane Stadler, *Effects of heat treatments on magneto-structural phase transitions in $MnNiSi-FeCoGe$ alloys*, Intermetallics **112**, 106547 (2019). [doi.org/10.1016/j.intermet.2019.106547]

Anil Aryal, Sudip Pandey, Igor Dubenko, Dipanjan Mazumdar, Shane Stadler, and Naushad Ali, *Magnetostructural phase transitions and large magnetic entropy changes in Ag-doped $Mn_{1-x}Ag_xCoGe$ intermetallic compounds*, MRS. Comm. **1-6** (2019). [DOI: 10.1557/mrc.2018.228]

Yury Koshkid'ko, Sudip Pandey, Jacek Cwik, Igor Dubenko, Anil Aryal, Alexander Granovsky, Damian Szymanski, Shane Stadler, Erkki Lähderanta, and Naushad Ali, *Relaxation phenomena in adiabatic temperature changes near magnetostructural transitions in Heusler alloys*, J. Alloys Cmpds. **821** 153402 (2020). [doi.org/10.1016/j.jallcom.2019.153402]

Anil Aryal, Said Bakkar, Hassana Samassekou, Sudip Pandey, Igor Dubenko, Shane Stadler, Naushad Ali, and Dipanjan Mazumdar, *Mn_2FeSi : An antiferromagnetic inverse-Heusler alloy*, J. Alloy Cmpds. **823**, 153770 (2020). [doi.org/10.1016/j.jallcom.2020.153770]

J.T. Liang, K.C. Cheng, SH Chen, J.H. Chen, S. Stadler, C.L. Li, and C.H. Hsueh, *Study on the continuous phase evolution and physical properties of gas-atomized high-entropy alloy powders*, Materials Research Express **7** (2), 026545 (2020) [doi.org/10.1088/2053-1591/ab5ee2]

Anil Aryal, Igor Dubenko, Saikat Talapatra, Alexander Granovsky, Erkki Lähderanta, Shane Stadler, and Naushad Ali, *Magnetic field dependence of the martensitic transition and magnetocaloric effects in $Ni_{49}BiMn_{35}In_{15}$* , AIP Advances **10**, 015138 (2020). [10.1063/1.5130405@adv.2020.MMM2020.issue-1]

Anil Aryal, Igor Dubenko, Sudip Pandey, Jing-Han Chen, Saikat Talapatra, Vojtech Chlan, Helena Stepankova, Vladimir Matveev, Mikhail Blinov, Valerii Prudnikov, Alexander Granovsky, Erkki Lähderanta, Shane Stadler, and Naushad Ali, *NMR studies of the ground states of $Ni_{50-x}Co_xMn_{35}In_{15}$ ($x=1, 2.5$) and $Ni_{45}Co_5Mn_{37}In_{13}$ Heusler alloys*, AIP Advances **10**, 015328 (2020). [doi.org/10.1063/1.5129976]

A. B. Granovsky, E. A. Soboleva, E. A. Fadeev, I. S. Dubenko, A. Arial, H. Samasseku, S. Pandey, S. Stadler, D. Mazumdar, N. Ali, and E. Lahderanta, *Martensitic phase transition in magnetic thin films based on inverse Heusler alloys of Mn_2FeSi composition*, ZhETF **157** (1), 137 (2020).

Mikhail Blinov, Anil Aryal, Sudip Pandey, Igor Dubenko, Saikat Talapatra, Valeriy Prudnikov, Erkki Lähderanta, Shane Stadler, Vasiliy Buchelnikov, Vladimir Sokolovskiy, Mikhail Zagrebin, Alexander Granovsky, and Naushad Ali, *Effects of magnetic and structural phase transitions on the normal and anomalous Hall effects in Ni-Mn-In-B Heusler alloys*, Phys. Rev. B **101**, 094423 (2020) [doi.org/10.1103/PhysRevB.101.094423]

Timothy David Brown, Jing-Han Chen, Erick Braham, Shane Stadler, and Patrick J Shamberger, *Dynamic Re-equilibration Controlled Multi-step Transformations in $(Mn,Fe)_2(P,Si)$ Alloys*, J. Phys. D: Appl. Phys. **53**, 205303 (2020) [doi.org/10.1088/1361-6463/ab768a]

Jing-Han Chen, Aaron Trigg, Tej Poudel Chhetri, David P. Young, Igor Dubenko, Naushad Ali, and Shane Stadler, *The influence of Au substitution and hydrostatic pressure on the phase transitions and magnetocaloric properties of MnCoGe alloys*, J. Appl. Phys. **127**, 213901 (2020) [doi.org/10.1063/5.0007172]

Jing-Han Chen, Tej Poudel Chhetri, Chung-Kai Chang, Yu-Ching Huang, David P. Young, Igor Dubenkod, Naushad Ali, and Shane Stadler *The effects of hydrostatic pressure and annealing conditions on the magnetocaloric properties of MnCoGe, (Under Review)*

Sudip Pandey, Yury Koshkid'Ko, Igor Dubenko, Anil Aryal, Alexander Granovsky, Shane Stadler, and Naushad Ali *Magnetic and magnetocaloric properties of Co doped Ni-Mn-Sn Heusler alloys at high magnetic field and pressure*, J. Appl. Phys. (2019) **(Under review)**.

Tej Poudel Chhetri, Jing-Han Chen, David P. Young, Igor Dubenko, Naushad Ali, and Shane Stadler *The magnetic, structural, and magnetocaloric properties of $Ni_2Mn_{0.75}Cu_{0.25}Ga$ synthesized at high pressure and temperature, (Submitted for Publication)*

* Two additional manuscripts are in preparation.

Session XII

Phase Transitions in Mesoscopic Systems

P.I. Raymond L. Orbach

(The University of Texas at Austin)

Co-P.I. E. Dan Dahlberg

(University of Minnesota)

Co-P.I. Gregory G. Kenning

(Indiana University of Pennsylvania)

Program Scope

Our research focuses on developing an understanding of the correlated state in glassy systems using spin glasses as the model system; the goal is to establish a firm experimental and theoretical basis for their dynamics. Our research is complimentary to that on glass forming liquids¹ that have recently demonstrated correlated behavior using up to 5th order electrical dielectric susceptibilities. The focus on magnetic spin glasses demonstrates both the correlated nature of the condensed glassy state, and its dynamical properties. We have single crystals (a first) of the canonical metallic spin glass, CuMn, and have observed the consequences of large correlation lengths never before attained in polycrystalline materials. This includes studies of their non-linear magnetization properties. In polycrystalline films, we have explored their contributions to 1/f noise and have been able to determine the energy barrier distribution that determines many of the dynamical properties. There remain properties of glassy systems associated with temperature chaos and memory effects that remain elusive. Our current research focuses on the yet-to-be-understood dynamical processes underlying these phenomena.

Importantly, our research is synergized by our collaboration with the Janus II group.² They have constructed a special purpose computer that is able to simulate the dynamical properties of the 3D Ising spin glass at time and length scales comparable to experiment. The relationship between our research program and their simulations has created an extraordinary opportunity for scientific discovery not previously possible. The interaction between experiment, simulation, and theory has produced new insights into the nature of the growth of the correlated state. For example, we have discovered a new non-linear magnetization scaling law near the condensation temperature, T_g, far superior to previous relationships. Concomitantly, we have also clarified the nature of the Zeeman interaction in spin glasses, settling a decades old controversy.

The three laboratories involved in this DOE sponsored program collaborate in a complementary fashion. The group at The University of Texas at Austin provides theoretical guidance and SQUID magnetization measurements over a large time scale; the Indiana University of Pennsylvania group utilizes an ultra-sensitive home-built SQUID magnetometer to measure dynamics and grows thin film multilayer structures; the University of Minnesota group performs 1/f noise electrical resistance and very low frequency magnetic susceptibility measurements, and can also supply thin film multilayer structures. A weekly ZOOM collaboration call coordinates the research programs of the three laboratories. The combined group's publications are a consequence of this close collaboration.

Recent Progress

As an example of the fruits of the collaboration with the Janus II Collaboration, a new scaling law for the dynamical non-linear magnetization of spin glasses in the vicinity of the condensation temperature T_g has been proposed and evidenced through our combination of experiments and simulations.³ One can write the non-linear magnetization, M , for a spin glass at time t after aging the system for a time, t_w , in a magnetic field, H , with the non-linear susceptibilities χ_{2n-1} as³

$$M(t, t_w; H) = \chi_1 H + \frac{\chi_3}{3!} H^3 + \frac{\chi_5}{5!} H^5 + \mathcal{O}(H^7),$$

Then, according to the proposed new scaling relationship, the non-linear susceptibilities, χ_{2n-1} , above can be written in term of the spin glass correlation length $\xi(t, t_w; H)$ as,

$$\chi_{2n-1} \propto b_{2n}(T) [\xi(t_w)]^{(n-1)D - [n\theta(\bar{x})/2]}$$

where the coefficients $b_{2n}(T)$ are assumed to be smooth functions of temperature T . Here, $\xi(t_w)$ is the spin glass correlation length, having grown from nucleation to a length $\xi(t_w)$ during the aging time t_w . The dimensionality is D (here, $D = 3$), $\theta(x)$ is the replicon exponent,⁴ and $x = \ell_J(T)/\xi(t_w)$ where $\ell_J(T)$ is the Josephson length.⁵

To test this relationship, the following protocol was followed using a commercial dc SQUID to measure the magnetization of a Cu₉₄Mn₆ single crystal ($T_g = 31.5$ K). The sample was quenched from 40 K at 10 K/min to the measuring temperature T_m in zero magnetic field. After the temperature was stabilized, the system was aged for a waiting time t_w before a magnetic field H was turned on, and the magnetization, $M_{ZFC}(t, t_w; T_m)$ recorded as a function of time t . The chosen temperatures were 28.5 K, 28.75 K, and 29 K, selected to be $\geq 0.9 T_g$. The magnetic fields ranged from 16 to 59 Oe.

In parallel with experiments, the simulations used the Ising-Edwards-Anderson (IEA) model with the Hamiltonian

$$\mathcal{H} = - \sum_{\langle x,y \rangle} J_{xy} s_x s_y - H \sum_x s_x$$

where s_x is the spin at site x (with $s_x = \pm 1$) and J_{xy} is the exchange coupling between spins ($J_{xy} = \pm 1$). The sample is a cubic lattice of linear size $L = 160$ with random J_{xy} . In these natural units, for $H = 0$, the IEA model undergoes a spin glass phase transition at the critical temperature $T_g = 1.103$.⁶ The non-equilibrium dynamics were simulated by means of a Metropolis algorithm using periodic boundary conditions. The magnetic field $H = 1$ corresponds to 5×10^4 Oe. The lowest magnetic field for which the simulations can be measured is $H = 0.005$, corresponding to a laboratory equivalent of approximately 250 Oe. Although H in the simulations is considerably larger than experimental fields, two relationships were utilized to reach the laboratory values.³

In order to mimic the experimental setup in the simulations, an initial random spin configuration is placed instantaneously at the temperature T_m and left to relax for a time t_w with $H = 0$. At time t_w , the external magnetic field is turned on and the magnetization $M(t, t_w; H)$ and the correlation function are recorded.

The dynamics are measured through the relaxation function $S(t) = d(M/H)/d \ln t$. Figure 1 below displays both the experimental and simulation data for $S(t)$:

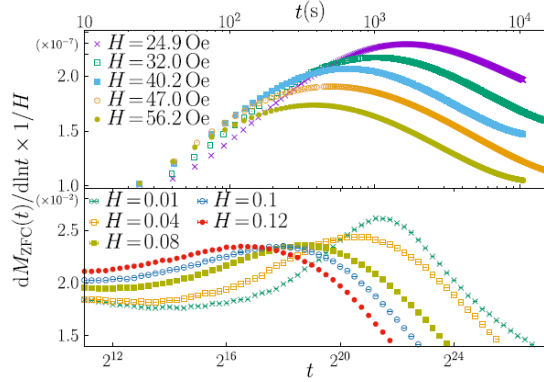


Fig. 1. A representative set of relaxation curves $S(t) = d(M/H)/d \ln t$ for CuMn at $T = 29$ K and $t_w = 10^4$ s (top) and for the IEA model at $T = 0.9$ and $t_w = 2^{22}$ lattice sweeps (bottom).

The time t at which $S(t)$ peaks, $t_{\text{peak}} \equiv t_w^{\text{eff}}$ describes the characteristic response time of the spin glass system, and is related to the excess free energy per spin in a magnetic field H . By integrating the above expression for $M(t, t_w; H)$ with respect to H (values for the individual χ_{2n-1} are extracted from a polynomial fit of $M(t, t_w; H)$ to the experimental data):

$$\Delta F = - \left[\frac{\chi_1}{2} H^2 + \frac{\chi_3}{4!} H^4 + \frac{\chi_5}{6!} H^6 + \mathcal{O}(H^8) \right].$$

One can relate ΔF to the effective response time t_w from the usual Arrhenius law, $t_H^{\text{eff}}/t_{H=0}^{\text{eff}} = \exp[N\Delta F/(k_B T)]$, where we have taken explicit recognition of the dependence of t_w^{eff} on H by changing notation from t_w^{eff} to t_H^{eff} , so that t_w becomes an implicit variable. We extract the χ_{2n-1} from both the experimental measurements and simulations, and use ΔF and the associated Arrhenius law to determine $t_H^{\text{eff}}/t_{H=0}^{\text{eff}}$. This is plotted against H^2 in Fig 2.

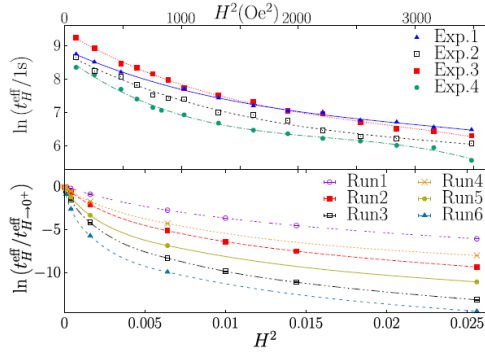


Fig. 2. Experimental and numerical $\ln t_w^{\text{eff}}$ from the maximum of the response function in Fig. 1. Top: data from the experiments with Exp 1: $T_m = 28.50$ K, $t_w = 10,000$ s; Exp. 2: $T_m = 28.75$ K, $t_w = 10,000$ s; Exp. 3: $T_m = 28.75$ K, $t_w = 20,000$ s; Exp. 4: $T_m = 29.00$, $t_w = 10,000$ s. Lines are a fit to a polynomial in H^2 . Bottom: numerical data for the Runs 1-3, $T_m = 0.9$, $t_w = 2^{22}, 2^{26.5}, 2^{31.25}$, respectively; Runs 4-6, $T_m = 1.0$, $t_w = 2^{33.75}, 2^{37.625}, 2^{41.25}$, respectively. Lines are guides for the eye.

This melding of experiment, theory, and simulations, as exhibited by Figs. 1 and 2, is a spectacular success of statistical mechanics.

Future Plans

The above demonstrates that if the right questions are asked for glassy systems, a truly schematic model (here the Ising-Edwards-Anderson spin glass model) can be quantitatively compared to experiment (here the CuMn spin glass). The crucial ingredients to uncover universal behavior are detailed measurements on single crystal spin glasses, combined with high-quality simulations carried out on a custom-built computer. Careful experiments capable of addressing the relevant regime of very large correlation lengths close to the glass temperature are compared to a non-equilibrium extension of classical equilibrium scaling theory.

We are now able to determine responses, autocorrelation lengths, and energy barriers in three dimensional spin glasses quantitatively, both through experiment and numerical simulation. This allows us to address more exotic phenomena such as rejuvenation (temperature chaos) and memory effects. Moreover, because spin glasses are influential in so many other fields (such as economics, physics, biology, and optimization in computer science), our work shows that successful modelling of complex systems is feasible in finite dimensions.

The elusive concepts of temperature chaos and memory in spin glasses remain to be understood. The theoretical basis has been developed under equilibrium conditions, while experiments are always performed under non-equilibrium conditions. However, very recent theoretical and numerical investigations⁶ have shown that non-equilibrium dynamics exhibits temperature chaos. This theoretical foundation is being tested with experiments where the spin glass correlation length $\xi(t_w)$ is being used as a metric for temperature chaos and memory. Experiments are underway using zero-field magnetization studies (UT Austin), ultra-sensitive thermoremanent magnetization studies at Indiana University of Pennsylvania, and ultra-low frequency magnetic susceptibility studies (U Minnesota). The combination of these investigations, working with samples from the same CuMn single crystal boule, will test the dependence of both chaos and memory on $\xi(t_w)$. The non-equilibrium theoretical investigation⁶ exhibits a profound dependence of temperature chaos on $\xi(t_w)$, consistent with preliminary work of our group.⁷ Will the same be true for memory? If so, one may be able to construct a theory based on a length scale set by the correlation length as opposed to rather arbitrary length scales as previously suggested.⁸

References

1. S. Albert et al., Science **352**, 1308 (2016).
2. M. Baity-Jesi, et al., Comput. Phys. Commun. **185**, 550 (2014).
3. Q. Zhai et al. (Janus Collaboration), Phys. Rev. Lett. **125**, 237202 (2020).
4. E. Marinari et al., Phys. Rev. Lett. **76**, 843 (1996).
5. M. Baity-Jesi et al. (Janus Collaboration), Phys. Rev. Lett. **120**, 267203 (2018).
6. M. Baity-Jesi et al. (Janus Collaboration), arXiv:2011.09419v1 [cond-mat.dis-nm] (2020).
7. Q. Zhai et al., arXiv:2010.01214v1 [cond-mat.dis-nn] (2020).
8. Yoshino H. et al., European Physical J. B 20 (2001) 367.

Publications

“Effect of anisotropy on 1/f noise measurements of CuMn spin glasses,” D.C. Harrison, E.D. Dahlberg, and R.L. Orbach, Phys. Rev. B **100**, 064411 (2019).

“Slowing down of spin glass correlation growth: Simulations meet experiments,” Q. Zhai, V. Martin-Mayor, D.L. Schlagel, G.G. Kenning, and R.L. Orbach, Phys. Rev. **100**, 094202 (2019).

“Collapse of the waiting time effect in a spin glass,” D.M. Tennant and R.L. Orbach, Phys. Rev. **101**, 174409 (2020).

“Study of the low-field irreversibility line in the transverse component spin-glass phase of the amorphous Fe₉₀Zr₁₀ alloy,” D.R. Ratkovski, P.R.T. Ribeiro, F.L. de A. Machado, E.P. Raposo, and E.D. Dahlberg, Eur. Phys. J. B **93**, 149 (2020).

“Spin Glass Correlation length: a Caliper for Temperature Chaos,” Q. Zhai, R.L. Orbach, and D.L. Schlagel, arXiv: 2010.01214v1 [cond-mat.dis-nn] (2020).

“Experimental determination of the critical spin-glass correlation length in single-crystal CuMn,” G.G. Kenning, D.L. Schlagel, and V. Thompson, Phys. Rev. **102**, 064427 (2020).

“Scaling Law Describes the Spin-Glass Response in Theory, Experiments, and Simulations,” Q. Zhai, I. Paga, M. Baity-Jesi, E. Calore, A. Cruz, L.A. Fernandez, J.M. Gil-Navarro, I. Gonzalez-Adalid Pemartin, A. Gordillo-Guerrero, D. Iñiguez, A. Maiorano, E. Marinari, V. Martin-Mayor, J. Moreno-Gordo, A. Muñoz-Sudupe, D. Navarro, R.L. Orbach, G. Parisi, S. Perez-Gaviro, F. Ricci-Tersenghi, J.J. Ruiz-Lorenzo, S.F. Schifano, D.L. Schlagel, B. Seoane, A. Tarancon, R. Tripiccione, and D. Yllanes (Janus Collaboration), Phys. Rev. Lett. **125**, 237202 (2020).

“Spin-glass dynamics in the presence of a magnetic field: exploration of microscopic properties,” I. Page, Q. Zhai, M. Baity-Jesi, E. Calore, A. Cruz, L.A. Fernandez, J.M. Gil-Navarro, I. Gonzalez-Adalid Pemartin, A. Gordillo-Guerrero, D. Iñiguez, A. Maiorano, E. Marinari, V. Martin-Mayor, J. Moreno-Gordo, A. Muñoz-Sudupe, D. Navarro, R.L. Orbach, G. Parisi, S. Perez-Gaviro, F. Ricci-Tersenghi, J.J. Ruiz-Lorenzo, S.F. Schifano, D.L. Schlagel, B. Seoane, A. Tarancon, R. Tripiccione, and D. Yllanes (Janus Collaboration), J. Stat. Mech: Thy. Exp., accepted for publication, (2021).

Atomic Dynamics in Metallic and Other Liquids and Glasses

T. Egami, University of Tennessee and Oak Ridge National Laboratory,
Y. Shinohara, E. Zarkadoula, C. Hua and J. R. Morris, Oak Ridge National Laboratory,
W. Dmowski, University of Tennessee

Program Scope

The science of liquids and glasses is much less developed than that of crystalline materials, even though liquids and glasses are as important as crystalline materials in energy-related applications. The main origin of this slow progress is the non-periodicity of their structures, which eluded the application of modern condensed-matter theories, many of which presume lattice periodicity. The overarching goal of this program is to establish a fundamental understanding of atomistic mechanisms which control the structural and dynamic properties of liquids and glasses through combination of tightly coupled experiment, simulation and theory. To achieve this overarching goal this project focuses on the following three specific aims: (1) advance the science of bulk metallic glasses to improve mechanical properties, (2) develop better understanding of a basic unanswered question on the nature of liquid and glass and the origin of the glass transition, and (3) extend the study of local dynamics to various functional liquids relevant to the DOE mission. Owing to recent advances in experimental tools and computational power, we now have an excellent prospect of achieving substantial progress. In particular, we examine the mechanism of rapid increase in viscosity of liquid upon cooling, using a new approach with inelastic neutron and x-ray scattering combined with simulation. The outcome of this proposed work will guide us to the development of glasses and liquids with superior properties, and ultimately contribute to the DOE mission through the development of the general physics of liquids and glasses.

Recent Progress

1. Correlated Atomic Dynamics in Liquid

Liquid is a condensed matter with a physical density similar to that of a solid with the same composition. Thus, atoms are not free to move in liquid, and their motions are highly correlated. However, it has been difficult to assess such correlations because effective experimental tools to observe them were not available. Our breakthrough contribution is to develop a new technique, the Van Hove function (VHF) determined by inelastic x-ray or neutron scattering, to observe the correlated dynamics directly [1, P2, P24]. We measure the dynamic structure factor, $S(Q, \omega)$, where Q and $E = \hbar\omega$, are the momentum and energy transfer of scattering, by inelastic scattering over a wide range of Q and E , and double-Fourier-transform it to obtain the VHF, $G(r, t)$ [2]. Even though the VHF has been known for a long time only with the recent advances in the inelastic

scattering facilities made it possible to carry out such a measurement. Fig. 1 shows the VHF of water at $T = 303\text{K}$ determined by inelastic x-ray scattering (IXS) [P6]. It shows that as time evolves the nearest neighbors at 2.8\AA move away and replaced by second neighbors at 4.5\AA which move in. This demonstrates that the atomic motions in liquid are correlated. We found that such correlations result in the difference between the short-range diffusion and long-range diffusion in water [P19]. We also studied how addition of salt changes water-water and water-ion correlations [P5, P6] and affects the local dynamics. The VHF was measured for liquid metallic alloys by inelastic neutron scattering (INS) using electrostatic levitation to eliminate the effect of sample container [P26]. Earlier, through simulation we explained the origin of liquid viscosity in terms of the lifetime of atomic bond, τ_{LC} [3]. The decay of the VHF with time provides direct information on the bond cutting dynamics, and the result, shown in Fig. 2 [4], proves the prediction by simulation. In addition, we developed a new approach of using x-ray photon correlation spectroscopy (XPCS) with split-and-delay optics using x-ray free-electron laser (XFEL) at SACLAs Japan (Fig. 3) [P25]. This method potentially extends the timescale of the measurement to 500 ps or more. At the moment, however, heating of the sample by laser beam is limiting its application.

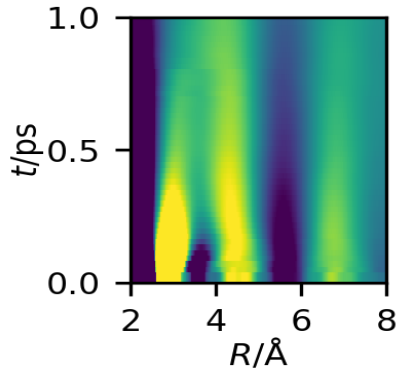


Fig. 1 The Van Hove function of water at $T = 303\text{K}$ [P6].

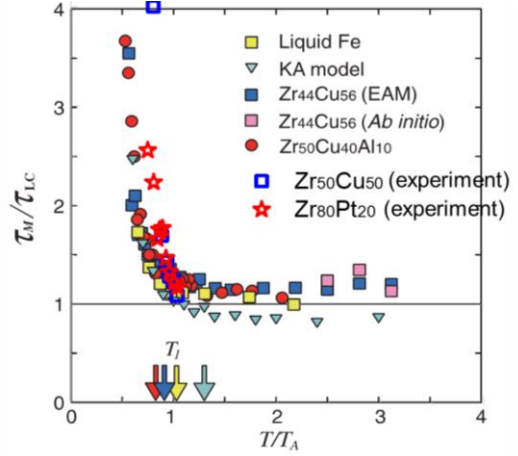


Fig. 2 The ratio, t_M/τ_{LC} , where τ_M is the Maxwell relaxation time ($= \eta/G_\infty$), as a function of T/T_A , predicted by simulation [3] and proven by the VHF determined by INS noted as experiment [4].

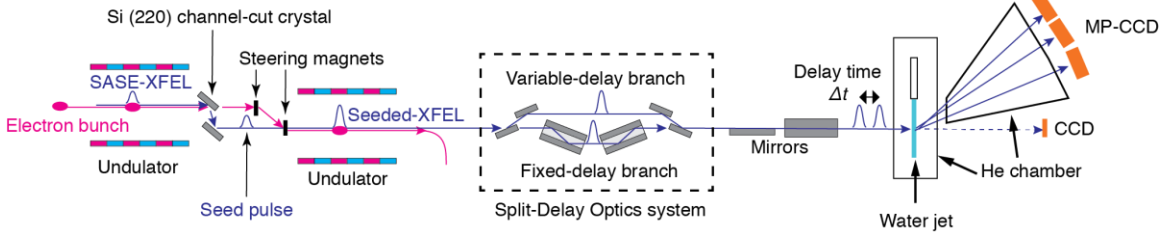


Fig. 3 Experimental setting of XFEL-XPCS using split-and-delay optics at BL3, SACLAs [P25].

2. Nature of Medium-Range Order in Liquid

The structure of liquid is described usually by the atomic pair-distribution function (PDF), $g(r)$, which shows the distribution of distances between atoms. The PDF can be determined by diffraction experiments through the Fourier-transformation of the structure function, $S(Q)$. The

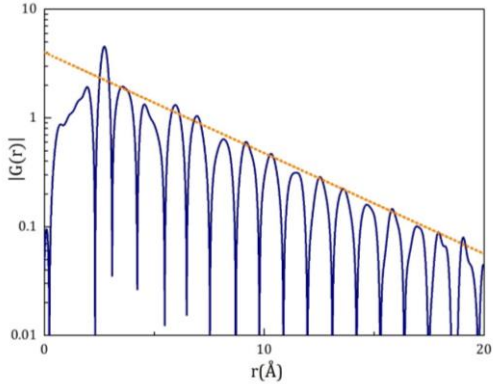


Fig. 4 The PDF of PdNiCuP liquid [P7].

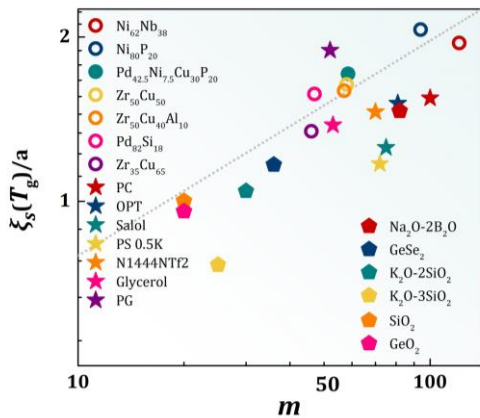


Fig. 5 Correlation between fragility, m , and the structural coherence length, $\xi_s(T_g)/a$, for various liquids [P23].

first peak of the PDF describes the short-range order (SRO) in the near neighbors, whereas the peaks beyond the first depict the medium-range order (MRO). It is widely believed that the MRO is just a consequence of the SRO, but we found that they are quite distinct in nature. Whereas the SRO depicts atomic bonds, the MRO describes correlation in coarse-grained density fluctuations, not the atomic-level structure [P16, P17, P20]. The MRO follows the Ornstein-Zernike form, $|g(r)-1| \approx \exp(-r/\xi_s)/r$, as shown in Fig. 4, which shows $|G(r)| = 4\pi r \rho_0 |g(r)-1|$ [P7]. The structural coherence length, ξ_s , is proportional to the height of the first peak of $S(Q)$, and characterizes the structural ideality [P17]. We found that it plays a key role in liquid viscosity. For instance, it is strongly correlated with the fragility, m , which characterizes the variation of viscosity, η , with temperature as shown in Fig. 5 [P23]. The activation energy of viscosity, $E_a = kT \ln(\eta/\eta_\infty)$, is proportional to the coherence volume, ξ_s^3 , above T_g [P7, P20]. The structural coherence length, ξ_s , follows the Curie-Weiss law as a function of temperature [P7]. We developed a theory to account for the temperature dependence based upon the concept of the atomic-level pressure fluctuation [5].

Future Plans

1. Collective dynamics in liquid

At high temperatures $T > T_A$ $t_M/t_{LC} = 1$, and the dynamics of cutting one bond determines viscosity [3]. Below T_A the ratio, t_M/t_{LC} , increases with decreasing temperature as shown in Fig. 2, suggesting that the atomic dynamics becomes correlated and cooperative. We will determine the nature of such dynamic correlations through the simulation and the analysis of the VHF measured by INS just below T_A . Well below T_A the timescale becomes longer, and we will use the neutron spin echo (NSE) method measured as a function of Q , for instance at the WASP spectrometer at the ILL. Traditionally the atomic transport in liquid and glass has been discussed in terms of structural defects, as in crystalline solids. However, defects cannot be uniquely defined in amorphous system which lack the well-defined ideal structure. Our view is that it is determined

by the collective bond-cutting dynamics determined by the MRO which is an equilibrium bulk property [P20]. We will extend the theory of the atomic-level pressure fluctuation [5] to explain the role of the MRO on atomic transport.

2. Topological excitation in glass

The action of cutting an atomic bond is a topological excitation in the atomic connectivity network. Even though the MRO freezes at the glass transition these excitations persist in the glassy state, and are most likely responsible for the β -relaxation. We will study the nature of these excitations through simulation as well as the VHF measured by INS in the glassy state. Recently, in collaboration with M. Chen at Johns Hopkins University we found that Au-Si metallic glass shows strong inverse spin Hall effect (ISHE) which is a measure of the strength of spin-charge coupling, and could be useful for spintronics. The effect is dramatically decreased when it is crystallized. We believe that the spin fluctuations induced by the topological excitations through spin-orbit coupling is responsible for the strong ISHE, and started the measurement of SHE by magneto-optical Kerr effect.

3. Universality of local dynamics in liquid

Various types of liquids and glasses (metallic, oxides, polymeric, molecular, and colloidal) share a number of salient features, such as the glass transition and relaxation, although they differ in temporal and spatial scales and some microscopic details. We hypothesize that there are universal principles that govern behaviors of all liquids and glasses, which are yet to be discovered. We will investigate the dynamics of various groups of liquid relevant to the DOE mission, including molten salts for nuclear reactor, electrolytes for energy storage, and chalcogenides for phase change memory, through simulation and VHF measurement. However, there are exceptions. For instance, water is quite unique because of hydrogen bond which is highly quantum-mechanical in nature. Recently we detected a slow (8 ps) collective relaxation in the VHF of heavy water by INS. We suspect this is responsible for the Debye relaxation used for heating water in microwave ovens [6]. We will pursue the study of such unique behaviors when they are relevant to useful properties.

References

1. T. Iwashita, B. Wu, W.-R. Chen, S. Tsutsui, A. Q. R. Baron, and T. Egami, *Sci. Adv.* **3**, e1603079 (2017).
2. L. Van Hove, *Phys. Rev.* **95**, 249 (1954).
3. T. Iwashita, D. M. Nicholson and T. Egami, *Phys. Rev. Lett.*, **110**, 205504 (2013).
4. Z. Wang, W. Dmowski, H. Wang, R. Ashcraft, K. F. Kelton, and T. Egami, unpublished.
5. T. Egami and C. W. Ryu, unpublished.
6. J. S. Hansen, A. Kisliuk, A. P. Sokolov, and C. Gainaru, *Phys. Rev. Lett.* **116**, 237601 (2016).

Publications supported by the DOE-BES [’19, ‘20]

- P1. H. Wang, W. Dmowski, Z. Wang, J. Qiang, K. Tsuchiya, Y. Yokoyama, H. Bei, and T. Egami, Transformation pathway from alpha to omega and texture evolution in Zr via high-pressure torsion, *Appl. Phys. Lett.* **114**, 061903 (2019).
- P2. T. Egami, Local dynamics of liquids and glassy materials, *J. Phys. Soc. Japan* **88**, 081001 (2019).
- P3. L. E. Sánchez-Díaz, T. Iwashita, T. Egami, and W.-R. Chen, Connection between the anisotropic structure and nonlinear rheology of sheared colloidal suspensions investigated by Brownian dynamics simulations, *J. Phys. Commun.* **3**, 055018 (2019).
- P4. Kh. Odbadrakh, D. M. Nicholson, G. M. Stocks, and T. Egami, Electronic structure and atomic level complexity in $\text{Al}_{0.5}\text{TiZrPdCuNi}$ high-entropy alloy in glass phase, *J. Appl. Phys.* **126**, 095104 (2019).
- P5. Y. Shinohara, R. Matsumoto, M. W. Thompson, C. W. Ryu, W. Dmowski, T. Iwashita, D. Ishikawa, A. Q. R. Baron, P. T. Cummings, and T. Egami, Identifying water–anion correlated motion in aqueous solutions through Van Hove functions, *J. Phys. Chem. Lett.* **10**, 7119 (2019).
- P6. Y. Shinohara, W. Dmowski, T. Iwashita, D. Ishikawa, A. Q. R. Baron, and T. Egami, Local correlated motions in aqueous solution of sodium chloride, *Phys. Rev. Mater.* **3**, 065604 (2019).
- P7. C. W. Ryu, W. Dmowski, K. F. Kelton, G. W. Lee, E. S. Park, J. R. Morris, and T. Egami, Curie-Weiss behavior of liquid structure and ideal glass state, *Sci. Rep.* **9**, 18579 (2019).
- P8. T. Egami and Y. Shinohara, Dynamics of water in real-space and time, *Mol. Phys.* **117**, 3227 (2019).
- P9. Z. Wang, T. Iwashita, L. Porcar, Y. Wang, Y. Liu, L. E. Sánchez-Díaz, W. A. Hamilton, T. Egami and W. R. Chen, Local elasticity in nonlinear rheology of interacting colloidal glasses revealed by neutron scattering and rheometry, *Phys. Chem. Chem. Phys.* **21**, 38 (2019).
- P10. H. S. Oh, S. J. Kim, K. Odbadrakh, W. H. Ryu, K. N. Yoon, M. Sai, F. Körmann, Y. Ikeda, C. C. Tasan, D. Raabe, T. Egami, and E. S. Park, Engineering atomic-level complexity in high-entropy and complex concentrated alloys, *Nature Commun.* **10**, 2090 (2019).
- P11. G.-R. Huang, Y. Wang, C. Do, L. Porcar, Y. Shinohara, T. Egami, and W.-R. Chen, Determining gyration tensor of orienting macromolecules through their scattering signature, *J. Phys. Chem. Lett.* **10**, 3978 (2019).
- P12. J. Brechtl, H. Wang, N. A. P. K. Kumar, T. Yang, Y.-R. Lin, H. Bei, J. Neufeind, W. Dmowski, S. J. Zinkle, Investigation of the thermal and neutron irradiation response of BAM-11 bulk metallic glass, *J. Nucl. Mater.* **526**, 151771 (2019).
- P13. S. Okamoto, T. Egami, and N. Nagaosa, Critical spin fluctuation mechanism for the Spin Hall effect, *Phys. Rev. Lett.* **123**, 196603 (2019).

- P14. G.-R. Huang, Y. Wang, C. Do, Y. Shinohara, T. Egami, and W.-R. Chen, Orientational distribution function of aligned elongated particles determined from their scattering signature, *ACS Macro Lett.* **8**, 1257 (2019).
- P15. T. Egami, Atomic dynamics in real space and time, in *High-resolution inelastic X-ray scattering*, ed. A. Cunsolo, M. K. K. Dias Franco, F. Yokaichiya (Intech Press, 2020) Chapter 3, pp. 108–150, ISBN: 978-1-78985-052-9.
- P16. T. Egami, Local density correlations in liquids, *Front. Phys.* **8**, 50 (2020).
- P17. C. W. Ryu, W. Dmowski, and T. Egami, Ideality of liquid structure: A case study for metallic alloy liquids, *Phys. Rev. E* **101**, 030601(R) (2020).
- P18. W. Dmowski, G. H. Yoo, S. Gierlotka, H. Wang, Y. Yokoyama, E. S. Park, S. Stelmakh, and T. Egami, High pressure quenched glasses: Unique structures and properties, *Sci. Rep.* **10**, 9497 (2020).
- P19. Y. Shinohara, W. Dmowski, T. Iwashita, D. Ishikawa, A. Q. R. Baron, and T. Egami, Local self-motion of water through Van Hove function, *Phys. Rev. E* **102**, 034604 (2020).
- P20. T. Egami and C. W. Ryu, Why is the range of timescale so wide in glass-forming liquid?, *Front. Chem.* **8**, 579169 (2020).
- P21. J. S. Langer, Brittle-ductile transition in a metallic glass, *Phys. Rev. E* **101**, 063004 (2020).
- P22. C. Hua and L. Lindsay, Space-time dependent thermal conductivity in nonlocal thermal transport, *Phys. Rev. B* **102**, 104310 (2020).
- P23. C. W. Ryu and T. Egami, Origin of liquid fragility, *Phys. Rev. E* **102**, 042615 (2020).
- P24. T. Egami and Y. Shinohara, Perspective: Correlated atomic dynamics in liquid seen in real space and time, *J. Chem. Phys.* **153**, 180902 (2020).
- P25. Y. Shinohara, T. Osaka, I. Inoue, T. Iwashita, W. Dmowski, C. W. Ryu, Y. Sarathchandran and T. Egami, Split-pulse X-Ray photon correlation spectroscopy with seeded X-rays from X-ray laser to study atomic-level dynamics, *Nature Commun.* **11**, 6213 (2020).
- P26. R. Ashcraft, Z. Wang, D. L. Abernathy, T. Egami, and K. F. Kelton, Experimental determination of the temperature-dependent Van Hove function in a Zr₈₀Pt₂₀ liquid - A structural origin for the dynamics at high temperature, *J. Chem. Phys.* **152**, 074506 (2020).
- P27. J. Ketkaew, R. Yamada, H. Wang, D. Kuldinow, B. S. Schroers, W. Dmowski, T. Egami, and J. Schroers, The effect of thermal cycling on the fracture toughness of metallic glasses, *Acta Mater.* **184**, 100 (2020).
- P28. I. Lobzenko, Y. Shiihara, T. Iwashita, and T. Egami, Shear softening in a metallic glass: First principle local stress analysis, *Phys. Rev. Lett.* **124**, 085503 (2020).
- P29. E. Novac, B. Haberl, L. Daemen, J. Molaison, T. Egami, and N. Jalarvo, Pressure-induced phase transition in barium hydride studied with neutron scattering, *Appl. Phys. Lett.* **117**, 011646 (2020).

- P30. X. Han, Y. Liu, M. L. Crespillo, E. Zarkadoula, Q. Huang, X. Wang and P. Liu, Latent tracks in ion-irradiated LiTaO₃ crystals: Damage morphology characterization and thermal spike analysis, *Crystals* **10**, 877 (2020).
- P31. G.-R. Huang, C.-H. Tung, D. Chang, C. N. Lam, C. Do, Y. Shinohara, S.-Y. Chang, Y. Wang, K. Hong and W.-R. Chen, Determining population densities in bimodal micellar solutions using contrast-variation small angle neutron scattering, *J. Chem. Phys.* **153**, 184902 (2020).
- P32. H. Chen, Y. Sun, S. Yang, H. Wang, W. Dmowski, T. Egami, J. Fu and S. Dai, Self-regenerative noble metal catalysts supported on high-entropy oxides, *Chem. Commun.* **56**, 15056 (2020).

Machine-Learned Structure-Property Relationship in Metallic Glass

Michael L. Falk, Departments of Materials Science and Engineering, Mechanical Engineering, Physics and Astronomy, Johns Hopkins University, Baltimore, MD 21218 USA

Formerly: Evan Ma, Department of Materials Science and Engineering, Johns Hopkins University, Baltimore, MD 21218 USA

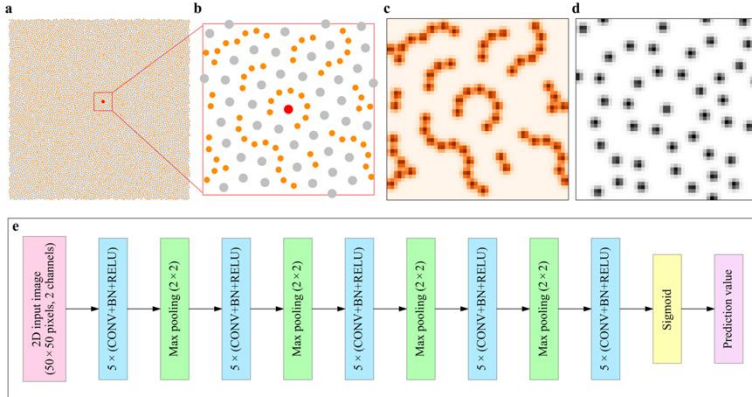
Program Scope

This project is designed to add new capabilities to recent machine learning achievements in connecting structure with properties of amorphous solids. Our preliminary analyses have indicated the advantage of these data-centric methods over other structural metrics in that they provide a more generic indicator of local structure, and thus can be used to correlate with various properties, not limited to just the specific property used as supervisory signal. When the machine learned indicator is assessed over different MG compositions in a given alloy (such as $\text{Cu}_x\text{Zr}_{100-x}$) system as well as for systems prepared with different processing protocols they allowing explanation and prediction of the compositional and processing dependence of properties. The overarching goal is to forecast properties from purely structural information in terms of atomic coordinates (relative locations) of the atoms. Preliminary results also point to salient local structural features detectable in the single-atom pair distribution functions that control relevant materials properties of the amorphous alloy.

These efforts in applying machine learning are aimed at improving our understanding of the unusual structural and mechanical heterogeneity inherent to a seemingly homogeneous amorphous solid. For engineering applications, our findings may facilitate the development of MGs, e.g., through judicious tuning of their internal structure based on what is learnt in our work as to how the composition and processing change the structural flexibility amongst other properties. As big data and machine learning are adding a new paradigm in the way we do materials science, the protocol and the understanding developed will be of broad interest to both experimentalists and modelers, and enrich materials science subjects, including structural, physical and mechanical behavior prediction.

Recent Progress

It has been a long-standing materials science challenge to establish structure-property relations in amorphous solids. In recent work we introduced a rotationally non-invariant local structure representation that enables different predictions for different loading orientations, which is found essential for high-fidelity prediction of the propensity for stress-driven shear transformations. This novel structure representation, when combined with a convolutional neural network (CNN), a powerful deep learning algorithm, leads to unprecedented accuracy for identifying atoms with high propensity for shear transformations (i.e., plastic susceptibility),



Atomic structure representation and model architecture for 2D glasses. (a) Snapshot of a 2D model glass. Orange and silver circles represent small (*S*) and large (*L*) particles, respectively. (b) A close-up showing a local configuration around the red particle in (a). (c) and (d) Corresponding spatial density map (SDM) of the *S* and *L* particles, respectively. (e) Architecture of the convolutional neural network (CNN) model used for 2D glasses, which contains 25 (5 in each blue box) 2D convolutional (conv.) layers. A 2D max-pooling layer is periodically inserted in-between the successive convolutional layers. The last convolutional layer is followed by the output layer which is a sigmoid neuron.

amorphous solids, i.e., particles that are most prone to rearrangements. First of all, a qualitative but crucial structural difference, in terms of a more non-uniform and asymmetric packing environment, was discovered for atoms with high plastic susceptibility relative to those with low plastic susceptibility. This insight may be tested by experiments if the orientational pair correlation functions can be mapped out in future such investigations. Second, we achieved unprecedented accuracy in predicting orientation-dependent local mechanical response over a wide range of shear strain, by designing a rotationally non-invariant structure representation coupled with a powerful deep learning algorithm. Third, once the optimized CNN model is in hand, all that is needed to predict plastic response are the atomic positions, without relying on other knowledge such as interparticle interactions required by previous approaches using parameters based on physical properties. Fourth, we have demonstrated that the CNN models trained on a single glass (with a particular composition and processing history) can be generalized to samples with different processing histories or at different compositions in the same alloy system. This is important for probing into the effects of processing procedure or chemical composition on properties, enabling the comparison between different glasses. These four merits open new avenues to the understanding of the structure-property relations in amorphous solids. Fifth and finally, we anticipate that our novel structure representation (SDM), in combination with the powerful CNN method, will find use in the studies of other forms of amorphous matter beyond metallic glasses, as well as in predicting rotation-variant properties of crystalline materials, via data augmentation.

solely from the static structure in both two- and three-dimensional model glasses. The data-driven models trained on samples at one composition and a given processing history were found to be transferrable to glass samples with different processing histories or at different compositions in the same alloy system. Our analysis of the new structure representation also provides valuable insight into key atomic packing features that influence the local mechanical response and its anisotropy in glasses.

Our analysis via machine learning has permitted a number of advances over previous efforts to identify structural “defects” in

Future Plans

We are now completing atomistic simulation studies that indicate that the location of shear banding in a metallic glass (MG) can be ascertained with reasonably high accuracy solely from the undeformed static structure. Correlation is observed between the location of the initiation of shear bands in a simulated MG and the initial distribution of the density of fertile sites for stress-driven shear transformations identified *a priori* based the above described deep learning model. This work validates that shear bands in MG arise from non-linear instabilities, and that the as-quenched structure contains inhomogeneities that control these instabilities. Interestingly, the isotropic nature of the as-quenched glasses is observed in some instances to lead to equivalent shear banding probabilities along the two maximal shear planes. This also reveals an important subtlety regarding the non-deterministic nature of althermal quasistatic shear simulations.

Publications

- 1) Fan, Z., Ding, J., & Ma, E. (2020). Machine learning bridges local static structure with multiple properties in metallic glasses. *Materials Today*, 40, 48-62.
- 2). Fan, Z., & Ma, E. (2021). Predicting orientation-dependent plastic susceptibility from static structure in amorphous solids via deep learning. *Nature Communications*, *in press*.
- 3). Fan, Z.. Ma, E. & Falk, M.L. (2021). Predicting shear band initiation in metallic glass simulations via deep learning. In preparation.

Phase-Field Modeling of Materials Interfaces and Nanostructures

Principal Investigator: Alain Karma

Address: Department of Physics and Center for Interdisciplinary Research on Complex Systems, Northeastern University, 360 Huntington Avenue, Boston, Massachusetts 02115

Email: a.karma@northeastern.edu

Program Scope

Nanostructured materials offer unique properties for a wide range of energy applications. Among various known processing methods, liquid metal dealloying (LMD)—the selective dissolution of a base alloy element into a metallic melt—has emerged as a powerful technique to produce a new class of nano-/meso-scale open porous and bicontinuous composite structures with ultra-high interfacial area. LMD has recently been complemented by the advent of vapor phase dealloying (VPD), a novel technique that exploits the selective evaporation of one element from a parent alloy containing elements with very different vapor pressures, thereby enabling to fabricate open nanoporous structures of various elements from less-noble metals to inorganic elements regardless of their chemical activity without requiring high LMD temperatures and chemical etching. Together LMD and VPD have greatly expanded the scope of dealloying techniques, limited by traditional electrochemical means to noble metals, and boosted the design of new functional and structural materials that combine a wide variety of elements. Topologically-connected open porous structures with ultra-high surface area allow mass transport within the structure while preserving structural integrity, enabling them to serve as catalysts, fuel cells, supercapacitors, or high-capacity battery materials. Bicontinuous composite structures in turn can display high strength and high ductility or superior radiation-damage resistance due to the ultra-high interface area between interpenetrating solid phases. This research program makes use of state-of-the-art computational methods to understand at a basic level the self-organizing dealloying process with main focus on dealloying kinetics and interfacial pattern formation at the dealloying front controlling initial structure size, topology, and phase compositions. Phase-field simulation studies of LMD focus on solid solutions, line compounds, and intermetallic systems that can form ternary composites by nucleation and growth of a new phase. Studies of VPD employ phase-field modeling and a hybrid method combining a kinetic Monte Carlo (KMC) model of evaporation and surface diffusion with molecular dynamics for vapor-phase transport inside nanopores. Simulations explore mechanisms of interface- and diffusion-controlled dealloying kinetics, both observed in VPD but not fundamentally understood. In addition, our newly developed multi-physics phase-field approach of large-volume-change phase transformations is being used to model novel 3D anode geometries based on dealloyed nanoporous structures including novel sandwiched graphene/Si/silica for high-rate Li ion battery. Those studies are aimed at elucidating geometric design principles that improve mechanical stability. We expect this research to enhance the capability to tailor nano-/mesoscale structures for a wide range of energy-related materials applications and to yield further advances in computational methodologies that benefit a broad materials research community.

Recent Progress

Nano-/meso-scale bicontinuous structures formed by LMD and VPD. To produce topologically connected bicontinuous structures, LMD has traditionally required minimally a ternary system consisting of the two elements of the base alloy and a different third element of the liquid melt chosen so as to selectively dissolve one of the elements of the base alloy, as exemplified

by dealloying of TaTi alloys by a Cu melt, which has served as model system for fundamental experimental studies of LMD structures and kinetics. However, a recent experimental study has shown that bicontinuous structures similar to those produced by LMD can be obtained by isothermal melting of a peritectic TiAg binary alloy [1]. Those observations raise the interesting question of whether the “topology-generating” interfacial pattern formation mechanism in a binary system differs fundamentally from the one previously elucidated for LMD in ternary systems [2]. In the latter, pattern formation involved both interfacial spinodal decomposition to form Ta-rich regions along the solid-liquid interface and two-phase coupled growth to propagate liquid channels

inside the base alloy [2]. They also raise the broader question of which of those mechanisms underlies structure formation in more complex alloy systems forming intermetallic compounds (e.g. dealloying of SiC by a Ge melt through the reaction $\text{SiC} \rightarrow \text{Si} + \text{C}$), which bear similarity to peritectic systems. To investigate the first question above, we used 2D and 3D simulations of a multiphase-field model of Lo et al. [3] previously developed in the PI’s group with model parameters adapted to model isothermal melting of a peritectic TiAg alloy. Melting decomposes the solid β phase of the base alloy of peritectic composition into a Ti-rich solid α phase and a Ag-rich liquid phase. Our 2D and 3D simulations results (Fig. 1) reveal striking similarities but also important differences between pattern formation in LMD and peritectic melting. During LMD in ternary systems (solid solution dealloyed by a liquid melt), the formation of the solid phase that is rich in the non-dissolving element has been shown to be controlled by interfacial spinodal decomposition [2], which is absent in peritectic melting. In the latter, formation of the analogous α phase is controlled by nucleation at the solid-liquid interface (Fig. 1A showing

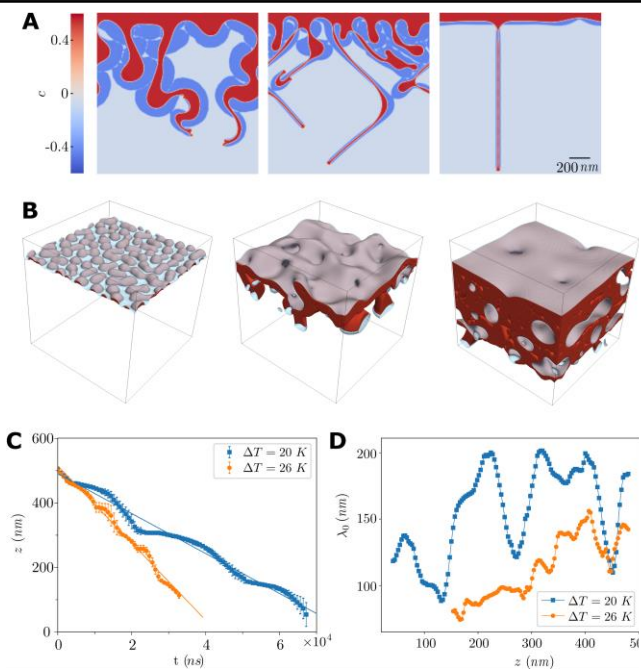


Fig. 1. Phase-field simulations of isothermal melting of a peritectic TiAg alloy showing the formation of bicontinuous composite structures. **(A)** Decreasing the nucleation rate in 2D simulations significantly affects the morphology. Snapshots of 3D simulations at successive times **(B)** showing that the growth of the dealloying front has a constant velocity **(C)**, which can be increased by increasing the processing temperature. **(D)** Dependence of the ligament size on temperature. The 2D and 3D simulation sizes are $1638 \text{ nm} \times 1638 \text{ nm}$ and $614 \text{ nm} \times 614 \text{ nm} \times 610 \text{ nm}$, respectively.

structures with nucleation rate of α at the β – liquid interface decreasing from left to right with liquid: red, blue: α , light blue: β). At a high nucleation rate, repeated heterogeneous nucleation events at the solid-liquid interface alters the growth direction of liquid channels forcing them follow tortuous paths and gives rise to polycrystalline structures with a grain size comparable to the ligament size. In contrast, at low nucleation rate, re-nucleation is absent, thereby alloying liquid channels to grow straight into the base alloy. In 3D simulations (Fig. 1B), porous structure formation occurs consistent with experimental observations [1]. In Fig. 1B, red indicates α phase,

brown the liquid- α interface, and light blue the β -liquid interface with the liquid and the β phase at the top and bottom, respectively. To characterize the dealloying kinetics, we measured the dealloying front position as a function of time. The result shows that the dealloying depth increases linearly in time (Fig. 1C), in contrast to LMD where the depth increases $\sim t^{1/2}$ [2]. This difference stems from the fact that peritectic melting does not involve the long-range diffusive transport of the dissolving element from the dealloying front to the edge of the dealloyed layer that is responsible for the $t^{1/2}$ behavior. However, like in LMD, dealloying involves the diffusive coupled growth of liquid channels and the nearby solid α phase that controls the velocity of the front associated with lamellar growth in 2D (Fig. 1A) and worm-like growth in 3D (Fig. 2A). To study the effect of thermodynamic driving force, we carried out 3D simulations at higher superheating $\Delta T = T - T_p$, where T is the isothermal processing temperature and T_p is the peritectic temperature. The results show that the dealloying velocity increases with ΔT (Fig. 1C), accompanied by a decrease of average ligament size (Fig. 1D). To gain further insight into the pattern formation process, we investigated the growth properties of individual liquid channels. The results show that, in both 2D and 3D, the channel width decreases as $\sim \Delta T^{-2}$ (Fig. 2B) and the growth velocity is inversely proportional to this width (Fig. 2C). The channel width at $\Delta T = 20\text{ K}$ and $\Delta T = 26\text{ K}$ are comparable to the ligament sizes in Fig. 1D, supporting the interpretation that worm-like growth of individual liquid channels is the dominant mechanism controlling the growth kinetics and ligament size of bicontinuous composite structures (Fig. 1B). Repeated nucleation events deflect the trajectories of liquid channels, promoting the formation of topologically connected structures in 3D, but do not alter significantly alter their growth velocity and width. In addition, we found that the growth velocity scales proportionally to the liquid diffusivity (green triangles in Fig. 2C), further supporting the theoretical expectation that coupled growth is diffusion-controlled.

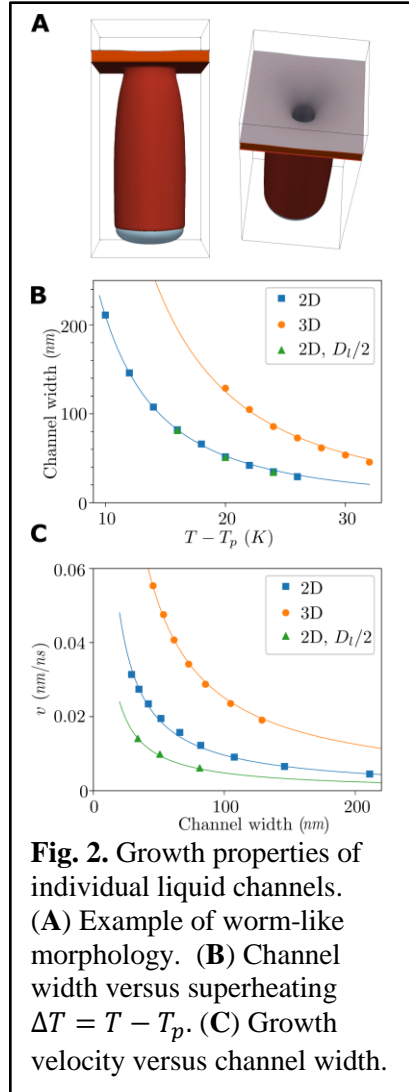


Fig. 2. Growth properties of individual liquid channels. (A) Example of worm-like morphology. (B) Channel width versus superheating $\Delta T = T - T_p$. (C) Growth velocity versus channel width.

Large-volume-change transformations in lithium-ion battery materials. With approximately ten times greater charge capacity over conventional carbon-based anodes, silicon and germanium have emerged as attractive anode materials for lithium-ion batteries. The improved charge capacity is accompanied by nearly 300% volume change during lithiation, which can lead to mechanical failure — notably fracture — and prevent these materials from seeing their full potential. Hence, research into Si- or Ge-based anodes has predominantly focused on shape design, for example hollow tubes [4] and nanoporous architectures fabricated via liquid metal dealloying [5]. To explore the role of anode shape on mechanical behavior, we have developed a model which couples phase-transition kinetics with volumetric swelling and elastoplastic material deformation at large strains. This model was previously applied to study lithiation of two-dimensional circular and annular domains (which represent the cross sections of cylinders and tubes, respectively) [6]. In

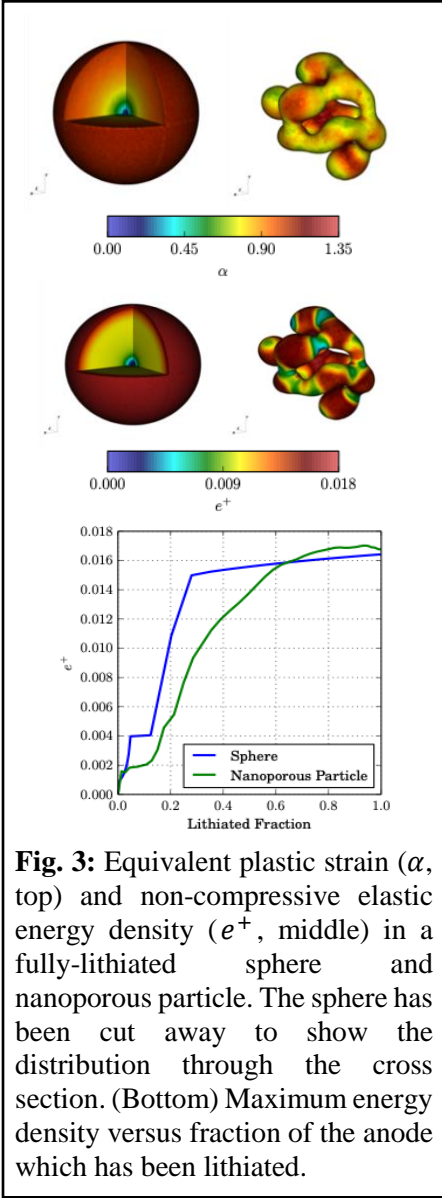


Fig. 3: Equivalent plastic strain (α , top) and non-compressive elastic energy density (e^+ , middle) in a fully-lithiated sphere and nanoporous particle. The sphere has been cut away to show the distribution through the cross section. (Bottom) Maximum energy density versus fraction of the anode which has been lithiated.

these domains, it was shown that plastic localization caused the formation of V-shaped notches along the outer edge of the domain, which served as initiation points for potential fracture. In 3D, we studied how equivalent plastic strain α and the non-compressive elastic energy e^+ are affected by the topology during isotropic lithiation. The latter is important in understanding where cracks may nucleate in the specimen; in phase-field models, cracks nucleate when e^+ exceeds a critical threshold. Our first example was the comparison between a spherical particle and a nanoporous particle. The latter geometry was computed via simulation of liquid metal dealloying process and had approximately 50% porosity. We show the results for the two geometries in Fig. 3. The distribution of plastic strain and energy density was symmetric in the spherical particle. Meanwhile, the nanoporous particle experienced preferential accumulation of plastic strains in areas with negative surface curvature; V-shaped notches were absent. The same areas with plastic strain concentrations also experienced the highest energy densities; notably, these areas do not lie along the ligaments of the nanoporous geometry. Remarkably, the maximum energy density was comparable between the two geometries. The nanoporous geometry may be viewed as a collection of spheres connected by ligaments. To better understand the behavior of the ligaments, we considered two model geometries: the infinite cylinder and the torus. The nanoporous ligaments do not have uniform thickness; for the cylinder and torus, we also studied variations in the radii, shown in Fig. 4. The uniform cylinder (despite isotropic invasion) and torus experienced plastic strain concentrations along their length (in the case of the torus, along the inner wall), which can lead to V-shaped notches. Meanwhile, the non-uniform cylinder and torus did not see this behavior. Notably, the energy density pattern in the non-uniform torus

resembled that in the nanoporous geometry. Based on the results for the cylinder and torus, the variable thickness of the ligaments in the nanoporous particle appear to prevent strong plastic localization (notably, V-shaped notches) along their lengths. Thus, the thick portions of the particle, which behave like spheres, experience the highest energy densities. However, in the nanoporous particle, the effective radii of the spheres are smaller, which make them more resistant to fracture than a single, larger spherical particle with equivalent volume.

Future Plans

We will build on our novel insights into bicomposite structure formation during melting of peritectic alloys to explore dealloying kinetics of line compounds (SiC by liquid Ge). In particular, we will test the hypothesis that structure formation in this case shares common features with both peritectic melting, where nucleation gives rise to polycrystalline structures, and LMD where

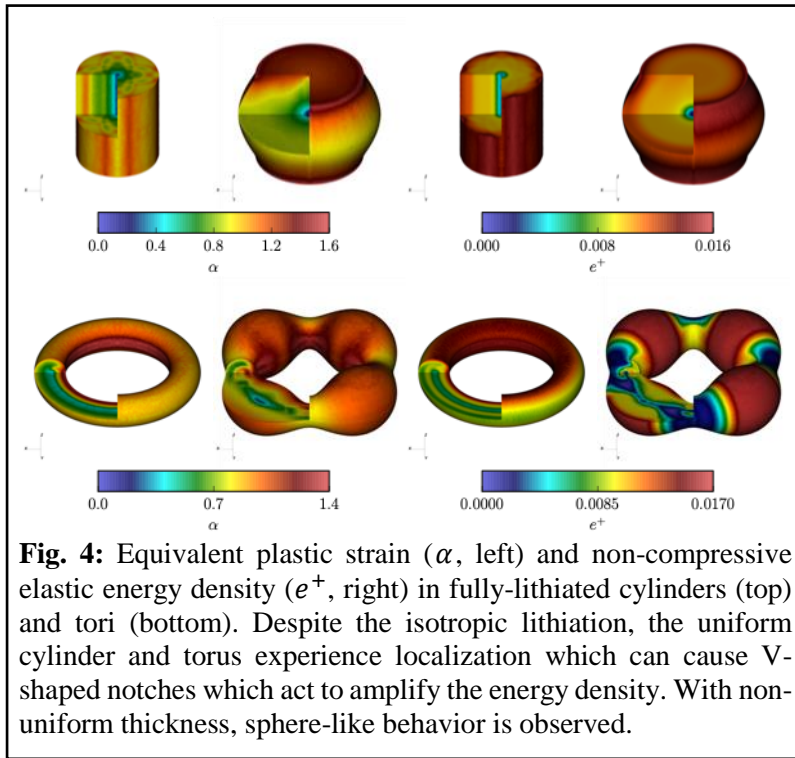


Fig. 4: Equivalent plastic strain (α , left) and non-compressive elastic energy density (e^+ , right) in fully-lithiated cylinders (top) and tori (bottom). Despite the isotropic lithiation, the uniform cylinder and torus experience localization which can cause V-shaped notches which act to amplify the energy density. With non-uniform thickness, sphere-like behavior is observed.

a novel class of nanoporous architectures for next generation Li-ion battery anodes based on a sandwich structure of silicate, silicon, and graphene [7].

References

1. Hu, W. *et al.*, Physical Review Materials, **3** (11), 113601 (2019).
2. Lo, T. *et al.*, Physical Review E, **63** (3), 031504 (2001).
3. Geslin, P.A. *et al.*, Nature Communications **6**, 8887 (2015).
4. Wu, H. *et al.*, Nature Nanotech **7**, 310–315 (2012).
5. Wada, T. *et al.*, Nano Letters **14** (8) 4505–4510 (2014).
6. Mesgarnejad, A. and Karma, A. *npj Comput. Mater.* **6**, 58 (2019).
7. Huang, G. *et al.*, ACS Nano **14** (4) 4374–4382 (2020).

DOE sponsored publications (2019 to date)

1. “Phase-field modeling of chemomechanical fracture of intercalation electrodes: Role of charging rate and dimensionality”, A. Mesgarnejad and A. Karma, *J. Mech. Phys. Solids* **132**, 103696 (2019).
2. “Configurational stability of a crack propagating in a material with mode-dependent fracture energy - Part I: Mixed-mode I + III”, J.B. Leblond, A. Karma, L. Ponson, A. Vasudevan, *J. Mech. Phys. Solids* **126**, 187–203 (2019).
3. “Influence of morphological instability on grain boundary trajectory during directional solidification”, S. Ghosh, A. Karma, M. Plapp, S. Akamatsu, S. Bottin-Rousseau, G. Faivre, *Acta Mater.* **175**, 214–221 (2019).
4. “Configurational stability of a crack propagating in a material with mode-dependent fracture energy - Part II: Drift of fracture facets in mixed-mode I+II+III”, A. Vasudevan, L. Ponson, A. Karma, J.B. Leblond, *J. Mech. Phys. Solids* **137**, 103894 (2020).
5. “Vulnerable window of yield strength for swelling-driven fracture of phase-transforming battery materials”, A. Mesgarnejad and A. Karma, *npj Computational Materials* **6**, 1–10 (2020).

diffusive transport of one element in the melt gives rise to $t^{1/2}$ kinetics. For VPD, we will use our hybrid KMC/MD simulation framework to study the cross-over from interface to diffusion controlled kinetics in manganese-zinc alloys. We will test the hypothesis that this cross-over bridges ballistic evaporation at early times, to Knudsen diffusion of Zn vapor in developed pore channels at later time, where the Zn partial pressure at the dealloying front reaches the local equilibrium between the solid and vapor phases. In addition, we will use our computational framework for simulating lithiation-induced swelling and elastoplasticity to study the mechanical stability of

Extraordinary Responsive Magnetic Rare Earth Materials

Vitalij K. Pecharsky, Yaroslav Mudryk, and Anis Biswas

Ames Laboratory of US DOE, Iowa State University, Ames, Iowa, 50011-2416

Program Scope

Examples of critical energy technologies reliant on rare earths are abundant. Well-known are wind turbines, hybrid and electric vehicles, solid state lighting, mobile devices, lasers and optical fibers, all of which owe most or some of their core functions to $4f$ -electron compounds. Enabled through basic science, this progress is often built upon serendipitous discoveries, as can be exemplified by rare-earth permanent magnets. Recognized recently, extraordinary responsiveness of certain magnetic rare-earth compounds with p and d elements covers a range of intriguing physical behaviors rooted in strongly coupled crystal and magnetic lattices. Giant magnetocaloric, magnetoresistive and magnetostrictive effects, spontaneous thermoelectricity, unusual dynamic, training and acoustic effects, magnetic deflagration, phase-separated glass-like states, and exchange bias highlight the remarkable sensitivity of these materials to temperature, pressure, and magnetic field. It is clear that responsive materials that take full advantage of $4f$ electrons will continue to transformatively change our lives when basic understanding of energy-relevant physics is sufficiently developed. Hence, this research program focuses on the fundamentals of $4f$ element interactions at varying energy, spatial and time scales, on predictive science of the physics and chemistry of $4f$ intermetallic compounds, and on functionality of $4f$ -electron materials.

Our *overarching aspiration* is to transform the field of responsive magnetic rare-earth compounds into predictive science. Our *principal objective* is to understand chemistry, structure and properties of $4f$ materials, and control of their behaviors at the electronic, atomic, and microscopic scales, leading to a priori design of materials with desired functionalities. Our *main hypothesis* is that fundamentally novel physics can be brought to light by tailoring interactions that involve $4f$ elements in intermetallic and related compounds that adopt layered or conventional crystal structures. Using a number of diverse lanthanide-based model systems, which represent a range of discontinuous responses, this FWP seeks answers to the following fundamental questions: a) why do magnetoelastic transitions occur in some compounds but not in others, and why are the former scarce but the latter are common? b) how do we account for the intimately coupled lattice and electronic (spin and orbital) phenomena, spin and valence fluctuations, loss and gain of inversion symmetry, and crystalline and magnetic anisotropies in our interpretation of the phase stability and properties? c) how do we control and manipulate non-equilibrium magnetic and structural states in metallic materials? d) how do we model and consistently predict the response of a lattice to both strong, e.g., temperature and pressure, and weak, e.g., magnetic field, external stimuli? e) how do we apply the predictive power of the refined computational tools to guide experimental design of novel rare-earth compounds with desired responsive behavior and functionality?

Recent Progress

By making use of our expertise in synthesis, characterization, and modeling of rare-earth compounds, we revealed and controlled metastability, sensitivity to a range of influences and, therefore, physical behaviors in a number of materials, where magnetism is governed by $4f$ electrons. A few of our recent achievements are highlighted below.

Anhysteretic first-order transformations in R_2In compounds.

Magnetoelastic isosymmetric first-order magnetic transitions (FOMTs) that show negligible hysteresis are rare, with only a handful of material families, almost exclusively transition metal-based, known to exhibit them. Of note is an extraordinarily sharp, first-order phase change that occurs in Eu_2In [1]. What makes this transition remarkable, is that it is associated with a giant magnetic field-induced entropy change, $|\Delta S| = 27 \text{ J/kg K}$, in response to a low field change of 20 kOe, yet with minute lattice discontinuities and negligible hysteresis. More recently we discovered that a similar anhysteretic FOMT also occurs in Pr_2In , even though the compound crystallizes in a hexagonal Ni_2In -type structure, which is different from the orthorhombic Co_2Si type of Eu_2In [2]. A combined experimental and theoretical study of Pr_2In [2] demonstrates that despite phenomenological similarity between the discontinuous phase transitions in Pr_2In and Eu_2In , nearly identical Curie temperatures (respectively, 57 K and 55 K), and the anhysteretic nature of both FOMTs, the underlying mechanisms are different [1,2]. While Eu_2In owes its unique physical behaviors to charge transfer from In 5p to Eu 5d bands, indium plays a minor role in the magnetism of Pr_2In [1,2]. Here, Pr 4f bands are located near E_F (Figure 1) and the resulting large electronic density of states (DOS) at E_F underpins instabilities. This scientific advance paves the way toward future discoveries of novel functionalities by precisely manipulating the crystal and electronic structures of 4f compounds without significant itinerant magnetism.

Enhancing responsiveness of competing 4f interactions with 3d electrons. We performed a comparative study of two systems, $Er_{1-x}Dy_xCo_2$ [3] and $Er_xDy_{1-x}Al_2$ [4], one formed with magnetic 3d-element, Co, and another with non-magnetic 3p-element, Al, to examine the role that both 4f and 3d electrons play in controlling lattice distortions. Individually, Dy leads to tetragonal, while Er underpins rhombohedral distortions in the magnetically ordered states of the binary parent compounds, independent of whether 3d electrons are present or not. These crystallographic distortions, occurring at the corresponding magnetic transition temperatures, become strongly suppressed in pseudobinary $Er_xDy_{1-x}Al_2$ [4]. The distortions, albeit very minor, remain when $x = 0.45$ and $x = 0.9$, yet when $x = 0.67$ the compound remains cubic down to 5 K. These experimental results agree with the mean-field theory model that confirms the easy magnetization axis (EMA) $\langle 100 \rangle$ for $x = 0.45$, $\langle 111 \rangle$ for $x = 0.9$, and the lack of a distinct EMA for $x = 0.67$. The behavior observed in $Er_xDy_{1-x}Al_2$ is contrasting with that of earlier studied $Er_{1-x}Dy_xCo_2$, where clear and strong low-temperature lattice distortions are present. Combined, the results of two studies show that in these simple and common intermetallic structures, the presence of 3d-electrons and magnetocrystalline anisotropy leads to a rather strong responsiveness, but without them the responses are largely suppressed.

Future Plans

Focusing on model systems well-suited for anticipated breakthroughs in materials science, chemistry, and physics of rare-earth intermetallics, we will develop basic understanding of magneto-responsive behaviors that stem from complex interactions involving 4f electrons. Innovative science of intricate relationships among chemistry, crystallography, electronic,

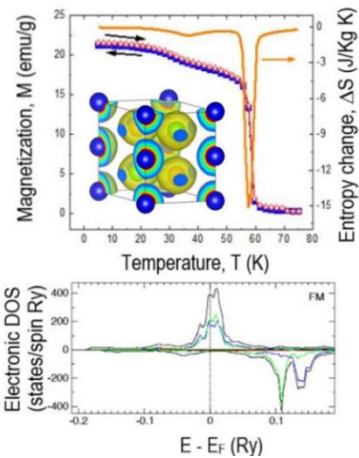


Fig. 1. Anhysteretic first-order phase transition in Pr_2In (top) and strongly enhanced 4f electron density of states at E_F (bottom).

magnetic, and microscopic structures, and physical properties of rare-earth compounds that the program is expected to create in the next few years will: i) advance the knowledge about key electronic and crystallographic features that control strong magnetic responsiveness in $4f$ systems; ii) establish a useful paradigm for design of rare-earth materials with sharp first-order transitions, extraordinary responsiveness, and no thermomagnetic hysteresis; iii) reveal the mechanisms of exchange bias and unusual memory effects in layered crystal structures composed of two or more rare-earth elements, in particular, in the $R'_{1-x}R''_xScT$ series of compounds; iv) explore the science of intra- and interlayer interactions and interfaces on the magnetic and transport properties of low-dimensional rare-earth materials, that is, thin films and multilayers (a new direction for the program); v) learn how to harness responsiveness of rare-earth materials for generation and manipulation of spin currents in support of potential breakthroughs in dissipationless information transfer and thermoelectrics (a new direction for the program); and vi) establish fundamental rules for virtual heterostructuring – an innovative approach to discovery of rare-earth compounds with desired responsive properties informed by density functional theory (DFT). Below we describe several research directions, each pursuing specific basic science goals, which we believe are well suited to achieve our basic science objectives.

Truly discontinuous magnetoelastic transitions. We will expand our study of the fundamentals of discontinuous phase transformations that occur without noticeable thermal and magnetic irreversibilities in R_2In compounds [1,2]. Here, we focus on chemical substitutions and predictive tailoring of $p-d$ charge transfer and $4f$ DOS instabilities near E_F – two mechanisms known to underpin borderline first-order phase transformations in, respectively, Eu_2In and Pr_2In . The R_2In compounds adopt Ni_2In -type (Pr_2In) and Co_2Si -type (Eu_2In) structures that are very common among both $3d$ and rare-earth intermetallics. The Ni_2In -type \leftrightarrow Co_2Si -type phase transformations coupled with magnetic transitions are well-documented and have been connected to strong responsiveness of some purely itinerant electron systems [5], but not for rare-earth compounds. The R_2In family will be used as model to verify a hypothesis whether Ni_2In -type \leftrightarrow Co_2Si -type transitions can also be realized in $4f-5p$ compounds. This will be achieved by a combined experimental (crystallography, magnetic, thermal, and transport properties) and first-principles study of $(R'_{2-x}R''_x)In$ compositions containing different lanthanides, such as a pseudobinary Pr_2In – Eu_2In system, where the end members adopt Ni_2In -type and Co_2Si -type structures.

Layered structures containing two or more rare-earth elements. Distributing different lanthanides orderly or randomly in a crystal lattice, brings about perturbations in exchange interactions, competing crystalline electric fields, and induces instabilities. On top of that, having two or more lanthanides increases complexity of magnetic structure, raises the number of spin degrees of freedom and, consequently, increases the potential for emergence of phase transitions sensitive to external stimuli. Our recent work on $Pr_{0.75}Gd_{0.25}ScGe$ [6] shows that when rare-earth atoms are confined to well-defined atomic monolayers spaced apart, strong spontaneous and conventional exchange bias, common in artificial multilayers, and exotic magnetic memory effect (Figure 2) can emerge in a three-dimensional lattice. When the compound is cooled in a weak magnetic field,

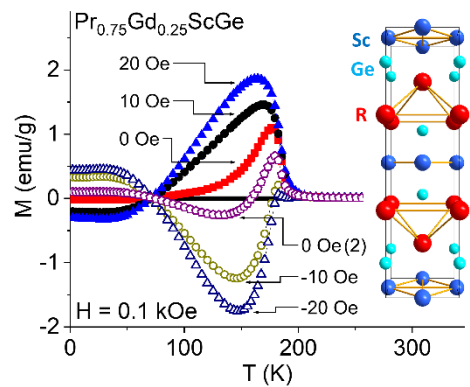


Figure 2. Magnetization measured during heating in $H = 100$ Oe after cooling in different fields as marked; one unit cell of $Pr_{0.75}Gd_{0.25}ScGe$ is shown on the right.

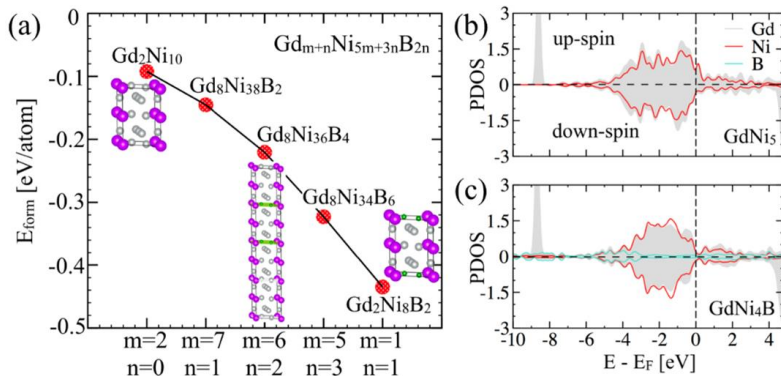


Figure 3. (a) Systematic variation of (m,n) in $\text{Gd}_{m+n}\text{Ni}_{5m+3n}\text{B}_{2n}$ helps in stabilizing intermetallic compounds by lowering the formation energy (E_{form}). DFT calculated trends suggest discovery of novel compounds is possible by virtual heterostructuring of geometrically compatible building blocks. (b,c) The partial densities of states for end points in (a), i.e., GdNi_5 and GdNi_4B .

it “remembers” the orientation of the magnetic field vector even when exposed to a much stronger “read-out” field. Our working hypothesis is that such phenomena can be created in many bulk rare-earth systems with layered crystallography when heavy and light lanthanides are randomly distributed in symmetrically identical monolayers. To test this hypothesis we will scrutinize pseudobinary $(\text{R}'_x\text{R}''_{1-x})\text{ScT}$ compounds, where R'' is a heavy lanthanide, such as Tb, Dy, Ho, and Er, and R' is a light lanthanide, such as Pr and Nd.

Harnessing predictive power of refined computational tools. Rare earths and rare-earth-containing compounds are often built from one- or two-dimensional combinations of structural fragments of simpler phases that exist within the same family. Hence, one can create models of intermetallic structures by way of what we call virtual heterostructuring, that is, by stacking structural elements found in nearby binary and/or ternary compounds, followed by rapid estimates of the models’ formation energies. Over the next few years we will demonstrate the predictive power of the virtual heterostructuring approach using a promising system of ternary borides $\text{R}_{m+n}\text{M}_{5m+3n}\text{B}_{2n}$ (Figure 3), where m is a number of CeCu_5 -type blocks and n is a number of CeCo_3B_2 -type blocks in the heterostructure, each block representing a single unit cell of the corresponding boride [7,8]. Formation energies, ranked against the RCO_5 (RNi_5) and RCO_3B_2 (RNi_3B_2) parents and known combinations in existing $\text{R}_{m+n}(\text{Co},\text{Ni})_{5m+3n}\text{B}_{2n}$ compounds, will be evaluated using DFT and employed to guide subsequent syntheses, targeting the lowest-energy regions of the computed convex hull(s) to reveal thermodynamically stable compositions and structures experimentally. Physical behaviors of these compounds will be also derived from the calculated electronic structures and experimentally validated.

References

- [1] F. Guillou, A.K. Pathak, D. Paudyal, Y. Mudryk, F. Wilhelm, A. Rogalev, and V.K. Pecharsky, Nat. Comm. **9**, 2925 (2018).
- [2] A. Biswas, N.A. Zarkevich, A.K. Pathak, O. Dolotko, I.Z. Hlova, A.V. Smirnov, Y. Mudryk, D.D. Johnson, and V.K. Pecharsky, Phys. Rev. B **101**, 224402 (2020).
- [3] A. K. Pathak, D. Paudyal, Y. Mudryk and V. K. Pecharsky, Phys. Rev. B **96**, 064412 (2017).
- [4] Y. Mudryk, B.P. Alho, P.O. Ribeiro, V.K. Pecharsky, Metals **10**, 1662 (2020).
- [5] A. Biswas, A.K. Pathak, N.A. Zarkevich, X.B. Liu, Y. Mudryk, V. Balema, D.D. Johnson, and V.K. Pecharsky, Acta Mater. **180**, 341 (2019).
- [6] T. Del Rose, A.K. Pathak, Y. Mudryk, and V.K. Pecharsky, J. Mater. Chem. C **9**, 181, (2021).
- [7] Y. Chen, J. Liang, X. Chen, and Q. Liu, J. Alloys Compd. **296**, L1 (2000).
- [8] Y. Suzuki, T. Ito, T. Uchida, O. Nashima, N.M. Hong, and H. Ido, J. Appl. Phys. **81**, 5141 (1997).

Publications

1. Y. Liu, Q.S. Lin, A.K. Pathak, D. Paudyal, and T.A. Lograsso, “Growth of PrCo₂ single crystals with a boron nitride crucible,” *J. Cryst. Growth* **507**, 209 (2019).
2. S.M. Harstad, A.A. El-Gendy, S. Gupta, V.K. Pecharsky, and R.L. Hadimani, “Magnetocaloric effect of micro- and nanoparticles of Gd₅Si₄,” *JOM* **71**, 3159 (2019).
3. Y. Mudryk, C. Ritter, D. Paudyal, A. Provino, S.K. Dhar, P. Manfrinetti, F. Fauth, and V.K. Pecharsky, “Magnetostructural behavior in the non-centrosymmetric compound Nd₇Pd₃,” *J. Phys. Condens. Matter* **31**, 265801 (2019).
4. A. Biswas, Y. Mudryk, A.K. Pathak, L. Zhou, and V.K. Pecharsky, “Managing hysteresis of Gd₅Si₂Ge₂ by magnetic field cycling,” *J. Appl. Phys.* **126**, 243902 (2019).
5. D.H. Ryan, D. Paudyal, F. Guillou, Y. Mudryk, A.K. Pathak, and V.K. Pecharsky, “The first-order magnetoelastic transition in Eu₂In: A ¹⁵¹Eu Mössbauer study,” *AIP Adv.* **9**, 125137 (2019).
6. T. Alammar, I.Z., Hlova, S. Gupta, A. Biswas, T. Ma, L. Zhou, V. Balema, V.K. Pecharsky, and A.-V. Mudring, “Mechanochemical synthesis, luminescent and magnetic properties of lanthanide benzene-1,4-dicarboxylate coordination polymers (Ln_{0.5}Gd_{0.5})₂(1,4-BDC)₃(H₂O)₄; Ln = Sm, Eu, Tb,” *New J. Chem.* **44**, 1054 (2019).
7. P. Malavi, Y. Deng, F. Guillou, Y. Mudryk, V. Pecharsky, and J.S. Schilling, “Antiferromagnetism of β-Ce under hydrostatic pressure,” *Solid State Commun.* **294**, 36 (2019).
8. P.J. Bora, S. Gupta, V.K. Pecharsky, K.J. Vinoy, P.C. Ramamurthy, and R.L. Hadimani, “Enhancement of microwave absorption bandwidth of polymer blend using ferromagnetic gadolinium silicide nanoparticles,” *Mater. Lett.* **252**, 178 (2019).
9. M.Q. Farooq, D. Chand, G.A. Odugbesi, M. Varona, Y. Mudryk, and J.L. Anderson, “Investigating the effect of ligand and cation on the properties of metal fluorinated acetylacetone based magnetic ionic liquids,” *New J. Chem.* **43**(28), 11334 (2019).
10. D. Chand, M.Q. Farooq, A.K. Pathak, J.Z. Li, E.A. Smith, and J.L. Anderson, “Magnetic ionic liquids based on transition metal complexes with N-alkylimidazole ligands,” *New J. Chem.* **43**, 20 (2019).
11. T. Gottschall, M.D. Kuz'min, K.P. Skokov, Y. Skourski, M. Fries, O. Gutfleisch, M.G. Zavareh, D.L. Schlagel, Y. Mudryk, V. Pecharsky, and J. Wosnitza, “Magnetocaloric effect of gadolinium in high magnetic fields,” *Phys. Rev. B* **99**, 134429 (2019).
12. K. Javed, S. Gupta, V.K. Pecharsky, and R.L. Hadimani, “Stability of magnetocaloric La(Fe_xCoySi_{1-x-y})₁₃ in water and air,” *AIP Adv.* **9**, 035239 (2019).
13. S.M. Hastrand, P. Zhao, N. Soin, A.A. El-Gendy, S. Gupta, V.K. Pecharsky, J. Luo, and R.L. Hadimani, “Gd₅Si₄-PVDF nanocomposite films and their potential for triboelectric energy harvesting,” *AIP Adv.* **9**, 035116 (2019).
14. B. T. Lejeune, D. L. Schlagel, B. A. Jensen, T. A. Lograsso, M. J. Kramer, and L. H. Lewis, “Effects of Al and Fe solubility on the magnetofunctional properties of AlFe₂B₂,” *Phys. Rev. Mater.* **3**, 094411 (2019).

15. A. Provino, V. Smetana, T.A. Hackett, D. Paudyal, M.K. Kashyap, C. Bernini, A. Bhattacharyya, S.K. Dhar, M. Pani, F. Gatti, A.-V. Mudring, and P. Manfrinetti, "Stability, crystal chemistry, and magnetism of $U_{2+x}Ni_{21-x}B_6$ and $Nb_{3-y}Ni_{20+y}B_6$ and the role of uranium in the formation of the quaternary $U_{2-z}Nb_zNi_{21}B_6$ and $U_8Nb_{3-\delta}Ni_{20}B_6$ systems," *Inorg. Chem.* **58**, 15045 (2019).
16. C.F. Sánchez-Valdés, R.R. Gimaev, M. López-Cruz, J.L. Sánchez Llamazares, V.I. Zverev, A.M. Tishin, A.M.G. Carvalho, D.J.M. Aguiar, Y. Mudryk, and V.K. Pecharsky, "The effect of cooling rate on magnetothermal properties of $Fe_{49}Rh_{51}$," *J. Magn. Magn. Mater.* **498**, 166130 (2019).
17. A. Biswas, A.K. Pathak, N.A. Zarkevich, X.B. Liu, Y. Mudryk, V. Balema, D.D. Johnson, and V.K. Pecharsky, "Designed materials with the giant magnetocaloric effect near room temperature," *Acta Mater.* **180**, 341-348 (2019).
18. K.N. Al-Milaji, R.L. Hadimani, S. Gupta, V.K. Pecharsky, and H. Zhao, "Inkjet printing of magnetic particles toward anisotropic magnetic properties," *Sci. Rep.* **9**, 16261 (2019).
19. A. Biswas, N.A. Zarkevich, A.K. Pathak, O. Dolotko, I.Z. Hlova, A.V. Smirnov, Y. Mudryk, D.D. Johnson, and V.K. Pecharsky, "First-order magnetic phase transition in Pr_2In with negligible thermomagnetic hysteresis," *Phys. Rev. B* **101**, 224402 (2020).
20. Y. Wu, Y. Mudryk, A. Biswas, V.K. Pecharsky, and Y. Long, "From a conventional ferromagnetism to a frustrated magnetism: An unexpected role of Fe in $Nd(Al_{1-x}Fe_x)_2$ ($x \leq 0.2$)," *J. Alloys Compd.* **830**, 154613 (2020).
21. F. Guillou, D. Paudyal, Y. Mudryk, A.K. Pathak, V. Smetana, A.-V. Mudring, and V.K. Pecharsky, "Metamagnetic transition, magnetocaloric effect and electronic structure of the rare-earth anti-perovskite $SnOEu_3$," *J. Magn. Magn. Mater.* **501**, 166405 (2020).
22. A.K. Pathak, Y. Mudryk, A. Provino, P. Manfrinetti, and V.K. Pecharsky, "Magnetic and transport behaviors of non-centrosymmetric Nd_7Ni_2Pd ," *AIP Adv.* **10**, 015103, (2020).
23. K.N. Al-Milaji, S. Gupta, V.K. Pecharsky, R. Barua, H. Zhao, and R.L. Hadimani, "Differential effect of magnetic alignment on additive manufacturing of magnetocaloric particles," *AIP Adv.* **10**, 015052 (2020).
24. Y. Liu, J.E. Beetar, M.M. Hossen, G. Dhakal, C. Sims, F. Kabir, M.B. Etienne, K. Dimitri, S. Regmi, Y. Liu, A.K. Pathak, D. Kaczorowski, M. Neupane, and M. Chini, "Extreme ultraviolet time- and angle-resolved photoemission setup with 21.5 meV resolution using high-order harmonic generation from a turn-key Yb:KGW amplifier," *Rev. Sci. Instrum.* **91**, 013102 (2020).
25. L. Petit, Z. Szotek, D. Paudyal, A. Biswas, Y. Mudryk, V.K. Pecharsky, and J.B. Staunton, "Magnetic structure of selected Gd intermetallic alloys from first principles," *Phys. Rev. B* **101**, 014409 (2020).
26. O. Dolotko, I.Z. Hlova, A.K. Pathak, Y. Mudryk, V.K. Pecharsky, P. Singh, D.D. Johnson, B.W. Boote, J.Z. Li, E.A. Smith, S.L. Carnahan, A.J. Rossini, L. Zhou, E.M. Eastman, and V.P. Balema, "Unprecedented generation of 3D heterostructures by mechanochemical disassembly and re-ordering of incommensurate metal chalcogenides," *Nat. Commun.* **11**, 3005 (2020).

27. O. Dolotko, I.Z. Hlova, Y. Mudryk, S. Gupta, and V.P. Balema, "Mechanochemical recovery of Co and Li from LCO cathode of lithium-ion battery," *J. Alloys Compd.* **824**, 153876 (2020).
28. F. Guillou, H. Yibole, R. Hamane, V. Hardy, Y.B. Sun, J.J. Zhao, Y. Mudryk, and V.K. Pecharsky, "Crystal structure and physical properties of Yb_2In and $\text{Eu}_{2-x}\text{Yb}_x\text{In}$ alloys," *Phys. Rev. Mater.* **4**, 104402 (2020).
29. B.P. Alho, P.O. Ribeiro, P.J. von Ranke, F. Guillou, Y. Mudryk, and V.K. Pecharsky, "Free-energy analysis of the nonhysteretic first-order transition of Eu_2In ," *Phys. Rev. B* **102**, 134425 (2020).
30. Y. Mudryk, B.P. Alho, P.O. Ribeiro, V.K. Pecharsky, "Low-temperature crystal structure and mean-field modeling of $\text{Er}_x\text{Dy}_{1-x}\text{Al}_2$ intermetallics," *Metals* **10**, 1662 (2020).
31. P.O. Ribeiro, B.P. Alho, R.S. de Oliveira, E.P. Nobrega, V.S.R. de Sousa, P.J. von Ranke, Y. Mudryk, and V.K. Pecharsky, "Magnetothermal properties of $\text{Tm}_x\text{Dy}_{1-x}\text{Al}_2$ ($x = 0.25, 0.5$, and 0.75)," *J. Alloys Compd.* **858**, 157682 (2021).
32. T. Del Rose, A.K. Pathak, Y. Mudryk, and V.K. Pecharsky, "Distinctive exchange bias and unusual memory effects in magnetically compensated $\text{Pr}_{0.75}\text{Gd}_{0.25}\text{ScGe}$," *J. Mater. Chem. C* **9**, 181, (2021).

Harnessing Order Parameter in Ternary II-IV-V₂ Semiconductors

Adele C. Tamboli, National Renewable Energy Lab

Program Scope

In this program, we are developing a fundamental understanding of cation order and its impact on properties in II-IV-V₂ semiconductors. Our work on II-IV-V₂ materials builds on a foundation of work in III-V ordering by exploring a set of materials with similar optoelectronic functionality to III-Vs but with wider tunability through chemical complexity. We study nitrides and phosphides, two structure types available in this class, shown in Fig. 1.^{P6} The underlying scientific questions this work addresses are:

- How does cation disorder affect properties such as band gap?
- What are the most important length scales for disorder, and how can we measure and simulate them?
- Can we use an understanding of disorder to guide materials discovery?

We aim to understand how a wide variety of physical properties are determined by site occupancy. Our materials of focus have strong technological relevance: II-IV-V₂s can be integrated with III-V materials and silicon, enabling optoelectronic applications spanning the visible spectrum.

Recent Progress

Controlling site disorder in complex semiconductors offers the possibility of achieving properties not available in perfectly ordered materials. This type of property tuning opens opportunities for discovering new or improved energy-relevant materials for applications such as light-emitting diodes, photovoltaics, photocatalysts, batteries, and thermoelectrics.^{P6} We have focused on understanding the impact of disorder on properties using energy-relevant model systems and using this knowledge to design new materials. Key areas of investigation are how to characterize and model site disorder, how to measure its impact on optical properties, and understanding the intersection of material “quality” with site disorder.

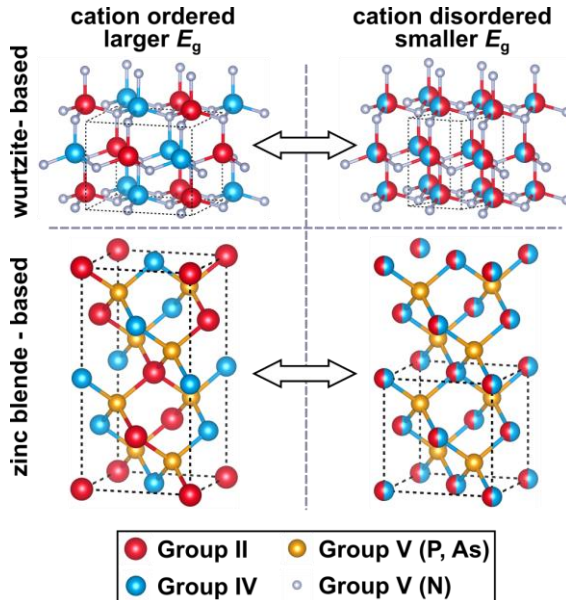


Fig. 1. II-IV-V₂ materials enable band gap tuning using cation disorder. This enables an alternative route to property tuning compared to traditional alloying approaches. In this project, we investigate nitride (wurtzite-based) and phosphide (zincblende-based) model systems to understand this phenomenon. Image from publication P6.

Optical properties of ZnGeP₂

ZnGeP₂ is a semiconductor of interest for Si-based tandem photovoltaics due to its lattice match with Si and its wider band gap of 2.1 eV. However, its band gap tunability with disorder had not been experimentally demonstrated or understood. We studied this material as a case example to understand the impact of site disorder on optical properties and the details of how to conceptualize site disorder from a structural perspective. The simple picture of fully random site disorder in Fig. 1 is not physically realistic because the energetic penalties for high levels of disorder are large.^{1,2} Thus, we used two metrics to quantify the degree of disorder in ZnGeP₂:

1. A stretching parameter quantifying tetragonal distortion in the lattice: c/a , where $c/a = 2$ for fully random or 1.96 for fully ordered material
2. A long range order parameter S calculated using site occupancies, where S is the fraction of cations on the “correct” site, $S=1$ being fully ordered and $S=0$ being random disorder

Both of these order parameters can be extracted from X-ray diffraction data as shown in Fig. 2 (a-b). Described in P8, resonant and off-resonant X-ray energies must be compared to measure S since Zn and Ge have similar scattering factors. To correlate these structural metrics with optical properties, we measured the optical absorption of our ZnGeP₂ films using ellipsometry, and saw that as expected, the band gap decreases with disorder. The stretching parameter did not correlate well to the long-range order parameter S , but

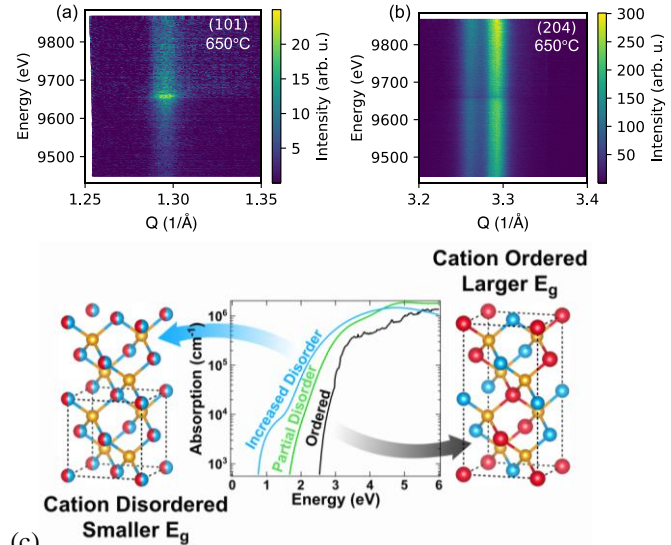


Fig. 2. Site disorder can be quantified accurately using resonant energy X-ray diffraction. (a) The superlattice peak is strongest on-resonance to enhance the difference in scattering factors between Zn and Ge. (b) Peak splitting which can be used to quantify stretching parameter. Optical absorption (c) changes with order parameter, verifying the predicted band gap tuning with cation disorder in ZnGeP₂.^{P6,P8}

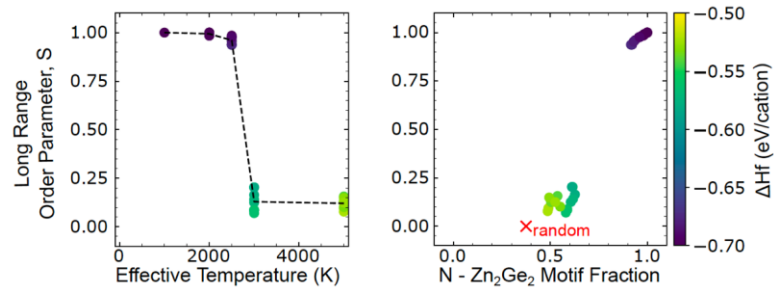


Fig. 3. Long range order parameter as a function of simulation temperature (left) and its correlation to local order parameter or “motif fraction” (right).^{P1}

¹ S. Lany, A.N. Fioretti, P.P. Zawadzki, L.T. Schelhas, E.S. Toberer, A. Zakutayev, and A.C. Tamboli, Phys. Rev. Materials **1**, 035401 (2017).

² P.C. Quayle, E.W. Blanton, A. Punya, G.T. Junno, K. He, L. Han, H. Zhao, J. Shan, W.R.L. Lambrecht, and K. Kash, Physical Review B **91**, 205207 (2015).

S better correlated to disorder-induced changes in optical properties. This study confirmed band gap tuning with site disorder, but also shows that metrics must accurately capture site occupancies, to characterize cation disorder.

Theoretical investigation of configurational disorder in ZnGeN_2

The discrepancy in order parameters described above prompted a theoretical investigation into more realistic models for partially-ordered materials. We have previously reported such a study on ZnSnN_2 ,^{R1} but materials such as ZnGeP_2 and ZnGeN_2 undergo structural deformations creating long range interactions which complicate modeling. We used a cluster expansion-based Monte Carlo method to generate structures corresponding to different temperatures in order to understand different physically realistic degrees of disorder (described in ref. P1). This approach allowed us to compare S to short-range order observed in anion coordination, where N bonded to 2 Zn and 2 Ge cations satisfies the local octet rule while other motif fractions create disorder. The long-range order parameter correlates well to local order parameter in highly ordered samples, but poorly in disordered samples (Fig. 3). Fully random disorder, as expected, was not found in our simulation due to it being energetically unfavorable. We also found that lattice parameter-based methods of characterizing disorder (e.g. stretching parameter) do not strongly correlate to site occupancy based metrics, in agreement with our experimental findings. We saw a steep “phase transition” between highly ordered and highly disordered samples, indicating that moderate disorder is unlikely to occur experimentally. This is visible in the gap between $S\sim 0.25$ and $S\sim 0.90$ in Fig. 3.

Epitaxial, disordered ZnGeN_2 on GaN

Cation site disorder can be thought of as a nonequilibrium defect; thus, it was not clear whether “high quality” materials could exhibit site disorder. Understanding the interplay between growth and disorder is important for understanding whether disorder can be expected in epitaxial thin films suitable for device applications. ZnGeN_2 is of interest for light-emitting diodes (LEDs), as its disordered structure may enable light emission in hard-to-reach areas of the visible spectrum such as green to amber, and it is lattice matched to GaN. We investigated this case example using molecular beam epitaxy (MBE) growth of ZnGeN_2 on AlN and GaN and found that high crystalline quality material can be grown with cation site disorder (Fig. 4). Integrating disordered nitrides in epitaxial stacks enables the discovery of new materials for a wide variety of applications, including UV LEDs, power electronics, and solar absorbers.^{P2} Fig. 5 shows a map of known and

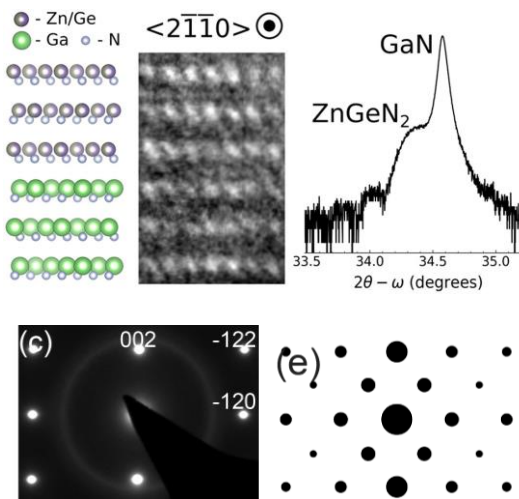


Fig. 4. Epitaxial $\text{ZnGeN}_2/\text{GaN}$ films by MBE. Electron diffraction shows that these films are cation-disordered due to the lack of superlattice reflections (visible in the simulated pattern). Disorder coexists with high crystalline “quality.” Images from P7.

predicted ternary nitride materials that could be grown with hexagonal symmetry, along with known binaries. All the materials are shown with their predicted, ordered band gaps; disorder can be expected to decrease their band gaps by 1-2 eV.

Combinatorial synthesis of MgSnN₂

The approach outlined in the previous section and Fig. 5 for the discovery of new ternary nitrides with disorder-based tunability motivated the exploration of MgSnN₂, a previously unknown material that is expected to have a band gap of 2.4 eV in its ordered form. This material is promising for photoelectrochemical reduction of CO₂ as well as solid state lighting applications. We used combinatorial methods to demonstrate the synthesis of MgSnN₂, which also exhibits a disorder-driven band gap reduction, and the ability to grow oriented MgSnN₂ films on GaN. Surprisingly, this material can also form in a rocksalt-derived crystal structure in addition to its wurtzite-derived ground state, and the rocksalt structure orients preferentially to GaN as well, with an even closer lattice match. These experiments, described in more detail in ref. P4, demonstrate both the promise of disorder-informed materials discovery and the need for experimental investigations to inform understanding of polymorphs.

Future Plans

Understanding local ordering in alloys

We previously reported on theoretical predictions that novel emergent behavior would be observed in the ZnSnN₂:ZnO alloy system, where at certain “magic” compositions, perfect short range order could coexist with long range disorder.^{P3} These compositions behave in some ways like line compounds, in that their energetics and predicted band gap are outliers from alloy trends, and they represent a new opportunity for materials by design as beneficial aspects of ordered systems (e.g. excellent carrier transport) may coexist with beneficial aspects of disordered alloys (e.g. tunability). We have now synthesized these ZnSnN₂:ZnO alloys in a wide range of compositions using combinatorial techniques. Our current work probes local ordering by measuring the motif fraction directly using X-ray absorption. Preliminary results indicate that annealing may induce perfect short-range order at these “magic” compositions, and that optical properties can be tuned with local ordering. We plan to continue our analyses to understand both the possibilities and limitations of these measurements of local ordering and apply these methods to discovery of new line-compound-like alloys that may exhibit similar behavior.

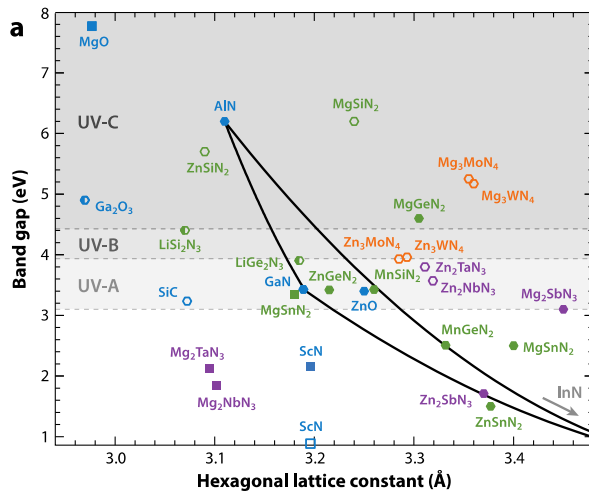


Fig. 5. A map of promising new ternary nitride materials that may be integrated with binaries such as GaN and ZnO. From ref. P2.

of CO₂ as well as solid state lighting applications. We used combinatorial methods to demonstrate the synthesis of MgSnN₂, which also exhibits a disorder-driven band gap reduction, and the ability to grow oriented MgSnN₂ films on GaN. Surprisingly, this material can also form in a rocksalt-derived crystal structure in addition to its wurtzite-derived ground state, and the rocksalt structure orients preferentially to GaN as well, with an even closer lattice match. These experiments, described in more detail in ref. P4, demonstrate both the promise of disorder-informed materials discovery and the need for experimental investigations to inform understanding of polymorphs.

We previously reported on theoretical predictions that novel emergent behavior would be observed in the ZnSnN₂:ZnO alloy system, where at certain “magic” compositions, perfect short range order could coexist with long range disorder.^{P3} These compositions behave in some ways like line compounds, in that their energetics and predicted band gap are outliers from alloy trends, and they represent a new opportunity for materials by design as beneficial aspects of ordered systems (e.g. excellent carrier transport) may coexist with beneficial aspects of disordered alloys (e.g. tunability). We have now synthesized these ZnSnN₂:ZnO alloys in a wide range of compositions using combinatorial techniques. Our current work probes local ordering by measuring the motif fraction directly using X-ray absorption. Preliminary results indicate that annealing may induce perfect short-range order at these “magic” compositions, and that optical properties can be tuned with local ordering. We plan to continue our analyses to understand both the possibilities and limitations of these measurements of local ordering and apply these methods to discovery of new line-compound-like alloys that may exhibit similar behavior.

Publications (Last 2 Years)

- P1. Jacob J. Cordell, Jie Pan, Adele C. Tamboli, Garrett J. Tucker, Stephan Lany, *Probing configurational disorder in ZnGeN₂ using cluster-based Monte Carlo*. *Phys. Rev. Mater.*, **2021**, 5, 024604. <https://doi.org/10.1103/PhysRevMaterials.5.024604>
- P2. Ann L. Greenaway, Celeste L. Melamed, M. Brooks Tellekamp, Rachel Woods-Robinson, Eric S. Toberer, James R. Neilson, Adele C. Tamboli. *Ternary Nitride Materials: Fundamentals and Emerging Device Applications*. *Annual Reviews of Materials Research*, accepted, **9/2020**. <https://arxiv.org/abs/2010.08058>
- P3. Jie Pan, Jacob Cordell, Garrett J. Tucker, Andriy Zakutayev, Adele C. Tamboli, and Stephan Lany, *Perfect short-range ordered alloy with line-compound-like properties in the ZnSnN₂:ZnO system*, *NPJ Computational Materials* **2020**, 6, 1-6. <https://doi.org/10.1038/s41524-020-0331-8>
- P4. Ann L. Greenaway, Amanda L. Loutris, Karen N. Heinselman, Celeste L. Melamed, Rekha R. Schnepf, M. Brooks Tellekamp, Rachel Woods-Robinson, Rachel Sherbondy, Dylan Bardgett, Sage Bauers, Andriy Zakutayev, Steven T. Christensen, Stephan Lany, Adele C. Tamboli, *Combinatorial synthesis of magnesium tin nitride semiconductors*. *Journal of the American Chemical Society* **2020**, 142, 8421-8430. <https://pubs.acs.org/doi/abs/10.1021/jacs.0c02092>
- P5. Celeste L. Melamed, Jie Pan, Allison Mis, Karen Heinselman, Rekha R. Schnepf, Rachel Woods-Robinson, Jacob Cordell, Stephan Lany, Eric S. Toberer, and Adele C. Tamboli, *Combinatorial investigation of structural and optical properties of cation-disordered ZnGeN₂*. *J. Mat. Chem. C* **2020**, 8, 8736-8746. <https://doi.org/10.1039/D0TC01675F>
- P6. Rekha R. Schnepf, Jacob J. Cordell, M. Brooks Tellekamp, Celeste L. Melamed, Ann L. Greenaway, Allison Mis, Geoff L. Brennecka, Steven Christensen, Garrett J. Tucker, Eric S. Toberer, Stephan Lany, and Adele C. Tamboli, *Utilizing site disorder in the development of new energy-relevant semiconductors*. *ACS Energy Letters*, **2020**, 5, 2027-2041. [Focus Review, Invited] <https://doi.org/10.1021/acsenergylett.0c00576>
- P7. M. Brooks Tellekamp, Celeste L. Melamed, Andrew G. Norman, and Adele Tamboli, *Heteroepitaxial Integration of ZnGeN₂ on GaN Buffers Using Molecular Beam Epitaxy*. *Crystal Growth & Design*, **3**, 1868 (2020). <https://doi.org/10.1021/acs.cgd.9b01578>
- P8. Rekha R. Schnepf, Ben L. Levy-Wendt, M. Brooks Tellekamp, Brenden R. Ortiz, Celeste L. Melamed, Laura T. Schelhas, Kevin H. Stone, Michael F. Toney, Eric S. Toberer, and Adele C. Tamboli, *Using resonant energy X-ray diffraction to extract chemical order parameters in ternary semiconductors*. *Journal of Materials Chemistry C*, **2020**, 8, 4350-4356. [Cover] <https://doi.org/10.1039/C9TC06699C>
- P9. Rekha R. Schnepf, Aaron D. Martinez, John S. Mangum, Laura T. Schelhas, Eric S. Toberer, and Adele C. Tamboli, *Disorder-tunable ZnGeP₂ for epitaxial top cells on Si*. *Proceedings of the 2019 IEEE Photovoltaic Specialists Conference*, p. 1052 **2019**. <https://doi.org/10.1109/PVSC40753.2019.8980697>

P10. Celeste L. Melamed, Brooks Tellekamp, John S. Mangum, Patricia Dippo, Eric S. Toberer, and Adele C. Tamboli, *Blue-Green Emission from Epitaxial Yet Cation-Disordered ZnGeN_{2-x}O_x.*, Phys. Rev. Mater. 3, 051602 2019.
<https://doi.org/10.1103/PhysRevMaterials.3.051602>

Effect of spatial variation of photon chemical potential on near-field thermophotovoltaics

Principle Investigator: Zhuomin Zhang
George W. Woodruff School of Mechanical Engineering
Georgia Institute of Technology, Atlanta, GA 30332

Program Scope

Nanoscale thermal radiation can significantly enhance the radiative heat flux and may have important applications in heat-to-electricity energy harvesting and electroluminescent refrigeration. This project aims at investigating near-field Radiative Thermoelectric Energy Converters (RTECs), such as thermoradiative energy generation and electroluminescent refrigeration devices. Additionally, radiation thermodynamics will be applied to examine the effect of luminescent emission on the performance in order to gain a deeper understanding of the fundamental processes. A recent study is presented in the following on an important aspect of the spatial profile of photon chemical potential and its impact on the near-field thermophotovoltaic (TPV) performance by solving the combined photon and charge transport equations.

Recent Progress

In most studies with moderate emitter temperatures and narrow gap cell materials [1,2], it is assumed that the photon chemical potential is uniform in the active region and equals the product of the bias voltage and fundamental charge: $\mu = Vq$. With the recent experimental demonstrations of near-field TPVs and electroluminescent cooling devices [3-5], realistic modeling of the photon chemical potential profile becomes imperative for future research and development of near-field RTECs. This requires a full solution of the coupled photon exchange and charge transport equations. The PI's group has initiated a collaborative effort to develop numerical solution methods and tools to fully address the coupled photon and charge transport problems [6,7]. The iterative method combines fluctuational electrodynamics with the full drift-diffusion model to solve the coupled charge and photon transport equations. The calculation results are used to assess the impact of the photon chemical potential on the performance of TPV systems. By comparison of the solution using the iterative method with that using the detailed balance analysis based on a constant (or zero) photon chemical potential, the errors caused by the assumption of a constant photon chemical potential across the TPV cell or by completely neglecting the luminescent effect (i.e., $\mu = 0$) can be quantified for different TPV systems.

A multilayer fluctuational electrodynamics (FE) formalism is applied to calculate photon exchange between any two layers in a 1D stratified medium. As an example, a thin InAs TPV cell (whose bandgap energy is $E_g = 0.35$ eV) with an Au film reflector is considered, and the emitter is made of tungsten covered by a thin ITO film. The charge transport equations for both majority and minority carriers are solved at steady state, using the photogeneration profile obtained from the near-field FE based on the modified Bose-Einstein statistics with a presumed photon chemical potential profile. The solution of the charge transport equations considering both bulk and surface nonradiative recombinations yields the spatial distributions of electron and hole quasi-Fermi levels. The difference between the quasi-Fermi levels gives the profile of photon chemical potential, $\mu(z)$, where z is perpendicular to the surfaces/interfaces. The new values of the photon chemical potential are used to repeat the near-field photon exchange calculation, followed by the charge transport solution, until the

prescribed convergence criteria are satisfied [7]. The iterative method has also been used to improve the modeling of thermoradiative (TR) cells [6].

The band diagram of an InAs TPV cell is shown in Fig. 1 for (a) $V = 0$ V (short-circuit case) and (b) $V = 0.17$ V (maximum-efficiency condition). The thicknesses of the p -region and n -region are both assumed to be 200 nm. The cell is at 300 K and the emitter is at 900 K, separated by a vacuum gap distance $d = 10$ nm. The difference between the quasi-Fermi levels, $\mu(z)$, is represented by the height of the shaded region. It can be seen that the depletion region is broadened and extended over the n -region, especially for the short-circuit case. Surface recombination can affect the band structure in the depletion region as manifested by the inflection of the curve. Note that a high-injection condition exists in the n -region with a donor concentration of 2×10^{16} cm $^{-3}$. As shown in Fig. 1(a), $\mu(z)$ is a strong function of z . High-quality surfaces with minimal defects for both holes and electrons are assumed here. Nevertheless, the surfaces can trap the free carriers inside the junction, giving rise to a nonzero quasi-Fermi level difference in the depletion region even with $V = 0$. When $V = 0.17$ V, as shown in Fig. 1(b), $\mu(z)$ is approximately a constant. However, the value of μ is about 0.195 eV, which is almost 15% greater than the product Vq . The nonuniform splitting of quasi-Fermi levels was previously demonstrated by Blandre et al. [8]; however, their study used a radiative recombination model to treat the luminescence effect and did not consider the near-field effect on luminescent emission.

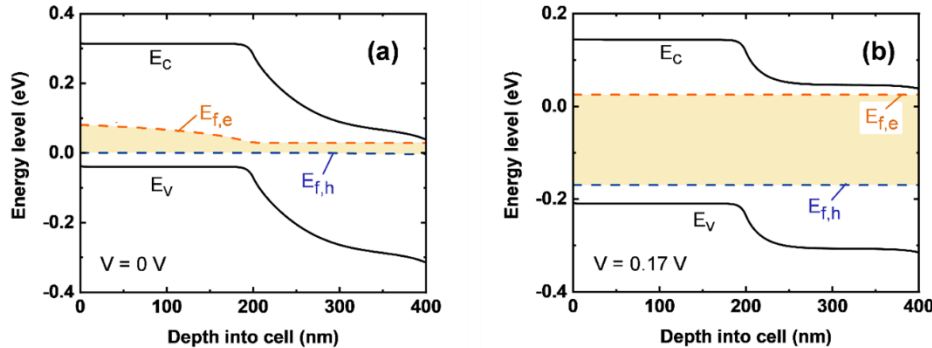


Fig. 1. The energy band diagrams of the thin near-field InAs TPV cell under (a) short-circuit ($V = 0$ V) and (b) maximum-efficiency ($V = 0.17$ V) conditions [7].

The characteristics of the InAs TPV cell performance is shown in Fig. 2, which demonstrates the luminescence effect and the importance of considering the nonuniform profile of the photon chemical potential. Note that the curve with $\mu = \mu(z)$ is based on the iterative method, while the curves with $\mu = Vq$ or 0 are based on the detailed balance analysis. As shown in Figs. 2(a) and (b), as V increases, the luminescence effect reduces both the photogeneration rate G_{cell} and absorbed energy rate Q as compared to the case with $\mu = 0$ (when the luminescence effect is completely neglected). Here, G_{cell} is calculated by integrating the local photogeneration rate over the active region of the cell. Since the iterative method yields a $\mu(z)$ that is always greater than Vq (based on the detailed balance analysis), the curve with $\mu = \mu(z)$ is always the lowest. The differences become larger as V increases to above 0.12 V. The maximum relative error in G_{cell} for $\mu = Vq$ is 21% taking the iterative method as the reference, which occurs at $V = 0.22$ V. The iterative method predicts that the maximum efficiency occurs at $V = 0.17$ V, where the relative error in G_{cell} is 6.1% with $\mu = Vq$ and 9.7% with $\mu = 0$. The current density and efficiency are displayed in Figs. 2(c) and (d).

The detailed balance analysis overpredicts the current density in particular as V increases to beyond 0.13 V. The difference between the current densities with $\mu = Vq$ and $\mu = 0$ is purely due to the net photogeneration rate as the recombination rates are the same according to the detailed balance analysis. Since the recombination rate increases with V , the current density drops to zero as V increases to the open-circuit voltage V_{oc} , which is slightly larger for $\mu = Vq$ than for $\mu = \mu(z)$, but much larger with $\mu = 0$. The maximum efficiencies are 39.8% at $V = 0.205$ V with $\mu = 0$, 37.4% at $V = 0.19$ V with $\mu = Vq$, and 32.7% at $V = 0.17$ V with $\mu = \mu(z)$. These differences are due to the combined effects caused by the profile of μ and the underlying charge transport modeling.

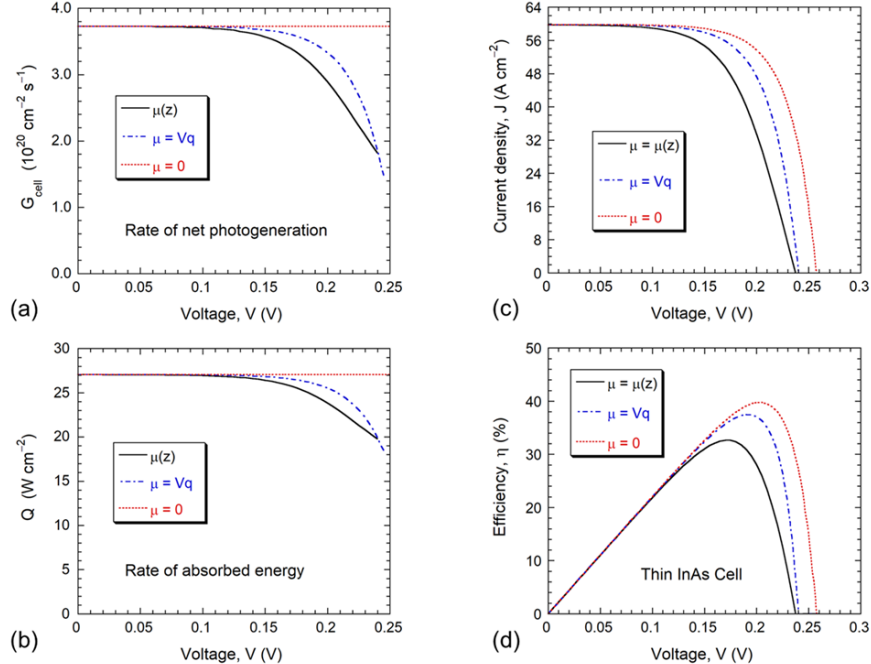


Fig. 2. (a) Net absorbed energy density, (b) net photogeneration density, (c) current density, and (d) efficiency versus bias voltage for the InAs TPV cell. Here, $\mu(z)$ is obtained from the iterative method, $\mu = Vq$ is from detailed balance analysis, and $\mu = 0$ is from detailed balance analysis by ignoring luminescent emission [7].

Comparisons of the major characteristics suggest that accurate modeling of the photon chemical potential and the charge transport are critical to predicting the performance of near-field TPV systems. These results show that the detailed balance approach by ignoring the luminescence effect ($\mu = 0$) or by using a constant photon chemical potential ($\mu = Vq$) cannot properly describe the characteristics of both the thin and thick TPV systems and could cause 10-30% error in efficiency and output power when compared to the iterative solutions. This study demonstrates that the photon chemical potential is an important parameter in near-field semiconductor radiative energy converters and need to be carefully considered when the emitter is at a moderate temperature. It should be noted that with even higher level of injection, the Boltzmann distribution used to approximate the Fermi-Dirac distribution of electron and hole systems may be questionable; hence, more comprehensive models that consider degenerate semiconductors may be necessary to accurately describe the band diagrams.

Future Plans

The PI's group recently demonstrated a near-field effect on the reverse saturation current due to radiative recombination. Work is in progress to develop the experimental characterization tools and measurements to demonstrate such near-field effect using a dielectric film as the gap rather than a vacuum gap. Because the measurements will be performed under "dark" conditions where the temperature of the cell and emitter is uniform, conduction heat transfer is excluded. This could offer a unique method for studying the near-field photon exchange. Furthermore, since the current project will end in June 2021, a renewal proposal has been submitted. The coupled photon and charge transport method will be extended to study various practical semiconductor devices, including heterojunction structures under degenerate conditions. The effect of an air gap that separates the TPV cell and the Au reflector will also be investigated. Furthermore, a comprehensive study will be performed on the radiative recombination processes and "spontaneous" emission under nonequilibrium conditions (such as illumination or voltage biasing) in order to better understand photon-semiconductor interactions under nonequilibrium conditions. In addition to the experimentally demonstration of the near-field effect on the dark current for selected photovoltaic cells, the PI's group will perform far-field electroluminescent measurements with narrow bandgap semiconductor diodes to obtain further evidence of the modified Bose-Einstein distribution.

References

1. E.J. Tervo, E. Bagherisereshki, and Z.M. Zhang, Near-Field Radiative Thermoelectric Energy Converters: A Review, *Frontiers in Energy*, Vol. 12, pp. 5-21, 2018.
2. B. Zhao and S. Fan, Chemical Potential of Photons and Its Implications for Controlling Radiative Heat Transfer, *Annual Review of Heat Transfer*, Vol. 23, pp. 397-431, 2020.
3. A. Fiorino, L. Zhu, D. Thompson, R. Mittapally, P. Reddy, and E. Meyhofer, Nanogap Near-field Thermophotovoltaics, *Nature Nanotechnology*, Vol. 13, pp. 806-811, 2018.
4. L. Zhu, A. Fiorino, D. Thompson, R. Mittapally, E. Meyhofer, and P. Reddy, Near-field Photonic Cooling through Control of the Chemical Potential of Photons, *Nature*, Vol. 566, pp. 239-244, 2019.
5. G.R. Bhatt, B. Zhao, S. Roberts, I. Datta, A. Mohanty, T. Lin, J.-M. Hartmann, R. St-Gelais, S. Fan, and M. Lipson, Integrated Near-field Thermo-photovoltaics for Heat Recycling, *Nature Communications*, Vol. 11, p. 2545, 2020.
6. W.A. Callahan, D. Feng, Z.M. Zhang, E.S. Toberer, A.J. Ferguson, and E.J. Tervo, Coupled Charge and Radiation Transport Processes in Thermophotovoltaic and Thermoradiative Cells, submitted to *Physical Review Applied*, 2021: arXiv:2101.04746v1.
7. D. Feng, E.J. Tervo, D. Vasileska, S.K. Yee, A. Rohatgi, and Z.M. Zhang, Spatial Profiles of Photon Chemical Potential in Near-field Thermophotovoltaic Cells, submitted to *Journal of Applied Physics*.
8. E. Blandre, P.-O. Chapuis, and R. Vaillon, High-injection Effects in Near-field Thermophotovoltaic Devices, *Scientific Reports*, Vol. 7, p. 15860, 2017.
9. D. Feng, E.J. Tervo, S.K. Yee, and Z.M. Zhang, Effect of Evanescent Waves on the Dark Current of Thermophotovoltaic Cells, *Nanoscale and Microscale Thermophysical Engineering*, Vol. 24, pp. 1-19, 2020.

Publications 2019-2021 (with support by the DOE-BES Grant DE-SC0018369)

1. Z.M. Zhang, *Nano/Microscale Heat Transfer*, 2nd edn., Springer Nature, Cham, Switzerland, 2020.
2. Z.M. Zhang, Overview of Micro/Nanoscale Thermal Radiation, *Annual Review of Heat Transfer*, Vol. 23, Chap. 1, pp. 1-12, 2020.
3. E.J. Tervo, B.A. Cola, and Z.M. Zhang, Dipole Approximations for Near-field Radiative Heat Transfer, *Annual Review of Heat Transfer*, Vol. 23, Chap. 5, pp. 131-166, 2020.
4. Z.M. Zhang, X.H. Wu, and C.J. Fu, Validity of Kirchhoff's Law for Semitransparent Films Made of Anisotropic Materials, *Journal of Quantitative Spectroscopy and Radiative Transfer*, Vol. 245, p. 106904, 2020.
5. E.J. Tervo, B.A. Cola, and Z.M. Zhang, Comparison of Kinetic Theory and Fluctuational Electrodynamics for Radiative Heat Transfer in Nanoparticle Chains, *Journal of Quantitative Spectroscopy and Radiative Transfer*, Vol. 246, p. 106947, 2020.
6. D. Feng, E.J. Tervo, S.K. Yee, and Z.M. Zhang, Effect of Evanescent Waves on the Dark Current of Thermophovoltaic Cells, *Nanoscale and Microscale Thermophysical Engineering*, Vol. 24, pp. 1-19, 2020.
7. X.H. Wu, C.J. Fu, and Z.M. Zhang, Near-field Radiative Heat Transfer between Two α -MoO₃ Biaxial Crystals, *Journal of Heat Transfer*, Vol. 142, p. 072802, 2020.
8. X.H. Wu, C.J. Fu, and Z.M. Zhang, Chiral Absorbers Based on Polarization Conversion and Excitation of Magnetic Polaritons, *ES Energy & Environment*, Vol. 8, pp. 5-14, 2020.
9. P. Yang and Z.M. Zhang, Bidirectional Reflection of Semitransparent Polytetrafluoroethylene (PTFE) Sheets on a Silver Film, *International Journal of Heat and Mass Transfer*, Vol. 148, p. 118992, 2020.
10. P. Yang, H. Ye, and Z.M. Zhang, Experimental Demonstration of the Effect of Magnetic Polaritons on the Radiative Properties of Deep Aluminum Gratings, *Journal of Heat Transfer*, Vol. 141, p. 052702, 2019.
11. X.H. Wu, C.J. Fu, and Z.M. Zhang, Effect of Orientation on the Directional and Hemispherical Emissivity of Hyperbolic Metamaterials," *International Journal of Heat and Mass Transfer*, Vol. 135, pp. 1207-1217, 2019.
12. X.H. Wu, C.J. Fu, and Z.M. Zhang, Chiral Response of a Twisted Bilayer of Hexagonal Boron Nitride, *Optics Communications*, Vol. 452, pp. 124-129, 2019.
13. E.J. Tervo, M.E. Gustafson, Z.M. Zhang, B.A. Cola, and M.A. Filler, Photonic Thermal Conduction by Infrared Plasmonic Resonators in Semiconductor Nanowires, *Applied Physics Letters*, Vol. 114, p. 163104, 2019.
14. E.J. Tervo, M. Francoeur, B.A. Cola, and Z.M. Zhang, Thermal Radiation in Systems of Many Dipoles, *Physical Review B*, Vol. 100, p. 205422, 2019.
15. J.L. Song, Q. Cheng, Z.X. Luo, X.P. Zhou, and Z.M. Zhang, Modulation and Splitting of Three-Body Radiative Heat Flux via Graphene/SiC Core-Shell Nanoparticles, *International Journal of Heat and Mass Transfer*, Vol. 140, pp. 80-87, 2019.
16. D.Y. Xu, A. Bilal, J.M. Zhao, L.H. Liu, and Z.M. Zhang, Near-Field Radiative Heat Transfer between Rough Surfaces Modeled Using Effective Media with Gradient Distribution of Dielectric Function, *International Journal of Heat and Mass Transfer*, Vol. 142, p. 118432, 2019.

Synthesis of Ta₂S₅ wires with steel-like strength and superconductivity in Ta₂O_{5-x}S_x wires

Shermane M. Benjamin, Nathaniel F. Rieders, M. G. Smith, and John J. Neumeier, Physics Department, Montana State University, Bozeman, MT 59717 USA.

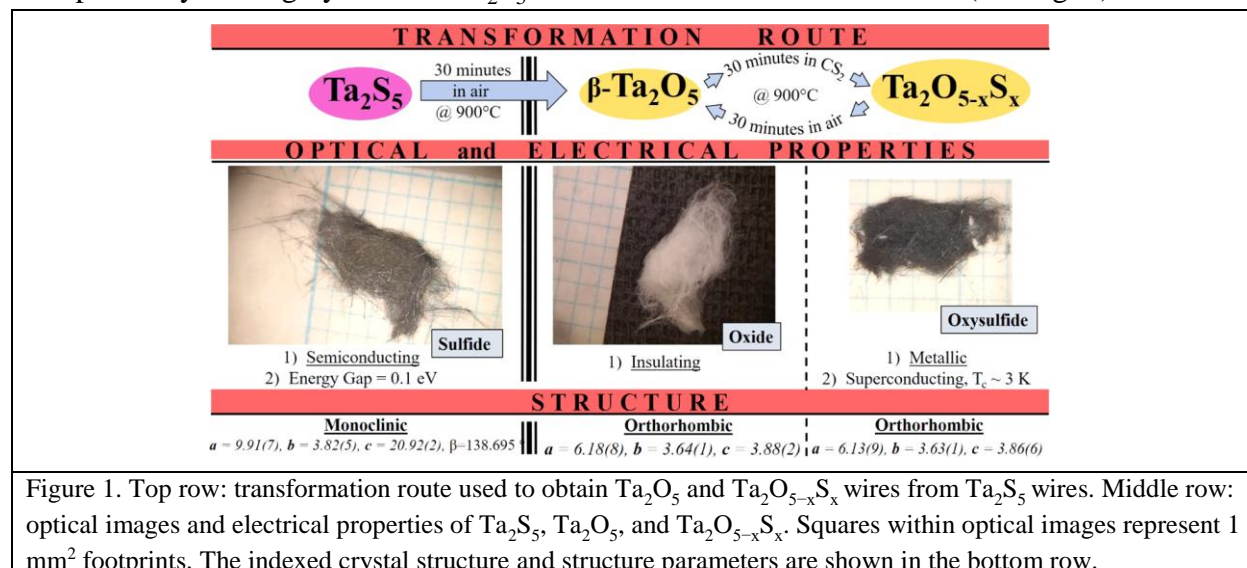
Program Scope

The synthesis pathways to form advanced materials are not always direct. In this presentation, we describe the synthesis of Ta₂S₅, a compound never before grown. It was grown via vapor transport as wires that are a few microns in diameter, and centimeters in length. The wires are as strong as steel. The Ta₂S₅ wires can be oxidized to form Ta₂O₅ wires, an insulator with many applications, albeit never formed previously in wire form. Ta₂O₅ can then be sulfurized to form Ta₂O_{5-x}S_x wires, which are metallic and superconducting.

Recent Progress

Ta₂S₅ has only been reported as an unwanted nonmetallic inclusion in etched, pure Ta and as a byproduct in thin-film production [1-3]. Furthermore, there are no reports of the formation of binary tantalum chalcogenides with the ratio 2:5 (i.e. Ta₂S₅, Ta₂Se₅, Ta₂Te₅). In contrast, the oxide Ta₂O₅ is well-known and widely used in technology as a dielectric, antireflective coating, and in photocatalysis [4-9]. In our work, the first controlled synthesis of Ta₂S₅ was realized; it forms as wires. Oxidation of the Ta₂S₅ wires leads to Ta₂O₅ wires. These can be sulfurized to form wires of Ta₂O_{5-x}S_x, a new superconductor. All wires are mesoscopic in thickness and macroscopic in length. The synthesis routes for these three compounds present an experimental pathway for growing long wires of other inorganic compounds.

For the synthesis of single-crystalline Ta₂S₅ wires, polycrystalline XTa₂S₅ (X = Sr or Ba) was first prepared [10,11]. This compound was placed in an evacuated, sealed, quartz tube with 2 wt% of sulfur and TeCl₄. The TeCl₄ produces the vapor-transport agent chlorine when heated; Te and Cl were absent from the wires. The quartz tube was placed in a single-zone tube furnace with the contents at the tube end in the hottest region of the furnace, which was ramped to 900 °C in 24 h. The other end of the tube, approximately 19 cm away, was 80 °C cooler. The furnace was cooled to 600 °C over 14 days. Finally, the quartz tube was cooled to room temperature in 24 h. This process yielded gray-colored Ta₂S₅ wires on the cool side of the tube (see Fig. 1).



Attempts to form Ta_2S_5 by heating Ta_2O_5 powder in nitrogen gas laden with CS_2 led only to bulk TaS_2 powder, and attempts to form Ta_2S_5 wires from Ta_2O_5 powder, sulfur, and TeCl_4 under similar conditions failed. Apparently, Sr or Ba are required to drive the reaction toward Ta_2S_5 for reasons that are unclear.

The gray Ta_2S_5 wires are a few centimeters long and down to a few microns in diameter [12]. Remarkably, they possess a tensile strength comparable to steel at 1000 MPa (see Fig. 2). The electrical resistivity at 295 K was measured on a pelletized sample to be $1800 \mu\Omega \text{ cm}$. The wires are semiconducting with an approximate band gap $E_g = 110 \text{ meV}$ (see Fig. 3d). Energy-dispersive x-ray spectroscopy (EDS) reveals the ratio of tantalum to sulfur at 2:5 ($\pm 1\%$). Electron back-scattering diffraction (EBSD) patterns [12] reveal that the grown Ta_2S_5 wires are single crystalline with the same crystallographic orientation along lengths of more than a few microns. Ta_2S_5 's powder diffraction pattern can be indexed to a monoclinic primitive cell with space group P2/m and lattice parameters $a = 9.91(7) \text{ \AA}$, $b = 3.82(5) \text{ \AA}$, and $c = 20.92(2) \text{ \AA}$. The specific heat C/T at constant pressure (Fig. 3g) yielded the electron and phonon contributions to C as $\gamma = 0.0073(2) \text{ mJ/mol K}^2$ and $\beta = 0.0018(9) \text{ mJ/mol K}^4$. The Debye temperature, $\Theta_D = 97.0(5) \text{ K}$, is comparable to those of BaTa_2S_5 ($\Theta_D = 94 \text{ K}$) and SrTa_2S_5 ($\Theta_D = 89.4 \text{ K}$) [10,11].

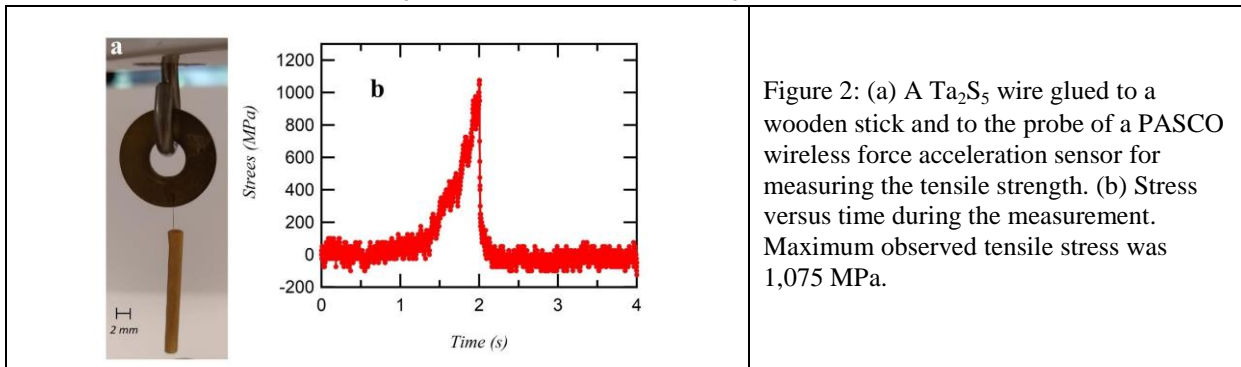


Figure 2: (a) A Ta_2S_5 wire glued to a wooden stick and to the probe of a PASCO wireless force acceleration sensor for measuring the tensile strength. (b) Stress versus time during the measurement. Maximum observed tensile stress was 1,075 MPa.

Ta_2O_5 wires can easily be formed from Ta_2S_5 wires within 30 min by exposing them to air at 900°C . The resulting wires are white in color; x-ray diffraction reveals that they possess the orthorhombic $\beta\text{-Ta}_2\text{O}_5$ structure. Thus, the Ta_2S_5 and Ta_2O_5 wires differ in color and crystal structure but retain the wire morphology (Fig. 1). EDS data for the Ta_2O_5 wires reveals that all sulfur is removed, within detection limits (Fig. 3a). After the synthesis of Ta_2S_5 and Ta_2O_5 wires, one might ask if the reaction is reversible. Exploring the idea further, the Ta_2O_5 wires were sulfurized in nitrogen gas laden with CS_2 for 30 min. This led to $\text{Ta}_{2-x}\text{S}_x$ wires that are black in color (Fig. 1). This process can be reversed by calcinating $\text{Ta}_{2-x}\text{S}_x$ in air for 30 min to recreate Ta_2O_5 wires. EDS data on $\text{Ta}_{2-x}\text{S}_x$ (Fig. 3a) reveals the sulfur content, $x \sim 3.6 (\pm 0.2)$; approximately 75% of oxygen is replaced with sulfur. X-ray diffraction (Fig 3c) reveals $\text{Ta}_{2-x}\text{S}_x$ wires to be crystalline, but further measurements are required to determine if they are single crystalline. $\text{Ta}_{2-x}\text{S}_x$ was indexed to the same orthorhombic structure and lattice parameters as Ta_2O_5 , within uncertainties (Figs. 1 and 3c). The formation of $\text{Ta}_{2-x}\text{S}_x$ wires from Ta_2O_5 wires is quite surprising since TaS_2 is the expected product after the reaction of Ta_2O_5 powder with CS_2 or H_2S [13]. Our results reveal that Ta_2O_5 in wire form seems to accept substitutions of sulfur for oxygen without undergoing a structural change to the 3R- TaS_2 rhombohedral structure, as one might expect. The physical properties of $\text{Ta}_{2-x}\text{S}_x$ are equally

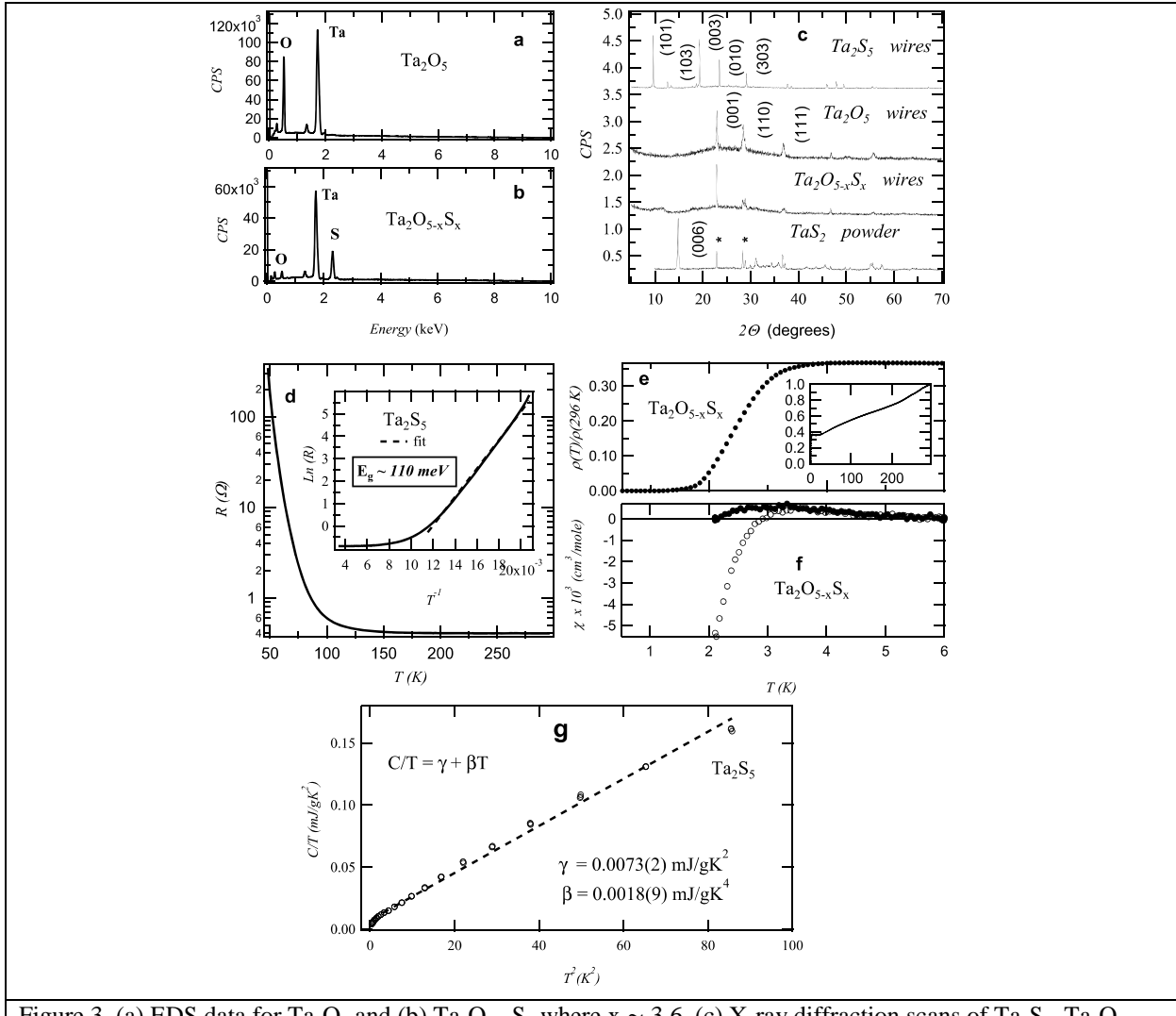


Figure 3. (a) EDS data for Ta_2O_5 and (b) $\text{Ta}_2\text{O}_{5-x}\text{S}_x$ where $x \sim 3.6$. (c) X-ray diffraction scans of Ta_2S_5 , Ta_2O_5 , $\text{Ta}_2\text{O}_{5-x}\text{S}_x$, and TaS_2 (Cu K α radiation); Ta_2O_5 and $\text{Ta}_2\text{O}_{5-x}\text{S}_x$ were indexed to orthorhombic β - Ta_2O_5 . X-ray pattern for TaS_2 indexed to rhombohedral 3R- TaS_2 , asterisks depict unreacted Ta_2O_5 . (d) Electrical resistance of pelletized Ta_2S_5 . The energy gap for $48 \text{ K} \leq T \leq 87 \text{ K}$ is $E_g = 110$ meV. (e) Electrical resistance of pelletized $\text{Ta}_2\text{O}_{5-x}\text{S}_x$ within the superconducting region where $T_c \sim 3 \text{ K}$. The inset displays data at higher temperature. (f) Magnetic susceptibility χ of pelletized $\text{Ta}_2\text{O}_{5-x}\text{S}_x$. χ data (open symbols) obtained after cooling the sample in zero magnetic field to 2.1 K, followed by application of the magnetic field $H = 38$ Oe and warming during the measurement; this is the shielding curve. The solid symbols are the Meissner curve, obtained by cooling from 6 K in $H = 38$ Oe. (g) Specific heat C/T vs T^2 of pelletized Ta_2S_5 below 10 K.

surprising. Its electrical resistance is metallic (inset Fig. 3e), dropping to approximately 40% of the room-temperature value before the onset of superconductivity at $T_c \sim 3 \text{ K}$ (Fig. 3e). Magnetic susceptibility measurements revealed Meissner and shielding volume fractions at $T = 2.1 \text{ K}$, the low-temperature limit of our equipment, of 0.58% and 5.2%, respectively (Fig. 3f). Note that it is not uncommon to observe small Meissner fractions in sulfides despite bulk superconductivity [11,12]. Thus, a narrow band gap semiconductor (Ta_2S_5) is oxidized to form an insulator (Ta_2O_5) that is then sulfurized to form a metallic superconductor ($\text{Ta}_2\text{O}_{5-x}\text{S}_x$), all while maintaining the wire morphology.

Superconductivity in oxysulfides is exceedingly rare [14]. Since the first reported bulk oxysulfide superconductor [15], $\text{Bi}_4\text{O}_4\text{S}_3$ [$T_c = 4.4$ K], only bismuth-based, BiS-layered oxysulfide compounds have been reported. These include [16,17] LaOBiS_2 [$T_c = 3.6$ K] and $\text{La}_{1.7}\text{Eu}_{0.3}\text{O}_2\text{Bi}_3\text{Ag}_{0.6}\text{Sn}_{0.4}\text{S}_6$ [$T_c = 3.64$ K], which have between four and seven elements. In comparison, $\text{Bi}_4\text{O}_4\text{S}_3$ and $\text{Ta}_2\text{O}_{5-x}\text{S}_x$ are “simple oxysulfides,” composed of only a few elements. Thus, $\text{Ta}_2\text{O}_{5-x}\text{S}_x$ is one of the few known oxysulfide superconductors and the first simple transition-metal oxysulfide superconductor composed only of a transition metal, oxygen, and sulfur. Further work is needed to determine the nature of the superconductivity of $\text{Ta}_2\text{O}_{5-x}\text{S}_x$.

Future Plans

Our search for new advanced materials has led to investigations of transition metal sulfides. Most of this work has focused on metals, which in turn has led to the discovery of superconductivity in four compounds (BaNbS_3 , BaNb_2S_5 , $\text{Ba}_2\text{Nb}_3\text{S}_8\text{I}$, and $\text{Ta}_2\text{O}_{5-x}\text{S}_x$). While all of these exhibit low T_c values (< 3 K), they possess interesting low-dimensional crystal structures and we have learned a great deal about the synthesis of sulfides. We plan to expand this work to develop methods for the growth of single-crystalline transition-metal sulfides and to search for interesting thermoelectric and magnetic transition-metal sulfides.

References

- [1] W. J. de Haas and W. H. Capel, *Physica* 1 (1934) 929.
- [2] W. F. Gale and T. C. Totemeier, *Smithells Metals Reference Book*, (Elsevier, Holland, 2003).
- [3] F. Cardon, *Photovoltaic and Photoelectrochemical Solar Energy Conversion*, (Springer Science & Business Media, 2012).
- [4] T. J. Bright, J. I. Watjen, Z. M. Zhang, C. Muratore, A. A. Voevodin, D. I. Koukis, D. B. Tanner, D. J. Arenas, *J. Appl. Phys.* 114 (2013) 083515.
- [5] I. Porqueras, J. Marti, E. Bertran, *Thin Solid Films* 343 (1999) 449.
- [6] A. S. Markosyan, R. Route, M. M. Fejer, D. Patel, C. Menoni, *J. Appl. Phys.* 113 (2013) 133104.
- [7] S. Shibata, *Thin Solid Films* 277 (1996) 1.
- [8] S. Cheng, L. Sang, M. Liao, J. Liu, M. Imura, H. Li, Y. Koide, *Appl. Phys. Lett.* 101 (2012) 232907.
- [9] X. J. Lu, S. J. Ding, T. Q. Lin, X. L. Mou, X. Z. L. Hong, F. Q. Huang, *Dalton Trans.* 41 (2012) 622.
- [10] A. K. Drenner, S. M. Benjamin, M. G. Smith, J. J. Neumeier, *Physica C* 556 (2019) 19.
- [11] A. K. Drenner, S. M. Benjamin, M. G. Smith, J. J. Neumeier, *Physica C* 566 (2019) 1353522.
- [12] S. M. Benjamin, N. F. Rieders, M. G. Smith, J. J. Neumeier, *ACS Omega* (2021) <https://pubs.acs.org/doi/pdf/10.1021/acsomega.0c05656>.
- [13] F. F. Schmidt, *Tantalum and Tantalum Alloys: Report; Defense Metals Info. Center* (1960).
- [14] C. Larquet and S. Carenco, *Front. Chem.* 8 (2020) 179.
- [15] S. K. Singh, A. Kumar, B. Gahtori, Shruti, G. Sharma, S. Patnaik, V. P. S. Awana, *J. Am. Chem. Soc.* 134 (2012) 16504.
- [16] R. Jha, and Y. Mizuguchi, *Condens. Matter* 5 (2020) 27.
- [17] E. Uesugi, S. Nishiyama, H. Goto, H. Ota, Y. Kubozono, *Appl. Phys. Lett.* 109 (2016) 252601.

Publications (covering the last two years)

- S. M. Benjamin, M. G. Smith, J. J. Neumeier, Synthesis and superconductivity of MgTa₂S₅, submitted to Physical Review Materials.
- C. A. M. dos Santos, F. S. Oliveira, M. S. da Luz, J. J. Neumeier, On the Order Parameter of the Continuous Phase Transition in the Classical and Quantum Mechanical limits, submitted to the Brazilian Journal of Physics.
- F. S. Oliveira, C. A. M. dos Santos, M. S. da Luz, J. J. Neumeier, Anomalous magnetoresistivity in under-doped SrTiO_{3-δ}, submitted to Physics Status Solidi B.
- M. G. Smith, Qisheng Lin, S. M. Benjamin, M. T. Baker, J. J. Neumeier, Crystal structure and physical properties of Ba₂Nb₃S₈I: A new misfit-layered transition-metal dichalcogenide superconductor, submitted to J. Phys. Chem. Solids.
- S. M. Benjamin, N. F. Rieders, M. G. Smith, J. J. Neumeier, From Ta₂S₅ wires to Ta₂O₅ and Ta₂O_{5-x}S_x, ACS Omega (2021) <https://pubs.acs.org/doi/pdf/10.1021/acsomega.0c05656>.
- A. B. Christian, J. J. Neumeier, R. L. Cone, Economical Laue x-ray diffraction using photographic film and orientation of single crystals, Rev. Sci. Instrum. 91 (2019) 051401.
- A. K. Drenner, S. M. Benjamin, M. G. Smith, J. J. Neumeier, *Physical properties and superconductivity of SrTa₂S₅*, Physica C 556 (2019) 19.
- A. K. Drenner, S. M. Benjamin, M. G. Smith, J. J. Neumeier, *Physical properties and superconductivity of BaTa₂S₅*, Physica C 566 (2019) 1353522.

Properties, Electrochemical Activity, and Stability of Solid Oxide Cell Materials Under Extreme Conditions

Scott A Barnett, Northwestern University

Program Scope

This project focuses on reversible solid oxide cells (ReSOCs), a technology that can store electricity with high efficiency, reasonable cost, and high storage capacity, and can also be used for renewable (CO₂-neutral) fuel production. A key question is how to make ReSOC electrode materials that provide the requisite performance and efficiency, while at the same time keeping degradation rates very low. Although this is a practical engineering consideration, it motivates fundamental scientific questions about the properties and durability of electrode materials under extreme conditions. Thus, this project aims to develop a comprehensive understanding and mechanistic modeling of ReSOC electrode characteristics and degradation mechanisms. Various effects that contribute to degradation during cell operation will be studied, including particle coarsening, surface segregation, and the extremely high effective oxygen pressures that are present during electrolysis operation. The resulting in-depth understanding of electrode performance and degradation will provide a basis for developing improved materials, and for choosing cell operating conditions that yield desired efficiency and long-term durability.

Recent Progress

Novel Oxygen Electrode

We previously reported on the desirable properties of Sr(Ti_{1-x}Fe_x)O_{3-δ} (STF) with $x = 0.7$, and also with Co doping, for oxygen electrode applications in solid oxide cells (SOCs). During the present reporting period, we have studied a range of compositions from $x = 0.5$ to 0.9 . The polarization resistance of porous electrodes shows a minimum at $x = 0.7$, resulting from the interaction of two effects - the oxygen solid state diffusion coefficient increases with increasing x , but the electrode surface area and surface oxygen exchange rate decrease due to increased sinterability and Sr surface segregation for the Fe-rich compositions.

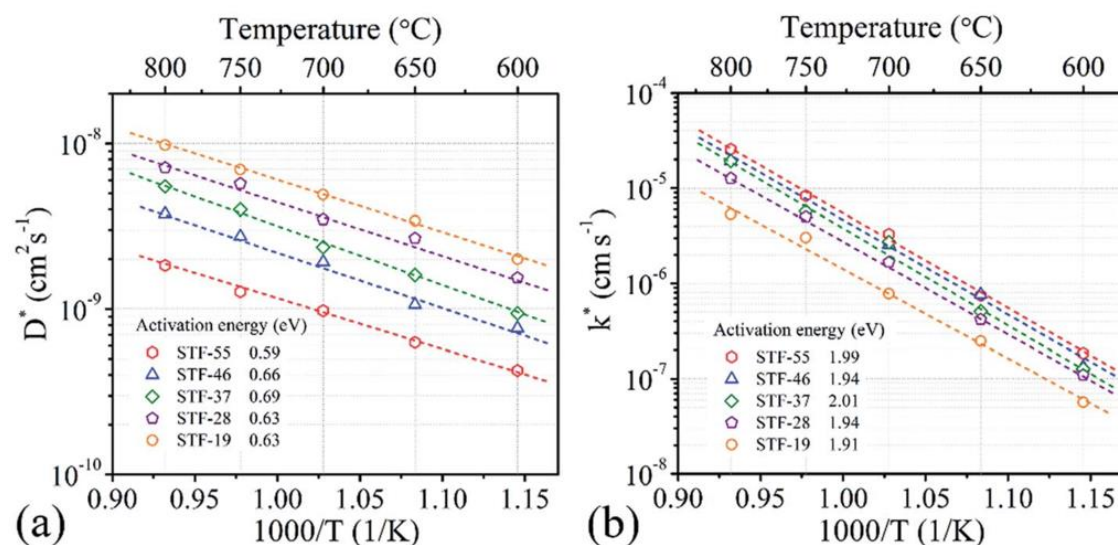


Figure 1. (a) Bulk oxygen diffusion coefficient D^* and (b) oxygen surface exchange rate coefficient k^* versus temperature for STF materials. Note that STF-37 corresponds to the 30% Ti – 70% Fe composition, i.e., $x = 0.7$.

Detailed analysis of impedance spectroscopy data using the Adler–Lane–Steele model analysis was used to determine the oxygen solid state diffusion coefficients D^* and the oxygen surface exchange coefficients k^* for the different compositions. The resulting D^* and k^* values are shown in Fig. 1. D^* increases continuously with increasing Fe content, with the biggest increase between $x = 0.5$ and 0.6 . k^* decreases slightly with increasing x from 0.5 – 0.7 . The results in Figure 1 are the first indication of how D^* varies with Fe content in STF, since prior thin-film studies did not yield D^* values. The increase in D^* with increasing Fe content can be explained by the increase in oxygen vacancy concentration implied by the increased oxygen non-stoichiometry. The decrease of k^* with increasing x may be related to increasing Sr surface segregation. In addition, the basic properties of the different STF compositions, including electronic conductivity, thermal expansion coefficient, and oxygen non-stoichiometry, have been determined.

Fuel Electrodes with Self-Assembled Nanoparticles

In previous DOE-supported work, we reported on a new fuel electrode composition, $\text{Sr}(\text{Ti},\text{Fe},\text{Ni})\text{O}_3$, where the spontaneous formation (exsolution) of Ni–Fe alloy nanoparticles results in remarkably good electrochemical performance by promoting H_2 dissociative adsorption. In the most recent work, $\text{Sr}(\text{TiFe})\text{O}_{3-\delta}$ (STF) and the associated exsolution electrodes $\text{Sr}_{0.95}(\text{Ti}_{0.3}\text{Fe}_{0.63}\text{Ru}_{0.07})\text{O}_{3-\delta}$ (STFR) and $\text{Sr}_{0.95}(\text{Ti}_{0.3}\text{Fe}_{0.63}\text{Ni}_{0.07})\text{O}_{3-\delta}$ (STFN) were characterized and compared with the Ni–YSZ fuel electrodes that are widely used in solid oxide cells (SOCs). They provide improved tolerance to redox cycling and fuel impurities, and may allow direct operation with hydrocarbon fuels. However, such perovskite-oxide-based electrodes present processing challenges for co-sintering with thin electrolytes to make fuel electrode supported SOCs. Thus, they have been mostly limited to electrolyte-supported SOCs. Here, we report the first example of the application of perovskite oxide fuel electrodes in oxygen electrode supported SOCs with thin YSZ electrolytes, and demonstrate their excellent performance. The cells have $\text{La}_{0.8}\text{Sr}_{0.2}\text{MnO}_{3-\delta}$ – $\text{Zr}_{0.92}\text{Y}_{0.16}\text{O}_{2-\delta}$ (LSM–YSZ) electrode-supports that are enhanced via infiltration of $\text{SrTi}_{0.3}\text{Fe}_{0.6}\text{Co}_{0.1}\text{O}_{3-\delta}$, with Ni–YSZ, STF, STFN, or STFR fuel electrodes. Figure 2 compares the electrolysis and fuel cell results. Cell performance improves with changes in the fuel electrode in the order Ni–YSZ < STF < STFN < STFR, with the STFC electrode cells yielding 60 – 72% higher current density than the Ni–YSZ-based cells. The high performance of the STFN and STFR electrodes is due to exsolution of catalytic metal nanoparticles. Fuel cell power density as high as 1.12 W cm^{-2} is obtained at 0.7 V with the STFR electrode, with electrolysis current density as high as -1.72 A cm^{-2} at 1.3 V .

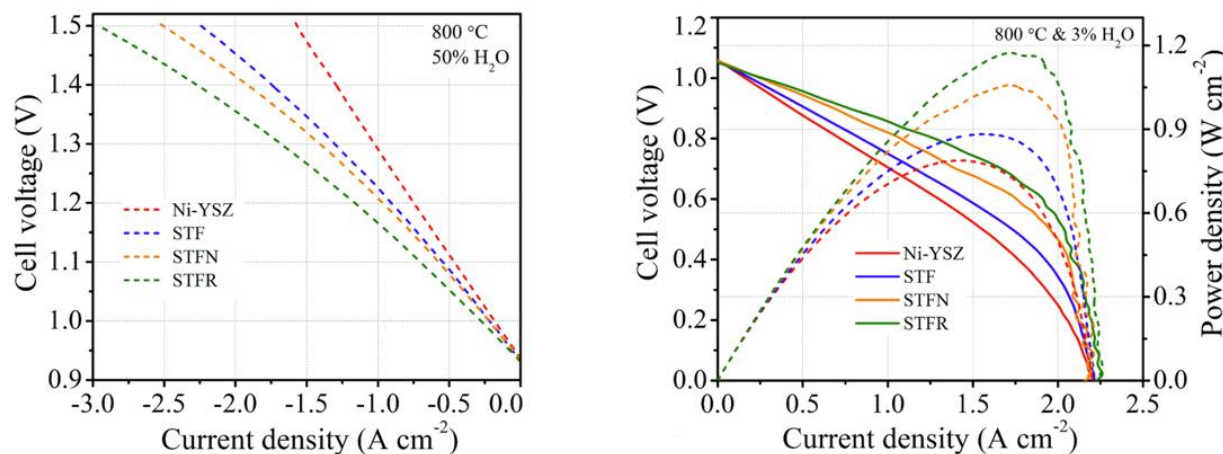


Figure 2. Electrolysis (left) and fuel cell (right) characteristic of cells with different fuel electrodes at $800 \text{ }^\circ\text{C}$.

The polarization resistance R_P value of a porous mixed ionic/electronic conducting electrode can be related to the materials' transport properties and the electrode microstructure using a transmission electrode model expression:¹

$$R_P = \sqrt{\frac{R_S}{\sigma_{ion}a}} \coth\left(L \sqrt{\frac{a}{\sigma_{ion}R_S}}\right) \quad (1)$$

where R_S is the surface oxygen exchange resistance, L is the electrode thickness (12-15 μm), a is the anode surface area ($4.6 \mu\text{m}^{-1}$), and the STF effective ionic conductivity σ_{ion} is given by the ionic conductivity times the anode solid fraction, 0.6-0.62, and divided by the solid-phase tortuosity, (1.24-1.26). Since an ionic conductivity has been measured for STF at 650 °C,² 0.025 S/cm, we carry out the calculation at this temperature (note that after exsolution the oxide matrix composition of STFN and STFR becomes approximately $\text{Sr}(\text{Ti}_{0.3}\text{Fe}_{0.7})\text{O}_3$,³ so the same value can be used for STF, STFN, and STFR). Although the electrodes are too thin to allow determination of oxygen diffusivities, values of R_S for the oxide electrodes were obtained to good approximation directly from electrochemical impedance spectroscopy measurements and fitting with the transmission line model. Figure 3 plots the resulting R_S values versus temperature. The only prior measurement of the surface oxygen exchange resistance of an oxide fuel electrode was for thin-film STF with the same composition, yielding R_S values that range from $25 \Omega \text{ cm}^2$ at 650 °C to $6 \Omega \text{ cm}^2$ at 800 °C. These values are somewhat higher than the values in Fig 3, probably due to the lower H_2 and H_2O partial pressures in the prior work. Fig. 3 confirms that the exsolution electrodes have lower intrinsic oxygen surface exchange resistances than STF, especially at the higher steam content.² This is the first such measurement for electrodes with exsolved nanoparticles.

Cell Degradation Under Extreme Conditions

The STFC-infiltrated LSM-YSZ electrodes noted above also have implications regarding cell degradation. It is well known that conventional LSM-YSZ electrodes can fracture during solid oxide electrolysis due to the high oxygen pressure that is produced by the applied cell voltage. In particular, previous work has shown that the pressure builds up exponentially with increasing electrode overpotential, and is higher for electrodes with higher polarization resistance R_P . The present results compare cells with STFC-infiltrated LSM-YSZ electrodes and conventional LSM-YSZ electrodes, the former having a substantially lower R_P . Figure 4 shows the results of life tests carried out at 700 °C and 0.5 A cm^{-2} DC current, conditions for which LSM-YSZ electrodes are known to delaminate. For the LSM-YSZ electrode cell, both the ohmic resistance R_{ohm} and R_P are observed to increase substantially during the test; the SEM image shows clear evidence of electrode/electrolyte delamination. For the STFC infiltrated electrode, on the other hand, there was little cell resistance increase, and the electrode/electrolyte interface appears to be free of any delamination or fracture. These results help validate the electrode pressurization theory.

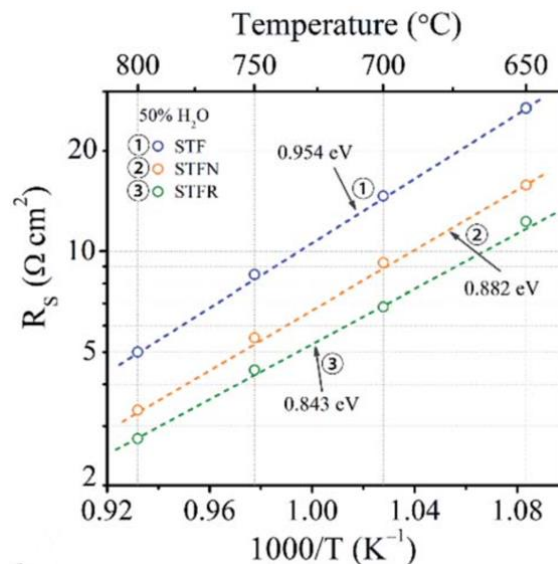


Figure 3. Surface oxygen exchange resistance R_S versus inverse temperature for the oxide fuel electrodes.

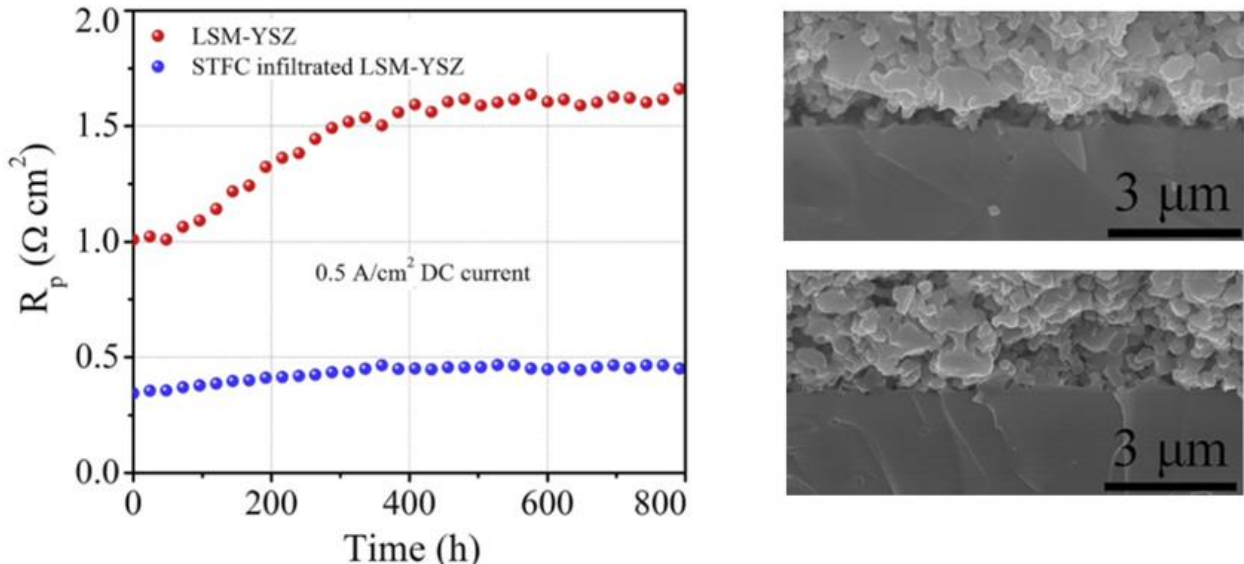


Figure 4. (left) Evolution of cell polarization resistance (R_p) versus at 750 °C with 0.5 A cm^2 DC current for cells with LSM-YSZ and STFC-infiltrated LSM-YSZ electrodes. Fracture cross sectional SEM images of the electrode/electrolyte interface after the life tests of the cell with the un-infiltrated LSM-YSZ electrode (top right) and the STFC-infiltrated LSM-YSZ electrode (bottom right).

The overpotential values during the life tests in Fig. 4 were estimated by assuming that the current-voltage follows a standard Butler-Volmer form and that the variation is similar for electrolysis and fuel cell modes. Given the initial R_p value of 1.02 $\Omega \text{ cm}^2$ for the LSM-YSZ electrode, the estimated overpotential is ~ 0.22 V, comparable to the critical overpotential of 0.23 V predicted to produce an oxygen pressure that can fracture the LSM/YSZ interface. Given that the initial R_p value of 0.3 $\Omega \text{ cm}^2$ for the STFC-infiltrated LSM-YSZ yields an overpotential of ~ 0.115 V, it is reasonable that fracture is not observed in this case.

Future Plans

The dynamics of exsolution processes from materials based on STFN will be further explored. Phase development during reduction and subsequent oxidation will be explored utilizing real time x-ray diffraction. The possibility of regenerating the electrodes by first re-dissolving the nanoparticles into the oxide under oxidizing conditions, and then re-reducing, will be studied. The role of perovskite stoichiometry changes and defect formation in determining electrochemical characteristics will be explored. The use of these materials for solid oxide fuel cell operation in bio-fuels, important for CO₂-neutral transportation application, will also be studied.

References

- 1 Fleig, J. R. *Annu. Rev. Mater. Res.* **33**, 361–382 (2003).
- 2 Nenning, A., Volgger, L., Miller, E., Mogni, L. V., Barnett, S. & Fleig, J. The Electrochemical Properties of Sr(Ti,Fe)O_{3-δ}for Anodes in Solid Oxide Fuel Cells. *J Electrochem Soc* **164**, F364-F371, doi:10.1149/2.1271704jes (2017).
- 3 Zhu, T., Troiani, H., Mogni, L. V., Santaya, M., Han, M. & Barnett, S. A. Exsolution and electrochemistry in perovskite solid oxide fuel cell anodes: Role of stoichiometry in Sr(Ti,Fe,Ni)O₃. *J Power Sources* **439**, doi:10.1016/j.jpowsour.2019.227077 (2019).

Publications

1. S. Zhang, H. Wang, T. Yang, M.Y. Lu, C. Li, C. Li and S. Barnett, "Advanced Oxygen-Electrode-Supported Solid Oxide Electrochemical Cells with Sr(Ti,Fe)O₃-δ-based Fuel Electrodes for Electricity Generation and Hydrogen Production," *Journal of Materials Chemistry A* **8** (2020) 25867–25879 Main DoE support.
2. T. Zhu, H. Troiani, L.V. Mogni, M. Santaya, M. Han and S.A. Barnett, "Exsolution and electrochemistry in perovskite solid oxide fuel cell anodes: Role of stoichiometry in Sr(Ti,Fe,Ni)O₃," *Journal of Power Sources* **439** (2019) Full DoE support.
3. S.L. Zhang, H.Q. Wang, M.Y. Lu, C.X. Li, C.J. Li and S.A. Barnett, "Electrochemical performance and stability of SrTi0.3Fe0.6Co0.1O₃-delta infiltrated La0.8Sr0.2MnO₃-Zr0.92Y0.16O₂-delta oxygen electrodes for intermediate-temperature solid oxide electrochemical cells," *Journal of Power Sources* **426** (2019) 233-241 Main support by DoE
4. S.-L. Zhang, H. Wang, C.-X. Li, C.-J. Li and S.A. Barnett, "Effect of SrTi0.3Fe0.6Co0.1O₃ Infiltration on the Performance of LSM-YSZ Cathode Supported Solid Oxide Fuel Cells with Sr(Ti,Fe)O₃ Anodes," *ECS Transactions* **91** (2019) Main support by DoE
5. S.-L. Zhang, D. Cox, H. Yang, B.-K. Park, C.-X. Li, C.-J. Li and S.A. Barnett, "High stability SrTi_{1-x}FexO₃-δ electrodes for oxygen reduction and oxygen evolution reactions," *Journal of Materials Chemistry A* **7** (2019) 21447-21458 Main support by DoE
6. T.A. Schmauss, J.G. Railsback, M.Y. Lu, K.Y. Zhao and S.A. Barnett, "ZrO₂ atomic layer deposition into Sr0.5Sm0.5CoO₃-δ-Ce0.9Gd0.1O₂-δ solid oxide fuel cell cathodes: mechanisms of stability enhancement," *Journal of Materials Chemistry A* 10.1039/c9ta09214e (2019) Main support by DoE
7. S.L Zhang, H. Wang, T. Yang, M. Lu, and S.A Barnett, "Characteristics of Oxygen Electrode Supported Reversible Solid Oxide Cells," *submitted to Journal of Power Sources*, Partial DOE support.
8. T.A. Schmauss and S.A. Barnett, "On the Viability of CO₂-Neutral Vehicles Utilizing Carbon-Based Fuels," *submitted to Joule*, Partial support by DoE

Collective Energy Transport of Excitons in Two-dimensional Materials

Principal Investigator: Steve Cronin, University of Southern California

Collaborator: Li Shi, University of Texas at Austin

PROGRAM SCOPE

The goal of this project is to explore collective behavior that exists in samples with large numbers of interacting particles. The behavior of these systems goes beyond the independent particle picture that is commonly used to describe a vast majority of solid-state phenomena, including the transport of quantized carriers of charge and heat in solids. While collective behavior gives rise to superconductivity at low temperatures, signatures of collective behaviors in both charge and heat transport appear at rather high temperatures in several recent studies of low-dimensional materials. One specific example of this collective behavior is the formation of excitons (i.e., bound electron-hole pairs), which is pronounced in two-dimensional (2D) materials such as transition metal dichalcogenides (TMDCs), with exciton binding energies exceeding the thermal energy at room temperature. In this project, we pursue, optical, electronic, thermal, and thermoelectric measurements to obtain unique insights into the unusual collective energy transport behaviors of excitons in 2D materials and heterostructures.

RECENT PROGRESS

Enhanced Thermoelectric Performance of Highly Correlated Electrons in Charge Density Waves

Charge density waves results from the collective behavior in materials due to strong electron-electron interactions, which create a condensed ground state of electrons and a gap in the Fermi surface at low temperatures. We have explored the effect of charge density wave (CDW) transitions on the in-plane thermoelectric transport properties of $(\text{PbSe})_1(\text{VSe}_2)_1$ heterostructures, illustrated in Figure 1a. In this materials system, we observe an abrupt 86% increase in the Seebeck coefficient, 245% increase in the power factor, and a slight decrease in resistivity over the CDW transition. This behavior is not observed in $(\text{PbSe})_1(\text{VSe}_2)_2$ (i.e., 2 layers of VSe₂ and 1 layer of PbSe per unit cell) and is rather unusual compared to the general trend observed in other materials. The abrupt transition causes a deviation from the Mott relationship (Eq. 1) through correlated electron states. Raman spectra of the $(\text{PbSe})_1(\text{VSe}_2)_1$ material show the emergence of additional peaks below the CDW transition temperature associated with VSe₂ material. Temperature dependent in-plane X-ray diffraction (XRD) spectra show a change in the in-plane thermal expansion of VSe₂ in $(\text{PbSe})_1(\text{VSe}_2)_1$ due to lattice distortion, consistent with the CDW transition. The increase in the power factor and decrease in the resistivity due to CDW suggest a potential mechanism for enhancing the thermoelectric performance at the low temperature region.

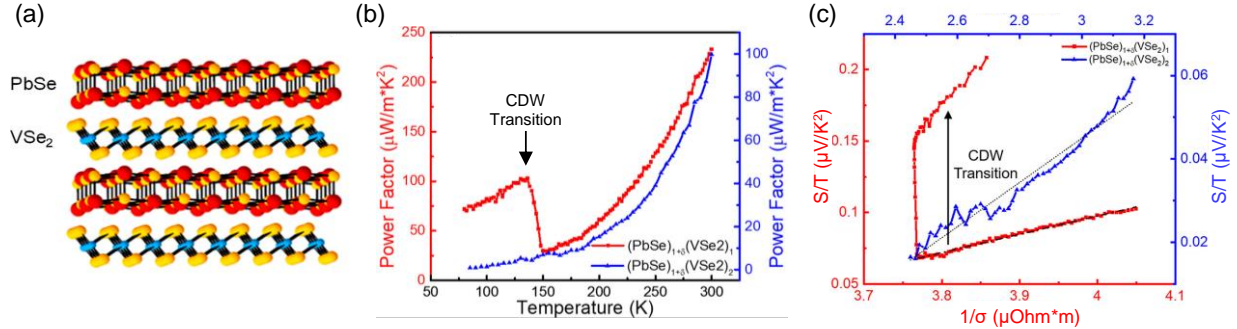


Figure 1. (a) Schematic diagram illustrating the $(\text{PbSe})_1(\text{VSe}_2)_n$ heterostructure material. (b) Power factor of $(\text{PbSe})_1(\text{VSe}_2)_n$ films plotted as a function of temperature. (c) S/T vs. $1/\sigma$ of $(\text{PbSe})_1(\text{VSe}_2)_{1,2}$ heterostructure materials. The black lines represent linear fits of the $(\text{PbSe})_1(\text{VSe}_2)_1$ and $(\text{PbSe})_1(\text{VSe}_2)_2$ films, respectively.

Figure 1b shows a comparison of the in-plane power factor (i.e., $S^2 \sigma$) plotted as function of temperature over the range 77–300 K for both the $(\text{PbSe})_1(\text{VSe}_2)_1$ and $(\text{PbSe})_1(\text{VSe}_2)_2$ heterostructures. For the $(\text{PbSe})_1(\text{VSe}_2)_1$ material, the power factor shows an abrupt increase from $30 \mu\text{W}/\text{m}\cdot\text{K}^2$ to $103 \mu\text{W}/\text{m}\cdot\text{K}^2$ above and below the CDW transition, respectively. The power factor of $(\text{PbSe})_1(\text{VSe}_2)_2$ is $4.4 \mu\text{W}/\text{m}\cdot\text{K}^2$. The ratio of power factors between these two materials increases from 7 above to more than 23 below the CDW transition. At 80 K, the ratio of the power factors has increased to 90 (the $(\text{PbSe})_1(\text{VSe}_2)_2$ film has a power factor $0.8 \mu\text{W}/\text{m}\cdot\text{K}^2$, while $(\text{PbSe})_1(\text{VSe}_2)_1$ has a power factor of $72 \mu\text{W}/\text{m}\cdot\text{K}^2$). Figure 1c shows the Seebeck coefficient over temperature (i.e., S/T) plotted as a function of one over the conductivity (i.e., $1/\sigma$) for the $(\text{PbSe})_1(\text{VSe}_2)_{1,2}$ heterostructures. Under the assumption of weak electron-electron interaction, the Mott relation (Eq. 1) is satisfied, where S is the Seebeck coefficient, k_B is the Boltzmann constant, T is the absolute temperature, e is electron charge, and σ is electrical conductivity. Eq. 1 can be rewritten as Eq. 2, which can be directly related to our experimental data plotted in Figure 1c, which contains a plot of S/T vs. $1/\sigma$ for both the 1:1 and 1:2 heterostructure materials. In the $(\text{PbSe})_1(\text{VSe}_2)_2$, the S/T vs. $1/\sigma$ relationship is linear over the entire measured temperature range (80–300 K) as indicated by the black dotted line, indicating that the density of states and mobility are roughly constant over this range. That is, $d\sigma/dE$ can be written as $(d\sigma/dn)(dn/dE) = e\mu(dn/dE)$, where e is electron charge, μ is the mobility, and dn/dE is the density of states. For $(\text{PbSe})_1(\text{VSe}_2)_1$, however, the Mott relation is only satisfied above the CDW transition of ~140 K. Below 140 K, there is a distinct change in behavior as the structure undergoes a structural distortion. The Mott relation is no longer valid below the CDW transition temperature because the conduction electron movements are highly correlated and no longer independent. The mechanism underlying these results may be used to provide a new approach for enhancing the thermoelectric performances of materials at low temperatures, where good thermoelectric materials are lacking.

$$S = -\frac{\pi^2 k_B^2 T}{3} \frac{d\sigma}{e \sigma dE} \Big|_{E_F} \quad (1)$$

$$\frac{S}{T} = \left(-\frac{\pi^2 k_B^2}{3} \frac{d\sigma}{e dE} \Big|_{E_F} \right) \frac{1}{\sigma} \quad (2)$$

Modulation of Exciton Luminescence in MoS₂ Nanoislands Formed via Plasma Treatment and Laser Exposure

As mentioned above, excitons in TMDC materials represent collective behavior that is particularly pronounced by the strong charge carrier interactions. In this work, we demonstrate a method for controlling the nature of exciton photoluminescence emission in molybdenum

diselenide (MoS_2) material using a plasma-based treatment of the material followed by laser exposure. Here, the plasma and laser treatments result in an indirect-to-direct band gap transition, which fundamentally changes the nature of the exciton that is primarily responsible for light emission in this system. The oxygen plasma creates a slight decoupling of the layers and converts some of the MoS_2 to MoO_3 . Subsequent laser irradiation further oxidizes the MoS_2 to MoO_3 , as confirmed via X-ray photoelectron spectroscopy (XPS), and results in localized regions of brightly luminescent MoS_2 monolayer triangular islands as seen in high-resolution transmission electron microscopy images. The photoluminescence lifetimes are found to decrease from 494 to 190ps after plasma and laser treatment, reflecting the smaller size of the MoS_2 grains/regions. Atomic force microscopic imaging shows a 2 nm increase in thickness of the laser-irradiated regions, which provides further evidence of the MoS_2 being converted to MoO_3 .

Figure 2a shows a transmission electron microscopy (TEM) image of a suspended MoS_2 bilayer, which is treated by oxygen plasma only. In this TEM image, we are able to clearly see the atomic lattice structure, which is almost the same as an untreated bilayer MoS_2 flake. Figure 2b shows a TEM image of a suspended MoS_2 bilayer after plasma and laser treatment, showing the formation of triangular and trapezoidal nano-islands, which is indicated by the different contrast (i.e., the difference of energy loss of the electron beam) in the TEM images. Here, the nano-islands of monolayer material are embedded within the bilayer MoS_2 , indicating the partial conversion of one of the MoS_2 layers to MoO_3 , consistent with the XPS data. It is also apparent from these images that the light-induced oxidation of the MoS_2 material follows the axes of the crystal, forming triangular patterns. These resulting monolayer nano-islands of MoS_2 are more than one order of magnitude more luminescent than the original bilayer material.

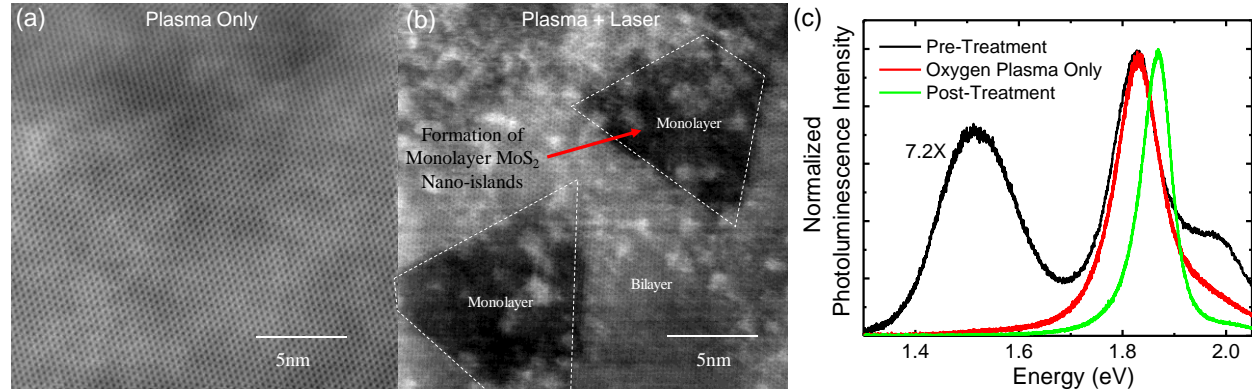


Figure 2. Transmission electron microscope (TEM) images of MoS_2 : (a) oxygen plasma treated only and (b) oxygen plasma treated and laser exposed. (c) Photoluminescence spectra for a bilayer MoS_2 flake taken before treatment, after oxygen plasma treatment only, and after oxygen plasma treatment and laser exposure.

Figure 2c shows the photoluminescence (PL) spectra of bilayer MoS_2 (indicated by the position of the indirect band gap emission) taken before and after plasma and laser exposure. Here, we see a 7.2-fold increase in the peak PL intensity after the treatment with a 22% linewidth narrowing and complete suppression of the indirect band gap transition. This Figure shows the PL spectra taken before treatment, after a 3 minute oxygen plasma exposure only, and after a 3 minute oxygen plasma and a 3 minute laser exposure. Here, the effect of the laser exposure is to increase the energy (i.e., 40 meV blueshift from 1.83 eV to 1.87 eV) of direct band gap emission while the PL intensity remains unchanged. The laser exposure also produces a narrower distribution (98.5 meV to 65.5 meV) as well as a decreased lifetime of the ground-state exciton. As a control

experiment, two few-layer MoS₂ flakes were thermally annealed at 500 °C in argon after the plasma treatment step instead of laser exposure. This showed a significant worsening of the PL emission rather than enhancement.

FUTURE PLANS

During the next reporting period, we will continue to work in collaboration with Prof. Shi to complete thermoelectric transport measurements of MoSe₂/barrier/WSe₂ heterostructures, as illustrated in Figure 3. In this the counterflow Seebeck measurement device configuration, holes flow from hot to cold in the WSe₂ layer while electrons flow from hot to cold in the MoSe₂ layer. With the two layers wired in series, this transport occurs as a bound exciton. This interlayer exciton enables us to evaluate Bosonic (i.e., excitons) thermoelectric transport as distinctly different from Fermionic (i.e., free electrons) thermoelectric transport. The device includes a top graphene gate layer and a bottom silicon gate, which enable independent tuning of the Fermi levels in both WSe₂ and MoSe₂ layers. Figure 3c shows the calculated interlayer exciton binding energy in the MoSe₂/BN/WSe₂ heterostructures as a function of BN thickness. The device shown in Figure 3a required 5 aligned transfers of 2D materials and 6 electron-beam lithography steps. Both the fabrication and measurement of these devices are significantly challenging and have faced delays due to the COVID 19 shutdown.

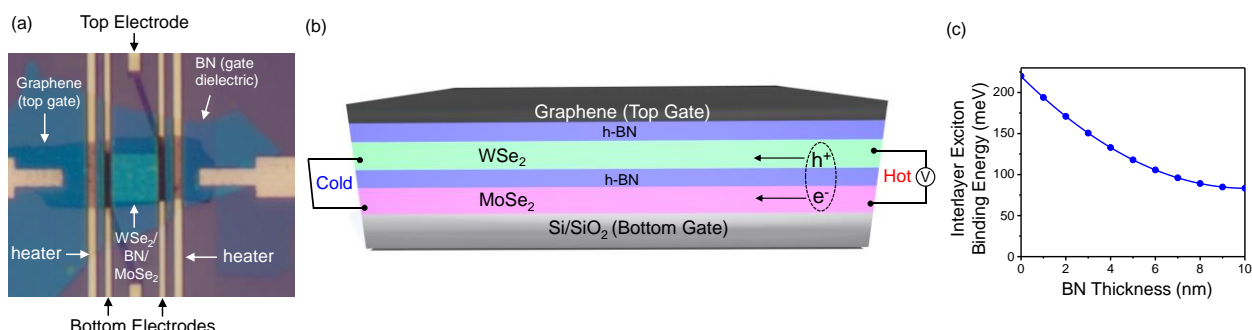


Figure 3. (a) Optical image and (b) schematic diagram of the counterflow Seebeck measurement of a MoSe₂/BN/WSe₂ heterostructure and (c) corresponding interlayer exciton binding energies plotted as a function of BN thickness.

PUBLICATIONS

- 1. Enhanced Low-Temperature Thermoelectric Performance in (PbSe)₁(VSe₂)₁ Heterostructures due to Highly Correlated Electrons in Charge Density Waves**
Yu Wang, Danielle M. Hamann, Dmitri Leo M. Cordova, Jihan Chen, Bo Wang, Lang Shen, Zhi Cai, Haotian Shi, Evguenia Karapetrova, Indu Aravind, Li Shi, David C. Johnson, and Stephen B. Cronin. *Nano Letters*, 20, 8008-8014 (2020). <https://doi.org/10.1021/acs.nanolett.0c02882>
- 2. Formation of Brightly Luminescent MoS₂ Nanoislands from Multilayer Flakes via Plasma Treatment and Laser Exposure**
Bo Wang, Sisi Yang, Yu Wang, Younghee Kim, Han Htoon, Stephen K. Doorn, Brendan J. Foran, Adam W. Bushmaker, David R. Baker, Gregory T. Forcherio, and Stephen B. Cronin. *ACS Omega*, 5, 20543-20547 (2020). <https://doi.org/10.1021/acsomega.0c02753>

3. Auger Suppression of Nanotube Incandescence in Individual Suspended CNT *pn*-junctions

Bo Wang, Sisi Yang, Yu Wang, Ragib Ahsan, Xiaowei He, Younghiee Kim, Han Htoon, Rehan Kapadia, Demis D John, Brian Thibeault, Stephen K. Doorn, and Stephen B. Cronin *ACS Appl. Mater. Interfaces*, DOI: 10.1021/acsami.9b17519 (2020).

4. Measuring Nanoscale Thermal Gradients in Suspended MoS₂ with STEM-EELS

Lang Shen, Matthew Mecklenburg, Rohan Dhall, B. C. Regan, and Stephen B. Cronin *Applied Physics Letters*, 115, 153108 (2019). <https://doi.org/10.1063/1.5094443>

5. Effects of Proton Radiation-Induced Defects on Optoelectronic Properties of MoS₂

Brendan Foran, Colin Mann, Mark Peterson, Adam Bushmaker, Bo Wang, Jihan Chen, Sisi Yang, and Stephen B. Cronin. *IEEE Transactions on Nuclear Science*, 66, 413-419 (2019). <https://doi.org/10.1109/TNS.2018.2886180>

Organic Multiferroics

Dr. Shenqiang Ren (University at Buffalo, The State University of New York), PI

Program Scope

The research objective of this project is to explore the unusual multiferroic properties of molecular electronic crystal materials, comprised of two chemically and electronically distinct donor and acceptor molecules, which combine two or more ferroic properties in the same crystal lattice in a manner that is difficult or impossible to achieve in continuous inorganic crystalline solids.

Recent Progress

1) Emerging Magnetic Interactions in van der Waals Heterostructures

Vertical van der Waals (vdWs) heterostructures based on layered materials are attracting interest as a new class of quantum materials, where interfacial charge-transfer coupling can give rise to fascinating strongly correlated phenomena. Transition metal chalcogenides are a particularly exciting material family, including ferromagnetic semiconductors, multiferroics, and superconductors. We describe an organic-inorganic heterostructure by intercalating molecular electron donating bis(ethylenedithio)tetrathiafulvalene into $(\text{Li},\text{Fe})\text{OHFeSe}$ (LFS), a layered material in which the superconducting ground state results from the intercalation of hydroxide layer. Molecular intercalation in this heterostructure induces a transformation from a paramagnetic to spin-glass-like state that is sensitive to the stoichiometry of molecular donor and an applied magnetic field. Besides, electron donating molecules reduce the electrical resistivity in the heterostructure and modify its response to laser illumination. This hybrid heterostructure provides a promising platform to study emerging magnetic and electronic behaviors in strongly correlated layered materials.

The vdWs forces and hydrogen bonds play a vital role in the structural engineering of FeSe-based layered materials where organic and inorganic molecules can be intercalated into the layers to tune its electronic and spin properties.^{1,2} The structure of FeSe consists of stacked and layered sheets stabilized by vdWs forces (Figure 1a). Besides, LFS shows a larger spacing between adjacent FeSe layers which are connected via hydrogen bonds with $(\text{Li},\text{Fe})\text{OH}$ layers (Figure 1b).³ Inspired by the formation of LFS heterostructure, we select electron donor ET molecule that often presents intermolecular interactions and hydrogen bonds, to explore the spin-dependent and charge-transfer behavior in LFS system. Based on the intercalated FeSe structures,^{2,4} a LFS·zET heterostructure is schematically shown in Figure 1c. The host material LFS for molecular interaction is superconducting, suggested from its diamagnetism and microwave spectroscopy. Figure 2a illustrates the diamagnetic transition at 40 K of the LFS powder under an applied magnetic field of 50 Oe while zero-field-cooled (ZFC) and field-cooled (FC). The inset of Figure 2a shows the ZFC diamagnetic transition near $T_c = 40$ K. The existence of superconductivity in the LFS powder sample is further investigated using temperature-dependent magnetic field modulated microwave spectroscopy

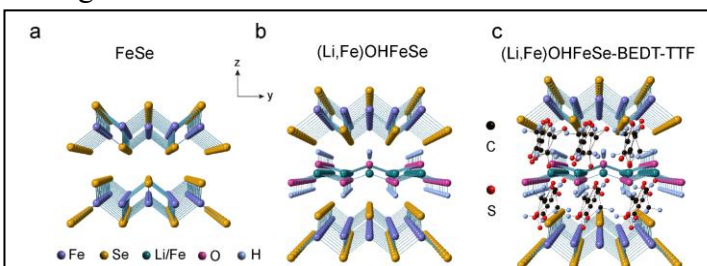


Figure 1. Crystal structures, morphologies and magnetic susceptibilities of FeSe and its derived heterostructures. (a-c) The layered crystal structures of FeSe (FS), $(\text{Li},\text{Fe})\text{OHFeSe}$ (LFS) and $(\text{Li},\text{Fe})\text{OHFeSe}\cdot z\text{BEDT-TTF}$ (LFS-ET) illustrate the FeSe-based heterostructures engineered with LiOH and the BEDT-TTF molecule at the layer scale. The derived heterostructures inherit the layered nature of FS and are governed by van der Waals forces and hydrogen bonds.

(MFMMS). The MFMMS signals (Figure 2b) at 50 Oe (ZFC and FC) show the sharp upturns at 35 K which suggests superconductivity and corroborates the diamagnetic transition at 40 K as a superconducting transition.⁵ The relatively small difference in temperature of 5 K between the onset of superconductivity in the magnetization ($T_c = 40$ K) and MFMMS ($T_c = 35$ K) measurements is not entirely understood but is possibly due to differences in thermometry.

The magnetic state in LFS-zET heterostructures is further studied as the spin-glass-like behavior and antiferromagnetic interactions. The inverse magnetic susceptibilities of LFS-zET samples exhibit negative intercepts ($-\theta$), suggesting its antiferromagnetic interactions (Figure 3a). Besides, the ZFC and FC magnetic susceptibility of LFS-zET heterostructure ($z=0.0065$) shows an irreversibility that is often observed in a spin glass⁶ (Figure 3b). Temperature-dependent AC magnetic susceptibility for LFS-zET sample ($z=0.0065$) at frequencies from 10 to 10 kHz further confirms its spin-glass behavior (Figure 3c). The inset shows the transition temperature T_s shifts to a higher temperature when the frequency is increased, which is the representative characteristic of a spin-glass state. The *Ab initio* calculations also reveal antiferromagnetic interaction in LFS-ET is more energetically stable than ferromagnetic interaction. All the *ab initio* calculations indicate the disordered or frustrated spin in LFS-zET which can be regarded as spin glass. Previous study on LFS system also revealed a spin-glass state at 12 K in its parent phase, non-superconducting and some superconducting samples⁷, even though it was claimed as a canted antiferromagnet³. The ET molecule in LFS-zET heterostructures seems to promote the spin-glass transition temperature, through spin interaction with (Li,Fe)OH and FeSe layers.

2) Cooperative transition in molecular electronic crystal

We select potassium-7,7,8,8-tetracyanoquinodimethane (K-TCNQ) as the model system to study the cooperative behavior in molecular electronic crystal. In K-TCNQ, the localized π electron on the TCNQ site forms an anion radical (TCNQ^-) and the system undergoes spin-Peierls transition below critical temperature (T_c , ~395 K) with the formation of a diamagnetic insulating

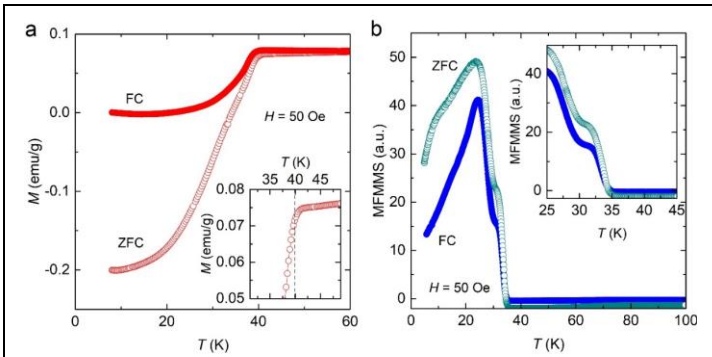


Figure 2. Superconducting properties of the LFS host material. (a) Zero field cooled (ZFC) and field cooled (FC) diamagnetic transition at 40 K of LFS suggests a superconducting transition under an applied field at 50 Oe. (b) At the same magnetic field of 50 Oe, magnetic field modulated microwave spectroscopy confirms the onset of a superconducting transition at 35 K.

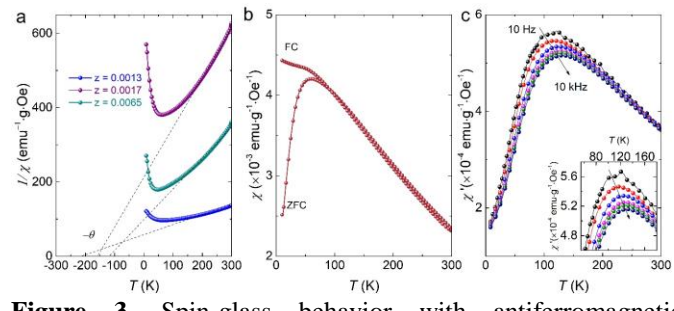
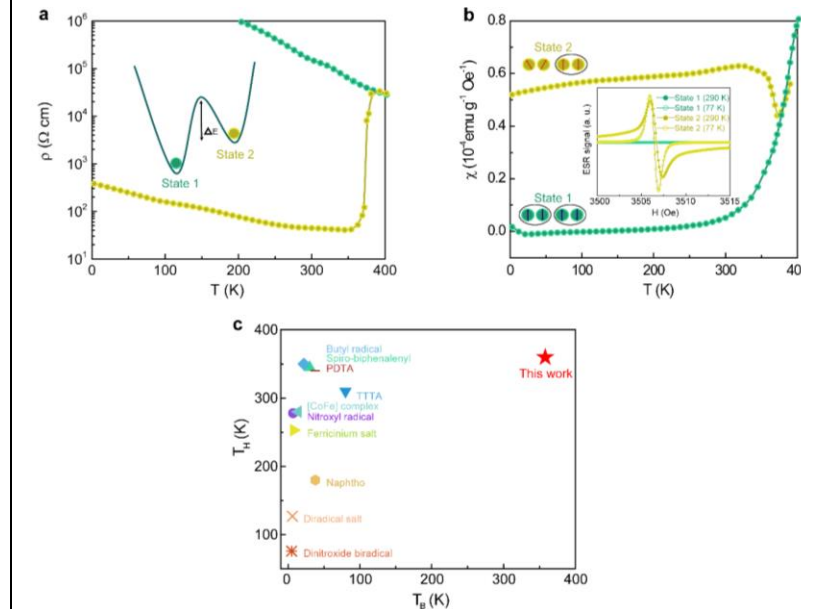
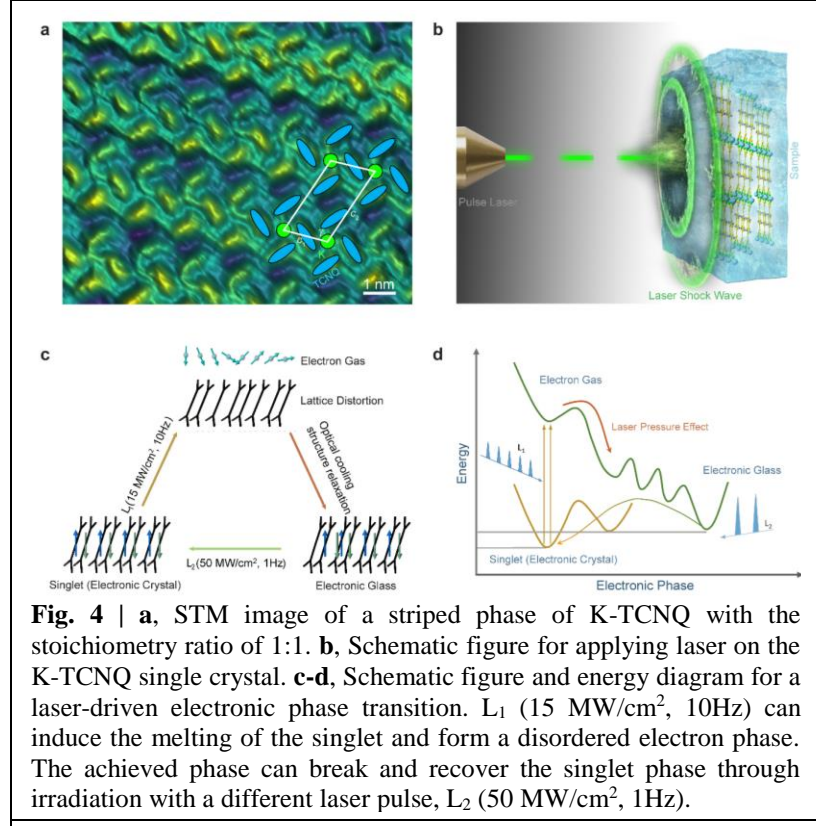


Figure 3. Spin-glass behavior with antiferromagnetic interactions in LFS-zET. (a) Inverse magnetic susceptibilities of LFS-zET samples exhibit negative intercepts ($-\theta$), suggesting antiferromagnetic interactions. (b) Zero-field-cooled (ZFC) and field-cooled (FC) magnetic susceptibility of LFS-zET ($z=0.0065$) at a magnetic field of 0.1 T. (c) Temperature dependent real part of AC magnetic susceptibility for LFS-zET sample ($z=0.0065$) at frequencies of 10, 100, 1,000, 3,000, 5,000, and 10,000 Hz. The inset shows the transition temperature shifts to higher temperature when the frequency is increased from 10 Hz to 10,000 Hz, confirming a spin-glass state.

singlet ground state. The packing motif of K-TCNQ perpendicular to the stacking *a* axis (*b-c* plane) can be visualized in the scanning tunneling microscopy (STM) images, where K atoms occupy the center sites of TCNQ mesh (Fig. 4a). Here, we found that delicately tuning the pulsed laser irradiation above certain threshold excitation could modify the degree of electronic ordering in K-TCNQ. The strong cooperativity among electronic and lattice degrees leads the system towards an equilibrium hidden state (Fig. 4b), which exhibits distinct electronic and magnetic properties that remain stable for over 400 days, significantly extending the lifetime of photoinduced transient state. Electric field from pulsed electromagnetic irradiation melts the electronic ordering in the spin-Peierls state (Fig. 4c-d) in K-TCNQ at room temperature, while the shockwave pressure further drives the system towards an electronic disordered phase (electronic glass), which is supported by the noise and vibration spectroscopy and scanning tunneling microscopy (STM) studies. The in-situ and atomic-scale mechanistic studies further suggest the pressure and electrical field effects on such cooperative phase transition, at which a switchable magneto-electronic bistability is achieved from 2 to 360 K.

The interplay of charge, spin, orbital and lattice degrees of freedom in K-TCNQ play a



crucial role in laser-driven phase transition and cooperativity. As shown in Fig. 5a, laser driven electronic bistability in K-TCNQ is shown from 2 to 360 K. The conducting phase is paramagnetic from its electron spin resonance (ESR, Fig. 5b), suggesting the conducting paramagnetic phase switched from the insulating diamagnetic singlet phase due to the strong coupling of charge, spin and lattice degrees. The magnetic state can also be maintained over the same temperature regime (2- 360 K) (Fig. 5b). It should be mentioned that the pristine K-TCNQ exhibits insulating behavior over the entire temperature regime below and above T_c without showing bistability. Thus, the achieved bistability is hidden from a dimerized phase, as the dimerization is thought to be the bane for developing conducting or magnetic molecular solids. The laser-induced phase transition in K-TCNQ simultaneously activates its magneto-electronic bistability from 2 to 360 K, a broad bistability temperature range among the reported molecular crystals (Fig. 5c).

Future Plans

The current program ends on April 2021, and the future plan focuses on the multiferroic orders of molecular ferroelectric-magnetic heterogeneous materials, consisting of high temperature molecular ferroelectric and magnetic building blocks with the control of their internal interfaces. The detailed experimental plan includes:

- 1) Molecular heterogeneous magnetoelectric material growth with the control of material composition and structure;
- 2) Study electric field-controlled magnetism and magnetic field-controlled polarization of molecular magnetoelectric materials;
- 3) Mechanistic understanding of charge mediated magnetoelectric coupling properties in molecular crystals;
- 4) Growth of high temperature molecular magnets and its strongly correlated behaviors.

References

- (1) Ying, T.; Chen, X.; Wang, G.; Jin, S.; Lai, X.; Zhou, T.; Zhang, H.; Shen, S.; Wang, W. Superconducting Phases in Potassium-Intercalated Iron Selenides. *J. Am. Chem. Soc.* **2013**, *135*, 2951-2954.
- (2) Burrard-Lucas, M.; Free, D. G.; Sedlmaier, S. J.; Wright, J. D.; Cassidy, S. J.; Hara, Y.; Corkett, A. J.; Lancaster, T.; Baker, P. J.; Blundell, S. J.; Clarke, S. J. Enhancement of the superconducting transition temperature of FeSe by intercalation of a molecular spacer layer. *Nat. Mater.* **2013**, *12*, 15-19.
- (3) Lu, X. F.; Wang, N. Z.; Wu, H.; Wu, Y. P.; Zhao, D.; Zeng, X. Z.; Luo, X. G.; Wu, T.; Bao, W.; Zhang, G. H.; Huang, F. Q.; Huang, Q. Z.; Chen, X. H. Coexistence of superconductivity and antiferromagnetism in (Li_{0.8}Fe_{0.2})OHFeSe. *Nat. Mater.* **2015**, *14*, 325-329.
- (4) Shi, M. Z.; Wang, N. Z.; Lei, B.; Shang, C.; Meng, F. B.; Ma, K.; Zhang, F. X.; Kuang, D. Z.; Chen, X. H. Organic-ion-intercalated FeSe-based superconductors. *Phys. Rev. Mater.* **2018**, *2*.
- (5) Ramirez, J. G.; Basaran, A. C.; de la Venta, J.; Pereiro, J.; Schuller, I. K. Magnetic field modulated microwave spectroscopy across phase transitions and the search for new superconductors. *Rep Prog Phys* **2014**, *77*, 093902.
- (6) Sagredo, V.; Morón, M. C.; Betancourt, L.; Delgado, G. E. Antiferromagnetic versus spin-glass like behavior in MnIn₂S₄. *J. Mag. Mag. Mater.* **2007**, *312*, 294-297.
- (7) Woodruff, D. N.; Schild, F.; Topping, C. V.; Cassidy, S. J.; Blandy, J. N.; Blundell, S. J.; Thompson, A. L.; Clarke, S. J. The Parent Li(OH)FeSe Phase of Lithium Iron Hydroxide Selenide Superconductors. *Inorg Chem* **2016**, *55*, 9886-9891.

Publications

1. Y. Huang and S. Ren*, Multifunctional Prussian Blue Analogue Magnets: Emerging Opportunities. *Applied Materials Today*, 22, 100886, (2021).
2. Y. Huang, C. Wolowiec, T. Zhu, Y. Hu, L. An, Z. Li, J. C. Grossman, I. K. Schuller and S. Ren*, Emerging Magnetic Interactions in van der Waals Heterostructures. *Nano Letters*, 20, 11, 7852–7859, (2020).
3. Y. Hu, Z. Guo, A. Ragonese, T. Zhu, S. Khuje, C. Li, J. C. Grossman, C. Zhou*, M. Nouha*, and S. Ren*, A 3D printed molecular ferroelectric metamaterial. *Proc. Natl. Acad. Sci. U.S.A.*, 117 (44) 27204-27210 (2020).
4. Y. Huang, Y. Hu, L. An, Z. Li, J. N. Armstrong, and S. Ren*, Electron transfer induced magnetic ordering of metal-cyanide magnets. *Materials Advances*, 1, 1061-1065, (2020)
5. A. Ahmed, Y. Guan, I. Hassan, C. Ling, Z. Li, S. Chang, P. R. Selvaganapathy, S. Ren, Multifunctional Smart Electronic Skin fabricated from Two-Dimensional like Polymer Film. *Nano Energy*, 75, 105044, (2020).
6. Y. Huang, S. Zhang, G. Zhong, Y. Hu, H. Zhou, F. Hu, C. Li, R. Yang, Z. Li, J. N. Armstrong, and S. Ren. Strongly Correlated Molecular Magnet with Curie Temperature above 60 K. *Matter*, 3, 1639–1650, (2020).
7. F. Hu, Y. Hu, Y. Huang, C. Li, R. Yang and S. Ren*, Molecular Conducting Magnetic Heterostructure, *J. Mater. Chem. C*, 8, 2228-2231 (2020).
8. F. Hu, C. Li, R. Yang, Y. Huang, Y. Hu, S. Ren*, Two-Dimensional Nanoconfined Channels for Heavy Metal Sensor, *ACS Applied Electronic Materials*, 2, 1, 41–47 (2020).
9. B. Xu, Z. Li, S. Chang and S. Ren*, Multifunctional Molecular Charge-Transfer Thin Films, *Nanoscale*, 11, 22585-22589 (2019)
10. Z. Wang, M. Gao, S. Ren, X. Hao, W. Qin*, Magnetic and Electric Control of Circularly Polarized Emission through Tuning Chirality Generated Orbital Angular Momentum in Organic Helical Polymeric Nanofibers, *Advanced Materials* 31, 1904857 (2019).
11. A. Ahmed,* I. Hassan, M. F. El-Kady, A. Radhi, C. K. Jeong, P. R. Selvaganapathy, J. Zu, S. Ren, Q. Wang, and R. B. Kaner, Integrated Triboelectric Nanogenerators in the Era of the Internet of Things, *Advanced Science* 6, 1802230 (2019).
12. Y. Huang, Y. Hu, F. Hu, R. Yang, C. Li, J. Armstrong and S. Ren*, Correlation at Two-Dimensional Charge-Transfer FeSe Interface, *Chemical Communications*, 55, 12643-12646 (2019).
13. Z. Zhang, Z. Li, S. Chang*, W. Gao, G. Yuan, R. Xiong, S. Ren*, Light-controlled molecular resistive switching ferroelectric heterojunction, *Materials Today*, 34, 51-57 (2019).
14. B. Xu, Z. Li, S. Chang, C. Li, S. Ren*, Crystallization-mediated magnetoelectric response in two-dimensional molecular charge transfer crystals, *ACS Applied Electronic Materials*, 1, 9, 1735–1739 (2019).
15. Y. Guan, Y. Hu, C. Li, and S. Ren*, Magnetoelectric Bistability of Molecular Ferroic Solids, *Journal of Materials Chemistry C*, 7, 9154-9158 (2019).
16. Y. Guan, Y. Hu, H. Zhang, G. Wu*, H. Yan* and S. Ren*, Highly Conductive, Transparent Molecular Charge-Transfer Salt with Reversible Lithiation, *Chemical Communications*, 55, 7179-7182 (2019).
17. Z. Wang, M. Gao, M. We, S. Ren, X. Hao, and W. Qin*, Organic Chiral Charge Transfer Magnets, *ACS Nano*, 13, 4, 4705–4711 (2019).
18. Y. Hu, G. Zhong, Y.Guan, J. N. Armstrong, C. Li, C. Liu, A.N'Diaye, A. Bhattacharya, S. Ren*, Strongly Correlated Aromatic Molecular Conductor, *Small*, 1900299 (2019).

19. Y. Hu, G. Zhong, Y. Guan, N. Lee, Y. Zhang, Y. Li, T. Mitchell, J. N. Armstrong, J. Benedict, S. W. Hla, and S. Ren*, Alkali-Metal-Intercalated Percolation Network Regulates Self-Assembled Electronic Aromatic Molecules, *Advanced Materials*, 31, 1807178, (2019)
20. B. Xu, Y. Hu, Y. Guan, Z. Zhang, and S. Ren*, Ubiquitous energy conversion of two-dimensional molecular crystals, *Nanotechnology*, 30, 15LT01 (2019).
21. A. Ahmed, I. Hassan, I. M. Mosa, E. Elsanadidy, M. Sharafeldin, J. F. Rusling, and S. Ren*, Ultra Shapeable, Smart Sensing Platform Basedon Multimodal Ferrofluid–Infused Surface, *Advanced Materials*, 31, 1807201 (2019)

Project Title: Collective Energy Transport of Excitons in Two-dimensional Materials

Principal Investigator: Li Shi, University of Texas at Austin

Collaborator: Steve Cronin, University of Southern California

Program Scope

The goal of this project is to explore collective behavior that exists in samples with large numbers of interacting particles. The behavior of these systems goes beyond the independent particle picture that is commonly used to describe a vast majority of solid-state phenomena, including the transport of quantized carriers of charge and heat in solids. While collective behavior gives rise to superconductivity at low temperatures, signatures of collective behaviors in both charge and heat transport appear at rather high temperatures in several recent studies of low-dimensional materials. One specific example of this collective behavior is the formation of excitons (i.e., bound electron-hole pairs), which is pronounced in two-dimensional (2D) materials such as transition metal dichalcogenides (TMDCs), with exciton binding energies exceeding the thermal energy at room temperature. In this project, we pursue optical, electronic, thermal, and thermoelectric measurements to obtain unique insights into the unusual collective energy transport behaviors of excitons in 2D materials and heterostructures.

Recent Progress

Phonon Interaction with Ripples and Defects in Thin Layered Molybdenum Disulfide

Due to thermal fluctuations, structural rippling is ubiquitous in monolayer and few-layer 2D materials, including both supported and suspended structures, such as molybdenum disulfide (MoS_2) and graphene. This rippling creates inhomogeneous strain fields due to the changed crystal structure that strongly affect electronic and lattice vibrational behaviors. For example, severe rippling in graphene was shown to generate a long-range scattering potential for electrons and strongly suppress their weak localization. In addition, the effects of ripples and kinks on thermal conductivity (κ) in 2D materials has been considered in several theoretical studies, including

unique strain effects, which can influence the performance and thermomechanical

reliability of emerging 2D devices. Contrary to bulk materials for which compressive and tensile strains generally increase and decrease κ , respectively, molecular dynamics studies have suggested that both tensile and compressive strains reduce the thermal conductivities of graphene and MoS_2 . In particular, compressive strain in 2D

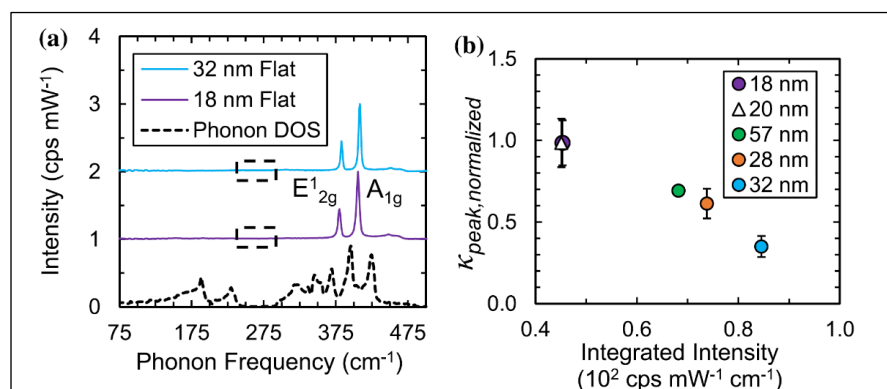


Fig. 1. (a) Raman spectra of two representative MoS_2 samples along with the phonon density of states from first principles calculations. The black dashed rectangles indicate the phonon frequency range where the Raman background intensities were integrated. (b) Measured peak thermal conductivity normalized by the calculated theoretical defect-free peak value for each sample thickness as a function of the integrated Raman spectra intensity in the frequency range between 245.5 to 288.75 cm^{-1} .

layers tends to drive the formation of buckling and rippling of the structure to relax the induced strain. Although a few theoretical studies have proposed that buckling or rippling due to compressive strains can increase phonon scattering rates, and thus reduce the thermal conductivity of 2D layers, it has also been suggested that the basal plane thermal conductivity of 2D layers is rather robust against rippling. Thus, the conditions and criteria for the importance of compression-induced ripple effects on thermal transport in 2D materials have remained unclear.

We have carried out four-probe thermal transport measurements of the intrinsic basal plane thermal conductivities of both rippled and flat multilayer MoS₂ samples, which are representative of 2D layered materials. Our experiments demonstrate that the basal plane thermal conductivity is robust against compression-induced ripples and kinks with radius of curvatures on the micrometer scale, but sensitive to phonon-defect scattering. A clear correlation is drawn between the peak thermal conductivity and the integrated Raman intensity caused by defects in the frequency range of the phonon band gap in MoS₂ (Fig. 1). In conjunction with experiments, first principles calculations of temperature, thickness, strain, and point defect concentration dependent κ provide physical insights into phonon-defect interactions and thermal resistance, and thus clarify the conditions for which ripples become an important mechanism for thermal conductivity suppression.

Electron-Phonon Interactions in Graphene encased in Hexagonal Boron Nitride

The highly tunable Dirac fermions in 2D graphene sheets have hosted an unprecedented variety of correlated electron behaviors including superconductivity, Bose-Einstein condensation of excitons, and electron hydrodynamics. These collective behaviors are closely associated with the elusive electron-phonon interaction behaviors in graphene. For common metals, measurements of the electronic thermal conductivity (κ_e) have provided unique insight into electron-phonon interaction. However, prior κ_e measurements of graphene have been limited to the low temperature (T) range in order to neglect electron-phonon scattering for analyzing the measurement data. Over the past several years, we have pursued a different method for κ_e measurement of graphene in a wide temperature range with a focus on the regime where electron-phonon scattering is dominant. During the past year, we have made further process in this pursue and are able to fabricate and measure the κ_e of clean edge-contacted graphene sample encased in hexagonal boron nitride (h-BN). The insets of Figure 2 show the optical photographs of a bottom-contacted graphene sample and our edge-contacted sample 29. This figure shows the measured Lorenz number, $L \equiv \kappa_e/\sigma T$ with σ being the electric conductivity, normalized by the Sommerfeld value (L_0), as a function of the charge carrier concentration (n).

When the Fermi level is near the Dirac point, bi-polar contribution increases the measured L of intrinsic graphene well above L_0 . In the degenerately doped regime, L is suppressed below L_0 at T higher than 120 K. This feature shows the dominance of inelastic scattering of electrons by high-energy optical and acoustic phonons, which decreases L/L_0 to only 0.3 as the temperature is decreased from 300 K to 120 K. This behavior is somewhat similar to the behavior of common metals. For common metals, L approaches L_0 both in the low temperature limit due to dominant elastic electron-defect scattering and at temperatures above the Debye temperature because of quasi-elastic scattering of electrons with much higher thermal energy than phonons. Meanwhile, inelastic electron-phonon scattering suppresses L of common metals below L_0 at an intermediate temperature below the Debye temperature. For doped graphene close to about 30 K, in comparison, L is suppressed below L_0 instead of approaching L_0 . The behavior at 30 K has been observed by

prior κ_e measurements of graphene and attributed to dominant electron-electron interaction that conserves the charge current but not the heat current in doped graphene. However, the measured L at an temperature close to 60 K approaches L_0 . Absent in common metals, this feature reveals the appearance of an elastic or quasi-elastic scattering mechanism that dominates inelastic electron-electron and electron-optical phonon scattering.

This peculiar feature at 60 K is observed in both the prior bottom-contacted sample and the recent edge-contacted sample 29, where the large L/L_0 peak near the Dirac point at 60 K reveals suppressed electron-hole puddle density compared to the prior bottom-contacted sample. Based on this experimental finding, we have proposed that quasi-elastic electron scattering by low-energy flexural phonons becomes dominant at temperatures 60 K. Based on prior theoretical studies, however, the reflection symmetry in suspended graphene leads to a stringent selection rule for electron scattering by flexural phonons. According to this selection rule, a pair of flexural phonons are required for electron-flexural phonon scattering. Due to this stringent selection rule, electron-flexural phonon scattering has been thought to be negligible in suspended graphene. In supported graphene, meanwhile, it has been suggested that the interaction with the support opens an energy gap in the flexural mode, making electron-flexural phonon scattering inelastic.

To better understand electron-phonon interaction in graphene, we have collaborated with Prof. Feliciano Giustino's group at UT Austin. Their first principles calculation have provided theoretical support to our proposed electron-phonon scattering mechanism. In graphene supported on h-BN, their results revealed the presence of both gapped and gapless flexural modes, which are caused by the out-of-phase and in-phase atomic vibration of the two adjacent layers, respectively. Furthermore, a weak breaking of the reflection symmetry in graphene/h-BN heterostructure relaxes the selection rule and considerably increases the electron-flexural phonon scattering rate.

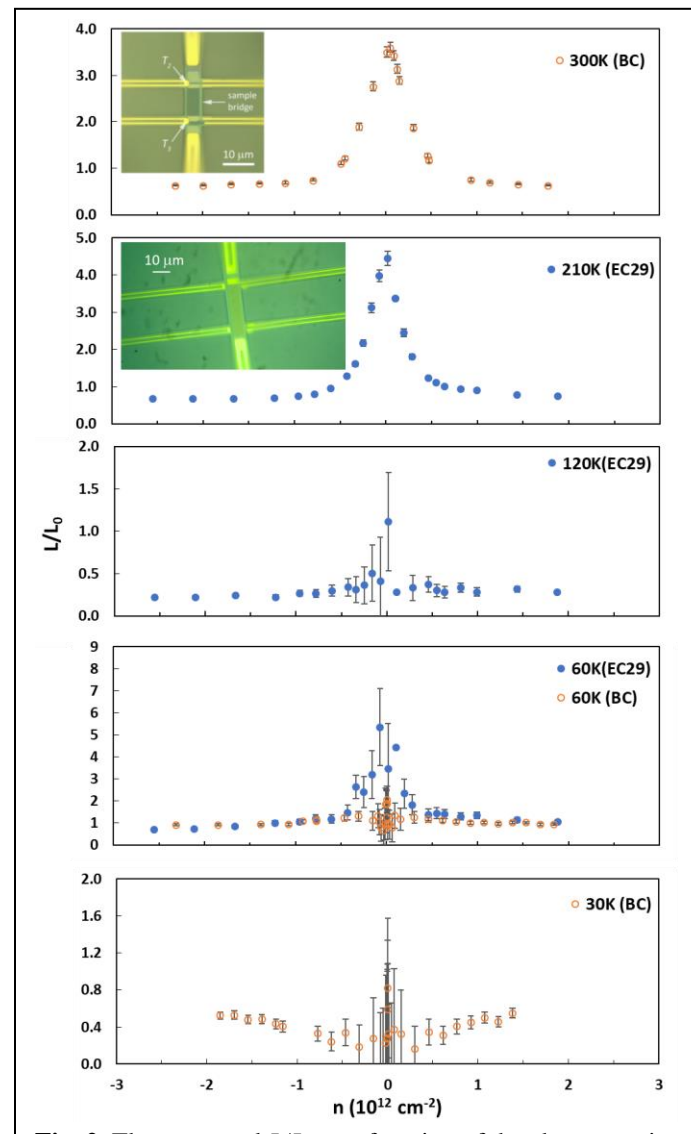


Fig. 2. The measured L/L_0 as a function of the charge carrier concentration (n) for a bottom contacted (BC) sample (upper optical graph) and edge-contacted sample 29 (lower optical graph) at ambient temperatures of 300 K, 210 K, 120 K, 60 K, and 30 K. Positive and negative n values are for hole- and electron- doped regimes, respectively.

This combined experimental and theoretical study has advanced the understanding of electron-phonon interaction processes in graphene/h-BN heterostructures, which are now explored as emerging electronic, optoelectronic, magnetic, and superconducting materials. The work has established a powerful method for measuring the electronic thermal conductivity of 2D materials. The method is being extended for probing the excitonic thermal conductivity in this project.

Counterflow Thermoelectric Transport Measurements of Interlayer Excitons

We have collaborated with Prof. Cronin's group to fabricate MoSe₂/h-BN/WSe₂ heterostructures, as illustrated in Figure 3(a,b), for thermoelectric probing of collective energy transport of interlayer exciton. With the two layers wired in series, the temperature gradient drive the transport of electrons and holes as bound excitons toward the same direction. Specifically, holes flow from hot to cold in the WSe₂ layer while electrons flow from hot to cold in the MoSe₂ layer in this counterflow Seebeck measurement. This exciton measurement is designed to evaluate Bosonic features that are distinctly different from Fermionic thermoelectric transport. The measurement device includes a top graphene gate layer and a bottom silicon gate, which enable independent tuning of the Fermi levels in both WSe₂ and MoSe₂ layers. Figure 3c shows the calculated interlayer exciton binding energy in the MoSe₂/h-BN/WSe₂ heterostructures as a function of the h-BN thickness. The device shown in Figure 3a required five aligned transfers of 2D materials and six electron-beam lithography (EBL) steps. The fabrication of these devices is as challenging as for the κ_e measurement devices shown in Fig. 2. Nevertheless, we have been able to fabricate the first sample shown in Fig. 3a and obtained preliminary measurement results. We are currently completing the last EBL step of the second sample, the design of which has been optimized based on the preliminary measurement results obtained for the first sample.

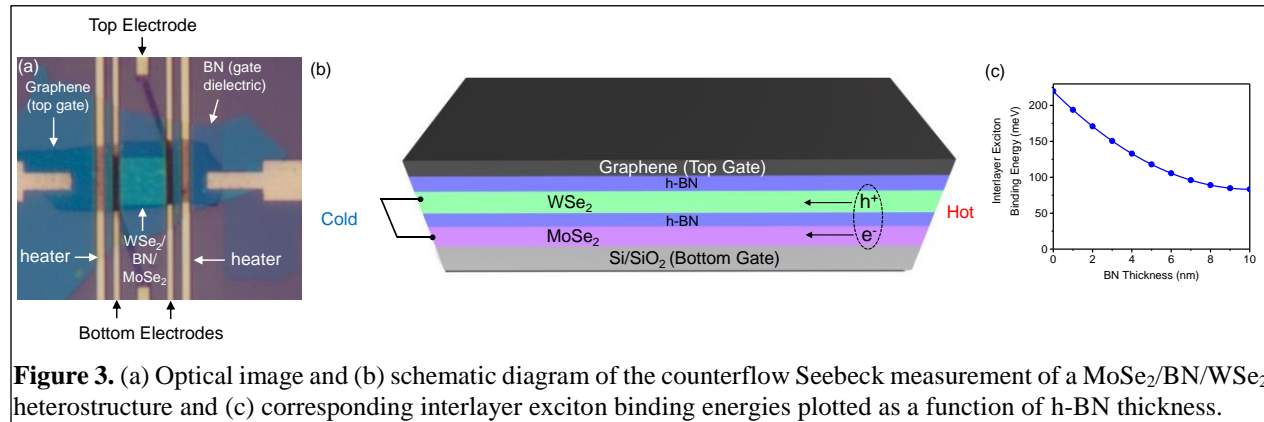


Figure 3. (a) Optical image and (b) schematic diagram of the counterflow Seebeck measurement of a MoSe₂/BN/WSe₂ heterostructure and (c) corresponding interlayer exciton binding energies plotted as a function of h-BN thickness.

Future Plans

We plan to complete the counter flow thermoelectric measurements of inter-layer excitons, and pursue excitonic thermal conductivity measurements in the coming year.

Publications

Y. Wang, D. M. Hamann, D. Leo M. Cordova, J. Chen, B. Wang, L. Shen, Z. Cai, H. Shi, E. Karapetrova, I. Aravind, L. Shi, D. C. Johnson, S. B. Cronin, "Enhanced Low-Temperature Thermoelectric Performance in $(\text{PbSe})_{1+\delta}(\text{VSe}_2)_1$ Heterostructures due to Highly Correlated Electrons in Charge Density Waves," *Nano Letters* 20, 8008–8014 (2020)

B. Smith, L. Lindsay, J.H. Kim, E. Ou, R. Huang, L. Shi, "Phonon Interaction with Ripples and Defects in Thin Layered Molybdenum Disulfide," *Applied Physics Letters* 114, 221902 (2019)

Title: Thermodynamic, Kinetic and Electrochemical Studies on Mixed Proton, Oxygen Ion and Electron (Hole) Conductors

PI: Anil V. Virkar, University of Utah

Program Scope

The principal objective of the project is to investigate multi-species transport in predominantly ionic conductors which have applications in fuel cells, electrolyzers, oxygen separators, hydrogen separators, and in sodium and lithium batteries. This includes all solid-state batteries. The work also includes proton exchange membrane (PEM) fuel cells. The literature is primarily focused on transport properties (e.g. conductivities) of such materials or charge transfer at electrode/electrolyte interfaces. In predominantly ionic conductors, the focus has been on ionic conductivity, the effects of which are measureable – e.g. current flowing through a device or electrocatalytic activity of electrodes. Local thermodynamic equilibrium (even when a system is away from thermodynamic equilibrium), however, determines stability [1-3]. Our work is on the measurement of electrode polarizations and their effects on both performance and stability of electrochemical devices and systems. Stability is governed by chemical potentials of electrically neutral species [4-6]. Thus, to investigate multi-species transport, electronic transport must be included in the general equations of transport [5-8]. It is equally important to include the role of electrode polarizations in the transport equations. To date electrode polarizations have been measured by electrochemical impedance spectroscopy (EIS). However, it is not possible to uniquely de-convolute EIS spectra. Also, EIS is AC technique but actual devices operate in a DC mode. The focus of the current effort is on measuring polarizations at the two electrodes separately by both EIS and DC methods. This approach allows one to separately determine polarizations for reduction reaction ($\frac{1}{2}\text{O}_2 + 2\text{e}^- \rightarrow \text{O}^{2-}$) and oxidation reaction ($\text{O}^{2-} \rightarrow \frac{1}{2}\text{O}_2 + 2\text{e}^+$). Additionally, we have been developing methods to measure electrode polarizations using a fully DC method. This is important since EIS is an AC method, but electrochemical devices operate in a DC mode. The overall transport equations must include Onsager coupling. The Onsager coefficients of the electrochemical device include transport properties of the electrolyte as well as electrode polarizations and interface electron/hole transport parameters. Our prior work has examined the effect of electrolytic and galvanic operations on stability. [6-9]. The fuel cell mode (or the battery discharge) is the galvanic mode. The electrolysis mode (or the battery charging mode) is the electrolytic mode. The electrochemical devices exhibit greater tendency to degradation in the electrolytic mode. Experimental evidence [10,11] of this behavior has been reported in the literature which confirms our theoretical predictions [5-8]. The origin of this result lies in non-equilibrium thermodynamics and Onsager coupling. The focus of our work is on predominantly oxygen ion conductors, proton conductors, and monovalent cation conductors and their behavior when removed from thermodynamic equilibrium.

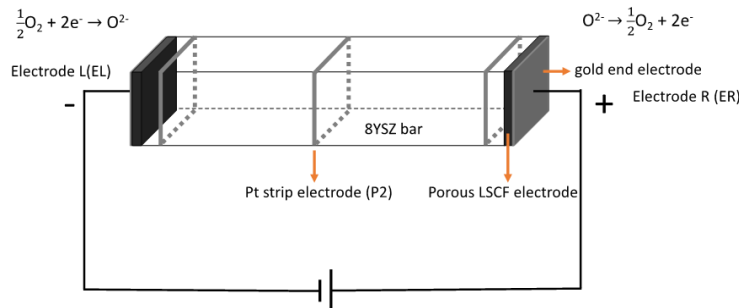


Figure 1

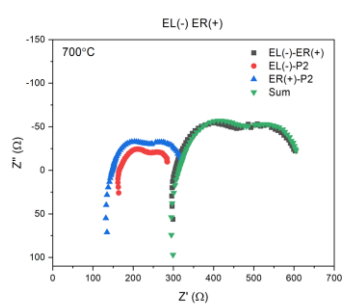


Figure 2(a)

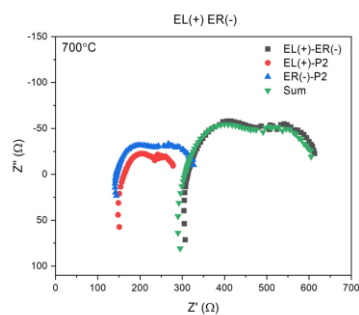


Figure 2(b)

Figure 1: A schematic of YSZ sample with identical LSCF electrodes and surface probes. Polarization measurements made by DC and AC methods for reduction and oxidation measurements.

Figure 2: EIS of between EL-P, P-ER and EL-ER.

By probes, EIS was measured under applied DC bias by changing polarities. In one case at left electrode, oxygen reduction reaction occurs. By changing polarities, oxidation reaction occurs at the left electrode. It is observed that polarization resistance for the reduction reaction is higher than for the oxidation reaction. This shows that identical electrodes exhibit different kinetics for the reduction and oxidation reactions.

Recent Progress

Recent work has been on the following topics: **(1)** Measurement of Electrode Polarizations in PEM Fuel Cells by Embedded Electrodes: PEM fuel cells with one and two embedded Ag-reference electrodes were synthesized. EIS spectra were obtained across the entire cell, as well as between the reference electrodes and anode/cathode and also across the reference electrodes (membrane with two reference electrodes). A paper based on this work was published in J. Electrochem. Soc. (2019) **(2)** Measurement of Electrode Polarization Resistance of LSM + YSZ electrodes by DC and EIS methods: A cylinder of YSZ was made by powder pressing and sintering. Four Pt strip electrodes were applied at equal distances along the cylinder. Polarization measurements were made in a DC mode under various loads. From these studies, electrode polarization measurements were made. A paper based on this work was published in SOFC-XVI, Kyoto, Japan (2019). **(3)** Garnet type LLZTO (Li-La-Zr-Ta-oxide) ceramic oxide is a promising solid-state electrolyte for use in Li-ion batteries because it has good stability, adequate mechanical strength. However, the ambiguity of lithium dendrite growth in electrolyte still needs to be studied. The opacity of the solid electrolyte hinders the in-situ investigation of dendrite growth. A wet ceramic processing method, pressure filtration, was developed to make dense LLZTO solid-state electrolyte with high ionic conductivity (1.47×10^{-4} S/cm) and adequate transmittance (17 –23% to visible light from 500 to 800 nm) to observe and monitor dendrite growth. **(4)** A solid cylinder of 8YSZ of diameter ~1 cm and length ~5 cm was made by powder pressing followed by sintering. LSM + YSZ electrodes were applied on the two end surfaces of the cylinder, upon which gold mesh was placed. Four Pt probes were painted along the

circumference at approximately 1.2 cm apart. Point by point additions of the electrode-1/probe 2 and probe 2/electrode-2 spectra matched electrode-1/electrode-2 spectra. There was good agreement between the DC and the EIS measurements. A paper was presented at SOFC-XVI in Kyoto, Japan (2019). (5) Polarization measurements by EIS were conducted on a porous LSCF/dense YSZ/porous LSCF and on porous LSCF/dense/LSCF/porous LSCF. On porous LSCF/dense YSZ/porous LSCF, clear impedance was observed, attributed to ohmic and electrode reaction. However, on porous LSCF/dense LSCF/porous LSCF, no capacitive impedance was observed; only ohmic. This conclusively shows that it is not possible to determine Warburg (diffusive) impedance with mixed ionic electronic conducting (MIEC) electrodes, due to electronic short. This conclusively shows that observed spectra in solid state electrochemistry cannot be attributed to gas diffusion or Warburg, unlike in aqueous electrochemistry. This shows that numerous papers which have used Warburg impedance are not accurate. (6) Two collaborative papers published with Prof. H-T. Lim of Chongwon University, South Korea. One is on the use of embedded probes fuel cells made proton conductors, with a bi-layer electrolyte. Results show that n-type conductivity in the electrolyte substantially increases stability. Cells with low electronic conductivity show degradation in reverse bias. Another paper is on YSZ electrolyte with and without n-type dopant. Here also n-type conductivity increases stability.

Future Plans

- 1) To synthesize and characterize ion conducting materials far removed from global thermodynamic equilibrium. Main emphasis in oxygen ion conductors in which large internal pressure can be developed internally.
- 2) To investigate the applicability of Gerischer impedance in solid state electrochemistry.
- 3) To synthesize lithium ion conductors and investigate dendritic growth, which limits potential use as solid electrolyte in solid state batteries.

References

- 1) D. Kondepudi and I. Prigogine, ‘Modern Thermodynamics: From Heat Engines to Dissipative Structures’, John Wiley, New York (1998).
- 2) S. Kjelstrup and D. Bedeaux, ‘Non-Equilibrium Thermodynamics of Heterogeneous Systems’, World Scientific, (2008).
- 3) R. Haase, ‘Thermodynamics of Irreversible Processes’, Dover Publications, (1990).
- 4) A. V. Virkar, *J. Electrochem. Soc.*, **138** (5) 1481-1487 (1991).
- 5) A. V. Virkar, *J. Power Sources*, **147** 8-31 (2005).
- 6) A. V. Virkar, *Int. J. Hyd. Energy*, **35** 9527-9543 (2010).
- 7) A. V. Virkar, *J. Power Sources*, **196** 5970-5984 (2011).
- 8) A. V. Virkar, *Int. J. Hyd. Energy*, **37** 12609-12628 (2012).
- 9) A. V. Virkar, in ‘Engineered Ceramics: Current Status and Future Prospects’, edited T. Ohji and M. Singh, p. 59-76, Wiley-Am. Ceramic Soc. (2016).
- 10) M. A. Laguna-Bercero, R. Campana, A. Larrea, J. A. Kilner, and V. M. Orera, *J. Power Sources*, **196** 8942-8947 (2011).
- 11) J. R. Mawdsley, J. D. Carter, A. J. Kropf, B. Yildiz, and V. A. Maroni, *Int. J. Hyd. Energy*, **34** 4198-4207 (2009).
- 12) A. Szendrei, T. D. Sparks, and A. V. Virkar, *J. Electrochem. Soc.*, **166** (12) F784-F795 (2019). .

Publications

- 1 ‘Measurement of Polarization Resistance of LSM + YSZ Electrodes on YSZ using AC and DC Methods’, A. Szendrei, T. D. Sparks and A. V. Virkar, , *ECS Transactions*, **91** (1), 1363-1369 (2019).
<http://dx.doi.org/10.1049/09101ecst>
- 2 ‘Modeling of Oxygen Chemical Potential Distribution in Solid Oxide Electrolyzer Cells’, L. Zhang, L. Zhu and A. V. Virkar, *J. Electrochem. Soc.*, **166** (6) F1275-F1283 (2019).
<http://dx.doi.org/10.1149/2.01219jes>
- 3 ‘Electrochemical Studies on Na- β'' -Alumina + Yttria-Stabilized Zirconia (YSZ) Composite Mixed Na⁺-Ion-O²⁻ Ion Conductors’, L. Ghadbeigi, T. D. Sparks, and A. V. Virkar.
J. Electrochem. Soc., **166** (10) F679-F686, (2019) <http://dx.doi.org/10.1149/2.0161912jes>
- 4 ‘Locally developed electronic conductivity in a yttria-stabilized zirconia (YSZ) electrolyte for durable solid oxide fuel cells’, M. J. Son, M. W. Kim, A. V. Virkar and H-T. Lim, *Electrochimica Acta*, **353** 136450 (2020). <https://doi.org/10.1016/j.electacta.2020.136450>
- 5 ‘Spatial investigation of electronic properties in composite electrolytes for solid oxide fuel cells using embedded probes’, A. K. Niaz, M. G. Jung, J-Y. Park, A. V. Virkar and H-T. Lim, *J. Power Sources*, **438**, 226945 (2019). <https://doi.org/10.1016/j.jpowsour.2019.226945>
- 6 ‘Three and Four-Electrode Electrochemical Impedance Spectroscopy Studies Using Embedded Composite Thin Film Pseudo-Refence Electrodes in Proton Exchange Membrane Fuel Cells’, A. Szendrei, T. D. Sparks, and A. V. Virkar, *J. Electrochem. Soc.*, **166** (12) F784-F795 (2019).
<https://doi.org/10.1149/2.0771912jes>

Book Chapter

A. V. Virkar and K. L. Reifsnider, ‘Work of electrochemical pressurization of a pore in an oxygen ion conducting solid electrolyte and implications concerning solid oxide electrolyzer degradation’, p. 341-362, ‘Durability of Composite Systems’, edited by K. L. Reifsnider, Elsevier publication (2020)

Author Index

Ager, Joel W.....	137
Alberi, Kirstin	313
Ali, Naushad.....	358
Alivisatos, A. Paul	187, 196
Anlage, Steven M.....	65
Apalkov, Vadym	73
Atwater, Harry A.....	154
Awschalom, David.....	3
Balandin, Alexander A.....	161
Bao, Zhenan	274
Barnett, Scott A.....	410
Beard, Matt.....	313
Benjamin, Shermane M.....	405
Beratan, David N.....	263
Bergman, Leah	255
Bhattacharya, Anand	131
Biaggio, Ivan	166
Biswas, Anis.....	387
Boehme, Christoph.....	82
Boltasseva, Alexandra.....	234
Brener, Igal.....	228
Briscoe, Jayson.....	228
Brongersma, Mark.....	217
Burch, Kenneth Stephen.....	15
Bustamante, C.	196
Cen, Cheng.....	41
Chang, Christopher	331
Chien, Chia-Ling.....	47
Chrzan, Daryl C.	137
Cohen, M. L.	196
Cohn, Joshua L.....	348
Crommie, Michael F.	196
Cronin, Steve.....	415, 426
Curtiss, Larry A.....	336
Dahlberg, E. Dan.....	367
Delaire, Olivier.....	353
Dery, Hanan	87
Dessau, Daniel.....	313
Dmowski, W.	372
Dubon, Oscar D.....	137
Egami, T.	372
Falk, Michael L.	379
Fan, Shanhui.....	217
Fei, Zhe	8
Ferguson, Andrew	331
Fischer, F. R.	196
Fluegel, Brian.....	313
Fong, Dillon	131
Forrest, Stephen	122
Gartstein, Yuri N.....	296
Giebink, Noel C.	268
Harutyunyan, Hayk	317
Heremans, Joseph.....	3
Heremans, Joseph P.	170
Hla, Saw Wai	336
Ho, Kai-Ming	8
Hruszkeywycz, Stephan	3
Hua, C.	372
Jarrahi, Mona.....	250
Javey, Ali	137
Jena, Purusottam	202
Jensen, Mark	331
Jiang, Sam	131
Jungfleisch, M. Benjamin	24
Kahn, Antoine	268
Kamat, Prashant	260
Karma, Alain	382
Kenning, Gregory G.....	367
Klem, John	228
Knezevic, Irena	301
Knowlton, William B.	32
Koschny, Thomas.....	222
Kuno, Masaru	260
Kuvayskaya, Anastasia	331
Lany, Stephan.....	313
Law, Stephanie	114
Lee, Dongkyu	326
Leone, Stephen R.	187
Li, Lian.....	41
Li, Xiaoqin Elaine	57
Li, Xin	41
Liao, Bolin	343
Limmer, David T.	187
Liu, Feng	103
Louie, S. G.	196
Luk, Willie	228
Luo, Liang	8
Lupton, John M.	82
Ma, Xuedan	336
Magana-Loaiza, Omar S.	28
Majetich, Sara A.....	92
Malko, Anton V.	296

Mallos, Thomas.....	331
Masson, Eric.....	336
McCluskey, Matthew D.	255
Menon, Vinod	122
Mishin, Yuri	284
Morris, J. R.....	372
Mudryk, Yaroslav	387
Naaman, Ron.....	263
Neumeier, John J.....	405
Ngo, Anh T.	336
Orbach, Raymond L.	367
Padilla, Willie J.	240
Pecharsky, Vitalij K.	387
Phan, Manh-Huong	96
Rabani, Eran.....	187
Rajh, Tijana.....	336
Rand, Barry P.	268
Ren, Shenqiang	420
Rice, Anthony	313
Rieders, Nathaniel F.	405
Robinson, J. A.	296
Rose, Volker.....	336
Ruoff, Kevin.....	331
Sarma, Raktim.....	228
Schelter, Eric	331
Sellers, Ian R.	306
Sellinger, Alan.....	331
Shi, Jing.....	50
Shi, Li.....	415, 426
Shinar, Joseph	8
Shinohara, Y.....	372
Sih, Vanessa	119
Sinclair, Michael B.	228
Smalyukh, Ivan I.	208
Smith, M. G.....	405
Soukoulis, Costas M.	222
Srikanth, Hari	96
Stadler, Shane.....	358
Steger, Mark	331
Sun, Dali.....	175
Suzuki, Yuri	53
Talapatra, Saikat.....	358
Tamboli, Adele C.	394
Thompson, Jeffrey.....	21
Tisdale, William A.	291
Tongay, Sefaattin	179
Tuan, Dinh Van.....	87
Türeci, Hakan.....	70
Ulloa, Sergio E.	336
Van de Walle, Chris G.	143
van Schilfgaarde, Mark	313
Vardeny, Z. Valy.....	77
Virkar, Anil V.	430
Waldeck, David H.	263
Walukiewicz, Wladek	137
Wang, Cai-Zhuang	8
Wang, Jigang.....	8, 222
Watzman, Sarah J.	322
Whittaker-Brooks, Luisa.....	109
Wolfowicz, Gary	3
Wu, Junqiao	137
Wu, Yiying.....	278
Yang, Min	87
Yang, Peidong	187
Yao, Yongxin	8
Zamkov, Mikhail.....	245
Zarkadoula, E.	372
Zettl, A.	196
Zevalkink, Alexandra.....	353
Zhang, Pengpeng.....	149
Zhang, Zhuomin.....	400
Zhao, Hui	36

Participant List

Name	Organization	Email_Address
Ager, Joel	Lawrence Berkeley National Laboratory	jwager@lbl.gov
Alberi, Kirstin	National Renewable Energy Laboratory	Kirstin.Alberi@nrel.gov
Anlage, Steven	University of Maryland	anlage@umd.edu
Apalkov, Vadym	Georgia State University	vapalkov@gsu.edu
Atwater, Harry	California Institute of Technology	haa@caltech.edu
Awschalom, David	Argonne National Laboratory	awsch@uchicago.edu
Balandin, Alexander	University of California, Riverside	balandin@ece.ucr.edu
Bao, Zhenan	Stanford University	zbao@stanford.edu
Barnett, Scott	Northwestern University	s-barnett@northwestern.edu
Beratan, David	Duke University	david.beratan@duke.edu
Bergman, Leah	University of Idaho	Lbergman@uidaho.edu
Bhattacharya, Anand	Argonne National Laboratory	anand@anl.gov
Biaggio, Ivan	Lehigh University	biaggio@lehigh.edu
Boehme, Christoph	University of Utah	boehme@physics.utah.edu
Boltasseva, Alexandra	Purdue University	aeb@purdue.edu
Brener, Igal	Sandia National Laboratories	ibrener@sandia.gov
Burch, Kenneth	Boston College	ks.burch@bc.edu
Cen, Cheng	West Virginia University	chcen@mail.wvu.edu
Chang, Chris	National Renewable Energy Laboratory	christopher.chang@nrel.gov
Chien, Chia-Ling	Johns Hopkins University	clchien@jhu.edu
Chrzan, Daryl	University of California, Berkeley	dcchrzan@berkeley.edu
Cohn, Joshua	University of Miami	jcohn@miami.edu
Crommie, Michael	University of California, Berkeley	crommie@berkeley.edu
Cronin, Steve	University of Southern California	scronin@usc.edu
Dahlberg, Dan	University of Minnesota	dand@umn.edu
Davis, Paul	Boise State University	pauldavis2@boisestate.edu
Delaire, Olivier	Duke University	olivier.delaire@duke.edu
Dery, Hanan	University of Rochester	hanan.dery@rochester.edu
Dinh, Van Tuan	University of Rochester	vdinh@ur.rochester.edu
Doiron, Chloe	Sandia National Laboratories	cfdoiro@sandia.gov
Dubon, Oscar	University of California, Berkeley	oddubon@berkeley.edu
Egami, Takeshi	Oak Ridge National Laboratory	egami@utk.edu
Falk, Michael	Johns Hopkins University	mfalk@jhu.edu
Fan, Shanhui	Stanford University	shanhai@stanford.edu
Fecko, Chris	U.S. Department of Energy	christopher.fecko@science.doe.gov
Ferguson, Andrew	National Renewable Energy Laboratory	andrew.ferguson@nrel.gov
Fiechtner, Gregory	U.S. Department of Energy	gregory.fiechtner@science.doe.gov
Fitzsimmons, Tim	U.S. Department of Energy	tim.fitzsimmons@science.doe.gov
Forrest, Stephen	University of Michigan	stevefor@umich.edu
Gennaro, Sylvain	Sandia National Laboratories	sdgenna@sandia.gov
Gersten, Bonnie	U.S. Department of Energy	bonnie.gersten@science.doe.gov
Giebink, Noel	The Pennsylvania State University	ncg2@psu.edu
Graf, Matthias	U.S. Department of Energy	matthias.graf@science.doe.gov
Hall, John	Boise State University	johnhall440@boisestate.edu
Harutyunyan, Hayk	Emory University	hayk.harutyunyan@emory.edu
Heremans, F. Joseph	Argonne National Laboratory	heremans@anl.gov
Heremans, Joseph P.	Ohio State University	heremans.1@osu.edu
Hla, Saw Wai	Argonne National Laboratory	shla@anl.gov
Horwitz, Jim	U.S. Department of Energy	james.horwitz@science.doe.gov
Iyer, Prasad	Sandia National Laboratories	ppadma@sandia.gov

Jarrahi, Mona	University of California, Los Angeles	mjarrahi@ucla.edu
Javey, Ali	University of California, Berkeley	ajavey@berkeley.edu
Jena, Puru	Virginia Commonwealth University	pjena@vcu.edu
Jung, Hyunseung	Sandia National Laboratories	hjung@sandia.gov
Jungfleisch, Benjamin	University of Delaware	mbj@udel.edu
Kahn, Antoine	Princeton University	kahn@princeton.edu
Kamat, Prashant	University of Notre Dame	pkamat@nd.edu
Karma, Alain	Northeastern University	a.karma@northeastern.edu
Kenning, Gregory	Indiana University of Pennsylvania	Gregory.Kenning@iup.edu
Knezevic, Irena	University of Wisconsin	irena.knezevic@wisc.edu
Knowlton, Bill	Boise State University	bknowlton@boisestate.edu
Kortan, Refik	U.S. Department of Energy	refik.kortan@science.doe.gov
Koschny, Thomas	Ames Laboratory	koschny@ameslab.gov
Kuno, Masaru	University of Notre Dame	mkuno@nd.edu
Kuvayskaya, Anastasia	Colorado School of Mines	kuvayskaya@mymail.mines.edu
Law, Stephanie	University of Delaware	slaw@udel.edu
Lee, Dongkyu	University of South Carolina, Columbia	dongkyu@cec.sc.edu
Lee, Jeunghoon	Boise State University	jeunghoonlee@boisestate.edu
Li, Lan	Boise State University	lanli@boisestate.edu
Li, Lian	West Virginia University	lian.li@mail.wvu.edu
Li, Xiaoqin Elaine	University of Texas, Austin	elaineli@physics.utexas.edu
Liao, Bolin	University of California, Santa Barbara	bliao@ucsb.edu
Liu, Feng	University of Utah	fliu@eng.utah.edu
Lupton, John	University of Utah	lupton@physics.utah.edu
Magana-Loaiza, Omar	Louisiana State University	maganaloaiza@lsu.edu
Majetich, Sara	Carnegie Mellon University	sara@cmu.edu
Malko, Anton	University of Texas, Dallas	anton.malko@utdallas.edu
Mass, Olga	Boise State University	olgamass@boisestate.edu
McCluskey, Matt	Washington State University	mattmcc@wsu.edu
Menon, Vinod	The City College of New York	vmenon@ccny.cuny.edu
Mishin, Yuri	George Mason University	ymishin@gmu.edu
Mudryk, Yaroslav	Ames Laboratory	slavkomk@ameslab.gov
Neumeier, John	Montana State University	neumeier@montana.edu
Orbach, Raymond	University of Texas, Austin	orbach@utexas.edu
Padilla, Willie	Duke University	willie.padilla@duke.edu
Parazzoli, Paul	U.S. Department of Energy	paul.parazzoli@science.doe.gov
Pechan, Mick	U.S. Department of Energy	michael.pechan@science.doe.gov
Pecharsky, Vitalij	Ames Laboratory	vitkp@ameslab.gov
Pensack, Ryan	Boise State University	ryanpensack@boisestate.edu
Rand, Barry	Princeton University	brand@princeton.edu
Ren, Shenqiang	The State University of New York, Buffalo	shenren@buffalo.edu
Ruoff, Kevin	University of Pennsylvania	kruoff@sas.upenn.edu
Rustad, Jim	U.S. Department of Energy	james.rustad@science.doe.gov
Schwartz, Andrew	U.S. Department of Energy	andrew.schwartz@science.doe.gov
Scott, Mary	University of California, Berkeley	mary.scott@berkeley.edu
Sefat, Athena	U.S. Department of Energy	athena.sefat@science.doe.gov
Sellers, Ian	University of Oklahoma	sellers@ou.edu
Sennett, Michael	U.S. Department of Energy	michael.sennett@science.doe.gov
Severs, Linda	Oak Ridge Associated Universities	linda.severs@orau.org
Shi, Jing	University of California, Riverside	jing.shi@ucr.edu
Shi, Li	University of Texas, Austin	lishi@mail.utexas.edu

Siddiqi, Irfan	Lawrence Berkeley National Laboratory	iasiddiqi@lbl.gov
Sih, Vanessa	University of Michigan	vsih@umich.edu
Sinclair, Michael	Sandia National Laboratories	mbsincl@sandia.gov
Smalyukh, Ivan	University of Colorado, Boulder	ivan.smalyukh@colorado.edu
Spitzer, Christopher	Lawrence Berkeley National Laboratory	cspitzer@lbl.gov
Srikanth, Hari	University of South Florida	sharihar@usf.edu
Stadler, Shane	Louisiana State University	stadler@phys.lsu.edu
Sun, Dali	North Carolina State University	dsun4@ncsu.edu
Suzuki, Yuri	Stanford University	ysuzuki1@stanford.edu
Tamboli, Adele	National Renewable Energy Laboratory	adele.tamboli@nrel.gov
Thiyagarajan, Thiyaga	U.S. Department of Energy	p.thiyagarajan@science.doe.gov
Thompson, Jeff	Princeton University	jdthompson@princeton.edu
Tisdale, William	Massachusetts Institute of Technology	tisdale@mit.edu
Tongay, Sefaattin	Arizona State University	sefaattin.tongay@asu.edu
Türeci, Hakan	Princeton University	tureci@princeton.edu
Turner, Daniel	Boise State University	danielturner926@boisestate.edu
Van de Walle, Chris	University of California, Santa Barbara	vandewalle@mrl.ucsb.edu
Vardeny, Zeev Valy	University of Utah	valy_vardeny@yahoo.com
Virkar, Anil	University of Utah	anil.virkar@utah.edu
Waldeck, David	University of Pittsburgh	dave@pitt.edu
Wang, Jigang	Ames Laboratory	jwang@ameslab.gov
Watzman, Sarah	University of Cincinnati	watzmasj@ucmail.uc.edu
Whittaker-Brooks, Luisa	University of Utah	luisa.whittaker@utah.edu
Wu, Junqiao	University of California, Berkeley	wuj@berkeley.edu
Wu, Yiyi	The Ohio State University	wu.531@osu.edu
Yang, Min	University of Rochester	myang30@ur.rochester.edu
Yang, Peidong	University of California, Berkeley	p_yang@berkeley.edu
Yurke, Bernard	Boise State University	BernardYurke@BoiseState.edu
Zamkov, Mikhail	Bowling Green State University	zamkovm@bgsu.edu
Zevalkink, Alexandra	Michigan State University	alexzev@msu.edu
Zhang, Pengpeng	Michigan State University	zhangpe@msu.edu
Zhang, Zhuomin	Georgia Institute of Technology	zhuomin.zhang@me.gatech.edu
Zhao, Hui	University of Kansas	huizhao@ku.edu
Zhu, Jane	U.S. Department of Energy	jane.zhu@science.doe.gov